AGH University of Science and Technology

DEPARTAMENT OF POWER ELECTRONICS AND ENERGY CONTROL SYSTEMS

FACULTY OF ELECTRYCAL ENGINEERING, AUTOMATICS, COMPUTER SCIENCE AND BIOMEDICAL

Doctoral dissertation

M. Sc. Chamberlin Stéphane Azebaze Mboving

Methods for Reducing Voltage and Current Distortion Caused by Power Electronic Converters in Power Systems

Metody redukcji odkształcenia napięć i prądów powodowanych przez przekształtniki energoelektroniczne w sieciach elektroenergetycznych

Supervisor:
prof. dr hab. inż. Zbigniew Hanzelka

Co-supervisor:
dr inż. Ryszard Klempka

CRACOW 2020

Psaumes 23: Cantique de David.

1. *L'ETERNEL est mon berger: je ne manquerai de rien.*
2. *Il me fait reposer dans de verts pâturages, Il me dirige près des eaux paisibles.*
3. *Il restaure mon âme, Il me conduit dans les sentiers de la justice, A cause de son nom.*
4. *Quand je marche dans la vallée de l'ombre de la mort, Je ne crains aucun mal, car tu es avec moi: Ta houlette et ton bâton me rassurent.*
5. *Tu dresses devant moi une table, En face de mes adversaires; Tu oins d'huile ma tête, Et ma coupe déborde.*
6. *Oui, le bonheur et la grâce m'accompagneront Tous les jours de ma vie, Et j'habiterai dans la maison de l'Eternel Jusqu'à la fin de mes jours.*

Psaumes 121: Cantique des degrés.

1. *Je lève mes yeux vers les montagnes… D'où me viendra le secours?*
2. *Le secours me vient de l'Eternel, Qui a fait les cieux et la terre.*
3. *Il ne permettra point que ton pied chancelle; Celui qui te garde ne sommeillera point.*
4. *Voici, il ne sommeille ni ne dort, Celui qui garde Israël.*
5. *L'Eternel est celui qui te garde, L'Eternel est ton ombre à ta main droite.*
6. *Pendant le jour le soleil ne te frappera point, Ni la lune pendant la nuit.*
7. *L'Eternel te gardera de tout mal, Il gardera ton âme;*
8. *L'Eternel gardera ton départ et ton arrivée, Dès maintenant et à jamais.*

Składam serdeczne podziękowania

Panu profesorowi Zbigniewowi Hanzelce

za pomoc merytoryczną konieczną do powstania

niniejszej pracy

***Pragnę również podziękować* Panom**

dr inż. Ryszardowi Klempce,

dr inż. Krzysztofowi Piątkowi,

Bogusławowi Spyrce,

Markowi Hajto,

dr inż. Andrzejowi Firlitowi,

dr inż. Krzysztofowi Chmielowcowi,

***a także* innym kolegom Katedry**

Pracę tę dedykuję mojemu tacie AZEBAZE i mojej mamie DONGMO JEANNE D'ARC.

I dedicate this work to my father AZEBAZE and my mother DONGMO JEANNE D'ARC.

Je dédie ce travail à mon père AZEBAZE et à ma mère DONGMO JEANNE D'ARC.

Streszczenie

W dzisiejszych społeczeństwach rośnie bardzo szybko produkcja odbiorników nieliniowych, takich jak urządzenia gospodarstwa domowego i przemysłowe odbiorniki energii elektrycznej. Ich masowe przyłączenie do sieci zasilającej (pomimo zgodności z normami emisyjnymi EMC) może powodować pogorszenie jakości dostarczanej energii elektrycznej.

Jakość energii odnosi się głównie, do jakości napięcia zasilającego (częstotliwość, amplituda, kształt przebiegi itp.), która powinna być zgodna z zaleceniami ustalonymi przez normy. W przypadku złej jakości napięcia zasilającego w punkcie wspólnego przyłączenia (PWP) jego poprawa jest zatem koniecznością, warunki norm i obowiązujących przepisów musza być spełnione. Energia elektryczna jest towarem i dbanie o jej jakość jest niezbędne. Zaburzenia jakości dostawy energii elektrycznej są liczne i różnorodne (spadki i wzrosty napięcia, wahania, odkształcenie itp.), co oznacza, że stosuje się wiele metod, żeby redukować ich poziom w systemie elektroenergetycznym. Niniejsza praca koncentruje się na łagodzeniu zaburzeń, takich jak asymetria, harmoniczne i moc bierna podstawowej harmoniczne, stosując do tego celu filtry pasywne, aktywne i hybrydowe.

Celem pracy jest zaprojektowanie hybrydowego filtru aktywnego, który jest połączeniem filtru aktywnego z filtrem pasywnym. W celu skutecznego zaprojektowania takiego filtru, w niniejszej pracy przedstawiono szczegółową analizę (symulacja i badania laboratoryjne) różnych struktur filtrów aktywnych i pasywnych. Omówiono także inne metody stosowane do redukcji zniekształceń napięcia i prądu.

Rozpatrywane są następujące struktury filtru pasywnego: równoległy (prosty), szeregowy, podwójnie nastrojony, szerokopasmowe (pierwszego, drugiego i trzeciego rzędu oraz typu C), a także hybrydowy filtr pasywny. Każdy z nich jest indywidualnie analizowany pod kątem charakterystyki impedancji w funkcji częstotliwości oraz wpływu zjawiska odstrojenia i rezystancji tłumienia na ich efektywność. Porównano niektóre struktury filtru pasywnego (grupa dwóch filtrów prostych & filtr podwójnie nastrojony, szeregowy filtr pasywny i hybrydowy filtr pasywny), a także metody podziału całkowitej mocy biernej w grupie filtrów. Wyniki symulacyjne zostały potwierdzone badaniami w laboratorium następujących struktur filtru pasywnego: filtr prosty, grupa dwóch filtrów prostych, filtry pierwszego i drugiego rzędu.

W niniejszej pracy analizowano równoległy filtr aktywny – trójfazowy, trójprzewodowy. Celem jego stosowania jest kompensacja asymetrii i odkształcenia napięcia oraz mocy biernej podstawowej harmonicznej przy użyciu oryginalnego algorytmu sterowania - opartego na teorii *p-q* - zaproponowanego przez autora. W pracy uwzględniono badania wpływu dławików: włączonego między PWP a sieć zasilającą, wejściowego prostownika, wejściowego równoległego filtru aktywnego oraz kondensatora strony DC na efektywność działania filtru. Eksperymenty laboratoryjne równoległego filtru aktywnego - potwierdzające wyniki badań symulacyjnych - zostały przeprowadzane z wykorzystaniem struktury czteroprzewodowej z dzieloną pojemnością po stronie DC.

Po szczegółowych badaniach filtru pasywnego i aktywnego, w następnej kolejności zostały przeanalizowane struktury hybrydowe filtru aktywnego: model równoległego filtru aktywnego (trójfazowy, trzygałęziowy) połączonego szeregowo z filtrem prostym (badania symulacyjne) i model równoległego filtru aktywnego (czteroprzewodowy z dzieloną pojemnością od strony DC) połączony równolegle z grupą dwóch filtrów prostych (badania laboratoryjne). Autor zaproponował oryginalny algorytm sterowania oparty na teorii mocy *p-q* dla tej struktury.

Abstract

In today societies, the production of non-linear loads such as household appliances and industrial electricity devices is growing rapidly. Their mass connection to the supply network (despite compliance with EMC emission standards) may cause a deterioration in the quality of the supplied electricity.

The power quality refers mostly to the supply voltage quality (frequency, amplitude, waveform, etc.) which should be in accordance with the recommendations set by the standards. Therefore, in case of poor quality of the supply voltage at the point common coupling (PCC), its improvement is a necessity, the standards conditions and applicable regulations must be met. The electrical power is as a commodity and taking care of its quality is essential. The disturbances in the quality of electricity supply are numerous and varied (voltage drops and swells, flickers, deformation, etc.), which means that many methods are used to reduce their level in the electrical power system. This work focuses on mitigating disturbances such as asymmetry, harmonics and reactive power of fundamental harmonics, using methods such as passive harmonic filter (PHF), active power filter (APF) and hybrid active power filter (HAPF).

The purpose of the work is to design a HAPF, which is the combination of PHF and APF. In order to effectively design such a filter, this work presents a detailed analysis (simulation and laboratory tests) of various PHF and APF structures. Other methods used to reduce voltage and current distortion are also discussed.

The following PHF structures are considered: single-tuned filter, the series PHF, the double-tuned filter, the broad-band filters (first-order, second-order, third-order and C-type filter) and Hybrid passive harmonic filter (HPHF). Each of them is individually analyzed focusing on the impedance versus frequency characteristics and influence of detuning phenomenon and damping resistance on their efficiency. Some PHF structures (group of two single-filters & double-tune filter, series PHF & hybrid PHF) are compared as well as the methods of sharing the total reactive power in the filter group. The simulation studies are confirmed after the investigation in the laboratory of the following PHF structures: single-tune filter, group of two single-tuned filters, first and second-order filters.

In this work, the SAPF (three legs three wire) is analyzed. The goal of its design is to compensate the load fundamental harmonic reactive power, harmonics, and asymmetry using the original control algorithm - based on *p*-*q* theory - proposed by author. The studies of the influence of the line reactor: connected between the PCC and the grid, rectifier input and SAPF input as well as the SAPF DC capacitor on the filter efficiency is considered in this work. The laboratory experiments of SAPF confirming the simulation results is carried out using the four wires three legs structure.

After detailed studies of PHF and SAPF structures, the HAPF structures: model of SAPF (three legs three wires) connected in series with the single-branch filter (simulation studies) and model of SAPF (three legs four wires) connected in parallel with the group of two single-branch filters (laboratory studies) were next analyzed. The author proposed an original control algorithm based on *p*-*q* theory for this structure.

Contents

Chapter 1 .... **15**

Introduction **15**

1.1 Literature review of passive harmonic filters 18

1.2 Literature review of shunt active power filter 19

1.3 Literature review of hybrid active power filter 20

1.4 Thesis, objective and scope of work 20

1.5 PhD thesis structure 21

Chapter 2 .... **22**

Techniques to mitigate the voltage and current distortion in the electrical network **22**

2.1 Increase of PCC short-circuit power 22

2.2 Transformers 24

2.2.1 Isolation transformers 24

2.2.2 Transformer and phase-shifting techniques for AC/DC multi-pulse rectifiers 25

2.3 High harmonic filters 25

2.3.1 Passive filters 26

2.3.1.1 AC line reactor 26

2.3.1.2 Interface filters for power inverters 26

2.3.2 Active power filters 30

2.3.2.1 Series active power filter 30

2.3.2.2 Shunt active power filters 31

2.3.2.3 Hybrid active power filters 32

2.3.3 Harmonic emission reduction by non-linear load configuration 34

2.3.3.1 PFC converters 34

2.3.3.2 Multi-level inverters 35

Chapter 3 .... **36**

Passive harmonic filters **36**

3.1 Resonance phenomena in electrical circuit 36

3.2 General concept of passive harmonic filters 38

3.3 Series passive harmonic filters 39

3.4 Shunt passive harmonic Filters 43

3.4.1 Single-tuned filter 43

3.4.1.1 Influence of the single-tuned filter reactive power on its efficiency............. 44
3.4.1.2 Analysis of single-tuned filter for different tuning frequency 46
3.4.1.3 Influence of single-tuned filter resistance on its efficiency 49
3.4.2 Double-tuned filter 53
3.4.2.1 Comparison between the group of two single-tuned filters and the double-tuned filter 55
3.4.3 BROAD-BAND FILTERS 58
3.4.3.1 1st order filter.. 58
3.4.3.2 2nd order filter... 67
3.4.3.3 3rd order filter 72
3.4.3.4 C-type filter 78
3.4.3.4.1 Detuning of C-type filter 85
3.5 Conclusion.. 97
3.6 Hybrid passive harmonic filter (HPHF) 99
3.7 Methods of sharing the total reactive power in the PHF groupη 101
3.7.1 Design methods description 102
3.7.2 Comparison of the methods 108
Chapter 4.. 117
Passive harmonic filters laboratory investigation 117
4.1 Laboratory model description 117
4.1.1 Load description.. 120
4.1.2 Electrical grid description 121
4.2 Load parameters analysis when connected to the PCC.............................. 122
4.3 Design of single-tuned filters 126
4.3.1 Single-tuned filter parameters computation 126
4.3.2 Verification of PHFs reactors and capacitors parameters in the laboratory. 127
4.3.3 Laboratory results of the 5th harmonic single-tuned filter........................... 130
4.3.3.1 Experiments with the programmable AC voltage source (Chroma)............ 133
4.3.3.2 Increase of electrical grid inductance 136
4.3.3.3 Analysis of the 5th harmonic single-tuned filter efficiency after electrical grid inductance increase 139
4.3.3.4 Detuning of 5th harmonic single-tuned filter 143
4.3.3.5 Experiments with the programmable AC voltage source (Chroma)............ 147
4.3.3.6 Investigation of the 7th order harmonic passive filter................................. 151
4.4 Group of single-tuned filters 153
4.5 Capacitor bank 156

4.6 Design of the 2nd order filter 159
Chapter 5 165
Shunt active power filter 165
5.1 Instantaneous *p-q* theory 165
5.1.1 Example of *p-q* theory application 168
5.1.1.1 Application of *p-q* theory under symmetrical but distorted supply voltage. 169
5.1.1.2 Application of *p-q* theory after supply voltage filtration 171
5.2 Investigation of three wires three legs SAPF in MATLAB SIMULINK 173
5.2.1 Simulation studies of three wires three legs SAPF 174
5.2.1.1 Influence of the inverter input reactor on the SAPF performances 176
5.2.1.2 Influence of the thyristor bridge input reactor on the SAPF performances . 180
5.2.1.3 Influence of invert DC capacitor parameters on the SAPF performances ... 184
5.3 Laboratory experiments on the three legs four wires shunt active power filter (model of Figure 2.11(b)) 189
5.3.1 Studies of thyristor bridge input reactor influence on the SAPF performance 190
5.3.2 Studies of the grid side line reactor influence on the SAPF performances.. 192
5.4 Laboratory experiments on the hybrid active power filter: model of Figure 2.13(l) 194
5.4.1 The first laboratory experiment 195
5.4.2 The second laboratory experiment 197
Chapter 6 199
Hybrid active power filter (topology nº2) 199
6.1 Functionality principle of HAPF2 199
6.1.1 Description of HAPF2 control system 201
6.2 HAPF2 Simulation studies 201
6.2.1 Simulation assumption and parameters computation 202
6.2.2 Simulation results 202
Chapter 7 210
Conclusion 210
7.1 Simulation study results 210
7.2 Laboratory study results 212
7.3 Further work direction 212
References 213
Annex I. Electrical grid model design in MATLAB/SIMULINK 227
Annex II. Model of the electrical grid with the load (MATLAB/SIMULINK) 228

Annex III. Data from chapter 3 ... 233
III.1 Series passive harmonic filters ... 233
III.2 Shunt Passive Filter ... 234
III.2.1 Single-tuned filter ... 234
III.2.1.1 Analysis of single-tuned filter for different tuning frequencies ... 234
III.2.1.2 Optimization technique in MATLAB (method f) ... 235
Annex IV. Technical data of the PHFs laboratory components (chapter 4) ... 236
IV.1 Load data ... 236
IV.2 Electrical grid parameters ... 238
IV.3 PHF reactors and capacitors technical data ... 240
IV.4 Connection of the capacitors bank to the PCC ... 244
Annex V. Presentation of the simulated power system with SAPF ... 245
V.1 Description of shunt active power filter (SAPF) simulated blocks ... 245
V.2 Proposed expressions to compute the three-wire three legs SAPF input reactor and DC side capacitor parameters ... 251
V.2.1 SAPF DC capacitor parameters computation ... 252
V.2.1.1 Proposed expressions to compute the inverter DC capacitor parameters ... 253
V.2.2 Computation of SAPF input reactor inductance ... 254
V.2.2.1 Proposed expression for SAPF input reactor inductance ... 255

Abbreviations and designations

Symbols

a-b-c	- three phase system coordinates
C	- Capacitance
D	- delta connection
f	- frequency
h	- number of filter in the filter group
I	- current RMS
i	- instantaneous current
K	- filter effectiveness
k	- coefficient
ℓ	- length of transmission line
L	- inductance
L	- line
L1,2,3	- phases of supply system
m, n	- harmonic order
P	- active power (fundamental harmonic)
p - q	- instantaneous real and imaginary powers in α-β coordinates
$\tilde{p}$, $\tilde{q}$	- variable components of instantaneous real and imaginary powers
$\bar{p}$, $\bar{q}$	- constant components of instantaneous real and imaginary powers
Q	- reactive power
q', q''	- quality factor of reactor and single-tuned filter respectively
R	- resistance
RMS	- root mean square
r	- resistance at the DC side of single-phase diode rectifier
S	- apparent power
Te	- electrical torque
U	- voltage RMS
u	- instantaneous voltage
W	- energy
wye	- star connection (also Y)
X	- reactance
x	- cross-section area of supply transmission line
Y, $\underline{Y}$	- admittance (module and complex form)
Z, $\underline{Z}$	- impedance (module and complex form)

Greek literary alphabet

α, β, 0	- rectangular coordinate system axis
ε	- Inverter DC voltage change ratio
η	- order number carried by one filter in the filter group
γ	- conductivity
Φ	- phase shift between voltage and current (fundamental harmonic)
θ	- thyristor bridge firing angle
ϑ	- transformer ratio

φ	- optimization function coefficient
ω	- angular frequency

Indexes

Al	- aluminium
Cu	- copper
F	- filter group
Fe	- iron
I	- current
i	- integral
MV	- medium voltage
N	- nominal value
p	- proportional
p-p	- peak to peak
r, T	- rectifier input
Sec	- secondary side of transformer
SC	- short-circuit
S	- electrical grid
U	- voltage
(1), (*n*)	- fundamental and other harmonic component order
(+), (-)	- positive and negative sequence

Abbreviations

AC	- alternative current
asym	- asymmetry
BPF	- band-pass filter
CSI	- current source inverter
*D*1-4	- diode
deg	- degree
DC	- direct current
DPF	- displacement power factor
DFT	- Discrete Fourier Transform
f	- filter
FFT	- fast Fourier Transform
g	- ground
HV	- high voltage
HPF	- high-pass filter
IGBT	- insulated gate bipolar transistor
h	- harmonic
Im	- imaginary
Inf	- infinity
In	- input
inv	- inverter
LV	- low voltage
LPF	- low-pass filter
MV	- medium voltage
max	- maximum
min	- minimum
Out	- output
PCC	- point of common coupling
PF	- power factor

PLL	- phase locked loop
Pri	- primary side of transformer
PWM	- pulse width modulation
re	- resonance
ref	- reference
rms, RMS	- root mean square
rvpmin	- revolution per minute
s	- second
SAPF	- shunt active power filter
SC	- short-circuit
*T*1-4	- Thyristor
THD	- total harmonic distortion
TTHD	- true total harmonic distortion
Tr	- transformer
VSI	- voltage source inverter

Chapter 1
Introduction

In recent years, the production of household appliances and industrial devices using power electronic components is in full growth. Due to the massive connection of such non-linear devices to the supply network (despite their standard accordance), the supplied power quality is in degradation mode.

The power quality refers mostly to the supply voltage quality (frequency, amplitude, waveform, phase shift between phase to phase or phase to ground voltage etc.) which should follow the recommendations fixed by standards (e.g. EN, IEC, IEEE etc.) in accordance to the country or continent. The standards concerning the power quality characteristics, measurements and monitoring are for instance EN 50160 [80], IEC 61000-4-30 [115] and IEEE standard 1159 [120] respectively.

The standard EN 50160 (for European countries) defines the voltage characteristics of the distribution systems (voltage dip and swell, harmonics, voltage interruption, transients, rapid voltage change, asymmetry, voltage fluctuation, etc.). The standard IEC 61000-4-30 focused on the power quality measurement techniques. The IEEE standard 1159 is for monitoring the electric power quality [115, 120].

If the supply voltage at the point of common coupling (PCC) of building or town, presents poor quality (harmonics, asymmetry, flickers etc.), its improvement is therefore necessary to comply the standards. The poor power quality does not come from the energy producer (because the voltage at the power plant production source is almost pure sinusoidal), but from the disturbing devices (used in the industries (e.g. converter drive systems etc.), houses (e.g. computers, printers, microwave kitchens, energy-efficient LED lighting etc.) etc.) connected to the power system, which despite their compliance to the emission standards, disturb the supplied power quality because of their huge number. In the further part of this thesis, the author will focus on the power quality disturbances such as harmonics; asymmetry and reactive power(1) flow because they are mainly caused by the power electronic devices.

The harmonic sources in power system can be organized in three important groups such as presented in [100]: saturated core devices (e.g. transformers (Figure 1.1), motors, generators

(1) The applied term "reactive power" used in this work refers to the reactive power in the fundamental harmonic domain.

etc.); arc devices (e.g. arc furnaces devices, welding devices, gas-discharge lamp etc.) and electronic or power electronic devices (Figure 1.2).

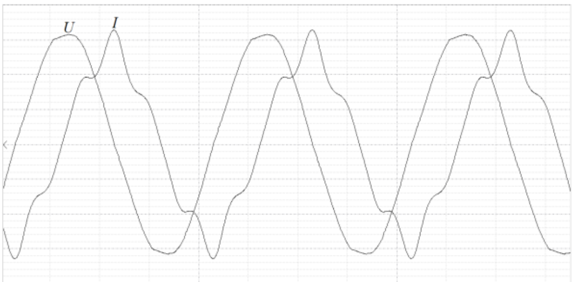

Figure 1.1 Example of the magnetizing current (with voltage) measured at the unloaded transformer primary side

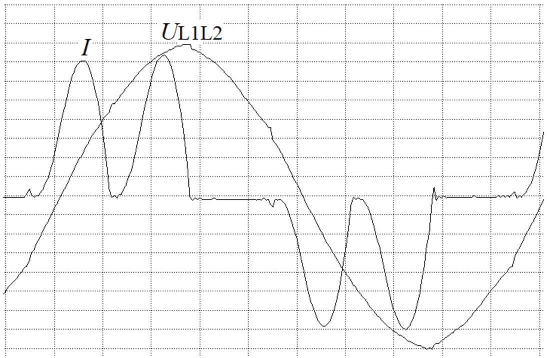

Figure 1.2 Example of distorted current and phase to phase voltage waveforms measured at the AC side of rectifier with capacitor at the DC side

The today non-linear loads are in the most of the cases devices equipped with power electronic components such as diodes, transistors and thyristors and which cause non-sinusoidal current flow (Figure 1.2) despite the fact that they are connected to an almost pure sinusoidal source voltage. The non-sinusoidal current contains harmonics and inter-harmonics that flowing to the supply network, interact with the supply network impedance, disturbing the supply voltage by causing distortions (Figure 1.2).

In the periodic non-sinusoidal current or voltage waveform, the components with frequency other than the fundamental frequency (50 Hz) and which are integral multiple of the fundamental frequency are call harmonics (e.g. 150Hz) [97, 100, 121]. The inter-harmonics are components, which are not integral multiple of the fundamental frequency (e.g. 55Hz) [119, 235].

In practical consideration, the harmonics can be neglected when their percentage in power system is very small compared to the fundamental (e.g. less than 1%). Figure 1.3 presents an example of 5^{th} and 7^{th} harmonic current and voltage characteristics registered during 7 hours at the point where the three-phase diode bridge were connected in an industry. Observing Figure 1.3(a), it can be seen that the 5^{th} harmonic current amplitude can reach up to 70% of the fundamental harmonic.

The harmonics presence in electrical network is accompanied by consequences such as: the increase of current RMS; the overloading, overheating and even damage of power system elements (e.g. transformers, generators, cables, electric motors, capacitors etc.) and other devices; the reduction of devices life span; the perturbation of the devices normal operation and power system operating costs increase; the inaccurate measurements of energy and power; decrease of power factor (PF) etc. [105, 106, 151, 171, 228, 237, 252].

The quoted harmonic source groups are not only responsible for the harmonics generation, but also for other power quality disturbances such as flicker effects, asymmetry (Figure 1.4) etc.

For a deformed current waveform signal (e.g. Figure 1.2), there are different methods used to separate the fundamental harmonic frequency component from the other frequencies. These methods are also call in literature methods for harmonics detection [15, 23, 119, 164, 176]. They are organized in frequency domain (e.g. Discrete Fourier Transformer (DFT) [4, 165]; Fast Fourier Transformer (FFT) [91, 166]; Recursive Discrete Fourier Transformer (RDFT) [216, 263] etc.) and in time domain (Synchronous fundamental *dq*-frame [65, 164]; synchronous individual harmonic *dq*-frame [46 ,164]; instantaneous power *pq*-theory [7, 8]; generalized integrator [262] etc.) and there are many others methods [53].

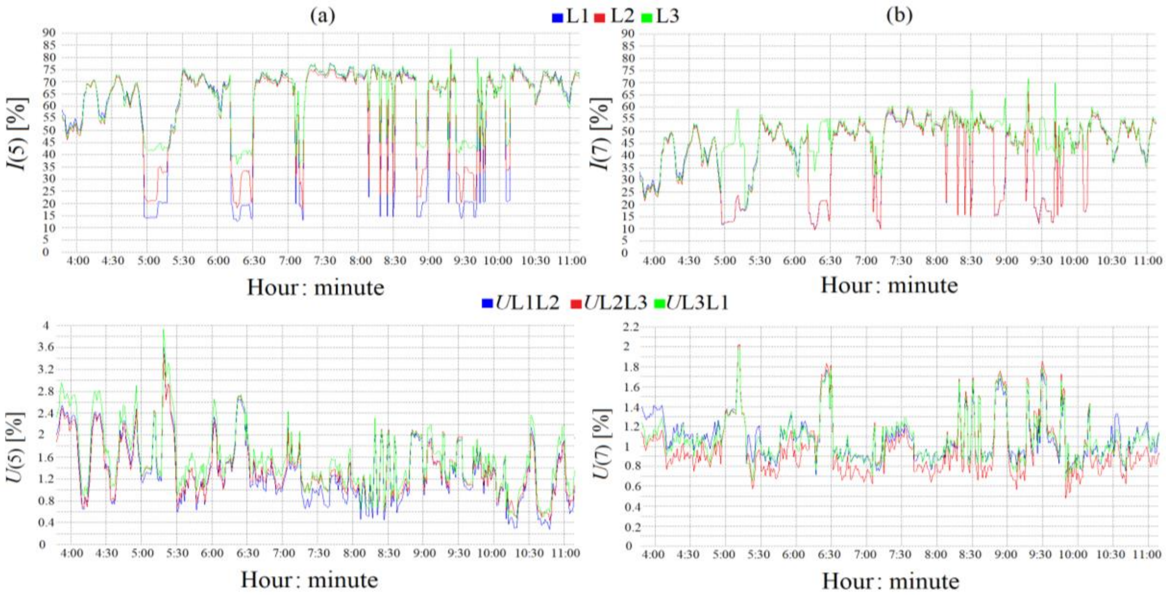

Figure 1.3 Example of 5th (a) and 7th (b) harmonic current and voltage (phase to phase) registered in the industry (during 7 hours) at the point of three phase diode rectifiers connection

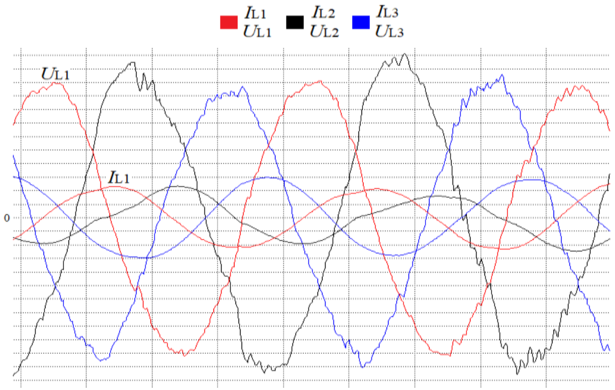

Figure 1.4 Unbalance voltage and current at the terminals of arc-furnaces

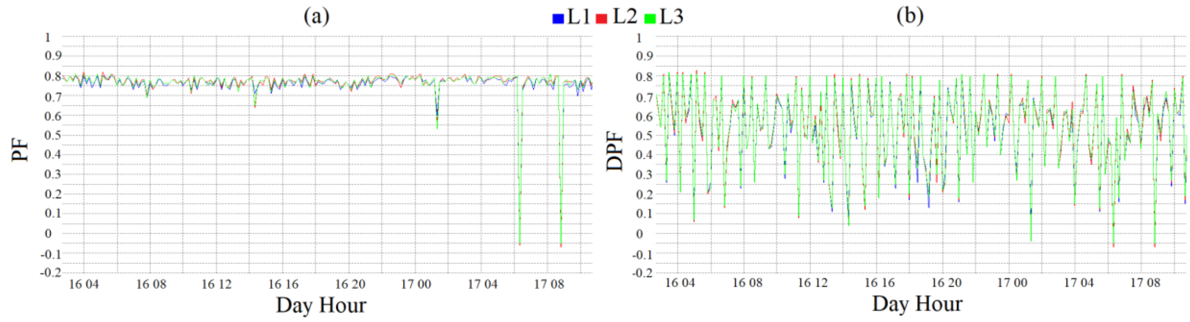

Figure 1.5 Example of: (a) power factor (PF) and (b) displacement power factor (DPF) measured in the industry at the arc-furnaces terminals

An example of voltage and current waveforms (in unbalance mode) registered in the industry equipped of arc-furnace device is shown in Figure 1.4. The amplitude of three-phase voltage is unequal as well as the amplitude of current. In each phase, the phase displacement between voltage and current can be observed. Figure 1.5 presents the power factor (PF) and displacement power factor (DPF) characteristics for the distorted and unbalance voltage and current of Figure 1.4.

The electrical power is as a commodity and taking care of its quality is essential. This is why it exist many standards for its regulation. To make the disturbing devices comply standards, there are several methods (see chapter 2 to 6).

The author will focus on the hybrid active power filter (HAPF) which is the combination of active power filter (APF) and passive harmonic filter (PHF) as presented in Figure 1.6.

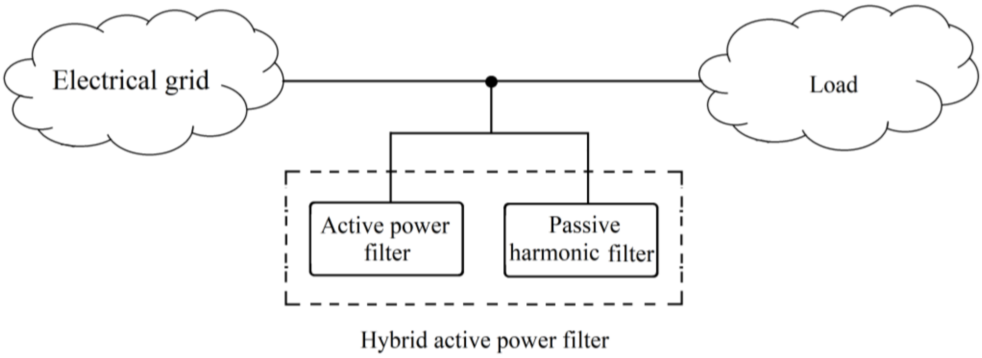

Figure 1.6 Example of hybrid active power filter configuration

1.1 Literature review of passive harmonic filters

The PHFs are the most common techniques applied in electrical network system to compensate the displacement power factor (DPF) and mitigate the harmonics [24, 102]. According to [224, 246] their first installation in the industries started in 1940. They are organized in different structures described in the literature [24, 47, 127, 271]: the single-tuned filter [62, 189, 218, 270], double-tuned filter [94, 184, 185, 186, 266, 272, 260], triple-tuned filter [41, 59], series passive filter [47, 48], hybrid passive filter [47, 48], damped filters (first, second, third-order filter and C-type filter) [24, 47], filter group [135, 141, 143] etc. The difference between filters is not only on their structure but also on their harmonics filtration efficiency(2), immunity on detuning phenomena due for intense to the capacitor or reactor aging, the power losses, harmonic filtering band, design method etc. Each of the highlighted features has influence on filter designing and its exploitation cost. Therefore, it is important to know the advantages and disadvantages of each topology while deciding on its choice and also in optimal decision-making in terms of technical and economical point of view.

The design of PHFs has not always been a small task since it took into account many parameters such as: the grid impedance (short circuit power) and voltage spectrum at point where the filter will be connected; the load fundamental harmonic reactive power and current spectrum; the filter power losses and investment cost etc. In certain PHF design procedure [2, 110, 136, 217], the optimization technique is introduced to select the optimal filter parameters basing on the constituted optimization function and conditions. Nowadays, the optimization techniques applied in PHF design procedure are very widespread in the literature. Some of them are: genetic algorithms [21, 146, 277], respond surface methodology [190, 218], swarm optimization [215], Particle Swarm Optimization (PSO) [161], bee colony optimization [208], Mixed Integer Distributed Ant Colony Optimization (MIDACO) [193], probabilistic approach [137], Multi-island Particle Swarm optimization (MIPSO) [225], Ant Colony Optimization (ACO) [255], Simulation annealing [192], optimal Multiobjective planning [267], Lagrange interpolation method [229] etc. The defined objective function can be based on maximization or minimization of some parameters in the power system such as for instance the gird current RMS (e.g. [192]) and power losses, the grid voltage and current THD and filter size (e.g. [208]), the gird specific voltage harmonic, the DPF or PF at the PCC (e.g. [193]), filter power losses and cost (e.g. [137]) etc. These techniques can be accompanied by constraints (e.g. maximum voltage capacitor and reactive power etc.).

The PHFs are mostly designed to be tuned only on one frequency (except the double and triple tuned filters) but depending on their structure and parameters, they can also mitigate

(2) The term harmonics filtration efficiency is clarified in chapter 3

harmonics in wide band. Therefore, to prevent more than one harmonic to inter the electrical grid (from the load side) the group of shunt PHFs is needed. The problem with the filter group design is based on the sharing of load reactive power (total reactive power to be compensated) to the individual filter in the group.

Because of the diversity of the shunt PHF topologies, the filter type and number in the group should be well chosen. In reference [13] the filter topology selection issue is investigated and an algorithm of filter selection is proposed. The maximum of three filters in the group is the most common situation in practice [13, 207].

The passive power filters present also certain disadvantages [72, 75, 90, 154] such as sensibility to load variation (e.g. designed for a selected load), grid parameters dependency, resonance (series and parallel) problem, can only reduce selected harmonic frequency or defined range frequencies, influence of the filter parameters tolerance on the tuning frequency, detuning phenomenon, the choice of the damping resistance etc. [47, 270]. Despite their drawbacks, the passive harmonic filters are still applied in practice [270] and from the economical point of view; they are more preferred than the active filter.

The PHF detuning phenomenon is characterized by the increase or decrease of the tuning frequency. This phenomenon can be cause by the variation of the PHF parameters over the time or the voltage fundamental harmonic frequency change at the point of PHF connection. The variation of the filter parameters (increase or decrease of the inductance or capacitance value) can be caused by their aging (mostly the capacitor), the atmospheric conditions (temperature, humidity etc.) or their damage. The filter inductance value decrease can takes place in the event of an inter-turn short circuit in the reactor (this condition leads to the reactor damage). The change in capacitor capacitance is mainly caused by the work temperature increase. The capacitors aging reduces their capacitance over the time [72, 178, 232, 270]. It is very important to take it into account the detuning phenomenon while designing the PHFs. In practice, it is advised to tune the PHF to the resonance frequency a bit lower than the frequency of the harmonic to be mitigated in the power system, but how lower should be that resonance frequency is controversial in the literature.

Compared to the shunt active power filters, they are low cost, simple in the structure, easy to maintain, high efficient in term of individual harmonic reduction, high power application. They can be applied in low voltage (LV) e.g. [82], medium voltage (MV) e.g. [73] and high voltage (HV) system e.g. [215]).

1.2 Literature review of shunt active power filter

The shunt active power filter (SAPF) is a power quality mitigation disturbances device applied for harmonics, reactive power, current asymmetry compensation [22, 47, 108, 169]. Its application in power electrical network dates from the years of 1971 [51, 89, 220]. It is more efficient in term of harmonic mitigation than the PHFs.

The structures of SAPF can be classified basing on: the type of electrical grid system (e.g. single-phase, three-phase three-wire SAPF and three-phase four-wire SAPF) [251], the type of energy storage at the their DC side (voltage source inverter (VSI) and current source inverter (CSI)) [35, 251], the structure of control system (closed or open loop) [83], the advanced inverters topologies (e.g. multi-level inverters etc.) [130, 251] and on the reference current generation algorithm (e.g. frequency domain algorithm, time domain algorithm etc.) [251, 274]. Additional information about the SAPF structures can be found in chapter 2.

The elements composing the SAPF can be organized in four parts: the input passive filter at the AC side (see chapter 2), the power electronic components constituted of semi-conductor such as transistors (IGBT-Diode, MOSFET [281, 282]. etc.), the control system (see chapter 5) and the DC storage unit.

The SAPF input passive filter is organized in different model and the simplest model is the first-order *L*-filter [139]. In the literature, it can be found many proposed expressions on how to compute the *L*-filter parameters [45, 75, 153, 204]. In the power system with for instance thyristor or diode rectifier load, the rate of current change at the commutation notches points is very high (see the current waveform example of Figure 1.2) and the connection of SAPF with not appropriate *L*-filter size in such of system can present the problem of handling the ripples at the commutation notches points [90]. This problem is not so often mentioned in the literature.

The IGBT-Diode and MOSFET are in the most cases the power electronic switching elements, which constitute the APFs. Because of its high voltage application, the IGBT transistor is the most used [281, 282].

Many types of SAPF control systems are proposed in the literature and most of them are constituted of the reference current extraction algorithm system based on the power theory. The control system algorithm can be developed in time (e.g. *p-q* theory, synchronous d-q frame method etc. [3, 7, 8, 9, 10, 11, 75, 140, 160]) or in frequency domain (e.g. sliding DFT, discrete Fourier transform theory, etc. [47, 230]). Another important part of the SAPF control system is the system (e.g. pulls width modulation (PWM) or hysteresis) which used the reference current to produce pulses to switch on and off the transistors.

1.3 Literature review of hybrid active power filter

The hybrid active power filter (HAPF) topologies are diversified in the literature [227]. They result from the combination of the shunt or series APF with parallel PHF or shunt APF with series APF together (see chapter 2 for more information). Their apparition in the scientific works dates from 1980s [174, 53].

The main advantages of their application in practice (industries) are that: (a) the power demand and performance cost of active part is less than when it is operating alone due to the presence of passive part, (b) the overcoming of passive part disadvantages (resonance phenomena, grid impedance dependency etc.) etc. [47, 93, 113].

Concerning the HAPF topologies in which the PHF (e.g. single-tuned filter) is connected in series with the SAPF, there is little information about the PHF tuning frequency choice.

1.4 Thesis, objective and scope of work

The growing number and unit power of non-linear load and electrical energy sources force the development and use of different technical solutions intended to reduce current and voltage distortion. Except for the passive methods, the active filtration and reactive power compensation systems are gaining more and more popularity. In their case, one of the highlighted disadvantages stills high price, especially in the systems with high power intended for use in medium or high voltage networks. However, it is possible to use the advantages of both solutions - passive and active. Such of systems are hybrid structures allowing to obtain the desired filtration effect and compensation of reactive power at moderate costs.

To build an effective hybrid filtration system, thorough knowledge of the *LC* filters frequency characteristics as well as active filters control algorithms are needed. The aim of the work was to acquire and present such knowledge by analyzing a very large number of different cases. Thanks to this, it was possible to formulate generalizing conclusions as a set of rules useful in the practice of designing such systems. Demonstrating that having such knowledge gives the opportunity to use the advantages of both components - passive and active, and allows to avoid the design errors is the main thesis that the author tried to prove in this work

The performance of passive harmonic filtration and reactive power compensation systems was analyzed in great detail. The sensitivity of the effectiveness of their work in response to the change in the value of their elements was examined as well as the impact of the power supply network and the parameters of the filtered/compensated load were analyzed. Theoretical and simulation considerations were confirmed by laboratory tests.

In the next parts of the work, the designed model of the active power filter electronic converter and its control system were checked in simulation tests. As in the case of passive filters, the impact of various factors on the active filter work efficiency was analyzed. The selected aspects of theoretical considerations were supplemented by studies on the physical model in the laboratory conditions.

In the final part of the thesis, the passive and active systems were combined into a very rarely considered hybrid structure and the advantages of such of solution were confirmed by simulation.

1.5 PhD thesis structure

This doctoral dissertation is organized into 7 chapters. The chapter 2 presents the area of PhD research concerning the techniques used to mitigate the voltage and current distortion in electrical network together with examples.

The chapter 3 presents the analysis of the most common PHF structures (single-tuned filter, double-tuned filter, hybrid passive filter, broad-band filters (first, second and third-order as well as C-type filter)). They are presented: the influence of the filter detuning phenomenon and damping resistance on the filters efficiency, a comparison study between the PHF selected topologies as well as between the methods of sharing the total reactive power in the PHF group.

The chapter 4 is about the laboratory investigation of the PHF chosen structures (single-tuned filters, group of single-tuned filter, first-order filter (capacitor bank) and 2nd order filter). The laboratory load and electrical grid are described, an electronic board (analogue PI controller) to externally control the thyristor rectifier pulse generator is proposed (system dynamicity verification when the SAPF or HAPF will be connected). The influence of the electrical grid parameters (impedance and voltage harmonics) as well as the filter parameters tolerances on the single-tuned filter efficiency is presented. The detuning of single-tuned filter is also presented.

In chapter 5, the SAPF is investigated (simulation and laboratory experiments). The instantaneous *p-q* theory is presented in detail and the three wires three legs SAPF control system with algorithm based on the *p-q* theory is proposed by the author. The studies of the influence of the electrical grid inductance, the inverter input reactor and DC capacitor parameters and the load input reactor parameters on the SAPF filtration efficiency are presented (simulation). The laboratory experiments presenting the influence of the thyristor bridge input reactor size and the electrical grid side line reactor size on the four wires three legs SAPF is considered. The laboratory experiment on a HAPF topology (four wires three legs SAPF connected in parallel with the group of PHF) is considered as well. It presents how much the SAPF power can be reduced when it is combined with the group of PHF.

The chapter 6 is focused on the HAPF (topology of three wires three legs SAPF connected in series with the single-tuned filter), presenting its functionality principle, control system (proposed by the author) as well as the studies based on the tuning frequency of its PHF.

Chapter 7 contains the conclusion from the work carried out and the direction of further works (laboratory realization of the HAPF model described in chapter 6).

Chapter 2

Techniques to mitigate the voltage and current distortion in the electrical network

The voltage and current distortion in the electrical power system can be mitigated by applying different filtration technics [24, 50, 71, 96, 114, 221]. Each of these techniques (Figure 2.1) is described in power quality literature and their application or choice is largely related with the power system parameters such as voltage level, short-circuit power, types of loads connected and so on [103, 187]. A brief overview of the most applied solutions in term of voltage and current harmonics mitigation in the electrical network is presented in this chapter.

2.1 Increase of PCC short-circuit power

The PCC voltage distortion depends upon the electrical grid (impedance). The more rigid (small impedance) is the electrical network, the less distorted is the PCC voltage [253]. The PCC short-circuit equivalent impedance is computed by considering the power system components such as transformers and lines resistance and inductance. An example of PCC short-circuit power calculation is described in Annex I (this example is considered in simulation part (chapter 3)).

According to [243], the transformer and line equivalent impedance should be chosen as low as possible for the PCC voltage quality improvement. Therefore, the reduction of line size (length and cross section) and transformer parameters (e.g. power increase or short-circuit voltage decrease), the electrical network reconfiguration, the AC line reactors elimination and the application of lines or transformers working in parallel are the possibilities (among others) of electrical grid short-circuit power increase (impedance reduction) [101].

On the other hand, in the electrical network the increase of short-circuit power can be a problem for the connected loads. The grid impedance plays an important role during the fault and load protection [196].

The simulation example of Figure 2.2 presents the grid current and voltage waveforms after increasing the grid equivalent inductance (from 681.18 μH to 10000 μH (Figure 2.2 (a))) and resistance (from 0.425 Ω to 3.4 Ω (Figure 2.2 (b)). In the both cases, the AC line reactor is considered (L) as the input reactor for three-phase six pulses thyristor bridge. The increase of

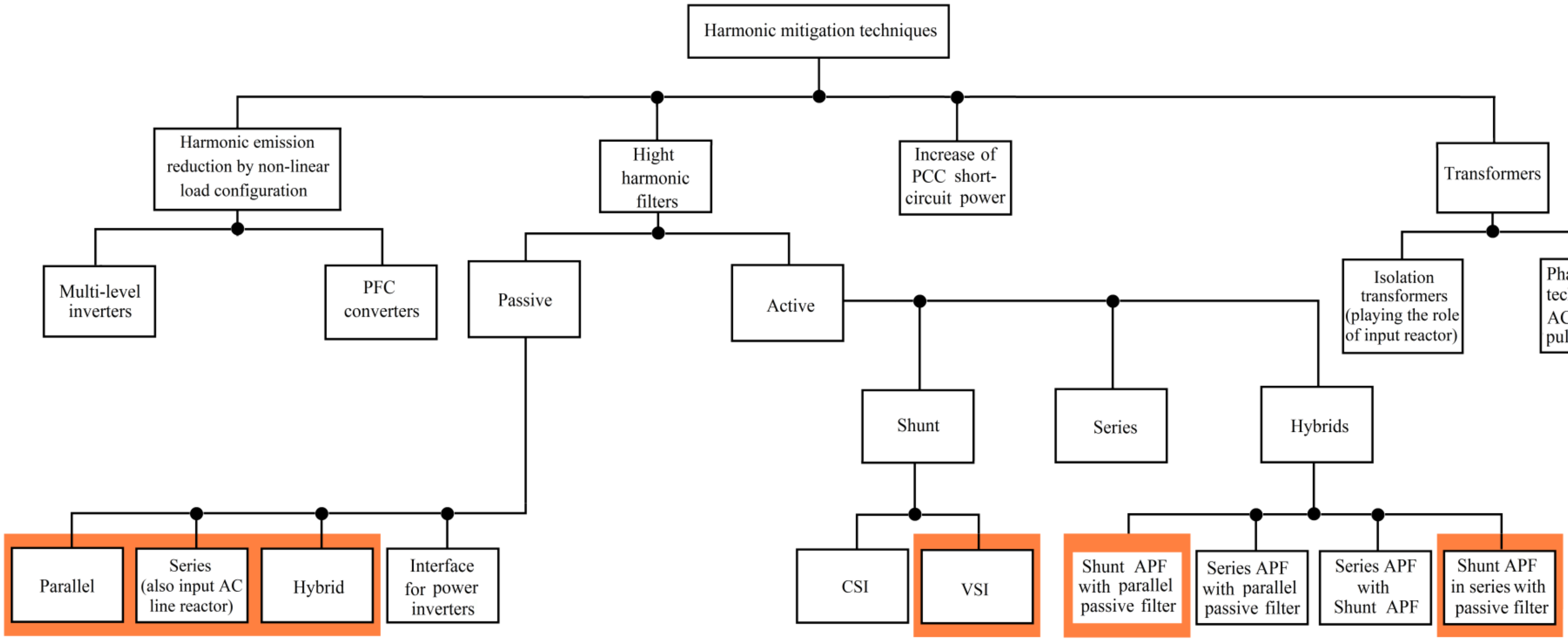

Figure 2.1 Classification of the harmonic mitigation methods in electrical network
(The distinctions in brown colour are explained in detail in the further part of the work)

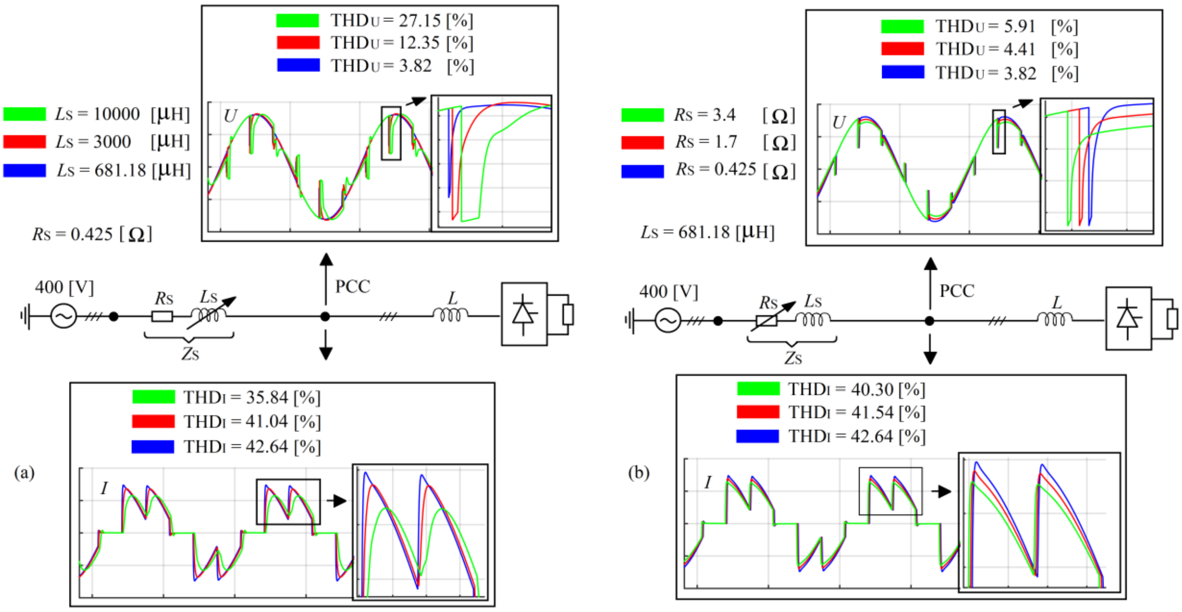

Figure 2.2 Influence of the grid parameters increase on the PCC current and voltage THD level: (a) increased of grid equivalent inductance (L_S), (b) increased of grid equivalent resistance (R_S) (for more detail information see Annex I)

the grid equivalent inductance (L_S) has more influence on the grid voltage and current harmonics variation than the increase of grid resistance (R_S). The PCC voltage presents better quality for a small value of grid equivalent inductance and resistance (L_S = 681.18 µH, R_S = 0.425 Ω, THD_U = 3.82 %). The smaller is the grid equivalent impedance, the less distorted is the grid voltage and the more distorted is the grid current (L_S = 681.18 µH, R_S = 0.425 Ω, THD_I = 42.64 %).

2.2 Transformers

On the one hand, the transformer can be a current harmonic source (distorted magnetizing current (see Figure 1.1) if its working point is located in its saturation area (non-linear part of transformer magnetization characteristic). This situation occurs if the transformer is working with the voltage higher than its nominal voltage [100]. On the other hand, they can be used for harmonics mitigation in power system (by playing the role of input reactor or using phase shifting technique with multi-pulse rectifiers [71, 211, 261]).

2.2.1 Isolation transformers

If the isolation transformers are sized properly, they can achieve the same level of harmonic reduction as the AC line reactor [221]. The higher is their equivalent reactance, the lower are distortions in the primary side voltage (assuming the nonlinear-loads connected to the secondary transformer windings). The isolation transformer typical structure used in power system for harmonics mitigation is in Delta (primary)/Wey (secondary) connection [100, 221]. It guarantees a low impedance of the delta connected windings for the triple-order harmonics and as result, the voltage waveform on the primary side does not undergo the deformation of these harmonics (Assuming the phase currents to be symmetrical). Another structure of insolation transformer is the Delta/Zigzag (it has low impedance for the zero sequence component and works in the same way like the Delta/Wye structure) [96, 105, 124].

2.2.2 Transformer and phase-shifting techniques for AC/DC multi-pulse rectifiers

Transformers with different windings coupling structures are widely used with multi-pulse power electronics devices (e.g. diode and thyrystor rectifiers) for harmonic components mitigation in the electrical network. The structures of transformer windings coupling for harmonic cancelation are based on phase-shifting techniques. The multi-pulse converters are organized in different topologies e.g. 6, 12, 18 pulses etc. [49, 50, 96, 131, 211].

For instance in the case of 12 pulse-rectifier (Figure 2.3), two three-phase 6 pulses rectifiers are connected to two transformers (it can also be a single transformer with two separated winding at the secondary side), one with delta (primary)/delta (secondary) connection and the other with delta (primary)/star (secondary) connection [96, 104, 113]. A phase-shift of 30° between the two transformers secondary side voltages is required for the 5th, 7th, 17th, 19th, 29th, 31st etc. harmonics generated by individual rectifier to cancel each other (the remain harmonics are expressed by: n = 12k±1, where k is natural number) [77,103]. If the DC side loads of rectifiers are different or if the system voltages are unbalance, the harmonics cancelation will be partial [96]. In the case of 18 pulse-rectifier, the phase-shifting of 20° is required to cancel the 5th, 7th, 11th, 13th etc. harmonics (the remain harmonics are expressed by: n = 18k±1) and for the 24 pulse-rectifier, the phase-shifting of 15° cancels the 5th, 7th, 11th, 13th, 17th, 19th etc. harmonics (the remain harmonics are expressed by: n = 24k±1) [113, 221]. With the growing of rectifier pulses (associate with transformer phase-shifting technique), the current distortion is more reduced [131].

Figure 2.3(a) shows a simulation example of 12 pulse-rectifier connected to the PCC through the transformers (Tr1 and Tr2) using phase-shifted technique. The grid current waveform with their spectrums are presented in Figure 2.3(b) and (c) and the rectifiers input currents (Figure 2.3(d)) with their spectrum in Figure 2.3(e) and (f). The PCC current presents a spectrum (Figure 2.3(c)) without the 5th, 7th, 17th, 19th, 29th, 31st etc. harmonics and its waveform is less distorted (Figure 2.3(b)). In Figure 2.3(d), the phase-shift between rectifiers input currents (I_1, I_2) can be seen.

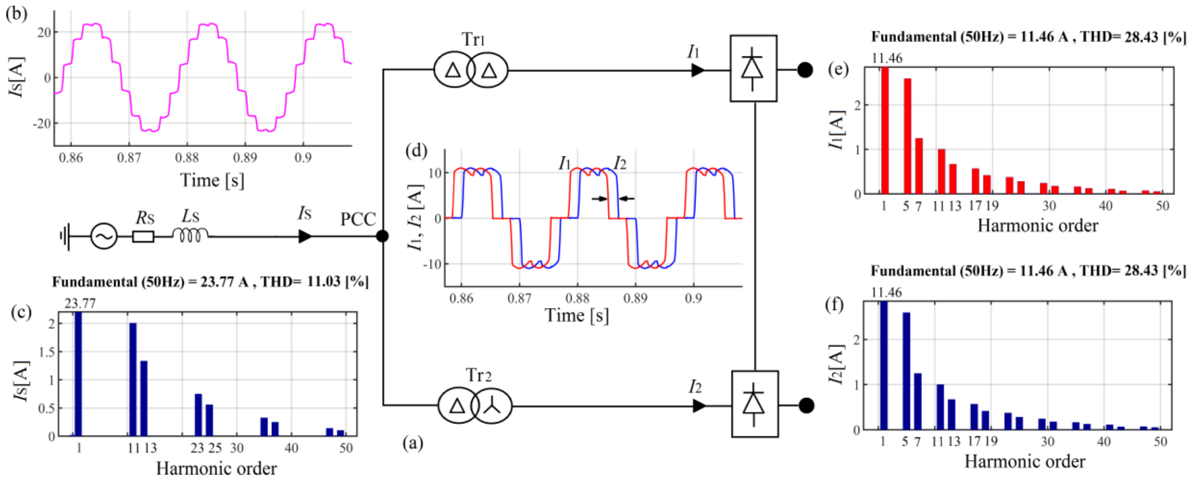

Figure 2.3 (a) electrical circuit of 12 pulse-rectifier connected to the PCC through transformers with different secondary side winding connection; (b) PCC current with its spectrum (c); (d) current waveforms (I_1 and I_2) at the input of rectifiers with respectively their spectrum (e) and (f)

2.3 High harmonic filters

The high harmonic filters can be divided into two main categories as presented in Figure 2.1 (passive and active). Both are used to reduce harmonics in wide range depending on the design technique.

2.3.1 Passive filters

The passive filters are electrical devices designed with passive elements such as resistance, capacitor and reactor. Combining different passive elements and basing on where they are connected, several passive filter structures can be set up for power quality improvement. They are widely used in practice despite their drawbacks (e.g. resonance, large size in comparison to the size of active filter, sensitive to the change of short-circuit power etc.). Some of the structures of passive filter applied as interface for power inverters are described later in the following chapter. The analyses of other passive filter topologies (such as the parallel, series and hybrid (Figure 2.1-brown colour)) are presented in chapter 3.

2.3.1.1 AC line reactor

The AC reactor (L) is connected between the PCC and the thyristor rectifier input (Figure 2.4 (a)). It is one of the easier and economical way to reduce grid voltage and current harmonics generated by power electronic devices. It is also very often used at the AC side of diode and thyristor rectifiers (Figure 2.4 (a)) to reduce the short-circuit current during the commutation. Its presence in electrical network increases the grid equivalent impedance (decreasing short-circuit power at the terminal of converter), improves the PCC voltage and current waveforms (harmonics reduction) [71, 96, 103, 114, 162, 212, 221, 243].

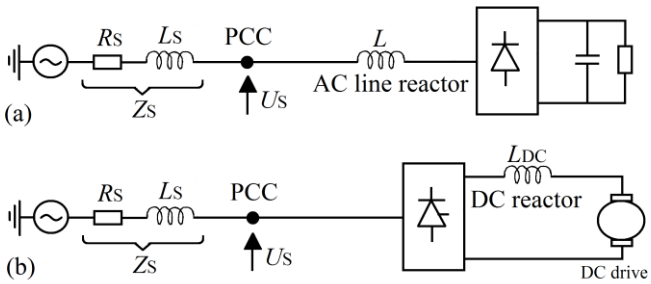

Figure 2.4 (a) AC line reactor connected between the PCC and the diode rectifier; (b) DC link reactor connected between the rectifier and the DC motor

The reduction level of harmonics amplitudes depends upon the choice of the line reactor parameters (which are also related to the load parameters) [221]. The simulation example of the line reactor inductance increase influence on the PCC voltage and current waveform is presented in Figure 2.5. With high value of line inductance, the grid voltage and current at PCC present lower THD. But the voltage at rectifier input is more distorted and its value is reduced by the line reactor voltage drop.

The phase shift between the fundamental harmonic grid voltage and current (Φ) has increased with the line reactor increased, but the grid inductance voltage drop has decreased as well as the rectifier DC voltage (Figure 2.5).

The DC link reactor (L_{DC}) as the AC line reactor (Figure 2.4(b)) reduces also the current THD value. It has almost the same functionality (in term of current harmonic reduction) as the AC line reactor. In comparison with the AC line reactor, it is bigger, more expensive and generates less power losses because it is air core reactor (in other to avoid the saturation phenomenon). The AC line and DC link reactor are less efficient than active and passive filter in term of harmonics reduction [52, 96, 162, 180, 212].

2.3.1.2 Interface filters for power inverters

The interface filters in power electric play two rules: the mitigation of harmonics below 2.5 kHz (see the example of Figure 2.6) and the reduction of converter switching components (see the example of Figure 2.7).

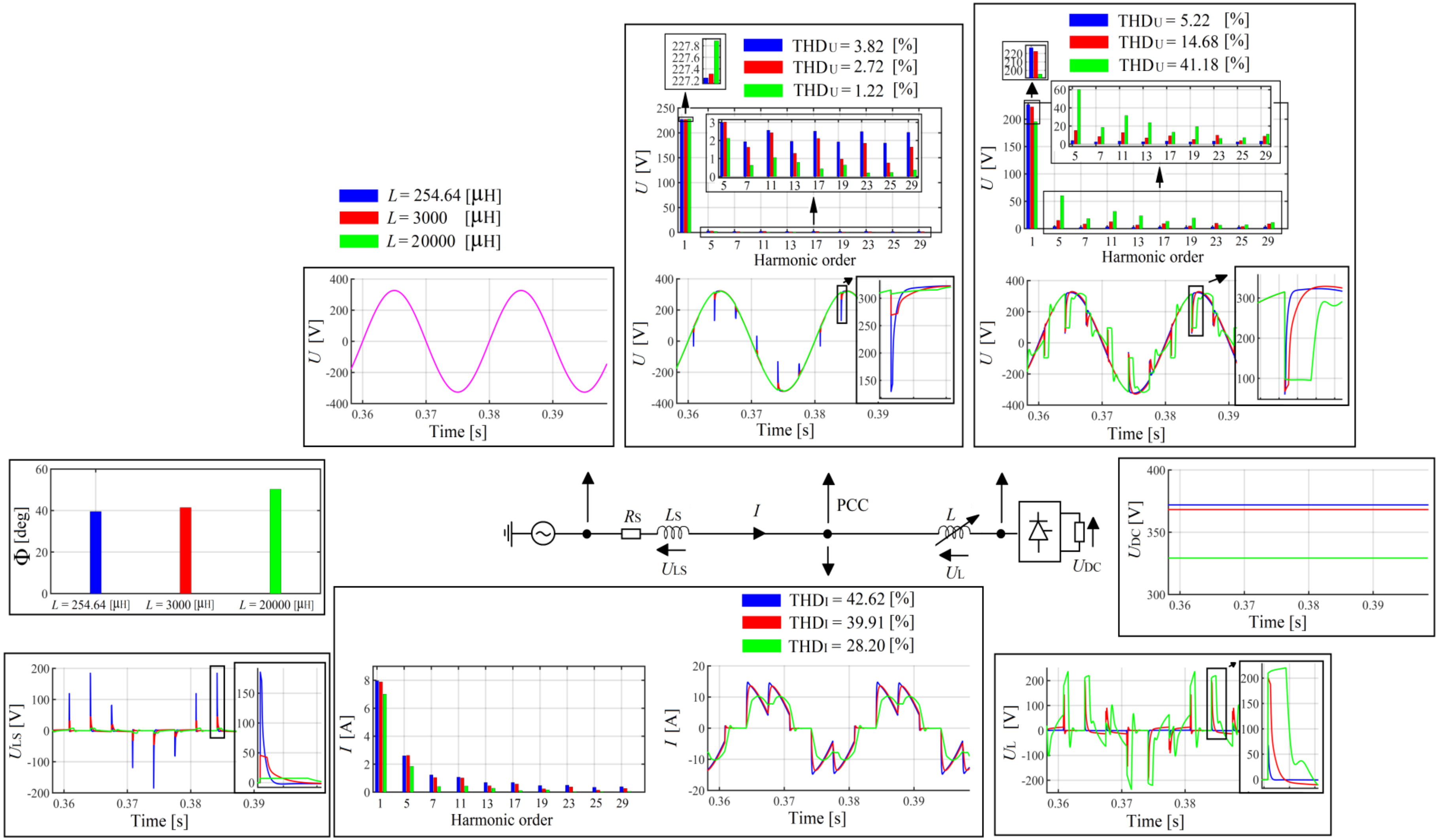

Figure 2.5 Influence of the increase of the AC line reactor (L) on the PCC voltage and current THD

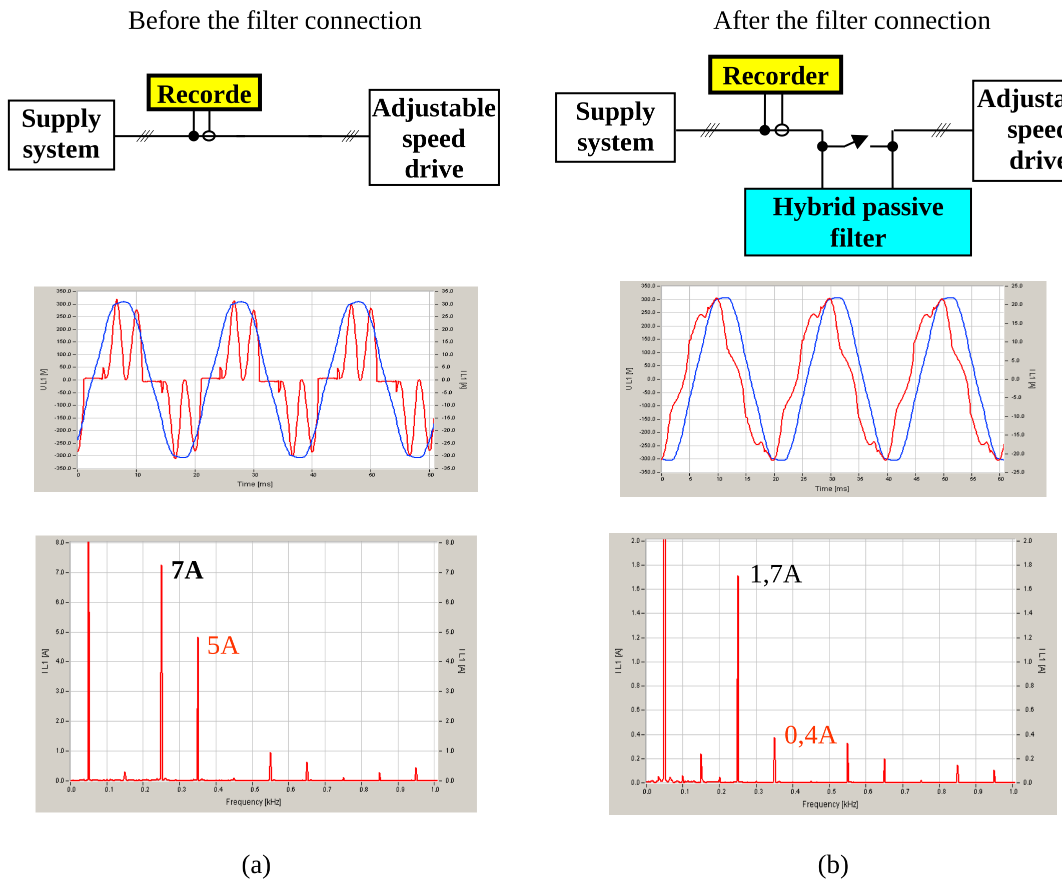

Figure 2.6 Voltage and current waveforms (and spectrums) measured at point of the adjustable speed drive connection: (a) without filter, (b) with the input hybrid passive filter

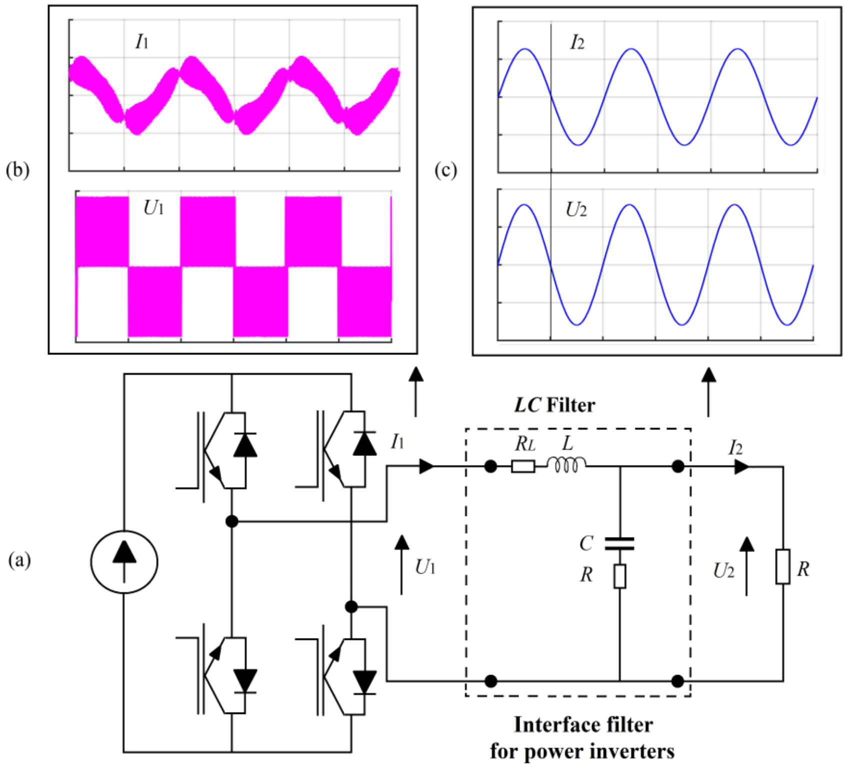

Figure 2.7 One phase transistor converter with interface filter at its input: (a) electrical circuit, (b) current and voltage waveforms at the inverter output (AC side), (c) current and voltage waveforms after the *LC* filter application

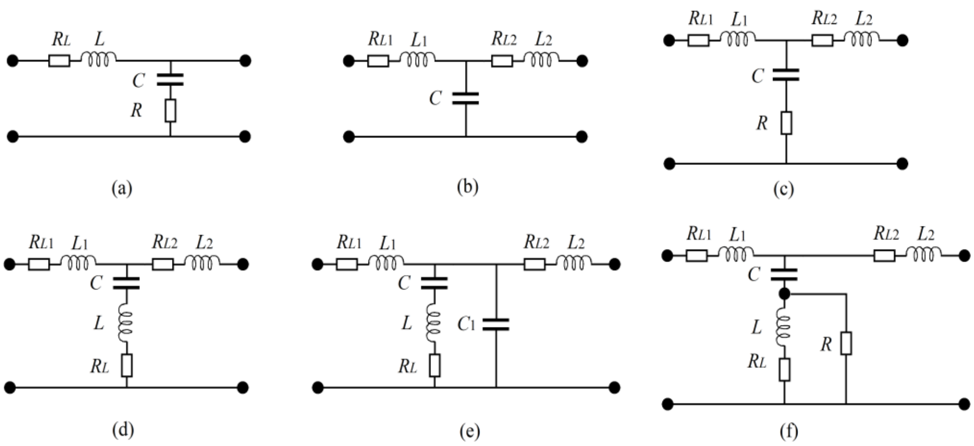

Figure 2.8 Example of power inverter interface filters for switching ripples reduction: (a) *LC* filter; (b) *LCL* filter, (c) *LCL* filter with damping resistance *R*, (d) *LLCL* filter; (e) *LCL-LC* filter; (f) *LCL-LC* filter with damping resistance *R* [139]

In the example of Figure 2.6, the interface filter (hybrid passive filter) is designed to mitigate the 5th and the 7th harmonics generated by the adjustable speed drive (it is designed for a specific load). The examples of such of configurations are presented in [48, 280] (see also chapter 3.6).

In the example of Figure 2.7, the interface filter which is in this case the *LC* filter (it can be also one of the structures of Figure 2.8) is applied at the converter output to mitigate in width band of voltage and current harmonics caused by the transistors switching frequency. The voltage and current waveforms at the inverter output and *LC* filter output are respectively shown in Figure 2.7(b) and (c) [14, 159].

The most common interface filter structures used for converter switching components mitigation are presented in Figure 2.8. The AC line reactor (Figure 2.4 (a)) can also be counted between them as first-order *L*-filter. Its performance in term of ripples reduction depends upon its size (the higher is the inductance, the better are reduced the switching frequencies components), load and grid inductances (see also chapter 5). In comparison to other filters (Figure 2.8(a) to (f)), its big size is a disadvantage because of the high power losses and performance cost (in the case for instance of APF) [14, 159, 179, 257].

The *LC*-filter (Figure 2.8(a)) is a type of secondary order filter not widely used as the first-order *L*-filter because its performances, which (in term of ripples mitigation) depends upon the electrical grid impedance. For a very small value of grid inductance, the capacitor is ineffective and the switching ripple reduction level is the same as the one of first-order *L*-filter [139] (with the same inductance). The damping resistance *R* in series with capacitor *C* is for resonance attenuation.

The *LCL*-filter (third-order filter) is the commonly used interface filter [179, 264]. It is constituted of two reactors and one capacitor as shown in Figure 2.8(b) and (c). Although it reduces the switching ripples with more efficiency than the *L*-filter [14, 63, 122], it presents also disadvantages such as: (a) resonance phenomena which can make the system unstable if not damped (see Figure 2.8(c) with the damping resistance *R*), (b) design parameters difficulties, (c) complicated control system (e.g. unstable closed-loop system) etc. [77,122, 159, 179].

Concerning the topology of Figure 2.8(d) (*LLCL* filter), the *LC* branch (connected in parallel between L_1 and L_2) is designed to resonate (series resonance) at the switching frequency. For the frequencies range located above the series resonance frequency, the *LLCL* presents the less harmonic reduction efficiency than the *LCL* filter [159]. According to [264], the structure of Figure 2.8(e) (*LCL-LC*) can strongly reduce the harmonics current around the switching frequency than the *LLCL* filter because of the capacitor (C_1) connected in parallel with the *LC* branch.

It exists many other interface input filter topologies, which present better filtration characteristics than the *LCL*-topology (e.g. Figure 2.8(e) etc.). Nevertheless, all the interface input filter topologies have a common problem of stability and resonance. The resonance problem can be solved by applying passive damping method (based on damping resistance utilization) and active damping methods (based on the control strategies) such as in the topologies of Figure 2.8(c) and (f) [122, 179].

2.3.2 Active power filters

The application of the active power filters (APFs) as harmonic mitigation techniques is in growth in the industries. Furthermore, they can be applied to mitigate other power quality disturbances such as flickers and slow voltage variation (stabilizer) [50], eliminate voltage dip and swell (DVR) [123], compensate the basic harmonic reactive power (STATCOM) [47] and balance the power system voltage or current [90]. Their main drawbacks are high cost, relatively complicated control system as well as limited application in MV and HV network because of the limited rate of semiconductor devices voltage and current. Basing on their structure and functionality, it can distinguish, between others: the series active power filter, the shunt active power filter and the hybrid active power filter.

2.3.2.1 Series active power filter

Connected between the PCC and the load mostly through a transformer (Figure 2.9), the series APF main role is to improve the supply voltage protecting the sensitive loads from disturbances such as voltage harmonics (Figure 2.10), fluctuation (voltage stabilizer), unbalance, dip and swell (DVR) [86, 226]. It ensures to the load almost a pure sinusoidal voltage waveform by eliminating harmonics in voltage supply (Figure 2.10) [83, 86, 113, 226]. Moreover, depending upon the adopted control strategy, it can block current harmonics flowing from the load to the AC network [16, 83, 133, 226].

The Series APF is less used in practice because of its complicated control system and fault condition at the terminals of the critical load [83, 86, 113].

A simulation example of series APF is shown in Figure 2.10(a). From the grid side, the voltage contains disturbances such as harmonics, dip and swell (Figure 2.10(b)) and at the load terminals, the voltage has better quality (Figure 2.10(c)).

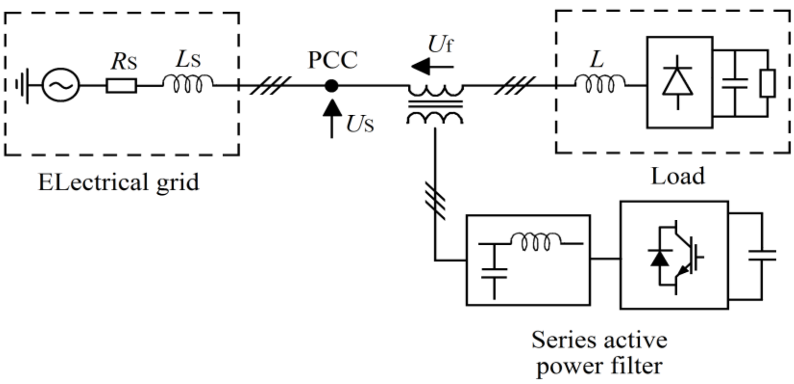

Figure 2.9 Series APF

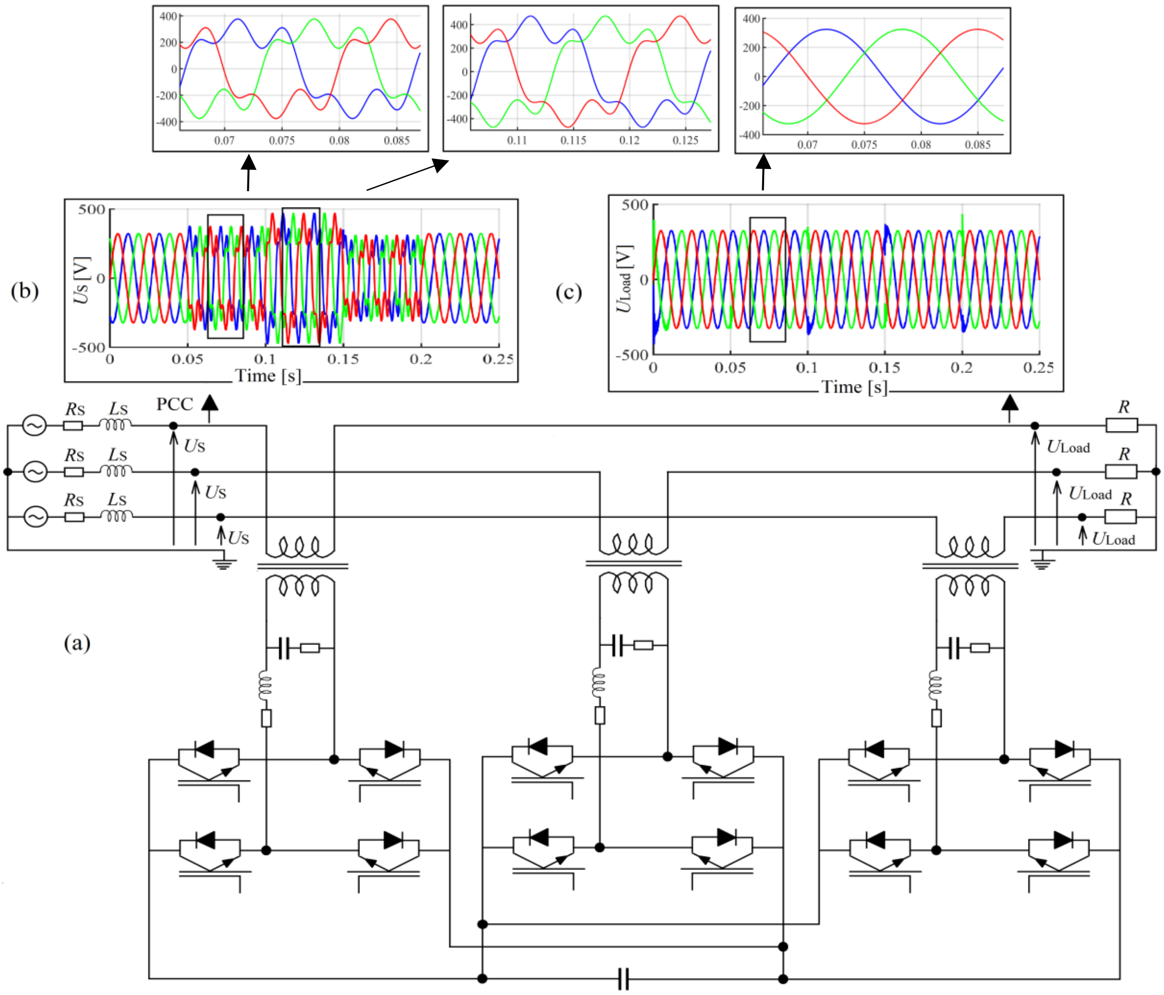

Figure 2.10 The series APF is connected between the PCC and the load (a); (b) distorted PCC voltage; (c) load voltage

2.3.2.2 Shunt active power filters

Despite their disadvantages (high cost [153], complex control system, difficulty for large scale implementation [3, 58, 134, 239] etc.), the SAPFs are more efficient when compared to the PHFs and their application is in growing in the industries and medium voltage system [3, 86, 239].

Their classification by basing on the type of power system, permits to distinguish the three and four wires structures (Figure 2.11). Concerning the four wires SAPF, it is organised in two structures (Figure 2.11(b) and (c)): the four wires three legs inverters with two DC capacitors (the neutral network wire is connected between capacitors (Figure 2.11(c)) and the four wires four legs inverters with one DC capacitor (Figure 2.11(b) [25, 56, 276]. The structure of Figure 2.11(a) will be under study in chapter 5.

The structures of Figure 2.11(a) to (c) are also called voltage source invert (VSI) and the structure in Figure 2.11(d) is the current source inverter (CSI). The VSI possess a capacitor as energy storage, whereas the CSI uses the reactor as energy storage at the DC side of converter. In comparison to the VSI, the CSI is rarely applied because of its disadvantages [43, 269].

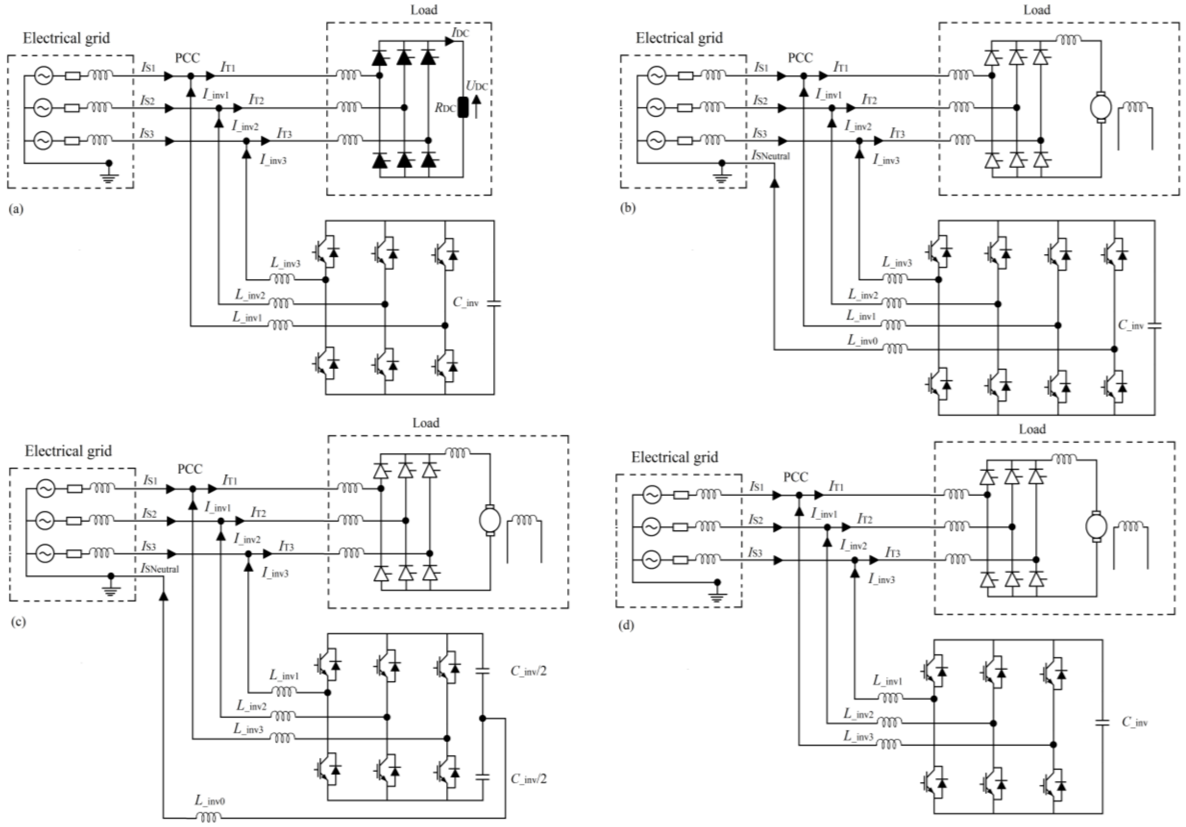

Figure 2.11 SAPF topologies: (a)(d) three wires three legs inverter, (b) four wires four legs inverter and (c) four wires three legs inverter

2.3.2.3 Hybrid active power filters

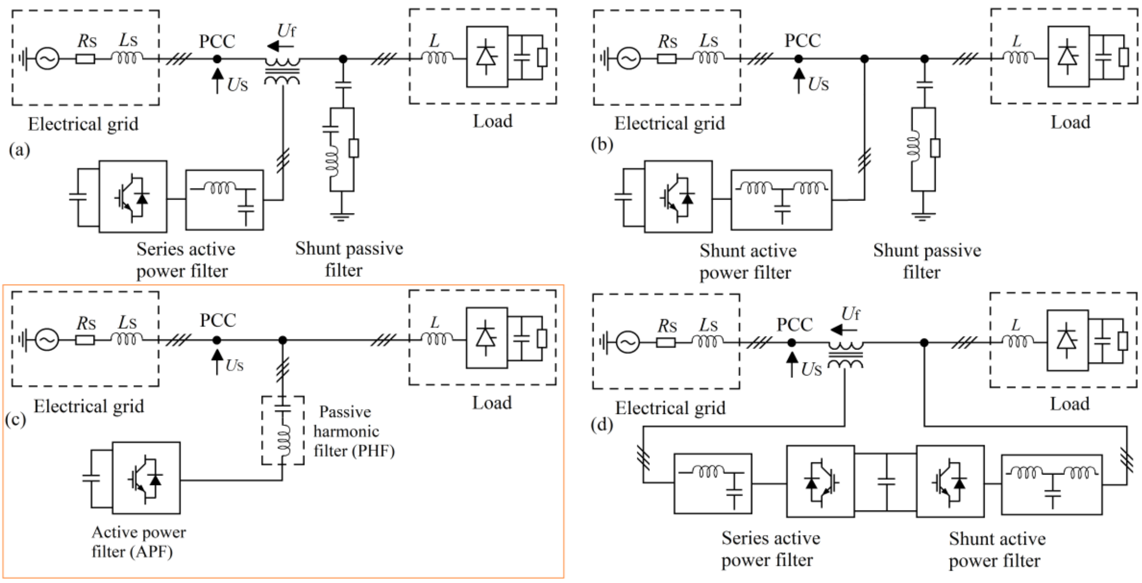

Figure 2.12 Hybrid APFs: (a) series APF in parallel with shunt passive filter; (b) shunt APF in parallel with shunt passive filter; (c) shunt APF connected in series with passive filter; (d) unify power quality conditioner (UPQC)

In the literature, the most common topologies of HAPF are presented in Figure 2.12 and Figure 2.13. Concerning the topology of Figure 2.12(a), the series APF can be control in such a way that its ensures high impedance for the selected harmonic generated by the non-linear load (it behaves as harmonic isolator for that harmonic) and in the same time very small impedance for the current fundamental harmonic in other to reduce power losses and voltage drops [133, 236, 245].

In the topology of Figure 2.12(b), the passive filter goal is to mitigate the load dominating harmonics and compensate the fundamental harmonic reactive power (which reduces the current level of SAPF), the shunt active power filter goal is to filter the remaining harmonics and compensate the remaining reactive power. With the SAPF, the resonance phenomena between the electrical grid and passive filter are eliminated [242, 265]. That topology is more used in practice than the one of Figure 2.12(c). For that reason, the author has focused its study on the topology of Figure 2.12(c) in chapter 6.

The topology presented in Figure 2.12(d) so call unified power quality conditioner (UPQC) is also analyzed in the literature [47, 51]. It can be control to improve (at the same time) the PCC RMS voltage (series part) and reduce the load current disturbances such harmonics, asymmetry (shunt part). It has also the possibility to compensate the reactive power.

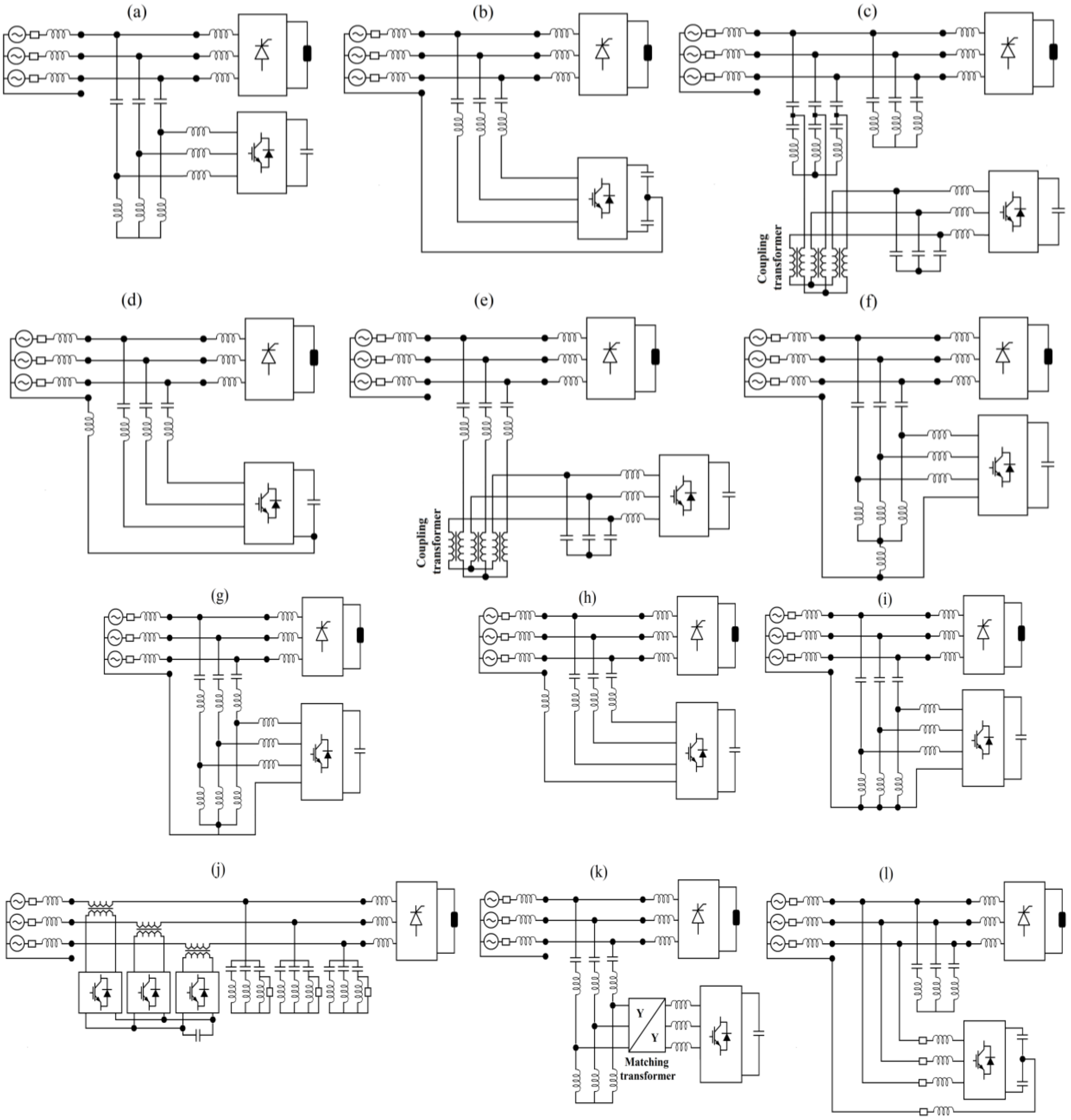

Figure 2.13 Examples of HAPF topologies: (a) to (l) [20, 60, 88, 95, 163, 167, 182, 200, 201, 205, 214, 238, 258]

The topology of Figure 2.13(a) was firstly proposed in [150, 238]. The active power filter is connected in parallel between the PHF capacitor and reactor. This parallel connection, in comparison to the topologies where PHF and active power filter are in series connection (e.g. Figure 2.12(c)), reduces the quantity of current flowing to the APF components. Because of the passive filter capacitor, this topology also ensures a small rate of the active power filter. One of the important advantages of that structure is that during the inverter maintenance break or failure situation, the PHF can continuous to operate [38, 39, 40, 60, 163, 167].

In the topology of Figure 2.13(e) the active power filter is connected in series with PHF through matching transformer. By imposing the voltage at the coupling transformer primary side, the active filter has an influence on the PHF compensation characteristics (e.g. the passive filter fundamental reactive power can be modified through the inverter imposed voltage at the transformer secondary side). The HAPF filtering characteristics depends upon the choice of PHF parameters as well. It presents as well an inverter DC side voltage reduction because of the large PHF capacitor voltage drop [20, 76, 112, 126, 172, 205, 209, 210, 258]. Not all the presented topologies in Figure 2.13 are described in this chapter (for more details see the literature).

2.3.3 Harmonic emission reduction by non-linear load configuration

2.3.3.1 PFC converters

One of the most common way to obtain sinusoidal PCC current in phase with the grid voltage is the application of power factor correction (PFC) converter [32,86]. They exist in several structures and an example is presented in Figure 2.14(b) and (c) [50, 113]. According to [32], they can be controlled in such a way to stabilize the DC capacitor voltage, shape the AC current and increase the displacement power factor (DPF) close to unity. They have different operating mode and one of them is used in the simulation example in Figure 2.14 (b). Comparing Figure 2.14(a) to Figure 2.14(b), it can be seen that the rectifier without any DC/DC converter at the back presents a distorted AC current and voltage [219].

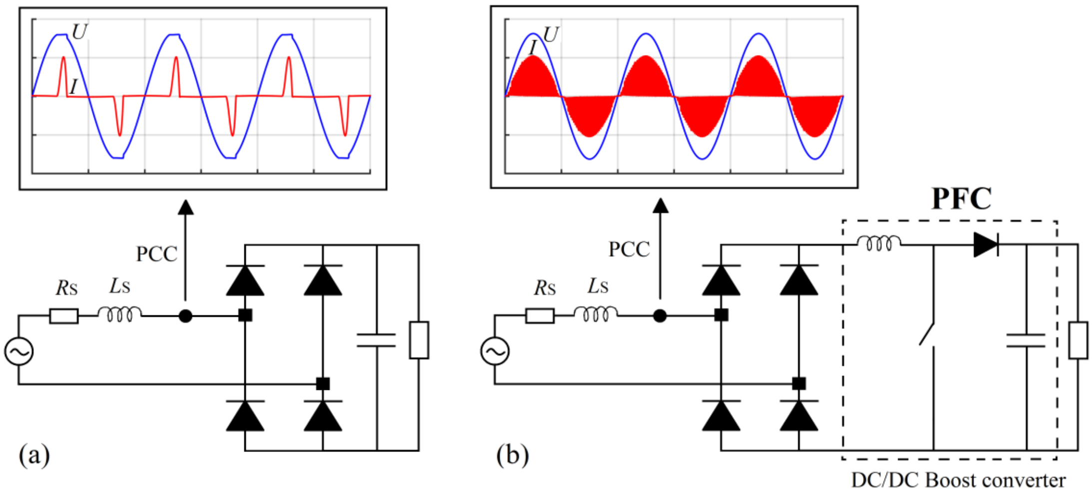

Figure 2.14 Comparison between AC voltage and current waveform generated by the rectifier without (a) and with (b) PFC converter

2.3.3.2 Multi-level inverters

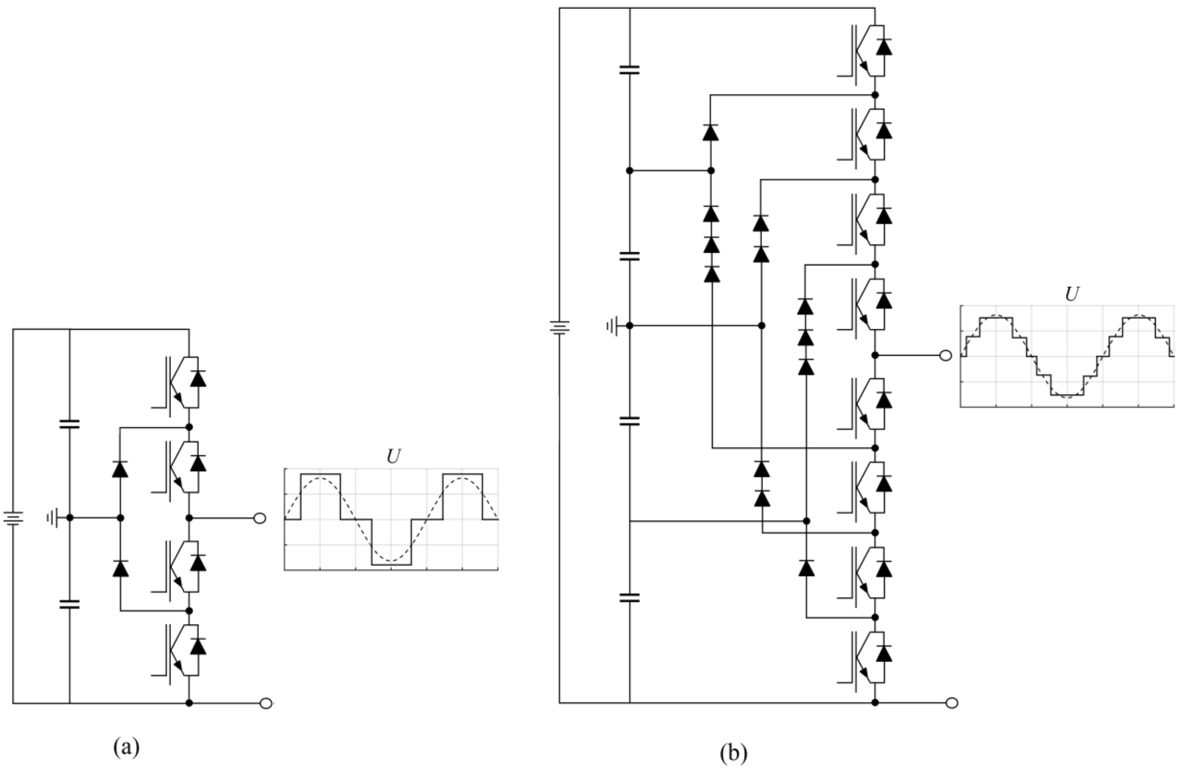

Figure 2.15 Waveforms of voltage at the output of three (a) and (b) five-level inverter

The multi-level inverters exist in different structures and their application is focus on low, medium and high voltage system. They are high power converters (because their high transistors number can easily manage HV), low switching frequency (in comparison to one level converter) and power losses (because the power electronic elements are not switched on at the same time), more efficient and produce less distorted voltage and current at their output than the conventional converter. They are mostly used in electrical drives, micro-grid installations such as interface of photovoltaic (PV) systems, wind generators etc. [19, 129, 157, 203, 213].

An example of multi-level inverter structures with output voltage waveform is presented in Figure 2.15. The output voltage of three-level inverter (Figure 2.15(a)) is more distorted than the output voltage of five-level topology (Figure 2.15(b)). The harmonics distortion reduction level depends upon the inverter level and the control strategies [128].

Chapter 3
Passive harmonic filters

The passive harmonic filters (PHFs) are classified into different groups (series, shunt and hybrid) and despite their disadvantages (robust construction, resonance phenomena with the grid impedance etc.), they are widely used in the industry and are applied in high, medium and low voltage distribution system because of their low cost, efficiency in reducting harmonics, simplicity in construction, ability to compensate the required reactive power (fundamental harmonic) etc. [47,72, 73, 102, 279].

The goal of this chapter is to analyze the most common PHFs topologies, focusing on their impedance vs frequency characteristics and their filtration and compensation properties. A comparison studies between selected PHFs topologies as well as between methods of sharing the total reactive power in the PHF group are also considered in this chapter.

3.1 Resonance phenomena in electrical circuit

The series and parallel resonances are the two types of resonance commonly observed in the electrical domain. Despite its negative influence on the electrical network components, this phenomenon is on the base of PHFs conception [82, 182, 256].

To illustrate the electrical resonance phenomenon, two RLC electrical circuit supplied by an ideal (without impedance) voltage source is presented in Figure 3.1(a) and (b). With the frequency increase, the capacitor reactance decreases whereas the reactor reactance increases (Figure 3.1(c)). The series and parallel resonance occur in an electrical circuit when the reactor and capacitor reactance modules are equal for a given frequency.

In the case of series resonance (Figure 3.1(a)), the impedance (Z_{Series}) of the R_1LC circuit is minimum and limited to the resistance R_1 (Figure 3.1(c)). The series resonance is also called voltage resonance because at that resonance the voltages at the capacitor and reactor terminals have the same amplitudes but in opposite sign (voltage cancelation) (Figure 3.2(a)). Therefore, for the frequency in resonating mode, the voltage at the terminals of the series connected R_1LC elements is only on the resistance R_1.

The parallel resonance is characterized by a very high impedance of the RLC circuit for the given frequency (Figure 3.1(c)). The parallel resonance is also called current resonance because at that circuit condition the currents flowing between the reactor and capacitor present the same amplitude but different sign (current cancelation) (Figure 3.2(b)).

Another example to clarify the resonance phenomenon in electrical domain is the electrical circuit of Figure 3.3 where the LC_1C_2 circuit (resonance circuit) is connected between the electrical network and the current harmonics source (load). The 5th and the 7th harmonics are generated by the load.

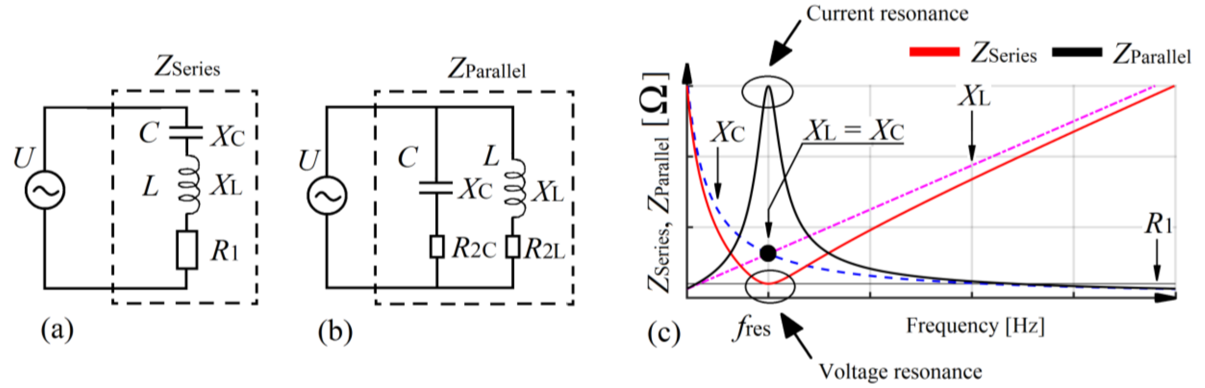

Figure 3.1 *RLC* electrical circuit used to illustrate the series (a) and parallel (b) resonances; (c) impedance vs frequency characteristics

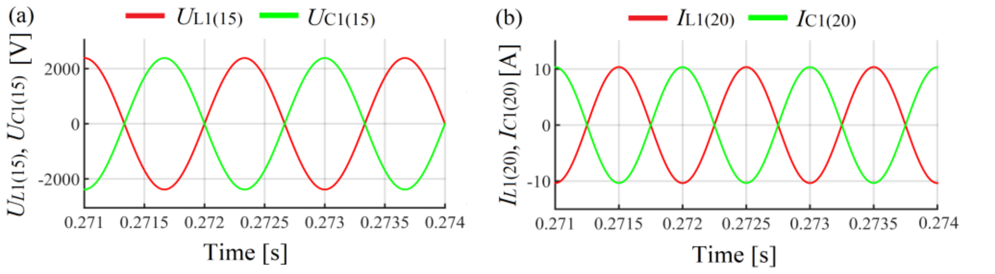

Figure 3.2 (a) Voltage at the capacitor and reactor terminals (series resonance at 750 Hz), (b) current flowing through reactor and capacitor (parallel resonance at 1 kHz)

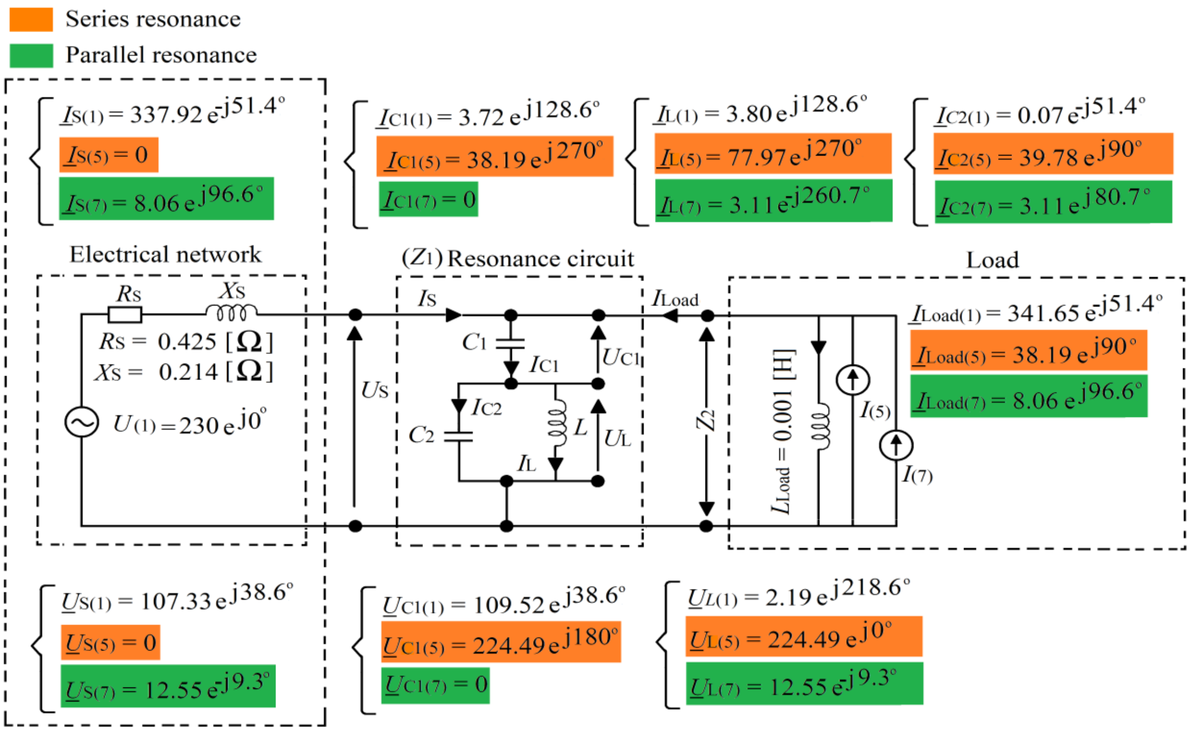

Figure 3.3 Electrical circuit with parameters after resonances (series and parallel)

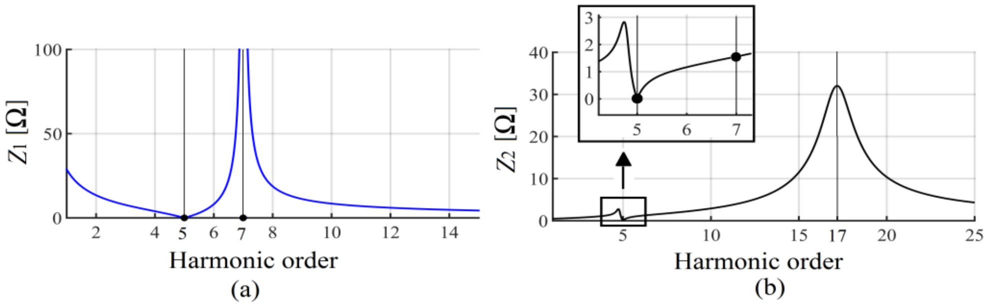

Figure 3.4 Impedance vesus frequency characteristic of (a) the resonance circuit (LC_1C_2) and (b) the electrical circuit seen from the load input

The LC_1C_2 circuit is designed to resonate at the frequency of 5th (series resonance) and 7th harmonic (parallel resonance) and the resistances of its elements are neglected. Its impedance vs frequency characteristic is set up in Figure 3.4(a).

The data in Figure 3.3 are obtained after simulation in MATLAB/SIMULINK. Due to the series resonance of the LC_1C_2 circuit, the 5th harmonic current ($I_{S(5)}$) coming from the load side did not flow to the electrical network (see data of Figure 3.3). The voltages of the 5th harmonic of capacitor ($U_{C1(5)}$) and reactor ($U_{L(5)}$) are high (in others cases can be higher than the source), presents the same amplitude and are in opposite sign, therefore cancel each other (there is a short circuit current for the 5th harmonic).

The 7th harmonic generated by the current source flows totally to the electrical network because of the parallel resonance (the LC_1C_2 circuit has a infinity impedance of the 7th harmonic). According to the parameters in Figure 3.3, the voltage of the 7th harmonic exits only on the reactor ($U_{L(7)}$). The current of 7th harmonic flowing through the capacitor C_2 and the reactor L are identical but in opposite sign.

The impedance versus frequency characteristic of circuit seen from the load input (Z_2) is presented in Figure 3.4(b).

3.2 General concept of passive harmonic filters

The PHF topologies vary by their components number, filtration band, immunity on detuning phenomena, power losses and so on. The design and operating cost of each topology depend on the highlighted features as well as on the grid and load parameters [102]. Therefore, it is important to know the disadvantages and advantages of each topology while deciding on its choice and in optimal decision taking in terms of technical and economical point of view.

The PHF topologies under studies in this chapter are presented in Figure 3.5(b). The influence of the filters parameters (tuning frequency, damping resistance and reactive power) on their efficiency is considered as well as the way how these parameters are computed.

To study the considered PHF topologies, the power system example modeled in MATLAB/SIMULINK is presented in Figure 3.5(a) (see also Annex II). It contains three-phase electrical power supply system with transformer (Tr) and line (L) feeding three-phase controlled thyristor bridge with DC motor at the DC side and input reactor (L) at the AC side. The PHFs are connected at the PCC.

The filters are tuned to the frequency a bit smaller than the frequency of the first high harmonic characteristic (after the fundamental harmonic) for 6-pulse thyristor rectifier, which is the 5th harmonic (4.85th). For each considered filter topologies, the capacitors resistance is neglected, the reactors resistance is computed basing on the quality factor, the compensating reactive power (fundamental harmonic) is constant: Q_f = -2172.5 Var (except in the case of single-tuned topology) as well as the rectifier firing angle. The voltage and current data and characteristics at the thyristor bridge AC side are considered at the steady state.

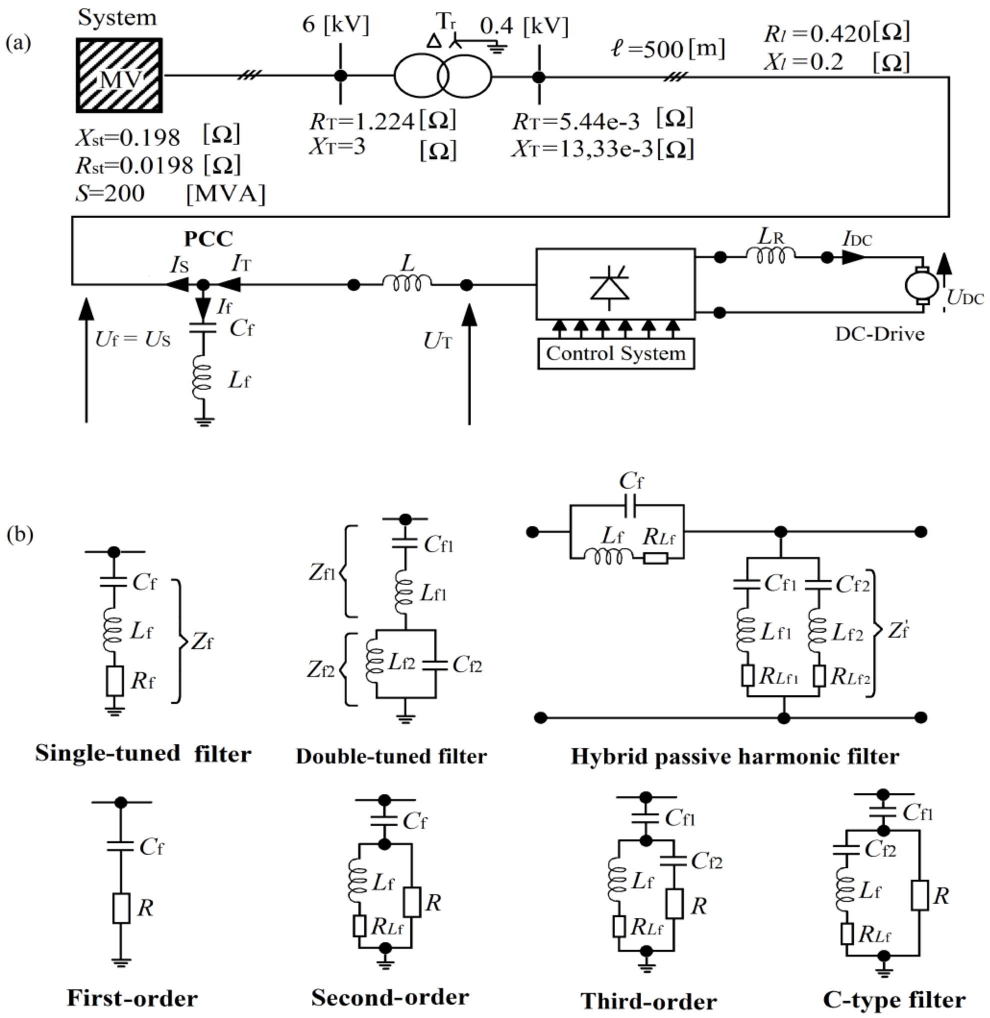

Figure 3.5 (a) Simulated power system, (b) considered passive parallel harmonic filter topologies

3.3 Series passive harmonic filters

The series PHFs are connected in series between the power source (PCC) and the nonlinear load. They exist in different topologies but the one under studies in this chapter is the basic structure (see Figure 3.6(a)). At the terminals of series PHF, the parallel resonance occurs for the selected harmonic to be eliminated. For that harmonic, the filter impedance is therefore very high (theoretically infinity), what prevents it (harmonic) to flow to the electrical grid (Figure 3.6(a)) [48, 149].

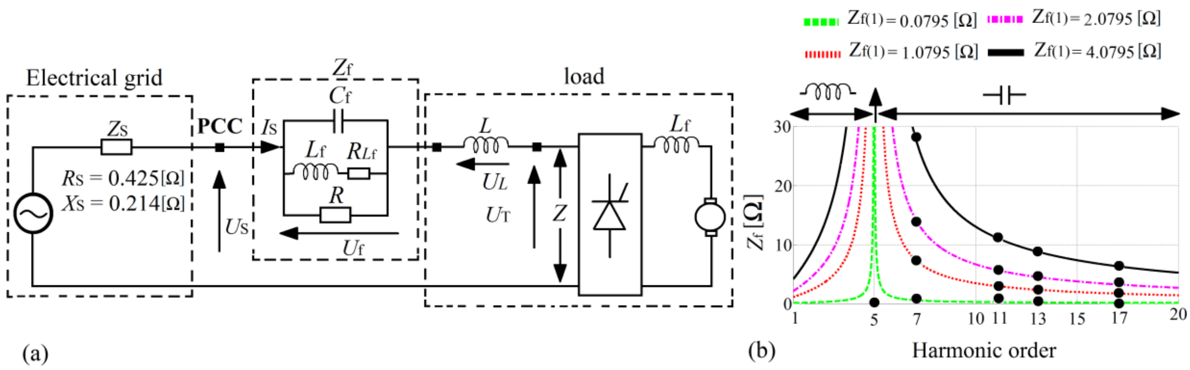

Figure 3.6 (a) series PHF configuration example cooperating with 6 pulses thyristor rectifier, (b) Series PHF impedance versus frequency characteristics for different value of its fundamental harmonic impedance (see Annex III - Table III.1 for the series PHF parameters)

Table 3.1 Formulas used to compute the series PHF parameters

For $R_{Lf} = R_{Cf} \approx 0$ and R infinity	For $R_{Lf} = R_{Cf} \approx 0$ and by considering R:
$\underline{Z}_{f(j\omega)} = j\dfrac{\omega L_f}{\omega^2 L_f C_f - 1}$ $\underline{Z}_{f(j\omega)} \to \infty \Rightarrow \omega^2 L_f C_f - 1 = 0 \Rightarrow \omega = \omega_{re} = \dfrac{1}{\sqrt{C_f L_f}} = n_{re}\omega_{(1)}$ $Z_{f(1)} = \frac{1}{(n_{re}^2 - 1)\omega_{(1)} C_f}$, $n_{re} > 1$ $C_f = \frac{1}{(n_{re}^2 - 1)\omega_{(1)} Z_{f(1)}}$, $L_f = \frac{1}{n_{re}^2 \omega_{(1)}^2 C_f}$	$\underline{Z}_{f(j\omega)} = \frac{\omega^2 L_f^2 R - j(\omega^2 L_f C_f - 1)\omega L_f R^2}{\omega^2 L_f^2 + (\omega^2 L_f C_f - 1)^2 R^2}$
$R_{Lf} = \frac{\omega_{(1)} L_f}{q'}$ (reactor resistance computation)	

In this chapter, the series PHF is designed to obtain high impedance Z_f (parallel resonance) for the harmonic to which it is turned (5th) and small impedance for the fundamental harmonic $Z_{f(1)}$ (minimum voltage drop and power losses). The formulas used to compute its parameters are presented in Table 3.1.

Figure 3.6(b) presents the series PHF impedance versus frequency characteristics for different values of the fundamental harmonic impedance (also different reactive powers for that harmonic). The filter impedance for the 5th harmonic increases with the increase of $Z_{f(1)}$ as well as the impedance of other harmonics. The seies PHF impedance is inductive below and capacitive above the resonance frequency (5th, Figure 3.6(b)).

If the series PHF is tuned to the frequency lower than the frequency of harmonic to be blocked (5th), the filter impedance of that harmonic will decrease and will be on the capacitive side of the filter characteristic (Figure 3.7(a)), therefore the filter will be less efficient to block that harmonic. See Annex III - Table III.2 for the filter parameters.

For the series PHF tuned to the frequency higher than the frequency of harmonic to be blocked (5th) (See Annex III - Table III.2), the filter impedance of that harmonic will also decrease and will be on the inductive part of the filter characteristic (Figure 3.7(a)) and the filter efficiency to block that harmonic will decrease as well. The impedance of harmonics higher than the 5th is small when the tuning frequency decreases and high when the tuning frequency increases (e.g. the 7th, Figure 3.7(a)).

With the increase of the filter capacity or inductor by +10% (see Annex III, Table III.3 and Table III.4), the filter characteristic has moved to the left side of 5th harmonic (Figure 3.7(b) and (c)), the filter impedance of harmonic to be blocked has decreased and is on the capacitive side of the filter characteristic (the 5th harmonic will be partially blocked by the filter) and the high harmonics filter impedance (e.g. $Z_{f(7)}$) has decreased as well.

For the decrease of filter capacity or inductor by -10% (see Annex III, Table III.3 and Table III.4), the filter characteristic has moved to the right side of 5th harmonic (Figure 3.7(b) and (c)). The filter impedance of high harmonics (e.g. $Z_{f(7)}$ - Figure 3.7(c)) has increased, whereas the filter impedance of 5th harmonic, which is inductive, has decreased. The filter efficiency to block the 5th harmonic is then reduced.

The inductor resistance influence on the filter characteristic is presented in Figure 3.7(d). The higher is the resistance, the smaller is the filter impedance of 5th harmonic. The series PHF is less efficient when the reactor is iron core with small quality factor (see Annex III, Table III.5).

The damping resistance (R) connected in parallel with filter reactor and capacitor (Figure 3.6(a)) is rarely applied in practice because of the power losses. Its influence on series PHF functionality is showed in Figure 3.8(a). The filter impedance for the 5th harmonic is equal to the value of damping resistance (see Annex III, Table III.6). The small damping resistance reduces the SPF efficiency.

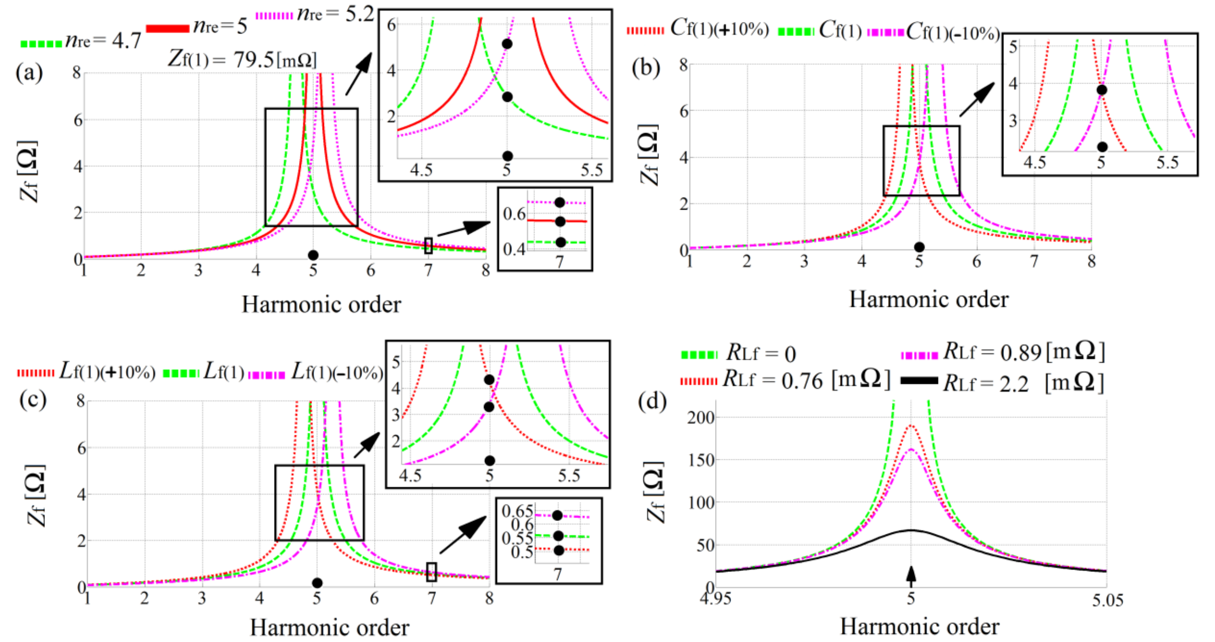

Figure 3.7 Series PHF impedance versus frequency characteristics: (a) different tuning frequency, (b) influence of filter capacitor change, (c) influence of filter inductor change and (d) influence of filter inductor resistance change (the filter parameters are presented in Annex III - Table III.2 to 5)

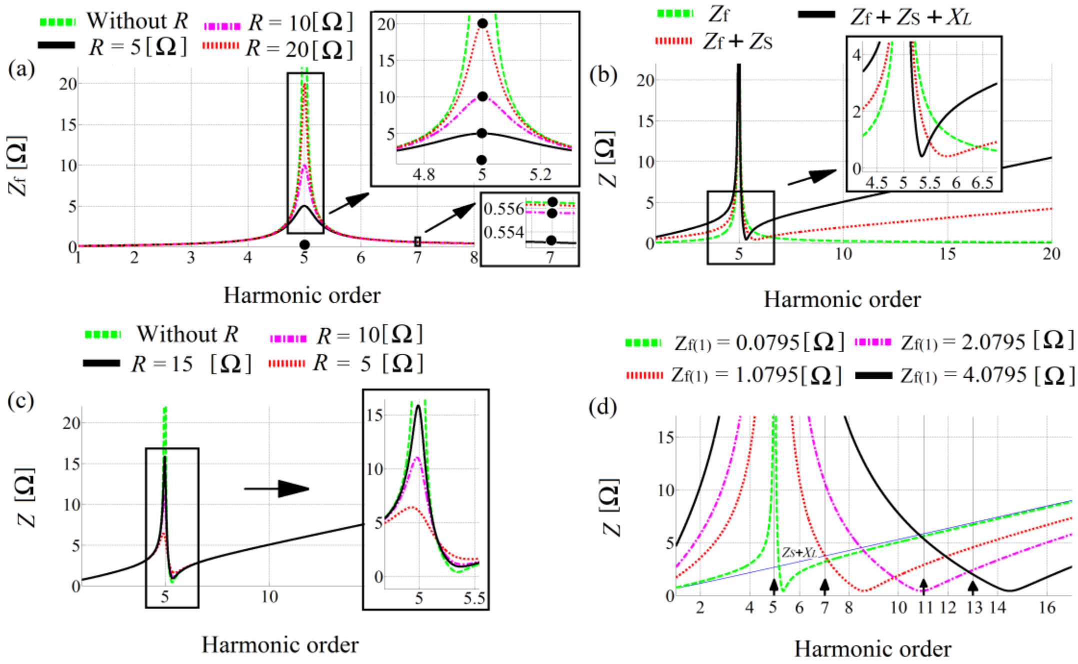

Figure 3.8 (a) series PHF impedance versus frequency characteristics for different value of its damping resistance R (see Figure 3.6(a)); (b) influence of the grid impedance Z_S (mostly the inductance) and rectifier input reactor X_L on the power system series resonance (see from the thyristor rectifier input - Figure 3.6(a)); (c) and (d) are respectively the power system impedance (see from the thyristor rectifier input) for different value of filter damping resistance R and fundamental harmonic filter impedance

The impedance frequency characteristics of power system (Z) observed from the thyristor rectifier input terminals (Figure 3.6(a)) presents the series and parallel resonance (Figure 3.8(b), (c) and (d)).

The power system series resonance (observed from the rectifier input) is influenced by the grid inductance and rectifier input reactor as well (Figure 3.8(b)). The influence of filter damping resistance and filter impedance of fundamental harmonic on the system impedance (Z) are presented in Figure 3.8(c) and (d). The power system parallel and series resonances are damped with the decrease of filter damping resistance (Figure 3.8(c)). The series resonance occurring for the harmonics higher than the 5th moves with the increase of filter impedance $Z_{f(1)}$ (see Figure 3.8(d)).

The comparison between the waveforms and spectrums of the grid current and voltage before and after the serie PHF connection is presented in Figure 3.9 (the filter resistances was negleted during the simulation process). The filter is tuned to the frequency of the 5th harmonic. The connection of series PHF in the power system has improved the grid voltage waveform by reducing the commutation dip (Figure 3.9(a)) as well as the THD_{Us} (Figure 3.11). The spectrums in Figure 3.9(b) and (d) present a significant reduction of the 5th harmonic amplitude at the grid side after the seire PHF connection and the amplification of the 7th, 11th, 13th, 17th, 19th and 25th harmonic.

The THD_{Is} of PCC current has little increased after the filter connection (Figure 3.11). The shape of grid current before and after the filter connection is presented in Figure 3.9(c). The voltage (U_T) at the thyristor bridge input terminals is more distorted after the filter connection (Figure 3.10(a) and (b)) and its THD higher (Figure 3.11).

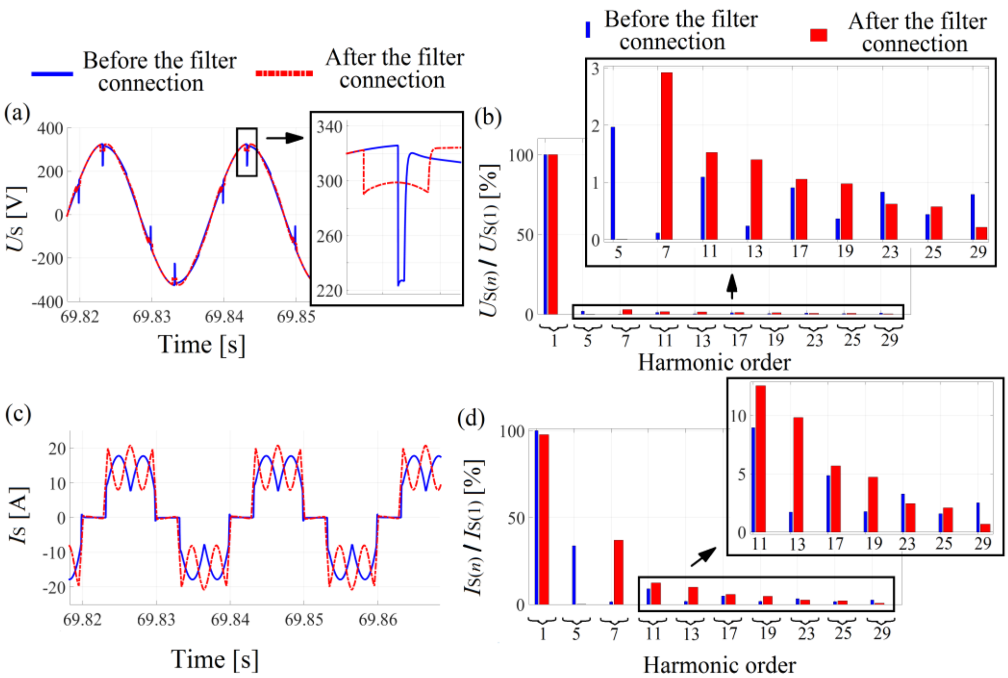

Figure 3.9 (a) grid voltage and (b) its spectrum, (c) grid current and (d) its spectrum

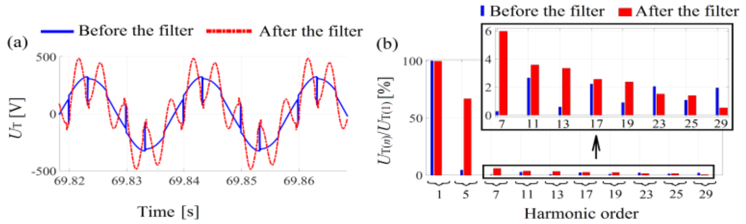

Figure 3.10 Voltage at the input of thyristor bridge and (b) its spectrum

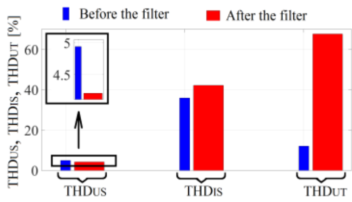

Figure 3.11 THD of grid voltage (U_S) and current (I_S) and voltage at the input of thyristor bridge (U_T)

The power system parameters (voltages, current and powers) obtained after simulation are presented in Table III.7 to 9 (see Annex III). The PCC reactive power (Q_S) has decreased after the filter connection (form 2140 Var to 2068 Var) (Table III.9 - Annex III).

To prevent (block) more than one harmonic to flow to the electrical grid, the serie PHFs can be designed in group as presented in Figure 3.12(a). The series PHFs are not communly used because their size depends on the full load voltage and current and they can be the source of harmonics amplification as presented in Figure 3.9(a)(b). An addition problem is their protection against the short current circuit at the coverter termonals.

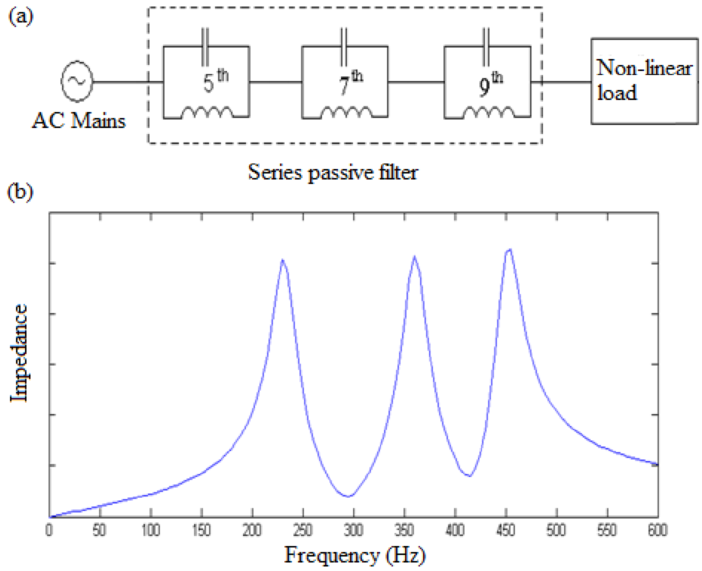

Figure 3.12 Example of SPFs tuned to the frequency of 5th, 7th and 9th harmonic (a) and (b) the impedance frequency characteristic

3.4 Shunt passive harmonic Filters

3.4.1 Single-tuned filter

Table 3.2 Single-tuned filter parameters computation formulas

$\underline{Z}_f(j\omega) = R_f + j\omega L_f - j\dfrac{1}{\omega C_f}$ $\underline{Z}_f(j\omega_{(n)}) = R_f + j\left(n\omega_{(1)}L_f - \dfrac{1}{n\omega_{(1)}C_f}\right)$ $\omega_{(n)} = n\omega_{(1)},\ R_f = \frac{1}{q''}\sqrt{\frac{L_f}{C_f}}$	
$R_f = 0$	
$\underline{Z}_f(j\omega_{re}) \to 0 \Rightarrow j\dfrac{\omega_{re}^2 L_f C_f - 1}{\omega_{re} C_f} = 0 \ \Rightarrow \omega_{re} = \dfrac{1}{\sqrt{L_f C_f}}$ $= n_{re}\omega_{(1)}$	$\underline{Z}_f(j\omega_{(1)}) = j\dfrac{\omega_{(1)}^2 - \omega_{re}^2}{\omega_{re}^2\omega_{(1)}C_f} = j\dfrac{1 - n_{re}^2}{n_{re}^2\omega_{(1)}C_f}$
$Q_f = U_f I_f = \dfrac{U_f^2}{Z_f}$	$C_f = \frac{n_{re}^2 - 1}{n_{re}^2}\frac{Q_f}{\omega_{(1)}U_f^2},\ n_{re}^2 > 1$
$L_f = \dfrac{1}{C_f\omega_{(1)}^2 n_{re}^2} = \dfrac{1}{n_{re}^2 - 1}\dfrac{U_f^2}{\omega_{(1)}Q_f}$	$X_{Cf} = \dfrac{n_{re}^2}{n_{re}^2 - 1}\dfrac{U_f^2}{Q_f}, X_{Lf} = \dfrac{1}{n_{re}^2 - 1}\dfrac{U_f^2}{Q_f}$
$X_{re} = \sqrt{\dfrac{L_f}{C_f}}$	$U_{Cf} = \dfrac{n_{re}^2}{n_{re}^2 - 1}U_f$

In this chapter, the single-tuned filter (see Figure 3.5(b)) is studied by presenting the influence of its reactive power, tuning frequency and resistance on its efficiency. The formulas used to compute the single-tuned filter parameters are presented in Table 3.2.

3.4.1.1 Influence of the single-tuned filter reactive power on its efficiency

The parameters of single-tuned filter for different values of its reactive power are presented in Figure 3.13(b). Three values of filter reactive power are consisdered: Q_f = 1172.5 Var (uncompensation), Q_f = 2172,5 Var (compensation) and Q_f = 3172.5 Var (overcompensation).

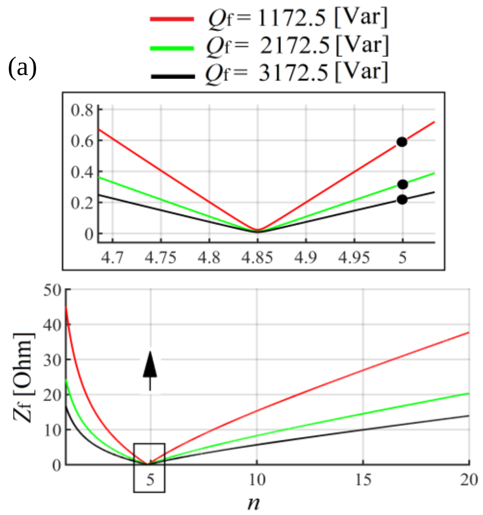

(b)

$Q_{f(1)}$ [Var]	$C_{f(1)}$ [μF]			$L_{f(1)}$ [mH]			R_{Lf} [mΩ]			q'
1172.5	67.55	-	-	6.4	-	-	23.6	-	-	85
2172,5	-	125.17	-	-	3.4	-	-	12.7	-	
3172.5	-	-	182.78	-	-	2.4	-	-	8.7	

Figure 3.13 (a) impedance frequency characteristics of single-tuned filter for different values of its reactive power, (b) single-tuned filter parameters

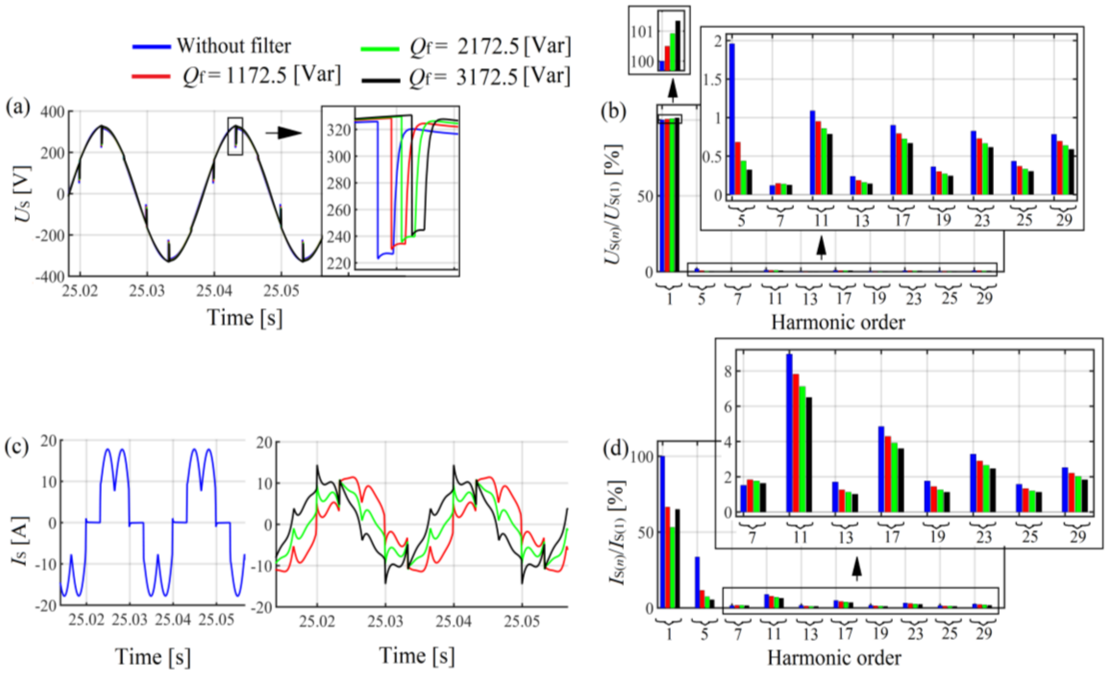

Figure 3.14 Grid voltage (a) and (b) its spectrum; (c) grid current and (d) its spectrum. The PCC voltage and current parameters were registered for different value of filter reactive powe

With the filter reactive power increased from 1172.5 Var to 3172.5 Var, the filter impedance of 5th harmonic has decreased (Figure 3.13(a)), the grid viltage waveform has improved (reduction of commutation dip - see Figure 3.14(a) and THD_{US} - see Figure 3.15(b)) as well as the grid current THD (Figure 3.15(b)).

The higher is the filter reactive power, the better is the reduction of grid voltage and current 5th harmonic (see spectrums of Figure 3.14(b) and (d)) and harmonics higher than the 5th (e.g. 11th to 29th). The filert power losses (P_f) has increased with the reactive power increase (Figure 3.15(a)).

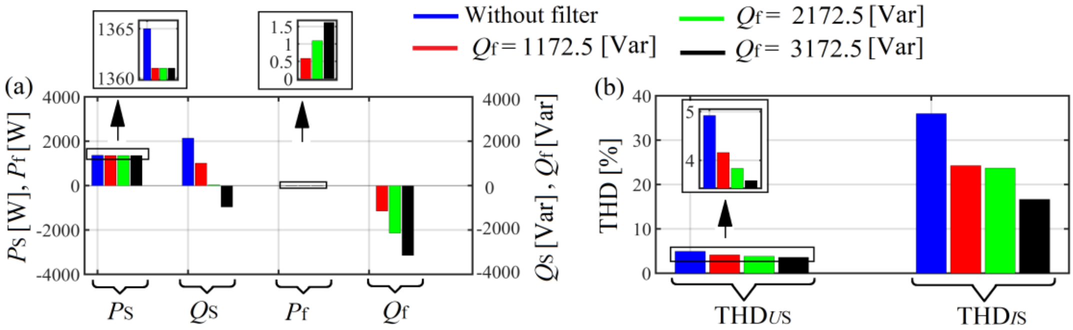

Figure 3.15 Powers (a) and (b) grid voltage and current THD for different value of single-tuned filter reactive power

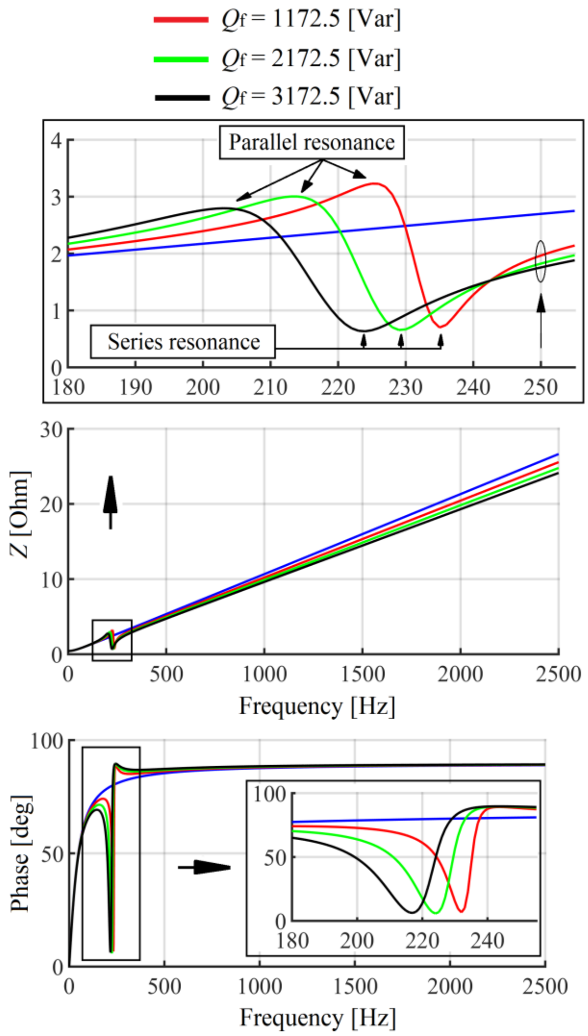

Figure 3.16 Characteristics of power system impedance versus frequency observed from the rectifier input when the filter reactive power is increased

The power system impedance versus frequency observed from the thyristor input (Figure 3.16) shows that with the filter reactive power increased, the power system 5th harmonic impedance has decreased and the parallel and series resonance amplitudes have moved to the lower frequency. The impedance value of the frequency at the parallel resonance have also decreased.

3.4.1.2 Analysis of single-tuned filter for different tuning frequency

Because of the aging (it concerns more the capacitor [79]) or work conditions etc., the single filter must be tuned to the frequency a bit smaller than the frequency of lowest generated harmonic (ω_{re}); in the considered example, the 5th order. There are different opinions on how much it should be detuned [69]. According to [189] the detuning frequency should be in the range of 3 to 15% below the frequency of harmonic to be eliminated. In this chapter, the detuning frequencies are chosen between 1% to 20% below the frequency of 5th harmonic (see Annex III, Table III.10) and the goal of the performed studies is to present the detuning phenomena influence on the single-tuned filter efficiency. The filter parameters are presented in Table III.10 and the power system parameters obtained after simulation are show in Table III.11 and Table III.12 of Annex III.

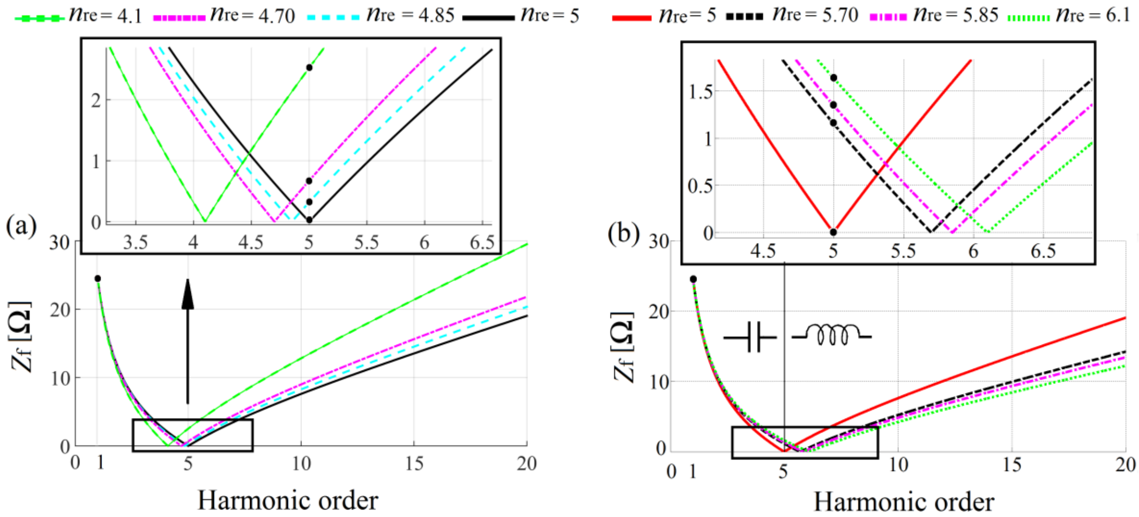

Figure 3.17 Impedance frequency characteristics of single-tuned filter for different values of tuning frequency order. The filter is tuned to the harmonic frequencies lower (a) and higher (b) than the frequency of 5th harmonic (R_f = 0)

For the tuning frequencies lower (Figure 3.17(a)) or higher (Figure 3.17(b)) than $\omega_{re(5)}$, the filter impedance of the 5th harmnic is high which reduces the filter filtration efficiency. In the case when the filter is detuned to the frequencies higher than $\omega_{re(5)}$, the amplification of the filtered harmonic (5th) can occur because of the parallel resosnamce phenomenon between the filter and the grid inductance.

The equivalent impedance of the filter is capacitive for all harmonics frequencies (also fundamental) lower than the resonance frequency and inductive for the harmonics higher than the resonance component (5th order in Figure 3.17(a) and (b)).

The waveforms of current and voltage at the PCC (Figure 3.5(a)) and their spectrums are presented in Figure 3.18. After the filter connection, it can be observed a little decrease of commutation notches depth (Figure 3.18(a)). The grid current waveforms before and after the filter connection is shown in Figure 3.18(c).

With the decrease of tuning frequency (5th to 4.1st), the amplitude of 5th harmonic of PCC voltage and current (Figure 3.18(b) and (d)) has increased as well as the amplitude of higher harmonics (11th to 29th). The THD of PCC current and voltage has also increased (Annex III, Table III.12).

The grid voltage and current fundamental harmonic amplitudes are almost constant during the change of the tuning frequency (Figure 3.18(b) and (d)). Nevertheless, after the filter connection, the current has considerably decreased (from 15.86 A to 8.43 A) because of the reactive component compensation.

The filter current spectrum is presented in Figure 3.19(b) and the waveform in Figure 3.19(a). The quantity of filtered harmonic (5^{th}) flowing through the filter depends upon the tuning frequency. Its value is high for the tuning frequency near to the frequency of the 5^{th} harmonic (250 Hz). The single-tuned filter is much loaded by the filtered harmonic than the other harmonics (Figure 3.19(b)).

The single-tuned filter effectiveness is presented in Figure 3.19(c) and (d). The filter is more effective when it is tuned to the frequency smaller but near to the frequency of the filtered harmonic.

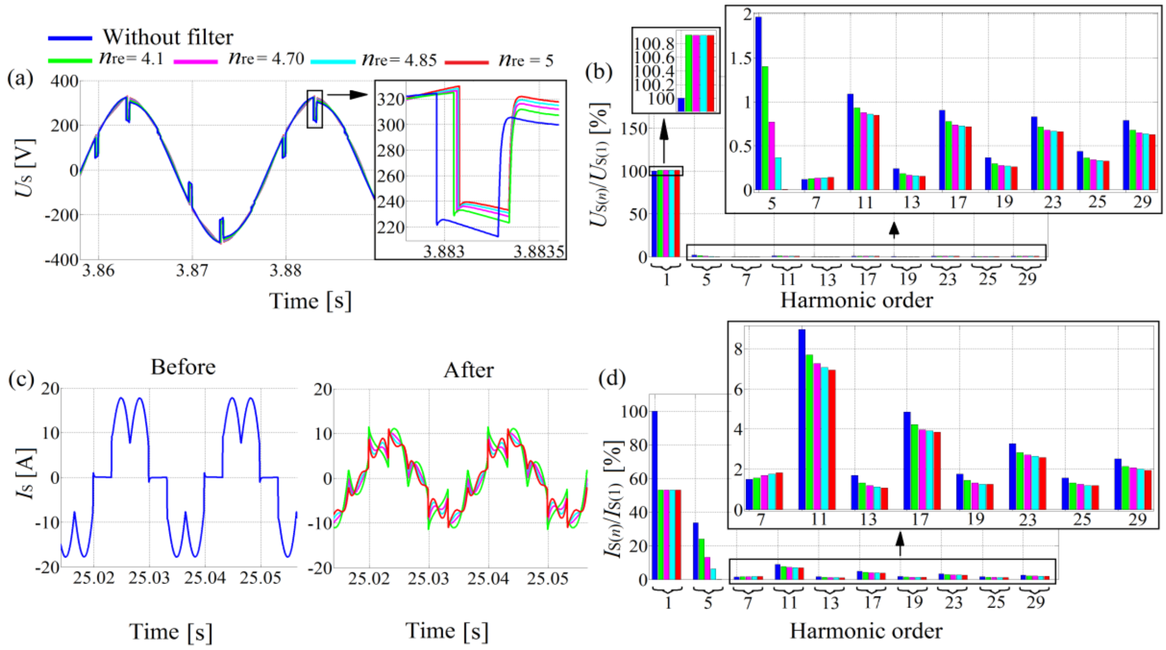

Figure 3.18 (a) grid voltage wavefoms with its spectrum (b), (c) grid current wavefoms with (d) its spectrum

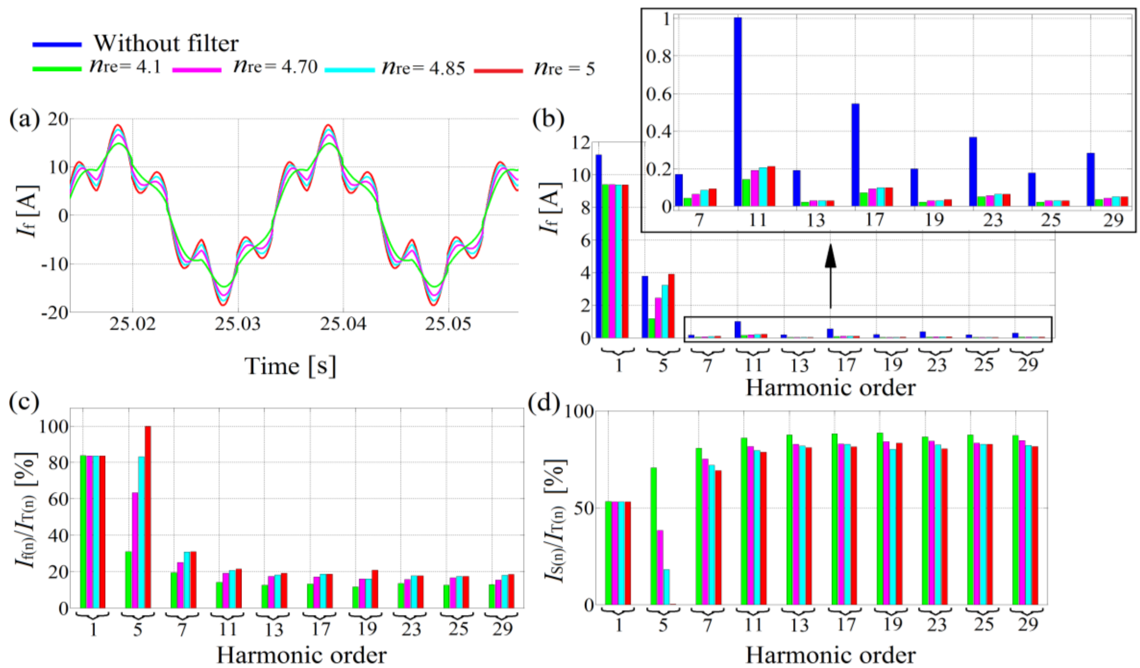

Figure 3.19 (a) filter current waveforms and (b) its spectrum; (c), (d) filter effectiveness

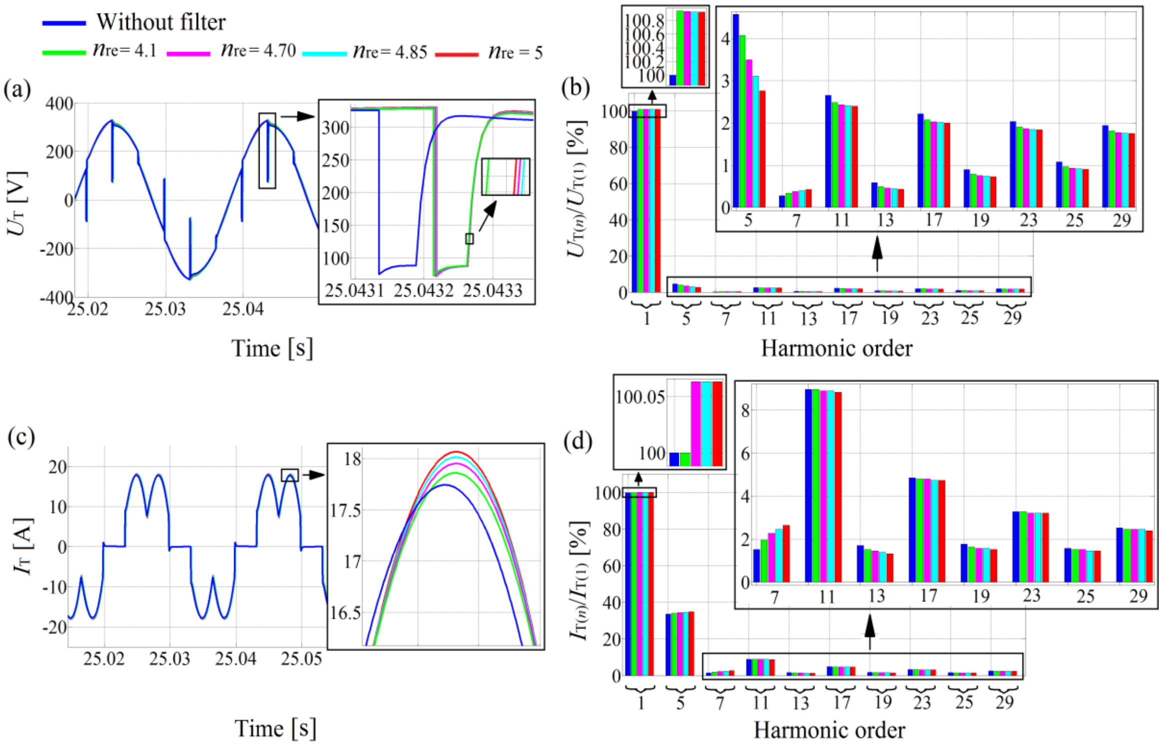

Figure 3.20 (a) voltage at the input of rectifier and (b) its spectrum, (c) current at the input of rectifier (d) its spectrum

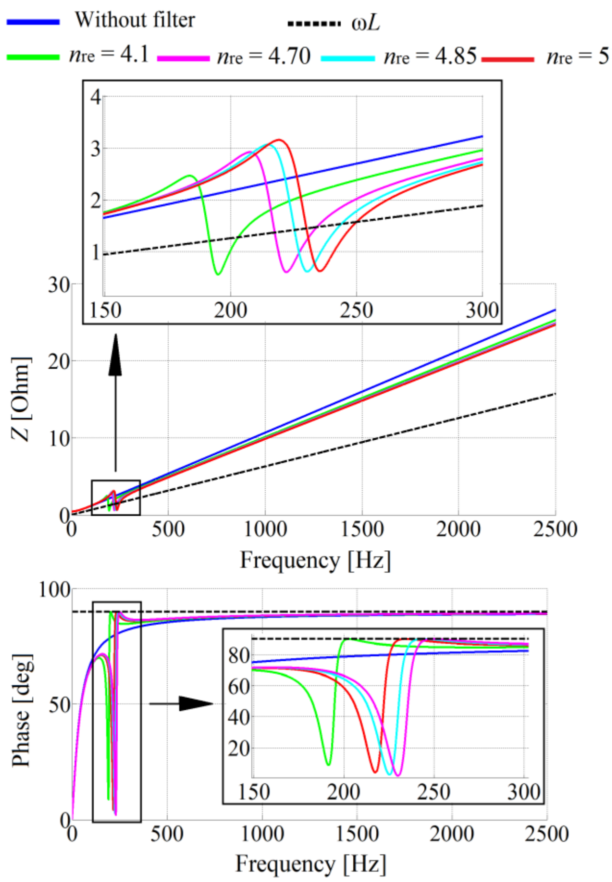

Figure 3.21 Characteristics of power system impedance versus frequency (module and phase) at the thyristor bridge input, ωL- input rectifier reactor reactance

The waveforms of voltage and current at the input of thyristor bridge and their spectrums are presented in Figure 3.20.

The power system impedance versus frequency measured from the input terminals of thyristor bridge is presented in Figure 3.21. On the zoom of that figure, the top of the characteristics represents higher impedance value (parallel resonance), and the bottom represents lower impedance value (series resonance). With the decrease of tuning frequency, the displacement of parallel and series resonances from the higher to lower frequency can be observed. The amplitude of power system impedance at the parallel resonance has decreased.

3.4.1.3 Influence of single-tuned filter resistance on its efficiency

The filter resistance is mostly related to the filter reactor resistance [249]. The q-factor of air-core reactor is between 50 and 150 (MV and HV) and for the iron-core reactor, it is between 20 and 50 (LV) [24, 127].

The goal of this analysis is to present the influence of the filter resistance on the 5th harmonic (takes as example) attenuation efficiency at the PCC. The single-tuned filter is designed to resonate at the frequency of 245.5 Hz (n_{re} = 4.85). The filter quality factor q'' (for the resistance computation – see Table 3.2) and other parameters are presented in Table 3.3.

By increasing of single-tuned filter resistance, the filter impedance of the filtered harmonic (5th) is increased (as shown in Figure 3.22) as well as the filter efficiency.

The grid current and voltage waveforms are shown in Figure 3.23(a) and (c) and the spectrums in Figure 3.23(b) and (d) respectively. After the filter connection, the amplitude of all (apart the grid voltage fundamental harmonic which has increased) gird voltage and current harmonics has decreased (Figure 3.23(b) and (d)).

With the filter resistance increased, the grid voltage fundamental harmonic has little decrease due to the filter resistance voltage drop increased Figure 3.23(b). The PCC current fundamental harmonic has increased because of the filter fundamental harmonic impedance increase (Table 3.3, Figure 3.23(d)).

Table 3.3 Single-branch filter parameters with the increase of its resistance

q''	R_f [mΩ]	$Z_{f(5)}$ [mΩ]	$Z_{f(1)}$ [Ω]	C_f [µF]	L_f [mH]	Q_f [Var] (capacitive)	n_{re}
Inf	0	319.5	24.3498	125.17	3.4	2172.5	4.85
70	74.9	328.1	24.3499				
21	250	405.5	24.3511				
10	524.3	614	24.3555				

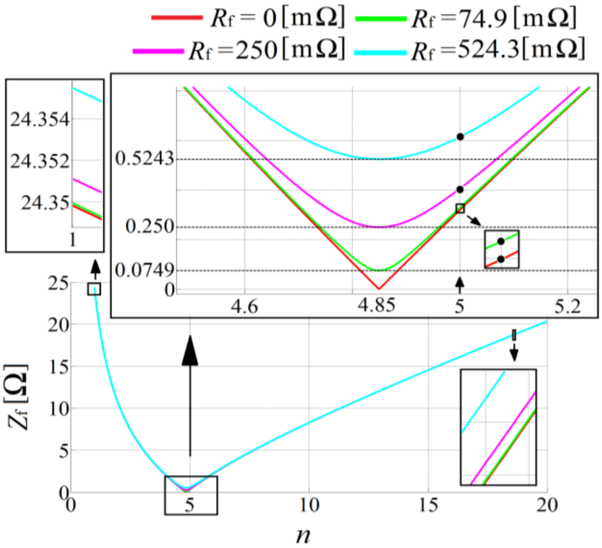

Figure 3.22 Impedance versus frequency characteristics for different filter resistance

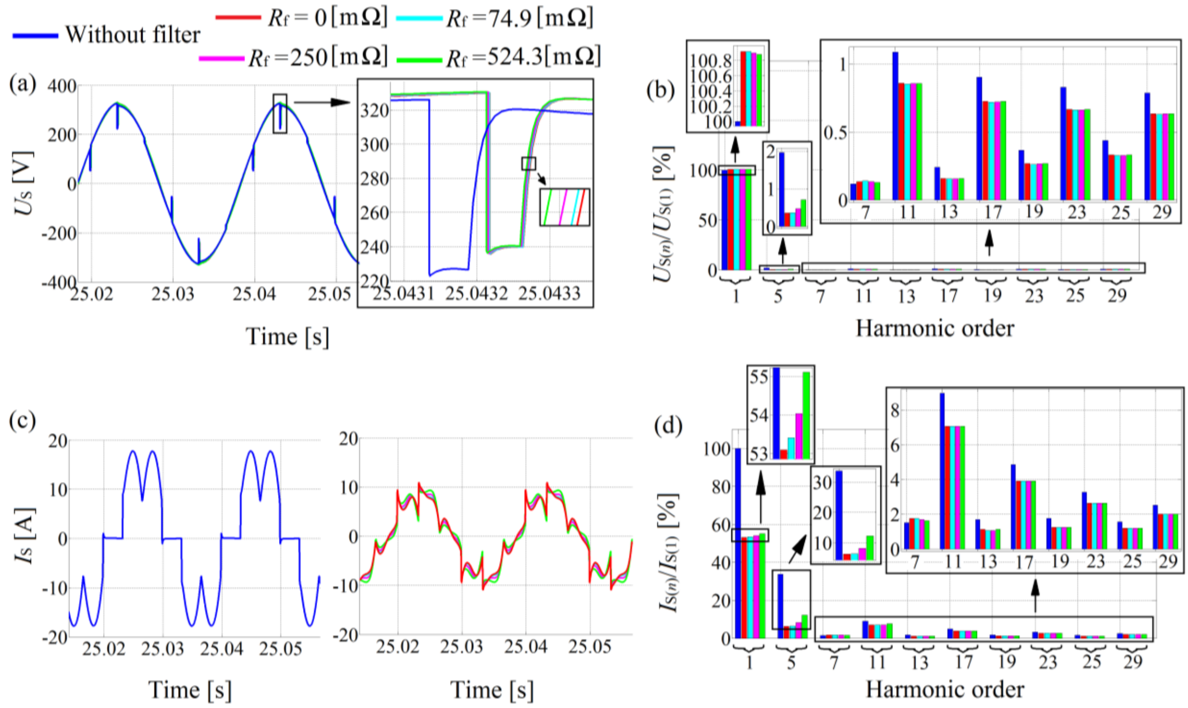

Figure 3.23 Grid voltage (a) and (b) its spectrum (p.u.), grid current (c) and (d) its spectrum (p.u.)

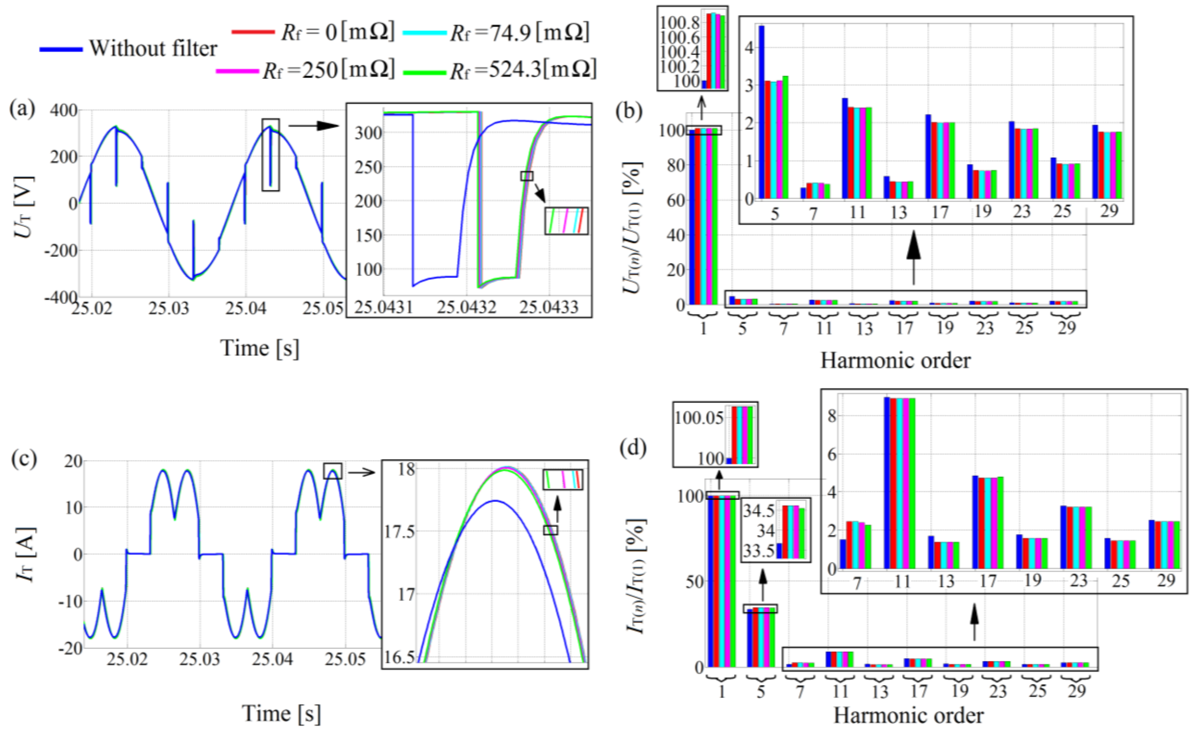

Figure 3.24 Voltage at the input of rectifier (a) and (b) its spectrum (p.c.), current at the input of rectifier (c) and (d) its spectrum (p.u.)

The PCC current and voltage 5th harmonic amplitude has increased with the filter resistance increase, whereas the one of higher harmonics (e.g. 11th to 29th) is almost the same (Figure 3.23(b) and (d)).

The waveforms of voltage and current measured at the input of thyristor bridge are presented in Figure 3.24(a) and (c). The input rectifier voltage and current high harmonics (11th

to 29th) amplitude have decreased after the filter connection and are almost constant during the filter resistance increased (Figure 3.24(b) and (d)).

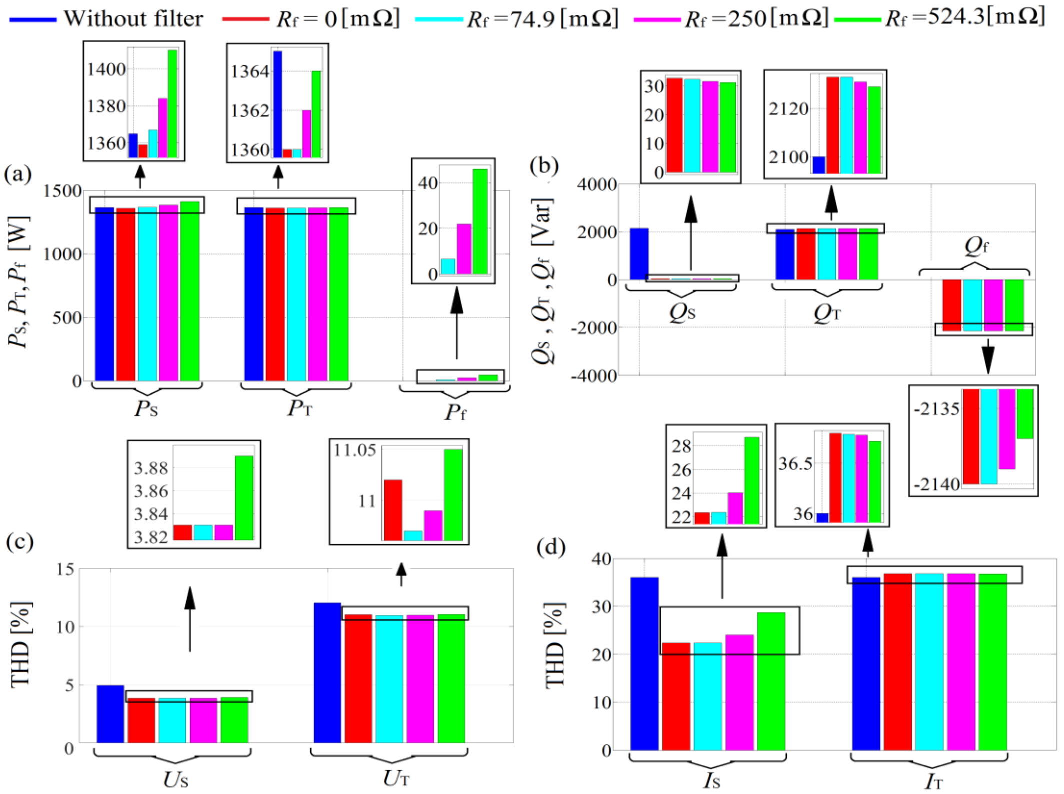

Figure 3.25 (a) and (b) are respectively the active and reactive power measured at the PCC (P_S), filter terminals (P_f) and input of rectifier (P_T), (c) THD of PCC voltage and voltage at the input of rectifier, (d) THD of PCC current and current at the input of rectifier

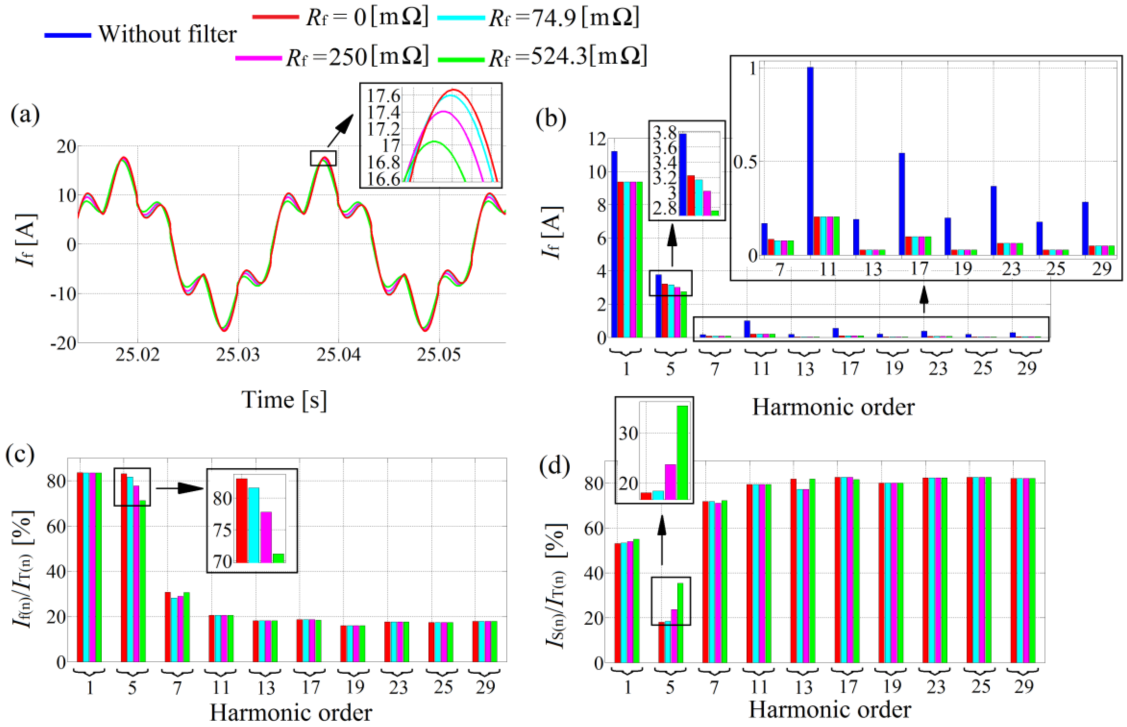

Figure 3.26 Filter current (a) and (b) its spectrum; (c), (d) filter effectiveness

The increase of filter resistance has increased the PCC and filter active power (Figure 3.25(a)). The active power at the input rectifier has decreased after the filter connection but its values has increased with the grow of filter resistance.

After the filter connection, the reactive power at the PCC has considerably decreased and has increased at the rectifier input (Figure 3.25(b)). With the filter resitanse increase, the PCC voltage and current distortion has increased (Figure 3.25 (c)) as well as the distortion of the input rectifier voltage (the one of the current (I_T) has little decreased) (Figure 3.25 (d)).

The filter current waveforms and their spectrum are respectively shown in Figure 3.26(a) and (b). Less current of 5th harmonic flows through the filter when its resistance is high (Figure 3.26(b)). The filter is less effective with high resistance (Figure 3.26(c) and (d)).

According to the characteristics of power system impedance seen from the rectifier input (Figure 3.27(a)), the parallel and series resonance are damped with the single-tuned filter resistance increase.

Figure 3.27(b) presents the influence of grid inductance variation (grid short circuit power variation as well) on the power system impedance seen form the thyristor bridge input. With the increase of the grid inductance (decreasing of the short circuit power), the system impedance increases at the parallel resonance, decreases at the series resonance and the frequencies at the parallel resonance decrease as well as the series resonance frequencies.

In the further part of this work, for certain filter damping resistance range, the properties of the later discussed passive harmonic filter structures (broad-band filters, e.g. second-order and C-type filter) will lead to those of the single-tuned filter structure.

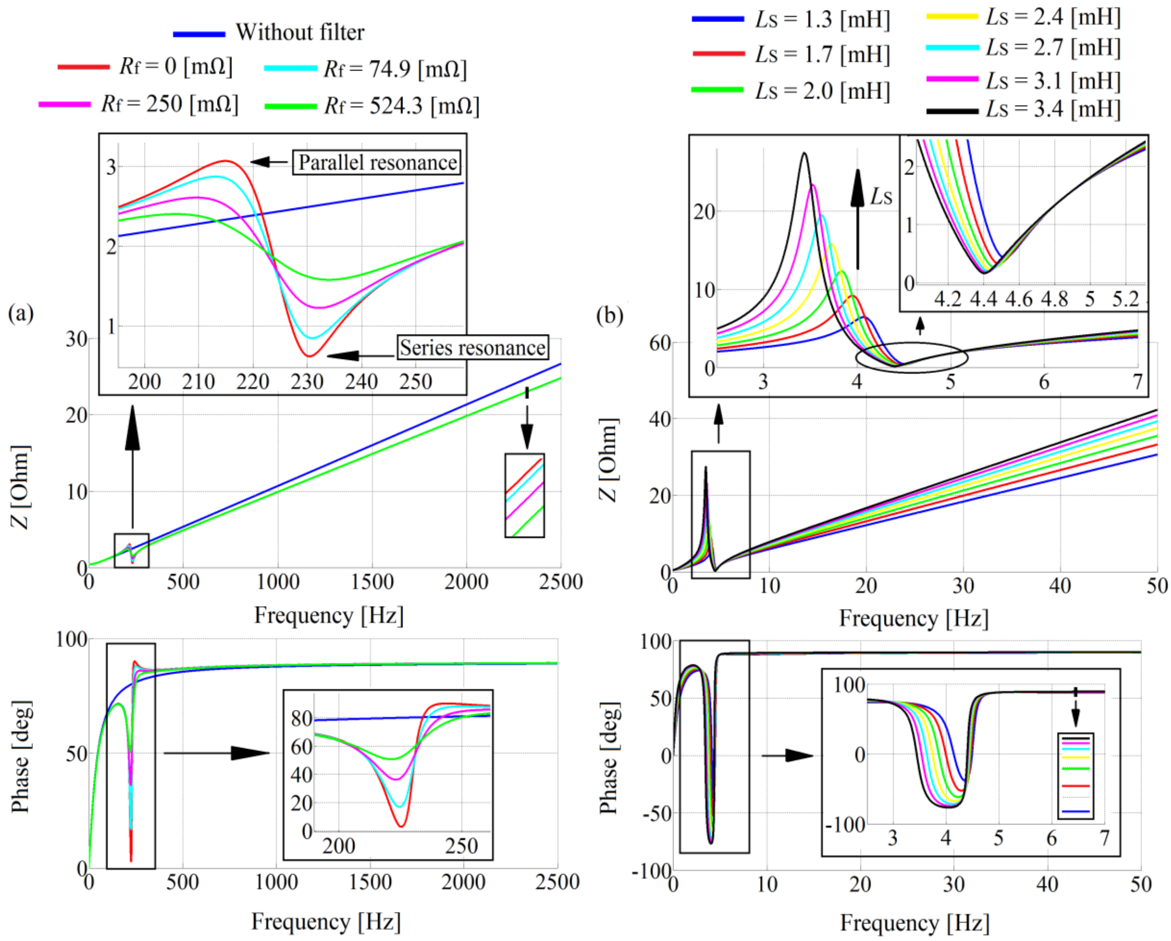

Figure 3.27 Power system impedance versus frequency characteristics (module and phase) measured at the thyristor bridge input terminals for: (a) different values of filter resistance, (b) different values of grid inductance

3.4.2 Double-tuned filter

The double-tuned filter presented in Figure 3.5(b) is constituted of series part (Z_{f1}) and parallel part (Z_{f2}). As its name indicates, it can be tuned to two different frequencies. According to [61, 217, 218, 266], the funtionality of the double-tuned filter is almost the same as the one of the group of two single-tuned filters. In this chapter, both topologies are compaired for more clarification. Many topologies of double-tuned filter exist [145, 275] and Figure 3.5(b) presents the most common one. Different algorithms [144, 184, 260, 275] are used for the double-tuned filter parameters computation. The parameters of double-tuned filter (designed and tested in the power system of Figure 3.5(a)) were computed basing on the equations of Table 3.4.

Table 3.4 Equations for double-tuned filter parameters computation ($R_f = 0$)

Resonance frequency of the series part	$\omega_a = \frac{1}{\sqrt{C_{f1}L_{f1}}} = n_a\omega_{(1)}$
Resonance frequency of the parallel part	$\omega_b = \frac{1}{\sqrt{C_{f2}L_{f2}}} = n_b\omega_{(1)}$
Series part equivalent impedance	$\underline{Z}_{f1}(j\omega) = j\omega L_{f1} - j\frac{1}{\omega C_{f1}} = j\frac{\omega^2-\omega_a^2}{\omega_a^2\omega C_{f1}}$
Parallel part equivalent impedance	$\underline{Z}_{f2}(j\omega) = j\frac{\omega L_{f2}}{1-\omega^2 C_{f2}L_{f2}} = j\frac{\omega}{C_{f2}(\omega^2-\omega_b^2)}$
Filter impedance	$\underline{Z}_f(j\omega) = \underline{Z}_{f1}(j\omega) + \underline{Z}_{f2}(j\omega) = j\frac{\omega^4 C_{f2} - \omega^2(C_{f2}\omega_b^2 + C_{f2}\omega_a^2 + C_{f1}\omega_a^2) + C_{f2}\omega_b^2\omega_a^2}{\omega_a^2\omega C_{f1}C_{f2}(\omega^2-\omega_b^2)}$
Filter series resonance angular frequencies (see also Figure 3.28)	$\omega_{re1,2} = \sqrt{\frac{C_{f2}\omega_b^2 + C_{f2}\omega_a^2 + C_{f1}\omega_a^2 \pm \sqrt{(C_{f2}\omega_b^2 + C_{f2}\omega_a^2 + C_{f1}\omega_a^2)^2 - 4\omega_b^2 C_{f2}\omega_a^2}}{2C_{f2}}}$ $\omega_{(re1)} = n_{re1}\omega_{(1)}$, $\omega_{(re2)} = n_{re2}\omega_{(1)}$
Relation between the resonance frequencies in the considered circuit	$\omega_a = \frac{\omega_{re1}\omega_{re2}}{\omega_b}$ (on the base of [145], this equation can be proved) $n_{re1} > n_b > n_{re2} > 1$
Relation between filter capacitors	$C_{f2} = C_{f1}\frac{\omega_{re1}^2\omega_{re2}^2}{\omega_b^2(\omega_{re1}^2+\omega_{re2}^2-\omega_b^2) - \omega_{re1}^2\omega_{re2}^2}$
Filter impedance represents in other way	$\underline{Z}_f(j\omega) = j\frac{(\omega^2-\omega_b^2)(\omega^2\omega_b^2-\omega_{re1}^2\omega_{re2}^2) - \omega^2\omega_{re1}^2\omega_b^2 - \omega^2\omega_{re2}^2\omega_b^2 + \omega^2\omega_{re1}^2\omega_{re2}^2 + \omega^2\omega_b^4}{\omega_{re1}^2\omega_{re2}^2\omega C_{f1}(\omega^2-\omega_b^2)}$
Filter impedance for the fundamental harmonic	$Z_{f(1)} = \frac{n_b^2(1-n_{re2}^2)(1-n_{re1}^2)}{n_{re1}^2 n_{re2}^2 C_{f1}(1-n_b^2)\omega_{(1)}} = \frac{U_f^2}{Q_f}$
$C_{f1} = \frac{n_b^2(1-n_{re2}^2)(1-n_{re1}^2)}{n_{re1}^2 n_{re2}^2(1-n_b^2)}\frac{Q_f}{\omega_{(1)}U_f^2}$	$L_{f1} = \frac{(1-n_b^2)}{(1-n_{re2}^2)(1-n_{re1}^2)}\frac{U_f^2}{\omega_{(1)}Q_f}$
$C_{f2} = \frac{n_b^2(1-n_{re2}^2)(1-n_{re1}^2)}{(1-n_b^2)(n_{re1}^2 n_b^2 + n_{re2}^2 n_b^2 - n_{re1}^2 n_{re2}^2 - n_b^4)}\frac{Q_f}{\omega_{(1)}U_f^2}$	$L_{f2} = \frac{(1-n_b^2)(n_{re1}^2 n_b^2 + n_{re2}^2 n_b^2 - n_{re1}^2 n_{re2}^2 - n_b^4)}{n_b^4(1-n_{re2}^2)(1-n_{re1}^2)}\frac{U_f^2}{\omega_{(1)}Q_f}$

Table 3.5 Example of double-tune filter parameters

Q_f = 2172.5 [Var] (capacitive); U_f = 230 [V]										q'
n_{re}	$C_{f1(1)}$ [μF]	$L_{f1(1)}$ [mH]	R_{Lf1} [mΩ]	$C_{f2(1)}$ [μF]	$L_{f2(1)}$ [mH]	R_{Lf2} [mΩ]	$Z_{f(1)}$ [Ω]	$Z_{f(5)}$ [Ω]	$Z_{f(7)}$ [Ω]	
n_{re1} = 4.85	126	2.6	8.7	1000	0.27	0.91	24.34	0.48	0.479	95
n_b = 6										
n_{re2} = 6.85										

In the further part of this work, the parameters in Table 3.5 are used to present the filter filtration properties. The filter reactors resistance (R_{Lf1}, R_{Lf2}) are considered in the simulation process (see Table 3.5).

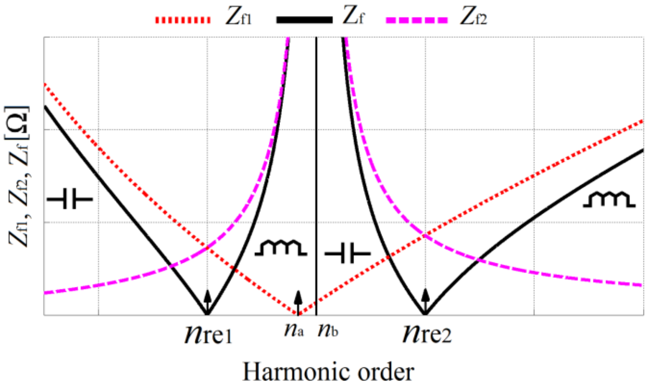

Figure 3.28 Impedance versus frequency characteristics of the series part (Z_{f1}), parallel part (Z_{f2}) and whole double-tuned filter (Z_f)

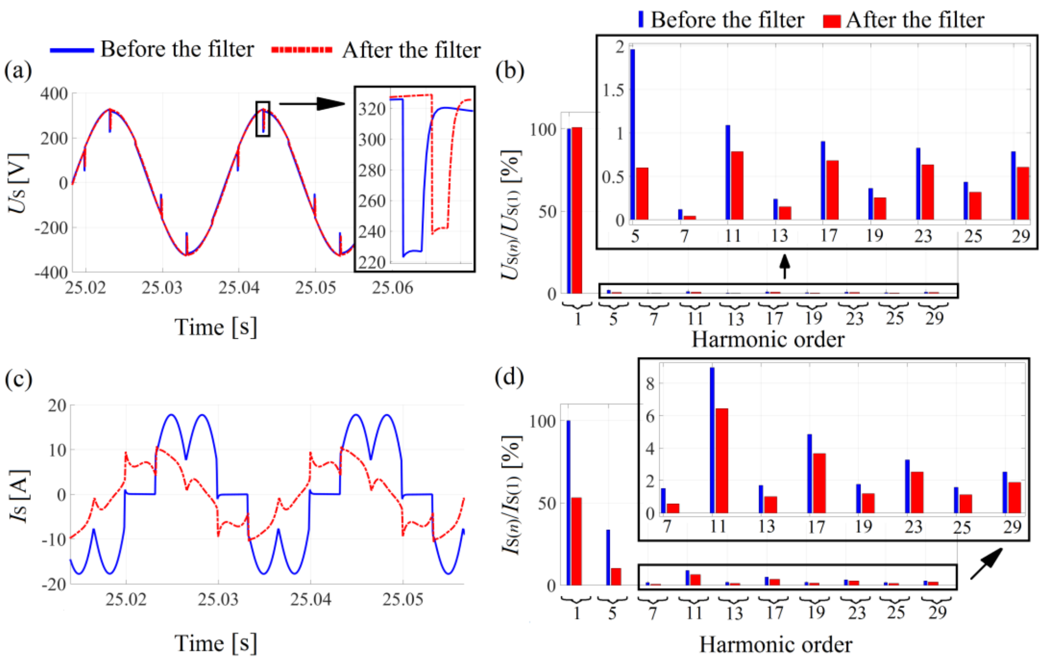

Figure 3.29 (a) grid voltage and (b) its spectrum, (c) grid current and (d) its spectrum

Table 3.6 Electrical system active and reactive power

	P_S [W]	Q_S [Var]	P_f [W]	Q_f [Var]	Q_L [Var]	P_T [W]	Q_T [Var]
Before	1365	2140	-	-	39.53	1365	2100
After	1361	31.2	0.82	-2141	11.58	1360	2133

Figure 3.28 presents the impedance versus frequency characteristics of the parallel part (Z_{f2}); series part (Z_{f1}) and of the whole filter (Z_f). In the considered example, the filter is tuned to the frequencies of 242.5 Hz (n_{re1} = 4.85) and 342.5 Hz (n_{re2} = 6.85). The filter is capacitive for the fundamental harmonic.

The 5th and 7th order harmonics (PCC) have considerably decreased after the filter connection (Figure 3.29(b) and (d)). The double-tuned filter has improved the grid current waveform (Figure 3.29(c)) and reduced the depth of the commutation notches (Figure 3.29(a)).

In Figure 3.29(b) and (d), it can be observed the reduction of harmonics higher than the 5th and the 7th after the filter connection. The system powers (active and reactive) before and after the double-tuned filter connection are presented in Table 3.6.

The power system impedance versus frequency characteristic observed from the thyristor rectifier terminals is presented in Figure 3.30. The parallel resonances between the filter and the grid can be observed.

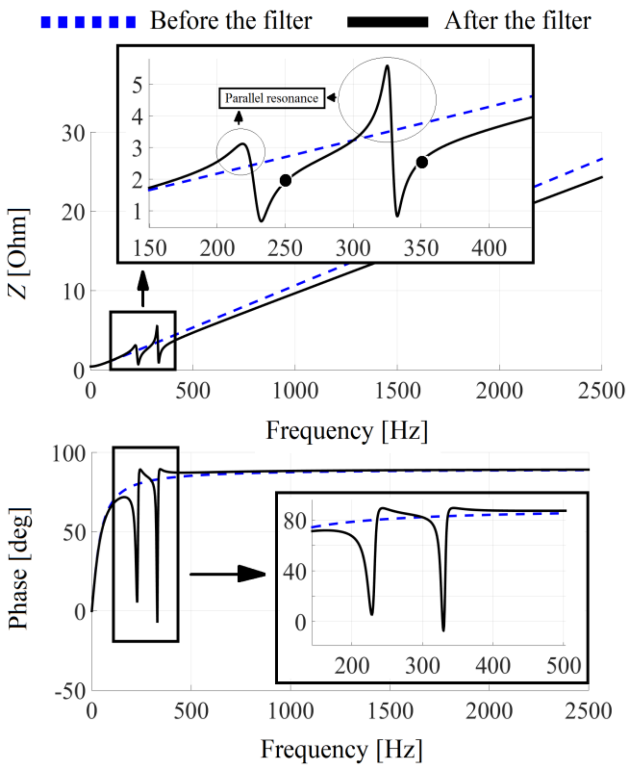

Figure 3.30 Power system impedance versus frequency characteristics (module and phase) measured at the thyristor bridge input terminals

3.4.2.1 Comparison between the group of two single-tuned filters and the double-tuned filter

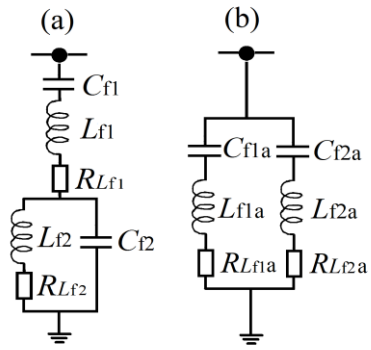

Figure 3.31 (a) double-tuned filter, (b) group of two single-tuned filters

The comparison is performed basing on the assumptions that the double-tuned filter and filter group (see Figure 3.31(a) and (b)) have the same reactive power (Q_f = 2172.5 [Var]), voltage (U_f = 230 [V]) and the reactors quality factor (q'=45). The capacitors resistances are neglected and the load parameters are constant.

The filter group and double-tuned filter parameters are presented in Table 3.7 (in comparison to Table 3.5, the double-tuned filter reactors quality factor is a bit small in Table 3.7 to increase the filter power losses). The filter group parameters are computed basing on Table 3.2.

The impedance versus frequency characteristics in Figure 3.32 show that the double-tuned filter has the lowest 5th harmonic impedance and the highest 7th harmonic impedance whereas the filter group has the lower impedance for the higher harmonics (e.g. from the 11th) in wide band.

Table 3.7 Filter group and double-tuned filter parameters

Q_f = 2172.5 [Var] (capacitive), U_f = 230 [V]										
Filter group										q'
n_{re}	Q_{f1} = 1086.3 [Var]			Q_{f2} = 1086.3 [Var]			$Z_{f(1)}$[Ω]	$Z_{f(5)}$[Ω]	$Z_{f(7)}$[Ω]	
	C_{f1a} [μF]	L_{f1a} [mH]	R_{Lf1a} [mΩ]	C_{f2a} [μF]	L_{f2a} [mH]	R_{Lf2a} [mΩ]				
4.85 6.85	62.58	6.9	48.1	63.96	3.4	23.6	24.35	0.74	0.30	45
Double-tuned filter										
n_{re}	$C_{f1(1)}$ [μF]	$L_{f1(1)}$ [mH]	R_{Lf1} [mΩ]	$C_{f2(1)}$ [μF]	$L_{f2(1)}$ [mH]	R_{Lf2} [mΩ]	$Z_{f(1)}$ [Ω]	$Z_{f(5)}$ [Ω]	$Z_{f(7)}$ [Ω]	
4.85 6 6.85	126	2.6	18.3	1000	0.27	1.9	24.35	0.48	0,48	

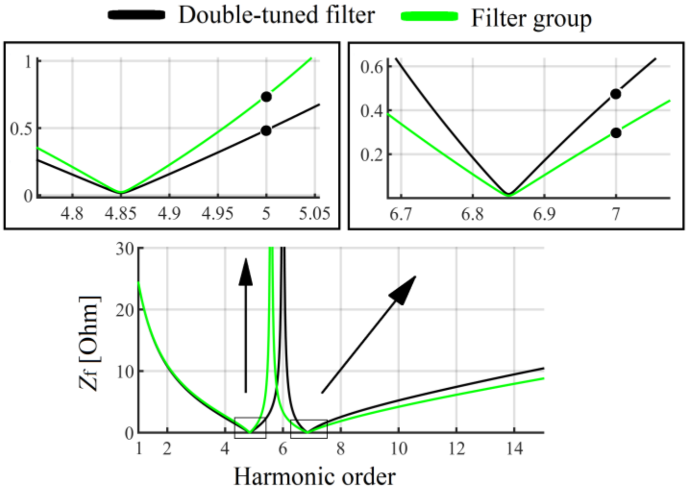

Figure 3.32 The impedance vs frequency characteristic of double-tuned filter (black color) is compared to the one of filter group (green color)

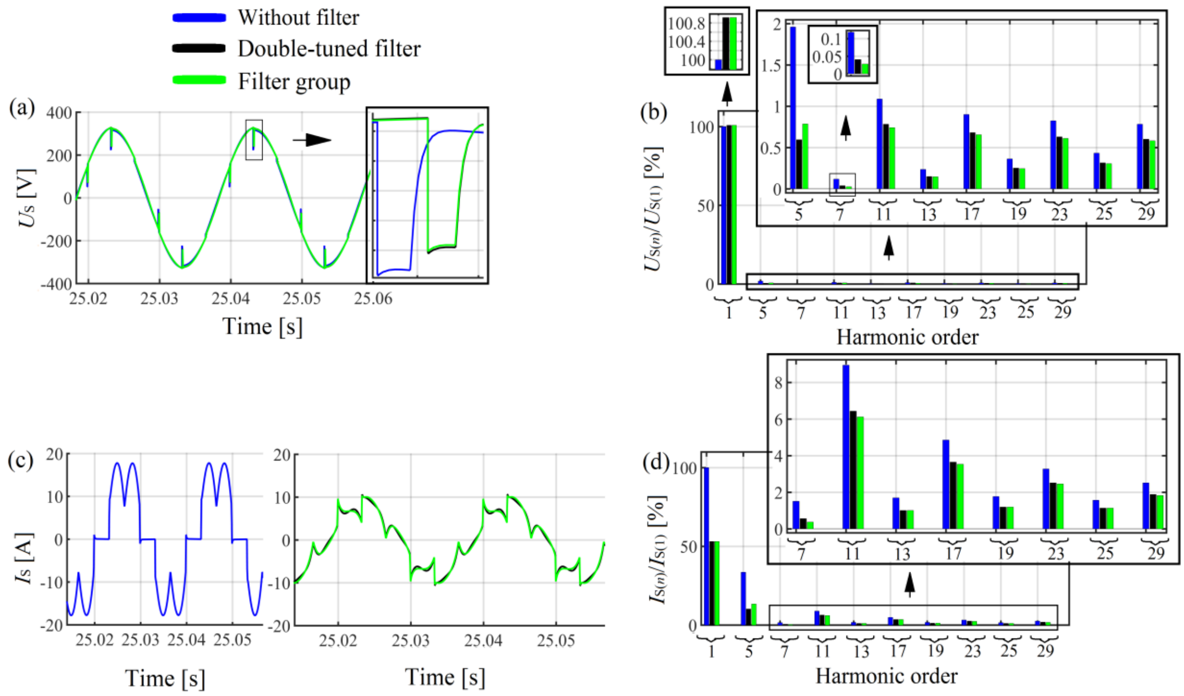

Figure 3.33 grid voltage waveforms and (b) their spectrums, (c) grid current waveforms and (d) their spectrums

The double-tuned filter and filter group have almost the same grid voltage and current waveforms (Figure 3.33 (a)(c)) but the double-tuned filter has the best filtered the grid voltage and current 5th harmonics and the worst filtered the grid voltage and current 7th harmonic (Figure 3.33(b) and (d)).

The filter group has lower grid reactive power (Q_S) and power losses (P_f) (Figure 3.34(a)) and its grid voltage THD is a bit smaller than the one of double-tuned filter (Figure 3.34(b)). The double-tuned filter has lower grid current THD (Figure 3.34(b)).

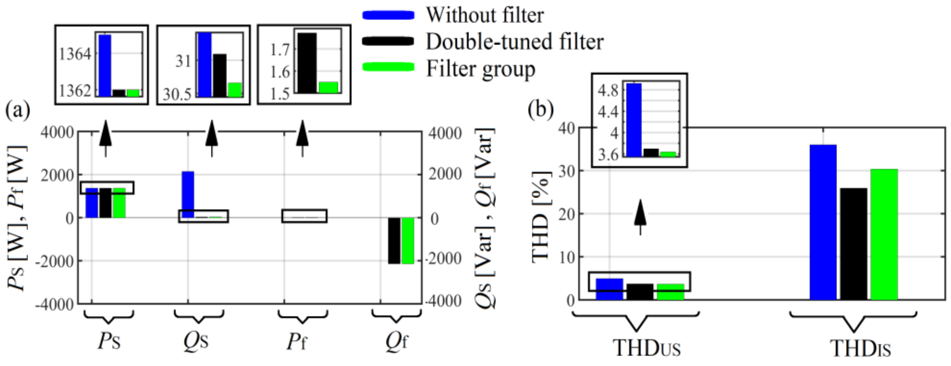

Figure 3.34 (a) grid and filters active and reactive powers; (b) grid voltage and current THD

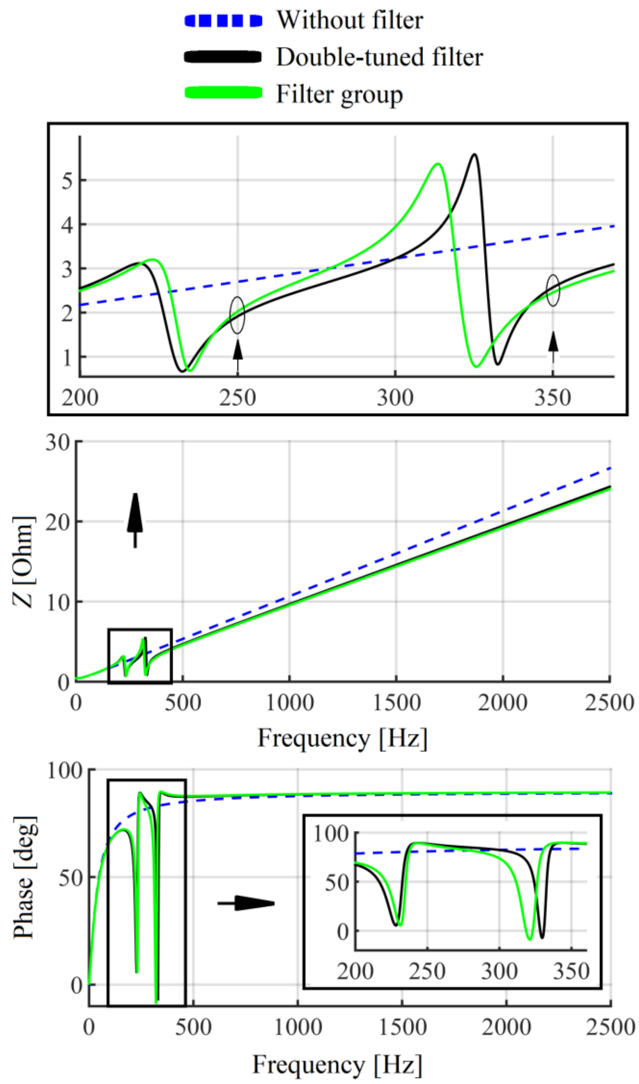

Figure 3.35 Characteristics (double-tuned filter and filter group) of power system impedance versus frequency observed from the thyristor bridge input (module and phase)

The power system impedance versus frequency characteristics (Figure 3.35) observed at the thyrystor bridge input show that for both configurations, the parallel resonances have occurred bellow 250 Hz and 350 Hz.

In the considered example, the double-tuned filter is more recommendable for the electrical systems in which the lowest generated current characteristic harmonic (after the fundamental) has the highest amplitude. However, from the power losses point of view and high harmonics reduction in width range, the filter group is better.

3.4.3 BROAD-BAND FILTERS

3.4.3.1 1st order filter

The capacitor bank (as shown in Figure 3.36(a)) designed for reactive power compensation can be included in the category of PHFs even though the harmonics filtration is not the goal of such installations. Its equivalent impedance versus frequency (see Figure 3.36(b)) shows that it possess better filtration properties for higher harmonics mostly for high capacitor reactive power (e.g. 20 kVar see Figure 3.36(b)) and low equivalent resistance circuit representing the power losses. In the case of nowadays capacitors bank, the power losses related to kVar are very small; therefore, their resistance can be neglected.

Two cases of study are considered in this chapter: in the first one, the capacitor bank (R_{Cf} and R neglected) is applied for reactive power compensation and in the second one, the capacitor bank (R = 0.25, R_{Cf} = 0) is applied with different value of reactive power.

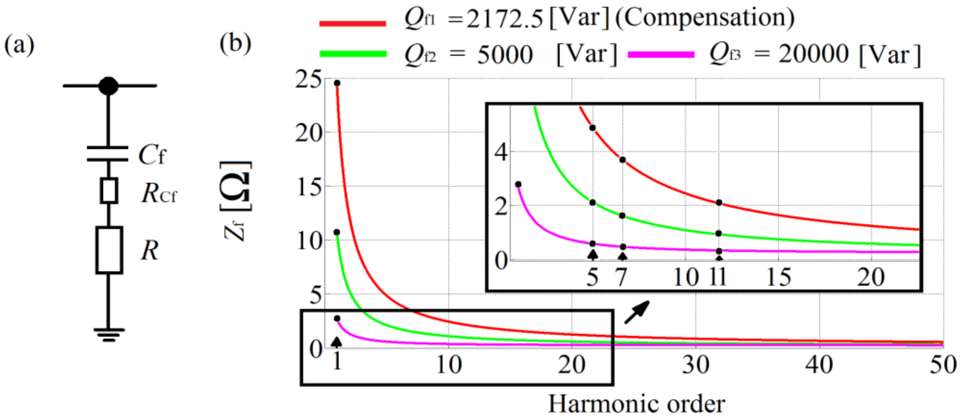

(c) Capacitor bank parameters (R_{Cf} = 0; R = 0.25 Ω)

	C_f [μF]	$Z_{f(1)}$ [Ω]	$Z_{f(5)}$[Ω]	$Z_{f(7)}$[Ω]
Q_{f1} = 2172.5 [Var]	130.72	24.3511	4.87	3.48
Q_{f2} = 5000 [Var]	300.86	10.58	2.13	1.53
Q_{f3} = 20000 [Var]	1200	2.656	0.58	0.45

Figure 3.36 (a) 1st order filter, (b) capacitor bank impedance versus frequency characteristics (R_{Cf} = 0; R = 0.25 Ω) and (c) capacitor bank parameters

Table 3.8 Capacitor bank equations

$R_{Cf} \neq 0$ and $R \neq 0$	
Capacitor bank impedance	$\underline{Z}_{Cf}(jn) = R_{Cf} + R - j\frac{1}{n\omega_{(1)}C_f}$
$R_{Cf} = R = 0$	
Capacitor bank reactance	$\underline{X}_{Cf}(j\omega) = -j\frac{1}{\omega_{(1)}C_f} = -j\frac{1U_{Cf}^2}{Q_{Cf}}$
Capacitor bank equivalent capacitance	$C_f = \frac{Q_{Cf}}{\omega_{(1)}U_{Cf}^2}$

In the considered example of the first case study, after the capacitor connection, the PCC reactive power has reduced (from 2140 Var to 19.97 Var) and the DPF has increased from 0.53 to 0.99 (Table 3.9). The compensation was done successfully but the reduction of voltage and current distortion remains a problem. The waveforms of PCC current and voltage before and after the capacitor connection are presented in Figure 3.37(a).

The capacitor bank connection has caused the resonance amplification of PCC voltage and current harmonics especially the 11th (Figure 3.37(b)). After the capacitor connection, the grid current and voltage waveforms have changed (Figure 3.37(a)) and their THD has increased from 4.93% to 6.03% for the voltage and from 36% to 116.29% for the current (Figure 3.37(b)).

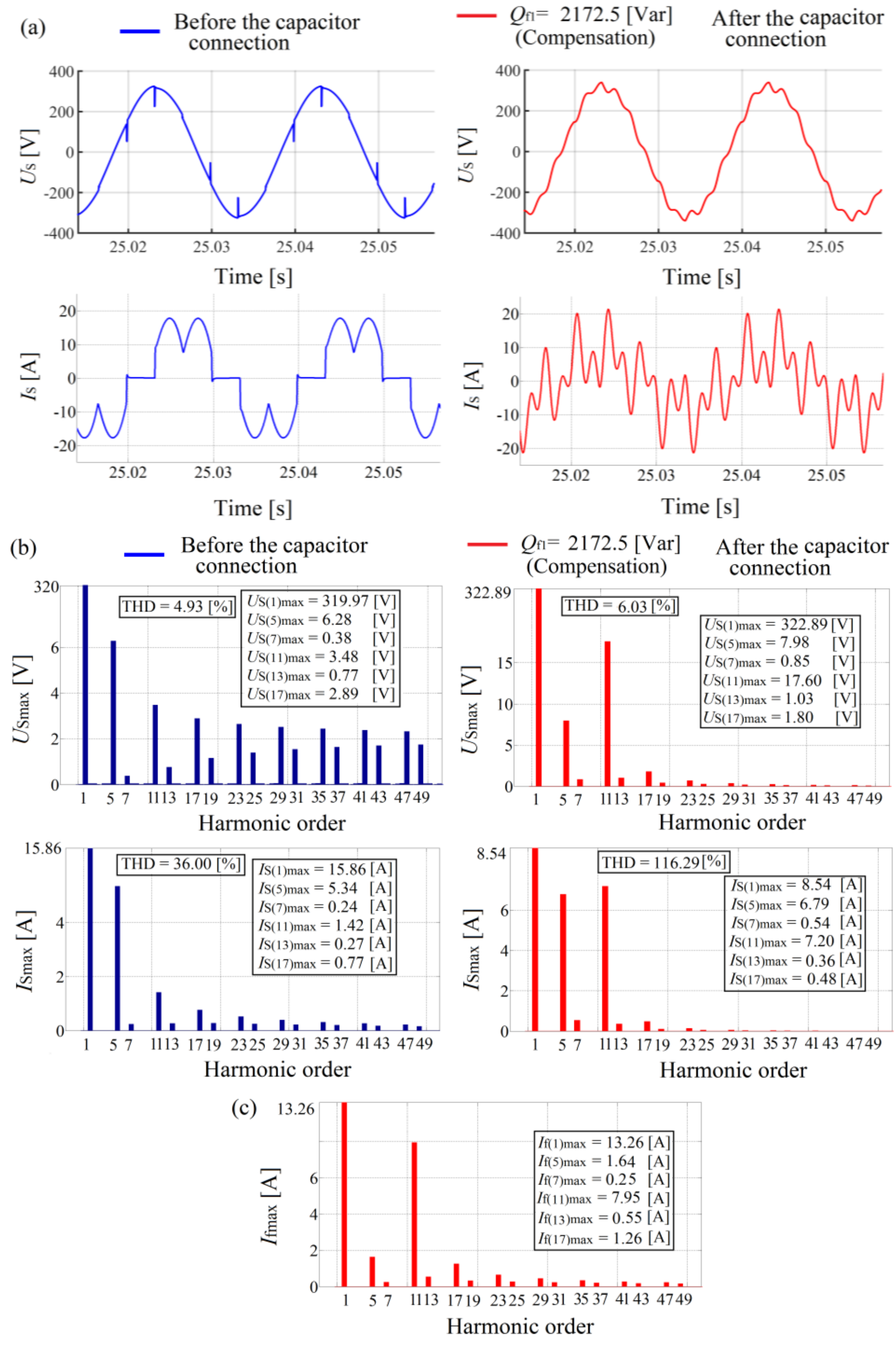

Figure 3.37 (a) grid Voltage and current waveforms and (b) their spectrums before and after the capacitor connection, (c) capacitor current spectrum. U_{Smax}, I_{Smax} and I_{fmax} are the amplitudes of sinusoidal waveforms ($R = R_{Cf} = 0$)

Table 3.9 Power system reactive and active power ($R = R_{Cf} = 0$)

	Measured values							
	Grid (PCC)			Capacitor		Line reactor (L)	Input of thyristor bridge	
	P_S [W]	Q_S [Var]	DPF	P_{Cf} [W]	Q_{Cf} [Var]	Q_L [Var]	P_T [W]	Q_T [Var]
Without filter	1365	2140	0.5378	-	-	39.53	1365	2100
With capacitor	1380	19.97	0.999	-	-2141	39.5	1380	2118

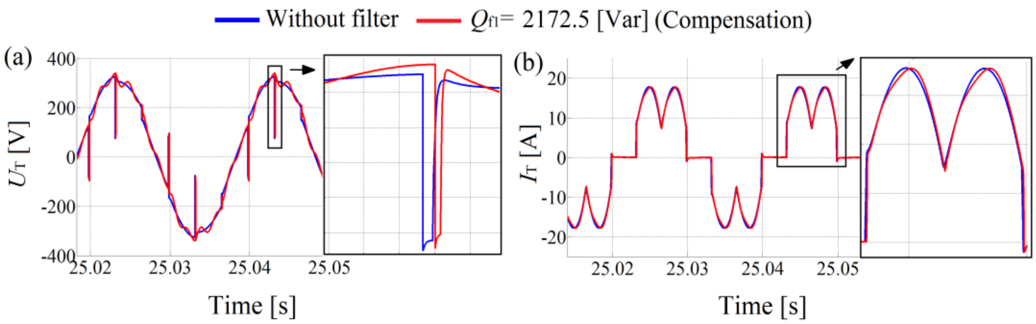

Figure 3.38 Rectifier input voltage (a) and current (b) waveforms ($R = R_{Cf} = 0$)

Table 3.10 Parameters of grid voltage and current ($R = R_{Cf} = 0$)

	$U_{S\,max}$ [V]				$I_{S\,max}$ [A]			
n	Without filter		Q_{Cf} = 2172.5 [Var]		Without filter		Q_{Cf} = 2172.5 [Var]	
	Ampl.	Phase	Ampl.	Phase	Ampl.	Phase	Ampl.	Phase
1st	319.97	30.7	322.89	29.7	15.86	-26.8	8.54	29.0
5th	6.28	-67.4	7.98	-79.1	5.34	43.9	6.79	32.2
7th	0.38	10.6	0.85	-33.9	0.24	116.7	0.54	71.7
11th	3.48	-34.3	17.60	207.7	1.42	65.7	7.20	-52.3
13th	0.77	-74	1.03	68.6	0.27	24.9	0.36	167.2
17th	2.89	-11.1	1.80	162.1	0.77	85.4	0.48	258.7
19th	1.17	-60.1	0.43	103.0	0.28	36	0.10	198.9
23rd	2.65	9.4	0.70	172.7	0.52	104.1	0.14	267.6
25th	1.4	-43.4	0.27	114.3	0.25	51.3	0.05	208.8
29th	2.52	28.6	0.38	184.7	0.4	122.3	0.06	-81.4
THD [%]	4.93		6.03		36		116.29	
Grey shaded area indicates the frequency (e.g. 17th) from which the capacitor has started to reduce the higher harmonics (e.g. 17th, 19th etc.) and to which it has amplified the lower harmonics (e.g. 5th, 7th and 13th) in comparison to the case without filter.								

The capacitor bank has reduced the amplitude of higher order harmonics (from the 17th) of grid current and voltage (Table 3.10, Q_{f1} = 2172.5Var). This situation occurs frequently when the capacitor bank is used (without the detuning reactor) to improve the DPF for the distorted voltages and currents. The spectrum of capacitor current is show in Figure 3.37(c).

The waveforms of voltage and current at the input of thyristor bridge are presented in Figure 3.38(a) and (b). The reduction of voltage commutation notches width is observed after the capacitor connection (Figure 3.38 (a)).

The filter current waveforms and spectrum are indicated in Figure 3.39(a) and (b). The filter current is capacitive (Figure 3.39(a)) and dominated by the fundamental harmonic though it is also bulked by the higher harmonics, which in comparison to the generated load harmonics (before the filter connection) have been a little bit amplified. Figure 3.39(c) and (d) shows that the capacitor bank can effective reduce the harmonics in width range (e.g. 17th - 29th).

The impedance of power system (Z) measured from the input of thyristor bridge is presented in Figure 3.40. When the line reactor (L) at the rectifier input is not connected, the characteristic (green color) presents only the parallel resonance (at 528 Hz, n_{re} = 10.56) between the grid inductance and capacitor bank. Observing the characteristic (red color) when the line reactor is considered, the parallel resonance remains but is shifted (from 528 Hz to 516 Hz (n_{re} = 10.32)). The series resonance between the parallel connected grid inductance with capacitor and input rectifier inductance can been seen as well.

In Figure 3.40, the characteristics allow to explain the amplification of certain harmonics and the reduction of others in power system at the PCC. The characteristics in red color (with line reactor) and green color have a common point (812 Hz, n = 16.24). On the one hand, all the frequencies (below the series resonance frequency 686 Hz (n = 13.72) - characteristic in red color) from the frequency of the 1st to 13th harmonic are under the parallel resonance (see also Table 3.10) and on the other hand, the frequencies above 686 Hz (From the 17th) are reduced (Table 3.10).

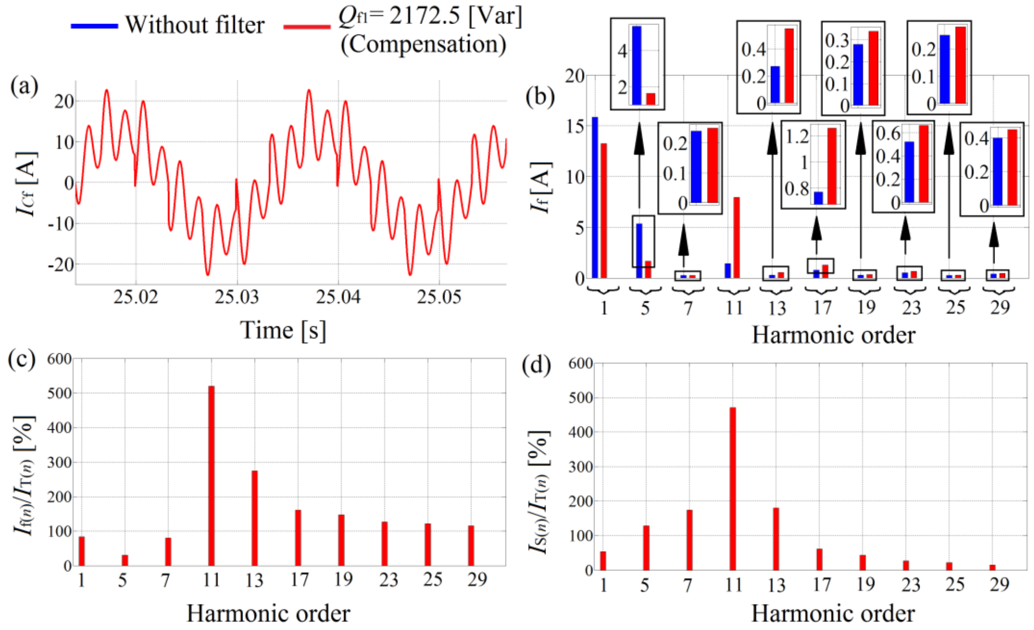

Figure 3.39 (a) Capacitor bank current characteristic and (b); (c) and (d) capacitor filtration efficiency ($R = R_{Cf}$ = 0)

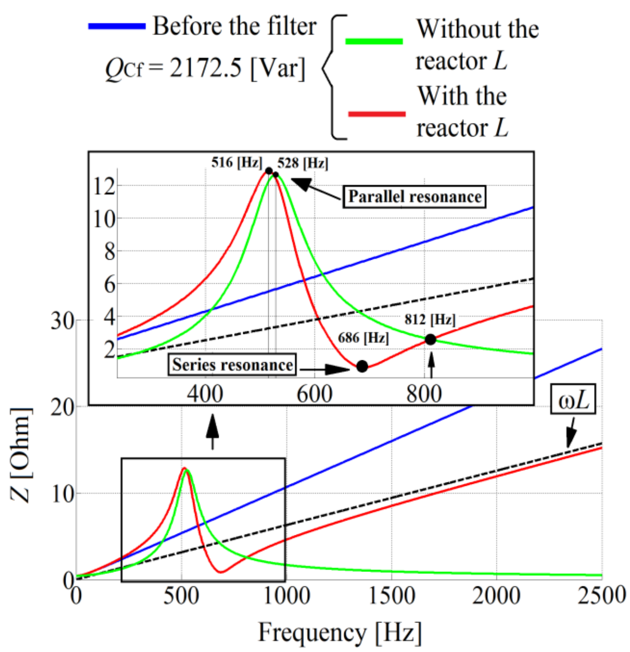

Figure 3.40 Power system impedance frequency characteristic measured at the input terminals of thyristor bridge with and without the line reactor at the rectifier input ($R = R_{Cf}$ = 0)

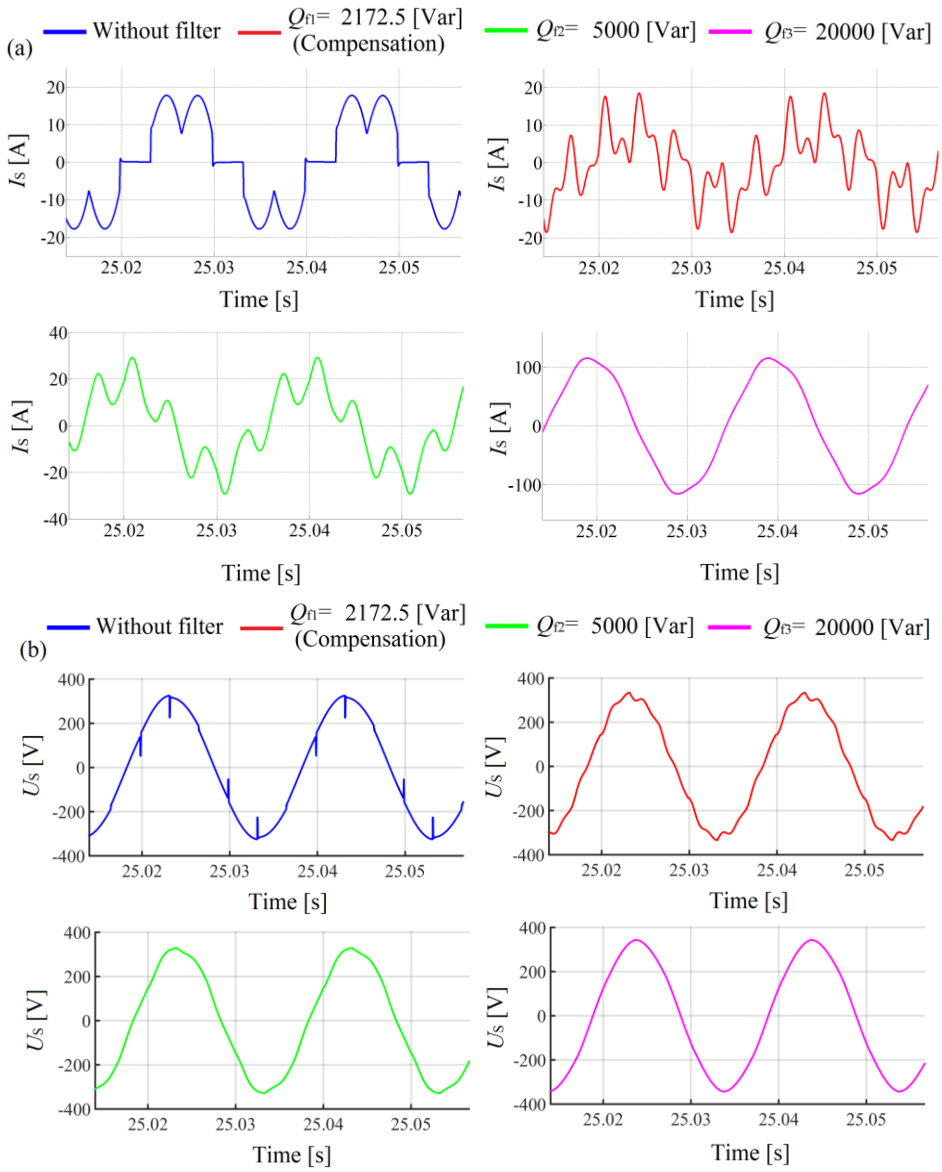

Figure 3.41 Grid current (a) and voltage (b) characteristics for different values of capacitors bank reactive power (R_{Cf} = 0, R = 0.25 Ω

The second case study example (R = 0.25 Ω, R_{Cf} = 0) shows that the increase of capacitor reactive power (capacitor capacitance as well) is characterized by the capacitor equivalent impedance reduction (e.g. in Figure 3.36(b); Q_{f3} = 20 kVar - the capacitor can be then more charged by harmonics) and the parallel and series resonances displacement to the lower frequencies (see Figure 3.47(a)).

The capacitor bank characteristics for different values of its capacity is presented in Figure 3.36(b). The impedances of 1st, 5th, 7th etc. harmonic have decreased with the reactive power increase (Figure 3.36(a)).

Figure 3.41(a) and (b) presents (respectively) the variation of PCC current and voltage waveforms with the increase of the capacitor reactive power. This increase has improved the THD of grid voltage and current (efficient harmonics reduction for 20 kVar) at the PCC, but a large overcompensation for fundamental harmonic (characterized by its amplification) is observed in the power system (see Table 3.11).

By increasing the capacitor bank reactive power from 2172.5 Var to 20 kVar, the reduction of the realative value of the grid voltage and current harmonics(in comparison to the case without filter) has started form the 17th for Q_{f1}, from the 11th for Q_{f2} and from the 5th for Q_{f3} (see also Figure 3.42(a) and (b)).

Table 3.11 PCC voltage and current parameters (R_{Cf} = 0, R = 0.25 Ω)

U_S [V]/ I_S [A]				
n	Without filter	Q_{f1}=2172.5 Var	Q_{f1}=5 kVar	Q_{f1}=20 kVar
1st	319.97/15.86	322.83/8.66	326.31/19.69	338.42/114.56
5th	6.28/5.34	7.93/6.75	10.9/9.28	4.48/3.82
7th	0.38/0.24	0.73/0.46	0.51/0.32	0.33/0.2
11th	3.48/1.42	11.31/4.63	2.23/0.91	0.53/0.21
13th	0.77/0.27	1.08/0.37	0.25/0.09	0.04/0.01
17th	2.89/0.77	1.79/0.48	0.61/0.16	0.22/0.06
19th	1.17/0.28	0.46/0.11	0.17/0.04	0.05/0.01
23rd	2.65/0.52	0.72/0.14	0.3/0.06	0.14/0.03
25th	1.4/0.25	0.29/0.05	0.13/0.02	0.05/0.01
29th	2.52/0.4	0.4/0.06	0.18/0.03	0.1/0.02
THD [%]	4.93/36	4.35/94.93	3.42/47.41	1.34/3.34
Grey shaded area indicates the frequency (e.g. 11th, Q_{f1} = 5kVar) from which the capacitor has started to reduce the higher harmonics (e.g. 13th, 17th etc.) and to which it has amplified the lower harmonics (e.g. 1st, 5th and 7th) in comparison to the case without filter.				

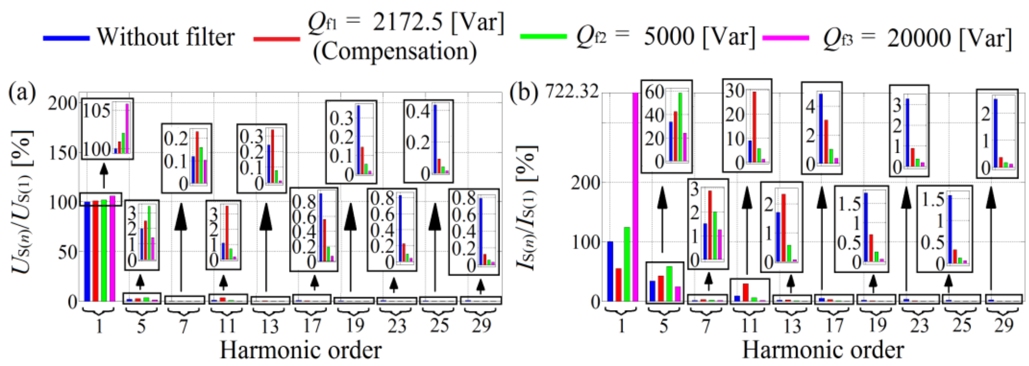

Figure 3.42 Spectrum (p.u) of grid voltage (a) and current (b) (R_{Cf} = 0, R = 0.25 Ω)

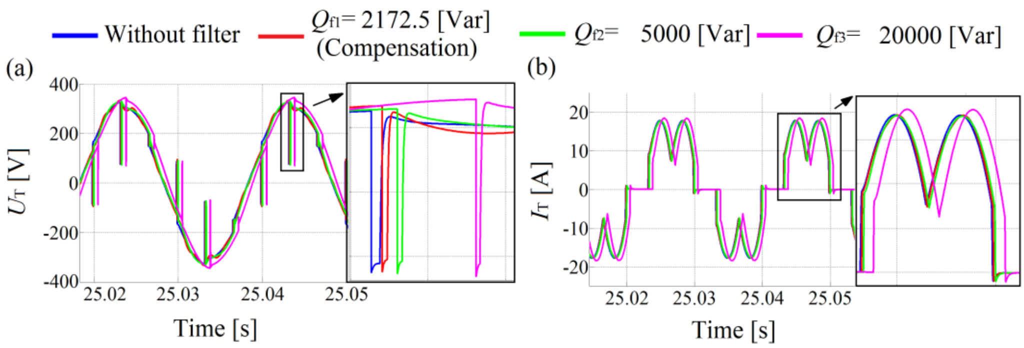

Figure 3.43 Waveforms of voltage (a) and current (b) at the input of rectifier (R_{Cf} = 0, R = 0.25 Ω)

In Figure 3.43, it is presented the input thyristor bridge voltage and current waveforms. The capacitor bank influence on the thyristors rectifier commutation time is clearly visible in Figure 3.43(a). The higher is the capacitor bank reactive power, the shorter is the commutation time. The current has shifted after the capacitor connection Figure 3.43(b).

The waveforms and spectrum of capacitor bank current are presented in Figure 3.44. With the high value of reactive power (e.g. 20 kVar) the filter is more efficient on the reduction of grid current and voltage harmonics although it is also the source of high power losses. The capacitor bank is more bulked by the current fundamental harmonic than other harmonics (Q_{f3} - Figure 3.44(d)).

The current and voltage at the DC side of thyristor bridge as well the DC drive speed are presented respectively in Figure 3.45(a), (b), (c) and (d)).

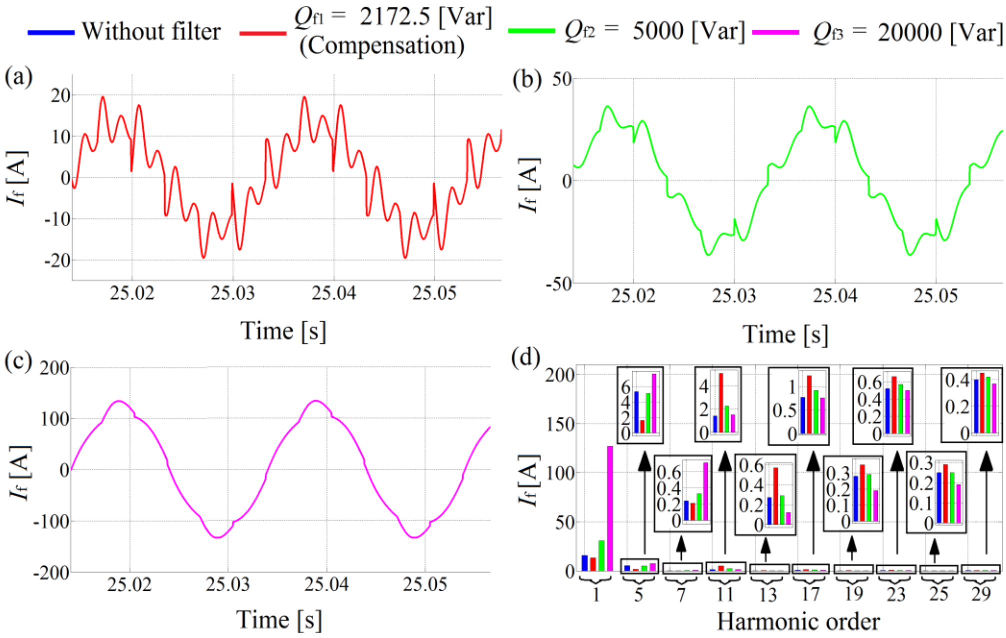

Figure 3.44 Waveform of filter current ((a), (b) and (c)), (d) the spectrum (R_{Cf} = 0, R = 0.25 Ω)

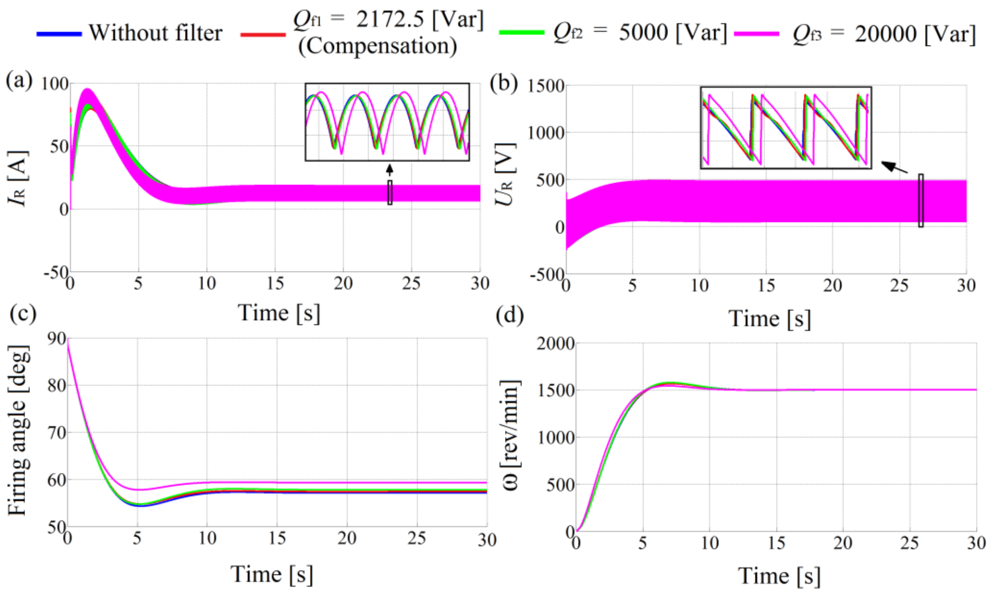

Figure 3.45 (a) current and (b) voltage at the DC side of thyrsitor bridge, (c) firing angle of the control system, (d) drive speed; when the capacitor bank reactive power is increased (R_{Cf} = 0, R = 0.25 Ω)

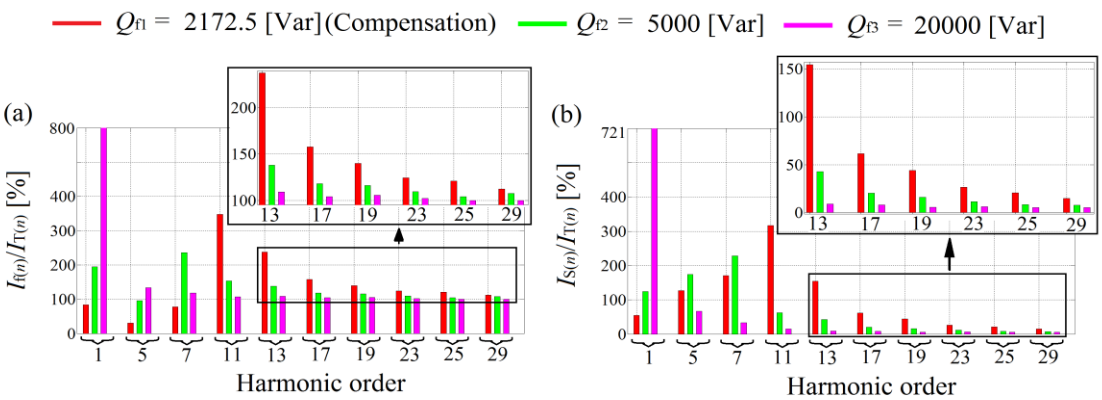

Figure 3.46 Capacitor bank efficiency ((a) and (b)) (R_{Cf} = 0, R = 0.25 Ω)

Figure 3.46(a) and (b) presents the capacitor bank effectiveness in term of harmonics reduction. The first-order filter is more effective when its capacity is high (high values of reactive power e.g.20 kVar).

The impedance of power system (Z) measured from the input terminals of thyristor bridge is presented in Figure 3.47. The parallel resonance has occurred because of parallel connection between capacitor and grid inductance, and the series resonance has occurred because of the series connection of the reactor (L), the capacitor and grid inductance (parallel connected). With the increase of the capacitor reactive power, the power system impedance at the parallel resonance has decreased and the series resonances have moved to the lower frequencies as well as the parallel resonance (Figure 3.47(a)).

The impedance of power system measured at the thyristor bridge input terminals for different damping resistance (Q_{f1} = 2172.5 Var) is presented in Figure 3.47(b). It can be observed that with the damping resistance increase, the impedance (at the resonance frequency) has decreased from 10.77 Ohm to 6 Ohm (parallel resonance) and has increased from 1.34 Ohm to 4.362 Ohm (series resonance). The capacitor resistance has damped the series and parallel resistance.

In the further part of this work, in certain filter damping resistance range, the properties of the later discussed board band filter structures will lead to those of capacitor bank structure.

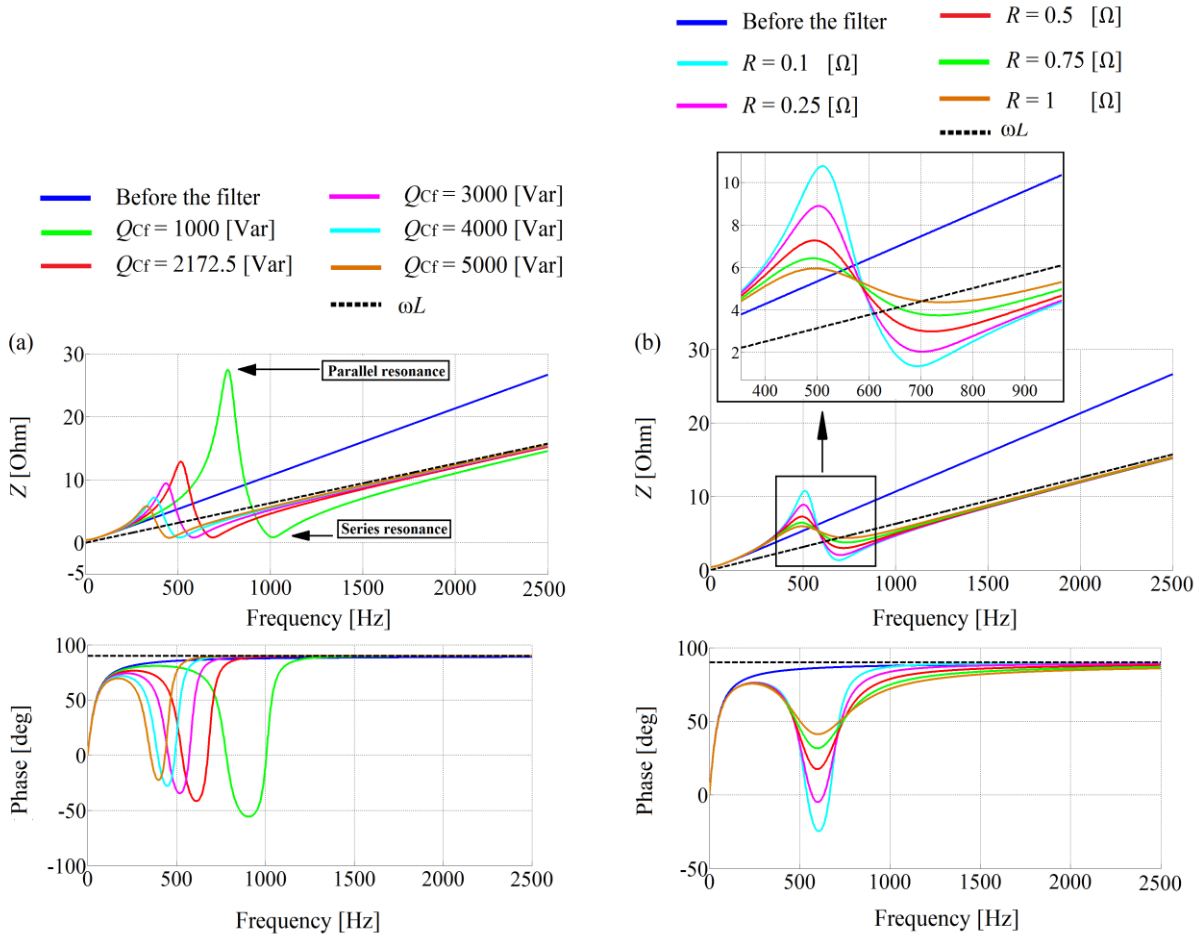

Figure 3.47 Power system impedance characteristic (module and phase) measured at the input terminals of thyristor bridge for different: (a) filter reactive power ($R_{Cf} = R = 0$) and (b) filter damping resistance (Q_{f1} = 2172.5 Var, R_{Cf} = 0)

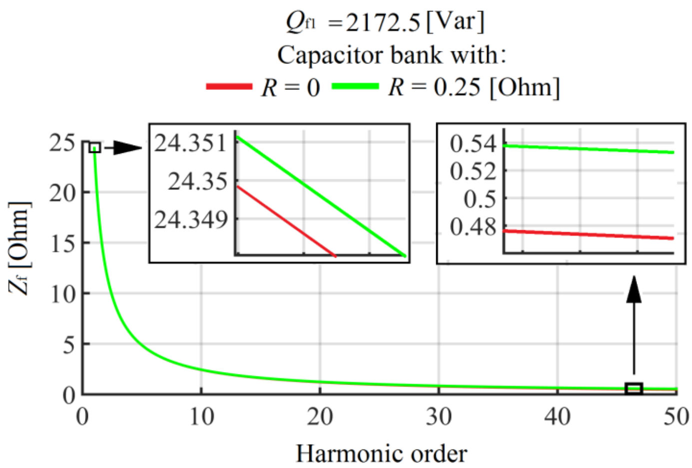

Figure 3.48 Capacitor bank impedance versus frequency characteristics when R is not considered and when it is considered (R_{Cf} = 0)

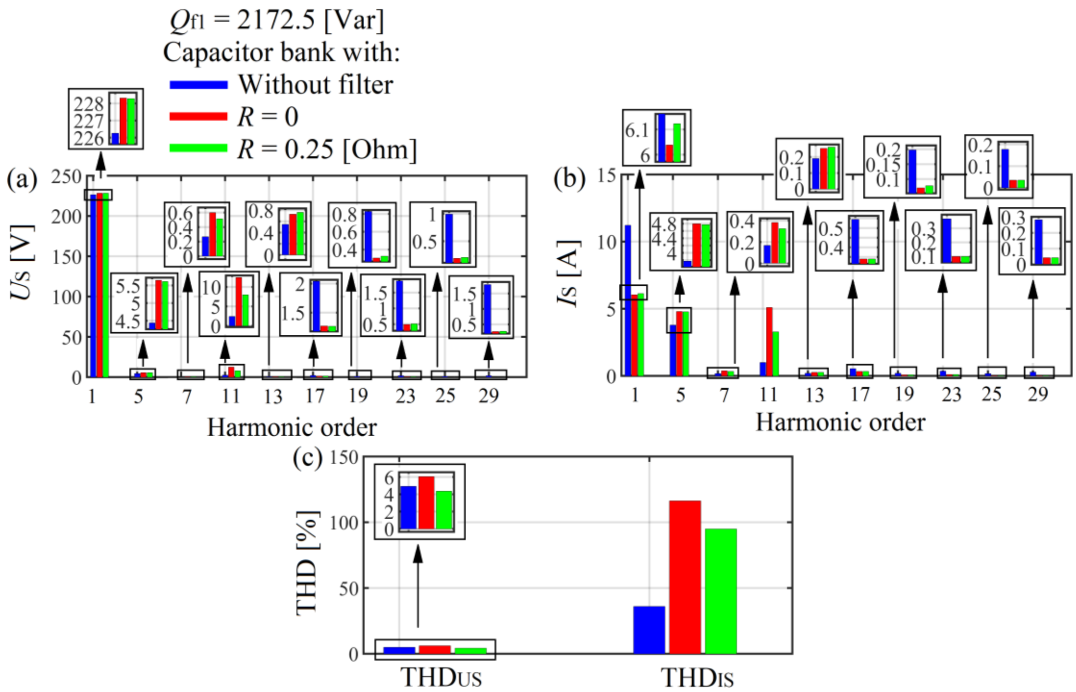

Figure 3.49 Comparison of the grid voltage (a) and current (b) spectrums as well as THD (c) when the capacitor bank resistance is considered (R = 0.25 Ω) and when is not (R = 0) (R_{Cf} = 0)

Figure 3.48 presents the capacitor bank impedance versus frequency characteristics when the resistance R is considered and when it is not considered. There is not a big difference between the two characteristics.

The comparison between the grid voltage and current harmonics as well as THD when the capacitor bank resistance is not considered and when it is considered, is presented in Figure 3.49. It can be noticed that after increasing the capacitor bank resistance from 0 to 0.25 **Ω**, the amplitude of the amplified grid voltage and current harmonics (e.g. 5th, 7th, 11th) has little reduced as well as the THDs (Figure 3.49(a)(b)(c)). The capacitor bank efficiency on the higher harmonic mitigation (e.g. from the 19th) reduces when its resistance increases (power losses increase as well).

3.4.3.2 2nd order filter

The single-tuned filter in Figure 3.5(b) has been used to design the second-order filter by connecting a resistance R in parallel with the reactor L_f and its resistance R_f (Figure 3.50(a)). The resistance R_f is considered as reactor resistance. The considered studies are mainly focused on the influence of filter resistance R on the filtration characteristic.

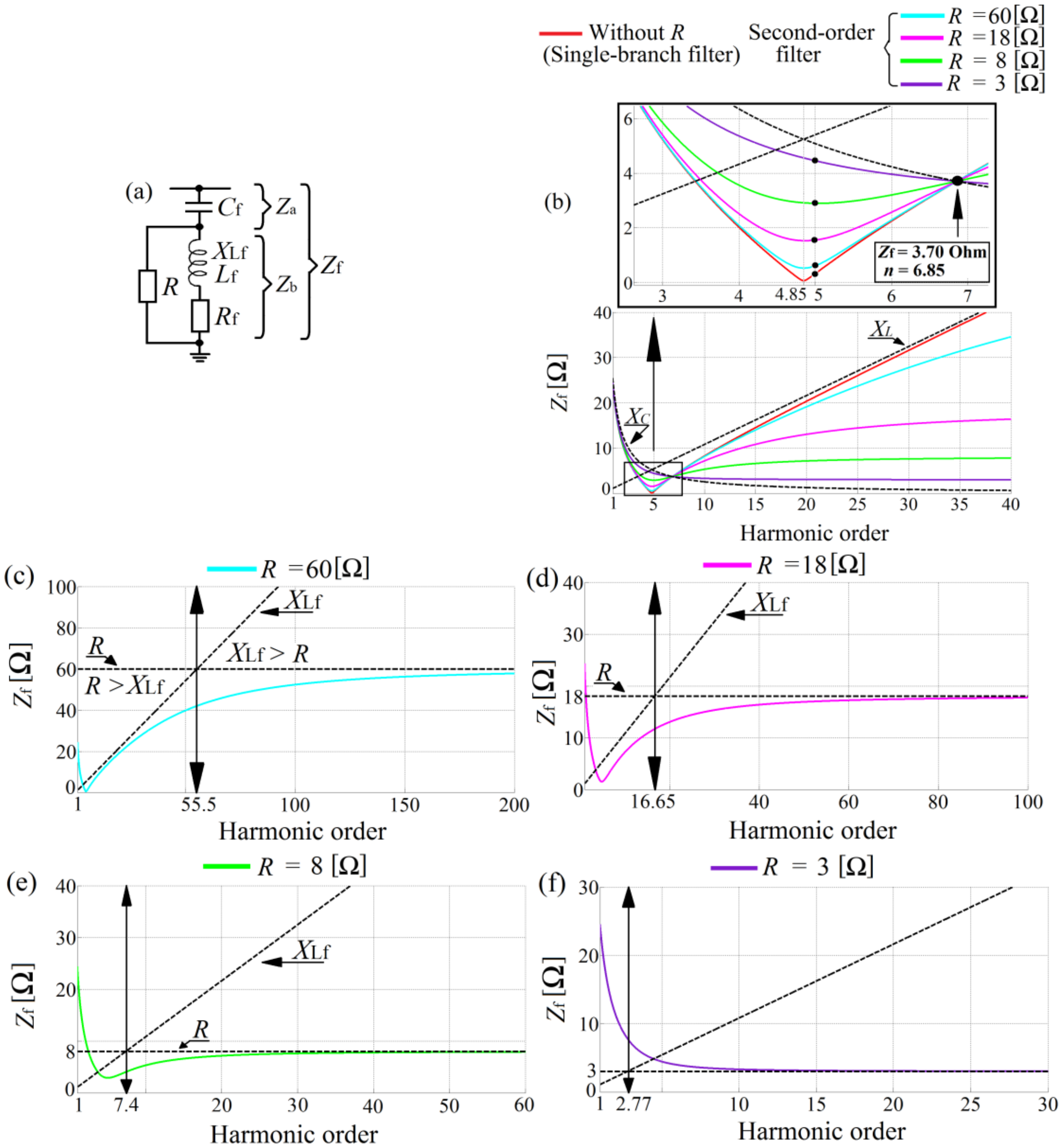

(g) Second-order filter parameters (one-phase)

R [Ω]	$Z_{f(5)}$ [Ω]	$Z_{f(1)}$ [Ω]	R_f [mΩ]	$C_{f(1)}$[μF]	$L_{f(1)}$ [mH]	$Q_{f(1)}$ [Var] (Compensation)	n_{re}
Without R	0.32	24.34	74.9	125.17	3.4	2172.5	4.85
60	0.61	24.35					
18	1.55	24.36					
8	2.89	24.38					
3	4.45	24.51					

Figure 3.50 Second-order filter equivalent circuit (a), (b) its impedance frequency characteristics for different values of damping resistance R: (c) $R = 60$ Ω, (d) $R = 18$ Ω, (e) $R = 8$ Ω and (f) $R = 3$ Ω and (g) its parameters. The case with $R = 3$ Ω will not be considered during the similation

Table 3.12 Second-order filter impedances equations

For $R_{\mathrm{Cf}} = 0$
$\underline{Z}_{\mathrm{a}} = -j\,\frac{1}{\omega C_{\mathrm{f}}}$
$\underline{Z}_{\mathrm{b}} = \frac{R_{\mathrm{f}}R(R_{\mathrm{f}}+R)+R\omega^2L_{\mathrm{f}}^2}{(R_{\mathrm{f}}+R)^2+\omega^2L_{\mathrm{f}}^2} + j\,\frac{R^2\omega L_{\mathrm{f}}}{(R_{\mathrm{f}}+R)^2+\omega^2L_{\mathrm{f}}^2}$
$\underline{Z}_{\mathrm{f}} = \frac{R_{\mathrm{f}}R(\mathrm{R_f}+R)+R\omega^2L_{\mathrm{f}}^2}{(R_{\mathrm{f}}+R)^2+\omega^2L_{\mathrm{f}}^2} + j\,\frac{R^2\omega^2C_{\mathrm{f}}L_{\mathrm{f}} - (\mathrm{R_f}+R)^2 - \omega^2L_{\mathrm{f}}^2}{\omega C_{\mathrm{f}}(R_{\mathrm{f}}+R)^2+\omega^3C_{\mathrm{f}}L_{\mathrm{f}}^2}$

The equations used to obtain the second-order filter impedance versus frequency characteristics are presented in Table 3.12 and the filter parameters are in Figure 3.50(g).

The 5$^{\mathrm{th}}$ harmonic second-order filter impedance has increased with the decrease of damping resistance (Figure 3.50(g)). The system active and reactive power are presented in Table 3.13. The filter reactor equivalent resistance power losses (P_{Rf}) have decreased with the damping resistance decreased whereas those of the damping resistance (P_{fR}) have increased (Table 3.13).

In Figure 3.50(b), it can be notice that the second-order filter with high damping resistance value (e.g. 60 **Ω**) has the characteristic close to the one of single-tuned filter characteristic. With small damping resistance value (e.g. 3 **Ω**), its characteristic is close to the one of capacitor bank (see also Figure 3.50(f)).

Independently on how high is the damping resistance, the second-order filter characteristic in comparison to the single-tuned filter characteristic will always presents a higher value of impedance for the resonance frequency and frequencies around it (e.g. the 5$^{\mathrm{th}}$ harmonic frequency) and smaller impedance value for the frequencies higher than the resonance frequency (Figure 3.50(b)).

The lower is the second-order filter damping resistance *R*, the better will be the higher frequencies components filtration (Figure 3.50(b)). The filter impedance of the 5$^{\mathrm{th}}$ harmonic for example, increases with the decrease of damping resistance value (reduction in the efficiency of reducing the 5$^{\mathrm{th}}$ harmony from the grid side (see also Table 3.14).

Table 3.13 Reactive and active power of power system (fundamental harmonic)

R [Ω]	Values after simulation									
	Grid (PCC)			Second-order filter				Input reactor (L)	Thyrystor bridge input	
	P_{S} [W]	Q_{S} [Var]	DPF	P_{f} [W]	Q_{f} [Var]	P_{fR} [W]	P_{Rf} [W]	Q_{L} [Var]	P_{T} [W]	Q_{T} [Var]
Without filter	1365	2140	0.53	-	-	-	-	39.53	1365	2100
Without *R*	1367	32.31	0.99	6.55	-2140	-	-	39.59	1360	2133
60	1374	29.39	0.99	8.23	-2139	1.67	6.56	39.6	1365	2129
18	1383	26.9	0.99	12.01	-2138	5.52	6.49	39.58	1371	2125
8	1392	26.64	0.99	18.42	-2136	12.1	6.32	39.55	1374	2123

The relation between the damping resistance (*R*) and filter reactor (*L*) is presented in Figure 3.50(c) to (f). It can be observed (in Figure 3.50(c)) that a large quantity of current harmonics (from 1$^{\mathrm{st}}$ to 55.5$^{\mathrm{th}}$) will flow through filter reactor (X_{Lf}) and a smaller quantity will flow through the damping resistance (*R*) because in that frequency range interval, the value of filter reactor reactance is smaller than the one of damping resistance. Concerning the current harmonics from 55.5$^{\mathrm{th}}$ order to infinity, the bigger quantity will flow through the damping resistance and the smaller quantity will flow through the filter reactor, because in that frequency interval the value of filter reactor reactance is higher than the damping resistance. The Figure 3.50(d), (e) and (f) can be interpreted in the same way.

The second-order filter impedance tends asymptotically to the damping resistance as it can be seen in Figure 3.50(c) to (f).

The Figure 3.51 presents the filter resistance and reactance current spectrums and their mutually relationship. For the damping resistance equal to 60 Ω, the value of filter reactor reactance (X_{Lf}) of the harmonics in the range between the 1st and the 55th (see also Figure 3.50(c)) is smaller than the value of damping resistance. Therefore, the amplitude of current harmonics flowing through the damping resistance is smaller than the amplitude of harmonics flowing through the filter reactor (e.g. the 13th harmonic). The same interpretation can be for R = 18 Ω. However, in the case of R = 8 Ω (Figure 3.51), the biggest part of filter current harmonics (apart the 1st, 5th and 7th) flows through the damping resistance (e.g. the 13th) because $R < X_{Lf}$ (see Figure 3.51 for R = 18 Ω).

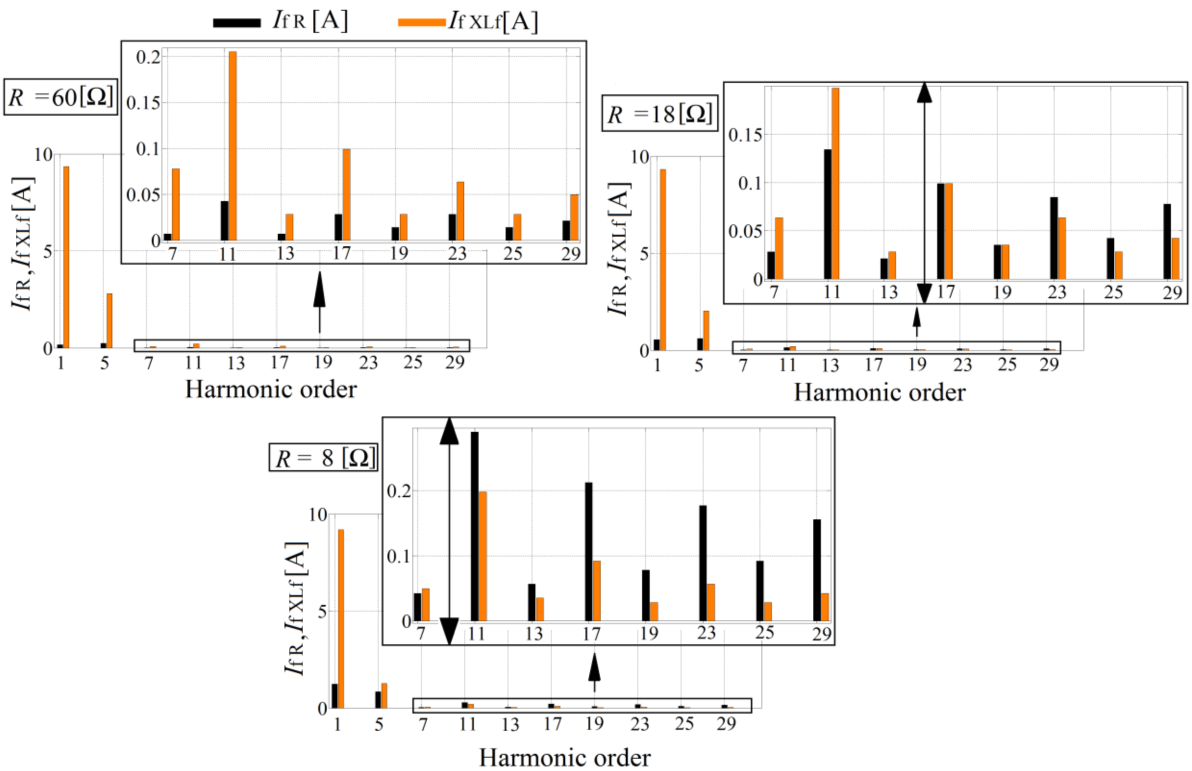

Figure 3.51 Spectrums of filter current flowing through the damping resistance R and reactance X_{Lf}

Table 3.14 Grid voltage and current parameters

$U_{s\,max}$ [V]/ $I_{s\,max}$ [A]												
n	Without filter		Single-branch filter		Second-order filter						
			Without R		R = 60 [Ω]		R =18 [Ω]		R = 8 [Ω]	
	Voltage	Current	Voltage	Current	Voltage	Current	Voltage	Current	Voltage	Current
1st	319.97	15.86	322.91	8.47	322.89	8.51	322.87	8.57	322.84	8.62
5th	6.28	5.34	1.19	1.01	2.31	1.97	4.59	3.91	6.21	5.29
7th	0.38	0.24	0.45	0.28	0.42	0.26	0.37	0.23	0.35	0.22
11th	3.48	1.42	2.73	1.12	2.72	1.11	2.72	1.11	2.79	1.14
13th	0.77	0.27	0.50	0.17	0.50	0.18	0.53	0.18	0.56	0.19
17th	2.89	0.77	2.30	0.62	2.29	0.61	2.27	0.61	2.22	0.59
19th	1.17	0.28	0.84	0.20	0.84	0.20	0.86	0.21	0.85	0.20
23rd	2.65	0.52	2.12	0.42	2.11	0.42	2.07	0.41	1.93	0.38
25th	1.4	0.25	1.05	0.19	1.05	0.19	1.04	0.19	0.98	0.18
29th	2.52	0.4	2.02	0.32	2.01	0.32	1.94	0.31	1.72	0.27
THD [%]	4.93	36	3.82	22.38	3.61	29.68	3.21	49.02	2.92	63.72

The waveforms of PCC voltage and current and their spectrums for different damping resistance are presented in Figure 3.52. It can be observed that the depth of the voltage commutation notches is less when the damping resistance decreases (Figure 3.52(a)). The grid current in term of THD presents better shape after the second-order filter connection (Figure 3.52(c)). The higher is the resistance R, the better is the reduction level of grid voltage and current 5th harmonic components (Figure 3.52(b) and (d)). With the decrease of damping resistance, the filter power losses have increased (Figure 3.53(a)) and the filter has more success on the high harmonics (e.g. 23rd to 29th) reduction (see Figure 3.52(b) and (d)).

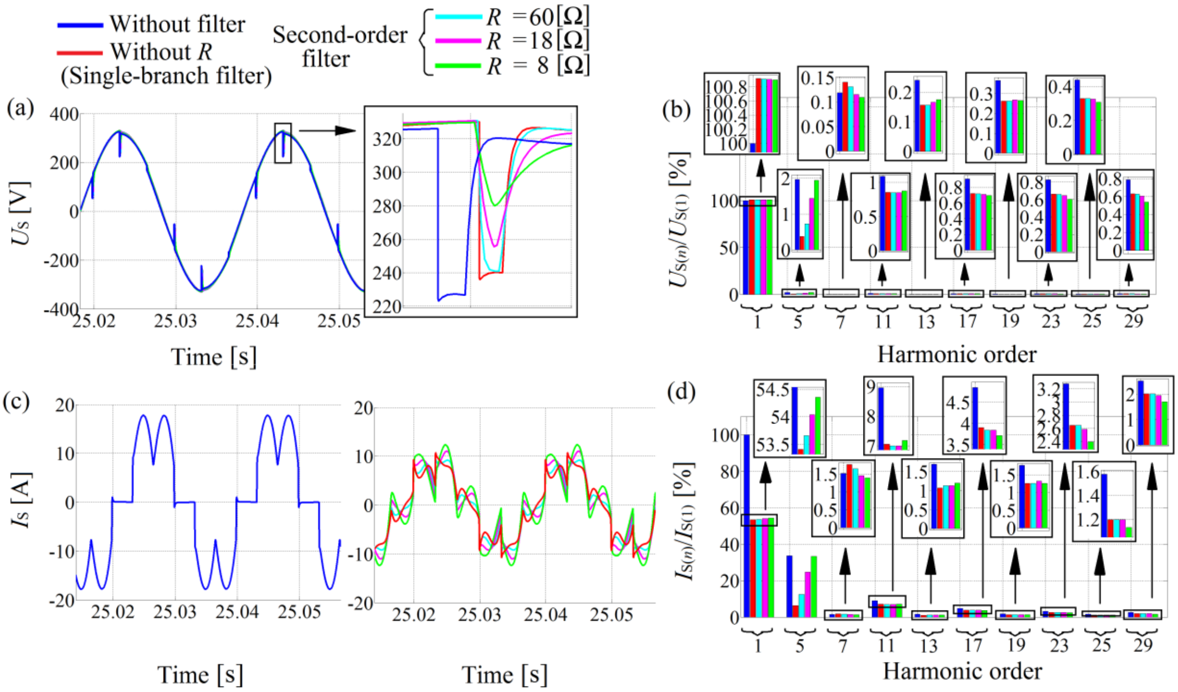

Figure 3.52 Grid voltage (a) and (b) its spectrum (p.u.); grid current (c) and (d) its spectrum (p.u.)

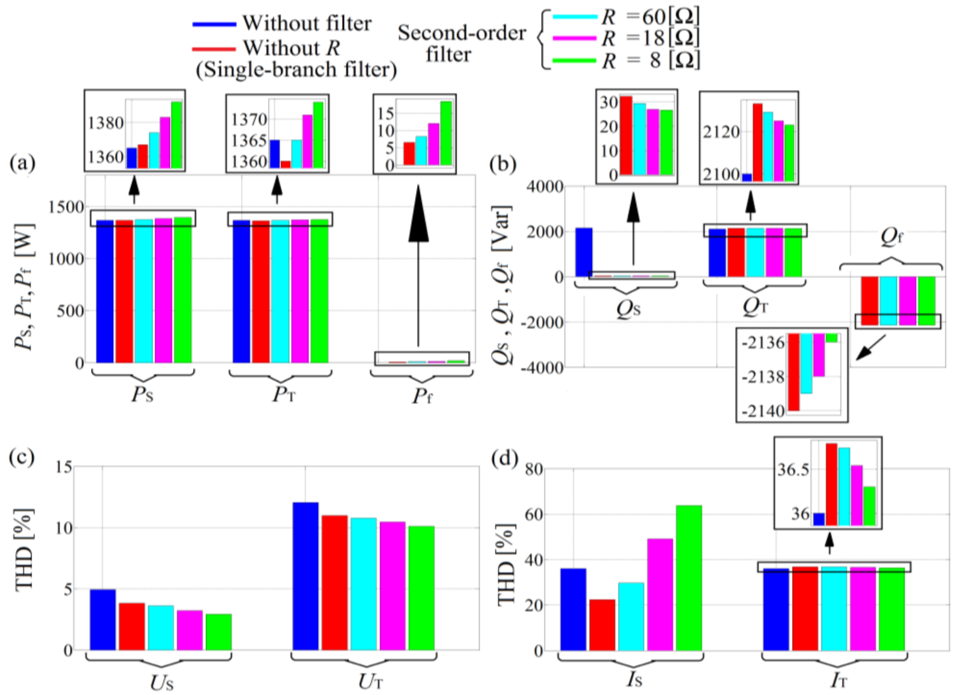

Figure 3.53 Active (a) and reactive (b) power measured at the PCC (P_S, Q_S), filter terminals (P_f, Q_f) and input of rectifier (P_T, Q_T); (c) THD of voltage at the PCC (U_S) and input of rectifier (U_T), (d) THD of current at the PCC (I_S) and input of rectifier (I_T)

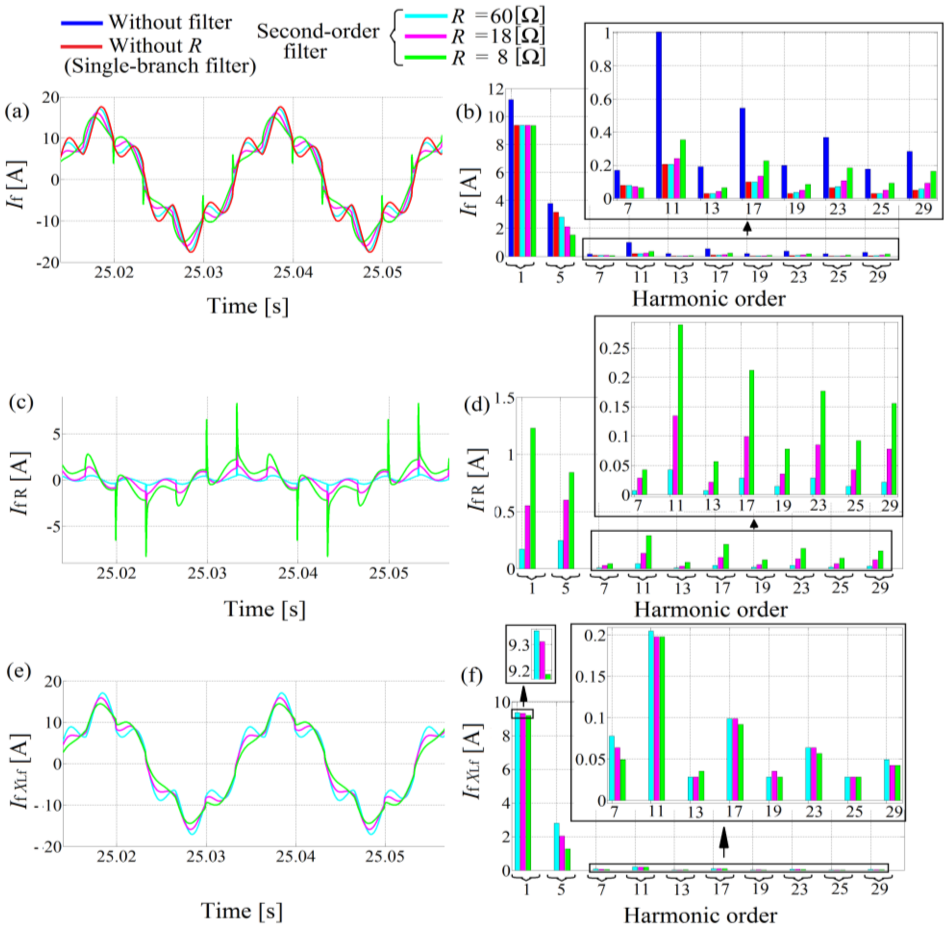

Figure 3.54 Filter current (a) and (b) its spectrum (the harmonics flowing through the filter are compared to the harmonics generated by the load – without filter), (c) resistance current (R) and (d) its spectrum; filter reactor current (e) and (f) its spectrum

The reactive power at the PCC has been well compensated (Figure 3.53(b)) after the filter connection. With the damping resistance decreased (Figure 3.53(d)), the THD of grid current has increased (because the 5th harmonic which is the dominated after the fundamental has considerably increased (from 1.01 A to 5.29 A, Figure 3.52)), whereas the THD of grid voltage and input rectifier voltage have decreased (Figure 3.53(c)). The single-tuned filter has the lower power losses (P_f) than the second-order filter (Figure 3.53(a)).

The filter current waveforms are presented in Figure 3.54(a), (c) and (e). With the decreased of damping resistance R, the filter 5th harmonic has decreased and the amplitudes of harmonics with frequencies higher than the 5th have increased (Figure 3.54(b)).

The waveforms (and spectrums) of filter current flowing through the damping resistance (R) and reactor (X_{Lf}) are respectively presented in Figure 3.54(c)(d) and (e)(f). Figure 3.55(a) shows that with the damping resistance decreased, the grid current is more distorted whereas the filter current is less distorted.

The characteristics of power system impedance seen from the inverter terminal and presented in Figure 3.55(b) shows that the parallel and series resonances are damped when the filter damping resistance decreases.

With the decrease of damping resistance value, the second-order filter is more effective for the reduction of high harmonics amplitude in wide range (e.g. from the 25th to infinity) than for the reduction of single harmonic amplitude (on which it is tuned) (Figure 3.56 (a) and (b)).

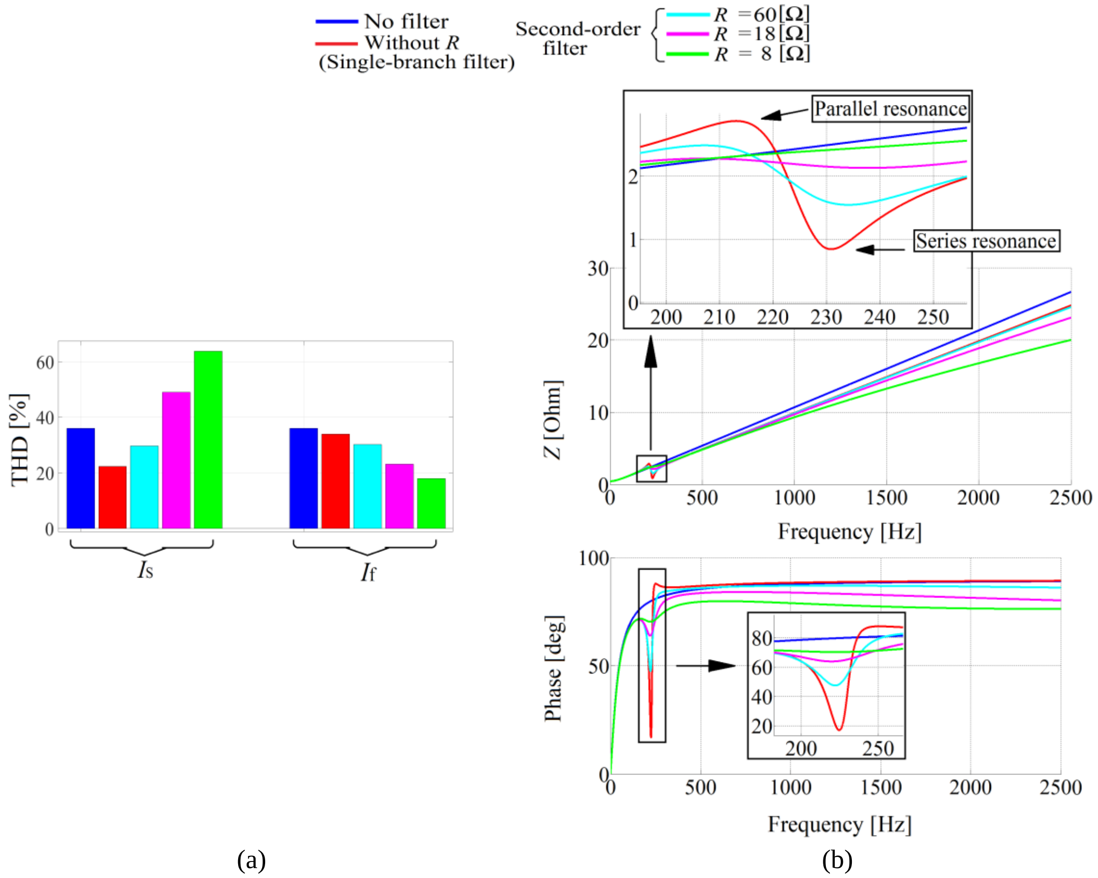

Figure 3.55 (a) grid current together with filter current THD, (b) impedance frequency characteristic measured at the thyristor bridge input terminals for different values of filter damping resistance

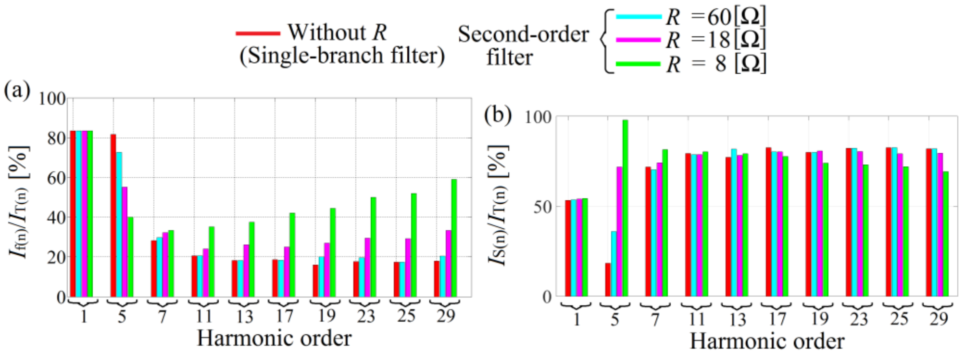

Figure 3.56 Filter effectiveness

3.4.3.3 3rd order filter

According to [127] the third-order filter is commonly used for low or medium voltage network [259]. The third-order filter topology and characteristics are presented in Figure 3.57(a) and (b). The studies are focused on the investigation of the third-order filter damping resistance R influence on the reduction level of 5th and higher harmonics amplitude at the PCC. The equations used for third-order filter parameters computation are shown in Table 3.15. In the literature, it can be found different algorithms of 3rd order-filter parameters computation but the one presented is this chapter is the must easier one.

A filter parameters example is presented in Figure 3.57(g). The filter is design in such a way that it can be decided at which frequency the parallel and series resonance will occur and the resistance (R) is just add to damp the resonances. The filter capacitor C_{f1} is mainly responsible for the reactive power compensation.

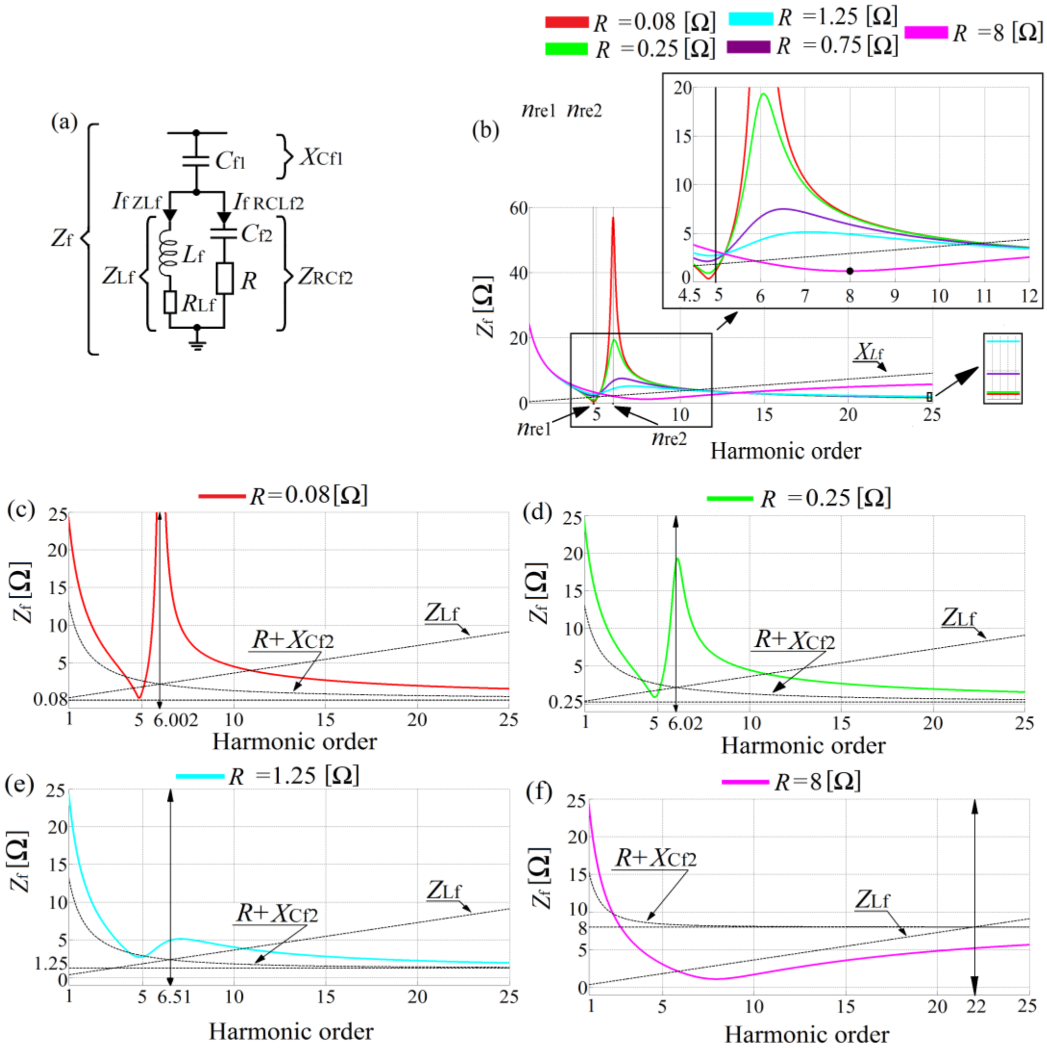

(g) Third-order filter parameters

R [mΩ]	$Z_{f(5)}$ [mΩ]	$Z_{f(1)}$ [mΩ]	R_{Lf} [mΩ]	C_{f1} [µF]	C_{f2} [µF]	L_f [mH]	Q_f [Var]	n_{re1}	n_{re2}
80	1070.3	24349.8							
250	1369.9	24349.8							
750	2282.3	24349.9	4.3	128.74	242.70	1.2	2172.5	4.85	6
1250	2701.5	24350.0							
8000	3112.0	24352.9							

Figure 3.57 Third-order filter equivalent circuit (a); (b) its impedance frequency characteristics for different values of damping resistance R: for (c) R = 0.08 Ω, (d) 0.25 Ω, (e) 1.25 Ω, (f) 8 Ω and (g) its parameters. X_{Cf2} - capacitor reactance, Z_{RCf2} - impedance of the branch containing the damping resistance

According to Figure 3.57(b), the parallel resonance has been chosen to occur at the frequency of 6th order harmonic and the series at the frequency of the component order 4.85. The filter impedance of 5th harmonic has increased from 1070.3 mΩ to 3112.0 mΩ with damping resistance increase and the filter fundamental harmonic impedance is almost the same (Figure 3.57(g)).

The resistance (R) increase has caused the damping of third-order filter series and parallel resonances. The filter impedance at the parallel resonance is reduced and increased at the series resonance (Figure 3.57(b)).

As it can be observed in Figure 3.57(b), with high value of damping resistance (e.g. 8 Ω), the third-order filter is practically tuned to a single frequency (around the 8th harmonic) and its characteristic looks like the one of single-tuned filter. The filter loses the ability to filter the 5th order harmonic and harmonics in wide range.

Table 3.15 Equations used to compute the third-order filter parameters

For $R_{\mathrm{Lf}} = R \approx 0$
$\underline{Z}_{\mathrm{f}}(j\omega) = j\frac{\omega^2 L_{\mathrm{f}}(C_{\mathrm{f1}}+C_{\mathrm{f2}})-1}{\omega C_{\mathrm{f1}}(1-\omega^2 C_{\mathrm{f2}} L_{\mathrm{f}})}$, $\underline{Y}_{\mathrm{f}(j)} = j\frac{\omega C_{\mathrm{f1}}(1-\omega^2 C_{\mathrm{f2}} L_{\mathrm{f}})}{\omega^2 L_{\mathrm{f}}(C_{\mathrm{f1}}+C_{\mathrm{f2}})-1}$ $\omega_{\mathrm{re1}} = \frac{1}{\sqrt{L_{\mathrm{f}}(C_{\mathrm{f1}}+C_{\mathrm{f2}})}} = n_{\mathrm{re1}}\omega_{(1)}$, $\omega_{\mathrm{re2}} = \frac{1}{\sqrt{L_{\mathrm{f}} C_{\mathrm{f2}}}} = n_{\mathrm{re2}}\omega_{(1)}, n_{\mathrm{re2}} > n_{\mathrm{re1}}$ $L_{\mathrm{f}} = \frac{\omega_{\mathrm{re2}}^2-\omega_{re1}^2}{\omega_{\mathrm{re2}}^2\omega_{\mathrm{re1}}^2 C_{\mathrm{f1}}} = \frac{n_{\mathrm{re2}}^2-n_{\mathrm{re1}}^2}{\omega_{(1)}^2 n_{\mathrm{re2}}^2 n_{\mathrm{re1}}^2 C_{\mathrm{f1}}}$, $C_{\mathrm{f2}} = \frac{1}{\omega_{(1)}^2 n_{\mathrm{re2}}^2 L_{\mathrm{f}}}$
Taking into account the PCC voltage and the load reactive power, the equation used to compute C_{f1} and the relation between C_{f1} and C_{f2} are set up. $\mathrm{Im}\{Z_{\mathrm{f}}\} = \frac{U_{\mathrm{f}}^2}{Q_{\mathrm{f}}} = \frac{n_{\mathrm{re2}}^2(1-n_{\mathrm{re1}}^2)}{C_{\mathrm{f1}} n_{\mathrm{re1}}^2(n_{\mathrm{re2}}^2-1)\omega_{(1)}}$ $C_{\mathrm{f1}} = \frac{n_{\mathrm{re2}}^2(1-n_{\mathrm{re1}}^2)}{n_{\mathrm{re1}}^2(n_{\mathrm{re2}}^2-1)}\frac{Q_{\mathrm{f}}}{\omega_{(1)} U_{\mathrm{f}}^2}$, $C_{\mathrm{f1}} = \frac{n_{\mathrm{re1}}^2}{(n_{\mathrm{re2}}^2-n_{\mathrm{re1}}^2)} C_{\mathrm{f2}}$
For $\mathrm{R} \neq 0,\ \mathrm{R_{Lf}} \neq 0$
$\underline{\mathrm{X}}_{\mathrm{Cf1}} = -j\frac{1}{\omega C_{\mathrm{f1}}}$
$\underline{Z}_{\mathrm{f}}(j\omega) = \frac{\omega^4 L_{\mathrm{f}}^2 C_{\mathrm{f2}}^2 R+\omega^2 C_{\mathrm{f2}}^2(R^2 R_{L\mathrm{f}}+R R_{L\mathrm{f}}^2)+R_{L\mathrm{f}}}{\omega^2 C_{\mathrm{f2}}^2(R+R_{L\mathrm{f}})^2+(\omega^2 L_{\mathrm{f}} C_{\mathrm{f2}}-1)^2}+$ $j\frac{\omega^4(-L_{\mathrm{f}}^2 C_{\mathrm{f2}}+L_f C_{\mathrm{f2}}^2 R^2)+\omega^2 C_{\mathrm{f1}}(L_f-R_{L\mathrm{f}}^2 C_{\mathrm{f2}})-\omega^2 C_{\mathrm{f2}}^2(R+R_{L\mathrm{f}})^2+(\omega^2 L_{\mathrm{f}} C_{\mathrm{f2}}-1)^2}{\omega^3 C_{\mathrm{f1}} C_{\mathrm{f2}}^2(R+R_{L\mathrm{f}})^2+(\omega^2 L_{\mathrm{f}} C_{\mathrm{f2}}-1)^2\omega C_{\mathrm{f1}}}$

The highest value of damping resistance should be chosen in a way to avoid the total damp of series and parallel resonances. The smaller is the damping resistance, the better will be the reduction level of 5th harmonic and harmonics in wide range at the PCC. The 7th harmonic impedance has decreased with the damping resistance increase (Figure 3.57(b)). in the considered example, the third-order filter should be designed in such a way that the parallel resonance does not occur near the 7th harmonic which is the characteristic one.

After the filter connection and for all damping resistance value, the inductive reactive power is compensated and the DPF is almost equal to one. The filter reactor power losses (fundamental harmonic) are practically the same when the damping resistance increases and the damping resistance power losses has increased from 0.0061 W to 0.44 W.

In Figure 3.57(c) to (f), the filter reactor impedance characteristic (Z_{Lf}) is compared to the characteristic of the filter branch having the capacitor reactance and damping resistance (X_{Cf2}, R). In Figure 3.57(c) it can be observed that for the harmonics between the 1st and the 6th, Z_{RCf2} ($X_{\mathrm{Cf2}} + R$) is higher than Z_{Lf}, therefore the big part of current harmonic will flow through Z_{Lf} and Z_{RCf2} will cause less power losses than Z_{Lf}. From the 6th harmonic, Z_{Lf} is higher than Z_{RCf2}, therefore the big part of current harmonic will flow through Z_{RCf2} (more power losses). Figure 3.57(d), (e) and (f) can be interpreted in the same way.

The damping resistance increase can either decrease the commutation notches depth, therefore improving the grid voltage waveform (Figure 3.58(a) with R from 0.08 Ω to 1.25 Ω) or have an weak influence on the commutation notches depth mitigation as presented in Figure 3.58(a) for R equal to 8 Ω (the filter is then less effective).

From Figure 3.58(a) it can be concluded that the percentage of the PCC voltage (fundamental harmonic) has little increased (not considerably) after the filter connection and is the same during the damping resistance increased.

The percentage of the PCC current (fundamental harmonic) has considerably decreased after the filter connection (because of the reactive component compensation) and has not considerably increased during the damping resistance increased (Figure 3.58 (b)).

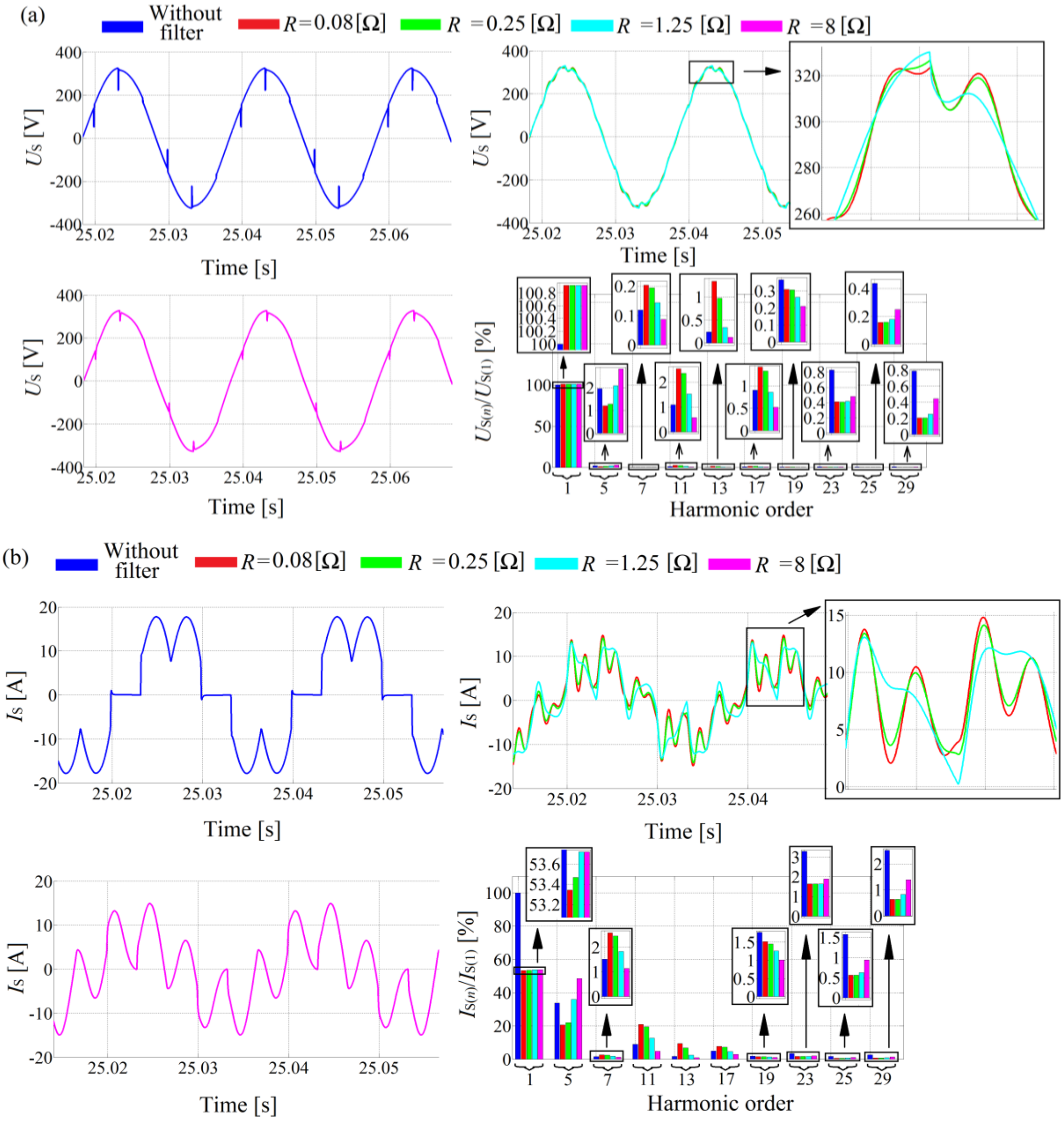

Figure 3.58 PCC voltage (a) and current (b) and their spectrums (p.u.) when the damping resistance filter is increased from 0.08 Ω to 8 Ω

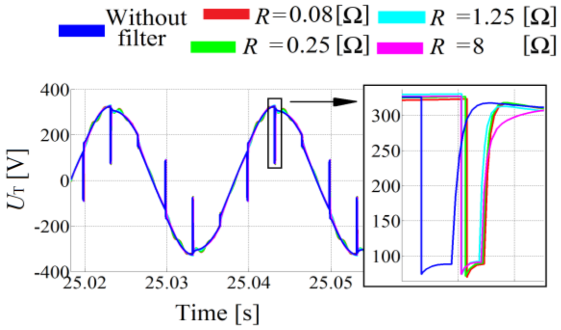

Figure 3.59 Voltage waveforms at the input of rectifier

In the spectrums in Figure 3.58(a) and (b) (PCC voltage and current), it can be observed that after the filter connection (for $R = 80$ mΩ), the amplitudes of 5th and higher harmonic (from the 19th) are reduced whereas those of the 7th, 11th, 13th and 17th harmonics are amplified (because they are near the parallel resonance zone according to frequency characteristics of

Figure 3.62(c)). But this harmonics amplification is damped by the filter damping resistance increased.

The waveforms of input rectifier voltage are presented in Figure 3.59. The width of commutation notches is reduced (reduction of commutation time) after the filter connection.

The filter active power has increased (Figure 3.60(a)) with the increase of R as well as the PCC active power. On the other hand, the PCC reactive power has decreased (Figure 3.60(b)).

After the filter connection, the gird voltage is less distorted (Figure 3.60(c)) and the grid current is more distorted (Figure 3.60(d)) taking into account the THD. However, with the damping resistance increase (with R from 0.08 Ω to 1.25 Ω), the grid voltage is less and less distorted whereas the grid current is more and more distorted.

Figure 3.61(a)(b) represents the filter current waveforms and their spectrums. By increasing R from 80 mΩ to 250 mΩ, the filter 5th harmonic amplitude has decreased from 2.16 A to 2.10 A. For the damping resistance between 250 mΩ and 8000 mΩ, the filter 5th harmonic amplitudes have increased.

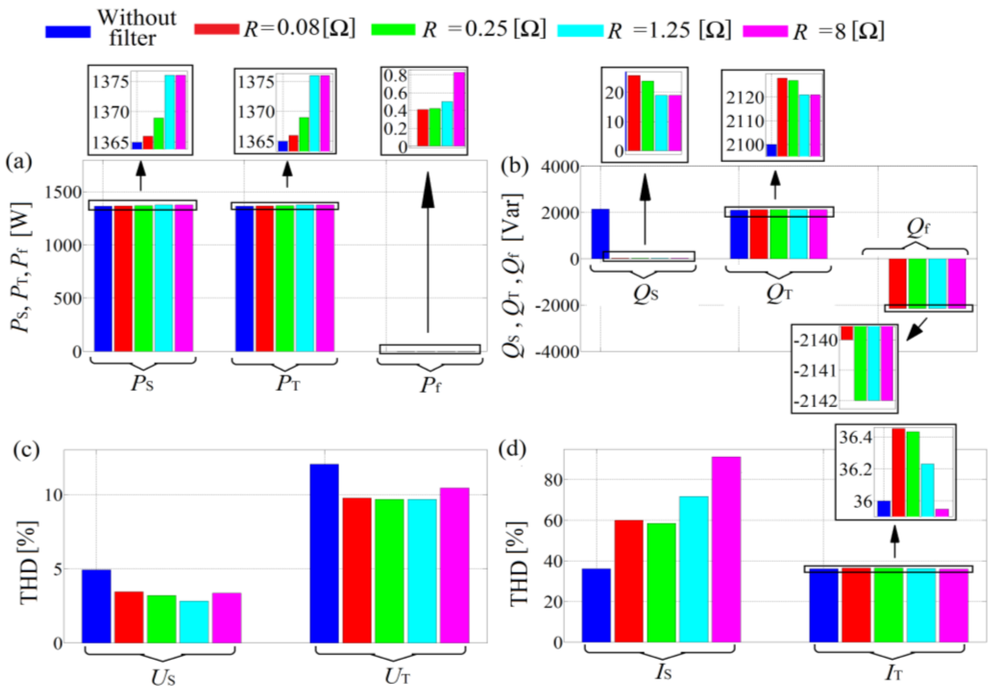

Figure 3.60 Active (a) and reactive (b) power measured at the PCC, filter terminals and input of rectifier; (c) THD of PCC voltage and voltage at the input of rectifier; d) THD of PCC current and current at the input of rectifier

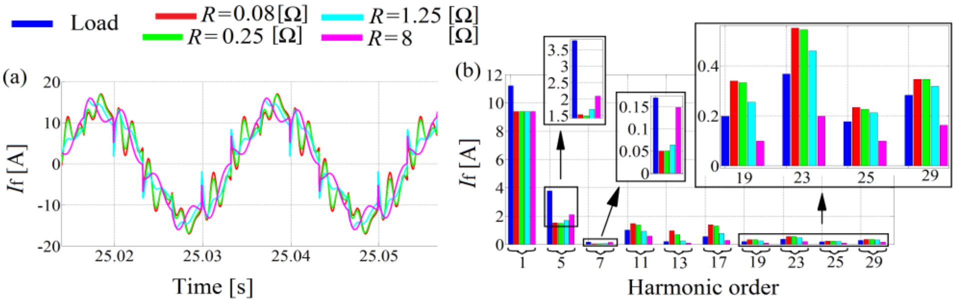

Figure 3.61 Filter current (a) and (b) its spectrum

The relationship between the filter parallel connected branches Z_{RCf2} and Z_{Lf} (see Figure 3.57(a) in term of current flow is illustrated by the spectrums in Figure 3.62(a). The filter current fundamental and 5th harmonic amplitudes (for 0.08 Ω, 0.25 Ω, 1.25 Ω and 8 Ω) are higher in the Z_{Lf} branch than in the branch containing the damping resistance (Z_{RC2}) (Figure 3.62 (a)).

The amplitude of the harmonics (from the 7th) flowing through the damping resistance is higher than the amplitude of those flowing through the reactor (for 0.08Ω, 0.25Ω and 1.25Ω); therefore from the power losses point of view, the damping resistance causes more power losses (for the high order harmonics).

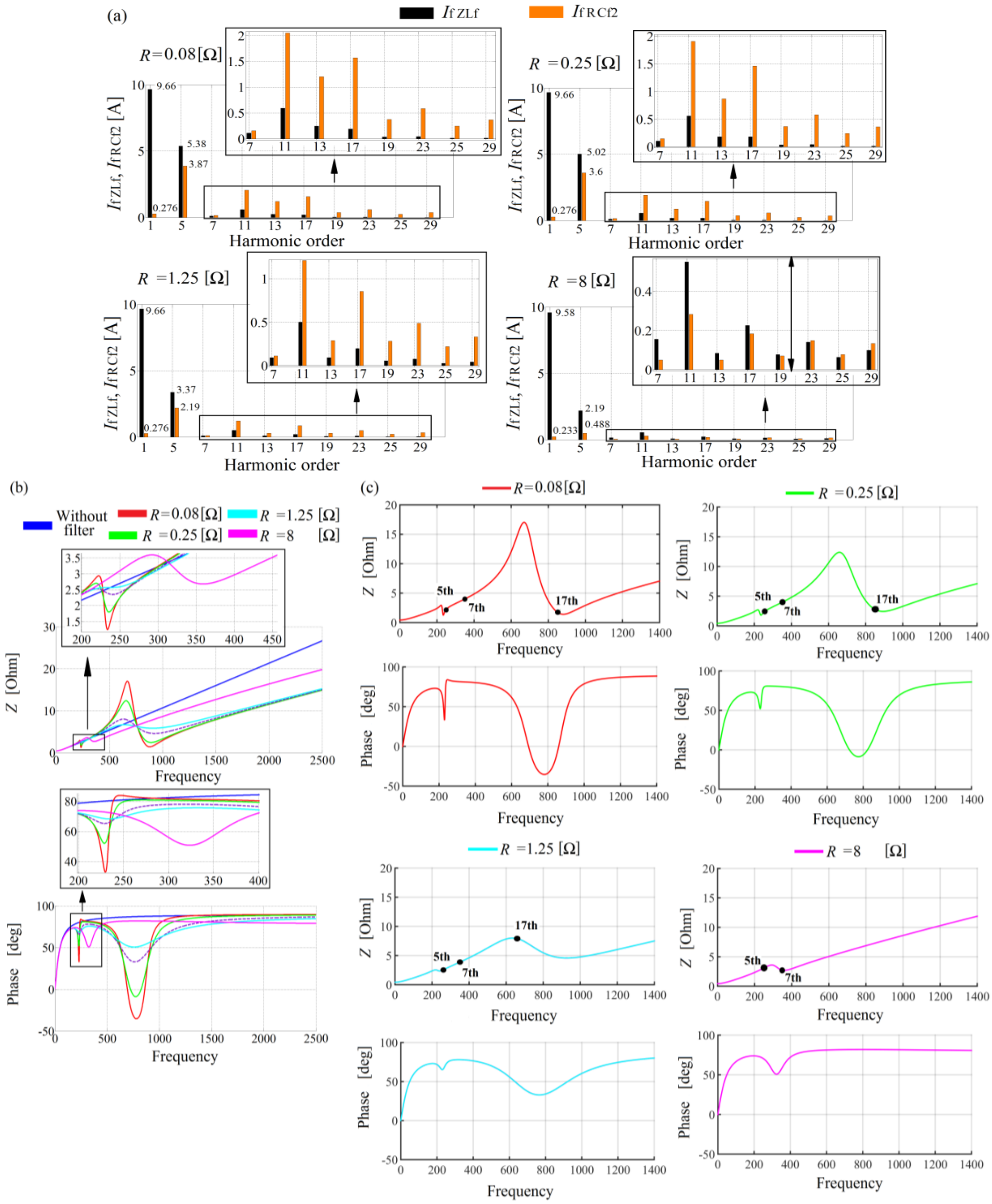

Figure 3.62 (a) spectrums of current flowing through the filter damping resistance R and reactor Z_{Lf} and (b) impedance versus frequency characteristics measured at the input terminals of thyristor bridge for different filter damping resistance

The power system impedances (seen from the rectifier terminals) versus frequency of Figure 3.62(b) and (c) show that between 200 Hz and 1000 Hz, there are parallel and series resonances. These resonances are damped when the filter damping resistance increases. In the case of Figure 3.62(c) for R equal to 8 Ω, the 5th harmonic is near the parallel resonance frequency, where it amplification at the grid side (see also spectrums of Figure 3.58(a) and (b)).

The Figure 3.63 shows that the filter efficiency on the reduction of harmonic near which it is tuned (e.g. 5^{th}) or high harmonics (higher than the 5^{th}) in width range depends upon its damping resistance. For instance in the case of 0.08 Ω, the filter is more efficient on the 5^{th} harmonic and high (from 25^{th}) harmonics reduction than in the case of 1.25 Ω (Figure 3.63). The filter parallel resonance (see Figure 3.57(b)) is a disadvantage because it occurs near the characteristic harmonics (e.g. 7^{th}, 11^{th}, 13^{th} and 17^{th}) which are amplified after the filter connection to the PCC.

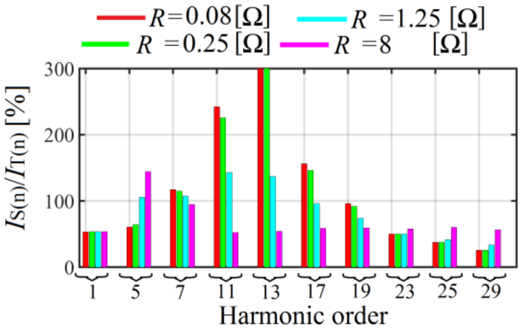

Figure 3.63 Third-order filter effectiveness

3.4.3.4 C-type filter

The filter which the equivalent circuit is shown in Figure 3.64(a) and (b) is a special type of 3^{rd} order filter [24]. Its main advantage is the power losses reduction in comparison to other filter structures [26, 142, 222, 268]. The filter design must be performed in such a way that less fundamental harmonic current flows through the damping resistance (R) connected in parallel with the branch containing reactor L_f and the capacitor C_{fb} [177]. Less current (or almost no current) of fundamental harmonic will flow through the damping resistance if the impedance Z_{LfCfb} is tuned to resonance frequency of fundamental harmonic (Figure 3.64(b)).

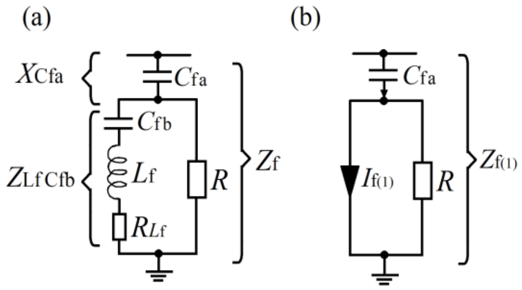

(c)

n_{re}	R [Ω]	$Z_{f(nre)}$ [Ω]	$Z_{f(5)}$ [Ω]	$Z_{f(1)}$ [Ω]	R_{Lf} [mΩ]	C_{fa} [µF]	C_{fb} [µF]	L_f [mH]	Q_f [Var]
-	1.25	-	4.73	24.34	12.7	130.72	2900	3.4	-2172.5
5.64	5	3.45	3.51	24.34					
4.99	8	2.67	2.67	24.34					
4.85	25	1	1.04	24.34					
4.85	2500	0.022	0.32	24.34					

Figure 3.64 C-type filter: (a) equivalent circuit, (b) equivalent circuit for the fundamental harmonic and (c) its parameters

The studies of C-type filter in this chapter is not only focused on its damping resistance but also on the increase and decrease of other parameters (detuning of C-type filter). The expressions used to compute the filter C-type filter parameters are presented in Table 3.16 (the resistances of capacitors C_{fa} and C_{fb} are neglected). The filter parameters example is introduced in Figure 3.64(c) and the filter reactor resistance is obtained from the reactor quality factor (R_{Lf}, C_{fa}, C_{fb}, and L_f were computed for n_{re} equal to 4.85 but with the damping resistance increase, n_{re} has also increase). The filter impedance of 5th harmonic has decreased with the damping resistance increase (Figure 3.64(c)).

Table 3.16 C-type filter equations used to compute the parameters

<table>
<tr><td rowspan="2">C-type filter equivalent impedance</td><td>For $R_{\mathrm{Lf}} \neq 0\ and\ R\ \neq 0$</td></tr>
<tr><td>$$\underline{Z}_{\mathrm{f}}(j\omega) = \left(\frac{1}{R} + \frac{1}{j\omega L_{\mathrm{f}} + R_{\mathrm{Lf}} - j\frac{1}{\omega C_{\mathrm{fb}}}}\right)^{-1} - j\frac{1}{\omega C_{\mathrm{fa}}} = \frac{R\omega^2 C_{\mathrm{fb}}^2 R_{\mathrm{Lf}}(R_{\mathrm{Lf}}+R) + R(\omega^2 L_{\mathrm{f}} C_{\mathrm{fb}}-1)^2}{(R_{\mathrm{Lf}}\omega C_{\mathrm{fb}} + R\omega C_{\mathrm{fb}})^2 + (\omega^2 L_{\mathrm{f}} C_{\mathrm{fb}}-1)^2} +$$ $$j\frac{C_{\mathrm{fb}} C_{\mathrm{fa}}(R^2\omega^4 L_{\mathrm{f}} C_{\mathrm{fb}} - 2RR_{\mathrm{Lf}}\omega^2 - R^2\omega^2) - (R_{\mathrm{Lf}}\omega C_{\mathrm{fb}} + R\omega C_{\mathrm{fb}})^2 - (\omega^2 L_{\mathrm{f}} C_{\mathrm{fb}}-1)^2}{\omega C_{\mathrm{fa}}(R_{\mathrm{Lf}}\omega C_{\mathrm{fb}} + R\omega C_{\mathrm{fb}})^2 + (\omega^2 L_{\mathrm{f}} C_{\mathrm{fb}}-1)^2}$$</td></tr>
<tr><td colspan="2">For $R_{Lf} = 0\ and\ R\ \Rightarrow \infty$</td></tr>
<tr><td colspan="2">For $n_{\mathrm{re}(1)} = 1,\ \underline{Z}_{\mathrm{LfCfb}}(\omega_{(1)}) = 0 \Rightarrow L_{\mathrm{f}} = \frac{1}{\omega_{(1)}^2 C_{fb}}$</td></tr>
<tr><td colspan="2">$$Z_{\mathrm{f}(1)} = \frac{1}{\omega_{(1)} C_{\mathrm{fa}}} = \frac{U_{\mathrm{f}}^2}{Q_{\mathrm{f}}} \Rightarrow C_{\mathrm{fa}} = \frac{Q_{\mathrm{f}}}{\omega_{(1)} U_{\mathrm{f}}^2}$$</td></tr>
<tr><td colspan="2">For $\mathrm{R_{Lf}} \Rightarrow 0,\ R\ \Rightarrow \infty$ and $Z_{\mathrm{f}} \Rightarrow 0$</td></tr>
<tr><td colspan="2">The filter resonance frequency is obtained after assuming the series resonance between the capacitors C_{fa}, C_{fb} and the inductance L_{f}</td></tr>
<tr><td colspan="2">$$\underline{X}_{\mathrm{Cfa}} + \underline{X}_{\mathrm{Cfb}} + \underline{X}_{\mathrm{Lf}}\Big|_{\omega=\omega_{\mathrm{re}}} = 0 \Rightarrow -j\frac{1}{\omega_{\mathrm{re}} C_{\mathrm{fa}}} - j\frac{1}{\omega_{\mathrm{re}} C_{\mathrm{fb}}} + j\omega_{\mathrm{re}} L_{\mathrm{f}} = 0 \Rightarrow \omega_{\mathrm{re}} = \sqrt{\frac{C_{\mathrm{fa}} + C_{\mathrm{fb}}}{C_{\mathrm{fa}} C_{\mathrm{fb}} L_{\mathrm{f}}}}$$</td></tr>
<tr><td>Relation between filter capacitors</td><td>$$\frac{C_{\mathrm{fb}}}{C_{\mathrm{fa}}} = \frac{\omega_{\mathrm{re}}^2 - \omega_{(1)}^2}{\omega_{(1)}^2} = (n_{\mathrm{re}}^2 - 1)$$</td></tr>
<tr><td colspan="2">For $R \neq 0, R_{\mathrm{Lf}} = 0$</td></tr>
<tr><td colspan="2">Another way to compute the filter equivalent impedance</td></tr>
<tr><td colspan="2">$$\underline{Z}_{\mathrm{f}}(j\omega) = \frac{j(R\omega^2 L_{\mathrm{f}} C_{\mathrm{fb}} - R)}{\omega R C_{\mathrm{fb}} + j(\omega^2 L_{\mathrm{f}} C_{\mathrm{fb}} - 1)} - j\frac{1}{\omega C_{\mathrm{fa}}} = \frac{(\omega^2 L_{\mathrm{f}} C_{\mathrm{fb}} - 1) + j[\omega^3 C_{\mathrm{fa}} R L_{\mathrm{f}} C_{\mathrm{fb}} - \omega C_{\mathrm{fa}} R - R\omega C_{\mathrm{fb}}]}{\omega^2 C_{\mathrm{fa}} R C_{\mathrm{fb}} + j(\omega^3 C_{\mathrm{fa}} L_{\mathrm{f}} C_{\mathrm{fb}} - \omega C_{\mathrm{fa}})}$$</td></tr>
<tr><td colspan="2">$$= \frac{(\omega^2 - \omega_{(1)}^2)\omega_{(1)}^2 U_{\mathrm{f}}^4 + j[U_{\mathrm{f}}^2 Q_{\mathrm{f}} \omega\omega_{(1)}(\omega^2 - \omega_{\mathrm{re}}^2)R}{Q_{\mathrm{f}}^2(\omega_{\mathrm{re}}^2 - \omega_{(1)}^2)\omega^2 R + j\omega_{(1)}\omega Q_{\mathrm{f}} U_{\mathrm{f}}^2(\omega^2 - \omega_{(1)}^2)} = \frac{\omega_{(1)}^2 U_{\mathrm{f}}^4}{Q_{\mathrm{f}}^2 R\omega_{\mathrm{re}}^2 + j\omega_{(1)}\omega_{\mathrm{re}} Q_{\mathrm{f}} U_{\mathrm{f}}^2} = \frac{U_{\mathrm{f}}^4 Q_{\mathrm{f}} R n_{\mathrm{re}} - jU_{\mathrm{f}}^6}{Q_{\mathrm{f}}^3 R^2 n_{\mathrm{re}}^3 + n_{\mathrm{re}} Q_{\mathrm{f}} U_{\mathrm{f}}^4}\ (\text{for } \omega = \omega_{\mathrm{re}})$$</td></tr>
<tr><td>The filter impedance expression at any resonance frequency</td><td>$$Z_{\mathrm{f\_re}} = \frac{U_{\mathrm{f}}^4}{n_{\mathrm{re}} Q_{\mathrm{f}}\sqrt{Q_{\mathrm{f}}^2 R^2 n_{\mathrm{re}}^2 + U_{\mathrm{f}}^4}}$$</td></tr>
</table>

The filter reactor inductance (Table 3.16) is obtained after assuming that the branch (C_{fb}, L_{f}) has a minimal impedance (series resonance) at the fundamental harmonic. The total impedance of C-type filter ($Z_{\mathrm{f}(1)}$) is then reduced to the capacitor reactance (X_{Cfa}) for the fundamental harmonic (Figure 3.64(b)). The C-type filter behave as a capacitor for the first harmonic and C_{fa} is in charge of filter reactive power compensation.

The C-type filter impedance versus frequency characteristics for different value of damping resistance are presented in Figure 3.65(a) and Figure 3.66. In Figure 3.65(a) it can be notice a common point for all the characteristics at the frequency of 339 Hz (*n* equal to 6.78). The filter impedance characteristics of resonance frequencies (Figure 3.65(b)) shows that with high value of damping resistance (e.g. 25Ω), the impedance of resonance frequencies is minimal (more close to zero). With the damping resistance decrease, it can be observed in the table of Figure 3.64 the increase of filter resonance frequency impedance as well as the filter resonance frequency (e.g. from 4.85 to 5.64 - see also Figure 3.65(a)).

The filter can be tuned to any resonance frequencies (ω_{re}) higher than the fundamental ($\omega_{(1)}$). For the two identical C-type filter tuned respectively to the 5th and the 7th harmonic, the resonance frequency filter impedance for the 7th harmonic is lower than the one of the 5th harmonic (Figure 3.65(c)).

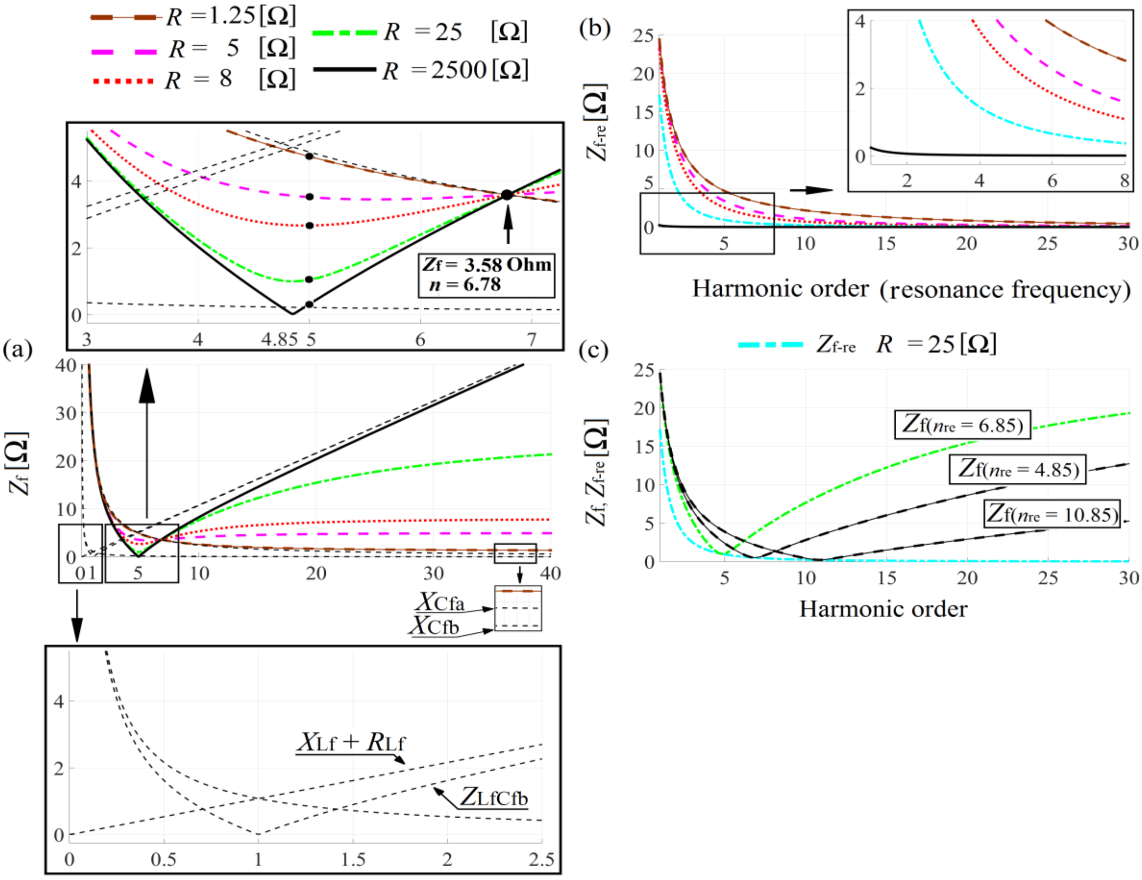

Figure 3.65 Filter impedance frequency characteristics: (a) for different value of damping resistance, (b) for resonance frequencies; (c) characteristics of filter impedance frequency (for the chosen frequencies; e.g. $Z_{f(n=4.85)}$) and filter resonance frequencies (Z_f) together

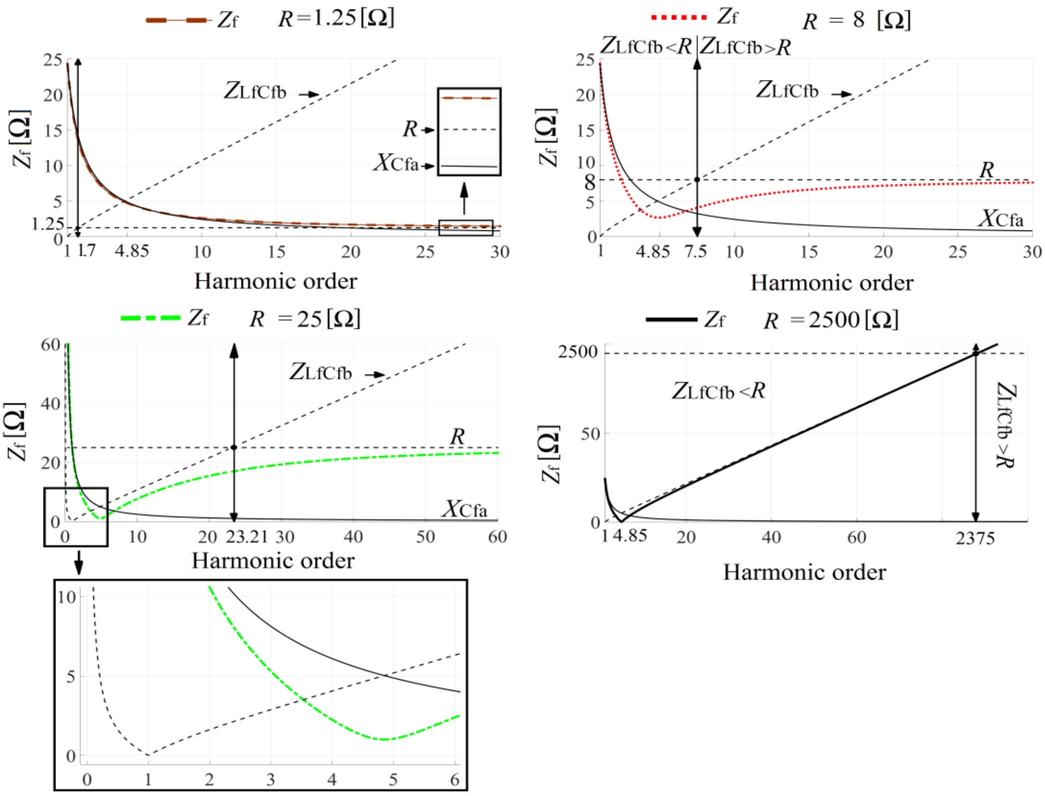

Figure 3.66 Filter impedance frequency characteristics for different value of damping resistance R ($\omega_{re} = 4.85$)

For high damping resistance, the C-type filter impedance frequency characteristic is like the one of single-tuned filter (Figure 3.66, e.g. 2500 Ω) and for the small values, it is similar to the one of the first-order filter (Figure 3.66, e.g. 1.25 Ω). On the one hand, when the damping resistance value is high, the 5th harmonic will be better filtered and the higher harmonics amplitude will be worse filtered. On the other hand, when the damping resistance is small, the situation will be in the opposite.

Figure 3.66 also sets for the comparison between the impedance Z_{LfCfb} (impedance of branch containing L_f and C_{fb}) and the damping resistance in point of view of harmonic current quantity, which can flow through the filter elements. For example, for 8 Ω, from the 1st to the 7.5th harmonic ($Z_{LfCfb} < R$) more current harmonic will flow through the L_f C_{fb} branch than the R branch. From the 7th harmonic ($Z_{LfCfb} > R$) more current harmonic will flow through R branch than the L_f C_{fb} branch. The same interpretation can be formulated for other characteristics in Figure 3.66 (25 Ω and 2500 Ω).

The PCC voltage and current waveforms and spectrums are presented in Figure 3.67 and Figure 3.68. The damping resistance has a big influence on the grid current and voltage characteristics. Its selection is very critical because an inappropriate choose of its value can makes the situation worse. In Figure 3.67 for instance, the damping resistance increase has improved the grid current waveform (see also THD of Figure 3.70(d)). But in the case of the grid voltage, the THD has increased (Figure 3.70(c)). The grid voltage waveform is less distorted (commutation notches reduction) for small damping resistance values (see Figure 3.68 for R = 1.25 Ω) than for high values (see Figure 3.68 for R between 8 Ω and 2500 Ω).

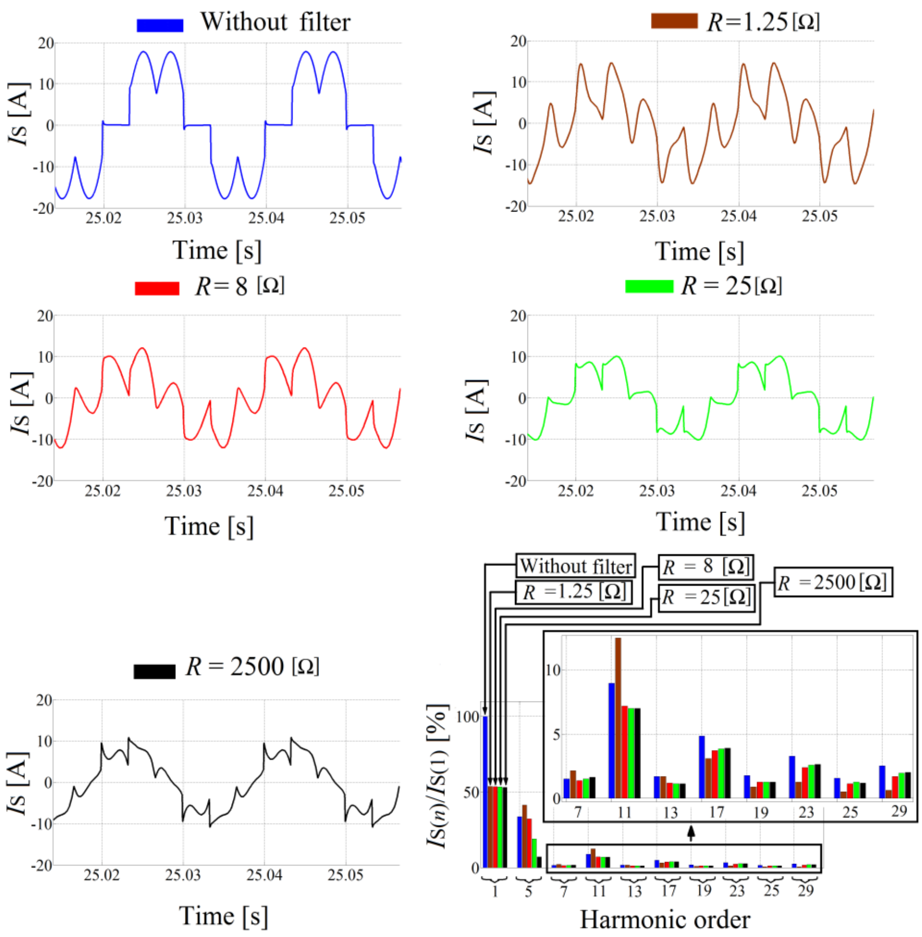

Figure 3.67 PCC current waveforms and spectrum

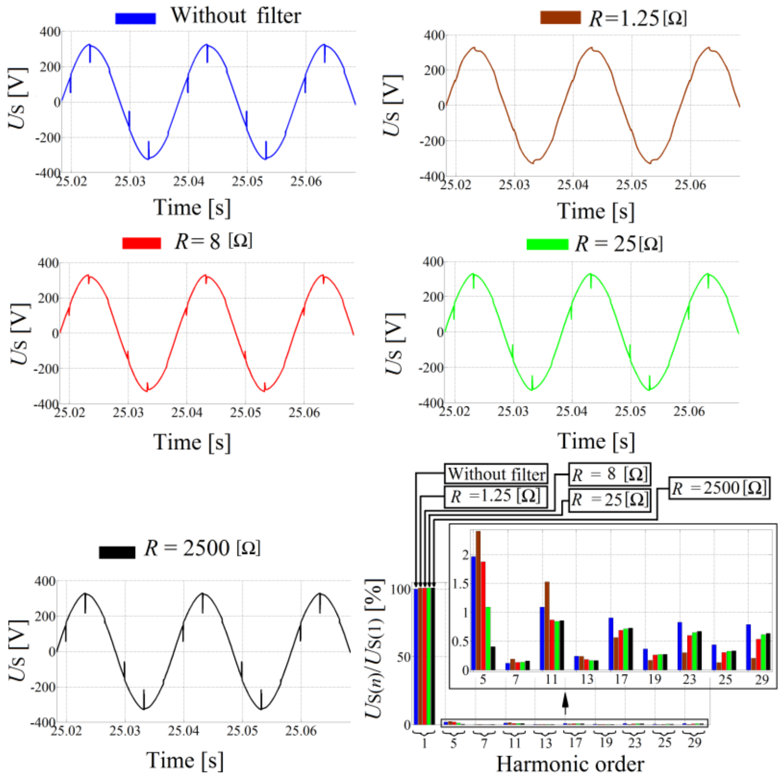

Figure 3.68 PCC voltage waveforms and spectrum

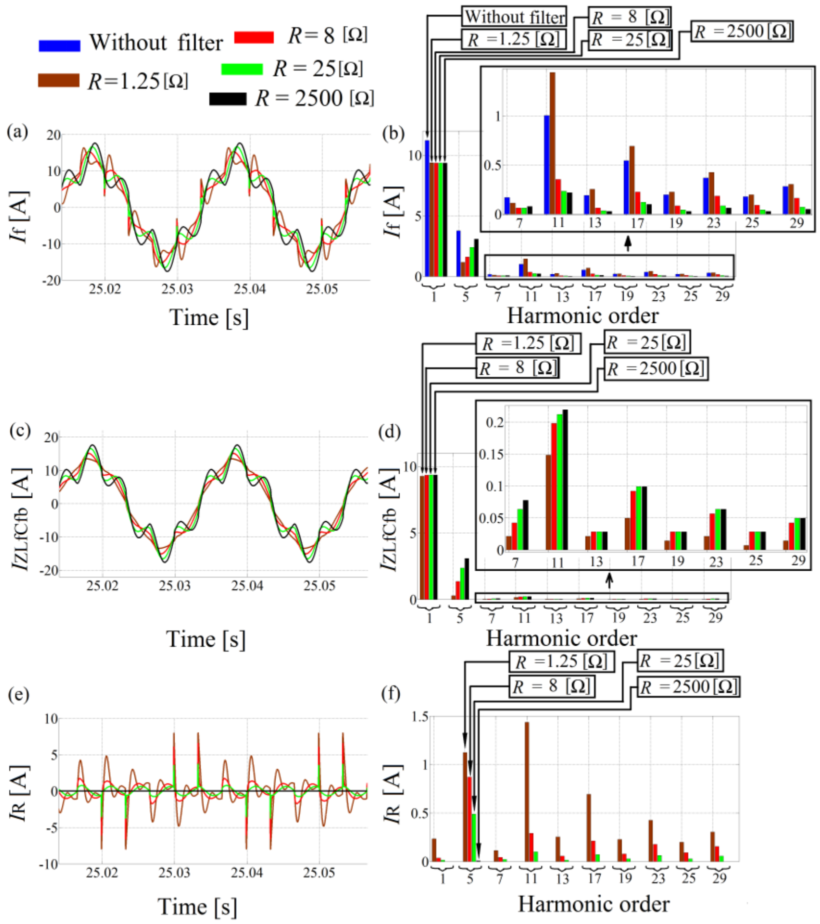

Figure 3.69 Filter current (a) and (b) its spectrum (the harmonics flowing through the filter are compared to the harmonics generated by the load - without filter); (c) filter current of the Z_{LfCfb} branch and (d) its spectrum; damping resistance current ($I_{f\,R}$) and (f) its spectrum

After the C-type filter connection, for R equal to 1.25 Ω, the 5th, 7th and 11th harmonics of grid viltage and current are amplified (because they are near the parallel resonance frequency caused between the grid and the filter – see Figure 3.73(b)) and the harmonics from 17th are reduced. However, with the resistance increase from 8 Ω to 2500 Ω, the 5th harmonc amplitude has considerably decreased (see spectrums of Figure 3.67 and Figure 3.68) whereas the amplitudes of high harmonics from the 17th have increased.

The filter current waveforms is presented in Figure 3.69(a), the current waveforms of the L_fC_{fb} branch and damping resistance are shown in respectively in Figure 3.69(c) and (e). The filter is less charged by the higher harmonics (from 7th) and more charged by the 5th order harmonic (Figure 3.69(b)) when the damping resistance is high (e.g. 2500 Ω). The fundamental harmonic flowing through the filter, flows largely through the L_fC_{fb} branch (Figure 3.69(d) and (f)). The quantity of current harmonic (apart of the fundamental) flowing through the damping resistance is high when its value (e.g. 1.25Ω) is small and small when its value is high (Figure 3.69(f)). The L_fC_{fb} branch is more charged by harmonics when the damping resistance increases (Figure 3.69(d)).

With the damping resistance increase, the active power at the PCC (P_S), filter terminals (P_f) and rectifier input (P_T) have decreased (Figure 3.70(a)). The reactive power of the PCC (Q_S) and of rectifier input (Q_T) have increased while the one of filter (Q_f) is remained almost the same (Figure 3.70(b)). The distortion of grid voltage and input rectifier voltage have increased whereas the one of the grid current has decreased (Figure 3.70(c) and (d)).

In Figure 3.71, it can be seen that the variation of current harmonics flowing between the filter parallel branches (Z_{LfCfb} and R) depends on their mutual relationship. For instance, the increase of the damping resistance (R) value has increased the current harmonics in the L_fC_{fb} branch (Figure 3.71(d)) and the decrease of damping resistance, has decreased the current harmonics in the L_fC_{fb} branch (Figure 3.71(a)).

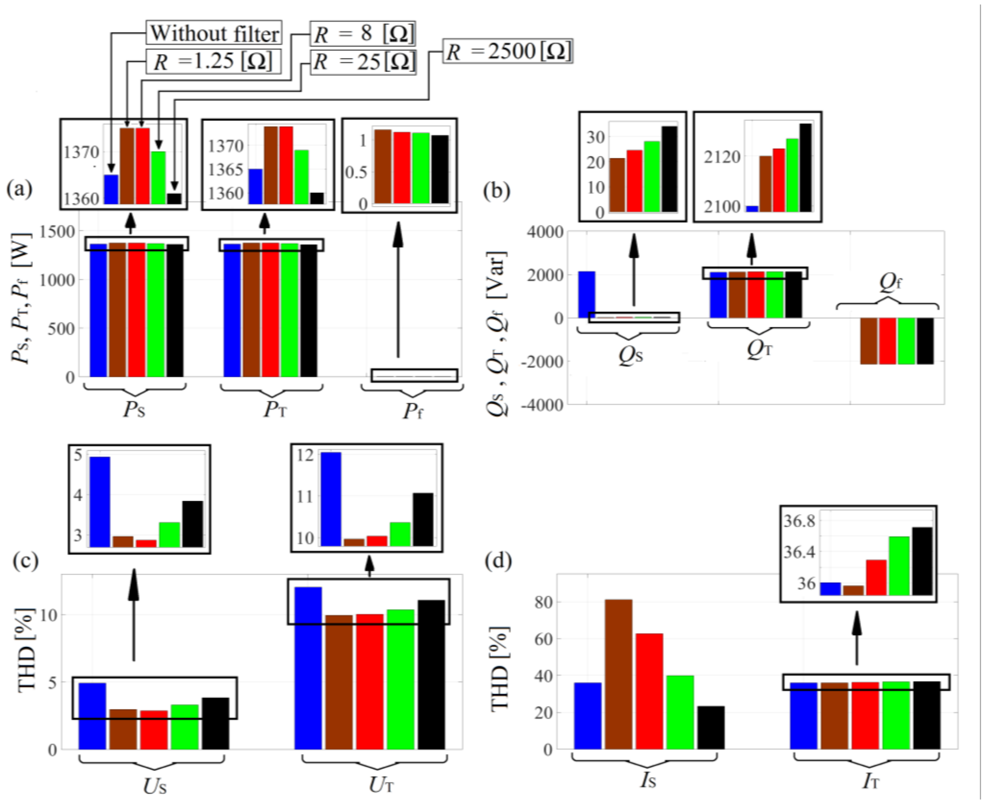

Figure 3.70 (a) active power at the PCC (P_S), filter terminals (P_f) and input of rectifier (P_T); (b) reactive power at the PCC (Q_S), filter terminals (Q_f) and input of rectifier (Q_T); (c) THD of PCC voltage (U_S) and voltage at the input of rectifier (U_T); (d) THD of PCC current (I_S) and current at the input of rectifier (I_T)

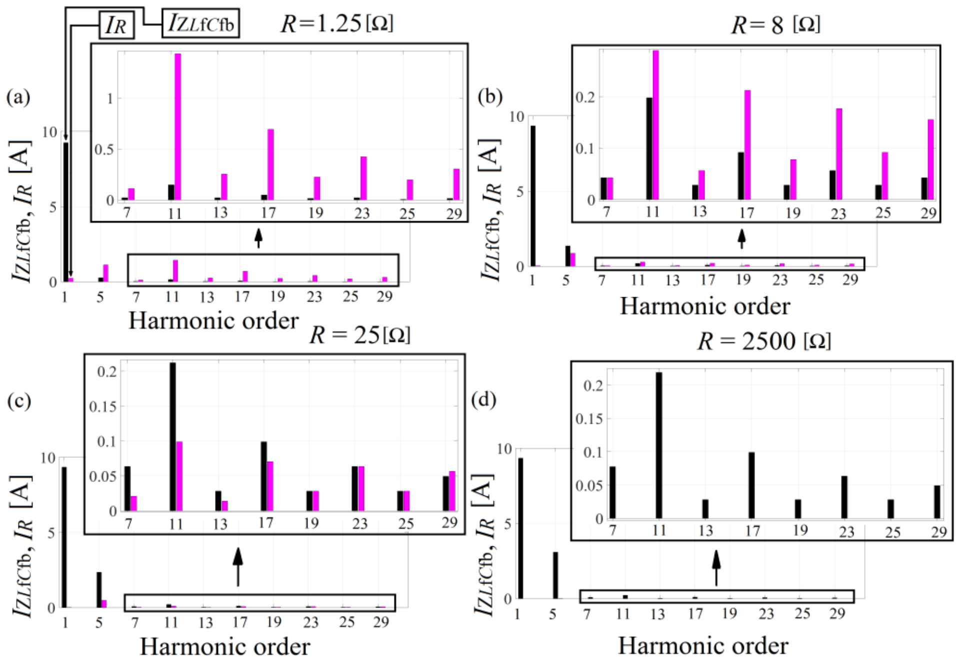

Figure 3.71 Spectrums of current flowing through the resistance R and reactance X_{Lf} for R equal to (a) 1.25Ω, (b) 8Ω, (c) 25Ω, (d) 2500Ω

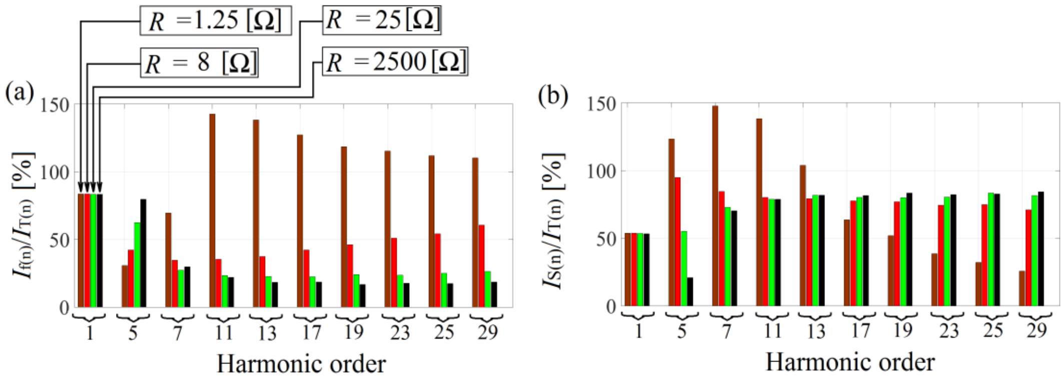

Figure 3.72 C-type Filter effectiveness: (a) from the filter side, (b) from the grid side

It is observed in Figure 3.72(a) that the filter is more efficient on the reduction of 5th harmonic when its damping resistance is high (e.g. 2500Ω). The amplitude of harmonics from the 7th to the 29th flowing through the filter is higher than the one generated by the load (e.g. the percentages are above 100 %). These harmonics have been amplified at the filter terminals (parallel resonance).

It is also observed in Figure 3.72(b) that the filter is less efficient on the reduction of 5th harmonic when its damping resistance is small (e.g. 1.25Ω). The grid current harmonics from the 5th to the 13th are above 100 %. The value of these harmonics have been amplified at the PCC (parallel resonance).

The impedance of the simulated power system measured at the rectifier input terminals (for different value of R) is presented in Figure 3.73. The series and parallel resonances are damped for the smaller values of damping resistance.

The choose of the C-type filter damping resistance depends on how much the harmonic to be eliminated should be reduced as well as on the reduction level of higher harmonics (higher than the harmonic to be eliminated) in width band.

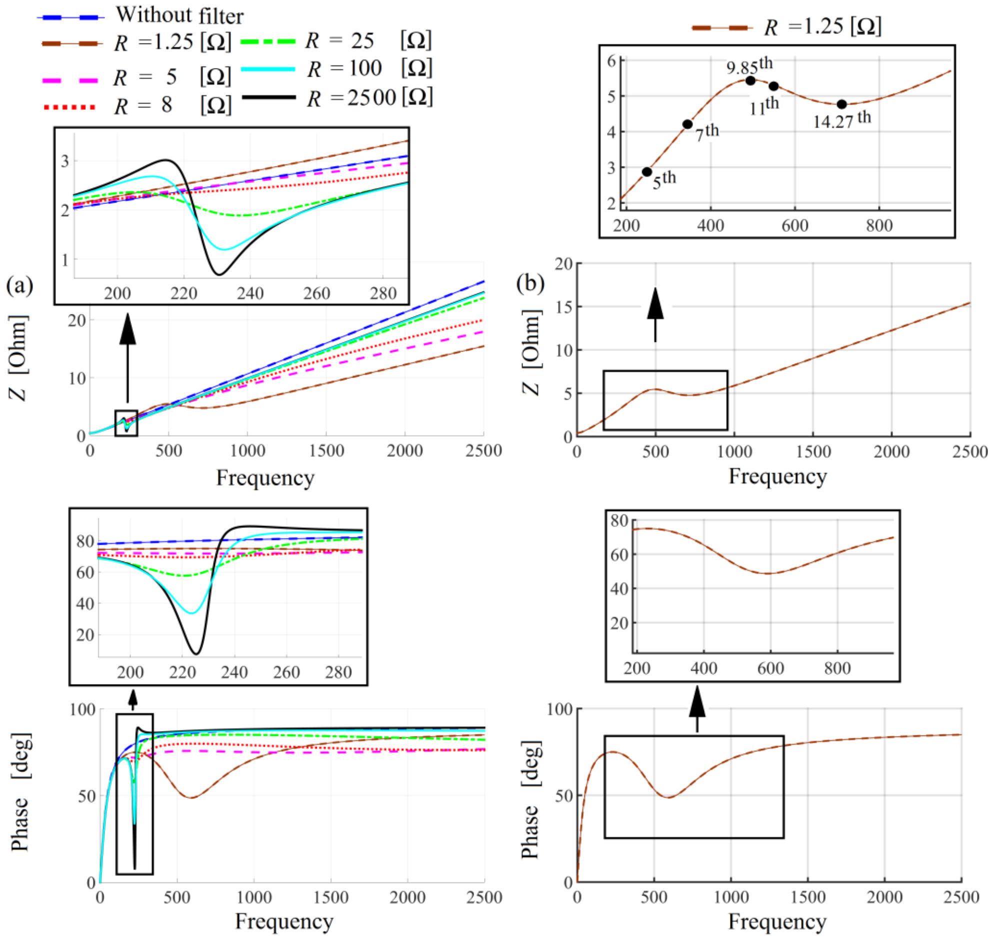

Figure 3.73 (a), (b) characteristics of power system impedance versus frequency observed at the input of thyristor bridge for different value of filter resistance

3.4.3.4.1 Detuning of C-type filter

The studies objective is to present the effects of C-type filter detuning phenomenon (due to the aging or faults on its elements etc.) on the reduction of the PCC voltage and current harmonic to be eliminated (e.g. 5th) and higher harmonics in the power system. That detuning is concerned by the increase and decrease of the nominal values of the capacitors (C_{fa}, C_{fb}) and reactor by ±10%. In practice the capacitor capacitance tolerance is around -5% to +10% and the reactor inductance tolerance is around ±10% (see Figure IV.4 and Figure IV.7 of Annex IV). The C-type filter damping resistance R is maintained to 25 Ω during the studies.

❖ ***The increase and decrease of the filter capacitor C_{fa} by ±10%***

The Figure 3.74(a) shows that with the increase of filter capacitor (C_{fa}) by +10 %, the characteristic has moved to the left side (n_{re} = 4.63) and the 5th harmonic impedance has increased and remains on the inductive side of the characteristic. With the decrease of C_{fa} by -10%, the characteristic has shifted to the right side and the impedance of 5th harmonic has increased and is on the capacitive side of the characteristic (its amplification can occur on the grid side (there is a resonance danger)). In the both cases (for the considered example), the impedance of 5th harmonic has increased, but is much higher in the case of the +10 % increase.

The PCC voltage and current waveforms as well as the spectrums are indicated in Figure 3.75. The amplitude of 5th harmonic of grid voltage and current has been slightly amplified by the filter when this latter was detuned to the frequency order of 5.1 ($C_{fa(-10\%)}$)).

The amplitude of grid voltage and current 5th harmonic is smaller when C_{fa} is increased by +10% than when it is decreased by -10% ($C_{fa(-10\%)}$). The C-type filter tuned to the frequency order of 4.85 presents the lowest amplitude of PCC voltage and current 5th harmonic (Figure 3.75).

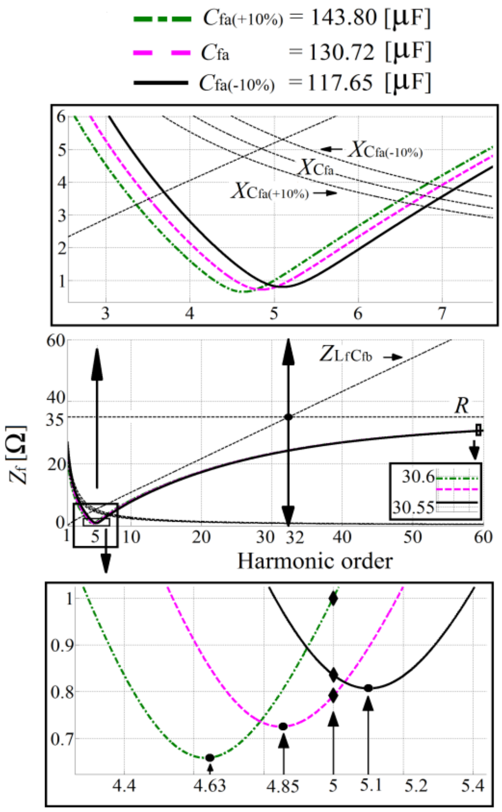

Figure 3.74 C-type filter impedance versus frequency characteristic for $C_{fa\pm10\%}$

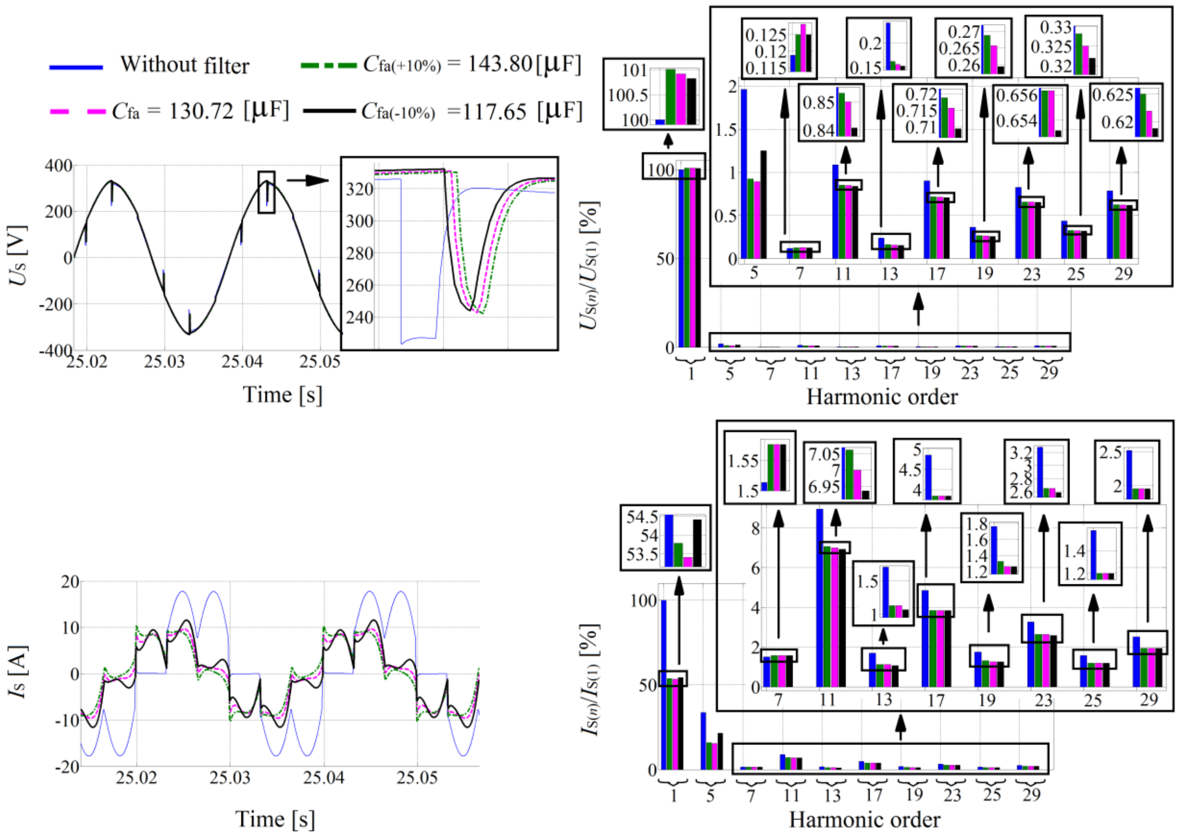

Figure 3.75 Grid voltage and current with their spectrums (p.u.) after detuning the C-type filter ($C_{fa\pm10\%}$)

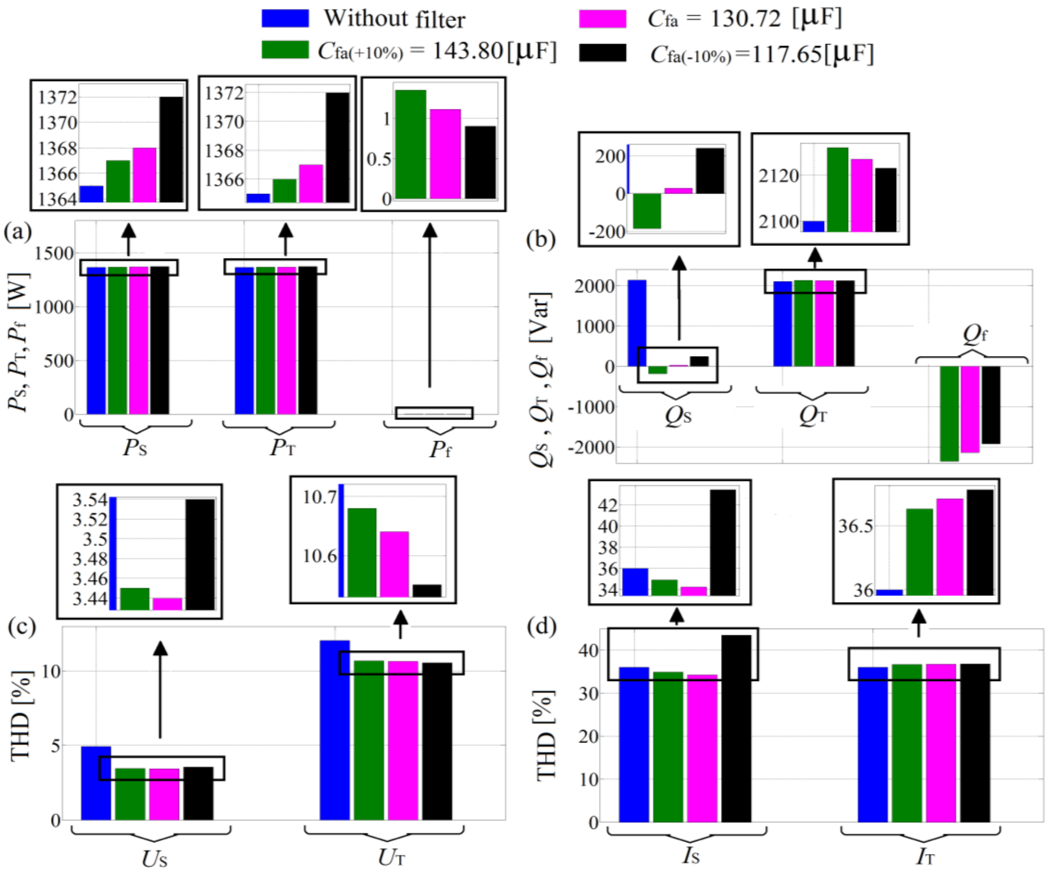

Figure 3.76 (a) Active power at the PCC (P_S), filter terminals (P_f) and input of rectifier (P_T); (b) reactive power at the PCC (Q_S), filter terminals (Q_f) and input of rectifier (Q_T); (c) THD of PCC voltage (U_S) and voltage at the input of rectifier (U_T); (d) THD of PCC current (I_S) and current at the input of rectifier (I_T) ($C_{fa\pm10\%}$)

The higher harmonics (from the 11th) of grid voltage and current are better reduced by the filter when the capacitor C_{fa} is decreased by -10% than when it is increased by +10% (Figure 3.75).

The variation of active and reactive powers at the PCC, filter terminals and rectifier input terminals are presented in Figure 3.76(a)(b). The PCC and input rectifier voltage and current THD for different C-type filter detuning frequency is presented in Figure 3.76(c) to (d).

The filter current waveforms and spectrums are presented in Figure 3.77. The amplification of 5th harmonic is also observed on the filter spectrum (I_f) for C_{fa} decreased by -10%.

The impedance of the branch (L_f, C_{fb}) (see Figure 3.74) is lower than the damping resistance (R) for the frequencies order from the fundamental to the 29th harmonic and higher than the damping resitance for the frequencies order from the the 29th harmonic. In the comparison spectrums of Figure 3.78, it can be noticed that by increasing or decreasing C_{fa} by ±10%, the amplitude of harmonics (from the fundamental) flowing through the damping resistance is smaller than the one of harmonics flowing through the Z_{LfCfb} branch (Figure 3.78(a) to (c)).

The impedance versus frequency characteristics of the simulated power system seen from the rectifier input is presented in Figure 3.79. On one hand, the decrease of C_{fa} by -10% has shifted the characteristic to the right and increased the system impedance of parallel and series resonance. On other hand, its increase by +10% has shifted the characteristic to the left by reducing the system impedance of parallel and series resonance (Figure 3.79).

The detuning of the C-type filter due to the variation of the capacitor C_{fa} (assuming L_f, C_{fb} and R constant) can reduce its efficiency in term of harmonics mitigation at the grid side.

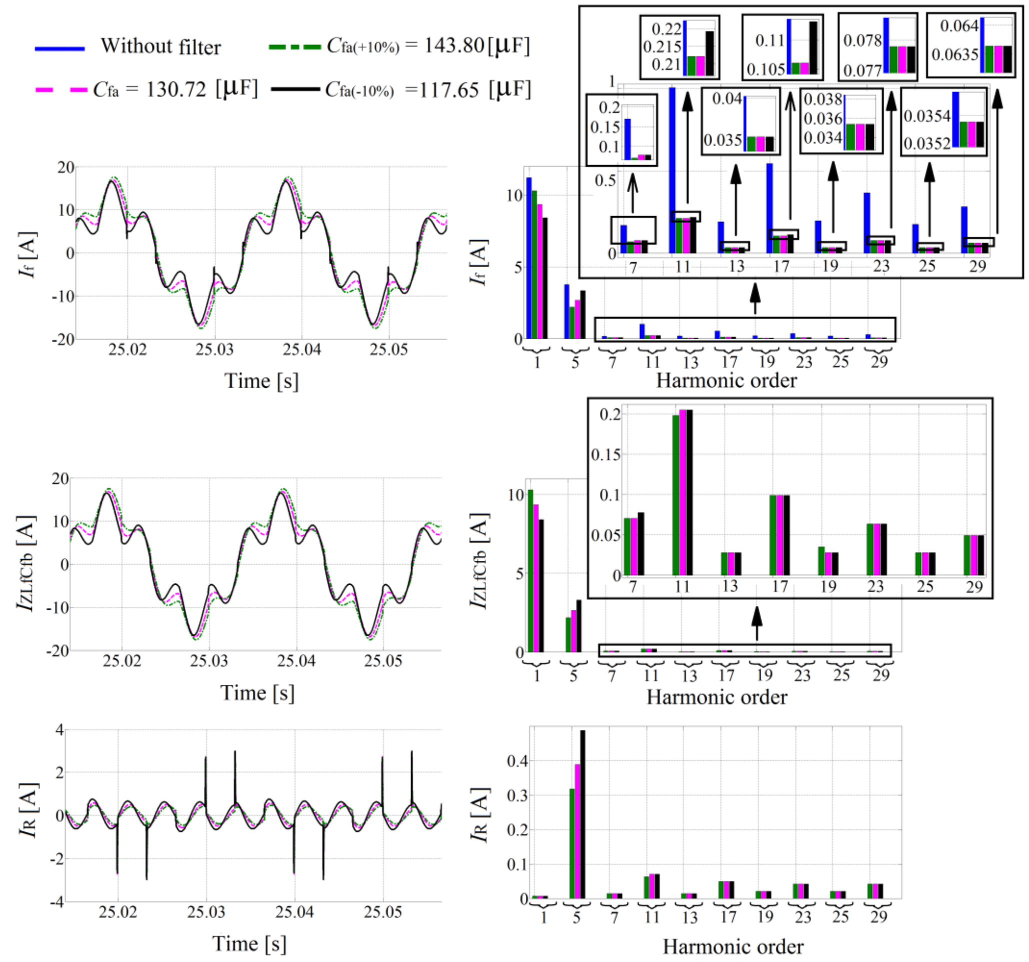

Figure 3.77 Filter current waveforms and their spectrums. I_{ZLfCfb} - current of Z_{LfCfb} branch, I_R - damping resistance current ($C_{fa\pm10\%}$)

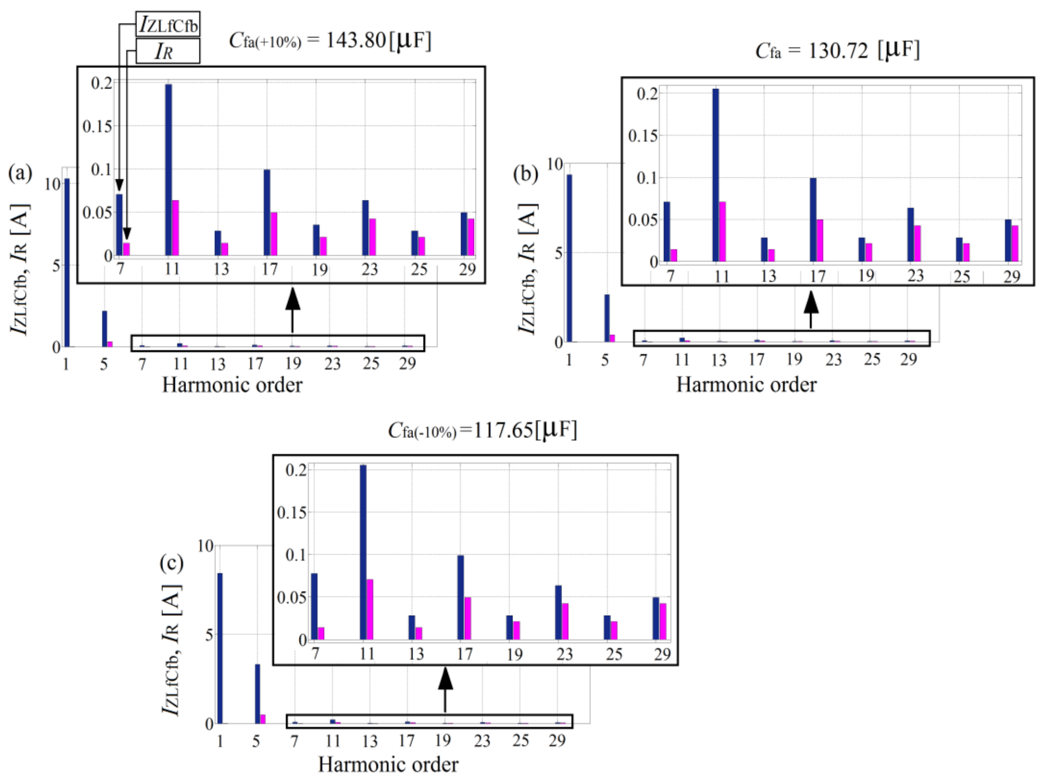

Figure 3.78 The spectrum of current flowing through the resistance R is compared to the spectrum of current flowing through the Z_{LfCfb} branch for: (a) $C_{fa(+10\%)}$, (b) C_{fa} and (c) $C_{fa(-10\%)}$

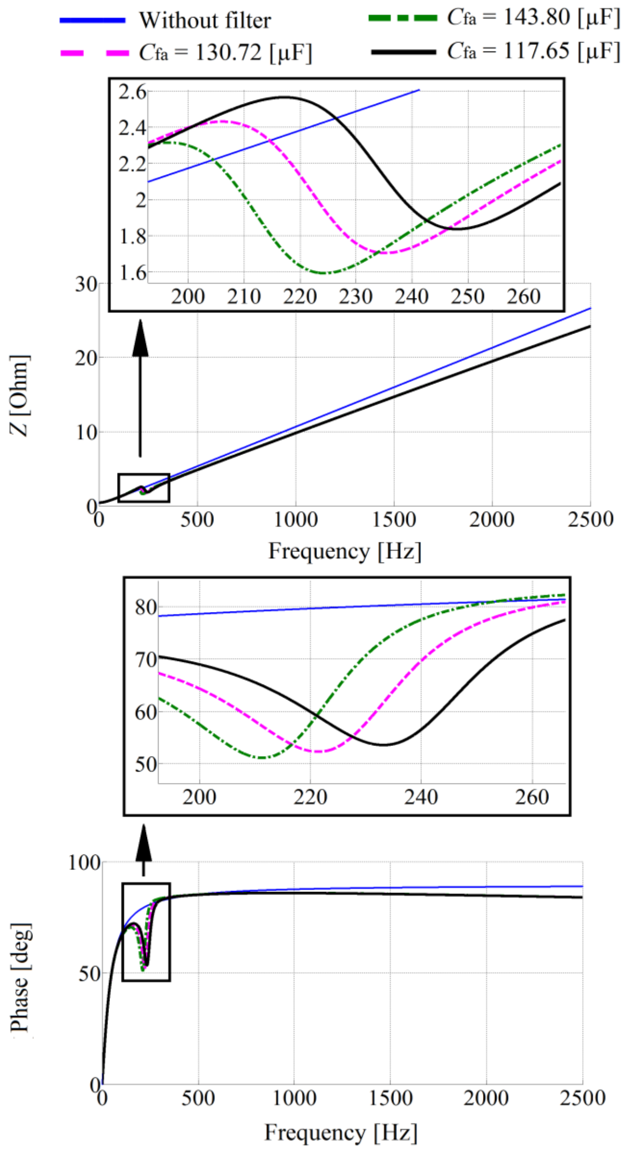

Figure 3.79 Characteristic of power system impedance measured at the input of thyristor bridge for different value of filter capacitor capacitance ($C_{fa\pm10\%}$)

❖ *The increase and decrease of the filter reactor inductance Lf by ±10%*

The increase and decrease of L_f have an influence on the resonance frequency (50 Hz) of the filter C_{fb} L_f branch. Therefore the change of L_f by ±10% has caused the reduction and augmentation of that frequency (50 Hz) (e.g. $f_{(1)+10\%}$ = 47.5Hz, $f_{(1)-10\%}$ = 52.5Hz).

For L_f increased by +10% the C-type filter is detuned from the frequency of 242.5 Hz (n_{re} = 4.85) to the frequency of 231 Hz (n_{re} = 4.62) (lower than 250Hz) and for L_f decreased by -10%, it is detuned from the frequency of 242.5 Hz to the frequency of 255.5Hz (n_{re} = 5.11) (higher than 250 Hz) (Figure 3.80).

On the one hand, the filter impedance of 5th harmonic has increased (characteristic shifted to the left – Figure 3.80) with the filter reactor inductance increase and remains on the inductive side of the characteristic. On the other hand, it has decreased (characteristic shifted to the right) with the reactor inductance decrease and is on the characteristic capacitive side (can be amplified from the grid side because of parallel resonance condition).

The spectrums of PCC voltage and current (Figure 3.81) shows that the harmonics higher than the 5th (e.g. from 11th) are better reduced by the C-type filter when L_f is decreased by -10% though the 5th harmonic is slightly amplified. By increasing L_f by +10%, the filter efficiency has reduced in term of 5th harmonic and higher harmonics reduction from the PCC side (Figure 3.81).

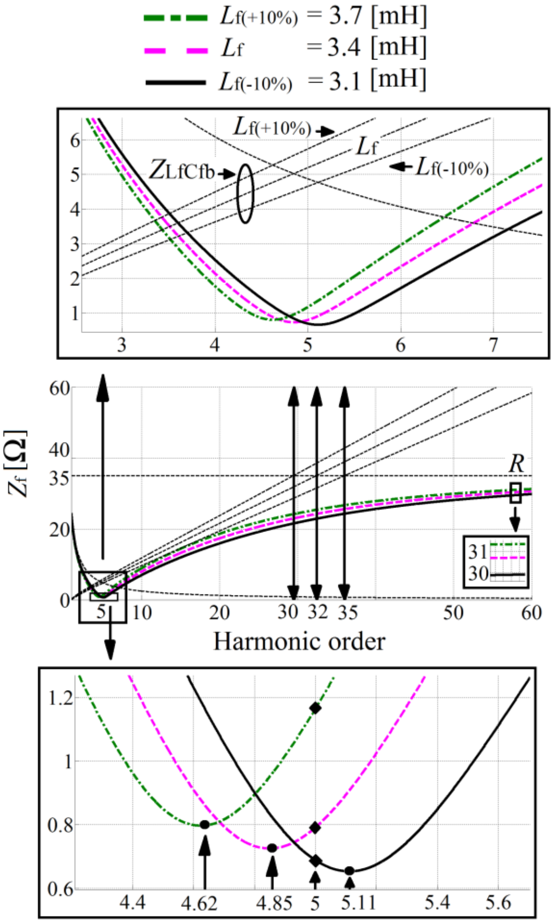

Figure 3.80 C-type filter impedance versus frequency characteristics ($L_{f\pm10\%}$)

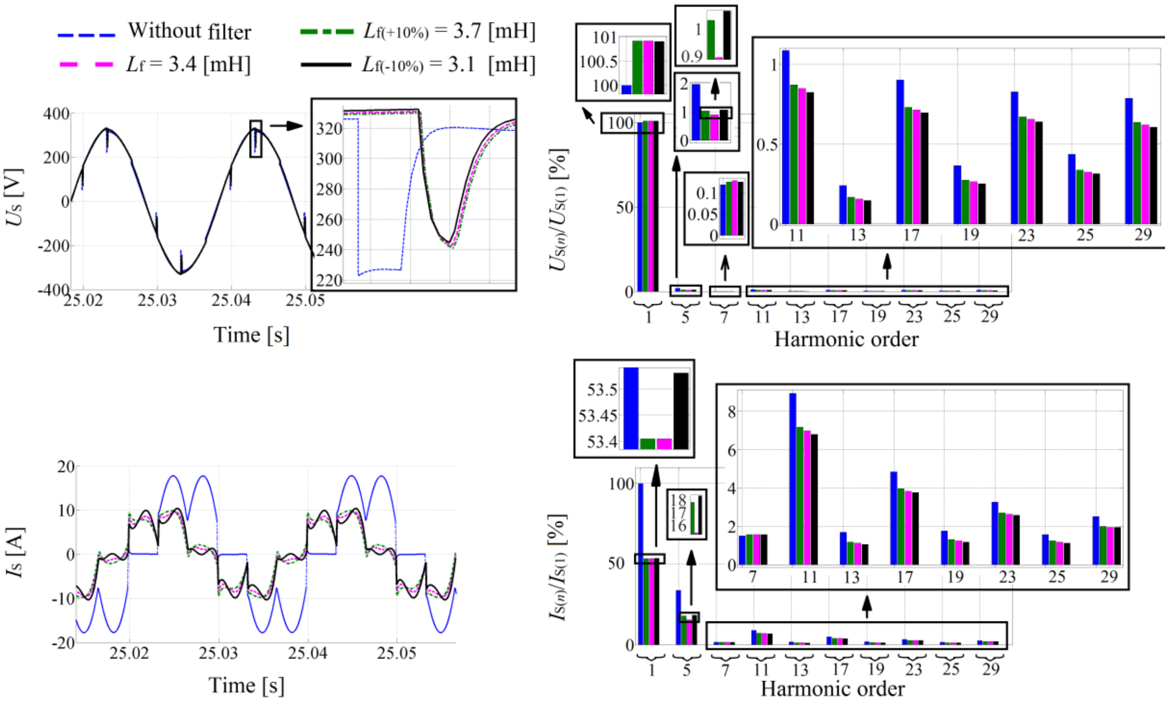

Figure 3.81 Grid voltage and current with their spectrums (p.u.) ($L_{f\pm10\%}$)

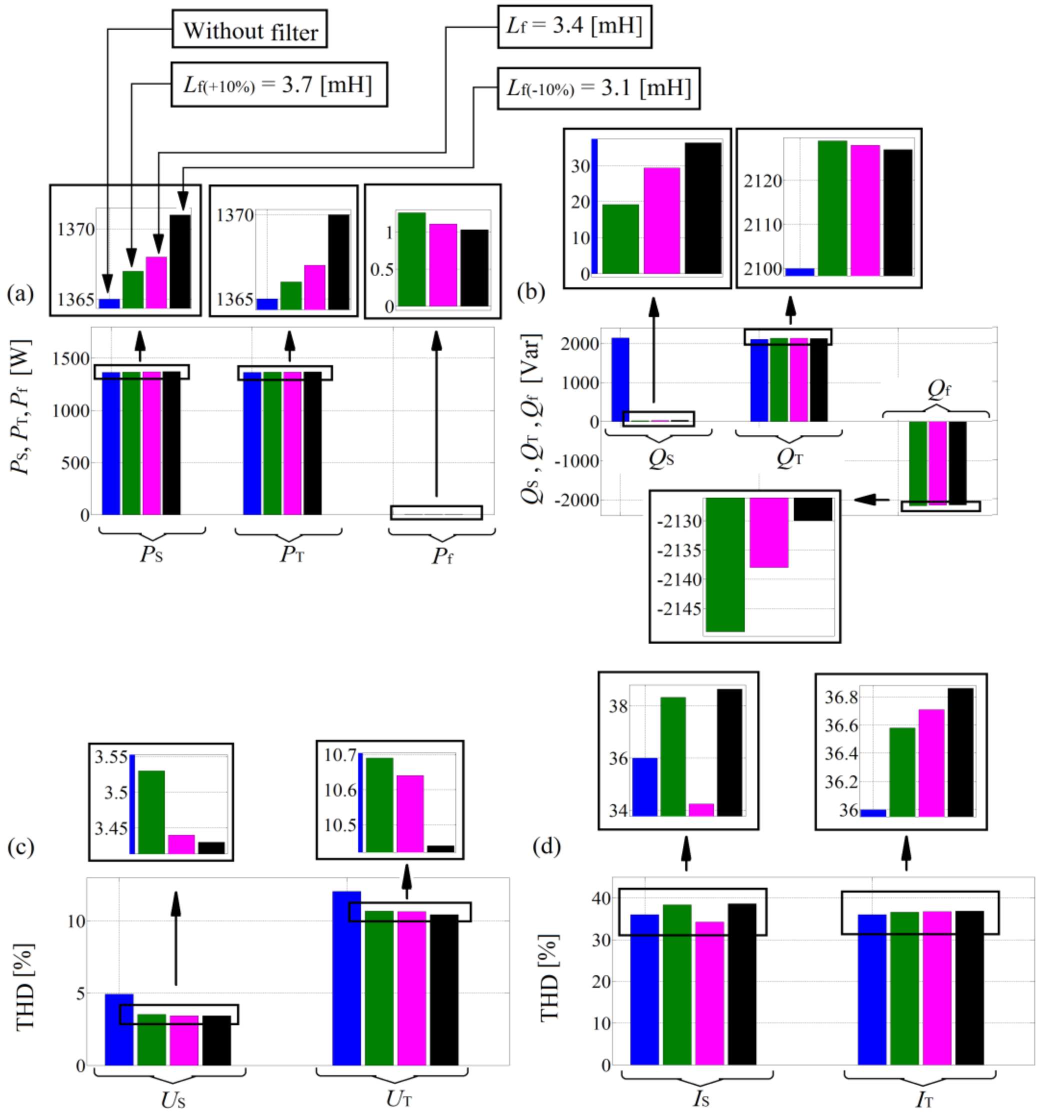

Figure 3.82 (a) Active power at the PCC (P_S), filter terminals (P_f) and input of rectifier (P_T); (b) reactive power at the PCC (Q_S), filter terminals (Q_f) and input of rectifier (Q_T); (c) THD of PCC voltage (U_S) and voltage at the input of rectifier (U_T); (d) THD of PCC current (I_S) and current at the input of rectifier (I_T) ($L_{f\pm10\%}$)

The influence of the C-type filter reactor value change on the active and reactive power at the particular points of the considered power system as well as on the voltage and current deformation rate is presented in Figure 3.82(a), (b), (c) and (d).

The filter current (I_f) waveform and spectrum of Figure 3.83 show that the 5th harmonic flowing through the filter has the highest amplitude (the 7th to 17th harmonics as well) for $L_{f(-10\%)}$ and the lowest for $L_{f(+10\%)}$.

The damping resistance (R) is higher than the filter impedance of the branch (Z_{LfCfb}) for the frequencies from the fundamental to the 30th and lower for the frequencies from the 30th ($L_{f(+10\%)}$, see also Figure 3.80). Observing Figure 3.80, For $L_{f(-10\%)}$, the resistance R is higher than the filter impedance of (C_{fb}, L_f) branch for the frequencies from the fundamental to the 35th and lower for the frequencies from the 35th. The current harmonics (I_{LfCfb}) flowing through Z_{LfCfb} presents the highest amplitude in comparison to those flowing through R (Figure 3.84(a), (b) and (c)).

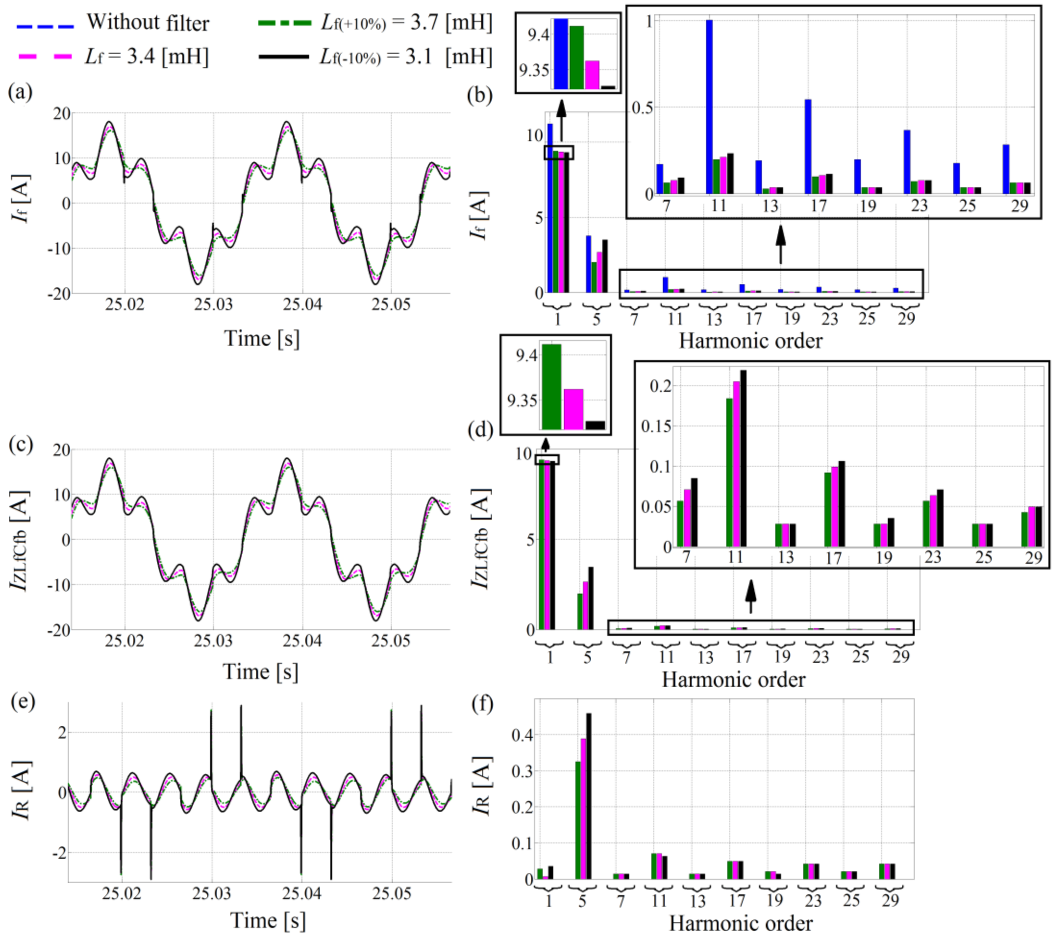

Figure 3.83 Filter current waveforms and their spectrums. I_{ZLfCfb} - current of Z_{LfCfb} branch, I_R – damping resistance current ($L_{f\pm10\%}$)

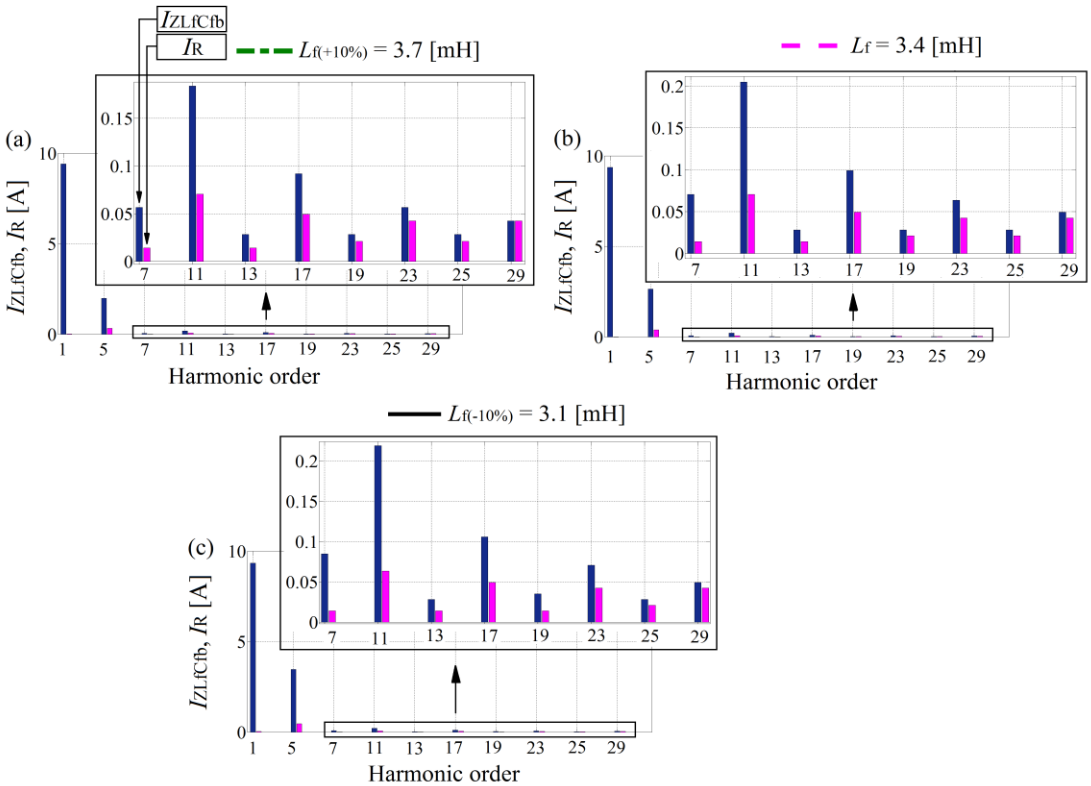

Figure 3.84 The spectrum of current flowing through the resistance R is compared to the spectrum of current flowing through the Z_{LfCfb} branch for: (a) $L_{f(+10\%)}$, (b) L_f and (c)

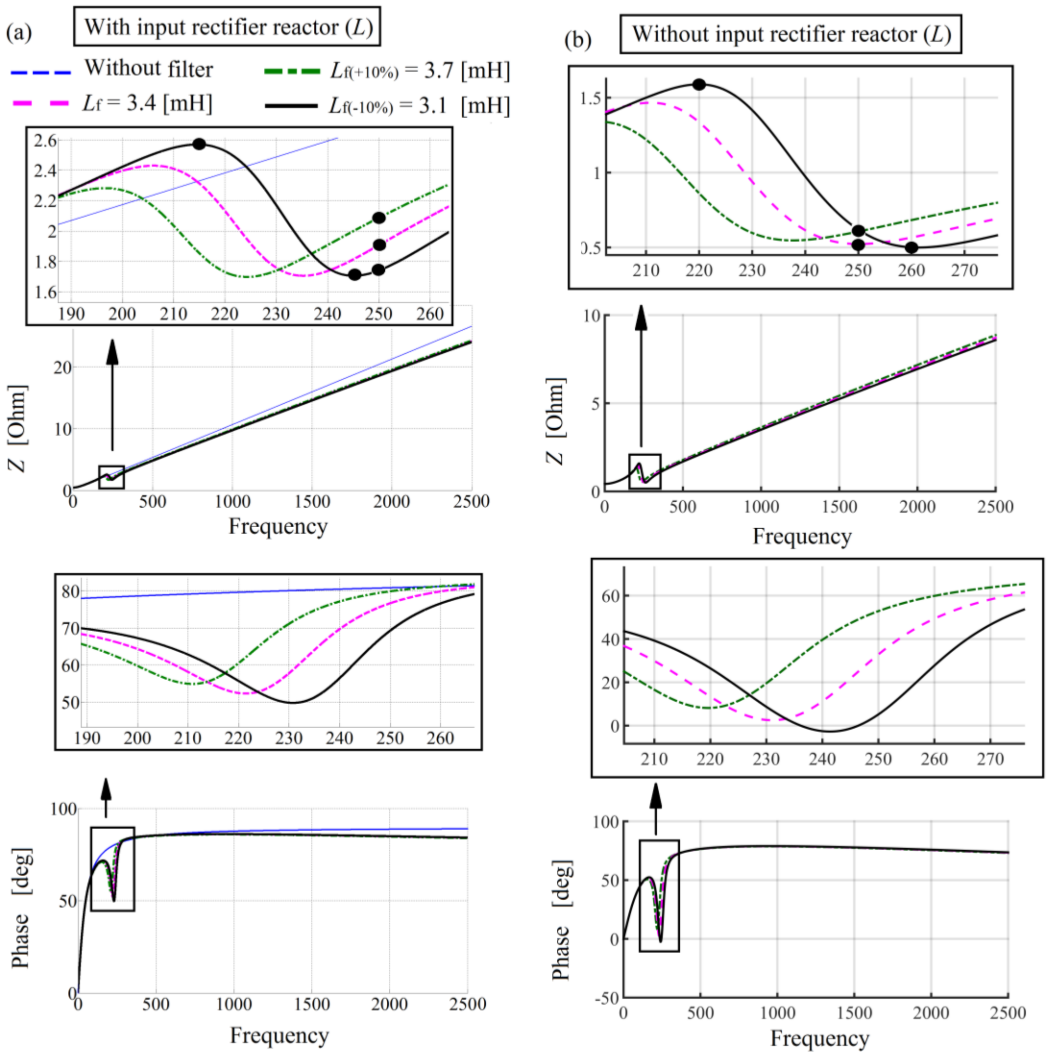

Figure 3.85 Characteristic of power system impedance measured at the input of thyristor bridge for different value of filter reactor inductances (L_f): (a) when the line reactor (L) at the rectifier is considered and (b) when it is not ($L_{f\pm10\%}$)

Two cases of study are considered for the power system impedance seen from the rectifier input. The first one by considering the line reactor at the rectifier input (Figure 3.85(a)) and the second one by neglecting the line reactor (Figure 3.85(b)). In the both cases (Figure 3.85(a) and (b)), the impedance frequency characteristic is shifted to the right for L_f decreased by -10% (the impedance of parallel resonance between the filter capacitors and grid reactor has increased and the impedance of series resonance caused by the filter has slightly decreased) and shifted to the left for L_f increased by +10% (the impedance of parallel resonance has decreased and the impedance of series resonance has slightly increased in Figure 3.85(b) and is almost the same in Figure 3.85(a)).

For $L_{f(-10\%)}$, the 5th harmonic power system impedance is fare from the parallel resonance when the input rectifier reactor (L) is considered (Figure 3.85(a)) and is near the parallel resonance frequency when L is not considered (Figure 3.85(b)). A slightly amplification of 5th harmonic from the grid side voltage and current is justified by Figure 3.85(b) ($L_{f(-10\%)}$).

❖ ***The increase and decrease of the filter capacitor Cfb by ±10%***

The resonance frequency of the C_{fb} L_f branch is 52.5 Hz for $C_{fb+10\%}$ and 47.5 Hz for $C_{fb-10\%}$. By increasing C_{fb} by +10% and decreasing it by -10%, the C-type filter resonance frequencies are respectively 242 Hz (n_{re} = 4.84) and 243 Hz (n_{re} = 4.86). Comparing the impedance versus frequency characteristics of Figure 3.86 to the one of Figure 3.80 and Figure 3.74, it can be noticed that the change of C_{fb} (detuned of C-type filter based on the variation of C_{fb} only) will have significantly less influence in the electrical power system than the change of L_f and C_{fa}.

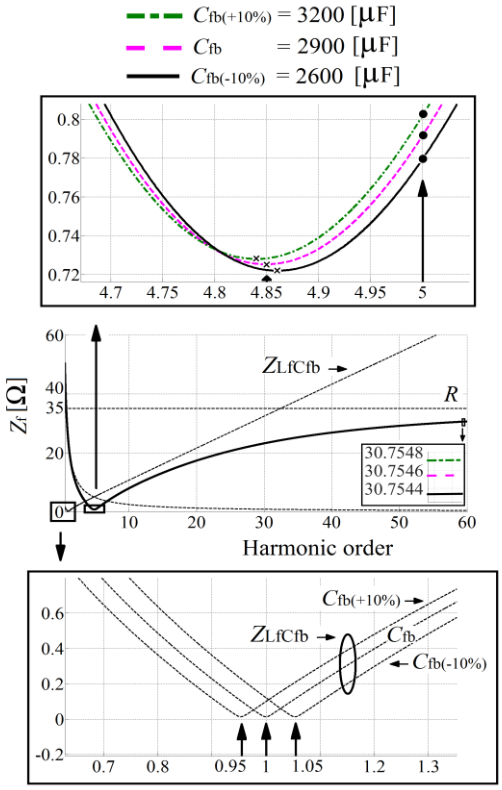

Figure 3.86 C-type filter impedance versus frequency characteristics for $C_{fb\pm10\%}$

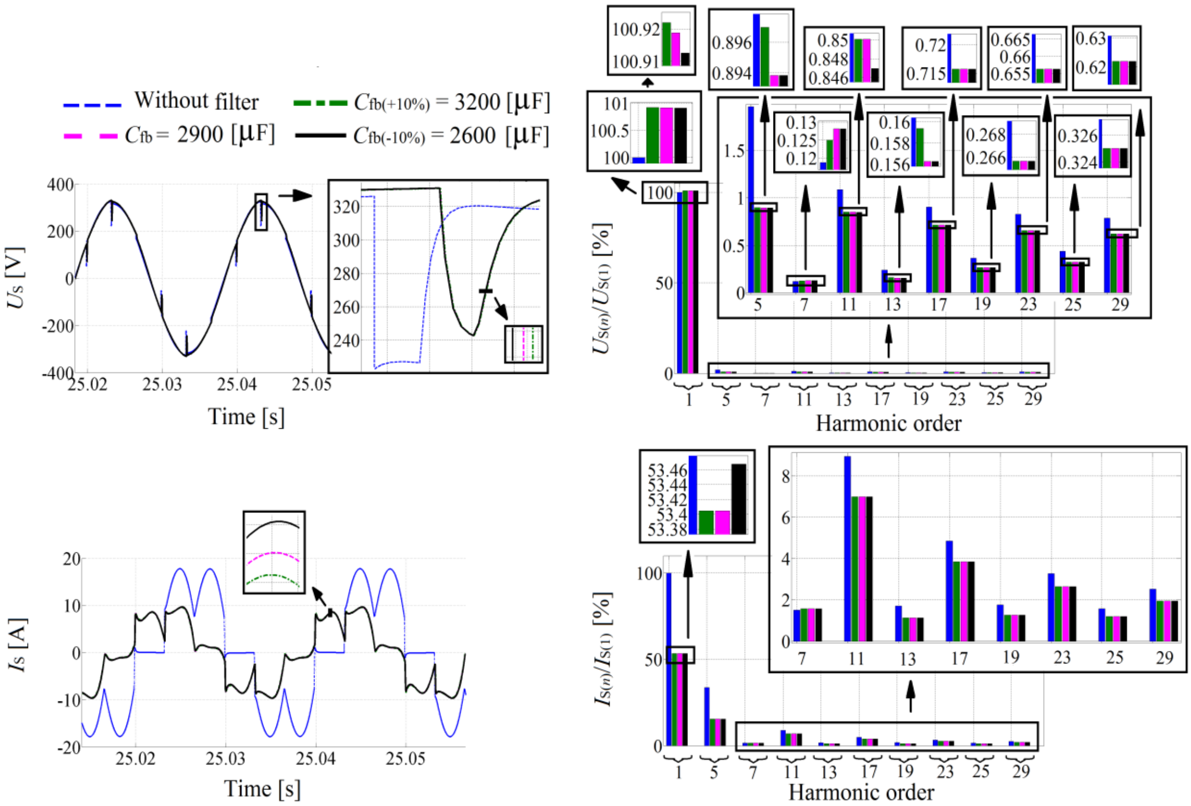

Figure 3.87 Grid voltage and current with their spectrums (p.u.)

The increased or decreased of C-type filter capacitor capacitance (C_{fb}) by ±10% does not have an significant influence on the grid voltage commutation notches (Figure 3.87); grid current 5th and higher harmonics (Figure 3.87); filter currents (Figure 3.88); power system active and reactive powers and THDs (Figure 3.89).

There is not significant difference between characteristics of Figure 3.90 when C_{fb} is increased or decreased by 10%. However, by considering the input rectifier reactor (L), the parallel and series resonance have been shifted to the left and their impedances have increased. In the case without L, the series resonance has occurred at the frequency of 250 Hz, whereas in the case with L, it has occurred at the frequency of 235 Hz and the system impedance of 5th harmonic has increased (Figure 3.90).

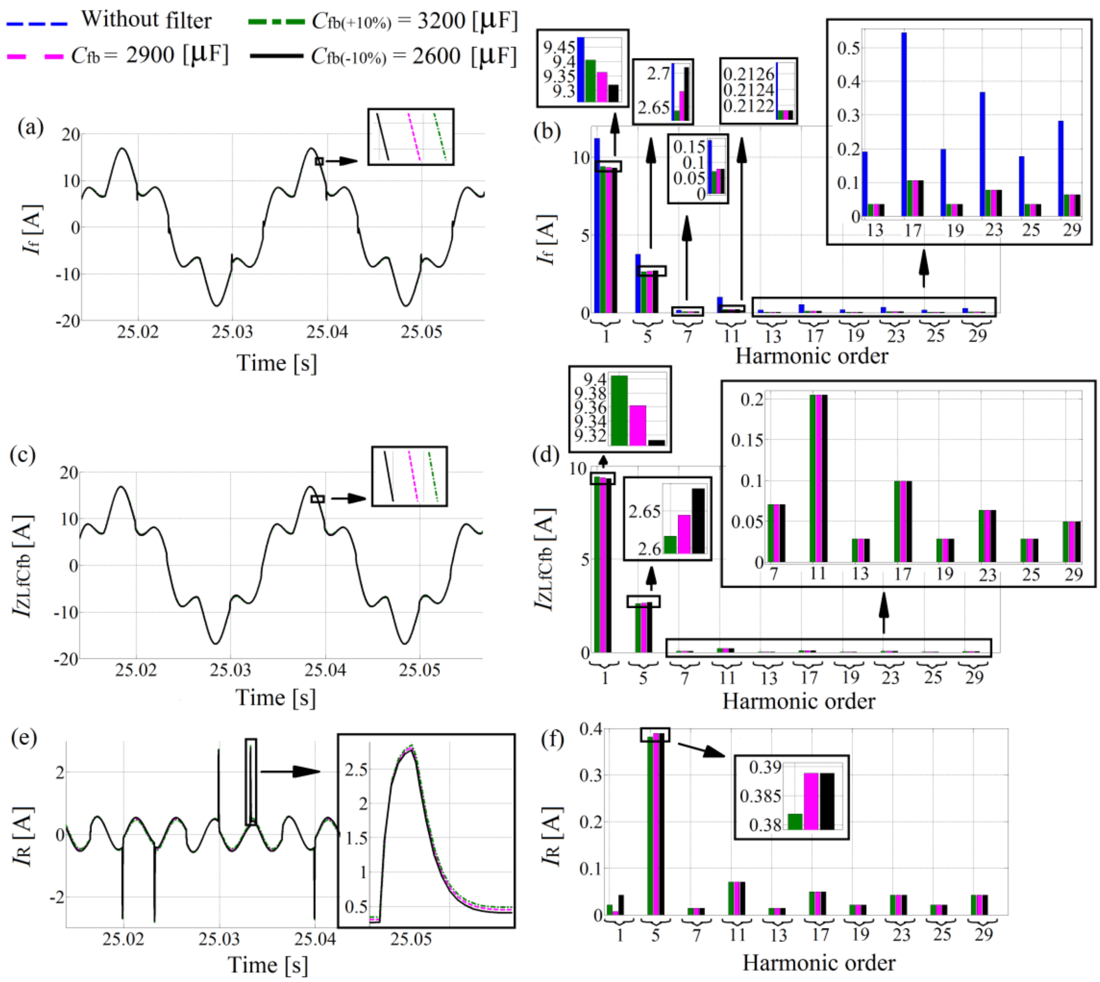

Figure 3.88 Current flowing though the filter with the spectrums. I_{ZLfCfb} - current of (L_f, C_{fb}) branch, I_R - damping resistance current

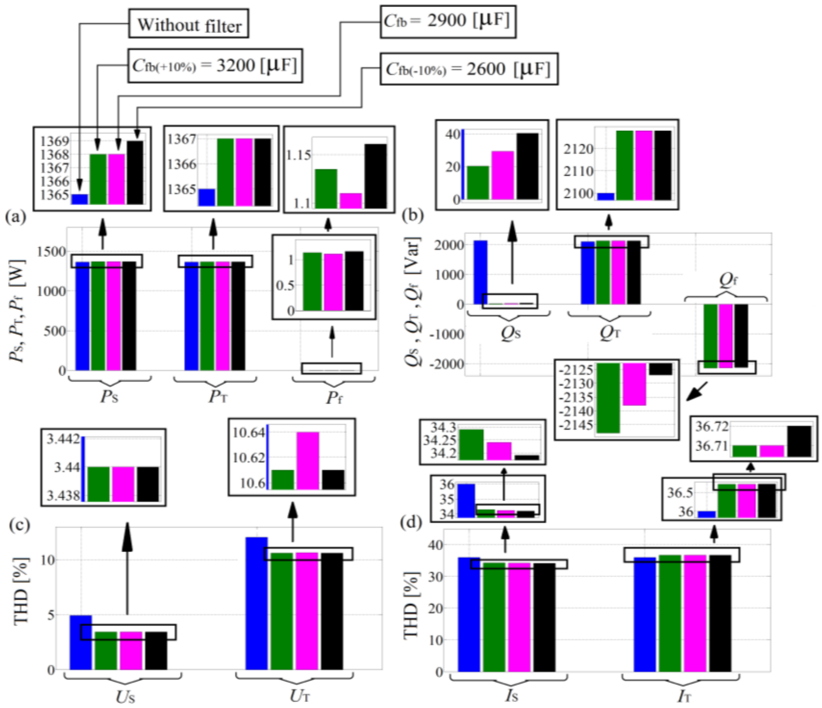

Figure 3.89 (a) Active power at the PCC (P_S), filter terminals (P_f) and input of rectifier (P_T); (b) reactive power at the PCC (Q_S), filter terminals (Q_f) and input of rectifier (Q_T); (c) THD of PCC voltage (U_S) and voltage at the input of rectifier (U_T); (d) THD of PCC current (I_S) and current at the input of rectifier (I_T)

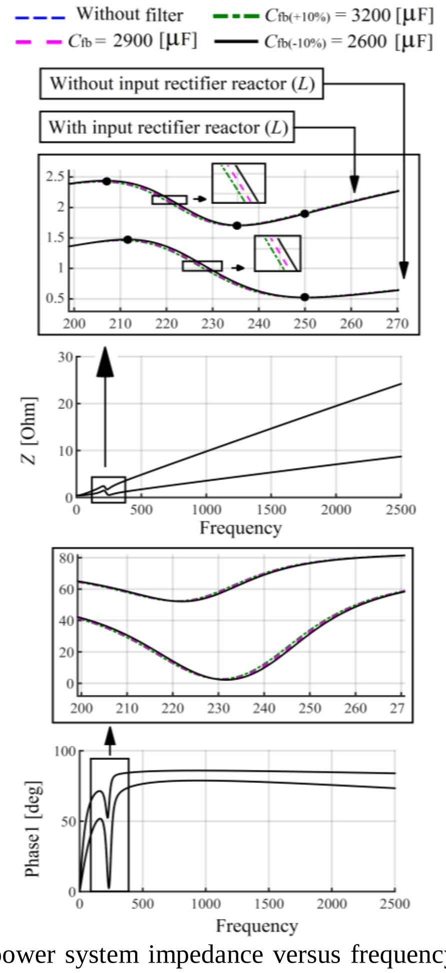

Figure 3.90 Characteristics of power system impedance versus frequency observed at the input of thyristor bridge for different value of filter capacitor capacitance C_{fb}, when the input rectifier reactor (L) is considered and when is not considered

3.5 Conclusion

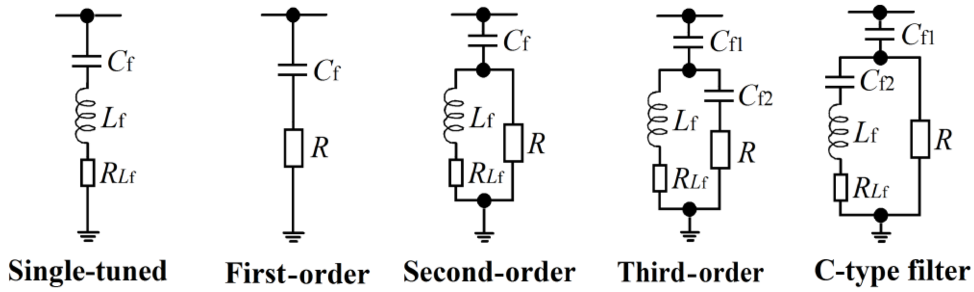

Figure 3.91 Compared topologies

Table 3.17 comparison assumptions

	Qf = -2172.5Var, θ = 57º, n_{re} = 4.85, q'= 85				
	First-order	Single-tuned	Second-order	third-order	C-type
R [Ω]	-	-	0.08	0.08	0.08
	-	-	1.25	1.25	1.25
	-	-	8	8	8
	-	-	25	25	25
R_{Lf} [Ω]	-	0.0127	0.0127	0.0043	0.0127

The broad-band filter (first-order, second-order, third-order and C-type filter) and single-tuned filter have been previously studied and their characteristics presented as well.

The single-tuned filter was analyzed by presenting the influence of its resistance, reactive power and variation of its tuning frequency (detuning phenomenon) on its efficiency. The capability of first-order filter to amplify the characteristic harmonics near the fundamental harmonic and to mitigate the higher harmonics in wide band was presented. The influence of the second-order, third-order and C-type filter damping resistance on their filtration efficiency was presented as well as the detuning of C-type filter.

This chapter is about the comparative study of the PHF topologies presented in Figure 3.91). The considered criteria for the comparison are the filter power losses (ΔP_f), the PCC voltage and current 5th harmonic amplitude ($U_{S(5)}$, $I_{S(5)}$) and the PCC voltage and current THD (THD_{US}, THD_{IS}). The compared filters are assumed to have the same reactive power (Q_f = 2172.5 Var), reactor quality factor (q'= 85) and tuning frequency (n_{re} = 4.85) (see Table 3.17).

The first-order filter resistance is neglected and the second-order, third-order and C-type filter are assumed to have the same damping resistances (e.g. 0.08 Ω, 1.25 Ω and 25 Ω, see Table 3.17). The single-tuned filter and the first-order filter are compared to the second-order, third-order and C-type filter when the damping resistance of these latest are increasing (from 0.08 Ω to 25 Ω). Other parameters (capacity and inductance) of single-tuned, first-order, second-order, third-order filter and C-type filter can be found respectively in the tables of Figure 3.13(b), Figure 3.36(c), Figure 3.50(g), Figure 3.57(g) and Figure 3.64(c).

All the broad-band filters present the problem of harmonics amplification. But depending on their damping resistance, this problem can be mitigated. From the point of view of individual harmonic mitigation, the single-tuned filter is more recommendable than other topologies because it has the lowest amplitude of grid voltage and current 5th harmonic (Figure 3.92(a)(b)).

With small values of damping resistance (e.g. 0.08 Ω, 1.25 Ω), the third-order filter is more recommendable for the reduction of individual harmonic than the second-order and C-type filter and then come the second-order filter (Figure 3.92(a)(b)).

With high values of damping resistance (e.g. 8 Ω, 25 Ω), the C-type filter is more recommendable for the reduction of individual harmonic than the second-order and third-order filter. The second-order filter is more recommendable than third-order the filter (Figure 3.92(a)(b)).

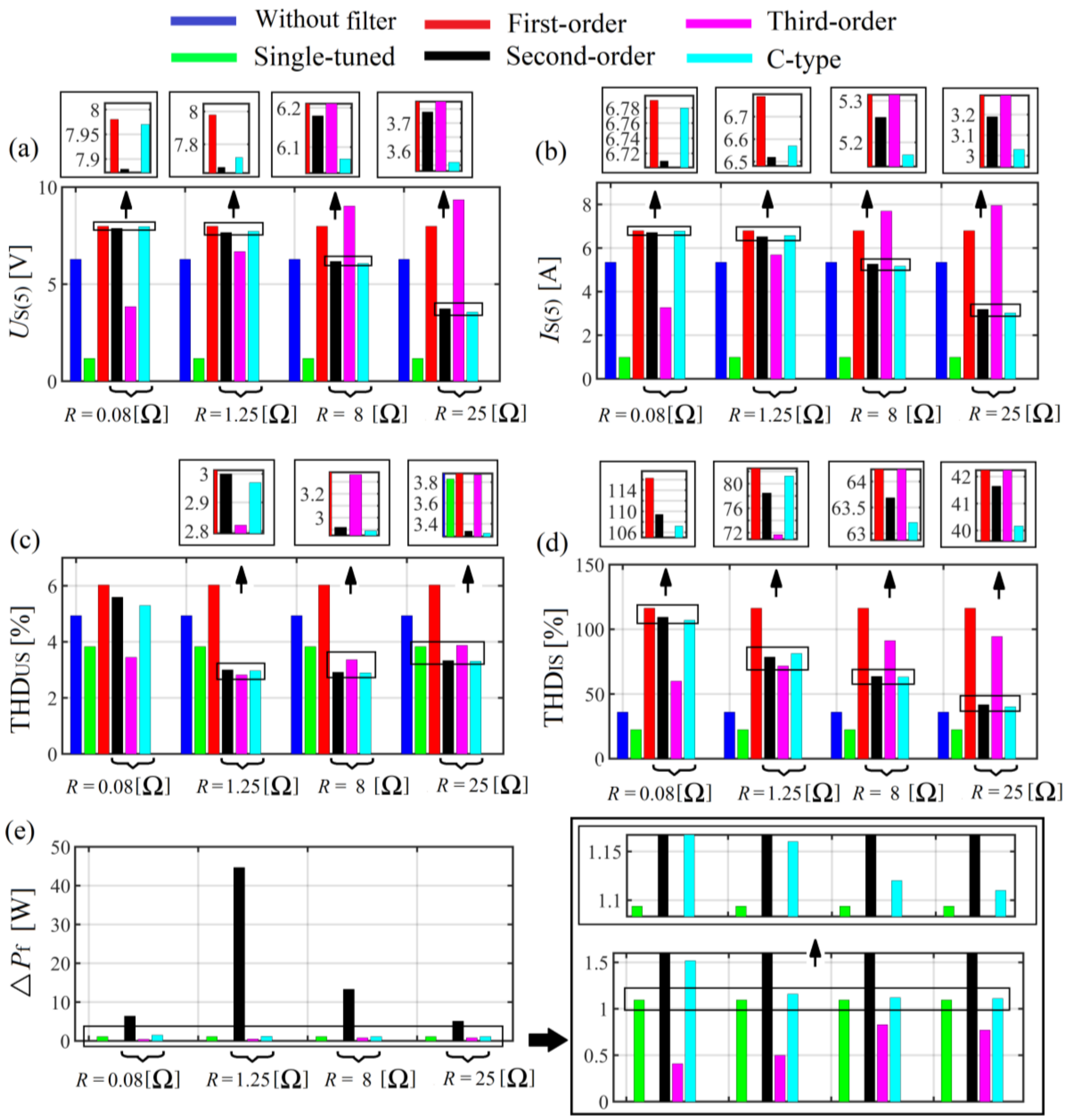

Figure 3.92 Comparison spectrums between the single-tuned, first-order, second-order, third-order filter and C-type filter: (a), (b) grid voltage and current 5th harmonic; (c), (d) grid voltage and current THD; (e) filter power losses

From the point of view of the 5th harmonic non-amplification (Figure 3.92(a)(b)), the single-tuned filter is more recommendable, then com the C-type filer with high damping resistance value (e.g. 25 Ω). The third-order filter with high damping resistance value has more probability to amplify the 5th harmonic than other filter.

From the grid voltage distortion point of view, it can be seen in Figure 3.92(c) that the third-order filter is more recommendable than other filters when its damping resistance is small (e.g. 0.08 Ω, 1.25 Ω), and the C-type filter is more recommendable than other filters for high damping resistance (e.g. 8 Ω, 25 Ω) (Figure 3.92(c)).

The single-tuned filter has the lowest PCC current THD than the broad-band filters (Figure 3.92(d)). For small values of *R* (e.g. 0.08 Ω, 1.25 Ω), the third-order filter is more recommendable than the second-order and C-type filter. For high values of *R* (e.g. 8 Ω, 25 Ω) it is better to apply the C-type filter than the second-order and third-order filter to improve the grid current THD. The first-order filter has the highest grid current and voltage THD and is not recommendable for harmonics mitigation.

The third-order filter generates less power losses than the single-tuned, second-order and C-type filter (Figure 3.92(e)) and then comes the single-tuned filter and at the end the C-type filter. The second-order filter is the one with the highest power losses.

Comparing the second-order filter to the C-type filter, it can be noticed in (Figure 3.92(a)(b)(c)(d) that, they have almost the same characteristics but from the power losses point of view, the C-type filter is more recommendable.

In the filter group where the basic harmonics such as the 5th, the 7th etc. (from e.g. the adjustable speed drive load) are reduced by the single-tuned filters, the damping filters such as the second-order, third-order or C-type filter can be added for better mitigation of high harmonics in wide band.

The knowledge of PHFs exists for many decades. Although it appears to be very rich, as indicates the experience of the authors. Still in the design process, often too little attention is paid on the analysis of changes filtration properties of these systems [111, 147]. They vary due to many factors, including e.g. aging or manufacturing tolerances of the reactors and capacitors during the manufacturing process etc. [84, 218, 273]. The aim of this chapter was to present the various topologies properties of PHFs using the impedance frequency characteristics [28, 33, 182, 217].

3.6 Hybrid passive harmonic filter (HPHF)

In power electronic systems, the passive filter in hybrid configuration is applied as input interface. The HPHF configurations are the result of different series and parallel passive filters connection and their purpose is to reduce the network current distortions. A simplified configuration example presenting a general concept of their resosnance frequency is shown in Figure 3.93(a). The hybrid passive filter under studies in this chapter is constituted of series passive harmonic filter (series PHF) and group of two single-branch filters parallel connected. In the considered example, the group of single-branch filters is constituted by two parallel *LC* filters. The series PHF is designed to block the harmonic to be eliminated forcing this latest to flow throw the filter group, which presents lower impedance for it resonance frequency. The single-branch filter group efficiency, in term of harmonics mitigation at the grid side, depends upon the grid impedance, but with the series PHF that dependency is strongly reduced.

The parameters of series PHF are the same as those used for the simulation in Table III.6 of Annex III and those of the filter group are presented in Figure 3.93(b). The filter reactor resistances are computed on the base of quality factor.

(a)

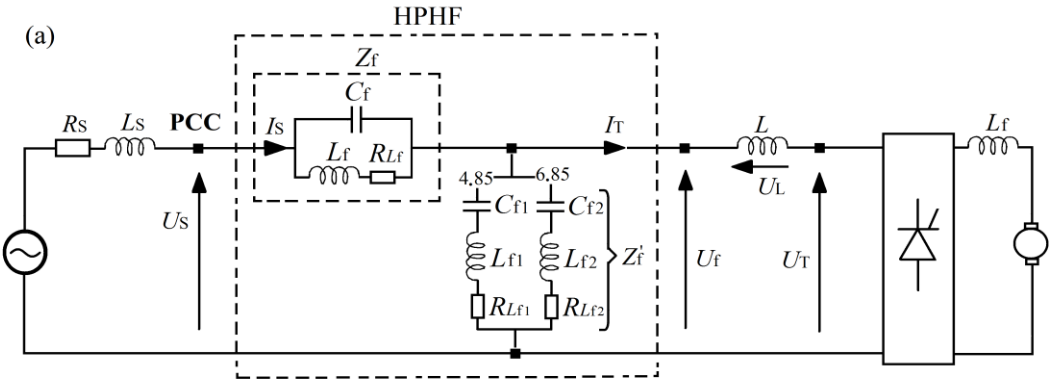

(b)

n	C_f [μF]	L_f [mH]	R_{Lf} [mΩ]	Q_f [Var]	U_f [v]	$Z'_{f(5)}$[mΩ]	$Z'_{f(7)}$[mΩ]
4.85	62.583	6.9	25.4	1086.3	230	741	303
6.85	63.969	3.4	12.5	1086.3	230		

Figure 3.93 (a) system equivalent circuit with the considered example of hybrid passive filter, (b) parameters of filter group connected in parallel. The parameters of the series PHF are presented in Table III.6 of Annex III (for R_{Lf} = 0.89 mΩ)

In Figure 3.93(b), the filter group total fundamental harmonic reactive power is equal to 2172.5 Var and for each filter in the group; the reactive power Q_f is equal to 1086.3 Var.

In the considered example, series PHF is tuned to the frequency of 5th order harmonic and the group of parallel connected filters is tuned to the frequencies a little bit lower than the harmonics frequencies to be eliminated (5th and 7th) (Figure 3.94).

The comparison (based on the system parameters) between the series PHF and HPHF is presented in Figure 3.95, Figure 3.96 and Figure 3.97.

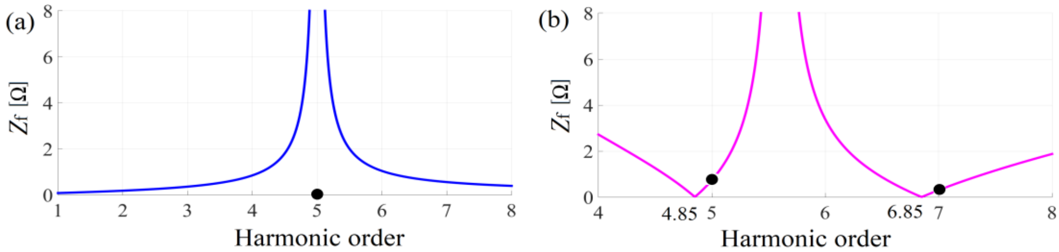

Figure 3.94 Impedance frequency characteristics: (a) Series PHF, (b) parallel connected filter group

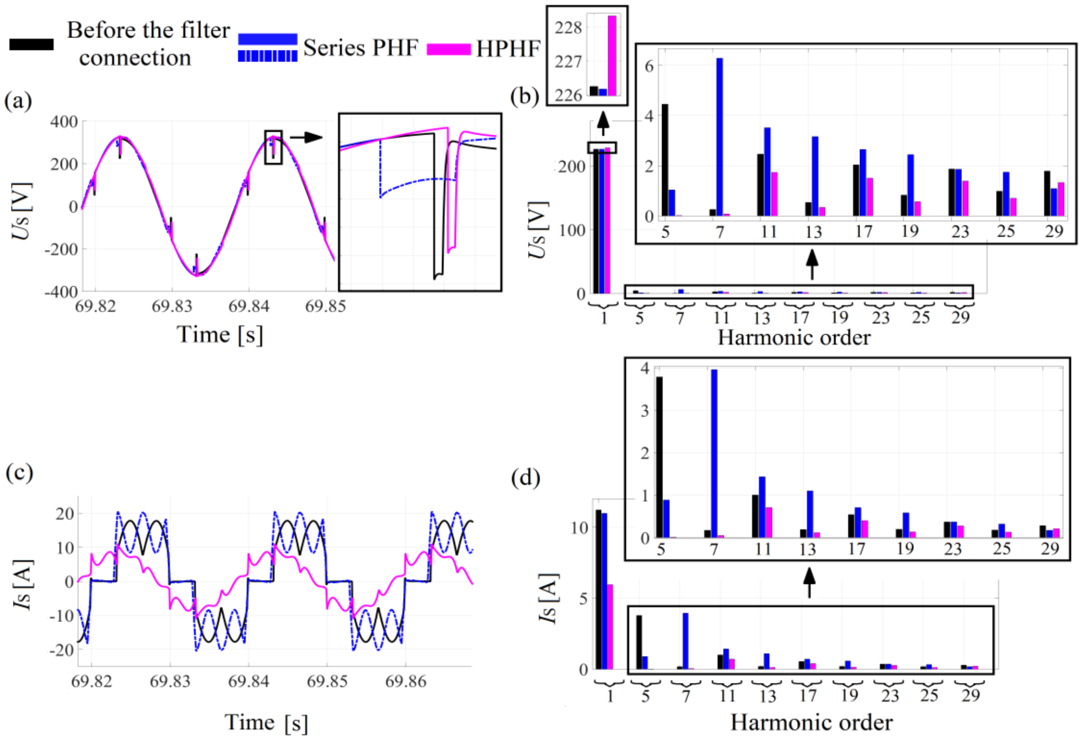

Figure 3.95 (a) grid voltage and (b) its spectrum; (c) grid current and (d) its spectrum

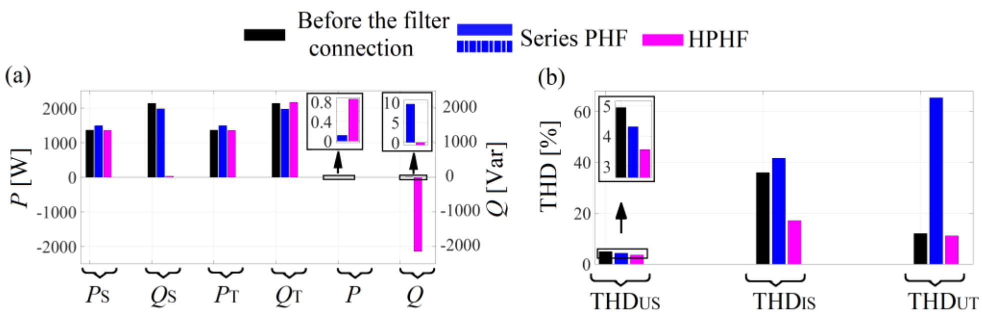

Figure 3.96 (a) power at the PCC (P_S, Q_S), rectifier input (P_S, Q_S) and HPHF terminal (P, Q); (b) THD of grid current (I_S) and voltage (U_S) and voltage at the rectifier input (U_T)

The parallel connection of the filter group together with the the series PHF has improved the grid current waveform (Figure 3.95(c)) and the PCC grid current and voltage THD (Figure 3.96(b)).

The harmonics amplification (7^{th} – 19^{th} and 25^{th}) observed in the case of series PHF (when working alone) is not observed in the case of HPHF (series PHF plus filter group - Figure 3.95(b) and (d)). The series PHF shows a better reduction of commutation notches depth than the HPHF (Figure 3.95(a)).

In Figure 3.97, is presented the power system impedance (Z) and phase versus frequency characteristics observed at the thyristor bridge terminals: when only the series PHF is considered and when the series PHF and filter group are considered (HPHF).

The HPHF has better filtered the 5^{th} order harmonic of grid current and voltage than the series PHF and can reduce the problems (harmonics amplification and waveform quality of grid current and voltage at the rectifier input) caused by the series PHF operating alone.

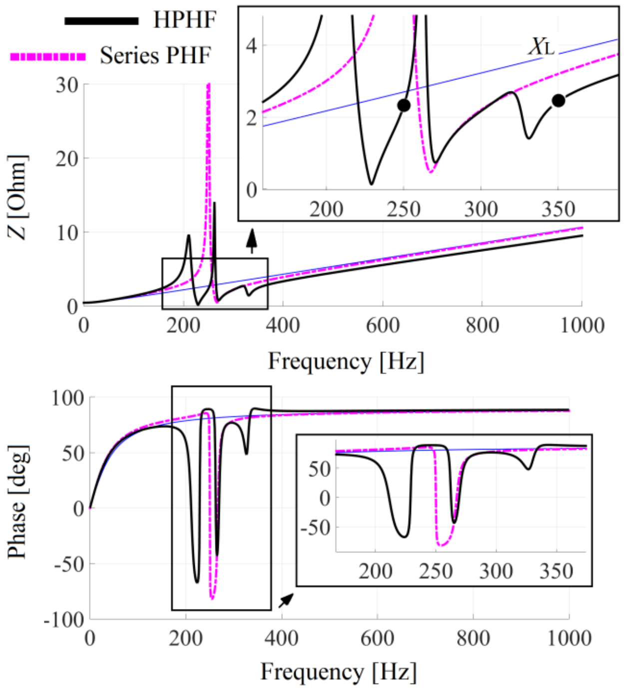

Figure 3.97 Characteristics of power system impedance vs frequency (module and phase) observed at the thyristor bridge terminals

3.7 Methods of sharing the total reactive power in the PHF groupη

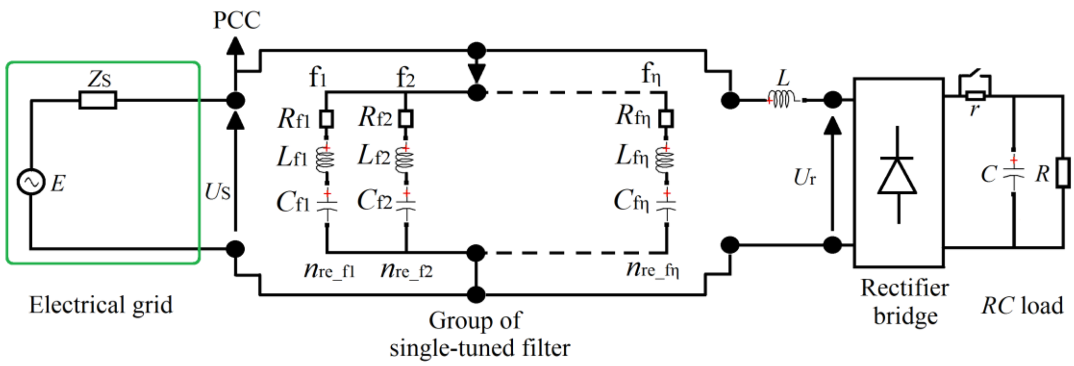

Figure 3.98 Electrical power sytem with the group of single-tuned filter

The group of PHFs is needed to prevent more than one harmonic from entering the electrical grid [102]. Its design depends principally upon the parameters such as load reactive power to be compensated, grid voltage spectrum (impedance as well) and load current characteristic harmonics (spectrum). Its efficiency is much more related on how much the grid current and voltage distortions should be reduced. The way on which the total reactive power should be shared (attributed to each filter) in the filter group (see Figure 3.98) is very controversial since decade and references [27, 29, 31] are the first to compare these methods.

The distribution of the total reactive power has an influence on the filter group impedance frequency characteristics and filtration efficiency as well [21, 107]. In this chapter, it is presented and compared (based on the simulated model) six exemplary methods used to split the total reactive power to individual filter in the group.

To perform the following studies, the single-phase model (see Annex II B) is considered, which does not reduce the generality presented in these studies because the symmetrical three-phase system in which filters are analyzed can lead to (or be simplified to) a single-phase system. To more illustrate each of the methods, the group of single-tuned filters is considered as example. The described methods can be applied to a group of different type of PHFs (apart method D). The reactive power value used so far is different from the one used in this chapter (e.g. 500 Var).

3.7.1 Design methods description

The methods used to distribute the total reactive power to a passive filter group are as follow:

Method A equal reactive power for each filter

Method B the reactive power of filters is inversely proportional to the harmonic order

Method C the reactive power of filters is inversely proportional to the square of harmonic order

Method D the reactive power of filters is calculated on the base of the filter group impedance versus frequency characteristic shaping [141, 256]

Method E the reactive power of filters is calculated by basing on the assumption that the reactors of filters are identical

Method F optimization - different form of objective function in optimization task can be considered e.g. the filters reactive power is computed on the base of the minimum or maximum value of the objective function y

Method A. Equal distribution of the total reactive power in the filter group

The total reactive power (Q_F) is shared equally in the filter group. For a filter group having *h* filters (*h* - number of filter) with each filter (f) carrying the number η (fη), the reactive power of individual filter is expressed by (3.7.1.3). The total reactive power is the sum of individual reactive power (3.7.1.1) and the each filter in the group has the same reactive power (3.7.1.2).

$Q_\mathrm{F} = Q_{\mathrm{f1}} + Q_{\mathrm{f2}} + \cdots + Q_{\mathrm{f}\eta} = \sum_{\eta=1}^{h} Q_{\mathrm{f}\eta}$ (3.7.1.1)	$Q_{\mathrm{f1}} = Q_{\mathrm{f2}} = Q_{\mathrm{f3}} = \cdots = Q_{\mathrm{f}\eta}$ (3.7.1.2)
$Q_{\mathrm{f}\eta} = \frac{Q_\mathrm{F}}{h}$ (3.7.1.3)	for $h, \eta \geq 1 \; and \; \in \mathbb{N}$
Example	
For $h = 3, n_{\mathrm{re\_f1}} = 2.8, n_{\mathrm{re\_f2}} = 4.8,$ $n_{\mathrm{re\_f3}} = 6.8$ and $Q_\mathrm{F} = 500$ Var	$Q_{\mathrm{f}\eta} = \frac{500}{3} = Q_{\mathrm{f1}} = Q_{\mathrm{f2}} = Q_{\mathrm{f3}} = 166.66$ Var

Method B. The reactive power of filters is inversely proportional to the harmonic order

The reactive power sharing is based upon the relationship between individual reactive powers in the filter group using the harmonic order ($n_{\mathrm{f}\eta}$) (3.9.1.4).

$n_{\mathrm{f\eta}}Q_{\mathrm{f\eta}} = n_{\mathrm{f(\eta+1)}}Q_{\mathrm{f(\eta+1)}}$	(3.7.1.4)
Example	
For $h = 3$, $n_{\mathrm{re\_f1}} = 2.8$, $n_{\mathrm{re\_f2}} = 4.8$, $n_{\mathrm{re\_f3}} = 6.8$ $Q_{\mathrm{F}} = 500\ \mathrm{Var}$	$\begin{cases} Q_{\mathrm{f1}} + Q_{\mathrm{f2}} + Q_{\mathrm{f3}} = Q_{\mathrm{F}} \\ n_{\mathrm{re\_f1}}Q_{\mathrm{f1}} = n_{\mathrm{re\_f2}}Q_{\mathrm{f2}} \\ n_{\mathrm{re\_f2}}Q_{\mathrm{f2}} = n_{\mathrm{re\_f3}}Q_{\mathrm{f3}} \end{cases} \begin{cases} Q_{\mathrm{f1}} = \frac{n_{\mathrm{re\_f2}}+n_{\mathrm{re\_f3}}}{n_{\mathrm{re\_f2}}n_{\mathrm{re\_f3}}+n_{\mathrm{re\_f1}}n_{\mathrm{re\_f3}}+n_{\mathrm{re\_f1}}n_{\mathrm{re\_f2}}}Q_{\mathrm{F}} \\ Q_{\mathrm{f2}} = \frac{n_{\mathrm{re\_f1}}+n_{\mathrm{re\_f3}}}{n_{\mathrm{re\_f2}}n_{\mathrm{re\_f3}}+n_{\mathrm{re\_f1}}n_{\mathrm{re\_f3}}+n_{\mathrm{re\_f1}}n_{\mathrm{re\_f2}}}Q_{\mathrm{F}} \\ Q_{\mathrm{f3}} = \frac{n_{\mathrm{re\_f1}}+n_{\mathrm{re\_f2}}}{n_{\mathrm{re\_f2}}n_{\mathrm{re\_f3}}+n_{\mathrm{re\_f1}}n_{\mathrm{re\_f3}}+n_{\mathrm{re\_f1}}n_{\mathrm{re\_f2}}}Q_{\mathrm{F}} \end{cases}$ $\begin{cases} Q_{\mathrm{f1}} = \frac{32.64}{65.15}500 = 250.61\ \mathrm{Var} \\ Q_{\mathrm{f2}} = \frac{19.04}{65.15}500 = 146.19\ \mathrm{Var} \\ Q_{\mathrm{f3}} = \frac{13.44}{65.15}500 = 103.19\ \mathrm{Var} \end{cases}$

Method C. The reactive power of filters is inversely proportional to the square of harmonic order

The share of reactive power is based upon the relationship between individual reactive powers in the filter group using the square of harmonic order $\left(n_{\mathrm{f\eta}}^2\right)$ (3.9.1.5).

$n_{\mathrm{f\eta}}^2Q_{\mathrm{f\eta}} = n_{\mathrm{f(\eta+1)}}^2Q_{\mathrm{f(\eta+1)}}$	(3.7.1.5)
Example	
For $h = 3$, $n_{\mathrm{re\_f1}} = 2.8$, $n_{\mathrm{re\_f2}} = 4.8$, $n_{\mathrm{re\_f3}} = 6.8$ $Q_{\mathrm{F}} = 500\ \mathrm{Var}$	$\begin{cases} Q_{\mathrm{f1}} + Q_{\mathrm{f2}} + Q_{\mathrm{f3}} = Q_{\mathrm{F}} \\ n_{\mathrm{re\_f1}}^2Q_{\mathrm{f1}} = n_{\mathrm{re\_f2}}^2Q_{\mathrm{f2}} \\ n_{\mathrm{re\_f2}}^2Q_{\mathrm{f2}} = n_{\mathrm{re\_f3}}^2Q_{\mathrm{f3}} \end{cases} \begin{cases} Q_{\mathrm{f1}} = \frac{n_{\mathrm{re\_f2}}^2+n_{\mathrm{re\_f3}}^2}{n_{\mathrm{re\_f2}}^2n_{\mathrm{re\_f3}}^2+n_{\mathrm{re\_f1}}^2n_{\mathrm{re\_f3}}^2+n_{\mathrm{re\_f1}}^2n_{\mathrm{re\_f2}}^2}Q_{\mathrm{F}} \\ Q_{\mathrm{f2}} = \frac{n_{\mathrm{re\_f1}}^2+n_{\mathrm{re\_f3}}^2}{n_{\mathrm{re\_f2}}^2n_{\mathrm{re\_f3}}^2+n_{\mathrm{re\_f1}}^2n_{\mathrm{re\_f3}}^2+n_{\mathrm{re\_f1}}^2n_{\mathrm{re\_f2}}^2}Q_{\mathrm{F}} \\ Q_{\mathrm{f3}} = \frac{n_{\mathrm{re\_f1}}^2+n_{\mathrm{re\_f2}}^2}{n_{\mathrm{re\_f2}}^2n_{\mathrm{re\_f3}}^2+n_{\mathrm{re\_f1}}^2n_{\mathrm{re\_f3}}^2+n_{\mathrm{re\_f1}}^2n_{\mathrm{re\_f2}}^2}Q_{\mathrm{F}} \end{cases}$ $\begin{cases} Q_{\mathrm{f1}} = \frac{1065.4}{1608.5}500 = 331.16\ \mathrm{Var} \\ Q_{\mathrm{f2}} = \frac{362.52}{1608.5}500 = 112.68\ \mathrm{Var} \\ Q_{\mathrm{f3}} = \frac{180.63}{1608.5}500 = 56.14\ \mathrm{Var} \end{cases}$

Method D. The reactive power of filter is calculated on the base of the filter group impedance versus frequency characteristic shape

This method is developed for the group of single-tuned filter. The expression (3.7.1.6) represents the single-tuned filter admittance for $R_{\mathrm{f}} = 0$ (see also Table 3.2).

The filter group admittance (fundamental harmonic) of (Y_{F}) is expressed by (3.7.1.7) and $Y_{\mathrm{f}\eta}$ is the admittance of individual filter carrying the number η. It is formulated after considering the filter group series resonance frequencies (e.g. $n_{\mathrm{re\_f1}}$, $n_{\mathrm{re\_f2}}$ . . . $n_{\mathrm{re\_f}\eta}$).

There is always parallel resonance between filters in the filter group. In this method, the parallel resonance (order - m) can be chosen. It is always located between series resonance frequencies. The filter group admittance after considering the parallel resonances frequencies ($\underline{Y}'_{\mathrm{F(m\lambda)}}$) is formulated in (3.7.1.8).

$$\underline{Y}_{\mathrm{f\eta}}\left(j\omega_{(1)}\right) = \frac{1}{\underline{Z}_{\mathrm{f\eta}}(j\omega)} = -j\,\frac{\omega_{\mathrm{re\eta}}^2\omega C_{\mathrm{f\eta}}}{\omega^2-\omega_{\mathrm{re\eta}}^2} \tag{3.7.1.6}$$

for $\omega = \omega_{(1)}$

$$Y_{\mathrm{F}} = \sum_{\eta=1}^{\mathrm{h}} Y_{\mathrm{f\eta}} = \frac{n_{\mathrm{re\_f1}}^2\omega_{(1)}}{1-n_{\mathrm{re\_f1}}^2}C_{\mathrm{f1}} + \frac{n_{\mathrm{re\_f2}}^2\omega_{(1)}}{1-n_{\mathrm{re\_f2}}^2}C_{\mathrm{f2}} + \frac{n_{\mathrm{re\_f3}}^2\omega_{(1)}}{1-n_{\mathrm{re\_f3}}^2}C_{\mathrm{f3}} + \cdots + \frac{n_{\mathrm{re_{f\eta}}}^2\omega_{(1)}}{1-n_{\mathrm{re_{f\eta}}}^2}C_{\mathrm{f\eta}} = \frac{Q_{\mathrm{F}}}{U_{\mathrm{f}}^2} \tag{3.7.1.7}$$

for $\omega = \omega_m = m\omega_{(1)}$, $n_{\mathrm{re\_f\eta}} < m_\lambda < n_{\mathrm{re\_f(\eta-1)}}$, $\lambda = h-1$ and $\in \mathbb{N}$,

$$\underline{Y}'_{\mathrm{F(m\lambda)}} = \sum_{\eta=1}^{h} -j\frac{n^2_{\mathrm{re\_f\eta}}\omega^2_{(1)}\omega_{m\lambda}}{\omega^2_{m\lambda}-n^2_{\mathrm{re\_f\eta}}\omega^2_{(1)}}C_{\mathrm{f\eta}};\ \sum_{\eta=1}^{h}\left(-j\frac{n^2_{\mathrm{re\_f\eta}}m_\lambda\omega_{(1)}}{m^2_\lambda-n^2_{\mathrm{re\_f\eta}}}C_{\mathrm{f\eta}}\right)/-j\,\omega_{(1)} \cong 0/-j\omega_{(1)} \Rightarrow$$

$$Y'_{\mathrm{F(m\lambda)}} = \sum_{\eta=1}^{h}\frac{n^2_{\mathrm{re\_f\eta}}m_\lambda}{m^2_\lambda-n^2_{\mathrm{re\_f\eta}}}C_{\mathrm{f\eta}} = \frac{n^2_{\mathrm{re\_f1}}m_\lambda}{m^2_\lambda-n^2_{\mathrm{re\_f1}}}C_{\mathrm{f1}} + \frac{n^2_{\mathrm{re\_f2}}m_\lambda}{m^2_\lambda-n^2_{\mathrm{re\_f2}}}C_{\mathrm{f2}} + \frac{n^2_{\mathrm{re\_f3}}m_\lambda}{m^2_\lambda-n^2_{\mathrm{re\_f3}}}C_{\mathrm{f3}} + \cdots + \frac{n^2_{\mathrm{re\_f\eta}}m_\lambda}{m^2_\lambda-n^2_{\mathrm{re\_f\eta}}}C_{\mathrm{f\eta}} \cong 0 \qquad (3.7.1.8)$$

λ - is the number of parallel resonance frequency (number of admittance equations $Y'_{\mathrm{F(m\lambda)}}$ (3.9.1.8)). If the filter group contains 3 filters (h = 3), λ ($\lambda = h-1$) will take the values 2. It means that there will be two equations representing the admittance for the parallel resonance frequencies.

The matrices of equation (3.7.1.9) are obtained from the equations (3.7.1.6) and (3.7.1.8). The reactive power of each filter in the groups (see (3.7.1.10)) is obtained after computing the filter group capacities (C_{f1}, C_{f2}, … $C_{\mathrm{f\eta}}$) (see example).

$$\begin{cases} Y'_{\mathrm{F}(m1)} = \dfrac{n^2_{\mathrm{re\_f1}}m_1}{m^2_1-n^2_{\mathrm{re\_f1}}}C_{\mathrm{f1}} + \dfrac{n^2_{\mathrm{re\_f2}}m_1}{m^2_1-n^2_{\mathrm{re\_f2}}}C_{\mathrm{f2}} + \dfrac{n^2_{\mathrm{re\_f3}}m_1}{m^2_1-n^2_{\mathrm{re\_f3}}}C_{\mathrm{f3}} + \cdots + \dfrac{n^2_{\mathrm{re_{f\eta}}}m_1}{m^2_1-n^2_{\mathrm{re_{f\eta}}}}C_{\mathrm{f\eta}} \cong 0 \\ Y'_{\mathrm{F}(m2)} = \dfrac{n^2_{\mathrm{re\_f1}}m_2}{m^2_2-n^2_{\mathrm{re\_f1}}}C_{\mathrm{f1}} + \dfrac{n^2_{\mathrm{re\_f2}}m_2}{m^2_1-n^2_{\mathrm{re\_f2}}}C_{\mathrm{f2}} + \dfrac{n^2_{\mathrm{re\_f3}}m_2}{m^2_2-n^2_{\mathrm{re\_f3}}}C_{\mathrm{f3}} + \cdots + \dfrac{n^2_{\mathrm{re_{f\eta}}}m_1}{m^2_2-n^2_{\mathrm{re_{f\eta}}}}C_{\mathrm{f\eta}} \cong 0 \\ \qquad\vdots \\ Y'_{\mathrm{F}(m\lambda)} = \dfrac{n^2_{\mathrm{re\_f1}}m_\lambda}{m^2_\lambda-n^2_{\mathrm{re\_f1}}}C_{\mathrm{f1}} + \dfrac{n^2_{\mathrm{re\_f2}}m_\lambda}{m^2_\lambda-n^2_{\mathrm{re\_f2}}}C_{\mathrm{f2}} + \dfrac{n^2_{\mathrm{re\_f3}}m_\lambda}{m^2_\lambda-n^2_{\mathrm{re\_f3}}}C_{\mathrm{f3}} + \cdots + \dfrac{n^2_{\mathrm{re_{f\eta}}}m_\lambda}{m^2_\lambda-n^2_{\mathrm{re_{f\eta}}}}C_{\mathrm{f\eta}} \cong 0 \end{cases} \qquad (3.7.1.9)$$

$$\begin{bmatrix} \frac{n^2_{\mathrm{re\_f1}}\omega_{(1)}}{1-n^2_{\mathrm{re\_f1}}} & \frac{n^2_{\mathrm{re\_f2}}\omega_{(1)}}{1-n^2_{\mathrm{re\_f2}}} & \frac{n^2_{\mathrm{re\_f3}}\omega_{(1)}}{1-n^2_{\mathrm{re\_f3}}} & \cdots & \frac{n^2_{\mathrm{re_{f\eta}}}\omega_{(1)}}{1-n^2_{\mathrm{re_{f\eta}}}} \\ \frac{n^2_{\mathrm{re\_f1}}m_1}{m^2_1-n^2_{\mathrm{re\_f1}}} & \frac{n^2_{\mathrm{re\_f2}}m_1}{m^2_1-n^2_{\mathrm{re\_f2}}} & \frac{n^2_{\mathrm{re\_f3}}m_1}{m^2_1-n^2_{\mathrm{re\_f3}}} & \cdots & \frac{n^2_{\mathrm{re_{f\eta}}}m_1}{m^2_1-n^2_{\mathrm{re_{f\eta}}}} \\ \frac{n^2_{\mathrm{re\_f1}}m_2}{m^2_2-n^2_{\mathrm{re\_f1}}} & \frac{n^2_{\mathrm{re\_f2}}m_2}{m^2_1-n^2_{\mathrm{re\_f2}}} & \frac{n^2_{\mathrm{re\_f3}}m_2}{m^2_2-n^2_{\mathrm{re\_f3}}} & \cdots & \frac{n^2_{\mathrm{re_{f\eta}}}m_2}{m^2_2-n^2_{\mathrm{re_{f\eta}}}} \\ \vdots & \vdots & \vdots & \ddots & \vdots \\ \frac{n^2_{\mathrm{re\_f1}}m_\lambda}{m^2_\lambda-n^2_{\mathrm{re\_f1}}} & \frac{n^2_{\mathrm{re\_f2}}m_\lambda}{m^2_\lambda-n^2_{\mathrm{re\_f2}}} & \frac{n^2_{\mathrm{re\_f3}}m_\lambda}{m^2_\lambda-n^2_{\mathrm{re\_f3}}} & \cdots & \frac{n^2_{\mathrm{re_{f\eta}}}m_\lambda}{m^2_\lambda-n^2_{\mathrm{re_{f\eta}}}} \end{bmatrix} \begin{bmatrix} C_{\mathrm{f1}} \\ C_{\mathrm{f2}} \\ C_{\mathrm{f3}} \\ \vdots \\ C_{\mathrm{f\eta}} \end{bmatrix} [-1] = \begin{bmatrix} \frac{Q_{\mathrm{F}}}{U^2_{\mathrm{f}}} \\ 0 \\ 0 \\ \vdots \\ 0 \end{bmatrix} \qquad (3.7.1.10)$$

$$\begin{cases} Q_{\mathrm{f1}} = \dfrac{n^2_{\mathrm{re\_f1}}\omega_{(1)}U^2_{\mathrm{f}}}{1-n^2_{\mathrm{re\_f1}}}C_{\mathrm{f1}} \\ Q_{\mathrm{f2}} = \dfrac{n^2_{\mathrm{re\_f2}}\omega_{(1)}U^2_{\mathrm{f}}}{1-n^2_{\mathrm{re\_f2}}}C_{\mathrm{f2}} \\ \qquad\vdots \\ Q_{\mathrm{f\eta}} = \dfrac{n^2_{\mathrm{re\_f\eta}}\omega_{(1)}U^2_{\mathrm{f}}}{1-n^2_{\mathrm{re\_f\eta}}}C_{\mathrm{f\eta}} \end{cases} \qquad (3.7.1.11)$$

Example	
For $h = 3$, $n_{\mathrm{re\_f1}} = 2.8$, $n_{\mathrm{re\_f2}} = 4.8$, $n_{\mathrm{re\_f3}} = 6.8$ $m_1 = 4$ $m_2 = 6$ $Q_{\mathrm{F}} = 500$ Var	$\left\{\begin{bmatrix} \frac{2.8^2.100\pi}{1-2.8^2} & \frac{4.8^2.100\pi}{1-4.8^2} & \frac{6.8^2.100\pi}{1-6.8^2} \\ \frac{2.8^2.4}{4^2-2.8^2} & \frac{4.8^2.4}{4^2-4.8^2} & \frac{6.8^2.4}{4^2-6.8^2} \\ \frac{2.8^2.6}{6^2-2.8^2} & \frac{4.8^2.6}{6^2-4.8^2} & \frac{6.8^2.6}{6^2-6.8^2} \end{bmatrix}\begin{bmatrix} C_{\mathrm{f1}} \\ C_{\mathrm{f2}} \\ C_{\mathrm{f3}} \end{bmatrix} = \begin{bmatrix} \frac{500}{230^2} \\ 0 \\ 0 \end{bmatrix}\right.$ $\begin{cases} C_{\mathrm{f1}} = 19.62\ \mu\mathrm{F} \\ C_{\mathrm{f2}} = 4.38\ \mu\mathrm{F} \\ C_{\mathrm{f3}} = 2.93\ \mu\mathrm{F} \end{cases}, \begin{cases} Q_{\mathrm{f1}} = 373.84\mathrm{Var} \\ Q_{\mathrm{f2}} = 76.24\mathrm{Var} \\ Q_{\mathrm{f3}} = 49.90\mathrm{Var} \end{cases}$

Method E. The reactive power of filters is calculated on the base of the assumption that the filters reactors are identical

In the industrial electrical system where the filter group is designed by applying that method, it is easier to replace the reactors during the fault.

The equations in (3.7.1.12) represent the steps on how the reactive power of individual filter is computed. For $L_{f1} = L_{f2} = L_{f3} = \ldots = L$, the reactive power ($Q_{f\eta}$) of each filter in the filter group is expressed in (3.9.1.13).

$$\begin{cases} \underline{Z}_{f1} = j\frac{\omega^2 LC_{f1}-1}{\omega C_{f1}} & \underline{Z}_{f2} = j\frac{\omega^2 LC_{f2}-1}{\omega C_{f2}} & \cdots & \underline{Z}_{f\eta} = j\frac{\omega^2 LC_{f\eta}-1}{\omega C_{f\eta}} \\ C_{f1} = \frac{1}{\omega_{re\_f1} L} & C_{f2} = \frac{1}{\omega_{re\_f2} L} & \cdots & C_{f\eta} = \frac{1}{\omega_{re\_f\eta} L} \\ Q_{f1} = \frac{U_f^2}{Z_{f1}} = \frac{U_f^2 \omega C_{f1}}{\omega^2 LC_{f1}-1} & Q_{f2} = \frac{U_f^2}{Z_{f2}} = \frac{U_f^2 \omega C_{f2}}{\omega^2 LC_{f2}-1} & \cdots & Q_{f\eta} = \frac{U_f^2}{Z_{f\eta}} = \frac{U^2 \omega C_{f\eta}}{\omega^2 LC_{f\eta}-1} \\ \omega_{re\_f1} = n_{re\_f1}\omega_{(1)} & \omega_{re\_f2} = n_{re\_f2}\omega_{(1)} & \cdots & \omega_{re\_f\eta} = n_{re\_f\eta}\omega_{(1)} \\ & \text{for } \omega = \omega_{(1)} & & \\ Q_{f1} = \frac{U_f^2}{\omega_{(1)} L(1-n_{re\_f1}^2)} & Q_{f2} = \frac{U_f^2}{\omega_{(1)} L(1-n_{re\_f1}^2)} & \cdots & Q_{f\eta} = \frac{U_f^2}{\omega_{(1)} L(1-n_{re\_f\eta}^2)} \end{cases} \tag{3.7.1.12}$$

$$\begin{cases} Q_F = Q_{f1} + Q_{f2} + \cdots + Q_{f\eta} = \frac{U_f^2}{\omega_{(1)} L}\left(\frac{1}{1-n_{re\_f1}^2} + \frac{1}{1-n_{re\_f2}^2} + \cdots + \frac{1}{1-n_{re\_f\eta}^2}\right) \\ L = \frac{U_f^2}{\omega_{(1)} Q_F}\left(\frac{1}{1-n_{re\_f1}^2} + \frac{1}{1-n_{re\_f2}^2} + \cdots + \frac{1}{1-n_{re\_f\eta}^2}\right) = \frac{U_f^2}{\omega_{(1)} Q_F}\sum_{\eta=1}^{\infty}\frac{1}{1-n_{f\eta}^2} \\ Q_{f\eta} = \frac{Q_F}{(1-n_{re\_f\eta}^2)\left(\frac{1}{1-n_{re\_f1}^2} + \frac{1}{1-n_{re\_f2}^2} + \cdots + \frac{1}{1-n_{re\_f\eta}^2}\right)} = \frac{Q_F}{(1-n_{re\_f\eta}^2)\sum_{\eta-1}^{\infty}\left(\frac{1}{1-n_{re\_f\eta}^2}\right)} \end{cases} \tag{3.9.1.13}$$

Example	
For $h = 3, n_{re\_f1} = 2.8, n_{re\_f2} = 4.8,$ $n_{re\_f3} = 6.8$ and $Q_F = 500$ Var	$\begin{cases} Q_{f1} = \frac{500}{(1-2.8^2)\left(\frac{1}{1-2.8^2} + \frac{1}{1-4.8^2} + \frac{1}{1-6.8^2}\right)} = 342.10 \text{ Var} \\ Q_{f2} = \frac{500}{(1-4.8^2)\left(\frac{1}{1-2.8^2} + \frac{1}{1-4.8^2} + \frac{1}{1-6.8^2}\right)} = 106.17 \text{ Var} \\ Q_{f3} = \frac{500}{(1-6.8^2)\left(\frac{1}{1-2.8^2} + \frac{1}{1-4.8^2} + \frac{1}{1-6.8^2}\right)} = 51.72 \text{ Var} \end{cases}$

Method F. Optimization method - different form of objective function in optimization task can be considered

In the proposed optimization method, the task of the objective function can be defined in different way. The example used to illustrate that method is the filter group (two single-tuned filters) connected in one-phase electrical grid system as presented in Figure 3.99(e). The reactive power of the individual filter in the group is determined by the search of the objective function (y) extremum value.

Firstly, the objective function is defined, then the characteristic of objective function versus one filter in the group reactive power (e.g. Q_{f1}) is set up and at the end, relying on the extremum of the objective function characteristic, the reactive power of each filter in the group is obtained. In the considered example, the minimum of the objective function is considered.

As presented in Figure 3.99(a), the electrical grid is simplified to a voltage source ($U_{S(1)}$ – fundamental harmonic) and equivalent impedance Z_S (according to Thevenin law) and the non-linear load is simplified to a current source (Norton law). The grid source voltage is assumed to not contain voltage harmonics and the non-linear load is the source of harmonics current.

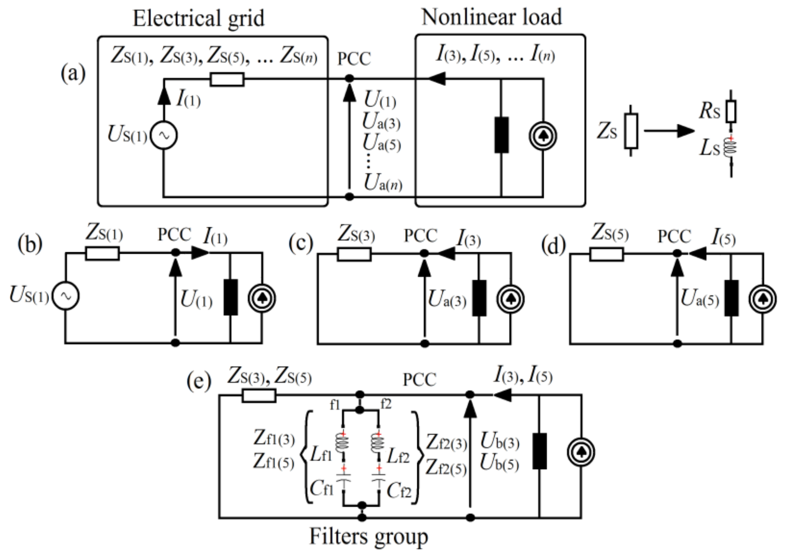

Figure 3.99 (a) equivalent circuit of considered electrical grid and nonlinear load; (b), (c), (d) electrical circuit representation based on superposition theory, (e) electrical circuit with the filter group

The current source characteristic harmonics corresponds to the one of one-phase diode rectifier (4k±1, k ≥ 1, where k ∈ ℕ) and the two single filters (f1 and f2) are tuned respectively on the frequency of harmonic order 2.8th and 4.8th. Each load harmonic current ($I_{(n)}$) flowing to the grid creates on the grid impedance (Z_S) voltage drop as shown in Figure 3.99(b), (c) and (d).

Two study cases are considered. In the first case (Figure 3.99(a)), the filter group is not connected and the voltage drops caused by the load current harmonics (3rd and 5th) on the grid impedance ($Z_{S(3)}$, $Z_{S(5)}$) are represented by $U_{a(3)}$ and $U_{a(5)}$ (see also Figure 3.99(c)(d)). In the second case (see Figure 3.99(e), the filter group is connected and the voltage drops caused by the load current of 3rd and 5th harmonics on the parallel connected grid impedance ($Z_{S(3)}$, $Z_{S(5)}$) and filter group impedance (($Z_{f1(3)}$, $Z_{f1(5)}$) (($Z_{f2(3)}$, $Z_{f2(5)}$))) are represented by $U_{b(3)}$ and $U_{b(5)}$ (Figure 3.99(e)).

The filter impedances of the two chosen frequencies ($Z_{f1(3)}$, $Z_{f1(5)}$) are expressed in (3.7.1.14). The filter group impedances of 3rd and 5th harmonic ($Z_{(3)}$, $Z_{(5)}$) are represented by (3.7.1.15) and the electrical grid impedance (see expression (3.7.1.15)) plus filter group impedance (parallel connection – see Figure 3.99(e)) for the 3rd and 5th harmonics ($Z''_{(3)}, Z''_{(5)}$) is expressed by (3.7.1.17).

By the assumption that the current harmonics ($I_{(3)}$ and $I_{(5)}$) generated by the non-linear load to the grid have the same values when the filter group is connected and when it is not, the expression (3.7.1.18) is set up. In that expression, $U_{a(3)}$ represents the voltage drop (Figure 3.99(c)) caused by the 3rd harmonic on the grid impedance ($Z_{S(3)}$) and $U_{b(3)}$ represents the voltage drop caused by the load current of 3rd harmonic on the grid impedance ($Z_{S(3)}$) together with the filter group impedance ($Z_{(3)}$) (Figure 3.99(e)). $U_{a(3)}$ is supposed to be higher than ($U_{b(3)}$) because, after the filter connection and due to the resonance phenomena, the impedance of 3rd harmonic of the first filter is near zero (short circuit) as well as its voltage (which is reduced almost to the voltage of its resistance (supposed to be very small). The same interpretation can be done for the 5th harmonic.

The example objective function (3.7.1.19) is defined from coefficients φ_1 and φ_2 of expression (3.7.1.18). The search of Q_{f1} is the optimization task.

The defined objective function in (3.7.1.19) allows to share the total reactive power in the filter group containing no more than 2 filters but in the case of 3 or more filters, it should be differently defined. It is important to notice that the optimization function (y) is also related with the grid inductance.

$$\begin{cases} \underline{Z}_{\mathrm{f1}(n_{\mathrm{f1}})} = j\dfrac{n_{\mathrm{f1}}^2\omega_{(1)}^2 L_{\mathrm{f1}}C_{\mathrm{f1}}-1}{n_{\mathrm{f1}}C_{\mathrm{f1}}\omega_{(1)}} = j\dfrac{(n_{\mathrm{f1}}^2-n_{\mathrm{re\_f1}}^2)U_{\mathrm{f}(1)}^2}{n_{\mathrm{f1}}(n_{\mathrm{re\_f1}}^2-1)Q_{\mathrm{f1}}} \\ \underline{Z}_{\mathrm{f2}(n_{\mathrm{f2}})} = j\dfrac{n_{\mathrm{f2}}^2\omega_{(1)}^2 L_{\mathrm{f2}}C_{\mathrm{f2}}-1}{n_{\mathrm{f2}}C_{\mathrm{f2}}\omega_{(1)}} = j\dfrac{(n_{\mathrm{f2}}^2-n_{\mathrm{re\_f2}}^2)U_{\mathrm{f}(1)}^2}{n_{\mathrm{f2}}(n_{\mathrm{re\_f2}}^2-1)Q_{\mathrm{f2}}} \end{cases} \text{for} \begin{cases} n_{\mathrm{f1}} = 3 \\ n_{\mathrm{f2}} = 5 \\ n_{\mathrm{re\_f1}} = 2.8 \\ n_{\mathrm{re\_f2}} = 4.8 \end{cases} \tag{3.7.1.14}$$

$$\begin{cases} \underline{Z}_{(n_{\mathrm{f1}})} = \dfrac{\underline{Z}_{\mathrm{f1}(n_{\mathrm{f1}})}\underline{Z}_{\mathrm{f2}(n_{\mathrm{f1}})}}{\underline{Z}_{\mathrm{f1}(n_{\mathrm{f1}})}+\underline{Z}_{\mathrm{f2}(n_{\mathrm{f1}})}} = j\dfrac{U_{\mathrm{f}(1)}^2}{\frac{(n_{\mathrm{re\_f2}}^2-1)}{(n_{\mathrm{f1}}^2-n_{\mathrm{re\_f2}}^2)}n_{\mathrm{f1}}Q_{\mathrm{f2}}+\frac{(n_{\mathrm{re\_f1}}^2-1)}{(n_{\mathrm{f1}}^2-n_{\mathrm{re\_f1}}^2)}n_{\mathrm{f1}}Q_{\mathrm{f1}}} \\ \underline{Z}_{(n_{\mathrm{f2}})} = \dfrac{\underline{Z}_{\mathrm{f1}(n_{\mathrm{f2}})}\underline{Z}_{\mathrm{f2}(n_{\mathrm{f2}})}}{\underline{Z}_{\mathrm{f1}(n_{\mathrm{f2}})}+\underline{Z}_{\mathrm{f2}(n_{\mathrm{f2}})}} = j\dfrac{U_{\mathrm{f}(1)}^2}{\frac{(n_{\mathrm{re\_f2}}^2-1)}{(n_{\mathrm{f2}}^2-n_{\mathrm{re\_f2}}^2)}n_{\mathrm{f2}}Q_{\mathrm{f2}}+\frac{(n_{\mathrm{re\_f1}}^2-1)}{(n_{\mathrm{f2}}^2-n_{\mathrm{re\_f1}}^2)}n_{\mathrm{f2}}Q_{\mathrm{f1}}} \end{cases} \tag{3.7.1.15}$$

$$\begin{cases} \underline{Z}_{\mathrm{S}(n_{\mathrm{f1}})} = n_{\mathrm{f1}}\omega_{(1)}L_{\mathrm{S}} \\ \underline{Z}_{\mathrm{S}(n_{\mathrm{f2}})} = n_{\mathrm{f2}}\omega_{(1)}L_{\mathrm{S}} \end{cases} \tag{3.7.1.16}$$

$$\begin{cases} \underline{Z}^{"}_{(n_{\mathrm{f1}})} = \dfrac{\underline{Z}_{(n_{\mathrm{f1}})}\underline{Z}_{\mathrm{S}(n_{\mathrm{f1}})}}{\underline{Z}_{(n_{\mathrm{f1}})}+\underline{Z}_{\mathrm{S}(n_{\mathrm{f1}})}} = j\dfrac{U_{\mathrm{f}(1)}^2\omega_{(1)}L_{\mathrm{S}}n_{\mathrm{f1}}}{U_{\mathrm{f}(1)}^2+\left[\frac{(n_{\mathrm{re\_f2}}^2-1)}{(n_{\mathrm{f1}}^2-n_{\mathrm{re\_f2}}^2)}n_{\mathrm{f1}}Q_{\mathrm{f2}}+\frac{(n_{\mathrm{re\_f1}}^2-1)}{(n_{\mathrm{f1}}^2-n_{\mathrm{re\_f1}}^2)}n_{\mathrm{f1}}Q_{\mathrm{f1}}\right]n_{\mathrm{f1}}\omega_{(1)}L_{\mathrm{S}}} \\ \underline{Z}^{"}_{(n_{\mathrm{f2}})} = \dfrac{\underline{Z}_{(n_{\mathrm{f2}})}\underline{Z}_{\mathrm{S}(n_{\mathrm{f2}})}}{\underline{Z}_{(n_{\mathrm{f2}})}+\underline{Z}_{\mathrm{S}(n_{\mathrm{f2}})}} = j\dfrac{U_{\mathrm{f}(1)}^2\omega_{(1)}L_{\mathrm{S}}n_{\mathrm{f2}}}{U_{\mathrm{f}(1)}^2+\left[\frac{(n_{\mathrm{re\_f2}}^2-1)}{(n_{\mathrm{f2}}^2-n_{\mathrm{re\_f2}}^2)}n_{\mathrm{f2}}Q_{\mathrm{f2}}+\frac{(n_{\mathrm{re\_f1}}^2-1)}{(n_{\mathrm{f2}}^2-n_{\mathrm{re\_f1}}^2)}n_{\mathrm{f2}}Q_{\mathrm{f1}}\right]n_{\mathrm{f2}}\omega_{(1)}L_{\mathrm{S}}} \end{cases} \tag{3.7.1.17}$$

$$\begin{cases} \varphi_1 = \dfrac{U_{\mathrm{b}(n_{\mathrm{f1}})}}{U_{\mathrm{a}(n_{\mathrm{f1}})}} = \dfrac{Z^{"}_{(n_{\mathrm{f1}})}}{Z_{\mathrm{S}(n_{\mathrm{f1}})}} = \dfrac{U_{\mathrm{f}(1)}^2}{U_{\mathrm{f}(1)}^2+\left[\frac{(n_{\mathrm{re\_f2}}^2-1)}{(n_{\mathrm{f1}}^2-n_{\mathrm{re\_f2}}^2)}Q_{\mathrm{F}}+\left(\frac{(n_{\mathrm{re\_f1}}^2-1)}{(n_{\mathrm{f1}}^2-n_{\mathrm{re\_f1}}^2)}-\frac{(n_{\mathrm{re\_f2}}^2-1)}{(n_{\mathrm{f1}}^2-n_{\mathrm{re\_f2}}^2)}\right)Q_{\mathrm{f1}}\right]\omega_{(1)}L_{\mathrm{S}}n_{\mathrm{f1}}^2} \\ \varphi_2 = \dfrac{U_{\mathrm{b}(n_{\mathrm{f2}})}}{U_{\mathrm{a}(n_{\mathrm{f2}})}} = \dfrac{Z^{"}_{(n_{\mathrm{f2}})}}{Z_{\mathrm{S}(n_{\mathrm{f2}})}} \dfrac{U_{\mathrm{f}(1)}^2}{U_{\mathrm{f}(1)}^2+\left[\frac{(n_{\mathrm{re_{f2}}}^2-1)}{(n_{\mathrm{f2}}^2-n_{\mathrm{re\_f2}}^2)}Q_{\mathrm{F}}+\left(\frac{(n_{\mathrm{re\_f1}}^2-1)}{(n_{\mathrm{f2}}^2-n_{\mathrm{re\_f1}}^2)}-\frac{(n_{\mathrm{re\_f2}}^2-1)}{(n_{\mathrm{f2}}^2-n_{\mathrm{re\_f2}}^2)}\right)Q_{\mathrm{f1}}\right]n_{\mathrm{f2}}^2\omega_{(1)}L_{\mathrm{S}}} \end{cases}$$

(3.7.1.18)

$$y = 1-(1-\varphi_1)(1-\varphi_2)$$

$$\text{for}\begin{cases} (1-\varphi_1) = \dfrac{\left[\frac{(n_{\mathrm{re\_f2}}^2-1)}{(n_{\mathrm{f1}}^2-n_{\mathrm{re\_f2}}^2)}Q_{\mathrm{F}}+\left(\frac{(n_{\mathrm{re\_f1}}^2-1)}{(n_{\mathrm{f1}}^2-n_{\mathrm{re\_f1}}^2)}-\frac{(n_{\mathrm{re\_f2}}^2-1)}{(n_{\mathrm{f1}}^2-n_{\mathrm{re\_f2}}^2)}\right)Q_{\mathrm{f1}}\right]\omega_{(1)}L_{\mathrm{S}}n_{\mathrm{f1}}^2}{U_{\mathrm{f}(1)}^2+\left[\frac{(n_{\mathrm{re\_f2}}^2-1)}{(n_{\mathrm{f1}}^2-n_{\mathrm{re\_f2}}^2)}Q_{\mathrm{F}}+\left(\frac{(n_{\mathrm{re\_f1}}^2-1)}{(n_{\mathrm{f1}}^2-n_{\mathrm{re\_f1}}^2)}-\frac{(n_{\mathrm{re\_f2}}^2-1)}{(n_{\mathrm{f1}}^2-n_{\mathrm{re\_f2}}^2)}\right)Q_{\mathrm{f1}}\right]\omega_{(1)}L_{\mathrm{S}}n_{\mathrm{f1}}^2} \\ (1-\varphi_2) = \dfrac{\left[\frac{(n_{\mathrm{re_{f2}}}^2-1)}{(n_{\mathrm{f2}}^2-n_{\mathrm{re_{f2}}}^2)}Q_{\mathrm{F}}+\left(\frac{(n_{\mathrm{re\_f1}}^2-1)}{(n_{\mathrm{f2}}^2-n_{\mathrm{re\_f1}}^2)}-\frac{(n_{\mathrm{re_{f2}}}^2-1)}{(n_{\mathrm{f2}}^2-n_{\mathrm{re_{f2}}}^2)}\right)Q_{\mathrm{f1}}\right]n_{\mathrm{f2}}^2\omega_{(1)}L_{\mathrm{S}}}{U_{\mathrm{f}(1)}^2+\left[\frac{(n_{\mathrm{re_{f2}}}^2-1)}{(n_{\mathrm{f2}}^2-n_{\mathrm{re_{f2}}}^2)}Q_{\mathrm{F}}+\left(\frac{(n_{\mathrm{re\_f1}}^2-1)}{(n_{\mathrm{f2}}^2-n_{\mathrm{re\_f1}}^2)}-\frac{(n_{\mathrm{re_{f2}}}^2-1)}{(n_{\mathrm{f2}}^2-n_{\mathrm{re_{f2}}}^2)}\right)Q_{\mathrm{f1}}\right]n_{\mathrm{f2}}^2\omega_{(1)}L_{\mathrm{S}}} \end{cases} \tag{3.7.1.19}$$

Example	
For $h = 2, n_{\mathrm{re\_f1}} = 2.8$, $n_{\mathrm{re\_f2}} = 4.8$ and $Q_{\mathrm{F}} = 500$ Var	$y = 1 - \left(1 - \frac{52900}{51384 + 14.38Q_{\mathrm{f1}}}\right)\left(1 - \frac{52900}{82980 - 58.02Q_{\mathrm{f1}}}\right)$ 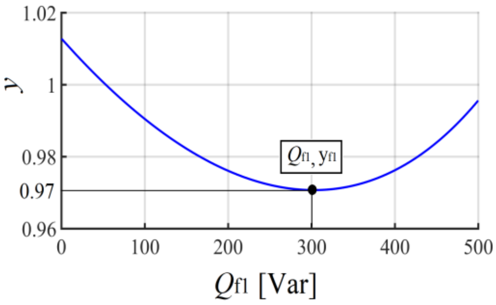 $Q_{\mathrm{f2}} = 500 - 325.54 = 174.46$ Var (The function used to design the characteristic y versus Q_{f1} is described in Annex III - Table III.13)

3.7.2 Comparison of the methods

To compare the six methods described in this chapter, it has been designed in the environment of MATLAB/SIMULINK a power grid system constituted of electrical network to which is connected a single phase rectifier (see Annex II-B). Between the PCC and the input reactor (L) of diodes bridge rectifier, the passive filter group constituted of two parallel connected single-branch filters (f1 and f2) is connected (Figure 3.100).

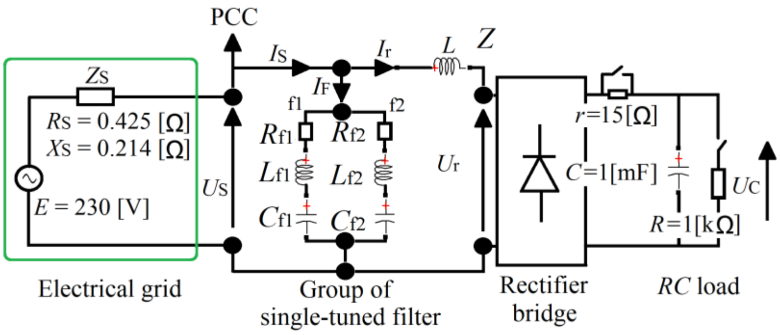

Figure 3.100 Equivalent circuit of the simulated power system

The comparison is mainly focused on filter power losses and the reduction of voltage and current distortion at the PCC. The set of criteria for the comparison does not include the production and operation cost of the filters.

It has been assumed that the filters are respectively tuned to the frequencies lower than the frequencies of the 3rd and 5th harmonic (2.9rd and 4.85th).

The total reactive power (basic harmonic) of the filter group (Q_{F} = -500Var) is the same for each method of parameters computation.

Table 3.18 Expressions used to compute the reactive power of each filter in the group for each method

Method A - equal reactive power for filters	$Q_{\mathrm{f1}} = Q_{\mathrm{f2}} = \frac{Q_{\mathrm{F}}}{2}$
Method B - the reactive power of filters is inversely proportional to the harmonic order	$\frac{Q_{\mathrm{f1}}}{Q_{\mathrm{f2}}} = \frac{n_{\mathrm{re\_f2}}}{n_{\mathrm{re\_f1}}} \Rightarrow 2.9Q_{\mathrm{f1}} = 4.85Q_{\mathrm{f2}} \Rightarrow Q_{\mathrm{f1}} = \frac{2.9}{7.75}Q_{\mathrm{F}}$

Method C - the reactive power of filters is inversely proportional to the square of harmonic order	$\frac{Q_{f1}}{Q_{f2}} = \frac{n^2_{re\_f2}}{n^2_{re\_f1}} \Rightarrow 8.41Q_{f1} = 23.52Q_{f2} \Rightarrow Q_{f1} = \frac{8.41}{31.93}Q_F$
Method D - the reactive power of filters is calculated on the base of the shaping of frequency characteristic of the filter impedance	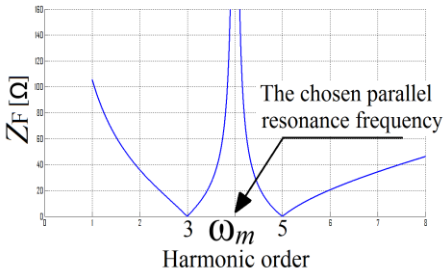 $\begin{cases}\begin{bmatrix}\frac{2.9^2*100\pi}{1-2.9^2} & \frac{4.85^2*100\pi}{1-4.85^2}\\ \frac{2.9^2*4}{4^2-2.9^2} & \frac{4.8^2*4}{4^2-2.9^2}\end{bmatrix}\begin{bmatrix}C_{f1}\\ C_{f2}\end{bmatrix} = \begin{bmatrix}\frac{Q_F}{230^2}\\ 0\\ 0\end{bmatrix}\end{cases}$
Method E - the reactive power of filters is calculated on the base of the assumption that the reactors of filters are identical	$Q_{f1} = \frac{Q_F}{(1-2.9^2)(\frac{1}{1-2.9^2}+\frac{1}{1-4.85^2})}$
Method F (optimization) - $y = 1-(1-\varphi_1)(1-\varphi_2)$	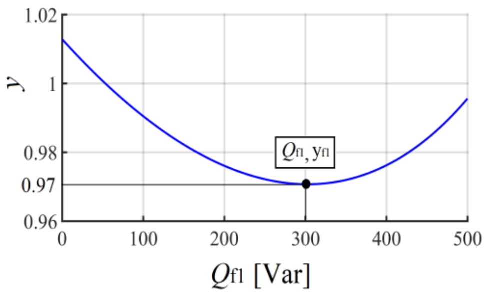 (see Annex III - Table III.13)

Table 3.19 Filter group parameters

Methods	Q_F = - 500 [Var], q' = 85									
	n_{f1} = 2.9					n_{f2} = 4.85				
	C_{f1} [μF]	L_{f1} [mH]	R_{Lf1} [Ω]	$Z_{f1(3)}$ [Ω]	Q_{f1} [Var]	C_{f2} [μF]	L_{f2} [mH]	R_{Lf2} [Ω]	$Z_{f2(5)}$ [Ω]	Q_{f2} [Var]
A	13.25	90.9	0.33	5.62	250	14.40	29.9	0.11	2.77	250
B	16.58	72.6	0.26	4.49	312.90	10.77	40.00	0.14	3.71	187.09
C	19.52	61.7	0.22	3.81	368.31	7.58	56.8	0.20	5.27	131.68
D	18.62	64.7	0.23	4.00	351.2	8.57	50.2	0.18	4.66	148.80
E	19.94	60.4	0.22	3.73	376.22	7.13	60.4	0.22	5.61	123.77
F	16.05	75.0	0.27	4.64	302.79	11.36	37.9	0.14	3.52	197.20

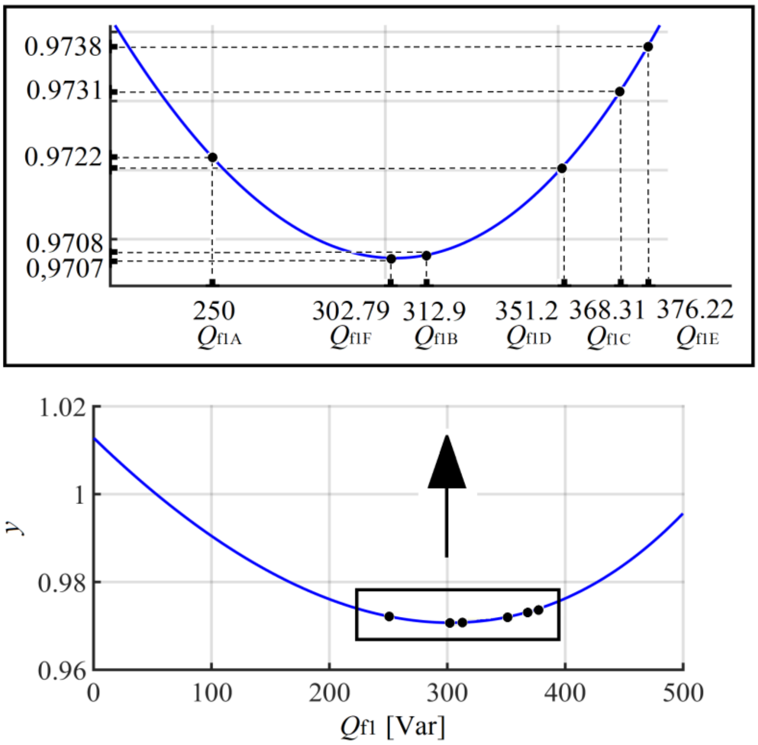

Figure 3.101 Objective function characteristic of method F with reactive powers of other methods (Q_{f1}(A-E))

Table 3.18 presents the formulas (Method A-C and E) and characteristics (methods D and F) used to obtain the reactive power of individual filter. The parameters of the filter group for each method (A-F) are presented in the Table 3.19 (the filter reactor resistances are computed basing on the quality factor (85)).

On the objective function characteristic of method F (see Figure 3.101), the reactive powers ($Q_{f1(A\text{-}E)}$) of other methods are also presented. It can be seen that for method F, the filter f1 has the lowest reactive power.

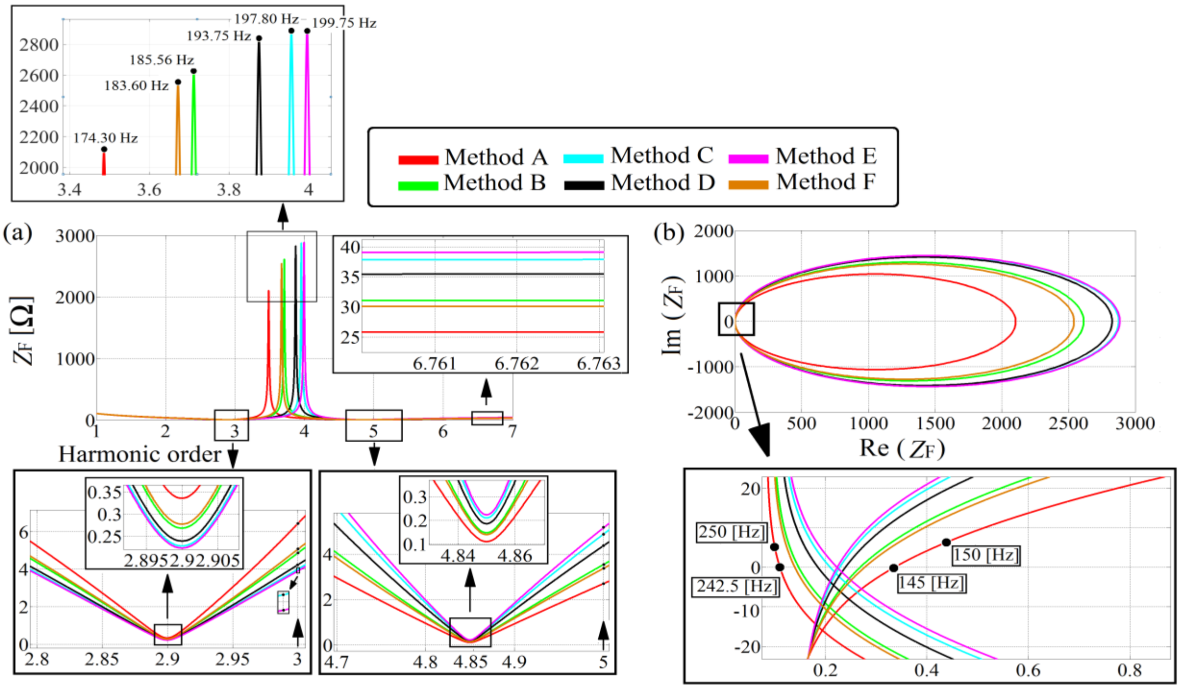

Figure 3.102 (a) impedance vs frequency characteristics for each method, (b) filter group impedance characteristic in complex plan

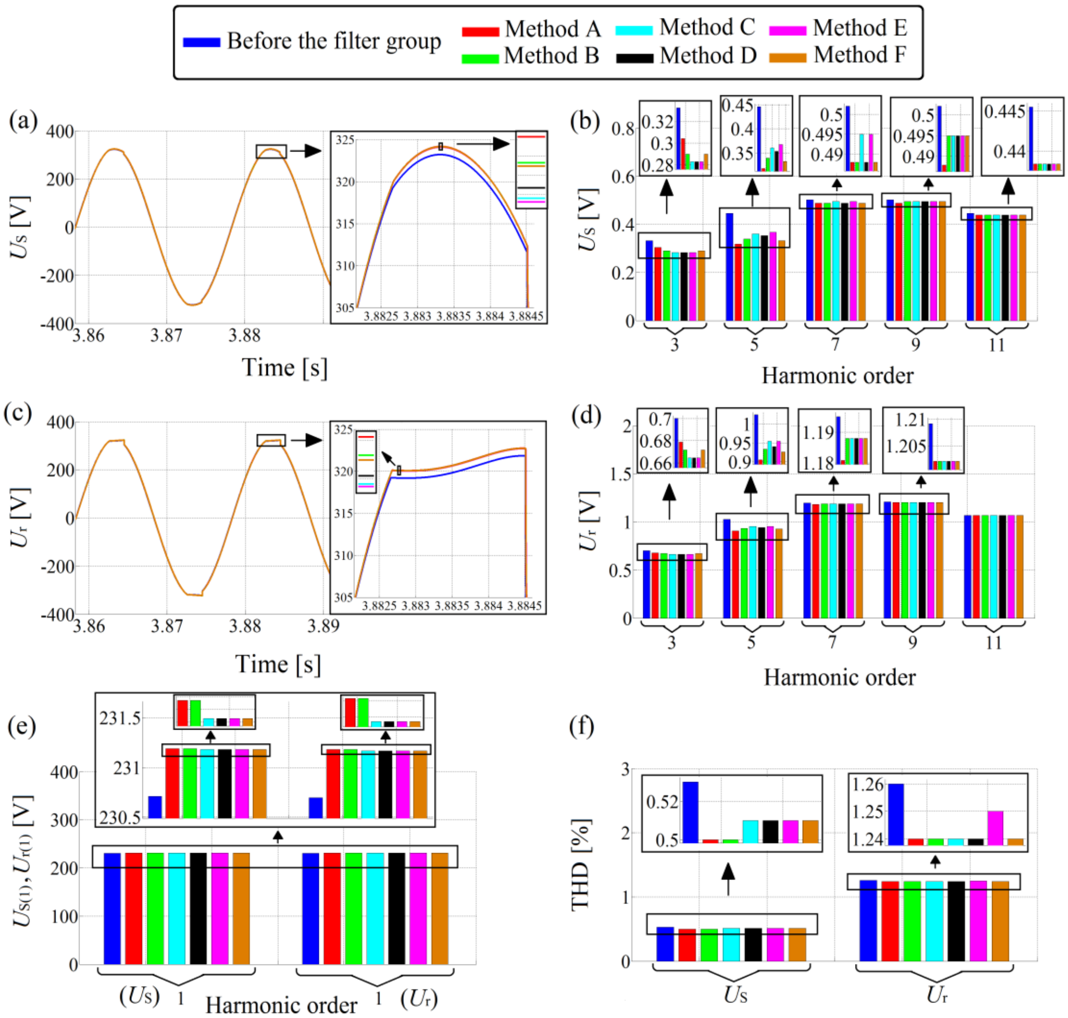

Figure 3.103 (a) grid voltage and (b) its spectrum, (c) voltage at the input of rectifier and (d) its spectrum, (e) first harmonic amplitude of grid and rectifier input voltage, (f) THD of grid and rectifier input voltage

The comparison criteria of the computation methods of the filter group is based on the frequency impedance characteristics, the amplitude of grid voltage and current harmonics and filter power losses as well.

Figure 3.102(a) presents the impedance frequency characteristics of filter groups whose parameters have been computed by the six methods. It can be observed that method A presents the highest value of impedance for the 3rd harmonic and the lowest value of impedance for the 5th harmonic. Focusing the comparison only on the 3rd and 5th harmonic filter group impedances, it is difficult to choose which method of parameters computation is the best.

Considering the filtration of the components with order higher than 5th, method A is the best because it can reduce more effectively the harmonics in a wide frequency range compering with others methods.

Figure 3.102(b) presents the filter group impedance characteristics for each method on the complex plan. The contact point of the characteristics with the horizontal axis represents the resonance frequencies (145Hz and 242.5Hz).

The amplitude of the fundamental harmonic of grid voltage (U_S) and rectifier input voltage (U_r) have increased for each method after the filter group connection (Figure 3.103(e)).

The waveforms and spectrums of the grid voltage are shown in Figure 3.103 (a) and (b) and those of input rectifier voltage in Figure 3.103(c) and (d). There is not considerable difference on voltages waveforms for all methods. For each method, after the filter connection, it can be observed in Figure 3.103(b) and (d) a reduction of harmonics amplitudes higher than the 3rd and 5th (e.g. 7th, 9th, 11th). Method A has the worse reduce the 3rd harmonic and the best reduce the 5th harmonic of the grid voltage (Figure 3.103(b)). Methods C, D and E present the lowest value of the third harmonic amplitude and method E the highest amplitude of 5th harmonic (Figure 3.103(b) and (d)). Methods A and B present the lowest THD of grid voltage (Figure 3.103(f)).

The filter group has improved the waveform of grid current (Figure 3.104(a)) reducing the 3rd and 5th harmonic amplitudes (in the considered example). Methods C and E show a better reduction of third harmonic grid current (Figure 3.104 (b)), then methods D and F and at the end methods B and A. The 5th harmonic is the best reduced by method A and the worse reduced by method C and E. The input rectifier current characteristics are presented in Figure 3.104(c) and the spectrums, which are almost the same (for all methods) before and after the filter group connection in Figure 3.104 (d).

One of the most important parameter in PHF design is the reactive power which is a quantity depending of load. In this analysis the load reactive power measured at the PCC before the filter group connection, is small (Q_S = 9.4Var). The filter group reactive power should be in the same scale as the load reactive power. The reactive power used to compute the filters parameters was chosen to be almost 50 time higher (Q_f = -500Var) than the load reactive power to present the phenomena of overcompensation in power system.

The overcompensation has caused the increase of fundamental harmonic of the grid voltage and current and voltage at the input of rectifier (Figure 3.103(e) and Figure 3.105(a)). It has affected the filter group fundamental current but almost did not influence the input rectifier fundamental current (Figure 3.105(a)). It has also increased the voltage at the DC side of diode bridge (Figure 3.106(d)). The power system together with the filter group (from the PCC) has turned to capacitive.

In practice, it exists the issue of the selection of filter with minimum reactive power. That means the filter with ability to eliminate harmonics and with minimal reactive power that does not overcompensate the load. In this paper, this issue is not taken into account.

The distortion of the PCC current has considerably decreased after the filters connection and method A presents the lowest THD and then com method F (Figure 3.105(b). A non-significant increase is observed on the input rectifier current THD.

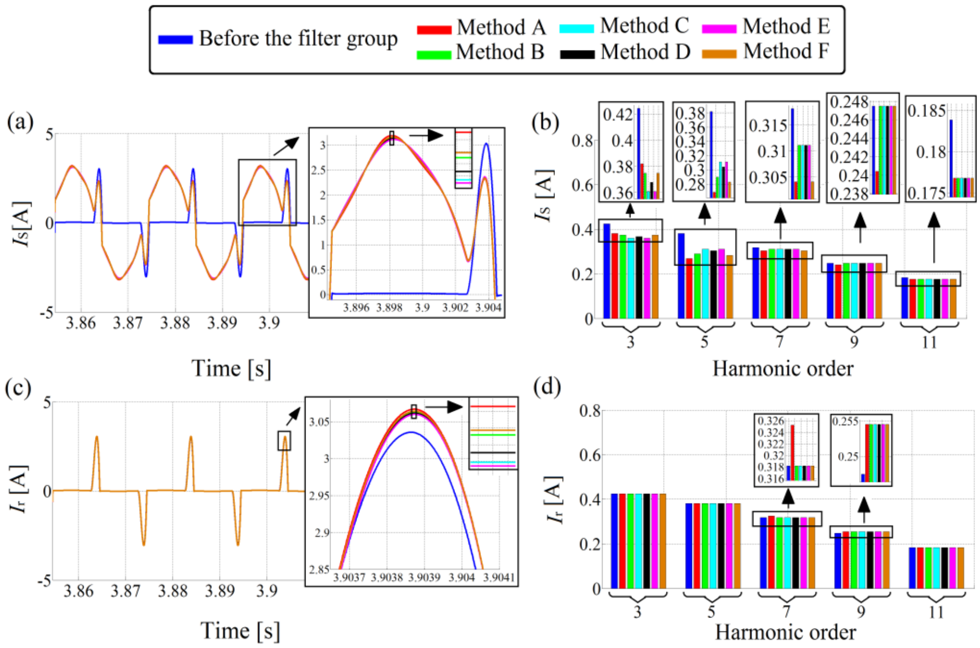

Figure 3.104 (a) grid current and (b) its spectrum, (c) current at the input of rectifier and (d) its spectrum, (e) spectrum (p.u.) of rectifier input voltage

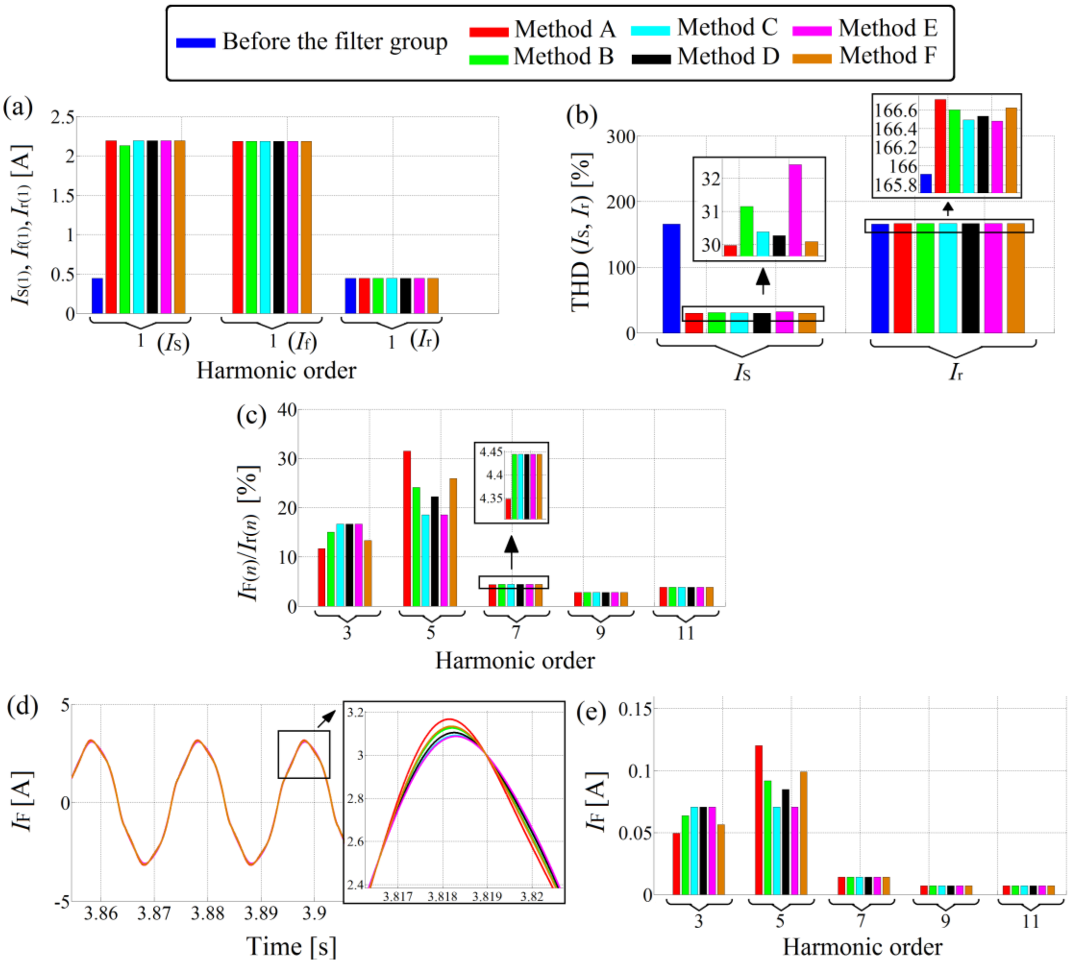

Figure 3.105 (a) fundamental harmonic of grid current, filter current and current at the input of rectifier, (b) THD of grid current and current at the input of rectifier, (c) filter group effectiveness, (d) waveforms of filter group and (e) the spectrum

The filter group current waveforms with the spectrums are respectively presented in Figure 3.105(d) and (e). For all methods, the filter group is more loaded by the harmonics that it is supposed to filter than the higher harmonics (Figure 3.105(f)).

Observing Figure 3.105(c), it can be seen that the filter group efficiency on the reduction of 3rd and 5th harmonics is below 35% for all methods because of the very low impedance of the grid. The filter groups designed by method C, D and E are more effective for the 3rd harmonic and less effective for the 5th harmonic. Method A has a better efficiency for the 5th harmonic than for the 3rd. The same interpretation can be formulated for the remaining methods (Figure 3.105(c)).

Before the filter group connection, the phase shift between the fundament harmonic of current and voltage at the PCC was positive (inductive). After the filter group connection (because of the overcompensation) it has changed to negative (capacitive) and its module has increased (Figure 3.106(c)). The DC side voltage is presented in Figure 3.106(d).

The power system impedance (Z) measured at the input of rectifier (see Figure 3.100) is presented in Figure 3.107. The series and parallel resonances are observed around each frequency to which the filter group is tuned. The series resonances have occurred because of the filter group connection and the parallel resonances because of the parallel connection between the filter group capacitors and the electrical grid reactor (L_S). The parallel resonances caused by each filter in the group has occurred bellow the frequencies of 145Hz and 242.5Hz.

To determine which method (A-F) is the best, a set of criteria has been established in Table 3.20. Observing that table, it can be noticed different filtration efficiency and in general sense it is difficult to indicate which method is the most effective because there is not big difference between the compared parameters.

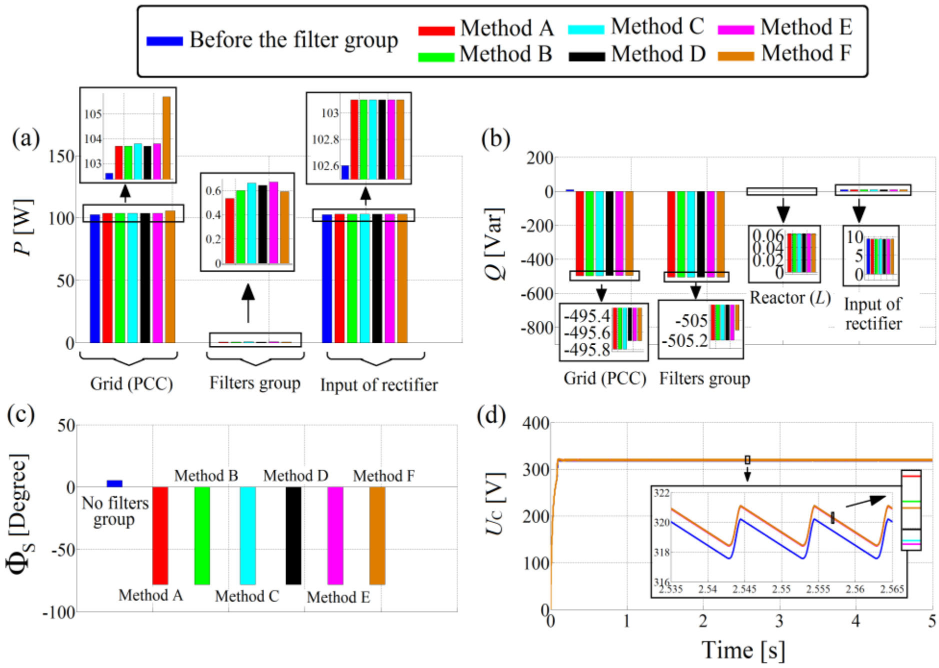

Figure 3.106 (a) PCC active and (b) reactive power, (c) phase shift between the grid fundament harmonic of current and voltage, (d) voltage at the DC side of rectifier

Table 3.20 Comparison of the methods basing on the selected criterions

Comparison criteria	Method A	Method B	Method C	Method D	Method E	Method F
$U_{S(3)}$ [v]	0.43	0.41	0.40	0.40	0.40	0.41
$U_{S(5)}$ [v]	0.45	0.48	0.51	0.50	0.52	0.47
$(I_{F(3)}/I_{r(3)})$ [%]	11.16	15	16.66	16.66	16.66	13.33
$(I_{F(5)}/I_{r(5)})$ [%]	31.48	24.07	18.51	22.22	18.51	25.92
THD_{Us}[%]	0.50	0.50	0.51	0.51	0.51	0.51
ΔP_F [w]	0.533	0.600	0.660	0.6418	0.6687	0.5897
The blue area indicates which method is the best in comparison to other methods.						

It has been noticed during the previous studies the influence of grid impedance on the filtration efficiency (it concerns all the methods). In the case of method C (another case could have chosen) for instance, 15% and 26.66% of the 3rd and 5th harmonic current respectively are reduced by the filter group. This is due to fact that the 3rd and 5th harmonic grid impedances are higher than the 3rd and 5th harmonic filter group impedances as presented in Table 3.21 (problem of the grid impedance dependency on the PHF efficiency).

Table 3.21 The 3rd and 5th harmonic impedances of filter group (e.g. $Z_{F(3)}$) are compared to those of grid impedance (e.g. $Z_{S(3)}$) when the line reactor L_{SS} is not connected

Methods	$Z_{S(3)}$ [Ω]	$Z_{F(3)}$ [Ω]	$Z_{S(5)}$ [Ω]	$Z_{F(5)}$ [Ω]
A	0.77	6.41	1.15	2.69
B		4.85		3.53
C		3.99		4.87
D		4.22		4.36
E		3.89		5.15
F		5.05		3.37

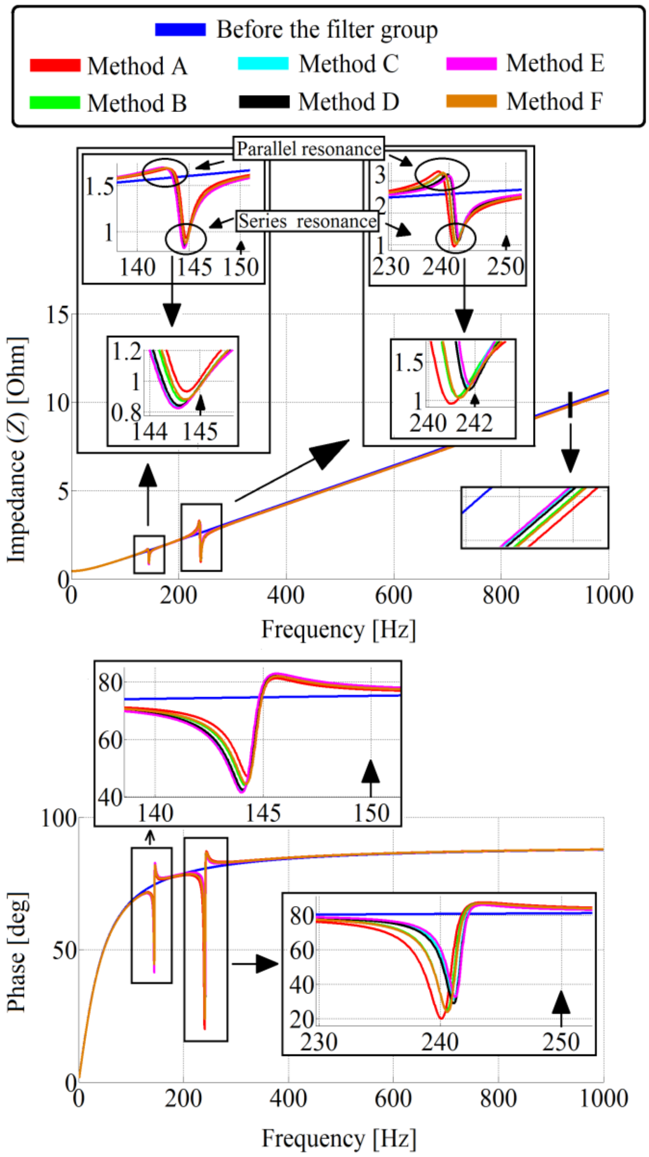

Figure 3.107 Frequency versus impedance characteristics measured at the input of rectifier bridge for all methods

To solve that problem, a line reactor (L_{SS} = 4.5 mH) is added between the PCC and the filter group (see Figure 3.108). The spectrums of grid voltage and current (for method C) are presented in Figure 3.109(a) and (b). It can be noticed that the harmonics (3rd to 11th) as well as THD of PCC voltage and current are better reduced after the line reactor connection. 60 % and 71.46 % of 3rd and 5th harmonic current respectively are reduced from the grid side.

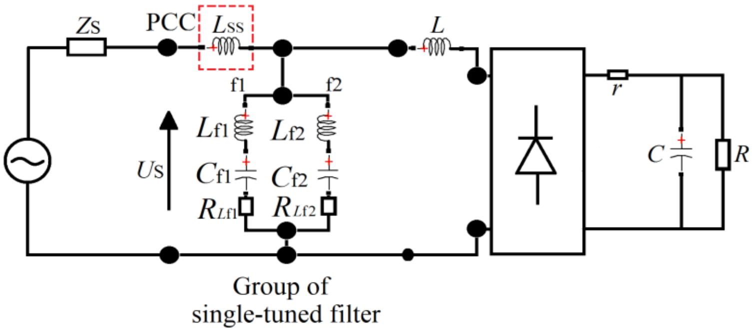

Figure 3.108 Equivalent circuit of the simulated power system with additional line reactor L_{SS} to improve the filter group efficiency

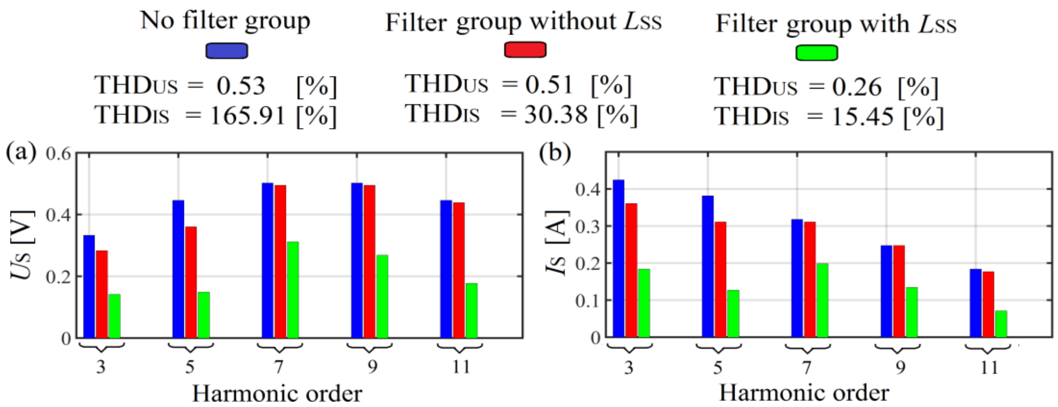

Figure 3.109 Grid voltage (a) and current (b) spectrums (e.g. method C)

Chapter 4

Passive harmonic filters laboratory investigation

In chapter 3, different filtration properties and frequency characteristics of the PHFs have been studied using simulation in MATLAB SIMULINK environment. This chapter is about the laboratory investigation of the chosen structures of PHFs: single-tuned filters, group of single-tuned filter, first-order filter (capacitor bank) and 2nd order-filter.

Figure 4.1 presents the overview of the laboratory set up. The further part of this chapter will concern the description of its elements (blocks in brown colour). The blocks without colour will be considered later in chapter 5 and 6.

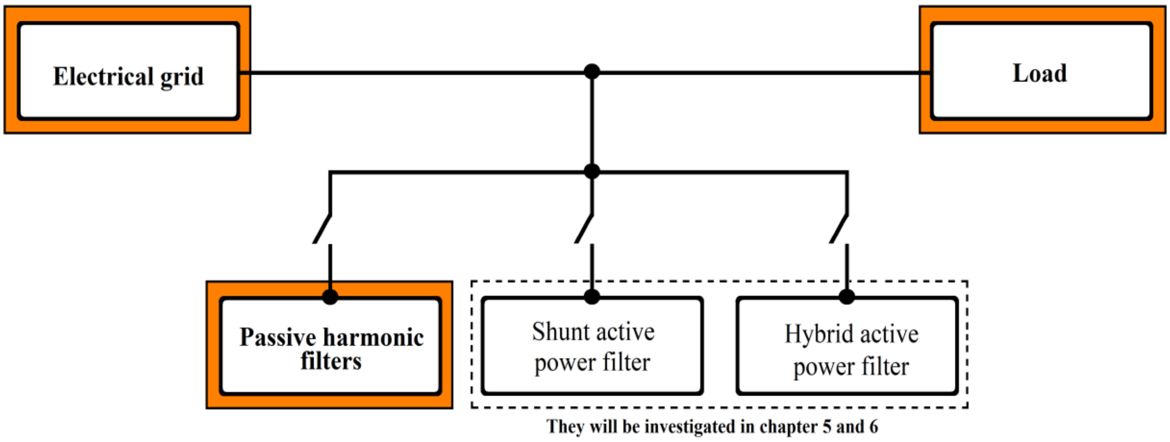

Figure 4.1 General representation of the investigated laboratory set up

4.1 Laboratory model description

The laboratory model equivalent circuit with pictures of the components is presented in Figure 4.2. The technical and other data are presented in Annex IV.

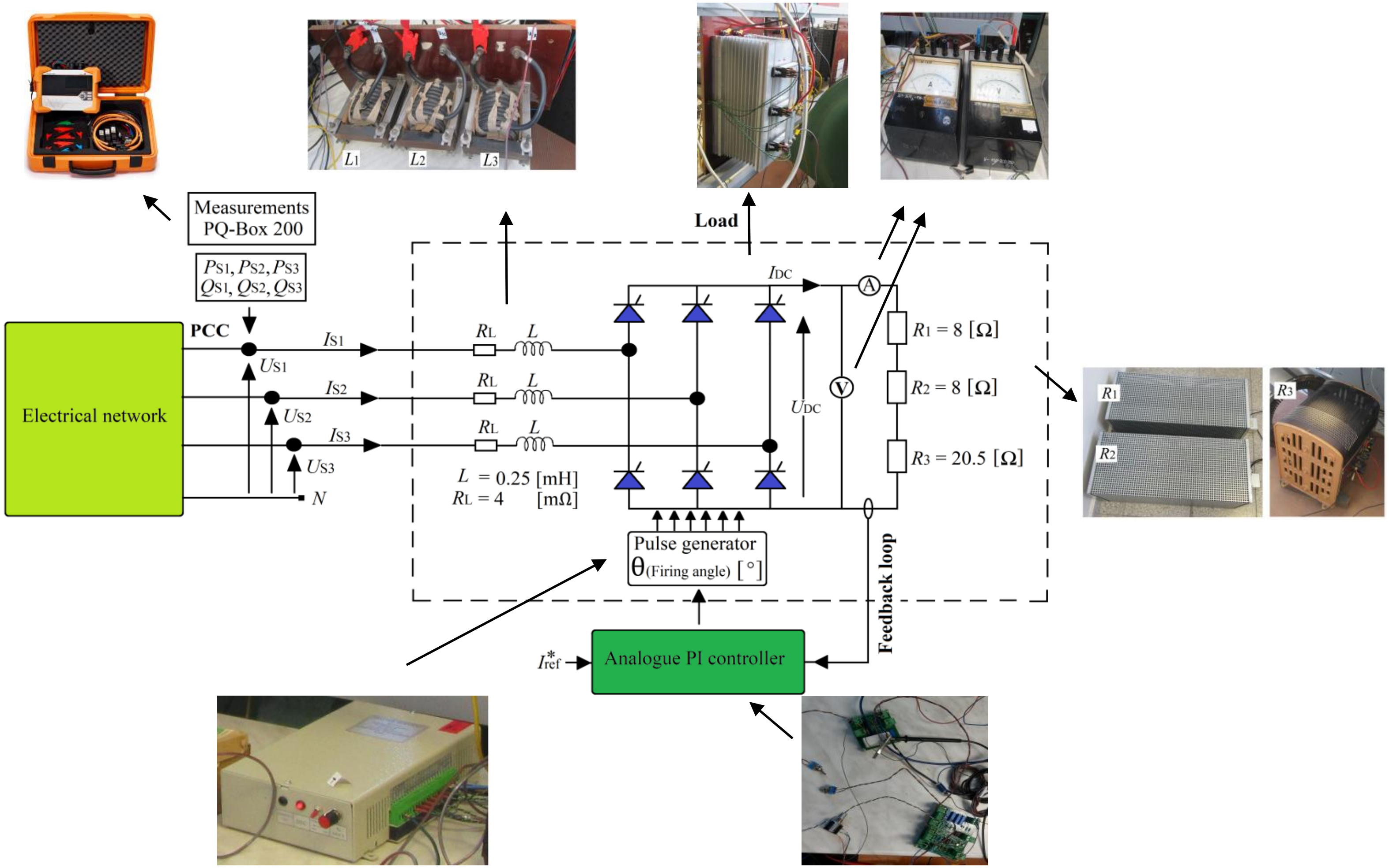

Figure 4.2 Block diagram of the non-linear load applied in the investigated laboratory model

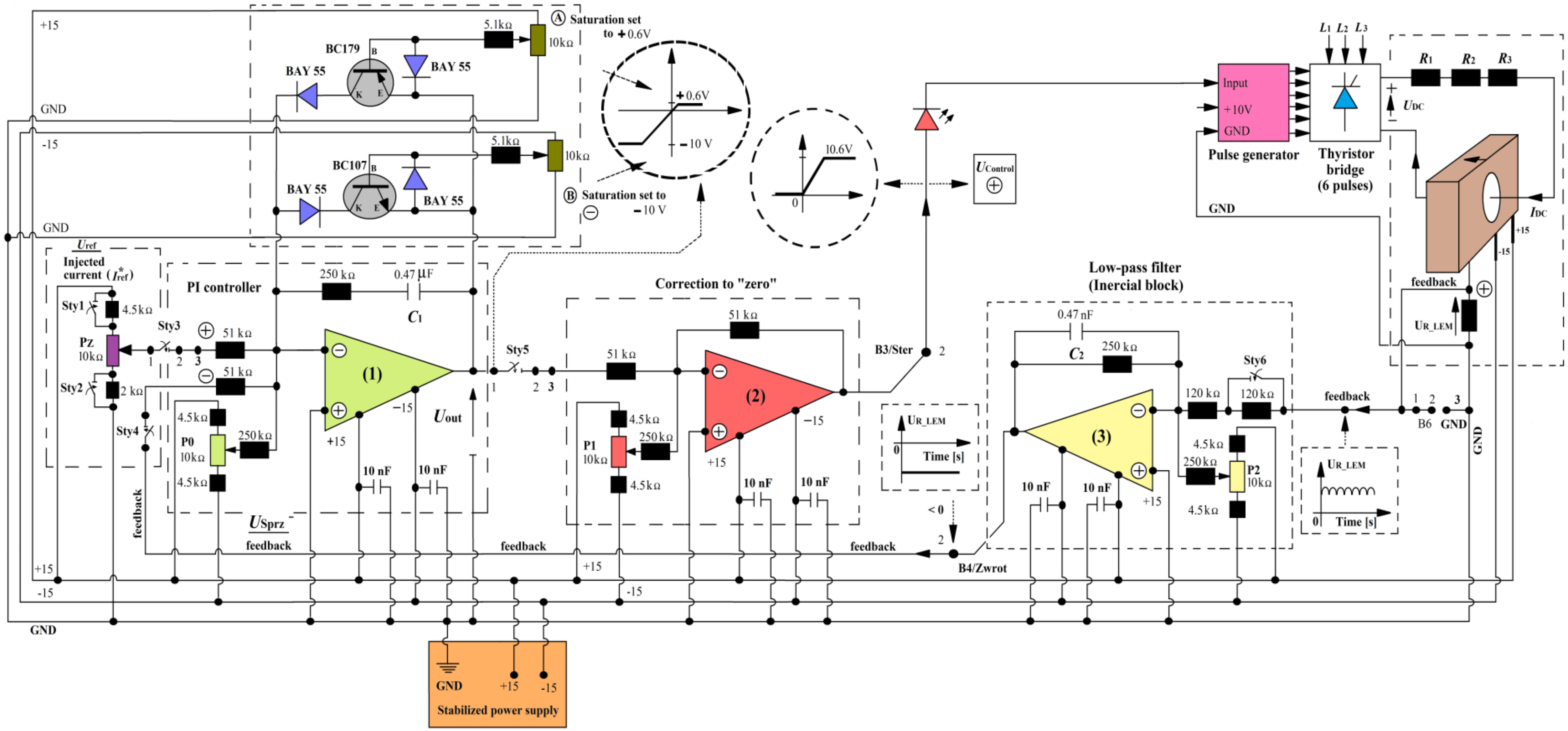

Figure 4.3 Equivalent circuit of the electronic board (analogue PI controller) used to control the thyristor pulse generator

4.1.1 Load description

The designed laboratory nonlinear load is constituted of six pules thyrystor bridge with input reactor at its AC side and resistance at the DC side (the total resistance of the DC load side is up to 36.5 Ω) (Figure 4.2). At the DC side of rectifier, the voltmeter and ampere-meter are used for voltage and current average value measurement and the smart meter "PQ-Box 200" [283] is used at the AC side to record the data (Figure 4.2).

The rectifier pulse generator can be control externally (by applying an external signal controller e.g. analogue PI controller - Figure 4.3) or internally (it possess its own internal control mode (potentiometer). The thyrystor bridge and its connection diagram are presented respectively in Table IV.2 and Figure IV.1 (Annex IV).

The goal of analogue PI controller board is to control the rectifier DC current (I_{DC}) by injecting an external signal at the rectifier pulses generator input (Figure 4.2 and Figure 4.3). It enables a control of the rectifier DC current in static and dynamic mode of operation.

The 10 kΩ potentiometer (Pz) (Figure 4.3) is used to generate the reference signal (I^*_{ref}). The step change of the reference current is performed by the switches "Sty1" or "Sty2". The transmittance of the PI controller (see Figure 4.3 – **(1)**) is expressed by (4.1) (C_1 = 0.47 µF, R_1 = R_2 = 51 kΩ, R_3 = R_4 = 250 kΩ; U_1, U_2 and U_3 are respectively the voltages at R_1, R_2 and R_3 terminals).

$$\underline{U}_{\mathrm{out}}(j\omega) = -\left(1 + \frac{1}{j\omega C_1 R_4}\right)\left[\frac{R_4}{R_1}\underline{U}_1(j\omega) + \frac{R_4}{R_2}\underline{U}_2(j\omega) + \frac{R_4}{R_3}\underline{U}_3(j\omega)\right] \quad (4.1)$$

The saturation block in Figure 4.3 (**Saturation set**) is used to fix the limits of the PI controller output voltage.

The potentiometer (**Correction to "zero"**) in Figure 4.3 is used to correct the signal at the output of PI controller (U_{out}), by making it start from zero (due to P1) and by changing its sign to positive.

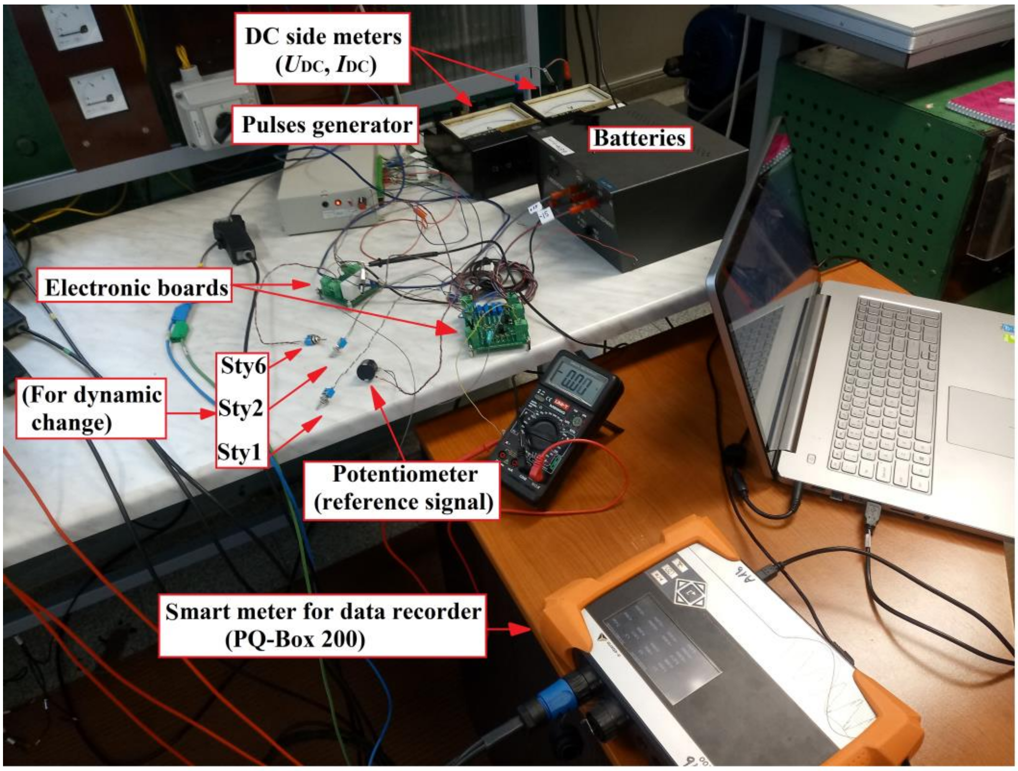

Figure 4.4 Laboratory equipment with analogue PI controller (electronic board)

The low-pass filter in Figure 4.3 is applied to mitigate the fluctuations contained in the feedback signal (coming from the current sensor). Its transmittance is expressed by (4.2) (C_2 = 0.47 nF, R_5 = 120 kΩ, R_7 = R_6 = 250 kΩ; U_5 and U_6 are respectively the voltages at R_5 and R_6 terminals).

$$\underline{U}_{\mathrm{R\_LEM}}(j\omega) = \left(\frac{1-j\omega C_2 R_7}{1+R_7^2\omega^2 C_2}\right)\left[\frac{R_7}{R_5}\underline{U}_5(j\omega) + \frac{R_7}{R_6}\underline{U}_6(j\omega)\right] \tag{4.2}$$

In the power electrical system, there are different types of sensors (or methods) used to measure and rescaling the current size. The sensor applied at the rectifier DC side (see Figure 4.3 - brown dark color) to reduce the current level (e.g. from 25 A to 25 mA) is type EL25P1 (see technical data in Annex IV, Figure IV.2).

The analogue PI controller equivalent circuit of Figure 4.3 has been physically realized (see the electronic boards of Figure 4.2) and tested in the laboratory (Figure 4.4). The result examples (grid voltage and current waveforms) are respectively shown in Figure 4.5. The step change of AC and DC current are performed by changing the position of switches “**Sty1**” and “**Sty2**”.

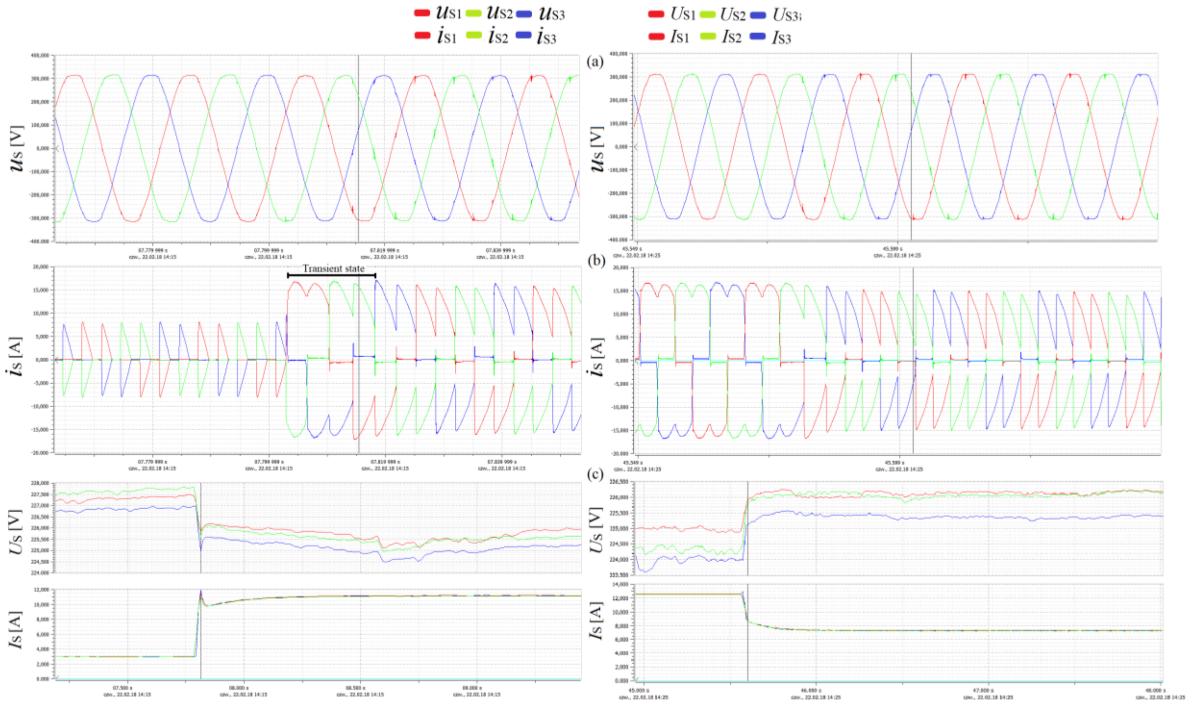

Figure 4.5 Waveform examples of the grid voltage (a) and current (b); (c) RMS voltage and current

4.1.2 Electrical grid description

The electrical grid feeding the laboratory in which the experimental studies were performed is presented by the equivalent circuit of Figure 4.6(a). The medium voltage system and transformer parameters are respectively presented in Table IV.3 and Table IV.4 of Annex IV.

The electrical network equivalent parameters (impedance, short circuit current and power) are presented in Figure 4.6(b) (See also Table IV.5 in Annex IV).

The electrical grid voltage (without the considered load) feeding the laboratory is symmetrical (the negative sequence represents 0.12% of the positive sequence) but not pure sinusoidal (Figure 4.7(a)) because of other connected non-linear loads. Its spectrum, limited on one phase as example (Figure 4.7(b)), shows that the dominated harmonics are the 5$^{\mathrm{th}}$ (around 2%) and then comes the 3$^{\mathrm{rd}}$ (more than 1%) and at the end the 7$^{\mathrm{th}}$ (almost 1 %). According to the IEC61000-2-4 standard, its THD and harmonics amplitude are acceptable (Figure 4.7(b)).

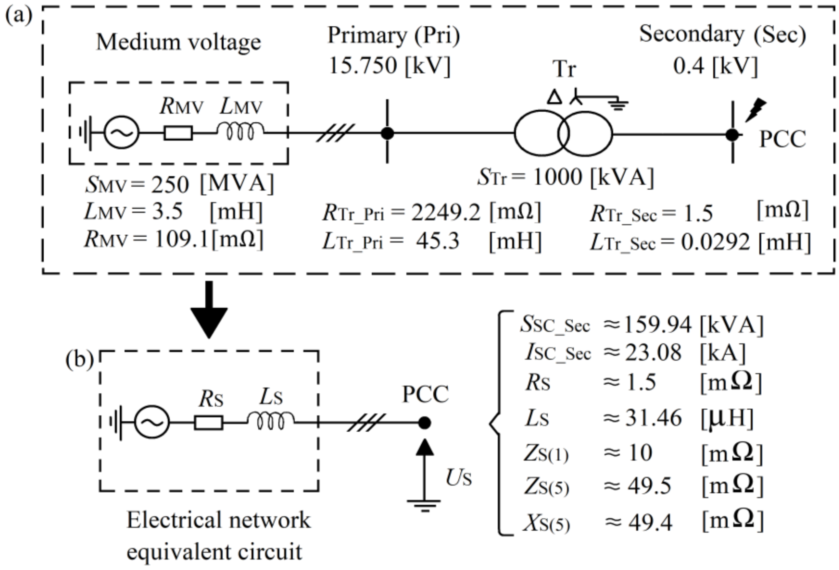

Figure 4.6 (a) laboratory electrical network, (b) electrical grid equivalent circuit

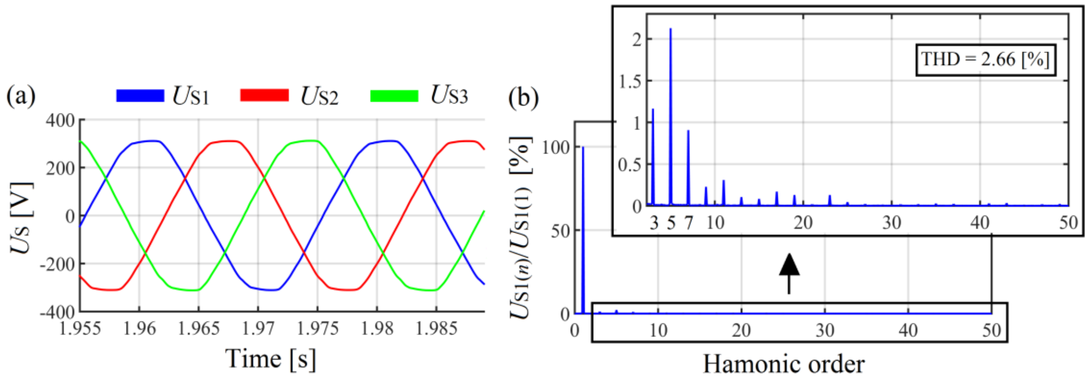

Figure 4.7 (a) PCC voltage waveforms without the considered load connected) and (b) its spectrum (p.u.)

4.2 Load parameters analysis when connected to the PCC

With the load connected at the PCC as presented in Figure 4.2, the laboratory model parameters has been analyzed by increasing the DC voltage from 0 V to 525 V (decreasing the thyristor bridge firing angle). The smart meter "PQ-Box 200" (AC side) and volt-meter (DC side) were used for data recording.

The PQ-Box scope data (10 periods) were analyzed through MATLAB tools by the means of Fast Fourier Transformer (FFT) function and the power system parameters (characteristics) such as harmonics, active and reactive power (fundamental harmonic) and displacement power factor (DPF) were obtained.

The firing angle used in some characteristics (e.g. Figure 4.10) has been estimated from the measured U_{DC} voltage by basing on the formulas (4.3) and (4.4) (the thyristors commutation is not considered and the rectifier DC side load is purely resistive) [188, 203, 250].

$$\theta = \operatorname{acos}\left(\frac{U_{\mathrm{DC}}}{1.35U_{\mathrm{L-L}}}\right) \quad \text{for } 0 \le \theta \le \frac{\pi}{3} \quad \text{continuous DC voltage and current} \tag{4.3}$$

$$\theta = \operatorname{acos}\left(\left(\frac{U_{\mathrm{DC}}}{1.35U_{\mathrm{L-L}}}\right) - 1\right) - \frac{\pi}{3} \quad \text{for } \frac{\pi}{3} \le \theta \le \frac{2\pi}{3} \quad \text{discontinuous DC voltage and current} \tag{4.4}$$

For $\frac{2\pi}{3} \le \theta \le \pi$, $U_{\mathrm{DC}} = 0$ [203])

$U_{L\text{-}L}$ is the line to line voltage and U_{DC} is the average voltage at the rectifier DC side

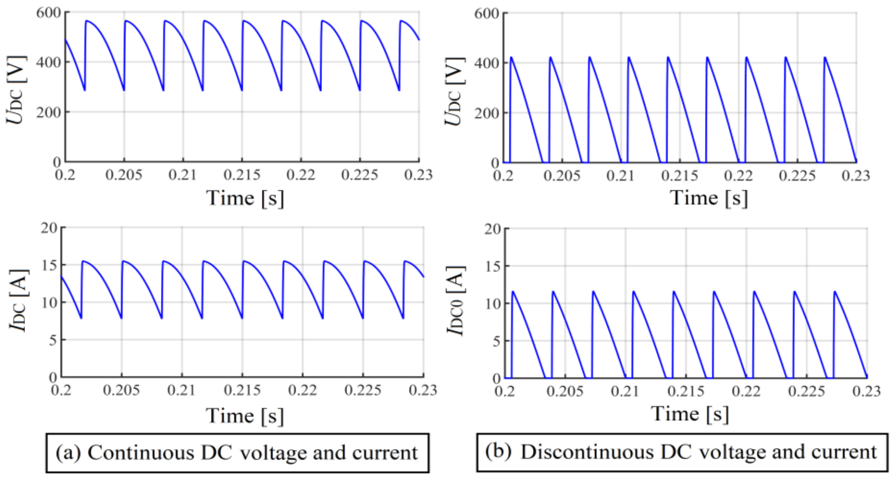

Figure 4.8 Voltage and current at the rectifier DC side for different firing angle: (a) continuous mode (θ = 30°); (b) discontinuous mode (θ = 60°) (simulation – see Annex IV, Figure IV.3)

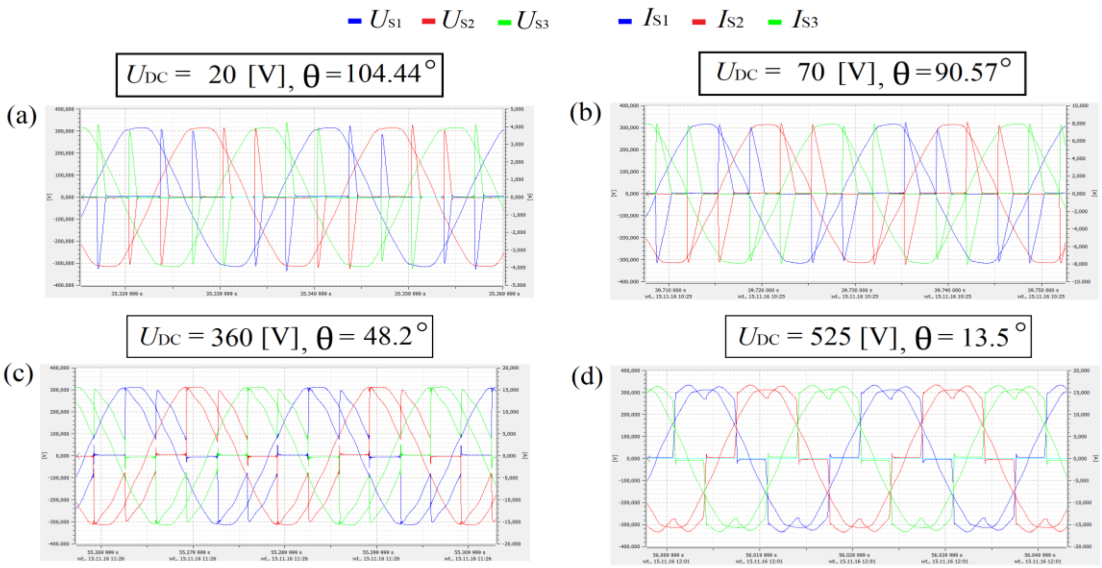

Figure 4.9 PCC phase voltage and current for different value of DC voltage (firing angle as well): (a) U_{DC} = 20 V; (b) U_{DC} = 70 V; (c) U_{DC} = 360 V and (d) U_{DC} = 525 V (measured)

The laboratory model (Figure 4.2) described above has been simulated in MATLAB/SIMULINK (see Annex IV, Figure IV.3) and in the further part of this work, the results from the laboratory as well as from the simulation are presented and compared.

The measured PCC voltage and current waveform examples (form the “PQ-Box 200”) are presented in Figure 4.9(a) - (d).

A comparison between characteristics obtained from the laboratory model and those obtained from the simulation are presented in Figure 4.10 to 4.13.

Figure 4.10(a)(b) represents the voltage and current (fundamental harmonic) versus rectifier firing angle and Figure 4.10(c)(d) represents the voltage and current (fundamental harmonic) versus rectifier DC voltage. A difference can be observed between the simulated grid voltage and the laboratory grid voltage, because in the case of simulation, other devices (apart the rectifier) are not connected to the electrical grid whereas in the case of laboratory other devices are connected and the grid is working continuously.

The voltage characteristics from the laboratory data (Figure 4.11(a) and (c)) are different to those from the simulation data (Figure 4.11(b) and (d)) because, before the rectifier connection, the laboratory PCC voltage contained already the 5th harmonic (see spectrum of

Figure 4.7(b)). The same phenomenon is observed for the 7th harmonic (see Figure 4.11(e) – (f)).

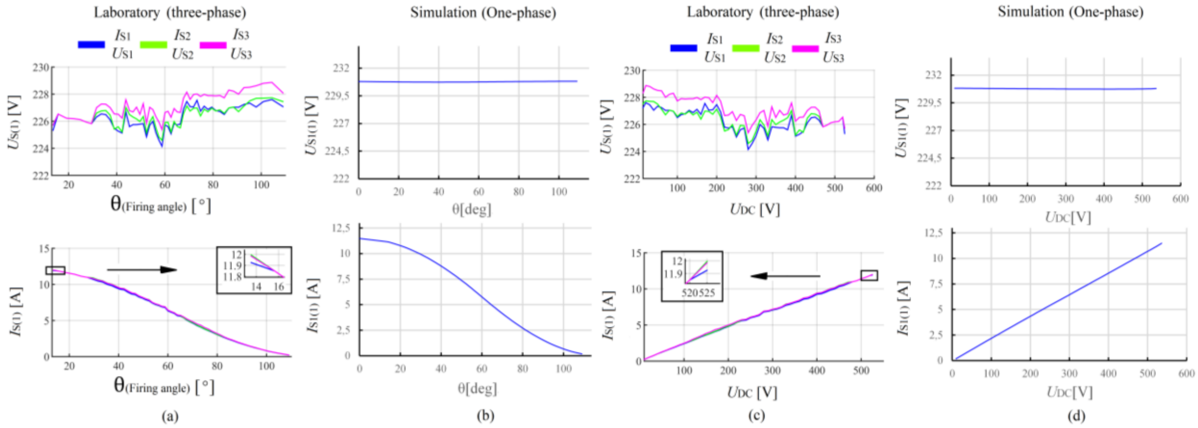

Figure 4.10 Comparison between laboratory and simulated characteristics: (a)(b) PCC voltage and current fundamental harmonic vs rectifier firing angle; (c)(d) PCC voltage and current fundamental harmonic vs rectifier DC voltage

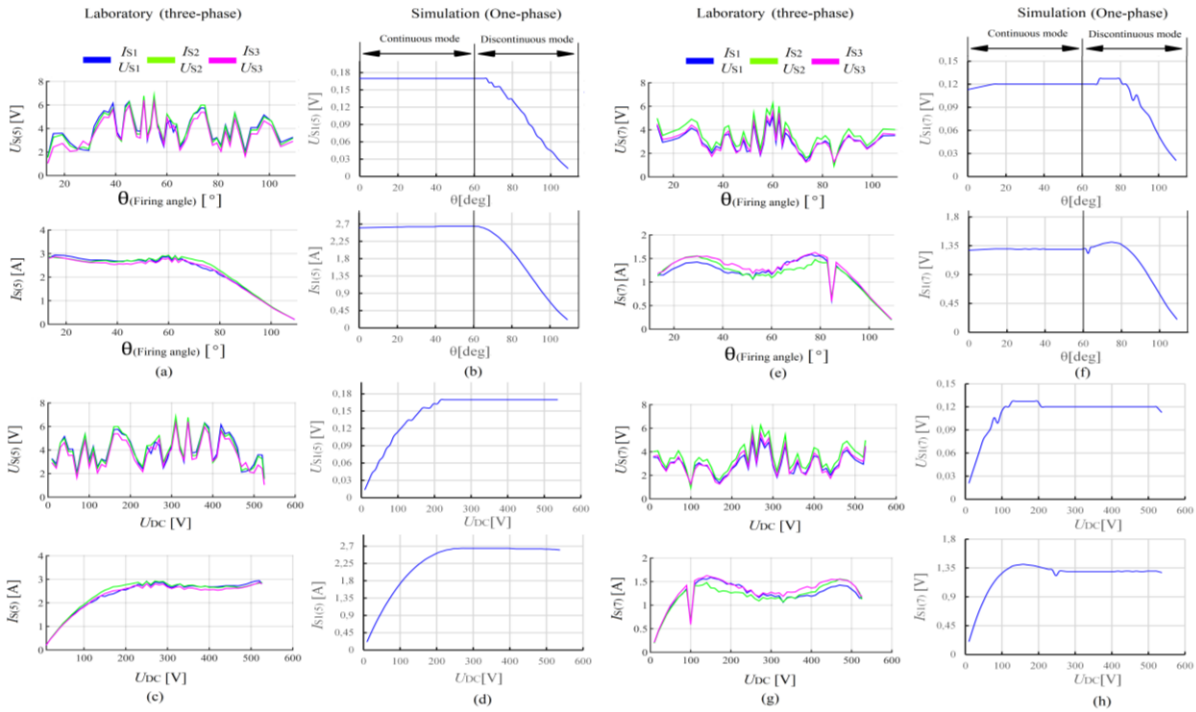

Figure 4.11 Comparison between laboratory and simulated characteristics: PCC voltage and current 5th harmonic vs rectifier firing angle (a)(b) and vs rectifier DC (c)(d); PCC voltage and current 7th harmonic vs rectifier firing angle (e)(f) and vs rectifier DC (g)(h)

The PCC active and reactive powers (fundamental harmonic) versus rectifier firing angle and versus rectifier DC voltage are shown in Figure 4.12(a) (laboratory) and Figure 4.12(b) (simulation). The active power decreases with the firing angle increase and increases with U_{DC} increase (Figure 4.12(a)). The reactive power characteristic achieves its maximum for θ equals to 50.23° for U_{DC} equal to 345.6 V (Figure 4.12(a)).

The spectrums in Figure 4.13 present the grid voltage and current harmonics for different values of rectifier firing angle and DC voltage. Owing to the fact that the power system of the designed laboratory model is symmetrical, the results are focussed one one-phase only (see waveforms of Figure 4.13).

Concerning the grid voltage fundamental harmonic, its amplitude has slightly decreased with U_{DC} increase (e.g. from 226.97 V (U_{DC} = 50 V) to 226.13 V (U_{DC} = 525 V)). The 5th

harmonic has the highest amplitude for U_{DC} equal to 250 V and the 7th harmonic for U_{DC} to 350V (Figure 4.13).

Apart the 3rd and 9th, there are other non-characteristic harmonics present in the PCC voltage and current spectrums (see Figure 4.14). Looking at the spectrum of Figure 4.14, it is noticed that with the harmonic order increase, some of the non-characteristic harmonics have higher amplitude than the amplitude of characteristic harmonics.

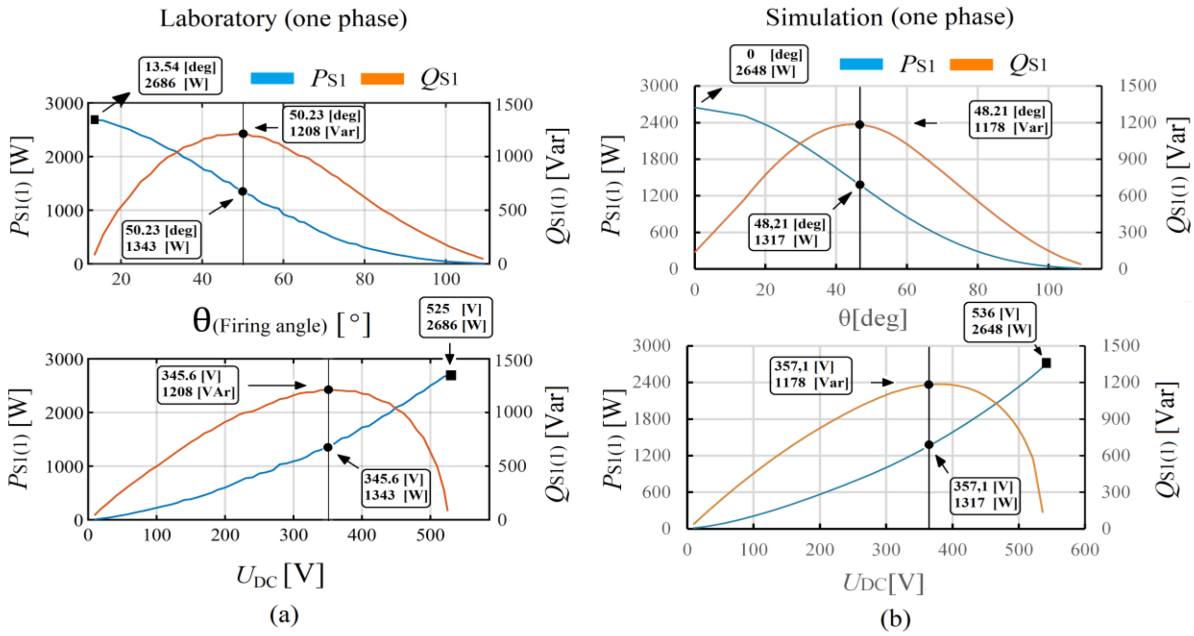

Figure 4.12 Fundamental harmonic PCC active and reactive powers vs firing angle and vs U_{DC}: (a) laboratory data; (b) simulated data

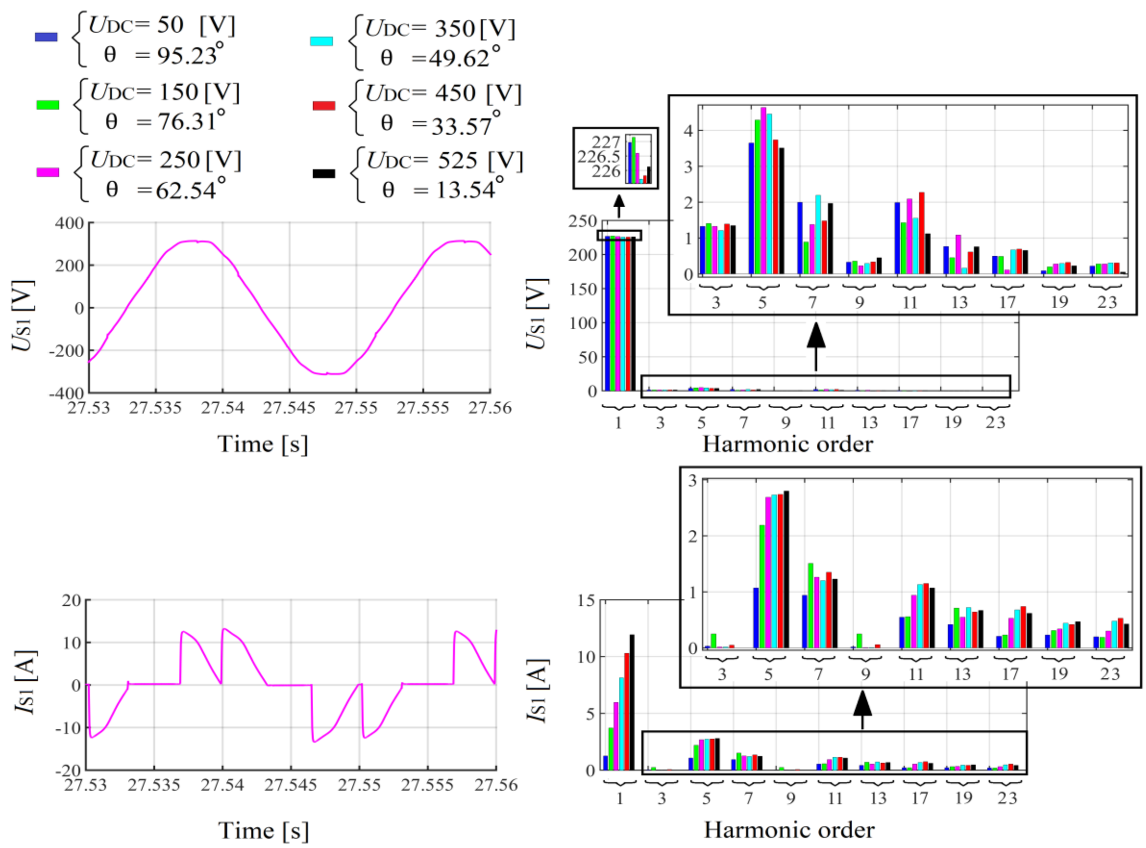

Figure 4.13 Grid voltage and current parameters measured from the laboratory model. The example of waveforms are for the U_{DC} equal to 250 V

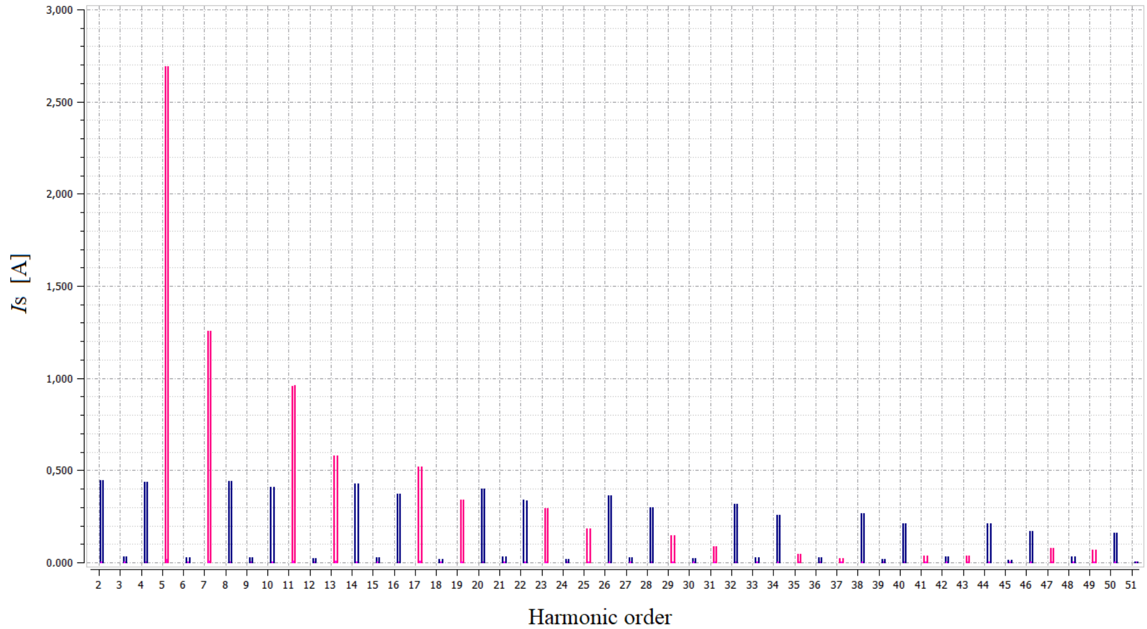

Figure 4.14 Example of grid current spectrum for U_{CD} = 250 V (the red manganese colour represents the characteristic harmonics)

4.3 Design of single-tuned filters

In this chapter, two single-tune filters are designed and tested in the laboratory. The first filter is for the 5th harmonic mitigation (the lowest load generated characteristic harmonic after the fundamental) and the second filter is used for the 7th harmonic mitigation from the grid side. The experimental studies are about the factors having influence on the filter filtration efficiency.

4.3.1 Single-tuned filter parameters computation

As presented in Figure 4.12(a), the highest load reactive and active power (one phase) are respectively around 1208 Var (inductive) and 2686 W. The filter used to mitigate the grid current 5th harmonic order is tuned to the frequency (f_{re} = 245 Hz, n_{re} = 4.9) a bit lower than the frequency of 250 Hz and its parameters (L_f = 7.3 mH, C_f = 19.2 µF – see “Parameters from producer” in Table 4.1, Table 4.2 and Annex IV - Figure IV.4 and Figure IV.7 for technical data) are calculated using the expressions of Table 3.2 (see chapter 3) with the chosen reactive power value of 966.6 Var (one phase). The reactive power value has been chosen to investigate in the laboratory the non-compensation, compensation and over-compensation mode of the power system after the rectifier firing angle change).

The detuning of the 5th order harmonic single-tuned filter is performed by increasing and decreasing (by ±5% and ±10%) the reactor inductance L_f and the following values are obtained: 8.03 mH, 7.665 mH, 6.935 mH and 6.57 mH. The designed filter reactor for that purpose is made with many terminals (see the “Parameters from producer” of Table 4.1 and the technical data of Annex IV - Figure IV.4).

The 7th order harmonic filter parameters (L_f = 7.3 mH, C_f = 9.6 µF) are presented in the “Parameters from produce” of Table 4.1, Table 4.2. It is tuned to the frequency a bit lower than the frequency of 350 Hz (f_{re} = 347.5 Hz) with the capacitor reactive power of 482.54 Var (one-phase). Its parameters are computed using the expressions of Table 3.2 (see chapter 3). The technical data are shown in Annex IV - Figure IV.6 and Figure IV.8.

4.3.2 Verification of PHFs reactors and capacitors parameters in the laboratory

The ractor and capacitor tolerance (from the producer) have an influence on the filter filtration efficiency and the experiments to verify the real PHFs reactors and capacitors parameters are necessary.

After receiving the reactors and capacitors from the producer, their parameters have been verified in the laboratory using the ammeter-voltmeter-wattmeter method (this method is very common and can be used in any condition in the industries, see Figure 4.15(b)). The equations (4.5) and (4.6) were used for the computation.

It can be noticed in Table 4.1 and Table 4.2 that the measured parameters are little different from the producer parameters, but are within the producer tolerances which are ± 10% for the reactors and -5% to 10% for the capacitor (see Annex IV - Figure IV.4, Figure IV.7 and Figure IV.8).

In the case of reactor with many terminals (Table 4.1), it can be seen that the measured parameters do respect the tolerance.

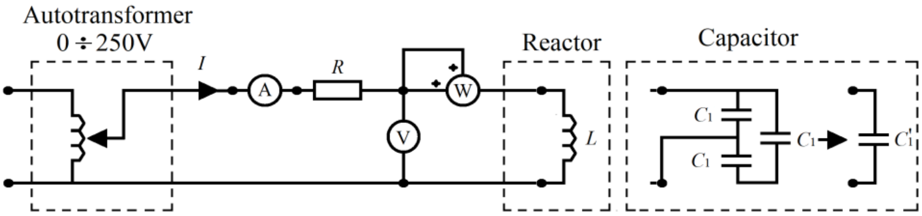

(a)

$$R_L = \frac{P}{I^2} \qquad L = \frac{\sqrt{\left(\frac{U}{I}\right)^2 - R_L^2}}{\omega_{(1)}} \qquad (4.5)$$

$$R_{C_1'} = \frac{P}{I^2} \qquad C_1' = \frac{1}{\omega_{(1)}\sqrt{\left(\frac{U}{I}\right)^2 - R_{C_1'}^2}} \qquad C_1 = \frac{2}{3}C_1' \qquad (4.6)$$

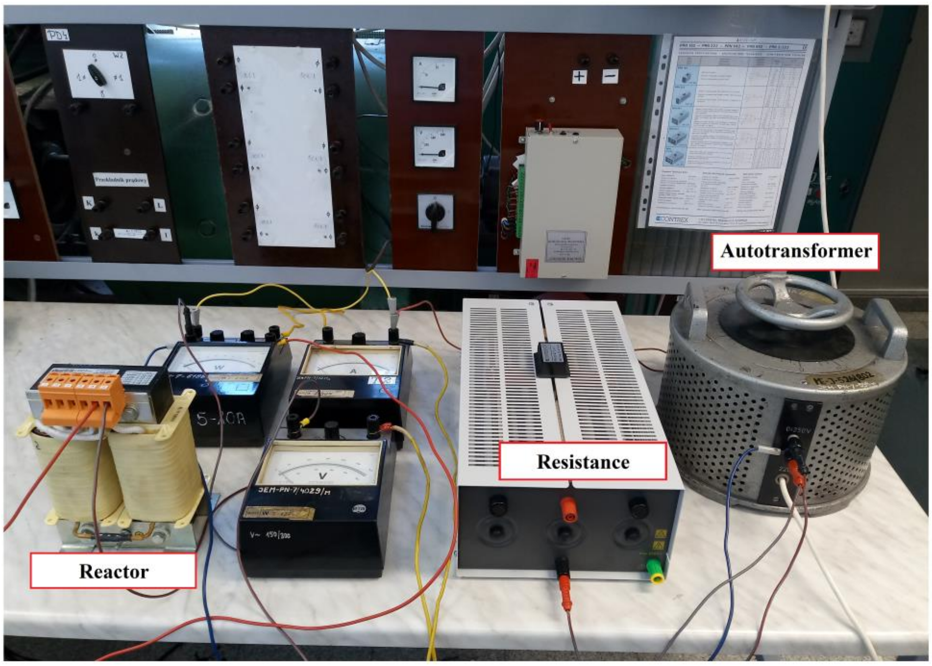

(b)

Figure 4.15 (a) equivalent circuit in which the PHFs capacitors and reactors parameters were verified, (b) laboratory model. The reactor with six terminals is connected

Table 4.1 Reactors parameters

Reactor with six terminals (5^{th} harmonic filter).

Parameters from producer (nominal)	Measured parameters					
L [mH]	U [V]	I [A]	P [W]	R_L [Ω]	L [mH]	$Z_{(1)}$ [Ω]
8.03	13.19	5	7.5	0.3	8.34	2.638
7.7	12.67	5	7.5	0.3	8.00	2.534
7.3	12.17	5	7.5	0.3	7.68	2.434
7	11.65	5	7.5	0.3	7.35	2.33
6.6	11.08	5	7.5	0.3	6.98	2.216

Reactor for the 7^{th} harmonic filter.

Parameters from producer (nominal)	Measured parameters					
L [mH]	U [V]	I [A]	P [W]	R_L [Ω]	L [mH]	$Z_{(1)}$ [Ω]
7.3	12.08	5	7.5	0.3	7.63	2.41

Table 4.2 Capacitors parameters

5^{th} harmonic filter capacitor.

Parameters from producer (nominal)	Measured parameters				
C_1 [µF]	U [V]	I [A]	P [W]	R_{C1} [Ω]	C_1 [µF]
19.2	241	2.2	0	0	19.4

7^{th} harmonic filter capacitor

Parameters from producer (nominal)	Measured parameters				
C_1 [µF]	U [V]	I [A]	P [W]	R_{C1} [Ω]	C_1 [µF]
9.6	215.1	1	0	0	9.87

Figure 4.16 presents the equivalent electrical circuit used to measure the PHFs impedance versus frequency characteristics and Table 4.3 presents the resonance frequencies comparison. The frequencies obtained from the producer data are compared to the frequencies obtained from the computed data of Table 4.1 and Table 4.2 and to the frequencies measured from the electrical circuit of Figure 4.16. The measured and computed resonance frequencies are almost the same for the 5th harmonic filter (Table 4.3). The tolerance of the PHFs elements (capacitors and reactors) have an influence on the expected resonance frequency (e.g. 245 Hz, Table 4.3).

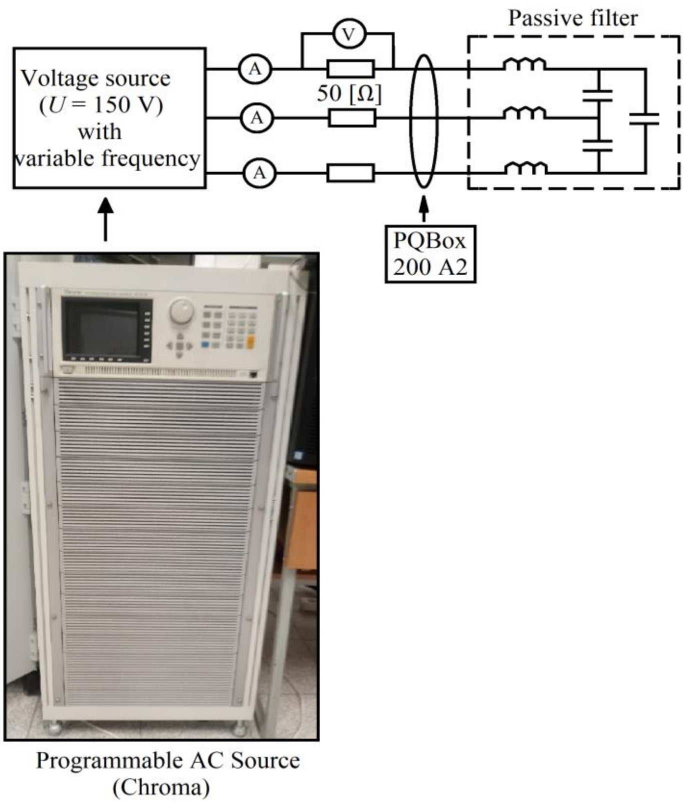

Figure 4.16 Equivalent electrical circuit used to measure the filters impedance versus frequency characteristics

Table 4.3 Comparison of single-tuned filters resonance frequencies: the frequencies from producer data are compared to the frequencies obtained from Table 4.1 and Table 4.2 and to the frequencies obtained from the electrical circuit of Figure 4.16

5th harmonic filter					
Frequencies from producer (nominal)		Computed frequencies (from Table 4.1 and Table 4.2)		Measured frequencies (Figure 4.16)	
n_{re}	f_{re} [Hz]	n_{re}	f_{re} [Hz]	n_{re}	f_{re} [Hz]
4.68	234	4.57	228.5	4.57	228.5
4.78	239	4.66	233	4.67	233.5
4.9	245	4.76	238	4.77	238.5
5.012	250.6	4.86	243	4.89	244.5
5.16	258	4.99	249.5	5.04	252
7th harmonic filter					
6.94	347	6.69	334.5	6.78	339

4.3.3 Laboratory results of the 5th harmonic single-tuned filter

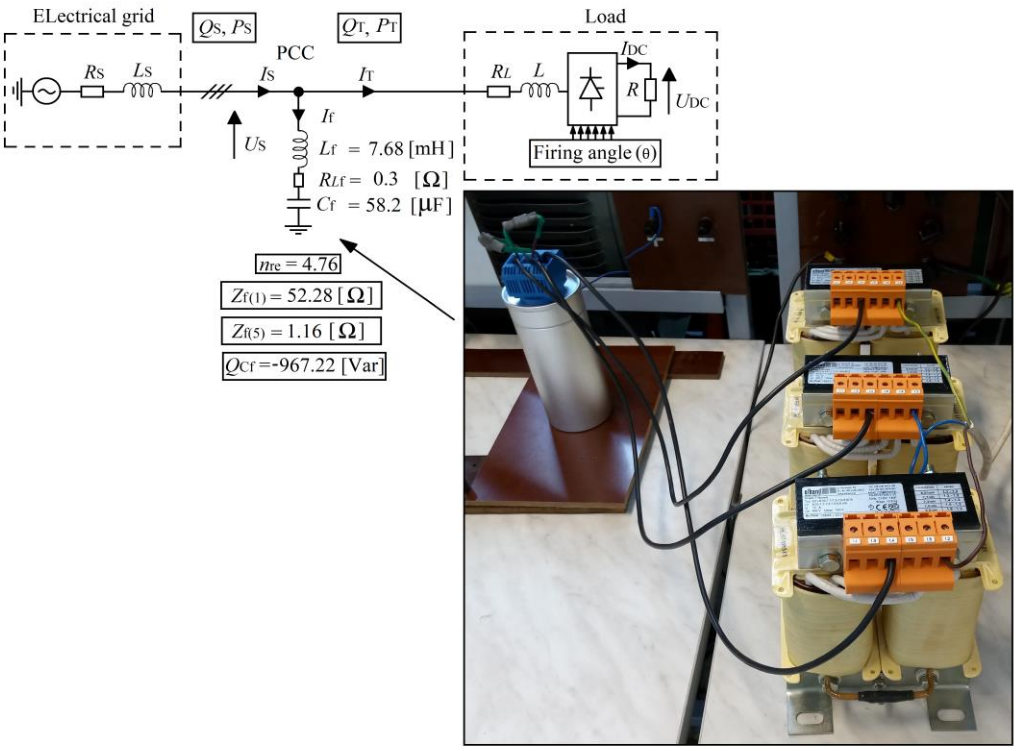

Figure 4.17 Equivalent circuit of laboratory model with 5th harmonic single-tuned filter (measured filter parameters)

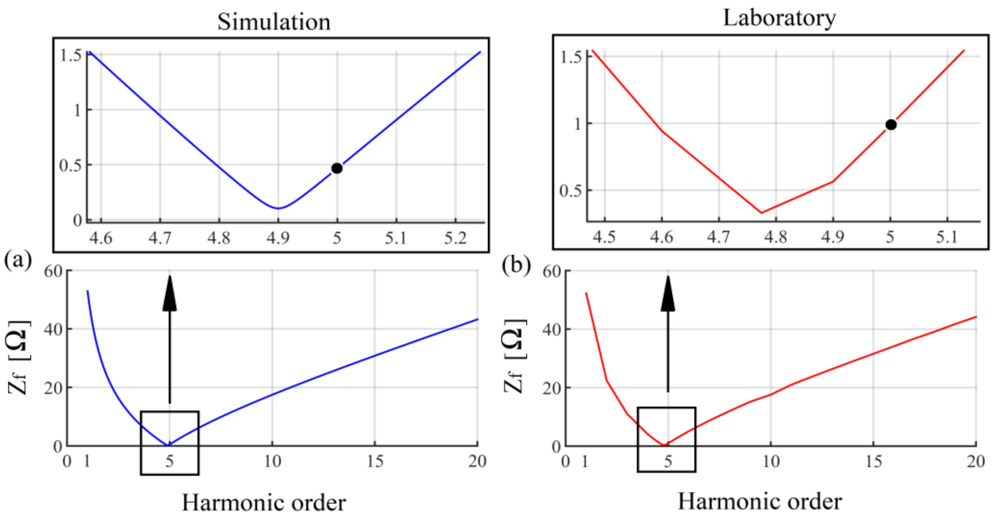

Figure 4.18 5th harmonic filter impedance versus frequency characteristics: (a) expected characteristic from simulation and (b) characteristic measured in the laboratory (see Figure 4.16)

The equivalent circuit of the laboratory model in which the 5th harmonic filter was designed is presented in Figure 4.17 and the filter impedance versus frequency of the simulated characteristic and the laboratory measured characteristic are respectively presented in Figure 4.18(a) and (b). Concerning the characteristic in Figure 4.18(b), the recorded dada have been obtained after each 50 Hz, but around the resonance frequency the interval of 10 Hz enven less were used (Chroma). The parameters in Figure 4.17 are computed basing on the measured parameters of Table 4.1 and Table 4.2.

The power system fundamental harmonic active and reactive powers as well as the grid current THD for different firing angles are presented in Table 4.4. It can be noticed in Table 4.4 that the grid voltage presents the highest THD for U_{DC} equal to 350 V and the grid current presents the lowest THD for U_{DC} equal to 525 V. For U_{DC} from 0 to around 220V and between 470V and 525V the power system is overcompensated (see $Q_{S1(1)}$ - Table 4.4). A partial compensation is observed between 250V and 450V (U_{DC}).

Table 4.4 Power system parameters measured in the laboratory for different rectifier firing angles (the 5th harmonic filter is connected)

U_{DC} [V]	θ [deg.]	THD_{US1} [%]	THD_{IS1} [%]	THD_{IT1} [%]	DPF	$P_{S1(1)}$ [W]	$P_{f1(1)}$ [W]	$Q_{S1(1)}$ [Var]	$Q_{f1(1)}$ [Var]	$Q_{T1(1)}$ [Var]
50	95.23	2.06	100.32	57.37	0.07	52.52	12.56	-757.17	-993.82	243.05
150	76.31	2.12	156.09	64.40	0.84	381.72	13.82	-242.01	-987.57	749.65
250	26.54	2.20	65.46	60.62	0.99	824.40	17.38	61.79	-983.80	1048.1
350	33.57	2.24	51.33	43.63	0.98	1396.3	19.39	233.94	-989.89	1225.4
450	33.57	2.06	55.62	35.14	0.99	2105.7	22.15	49.58	-989.38	1040.3
525	13.54	1.81	36.57	29.24	0.94	2680.2	24.60	-883.24	-975.21	95.52

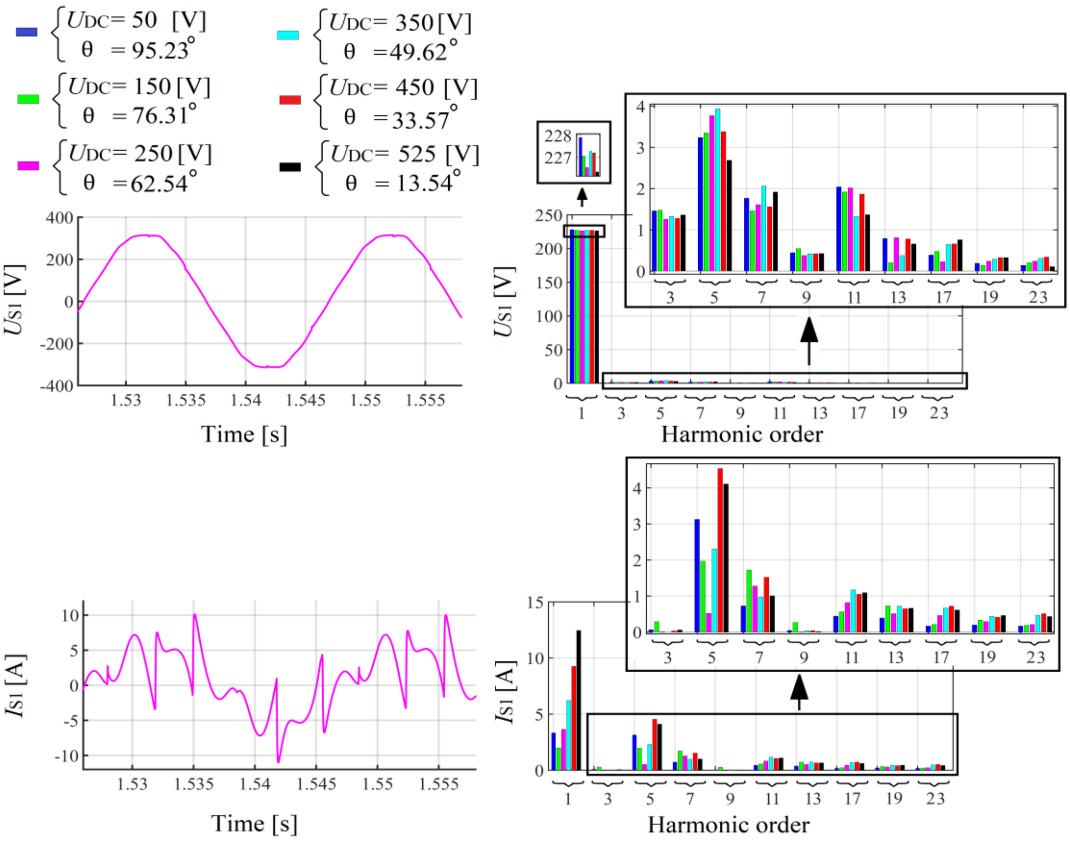

Figure 4.19 Grid voltage and current waveforms and spectrums (with the filter connected)

The grid voltage and current waveforms together with spectrums after the 5th harmonic filter connection are shown in Figure 4.19. The waveforms and spectrums of the rectifier input current and the filter current are presented in Figure 4.20. Comparing Figure 4.19 to Figure 4.13 it can be noticed that the grid voltage 5th harmonic amplitude has decreased after the filter connection (see also Figure 4.21(b)). The grid voltage waveform is improved after the filter connection (Figure 4.21(a)).

The grid voltage 7th harmonic amplitude before and after the filter connection is presented in Figure 4.21(c). For certain firing angles (e.g 95.23º) the 7th harmonic amplitude is reduced at the grid side after the filter connection and for others (e.g 76.31º), it is amplified.

The grid current spectrum in Figure 4.19 shows that the lowest amplitude of 5th harmonic is obtained for U_{DC} equal to 250V (when the filter reactive power 966.6 Var is around the thyristor bridge reactive power 1048.1Var and the firing angle around 62.54°). Despite the filter presence in power system, the PCC current presents higher THD than the input rectifier current (see Table 4.4) because of the fundamental harmonic reduction (reactive power compensation) and 5th harmonics amplification (comparing the spectrums of I_{S1} in Figure 4.19 to the one of I_{T1} in Figure 4.20). The filter current is more charged by the 5th harmonic than the other harmonics (see spectrum of I_{T1} in Figure 4.20).

The filter efficiency for the harmonics from the 1st to the 23rd is presented in Figure 4.22(a). The amplification of some harmonics can be observed (values higher the 100% of the input rectifier current). The grid current fundament harmonic is amplified (U_{DC} equal to 50V and 525V) because of the overcompensation.

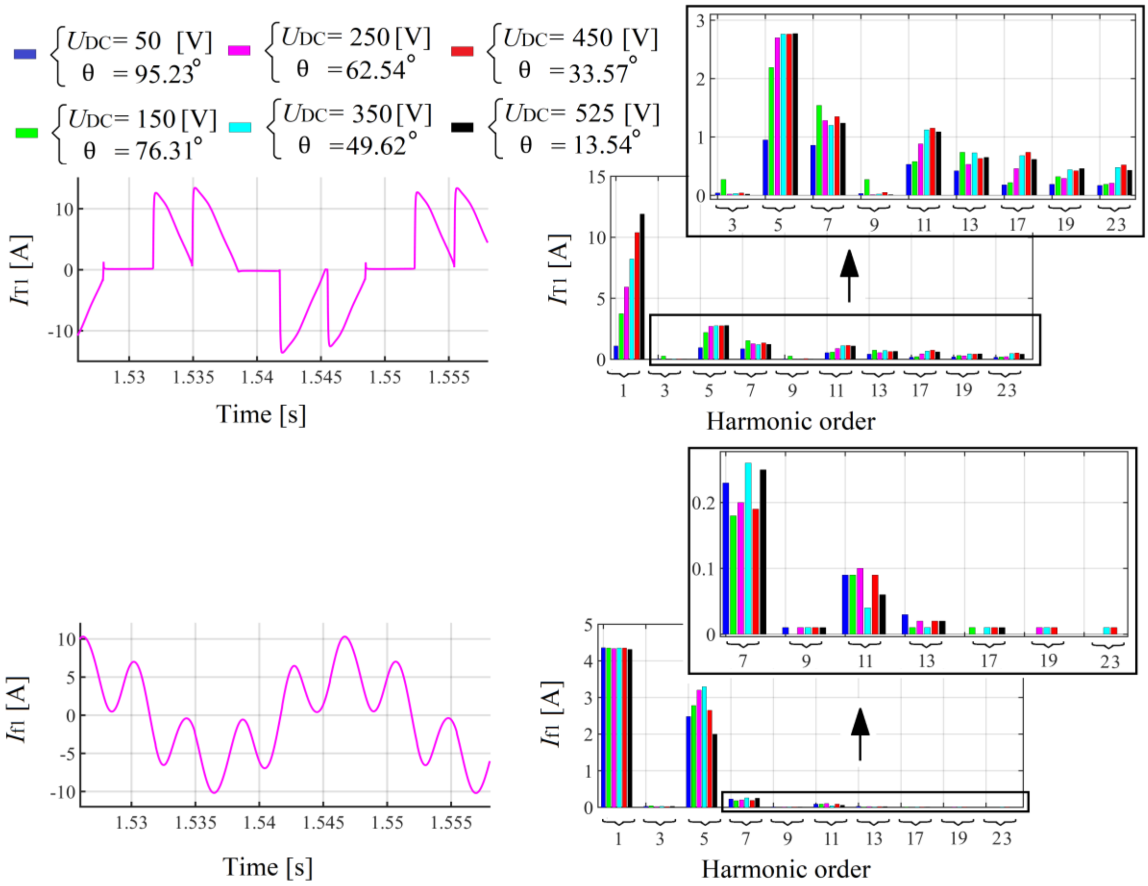

Figure 4.20 Input rectifier current with its spectrum and filter current with the spectrum

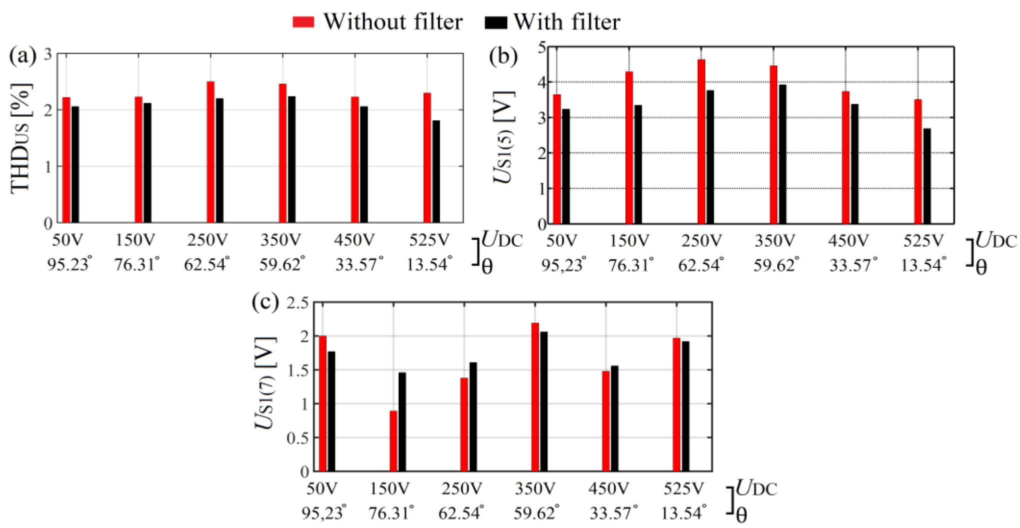

Figure 4.21 (a) grid voltage THD; grid voltage 5th (b) and 7th (c) harmonic amplitudes before and after the 5th harmonic filter connection

For U_{DC} equal to 250V (θ = 62.54°), the single-tuned filter efficiency on the grid current 5th harmonic mitigation is around 80.74% (see Figure 4.22(a) - only 19.26 % of 5th harmonic current generated by the load has flowed to the electrical grid). The filter efficiency varies with the rectifier firing angle.

In Figure 4.22(b), the 5th harmonic amplitude of the input rectifier current is compared to the 5th harmonic amplitude of the grid current for different firing angle. It can be noticed that for θ equal to 95.23º, 33.57º and 13.54º, the 5th harmonic amplitude in the grid side current is higher than the 5th harmonic amplitude in the load side current (Figure 4.22(b)). For θ equal to 76.31º, 62.54º and 59.62º the 5th harmonic amplitude in the grid side current is smaller than the 5th harmonic amplitude in the load side current.

For any value of thyristor bright firing angle, the filter should be able to mitigate the grid current 5th harmonic amplitude. In the further part of the theses, some experiments are performed to clarify the 5th harmonic current amplitude amplification (Figure 4.22(b)) at the grid side.

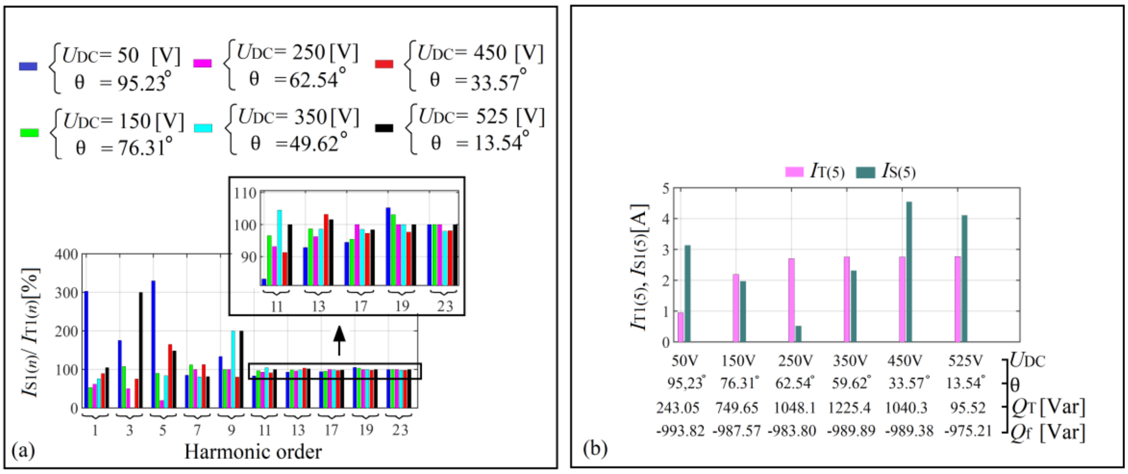

Figure 4.22 (a) 5th harmonic single-tuned filter efficiency, (b) the 5th harmonic current amplitude generated by the load (I_T) is compared to the 5th harmonic current amplitude at the grid side for different firing angle

4.3.3.1 Experiments with the programmable AC voltage source (Chroma)

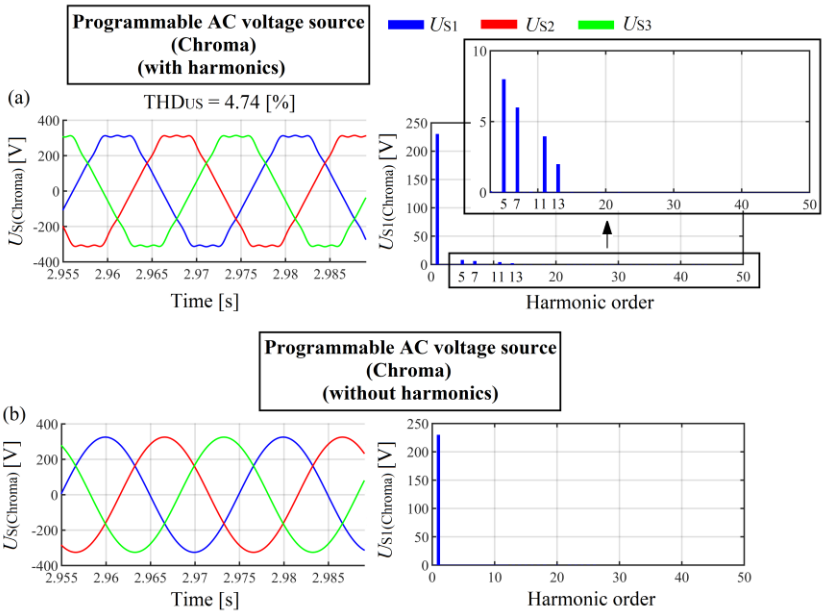

Figure 4.23 Voltages measured at the programmable AC voltage source (Chroma) with no load connected: (a) voltage with harmonics, (b) voltage without harmonics (with the load connected)

Laboratory model (load plus filter) is disconnected from the electrical grid and is supplied by the programmable AC voltage source named Chroma (Figure 4.16 [284]) with the cable of 0.11 Ω and inductance of 63.69 μH. Two experiments are carried out: Chroma voltage source with harmonics (5^{th}, 7^{th}, 11^{th} and 13^{th} - Figure 4.23(a)) and without harmonics (Figure 4.23(b)). The amplitudes of harmonics in Figure 4.23(a) have been chosen a bit higher than those in the electrical grid (when the laboratory model was not connected) to make the experiments more clear.

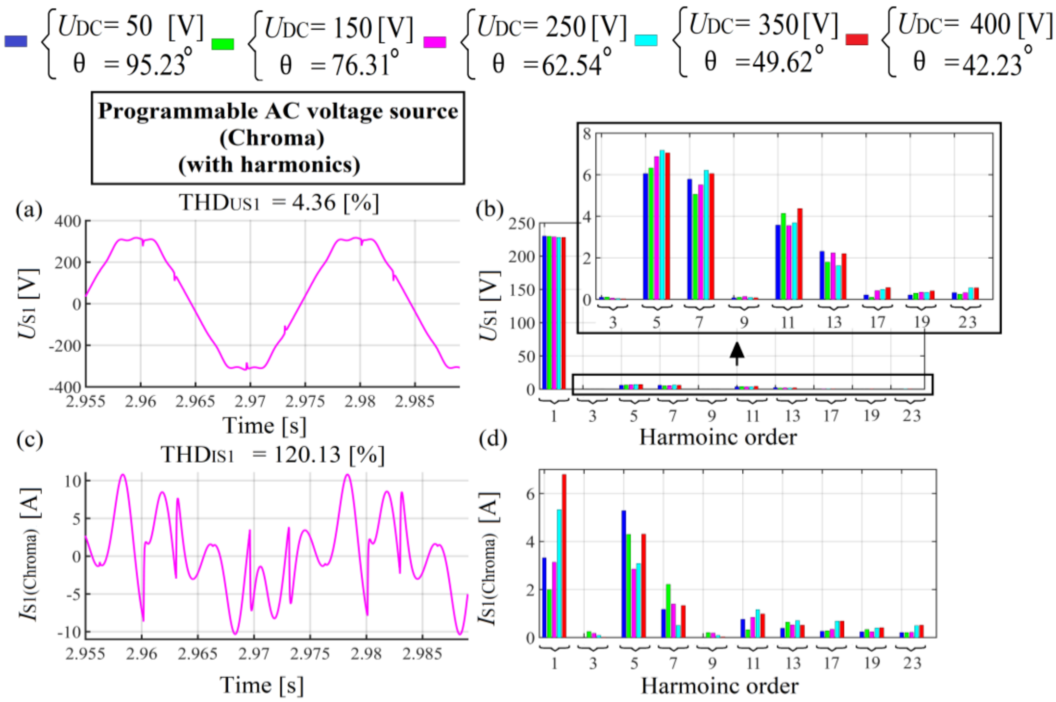

Figure 4.24 (a) PCC voltage waveform with (b) its spectrum, (c) voltage source input current with (d) its spectrum (with the load connected)

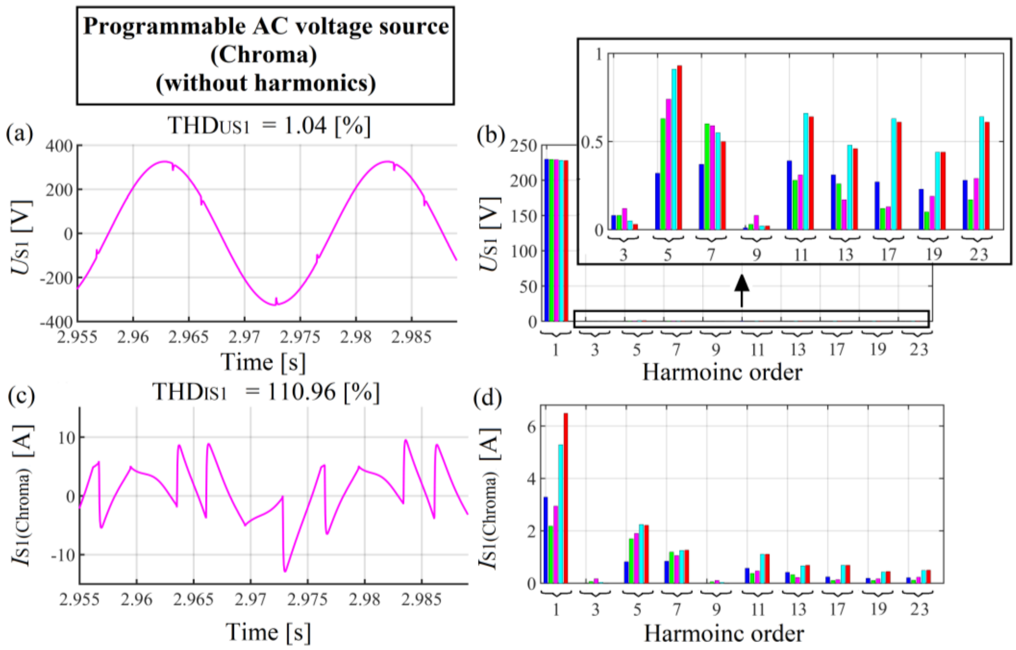

Figure 4.25 (a) PCC voltage waveform with the spectrum (b), (c) voltage source input current with the spectrum (d) (with the load connected)

The waveforms and spectrums of voltage and current at the Chroma input are presented in Figure 4.24 (voltage source with harmonics) and in Figure 4.25 (voltage source without harmonics). In the case of the voltage source with harmonics (Figure 4.24(d)), the current 5th harmonic amplitude is the smallest for U_{DC} equal to 250V (θ = 62.54°) as in the case of grid current spectrum of Figure 4.19.

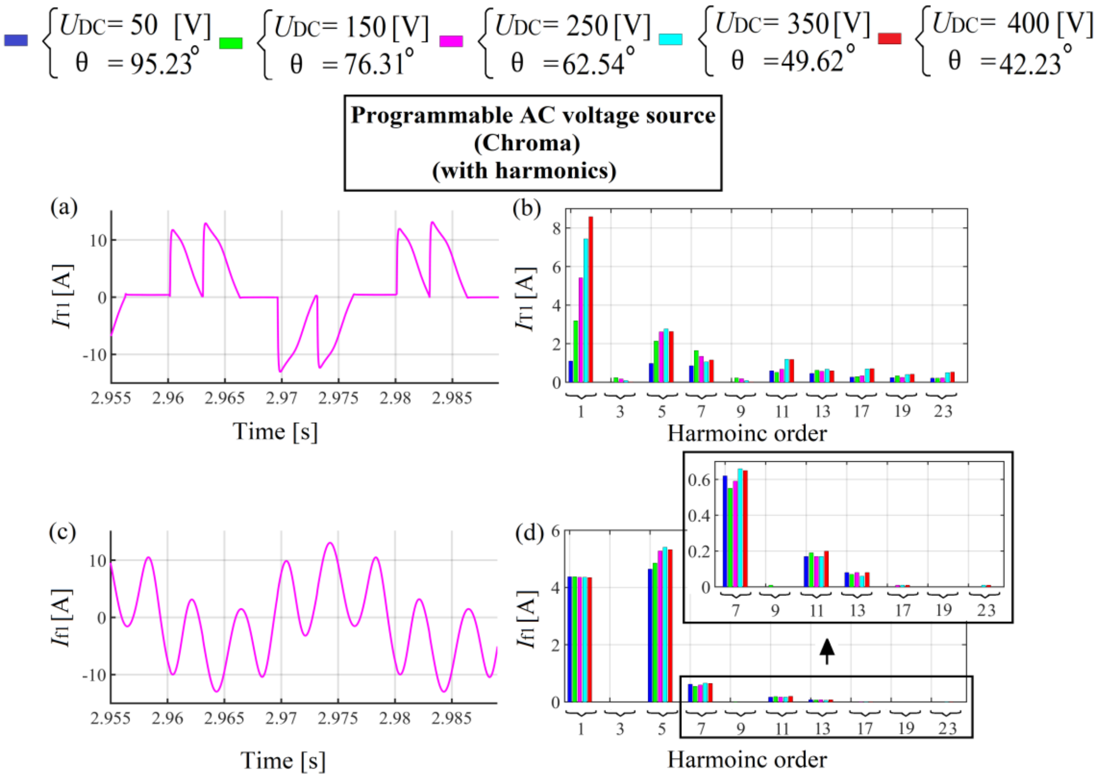

Figure 4.26 (a) rectifier input current waveform with (b) its spectrum, (c) filter current waveform with (d) its spectrum

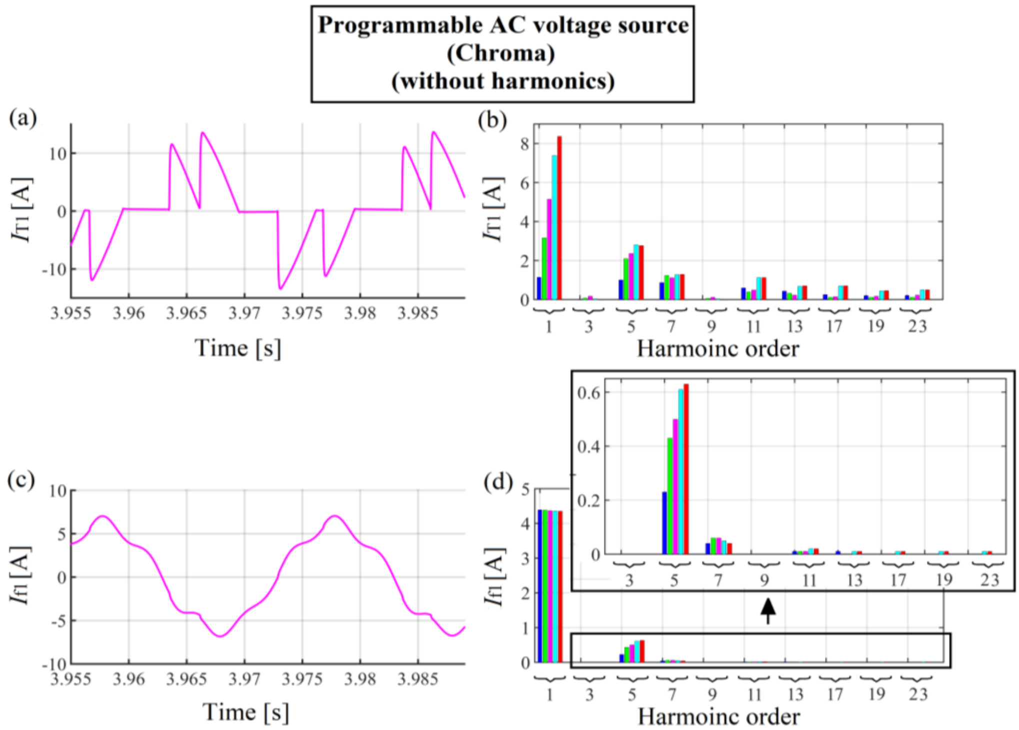

Figure 4.27 (a) rectifier input current waveform with (b) its spectrum, (c) filter current waveform with (d) its spectrum

The comparing Figure 4.24(b) to Figure 4.25(b), it can be observed that the programmable voltage source with harmonics presents the highest voltage harmonics amplitudes at its terminals.

The amplitudes of 5th harmonic current at the input of the voltage source with harmonic is higher in Figure 4.24(d) than in Figure 4.25(d) (voltage source without harmonic). At the input of the voltage source without harmonics, there is a part of non-filtred 5th, whereas at the input of the voltage source with harmonics, there is a part of non-filterd 5th harmonic plus the part of 5th harmonic flowing from the voltage source.

The load (I_T) and filter (I_f) current waveforms and spectrums are respectively presented in Figure 4.26 and Figure 4.27. Comparing the both figure it can be see that when Chroma is with or without harmonics, the rectifier input current spectrum in almost the same (see Figure 4.26(b) and Figure 4.27(b)).

Figure 4.26(d) compared to Figure 4.27(d) presents the highest current amplitude of the 5th, 7th, 11th and 13th harmonics, because the current harmonics generated by the voltage source flows through the filter.

On the base of the measurements performed during the experiments, it can be concluded that the single-tuned filter has more absorbed 5th harmonic current from the grid side than from the load side, whence the amplification of that harmonic at the grid side.

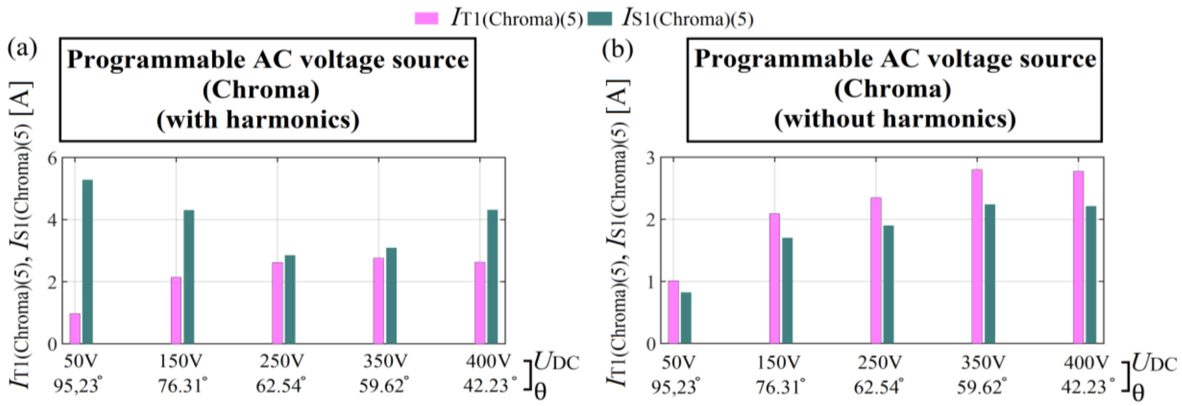

Figure 4.28 Comparison between the 5th harmonic current amplitude generated by the load (I_T) and the 5th harmonic current amplitude at the Chroma side: (a) the Chroma voltage source contains harmonics, (b) the Chroma voltage source do not contains harmonics (pure sinusoidal)

In Figure 4.28, the amplitude of 5th harmonic current measured at the thyristor bridge input ($I_{T1(5)}$) is compared to the amplitude of 5th harmonic measured at the voltage source input ($I_{S1(Chroma)(5)}$). In the case of the voltage source with harmonics (see Figure 4.28(a)) the amplification of the current 5th harmonic amplitude (at the voltage source input) is due to the fact that the voltage source is the source of 5th harmonic current which flows to the single-tuned filter. In the case of the voltage source without harmonics (see Figure 4.28(b)) the 5th harmonic is not amplified but is partially mitigated (at the Chroma input) due to the filter 5th harmonic impedance ($Z_{f(5)} = 1.16\ \Omega$ - Figure 4.17) which is almost 8 times higher than the Chroma cable 5th harmonic impedance ($Z_{Cable(5)} = 0.148\ \Omega$).

The influence of the distorted electrical grid voltage as well as the grid impedance on the filter efficieny were examined. The next chapter will concern the influence of the electrical grid impedance (Z_S) on the single-tuned filter efficiency.

4.3.3.2 Increase of electrical grid inductance

It has been decided to use the line reactor as solution to mitigate the current harmonics amplitude caused by the distorted electrical grid volataye and to increase the electrical grid 5th harmonic impedance (which is ($Z_{S(5)} = 49.5\ m\Omega$ - Figure 4.6(b)) around 23.43 times smaller than the filter 5th harmonic impedance ($Z_{f(5)}$ = 1160 mΩ)). The line reactor parameters are presented in Table 4.5 and Figure 4.29 presents the laboratory model equivalent circuit.

Table 4.6 presents the active and reactive power as well as the DPF measured at the PCC for different rectifier firing angle.

With the increase of grid inductance (L_{SS}), the PCC voltage is more distorted by commutation notches and the harmonics amplitudes have increased (comparing the voltage waveforms and spectrums of Figure 4.30 to those of Figure 4.13 when the line reactor is not connected). The grid current waveforms and spectrums are presented in Figure 4.30 and there is not big change in harmonics amplitudes when compared to the case without L_{SS} of Figure 4.13.

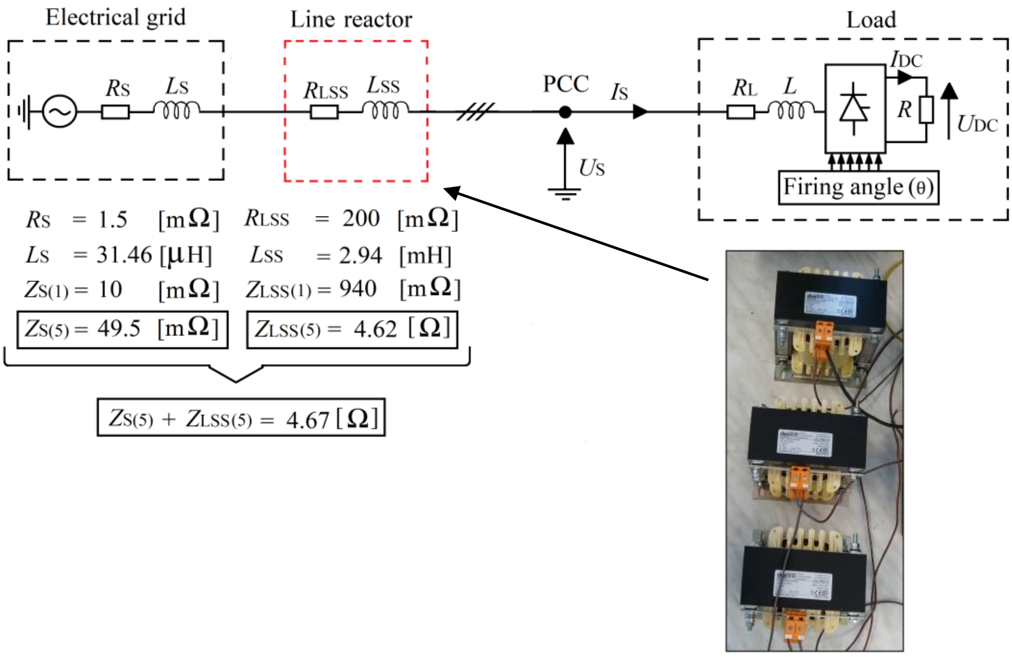

Figure 4.29 Equivalent circuit of laboratory model with line reactor

Table 4.5 Line reactor parameters (L_{SS})

Line reactor 						
Parameter from producer	Measured parameters					
L_{SS} [mH]	U [V]	I [A]	P [W]	R_{LSS} [Ω]	L_{SS} [mH]	$Z_{LSS(1)}$ [Ω]
2.5	4.74	5	5	0.2	2.94	0.94

Table 4.6 Parameters of fundamental harmonic active and reactive powers as well as DPF for different rectifier firing angle

U_{DC} [V]	θ [deg.]	$P_{S1(1)}$ [W]	$Q_{S1(1)}$ [Var]	DPF
50	95.23	73.13	269.02	0.26
150	76.31	387.71	743.75	0.46
250	26.54	805.26	1079	0.59
350	33.57	1371.8	1214.3	0.74
450	33.57	2091.1	995.88	0.90
525	13.54	2605.4	340.86	0.99

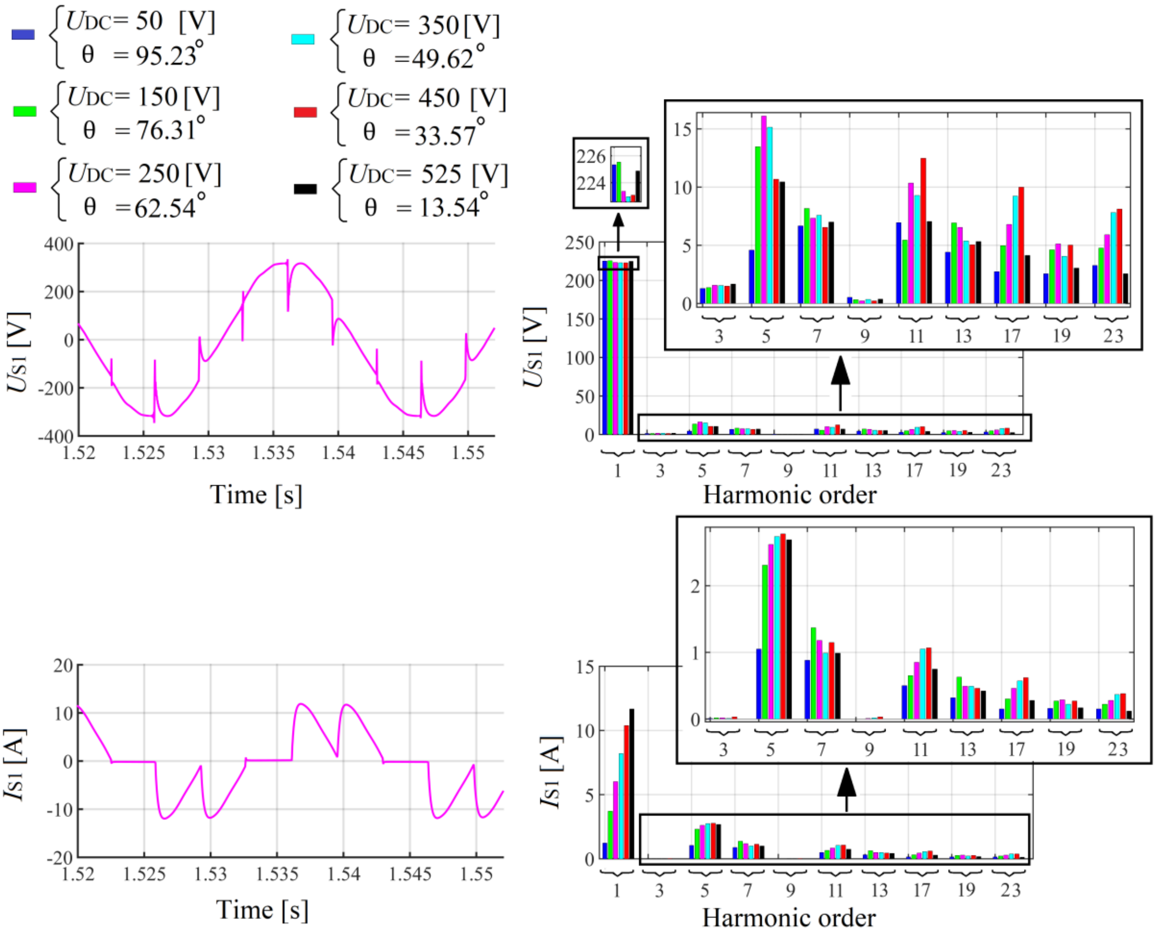

Figure 4.30 Grid voltage and current waveforms and spectrums (with L_{SS})

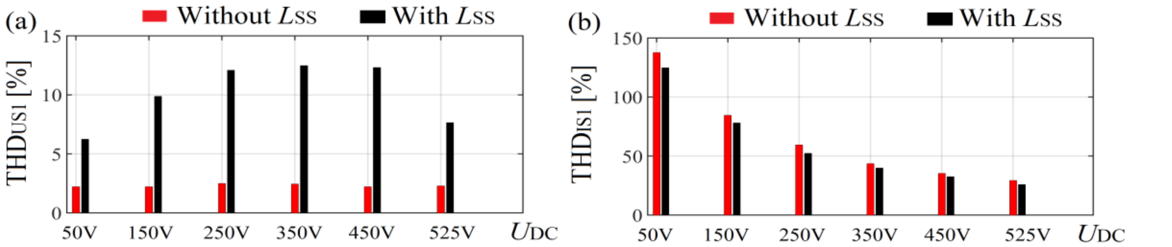

Figure 4.31 Comparison between the PCC voltage (a) and current (b) THD before and after the line reactor connection

The comparison between the PCC voltage and current THD as well as fundamental harmonic amplitude before and after the line reactor connection is presented in Figure 4.31 and Figure 4.32 respectively. The THD of the grid voltage has increased (Figure 4.31(a)), whereas its fundamental harmonic has decreased (Figure 4.32(a)) after the line reactor connection. The grid current THD has decreased (the line reactor has worked as a filter) (Figure 4.31(b)) and the fundamental harmonic is almost the same (Figure 4.32(b)) with the line reactor presence.

It has been theoretically demonstrated in chapter 2 that the depth of voltage commutation notches is more accented with the line reactor inductance increased. The laboratory measurements of Figure 4.33 shows that the higher is the line reactor inductance, the more dip are the voltage commutation notches (U_T). The voltage waveform at the PCC (U_S) is less distorted than the one at the rectifier input (U_T) (Figure 4.33).

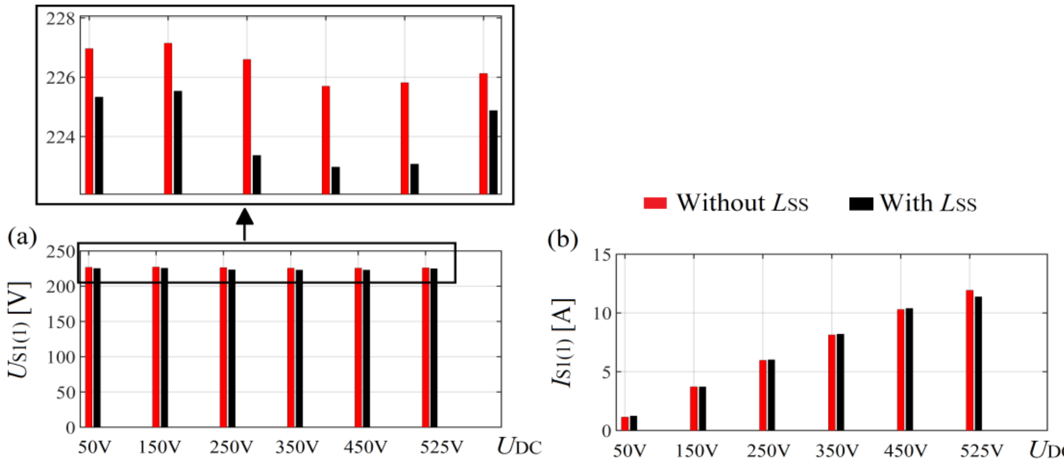

Figure 4.32 Comparison between the PCC voltage (a) and current (b) fundamental harmonic before and after the line reactor connection

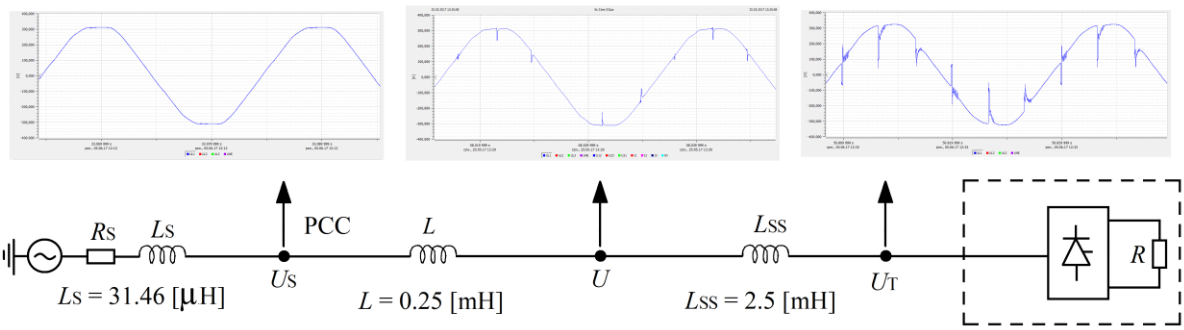

Figure 4.33 Voltage waveforms at different point of laboratory model

4.3.3.3 Analysis of the 5th harmonic single-tuned filter efficiency after electrical grid inductance increase

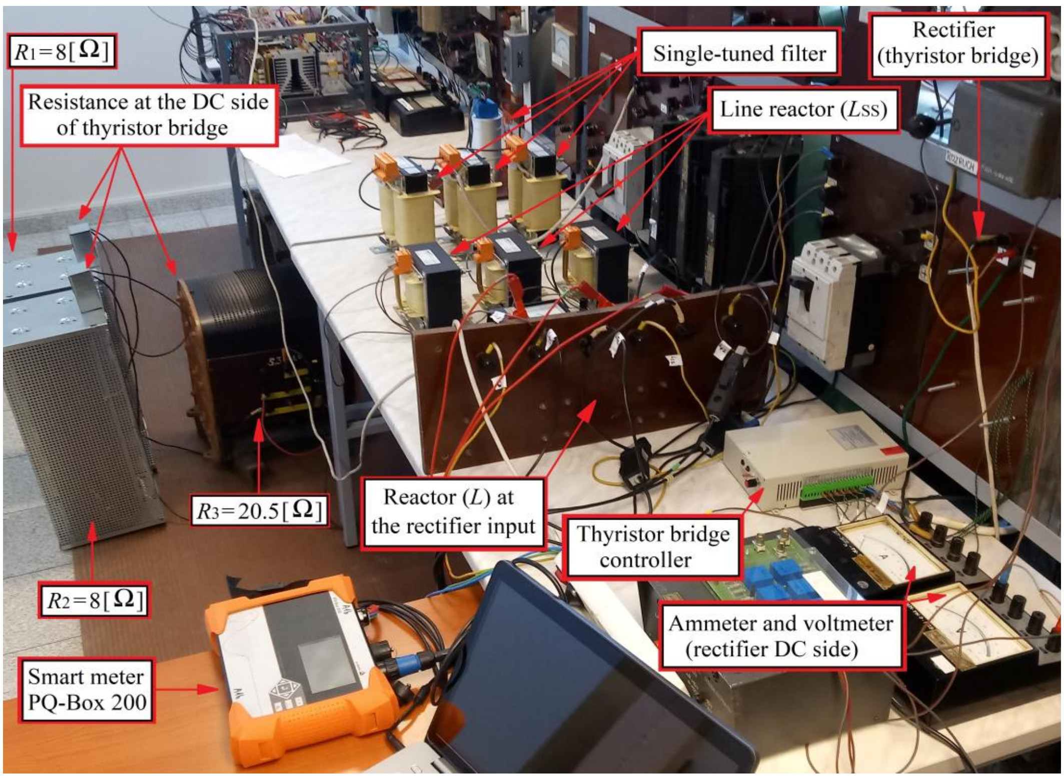

Figure 4.34 Laboratory model

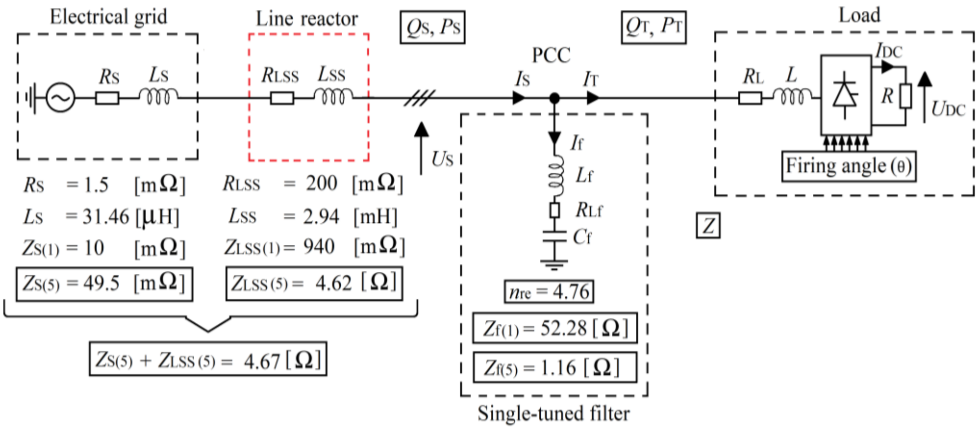

Figure 4.35 Laboratory equivalent circuit with filter and line reactor

The laboratory model is shown in Figure 4.34 and its equivalent circuit in Figure 4.35. The 5th harmonic grid impedance is around 4 times higher than filter impedance of the 5th harmonic (Figure 4.35). At the PCC, the grid inductance is almost 93.33 times higher than before the line reactor connection.

The parameters of Table 4.7 have been registered by increasing (with the filter connected) the rectifier DC voltage from 0 to 525V. The grid reactive power (Q_S) compensation is well performed for U_{DC} equal to 250V (Table 4.7).

The PCC voltage waveforms and spectrum are presented Figure 4.36. Compared to the case without line reactor L_{SS} (see voltage spectrums in Figure 4.19), the voltage spectrum of Figure 4.36 presents the highest amplitude of 7th, 11th, 13th, 17th, 19th, 23rd (see also Figure 4.33) and higher harmonics (because of the commutation notches depth increase) as well as the best reduction of 5th harmonic amplitude.

The grid current waveforms and spectrum are constituted by Figure 4.36 (the lowest value of 5th harmonic amplitude is obtained when thyristor bridge firing angle is set to 62.54° (U_{DC} =250V). Comparing the grid current spectrum in Figure 4.36 to the one in Figure 4.30 (grid with line reactor without filter), it can be observed that the 5th harmonic amplitude has considerably decrease after the filter connection.

Table 4.7 Power system parameters measured in the laboratory for different rectifier firing angles

U_{DC} [V]	θ [deg.]	THD_{US1} [%]	THD_{IS1} [%]	THD_{IT1} [%]	DPF	$P_{S1(1)}$ [W]	$Q_{S1(1)}$ [Var]	$P_{f1(1)}$ [W]	$Q_{f1(1)}$ [Var]	$Q_{T1(1)}$ [Var]
50	95.23	4.56	38.47	131.95	0.08	63.80	-743.27	13.31	-1022.6	283.91
150	76.31	6.72	77.46	85.33	0.82	394.58	-267.73	16.28	-1003.9	738.73
250	26.54	8.19	38.79	58.51	0.99	818.29	84.54	17.53	-992.40	1078.0
350	33.57	8.52	25.39	43.78	0.98	1370	244.61	18.62	-978.77	1223.5
450	33.57	9.10	19.77	34.74	0.99	2082.2	56.72	21.24	-972.86	1029.9
525	13.54	4.95	12.18	26.61	0.96	2668.1	-750.06	23.44	-982.17	235.02

Figure 4.37 presents the waveforms and spectrums of filter current and input rectifier current. On the top of that figure, an example of the measured current complex form is presented.

With the increase of grid inductance and for any DC rectifier voltage (Figure 4.38(a)), the filter is more efficient (when compared to the case without filter) on the 5th and higher harmonics reduction (values below 100% - Figure 4.38(a)). The amplification of the 3rd harmonic (grid side) observed in Figure 4.38(a) is due to its presence near the parallel reconance frequency occurring between the filter capacitor and the grid inductance.

The comparison between the 5th harmonic generated by the load ($I_{T(5)}$) and the one flowing to the electrical grid ($I_{S(5)}$) is presented in Figure 4.38(b). For any firing angle, there is none grid side 5th harmonic amplification (see Figure 4.22(b)). The line reactor has increased the filter efficiency (θ = 62.54°) on the 5th harmonic mitigation from 80.74 % (without L_{SS}) to 95 % (with L_{SS}).

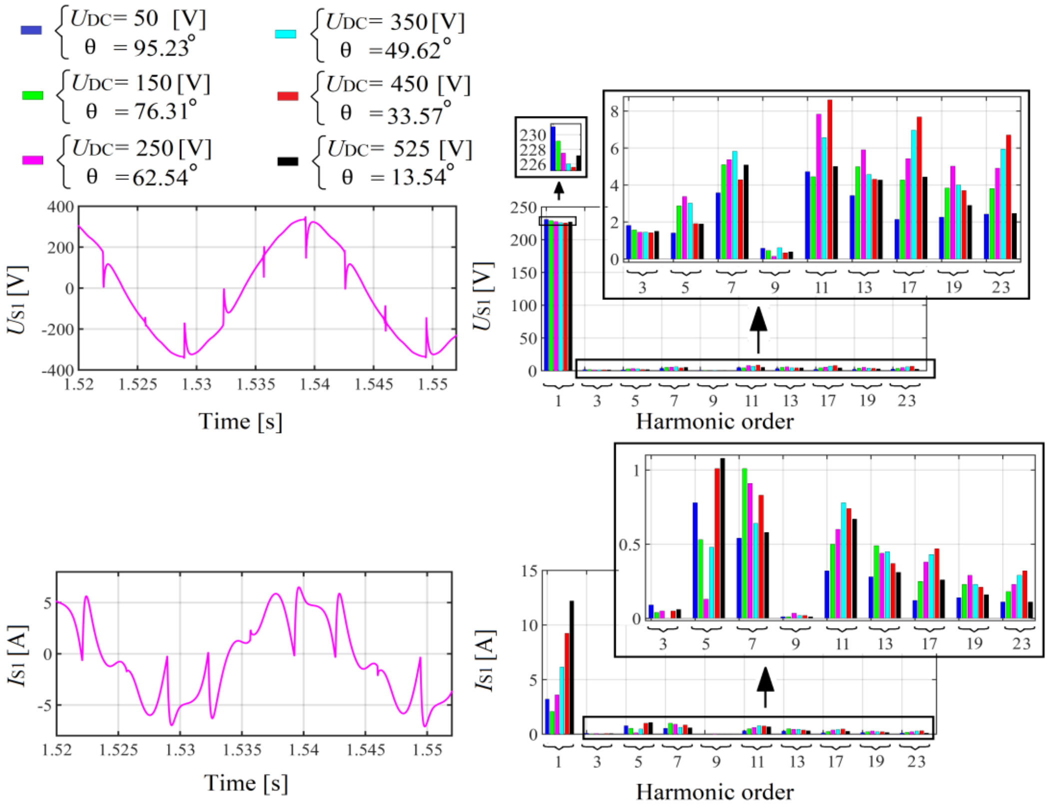

Figure 4.36 Waveforms and spectrums of grid current and voltage

$$\left.\begin{aligned} \underline{I}_{S1(1)} &= 3.61e\ j244.20 = -1.57 - j3.25 \\ \underline{I}_{T1(1)} &= 5.99e\ j197.86 = -5.70 - j1.83 \\ \underline{I}_{f1(1)} &= 4.36e\ -j18.87 = 4.12 - j1.41 \end{aligned}\right\} I_{S1(1)} = I_{T1(1)} + I_{f1(1)}$$

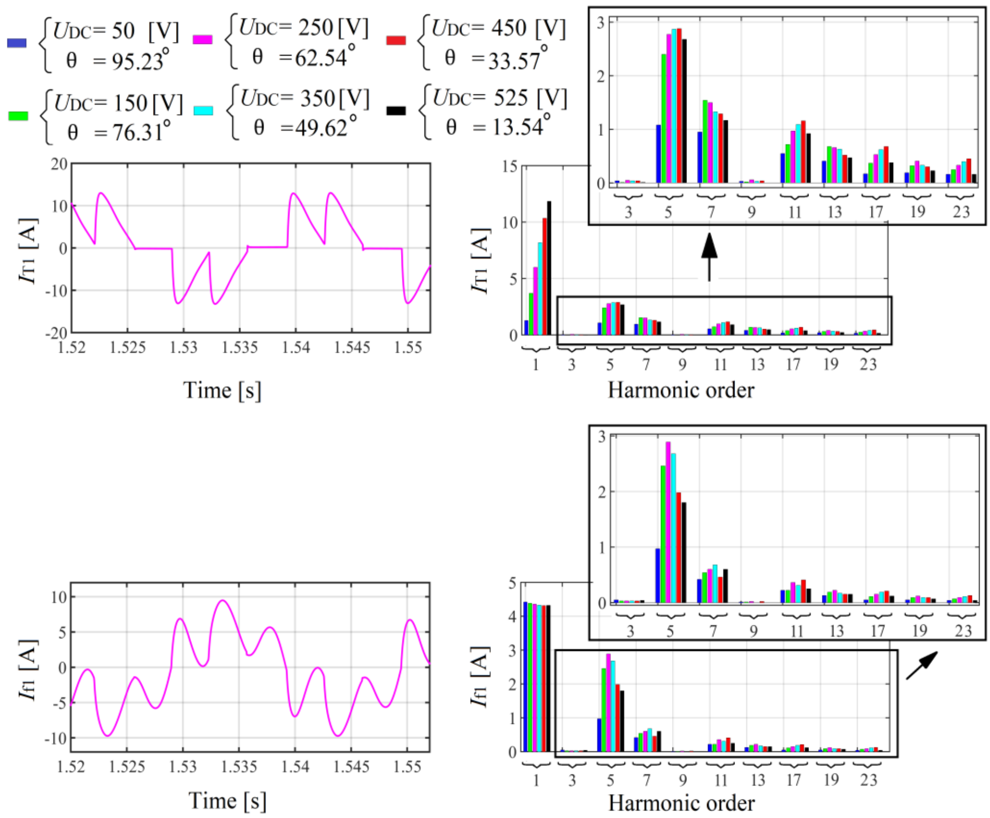

Figure 4.37 Waveforms and spectrums of input rectifier current (I_{T1}) and filter current (I_{f1})

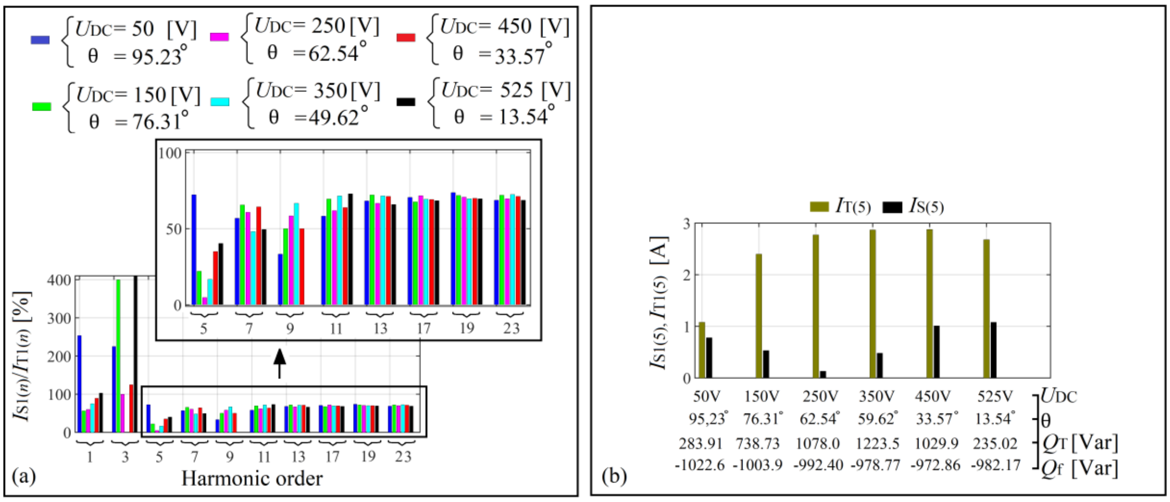

Figure 4.38 (a) filter electiveness, (b) comparison between the 5th harmonic current of grid (I_{S1}) and the input rectifier (I_{T1})

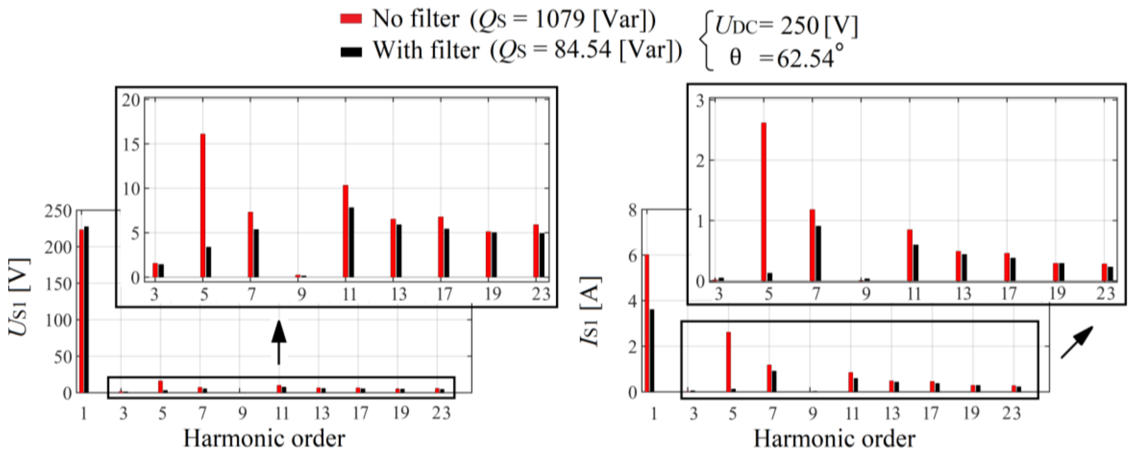

Figure 4.39 Grid voltage and current spectrum: the case without the filter is compare to the case with filter (U_{DC} = 250 V)

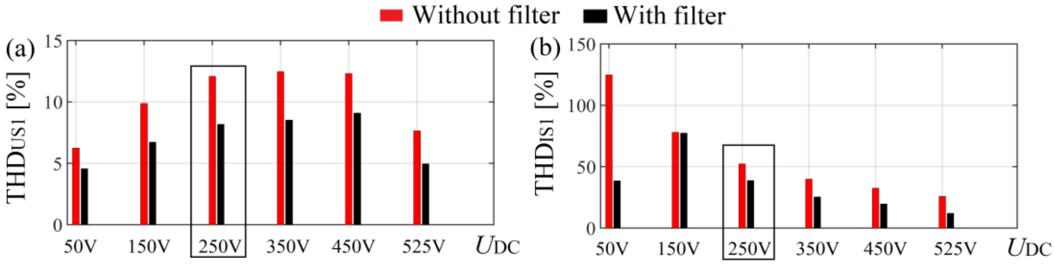

Figure 4.40 THD of grid voltage (a) and current (a) for different U_{DC}: the case without the filter is compare to the case with filter

A comparison of grid voltage and current spectrum and THD before and after the filter connection (with the line-rector) is considered in Figure 4.39 and in Figure 4.40. For almost all rectifier firing angle, the grid current and voltage THD have decreased after the filter connection Figure 4.40(a)(b).

The power system impedance frequency characteristic seen from the load input (from the simulated model) is presented in Figure 4.41 and it can be observed that the series (filter resonance) and parallel resonances (between the grid inductance and the filter) appears bellow the 5th harmonic frequency. Figure 4.41 and the results presented in this chapter show that the 5th harmonic filter was well designed.

Figure 4.41 also shows that if the filter is tuned to the frequency above the 5th harmonic frequency, this harmonic (5th) will be under the parallel resonance zone and can be amplified at the electrical grid side.

In the further part of this work, it is presented the case study in which the single-tuned filter is tune to the resonance frequencies very below the 5th harmonic frequency (e.g. 228.5 Hz which is 8.6 % below 250 Hz) as well as the case study in which the single-tuned filter tuned to the frequency above the 5th harmonic frequency (e.g. 334.5 Hz which is 33.6 % above 250 Hz).

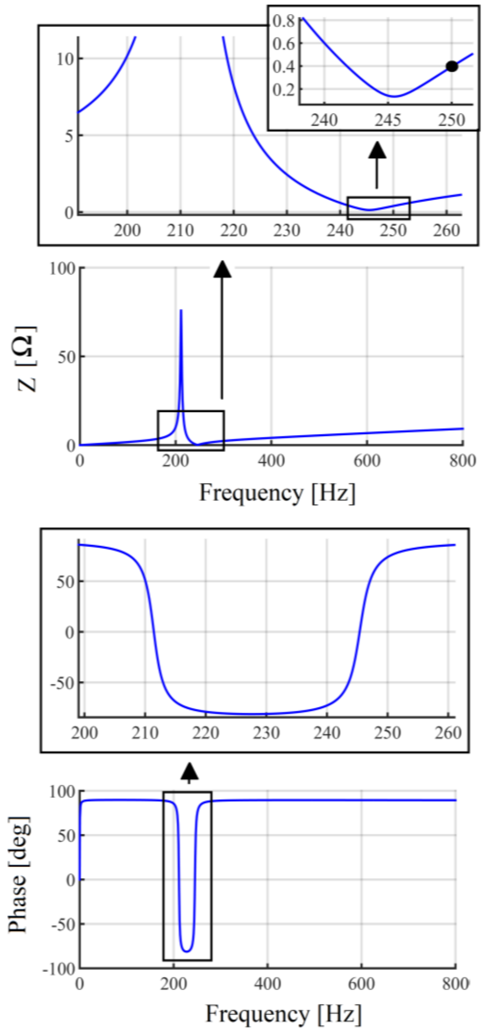

Figure 4.41 Impedance versus frequency characteristic observed at the rectifier input (from the simulated model)

4.3.3.4 Detuning of 5th harmonic single-tuned filter

The detuning of single-tuned filter is performed by increasing or decreasing its resonance frequency in the goal to observe its behaviour regarding the harmonic to be eliminated and higher order harmonics as well.

It has been theoretically demonstrated (chapter 3) that the single filter efficiency is reduced on the mitigation of harmonic to be eliminated (e.g. 5th) when its resonance frequency is lower and fare from the frequency of that harmonic and that the amplification of 5th harmonic amplitude can occur when the filter is tuned to the frequency higher than the 5th harmonic frequency because of the parallel resonance.

The single-tuned filter presented in Figure 4.42 (laboratory model) is tuned for the investigation on the frequencies lower than the frequency of the 5th harmonic (measured paramters - Figure 4.43(b)).

Figure 4.43 presents the filter impedance versus frequency characteristics obtained from the simulation (Figure 4.43(a) - expected characteristics based on the manufacture parameters) and measured in the laboratory Figure 4.43(b). The different observed between data and characteristics in the both figures is due to the filter parameters tolerance.

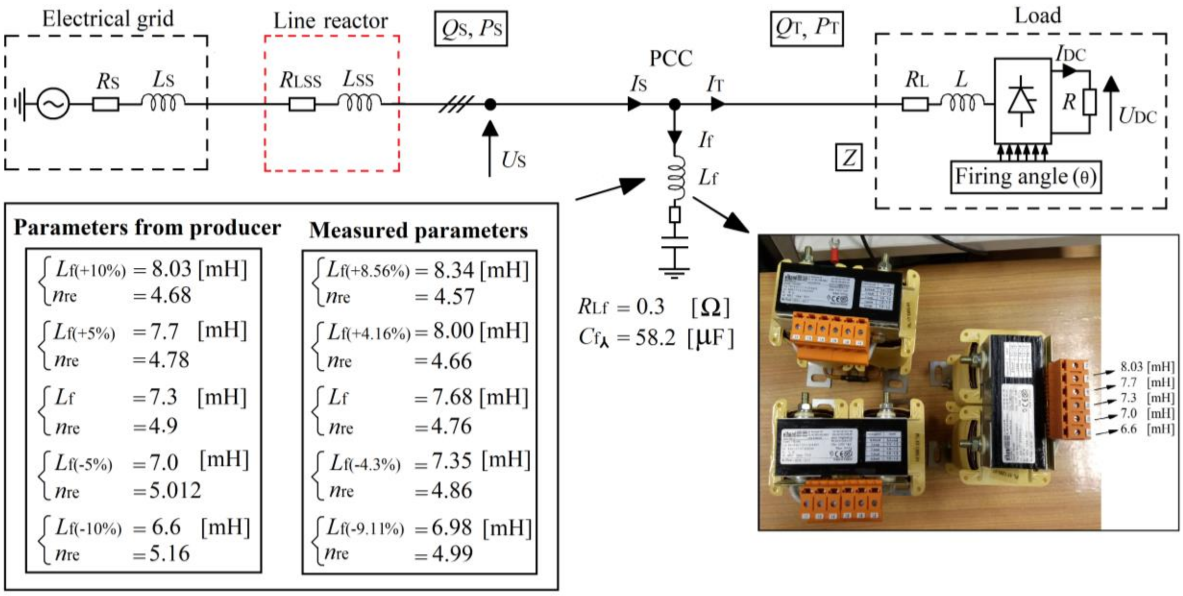

Figure 4.42 Power system equivalent circuit with filter reactor parameters

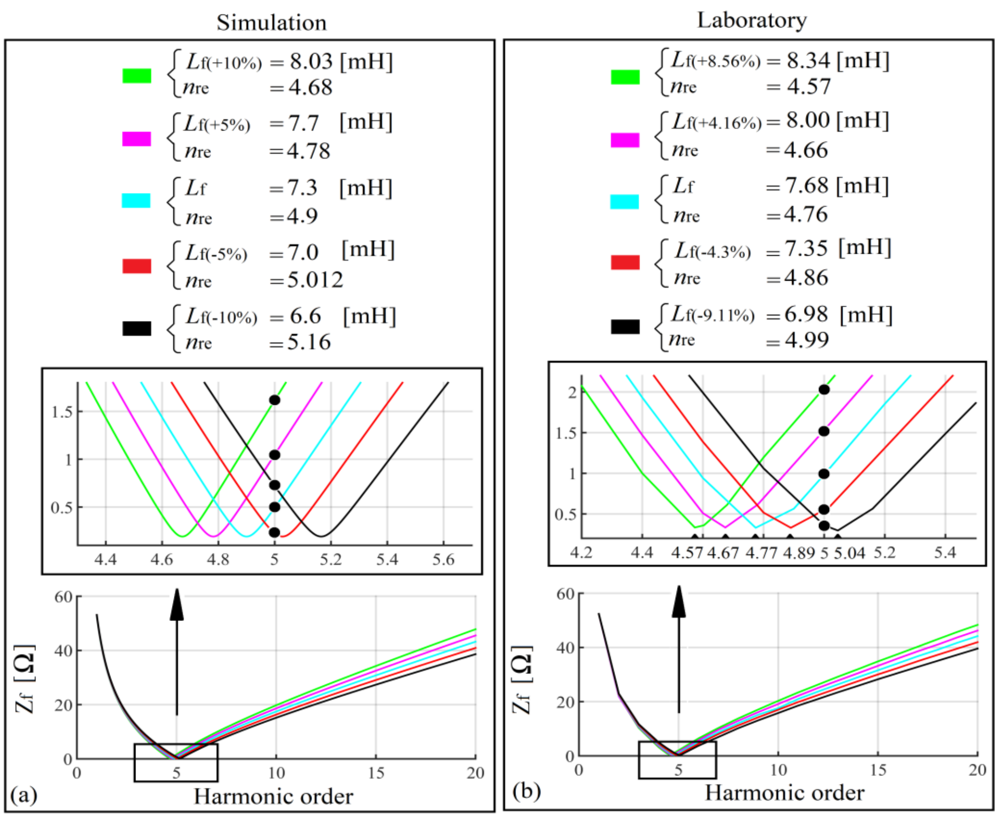

Figure 4.43 Filter impedance versus frequency characteristics: (a) expected characteristics from simulation and (b) characteristics measured in the laboratory

The following laboratory data are recorded by taking as example the rectifier DC voltage (U_{DC}) equal to 250 V (θ = 62.54°). For each tuning frequency the power system data were registered. The fundamental harmonic active and reactive power measured in the laboratory model at the grid side, filter terminals and rectifier input are presented in Table 4.8.

Table 4.8 Fundamental harmonic active and reactive power measured in the laboratory model

n_{re}	$P_{S1(1)}$ [W]	$Q_{S1(1)}$ [Var]	$P_{f1(1)}$ [W]	$Q_{f1(1)}$ [Var]	$Q_{T1(1)}$ [Var]
No filter connected	806.29	1065.6	-	-	-
4.57	821.66	83.81	16.99	-981.84	1067.4
4.66	826.15	83.53	16.10	-991.20	1076.4
4.76	815.84	83.21	16.90	-971.23	1056.1
4.86	807.39	94.73	16.10	-943.33	1039.5
4.99	819.69	78.11	17.46	-965.52	1045.1

The grid voltage and current waveforms and spectrums are presented in Figure 4.44 and the filter current and rectifier input current waveforms and spectrums are presented in Figure 4.45. The grid voltage and current THD and the filter effectiveness are respectively presented in Figure 4.46 and Figure 4.47

Observing Figure 4.44, it can be seen that the lowest value of the 5^{th} harmonic amplitude (the lowest THD as well - Figure 4.46(a)) in the grid voltage spectrum is obtained when the filter is tuned to the frequency of harmonic order 4.99, whereas in the case of grid current spectrum, the filter tuned to the frequency of 4.66 has the lowest 5^{th} harmonics amplitude as well as the lowest THD (Figure 4.46(b)). By increasing the filter tuning frequency from n_{re} equal to 4.57 to n_{re} equal to 4.99, the grid current 5^{th} harmonic amplitude should be decreasing as the 5^{th} harmonic amplitude observed in the grid voltage spectrum. This difference is due to the 5^{th} harmonic current flowing from the grid side to the laboratory model.

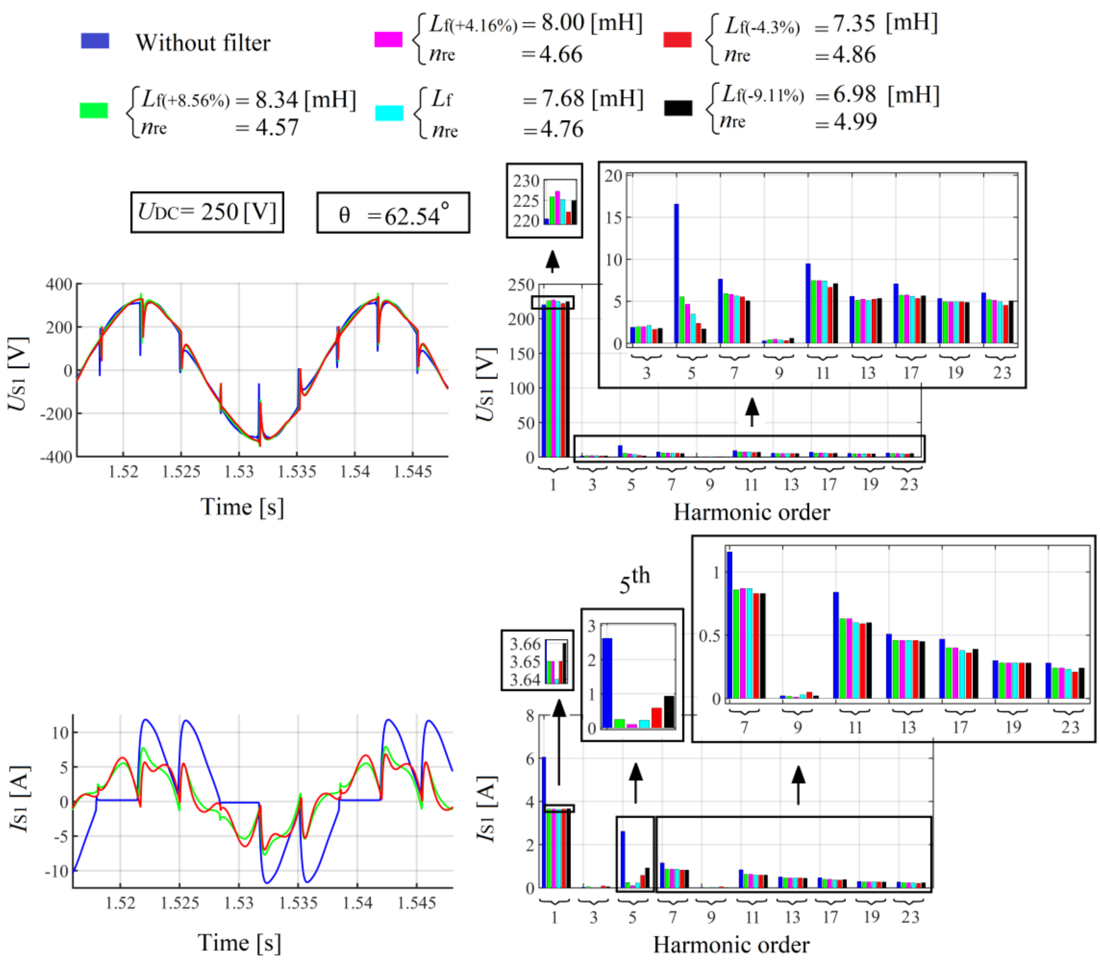

Figure 4.44 Point of common coupling voltage and current waveforms and spectrums

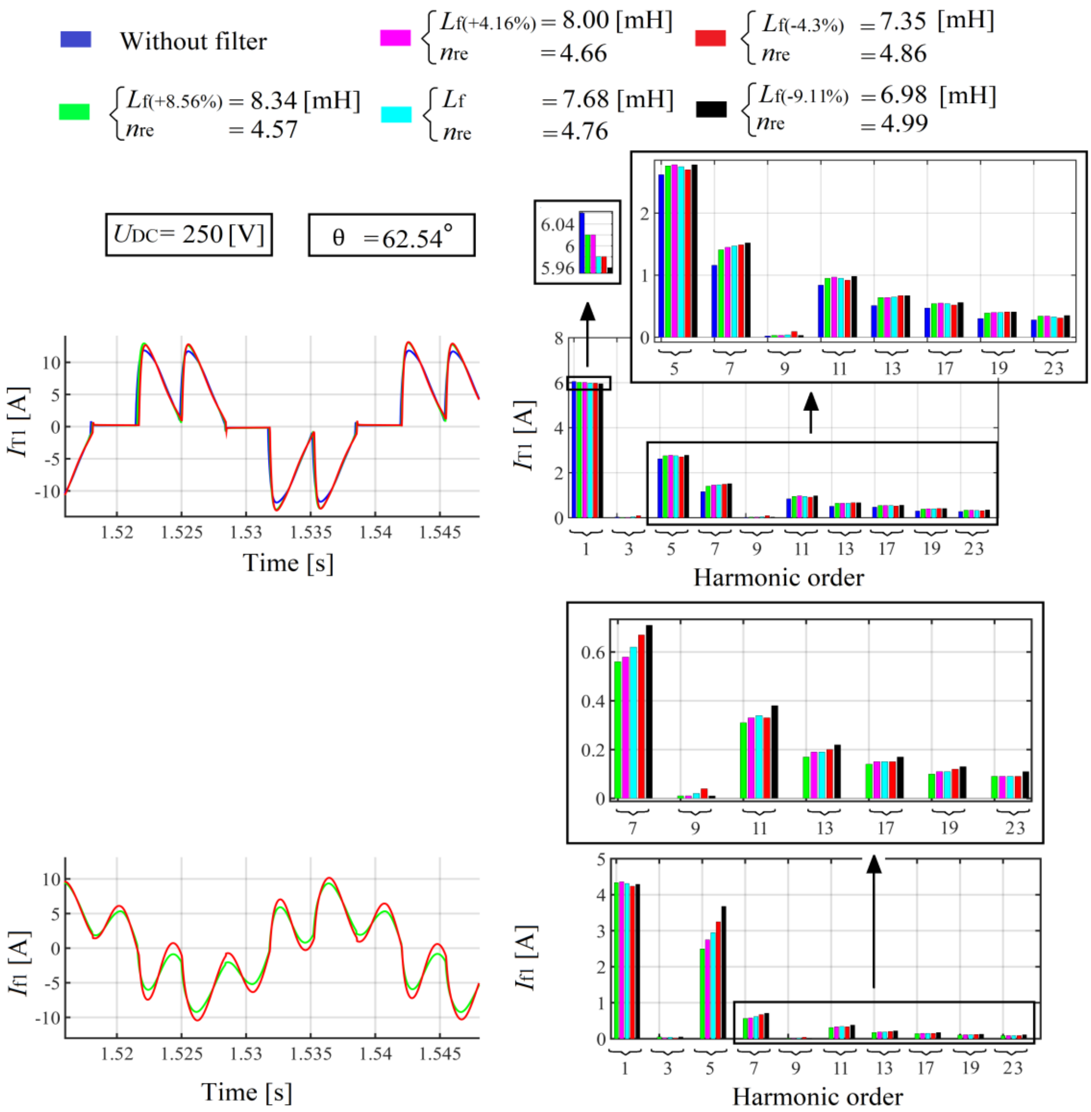

Figure 4.45 Input rectifier and filter current waveforms and spectrums

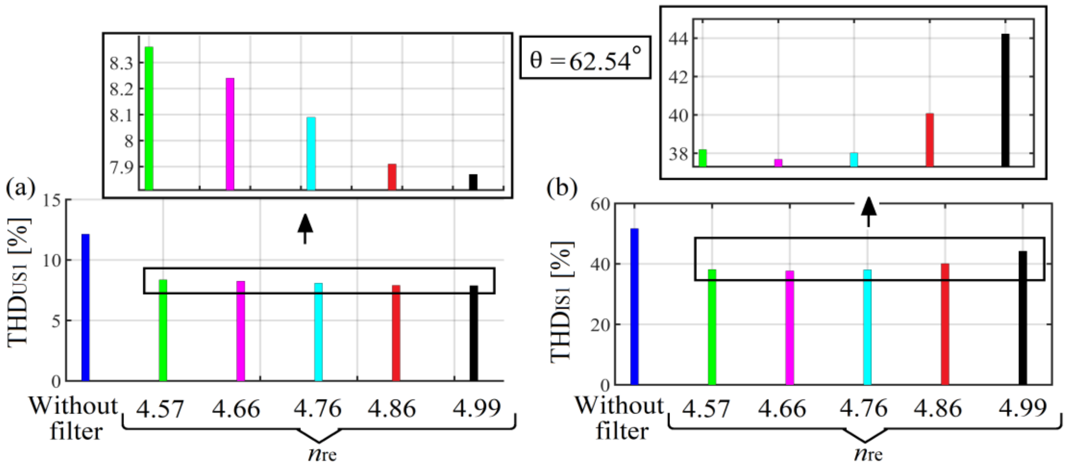

Figure 4.46 Grid voltage and current THD for different resonance frequency

The single-tuned filter efficiency presented in Figure 4.47 shows that the filter is more efficient on the 5th harmonic mitigation when its resonance frequency is on the harmonic order of 4.66, which is contrary to what can be observed in the characteristics of Figure 4.43(b).

According to the filter impedance versus frequency characteristics of Figure 4.43(b), the filter tuned to the frequency of 4.57 should present the highest 5th harmonic amplitude for both grid current and voltage and the filter tuned to the frequency of 4.99 should presents the lowest 5th harmonic amplitude for both grid current and voltage. But the reduction of the 5th harmonic amplitude in the grid current as presented in Figure 4.44 does not follow that principle and this is the reason for the next laboratory experiments using the programmable AC voltage source Chroma.

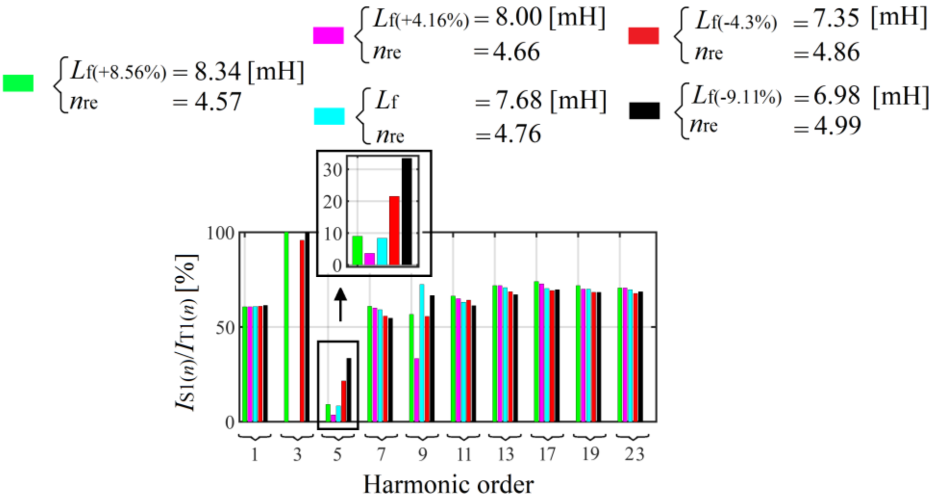

Figure 4.47 5th harmonic reduction efficiency

4.3.3.5 Experiments with the programmable AC voltage source (Chroma)

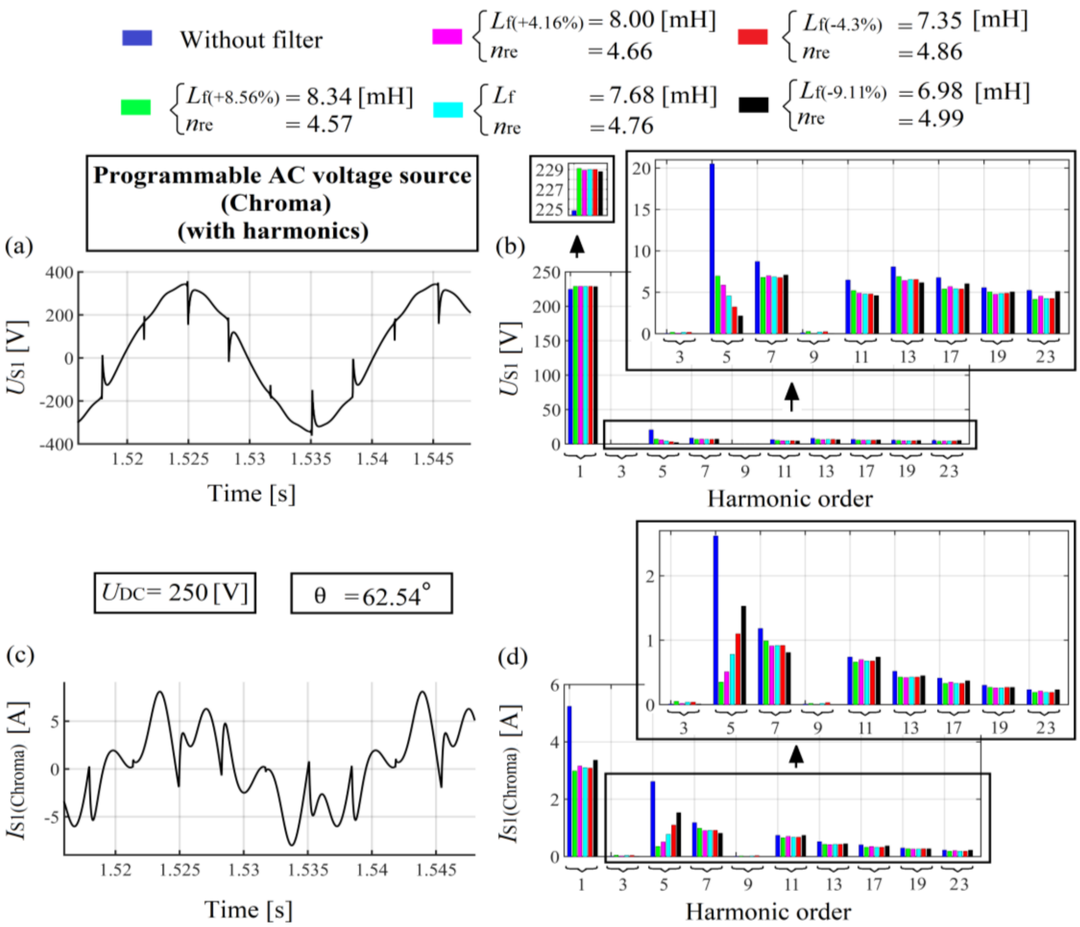

Figure 4.48 (a) PCC voltage waveform with (b) its spectrum, (c) Chroma input current with (d) its spectrum

The laboratory model of Figure 4.42 is disconnected from the electrical grid and is supplied by the programmable AC voltage source. As in the previous experiments, two case studies are considered: voltage source with (Figure 4.23(a)) and without (Figure 4.23(b)) harmonics.

The voltage and current waveforms and spectrums measured at the PCC are presented in Figure 4.48 and Figure 4.49. The filter current and rectifier input current waveforms and spectrums are presented in Figure 4.50 and Figure 4.51 respectively. The voltage and current THD measured at the PCC are shown in Figure 4.52 and Figure 4.53.

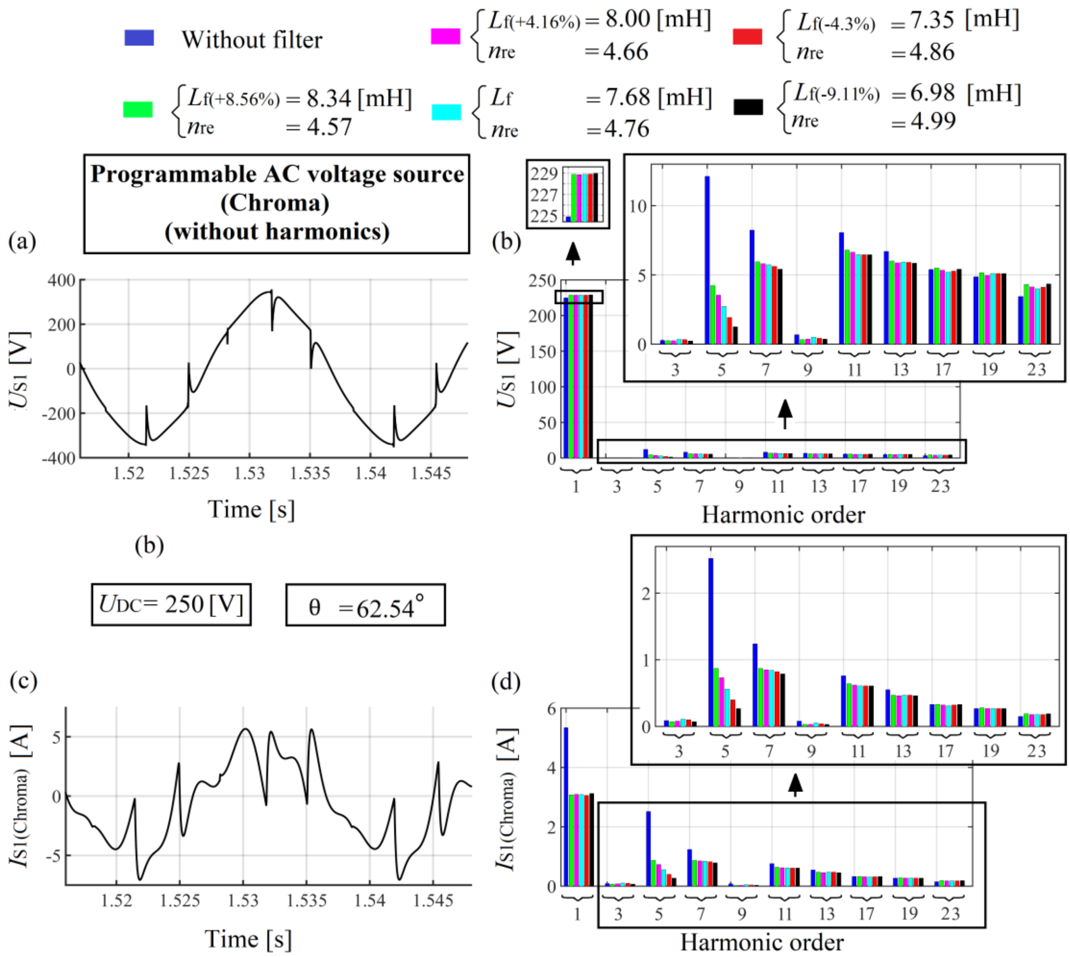

Figure 4.49 (a) PCC voltage waveform with the spectrum (b), (c) Chroma input current with the spectrum (d)

Comparing the spectrum of Figure 4.48(b) to the one of Figure 4.49(b) it can be noticed that in the case of voltage source with harmonics as well as without harmonics, the filter has reduced the 5th harmonic amplitude in the same way according to the measured characteristics of Figure 4.43. The same observation can be done when comparing Figure 4.52(a) to Figure 4.53 (a).

Concerning the voltage source input current spectrums, in the case of voltage source with harmonics (see Figure 4.48(d) and Figure 4.52(b), the filter behavior on the 5th harmonic amplitude mitigation is the same as in the case when the laboratory model was connected to the electrical grid (see spectrum and THD current of Figure 4.44 and Figure 4.46(b)). But observing Figure 4.49(d) and Figure 4.53 (b) it can be noticed that, the case with voltage source without harmonics presents the proper results (according to the characteristics of Figure 4.43(b)) of 5th harmonic amplitude mitigation.

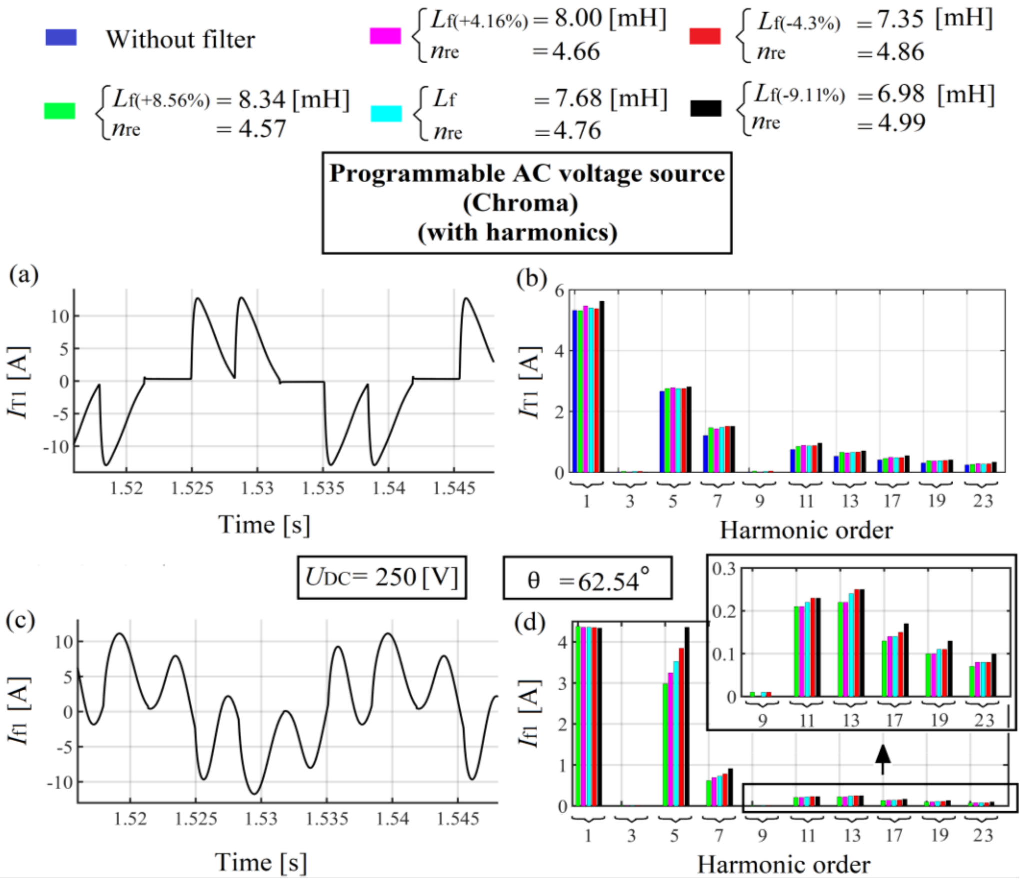

Figure 4.50 (a) rectifier input current waveform with (b) the spectrum, (c) filter current waveform with (d) the spectrum

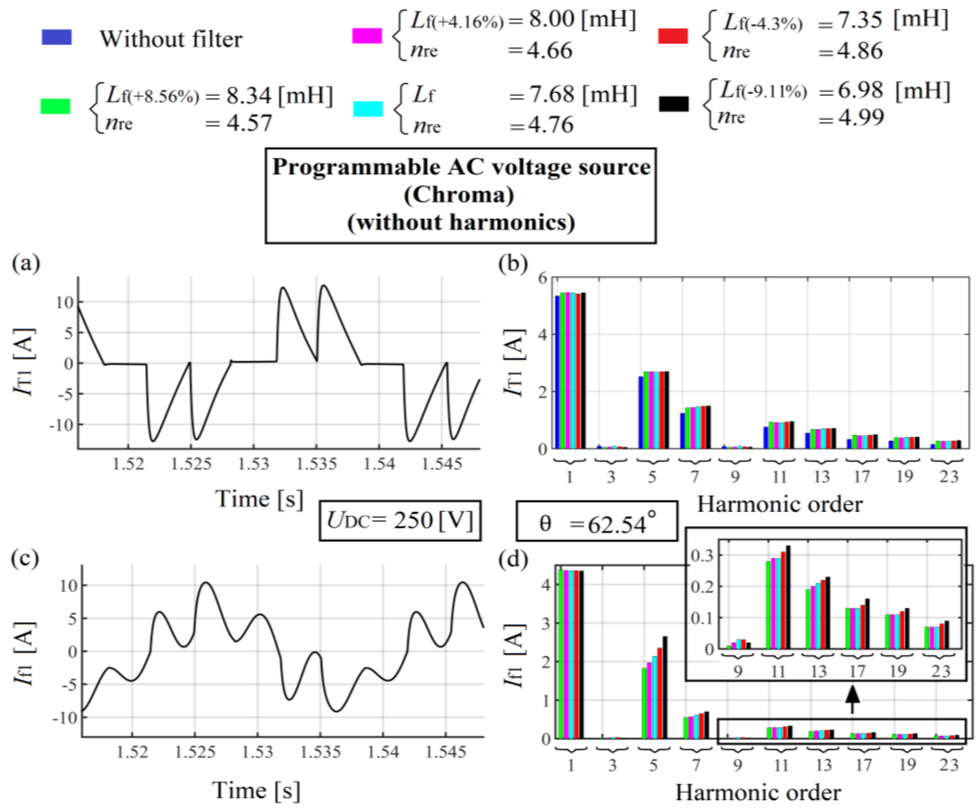

Figure 4.51 (a) rectifier input current waveform with (b) the spectrum, (c) filter current waveform with (d) the spectrum

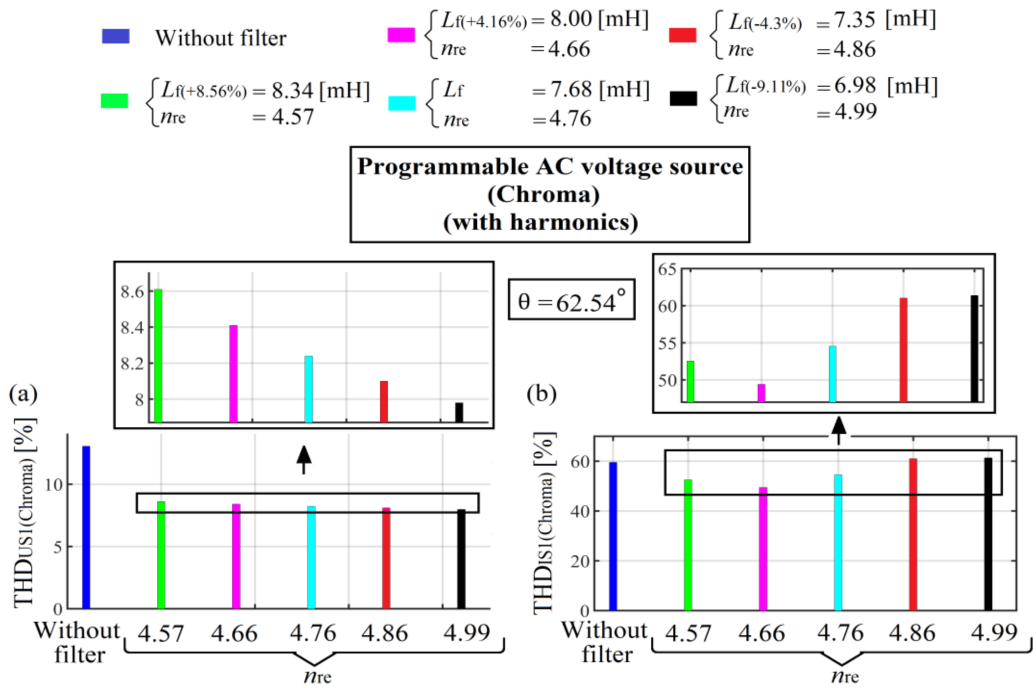

Figure 4.52 PCC voltage (a) and current (b) THD

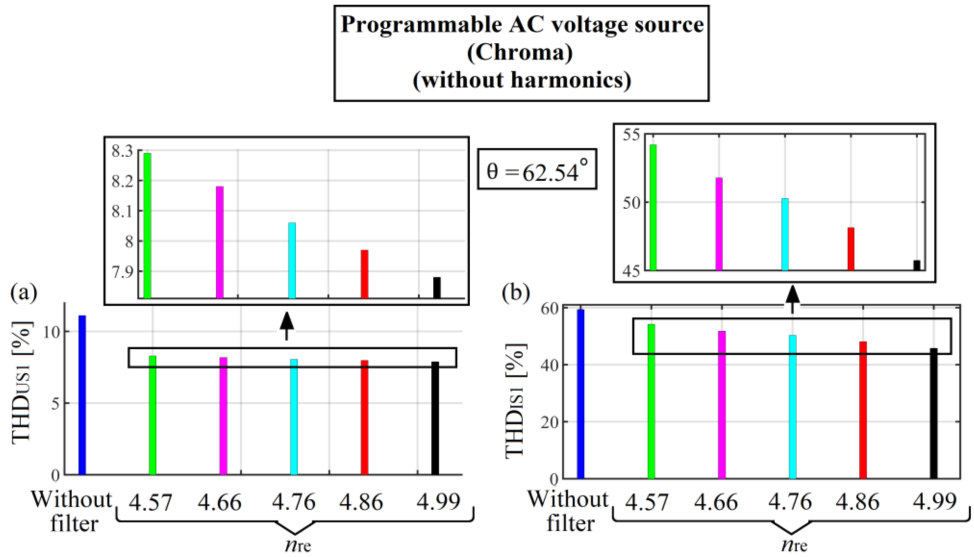

Figure 4.53 PCC voltage (a) and current (b) THD

The investigations done in this chapter have shown that the reactor and capacitor parameters tolerance has an influence on the PHF tuning frequency as well as on its work efficiency, therefor it is important to verifier the reactor and capacitor parameters after their reception from the producer. This varication should be based on the search of the filter parameters, which are close to the expected parameters. These investigations have also shown that the harmonics contains in the electrical grid flows through the filter, mostly those with frequencies close to the filter resonance frequency. The filter efficieny also depends upon the electrical grid impedance and that dependency can be reduced be additing the line reactor between the filter and the PCC. The line reactor presence does not only mitigates the current harmonics amplitude flowing from the electrical grid, but it increases also the grid voltage distortion.

4.3.3.6 Investigation of the 7th order harmonic passive filter

What can occur if the single-tuned filter is tuned to the frequency other (apart the fundamental) than the lowest generated one (which in this case is the 5th other harmonic frequency)? That question is answered after the laboratory experimental presented in this chapter.

The laboratory load current spectrums in Figure 4.13 shows that the lowest generated characteristic harmonic is the 5th. But for the investigation purposes, the single-tuned filter is tuned to the frequency very close the frequency of the 7th order harmonic (6.78).

The 7th order harmonic filter computed parameters are presented in Figure 4.54 as well as in Table 4.1 and Table 4.2. The filter impedance versus frequency characteristics presented in Figure 4.55(a) (characteristic based on the manifactur parameters) and Figure 4.55(b) (measured characteristic) show that the 5th harmonic is on the capacitive side of the characteristics.

The fundamental harmonic active and reactive powers before and after the filter connection are presented in Table 4.9 as well as the grid voltage and current THDs.

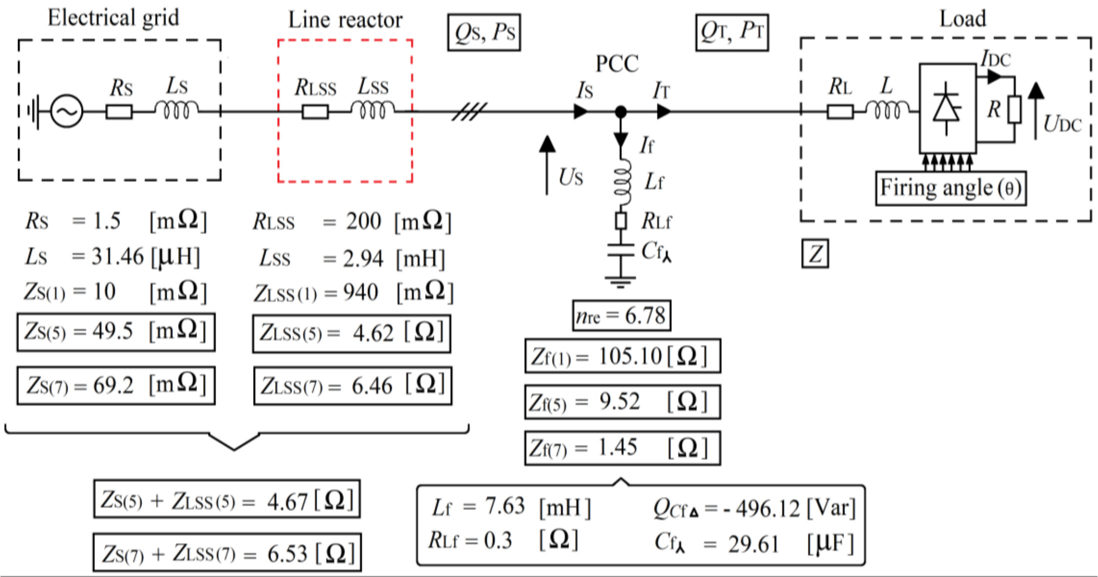

Figure 4.54 Power system equivalent circuit with the 7th harmonic passive filter

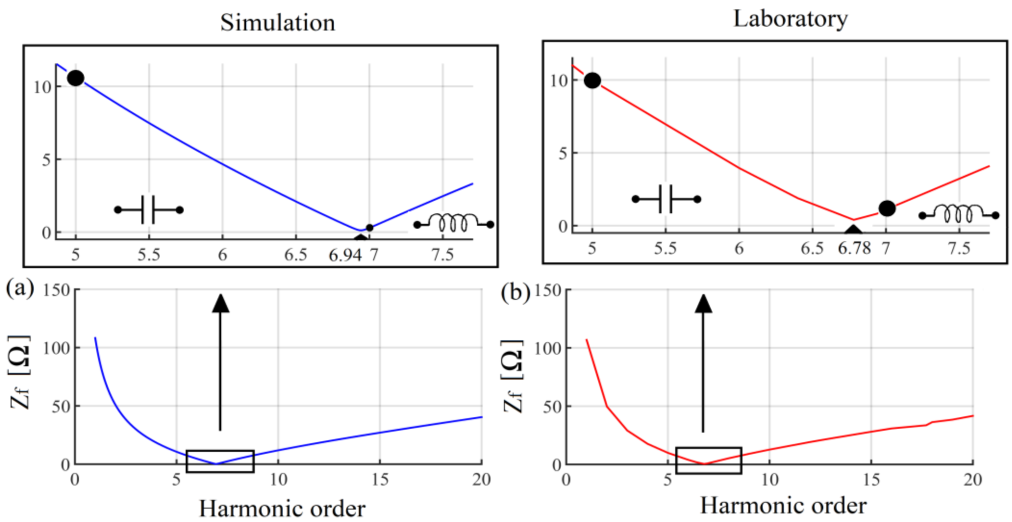

Figure 4.55 Impedance versus frequency characteristics of the seventh harmonic filter: (a) simulated (expected) characteristic, (b) measured characteristic (see also Figure 4.16)

Table 4.9 Fundamental harmonic active and reactive power as well as THDs measured in the laboratory model

	U_{DC} = 345V, θ = 50.29°							
	$P_{S1(1)}$ [W]	$Q_{S1(1)}$ [Var]	THD_{US1} [%]	THD_{IS1} [%]	$P_{f1(1)}$ [W]	$Q_{f1(1)}$ [Var]	$P_{T1(1)}$ [W]	DPF
Before the filter	1320	1172.5	12.89	39.60	-	-	-	0.74
After the filter	1275.2	755.33	14.48	75.38	13.57	-462.22	1292.3	0.86

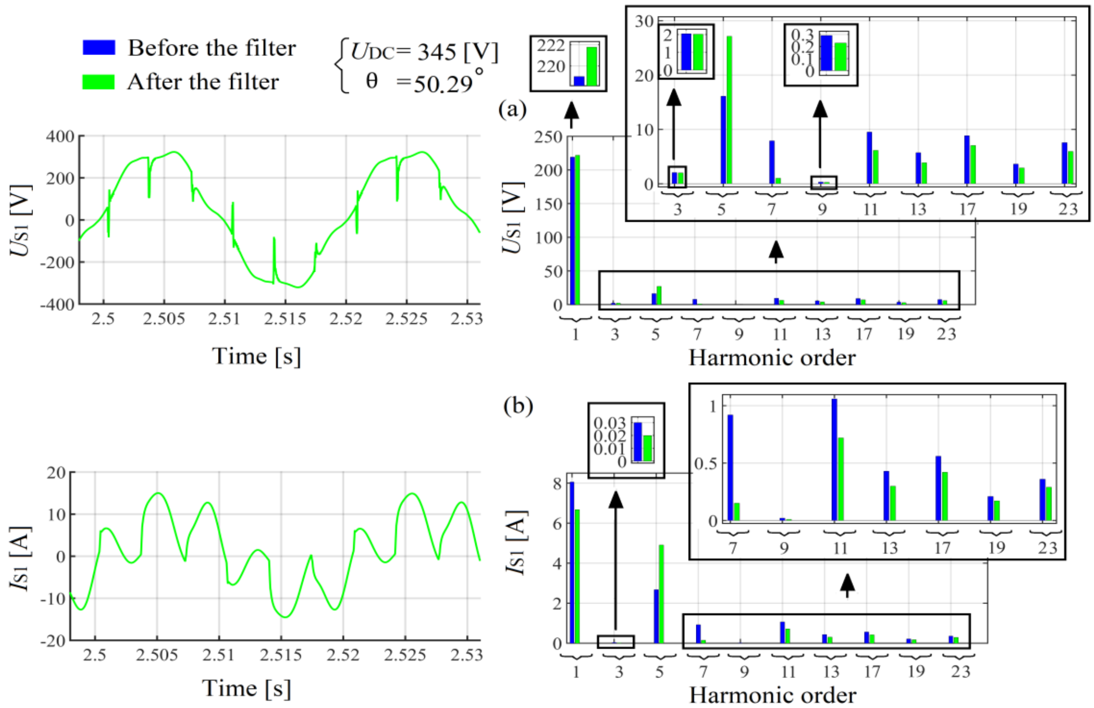

Figure 4.56 (a) grid voltage waveform with the spectrum; (b) grid current waveform with the spectrum

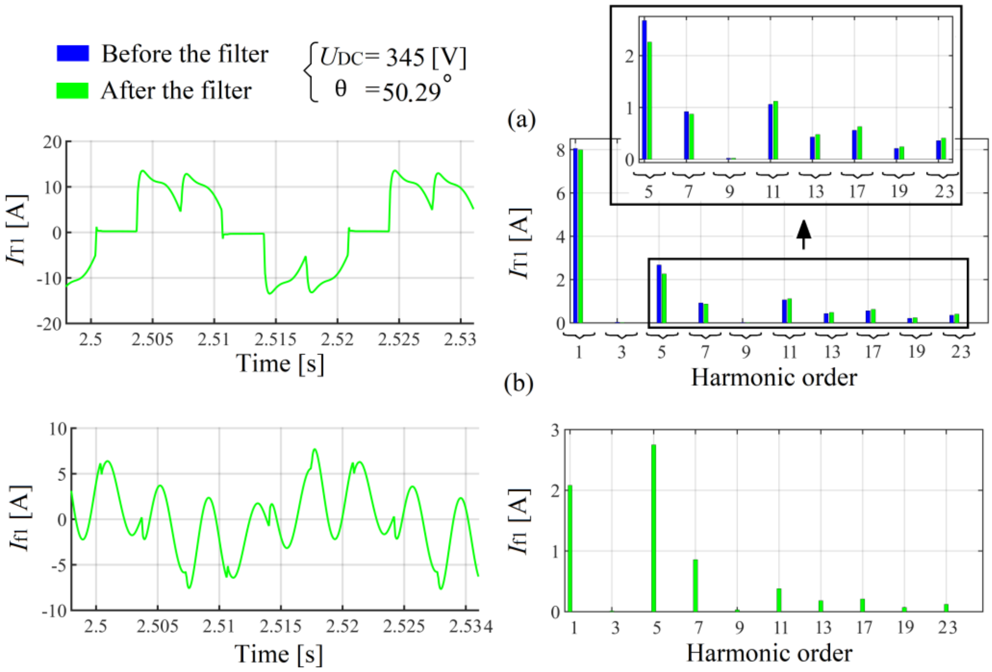

Figure 4.57 (a) input rectifier current waveform with the spectrum, (b) filter current waveform with its spectrum

The laboratory model parameters are measured after choosing (as example) the rectifier firing angle value equal to 50.29º (Compaired to other firing angle, it presents the best resuts in term of 7th harmonic mitigation). Observing the parameters in Table 4.9 it can be seen that after the filter connection, the fundamental reactive power is partially compensated at the grid side ($Q_{S1(1)}$ = 755.33 Var -) because of the filter capacitive reactive power $Q_{S1(1)}$ = 462.22 Var.

The PCC voltage and current spectrums in Figure 4.56(a)(b) show that the 7th harmonic is well reduced (as well as the higher order harmonics (e.g. 11th to 23rd)) after the filter connection, but the 5th harmonic is amplified. The THDs of Table 4.9 shows that the grid voltage and current waveforms are more distorted after the filter connection.

The load and filter current waveforms and spectrums are presented in Figure 4.57(a)(b). The filter is more charged by the 5th harmonic amplitude (Figure 51(b)).

Tuned to the frequency near the frequency of 7th harmonic (6.78th), the filter has prevented almost 82.76% of load 7th harmonic from entering the electrical grid (Figure 4.58(a)) but has amplified the 5th harmonic (at the grid side). That amplification is due to the presence of the 5th harmonic frequency near the parallel resonance occurring between the grid inductance and the filter capacitance as it can be observed in simulated characteristic of Figure 4.58(b). The 5th harmonic frequency is near 290 Hz which is the parallel resonance frequency.

If the designed filter is tuned to the frequency higher than the frequency of the lowest generated harmonic (apart the fundamental), that harmonic will be under parallel resonance phenomena, therefore in such of situation can be amplified.

The studies presented in this chapter confirm the principle of PHF design saying that the filter should be designed in the electrical system by starting from the lowest (apart the fundamental) load characteristic harmonic and no one should be neglected.

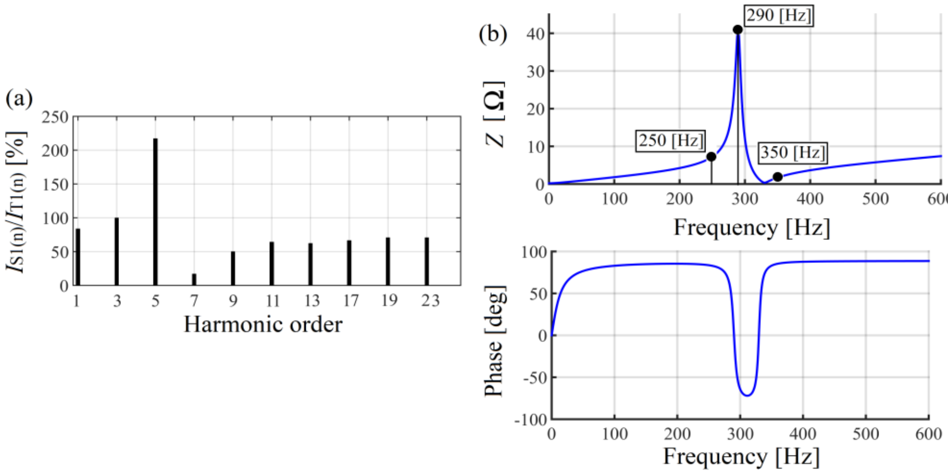

Figure 4.58 (a) filter efficiency, (b) Impedance versus frequency characteristic of power system observed from the rectifier input (simulated)

4.4 Group of single-tuned filters

In the considered example, the designed laboratory filter group is constituted of two single-branch filters as presented in Figure 4.59. The first filter (f1) is tuned to the frequency of 239 Hz (967.22 Var - Figure 4.59) and is dedicated to the 5th harmonic mitigation at the PCC. The second filter (f2) is tuned to the frequency of 339 Hz (492.08 Var – from Figure 4.59) and is dedicated to mitigate the 7th harmonic at the PCC. It can be noticed that the reactive power of filter (f1) is almost twice the reactive power of filter (f2).

Taking into account the measured parameters in Table 4.10, it can be seen that the filter group total reactive power is higher than load reactive power hence in consequence the overcompensation of -377.15Var at the grid side. That consequence is manifested by the grid voltage fundamental harmonic increased from 223.95V before the filters connection to 229.46V after the filter connection.

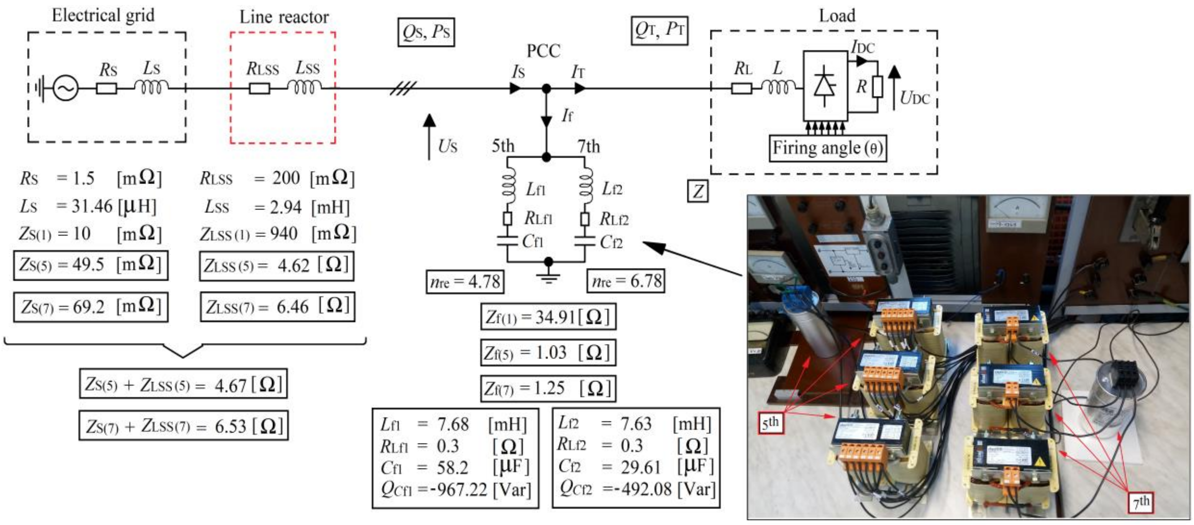

Figure 4.59 Power system equivalent circuit with filter group parameters

Table 4.10 Fundamental harmonic active and reactive power measured in the laboratory model at the grid side, filter terminals and rectifier input

	U_{DC} = 250 V				
	$P_{S1(1)}$ [W]	$Q_{S1(1)}$ [Var]	$P_{f1(1)}$ [W]	$Q_{f1(1)}$ [Var]	$Q_{T1(1)}$ [Var]
Before the filters connection	818.54	1067.7	-	-	-
After the filters connectio	877.92	-377.15	20.39	-1487.9	1113.3

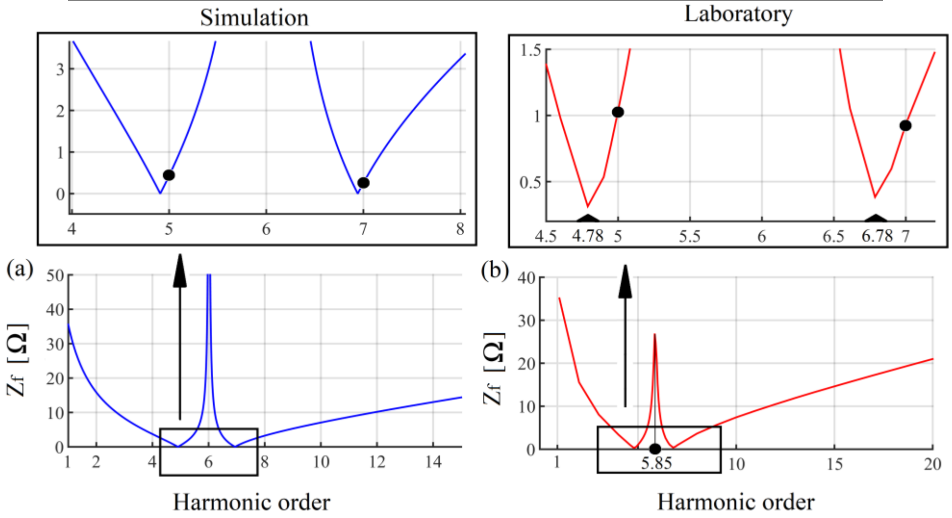

Figure 4.60 Filter group impedance versus frequency characteristics: (a) simulated (expected characteristic) characteristic, (b) measured characteristic

The filter group impedance versus frequency characteristics are shown in Figure 4.60(a) (characteristic based on the manufacture parameters) and Figure 4.60(b) (measured characteristic). In the measured characteristic of Figure 4.60(b) it is noticed that the filter group parallel resonance has occurred at the frequency of 292.5 Hz. The laboratory data are measured after fixing the rectifier firing angle at 62.54º (U_{DC} = 250 V).

According to the spectrums of Figure 4.61(a)(b) the grid voltage and current 5^{th} and 7^{th} harmonic amplitudes are efficiently reduced by the filter group as well as the higher harmonics from the 7^{th}.

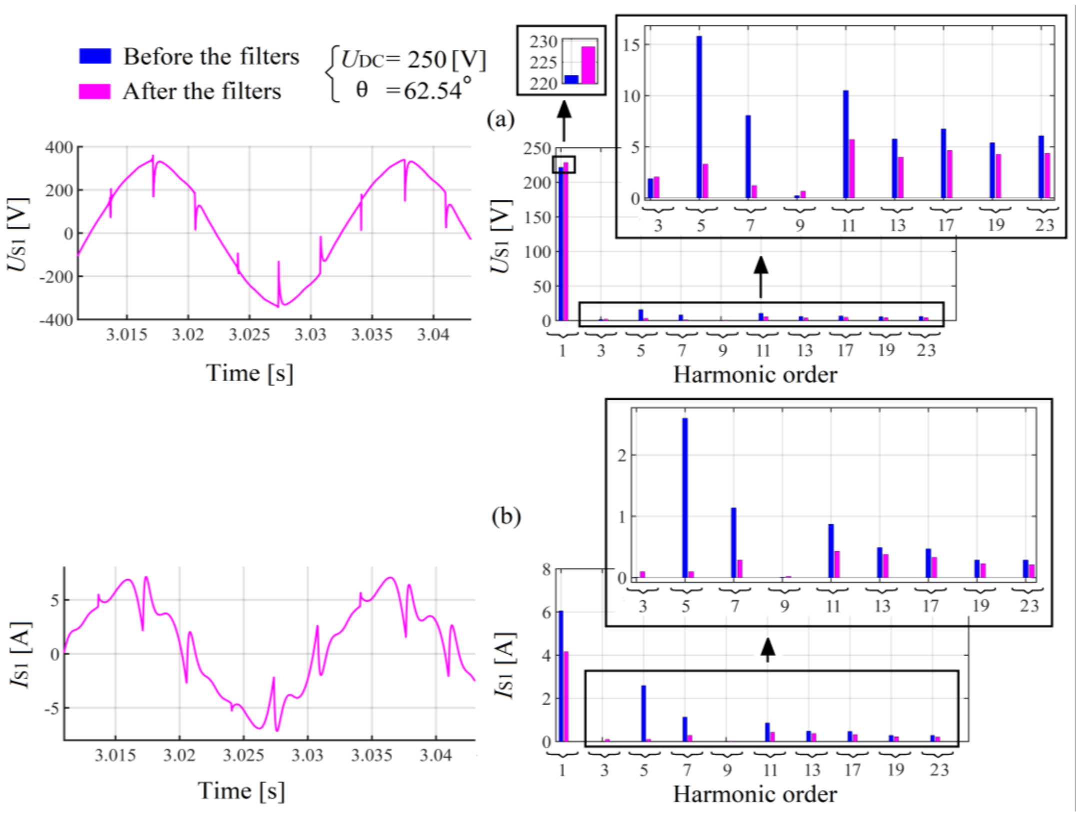

Figure 4.61 Grid voltage (a) and current (b) waveforms with the spectrums before and after the filter connection

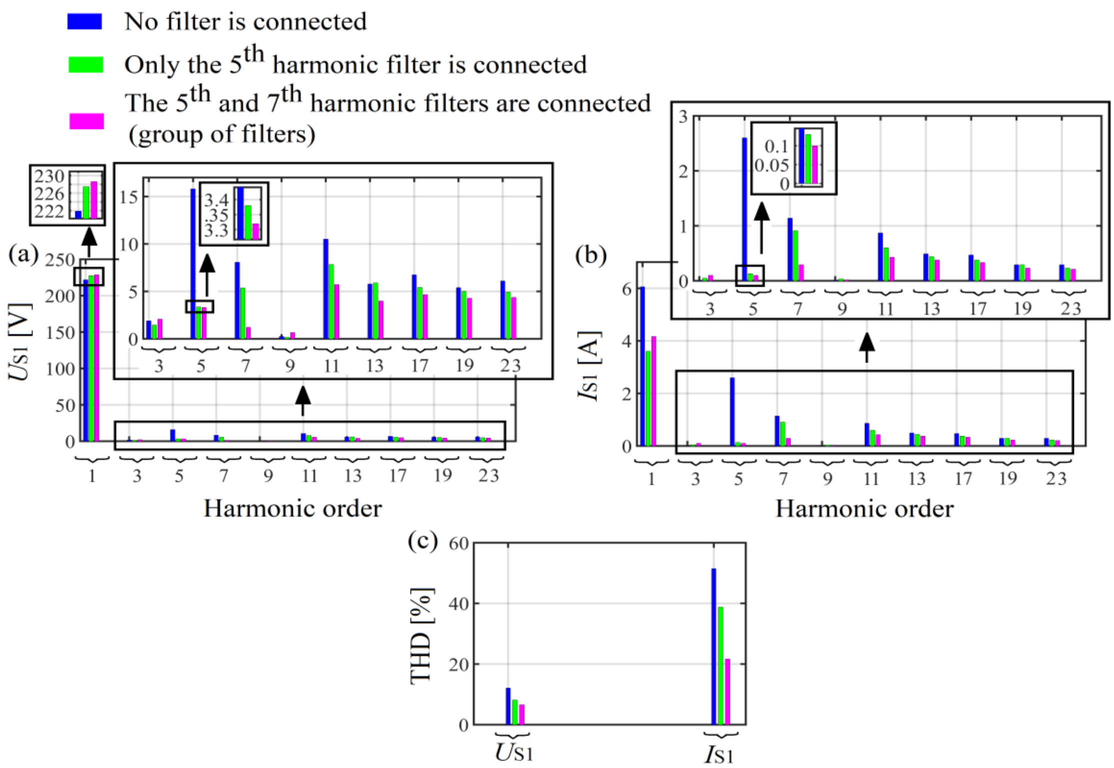

Figure 4.62 Harmonics comparison spectrums of grid voltage (a), current (b) and THD (c) when no filter is connected, when only the 5th harmonic filter is connected and when the 5th and 7th harmonic filters are connected (filter group)

Figure 4.62 presents a comparative study of the grid voltage and current harmonics and THD when no filter is connected, when only the 5th harmonic filter is connected and when the filter group is connected. It can be seen that the filter group has the best results in term of characteristic harmonics mitigation and presents the lowest THDs (Figure 4.62(a-c)).

The rectifier input and filter current waveforms are presented respectively in Figure 4.63(a) and (b). The designed filter group is more efficient on the 5th harmonic mitigation than on the 7th harmonic mitigation (Figure 4.64).

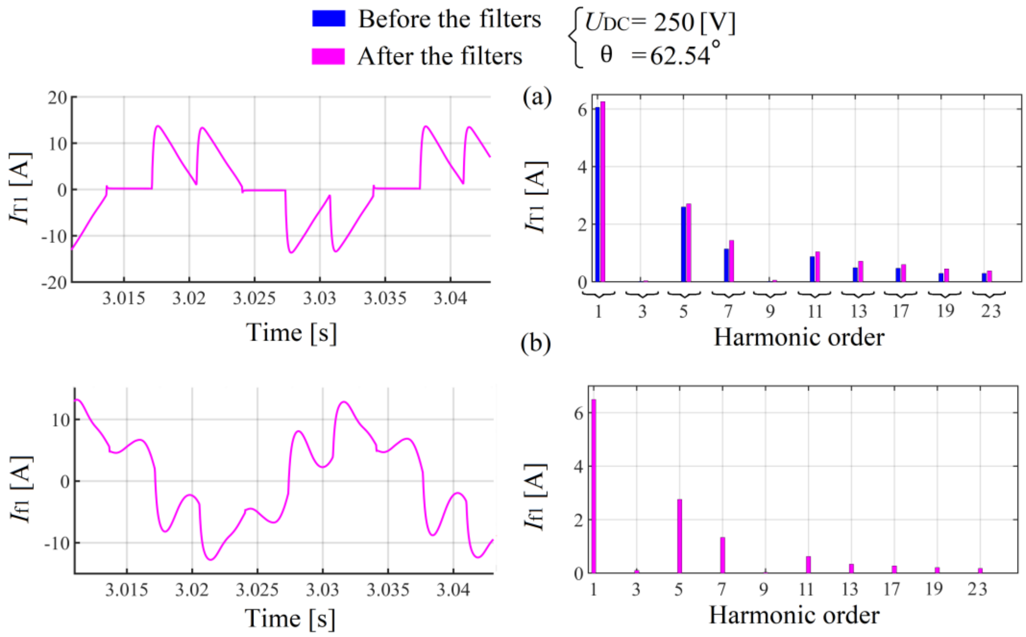

Figure 4.63 Currents of input rectifier (a) and filter (b) with spectrums

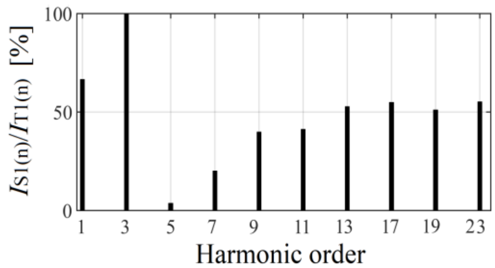

Figure 4.64 Filter group efficiency

4.5 Capacitor bank

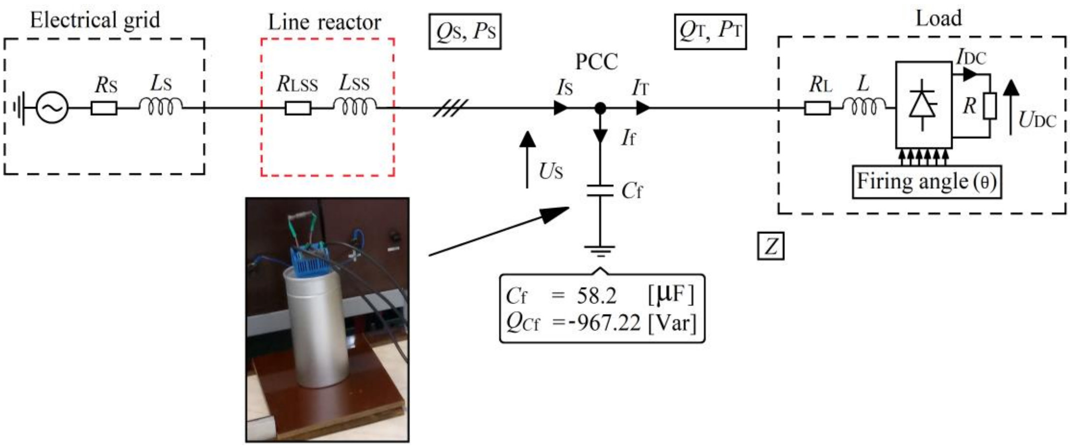

Figure 4.65 Power system equivalent circuit with the capacitor bank

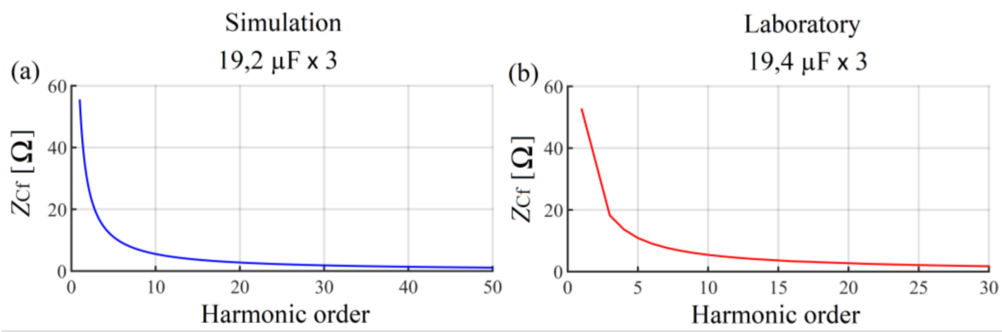

Figure 4.66 Capacitor bank characteristics: (a) simulated (expected) characteristic, (b) measured characteristic from the laboratory (see Table 4.2)

Table 4.11 Fundamental harmonic active and reactive powers as well as grid voltage and current THDs measured in the laboratory model

	U_{DC} = 250 V, θ = 62.54°							
	$P_{S1(1)}$ [W]	$Q_{S1(1)}$ [Var]	THD_{US1} [%]	THD_{IS1} [%]	$P_{f1(1)}$ [W]	$Q_{f1(1)}$ [Var]	$Q_{T1(1)}$ [Var]	DPF
Before the filter connection	809.11	1064.4	11.95	52.21	-	-	-	0.60
After the filter connection	756.33	145.03	14.62	165.33	21.92	-936.29	1080.1	0.98

The capacitor bank (first-order filter) widespread is used for the fundamental harmonic reactive power compensation in the industry environments where the voltage and current (of the compensated load) distortion is not considerable [99]. It has been theoretically demonstrated (in chapter 3) that the application of the capacitor bank in power system does not only compensate the reactive power, but also reduces or amplifies the harmonics (e.g. the 3rd, 5th 7th etc.

To confirm the correctness of theoretical studies, a laboratory experiment has been performed by connecting the capacitor bank between the load and the PCC as presented in Figure 4.65.

The capacitor parameters are presented in Figure 4.65 and its characteristics (simulated and measured in the laboratory) are respectively presented in Figure 4.66(a) and Figure 4.66(b).

The power system parameters measured before and after the capacitors bank connection are respectively presented in Table 4.11. Before the first-order filter connection the THD of the grid voltage was 11.95% and the one of the grid current was 52.21% (Table 4.11). But, after the filter connection it has increased to 14.62% for the voltage and to 165.33% for the current.

The laboratory capacitor bank (after its connection) has compensated the PCC reactive power (DPF increase from 0.60 to 0.98 - see Table 4.11) and by observing the grid voltage and current spectrums in Figure 4.67(b)(d), it can be noticed that, it has caused the 5th and 7th harmonics amplitude amplification and the reduction of higher harmonics amplitudes from the 11th.

The spectrum comparing the grid current harmonics and input rectifier current harmonics is presented in Figure 4.68. It can be seen that the grid current harmonics amplitude from the 2nd to the 10th are amplified and from the 11th are reduced. The current waveforms and spectrums measured at the rectifier input and capacitor bank terminal are presented in Figure 4.69.

From the compensation point of view, the first-order filter is efficient, but from harmonics reduction point of view, it is only efficient for higher harmonics (Figure 4.70(a), the harmonics under 100%). The amplification of the lowest generated harmonics (e.g. 3rd, 5th, 7th etc.) is due the parallel resonance phenomenon between the grid inductance and capacitor bank capacitance (Figure 4.70(b)).

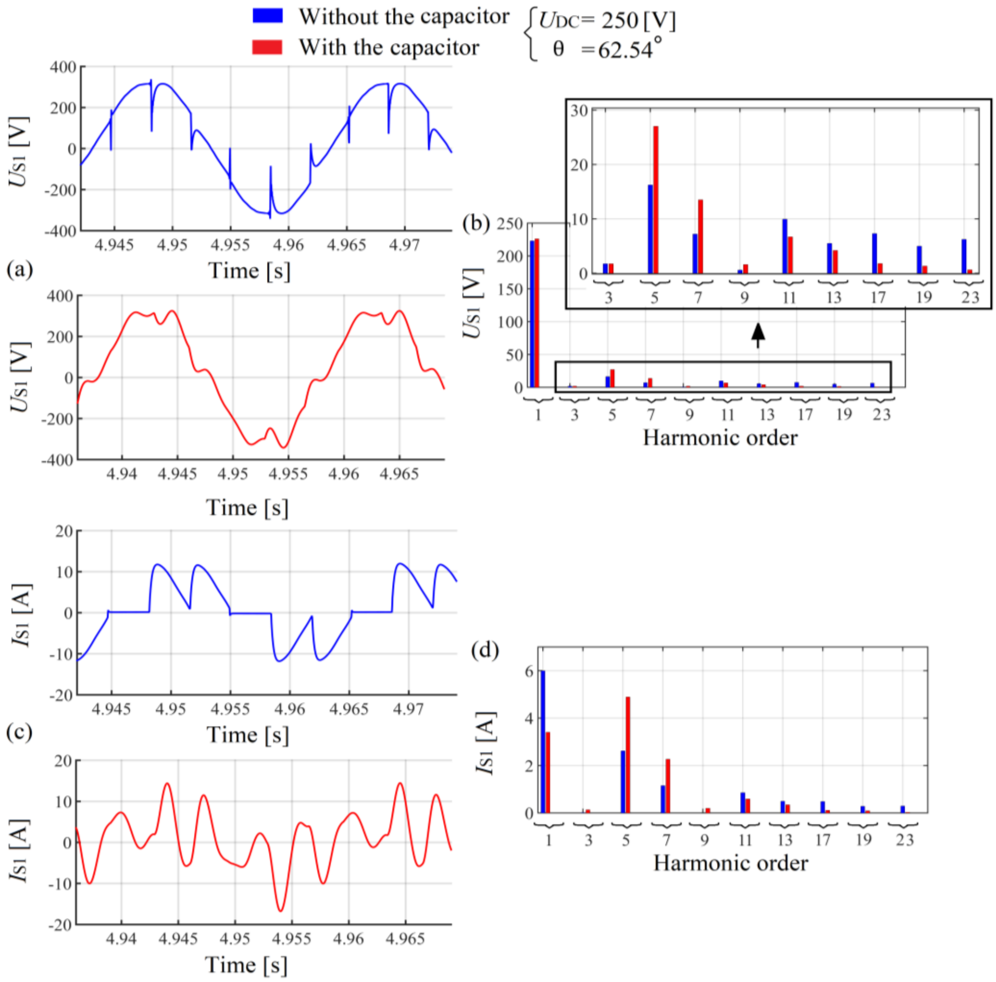

Figure 4.67 Measured grid voltage waveforms (a) and (b) their spectrums; measured grid current waveforms (a) and (d) thier spectrum

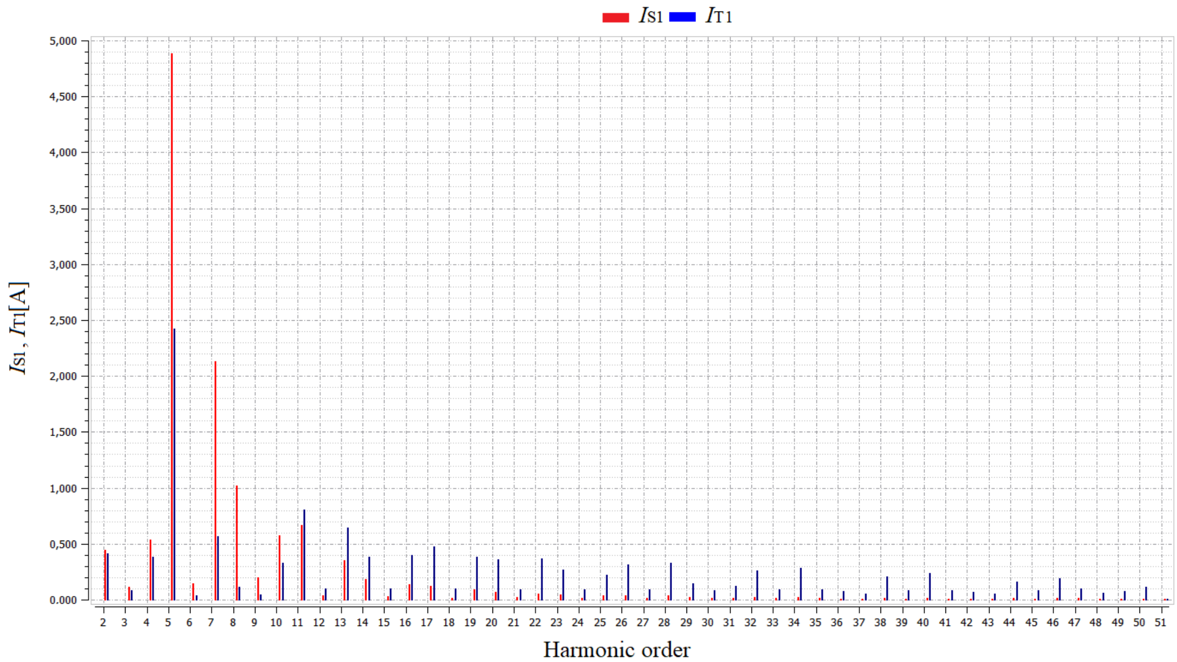

Figure 4.68 Grid and input rectifier current spectrum (measured)

In Figure 4.70(b), the cross point between the power system impedance seen from the rectifier input (characteristic in blue color) and the electrical grid plus line reactor inductance (characteristic in black broken line) is at the frequency of 532.1 Hz (n = 10.64) also called neutral frequency. Below that frequency, the grid current and voltage harmonics are amplified (e.g. 3^{rd}, 5^{th}, 7^{th} etc.) and above that frequency, they are mitigated (e.g. 11^{th}, 12^{th}, etc. - Figure 4.68).

The grid voltage and current waveforms are more distorted after the capacitor bank connection and in such of situation; the detuning reactor is needed to move the parallel resonance below the 5^{th} harmonic frequency.

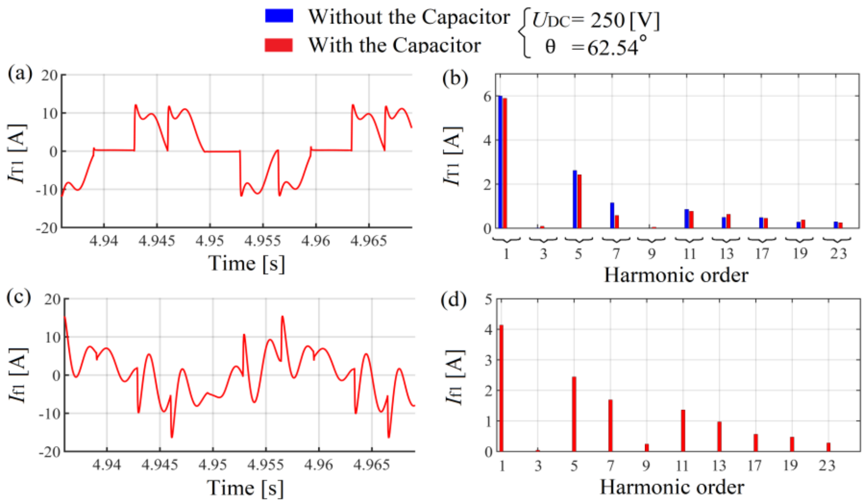

Figure 4.69 (a) input rectifier current and (b) its spectrum, (c) capacitor bank current and (d) its spectrum (meausred)

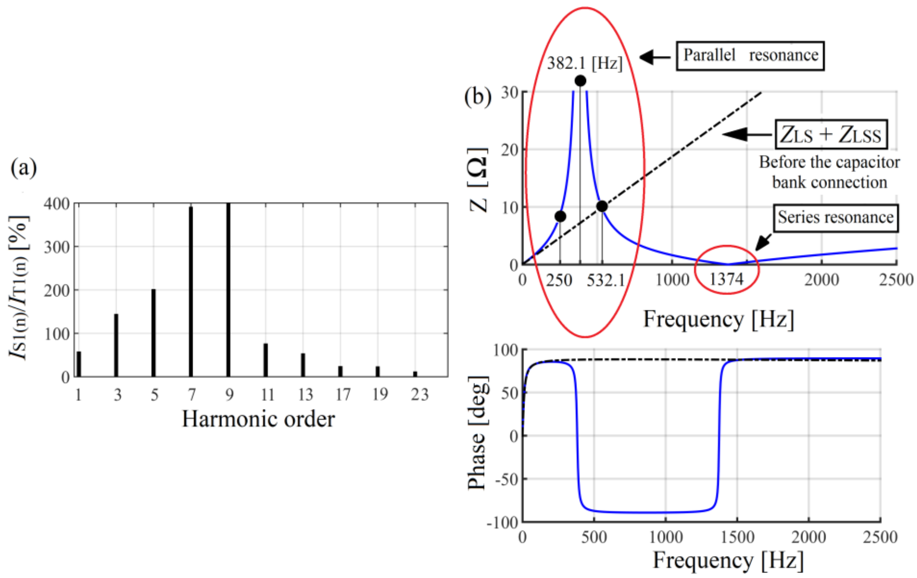

Figure 4.70 (a) capacitor bank efficiency in term of harmonics mitigation at the grid side (measured), (b) impedance versus frequency characteristic of power system simulated at the rectifier input

4.6 Design of the 2^{nd} order filter

The laboratory second order filter is designed by connecting the damping resistor R_{2nd} in parallel with the designed single-tuned filter reactor as presented in Figure 4.71.

The experimental study is set to confirm the theoretical explanation of the second-order filter behaviour when the damping resistance is changed. The power system data (see also Table 4.12) are recorded (for θ = 62.54°) when the damping resistance is not connected (R_{2nd} = inf, single filter) and when it is connected with the values sets to 28.7 Ω, 17.5 Ω, 11.7 Ω, and 2.2 Ω.

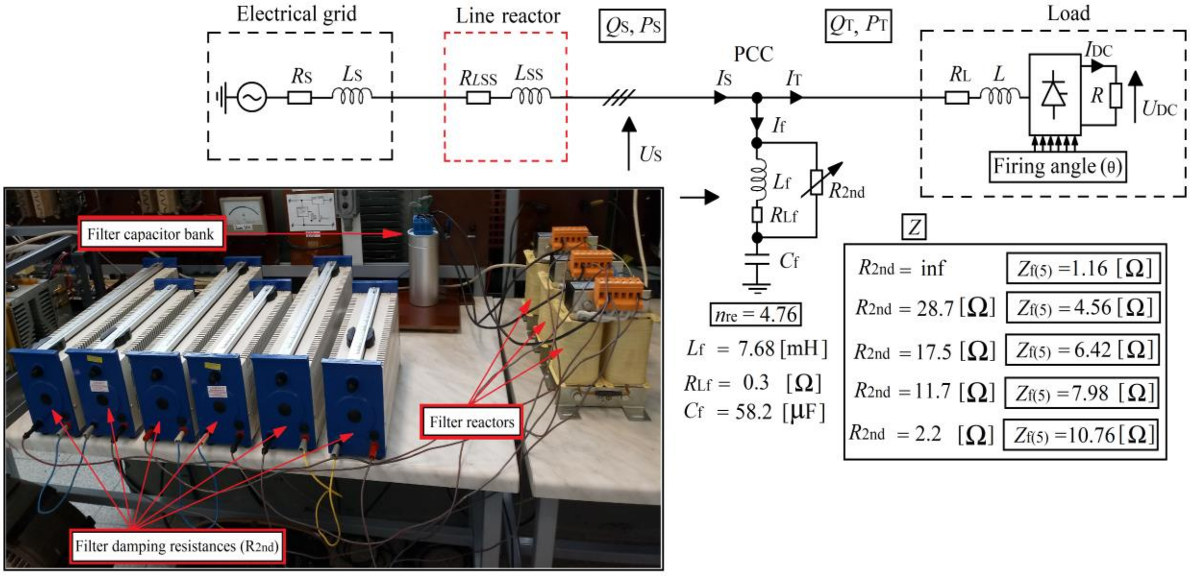

Figure 4.71 Power system equivalent circuit with the second-order filter

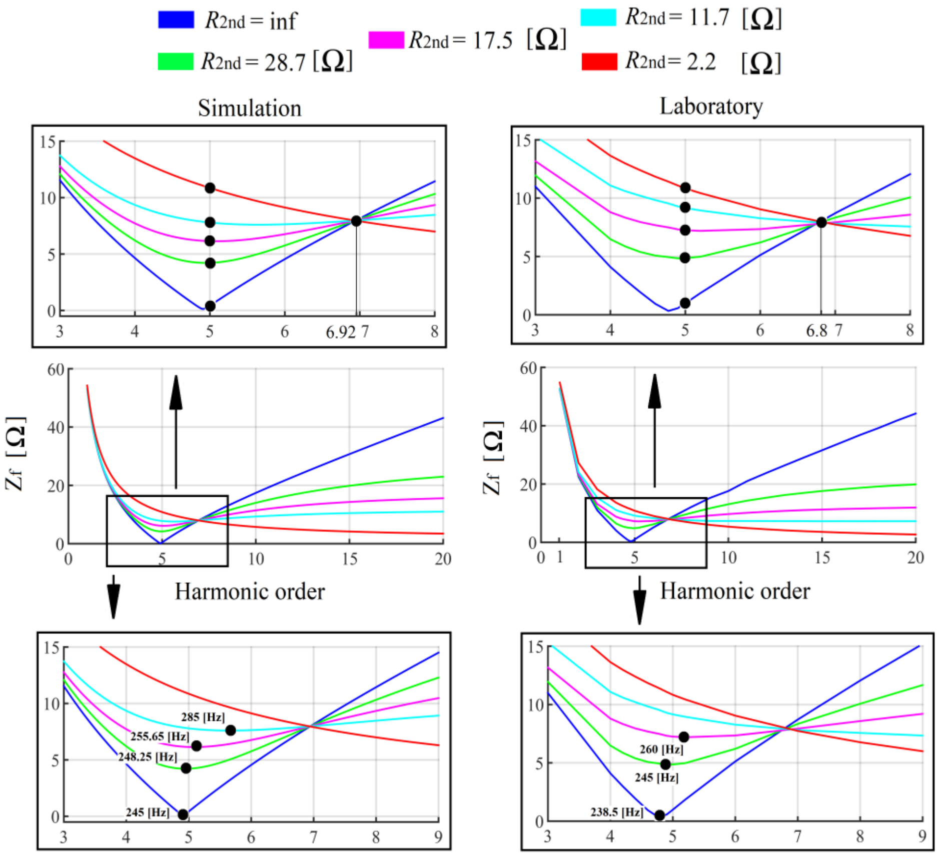

Figure 4.72 Second-order filter impedance versus frequency characteristics: (a) simulated (expected) characteristics, (b) measured characteristics

The impedance versus frequency characteristic of second-order filter resembles the one of single filter when damping resistance is very high (e.g. R_{2nd} = inf). When the damping resistance is very small (e.g. R_{2nd} = 2.2 Ω), it resembles the capacitors bank characteristic (Figure 4.72). With the damping resistance decrease, the filter impedance of 5th order harmonic increases as well as the filter resonance frequency (Form 245 Hz to 285 Hz in Figure 4.72(a) and from 238.5 Hz to 260 Hz in Figure 4.72(b)). The PCC reactive power has increased (From 84.54 Var to 151.27 Var) with the damping resistance increase (Table 4.12).

Table 4.12 Fundamental harmonic active and reactive power measured in the laboratory model at the grid side, filter terminals and rectifier input

U_{DC} = 250 V, θ = 62.54°					
R_{2nd} [Ω]	$P_{S1(1)}$ [W]	$Q_{S1(1)}$ [Var]	$P_{f1(1)}$ [W]	$Q_{f1(1)}$ [Var]	$Q_{T1(1)}$ [Var]
Inf. (single-tuned filter)	818.29	84.54	17.53	-992.40	1078.0
28.7	831.32	91.84	14.56	-975.15	1066.7
17.5	838.79	111.52	11.20	-975.88	1086.9
11.7	829.59	133.83	13.15	-964.91	1097.9
2.2	799.05	151.27	7.26	-945.67	1095.7

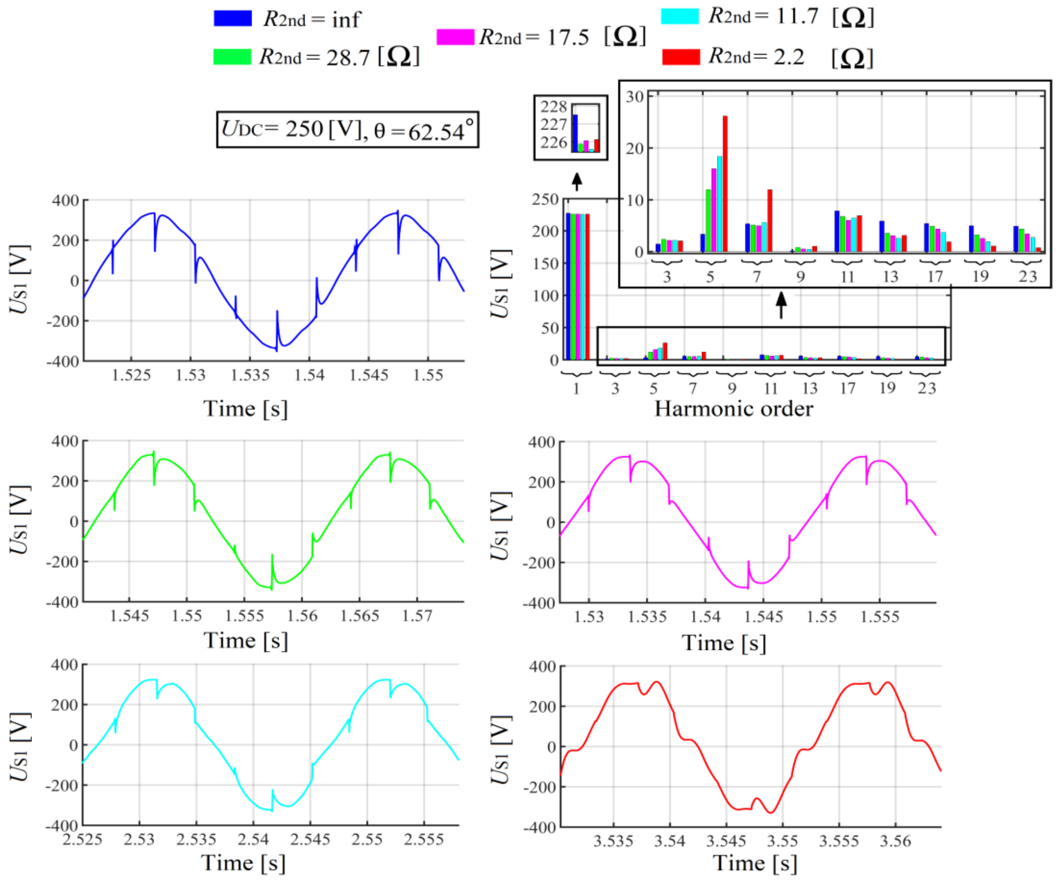

Figure 4.73 Grid voltage waveforms and spectrums (measured)

With the second-order filter damping resistance decrease, the grid voltage and current are more distorted (see waveforms of Figure 4.73 and Figure 4.74 as well as the THDs of Figure 4.77(a)(b)) and the 5th and 7th harmonics amplitudes are amplified (see spectrums of Figure 4.73 and Figure 4.74). Although the filter with small values of damping resistance (e.g.) gives a worse filtration of 5th harmonic, it ensures a batter reduction of higher harmonics in wide band (e.g. From the 17th harmonic – spectrums in Figure 4.73 and Figure 4.74). The waveforms and spectrums measured at the input rectifier and filter terminals are respectively presented in Figure 4.75 and Figure 4.76.

With small damping resistance, the second-order filter is more efficient on higher harmonics reduction (e.g. 13th to 23rd – Figure 4.77(c)). But that small value should be chosen in such a way to not amplified (grid side) the harmonic to be eliminated and hamonics around It. In Figure 4.78, it can be seen that the harmonic to be eliminated (e.g. 5th) is under the parallel resonance band when the damping resistance is very small (e.g. 2.2 Ω). The second-order filter with high damping resistance (R_{2nd} = inf, Single filter) presents the best results in term of 5th harmonic and THD reduction. Basing on its damping resistance, the second-order filter is better than the single filter in term of harmonics mitigation in wide band (higher harmonics).

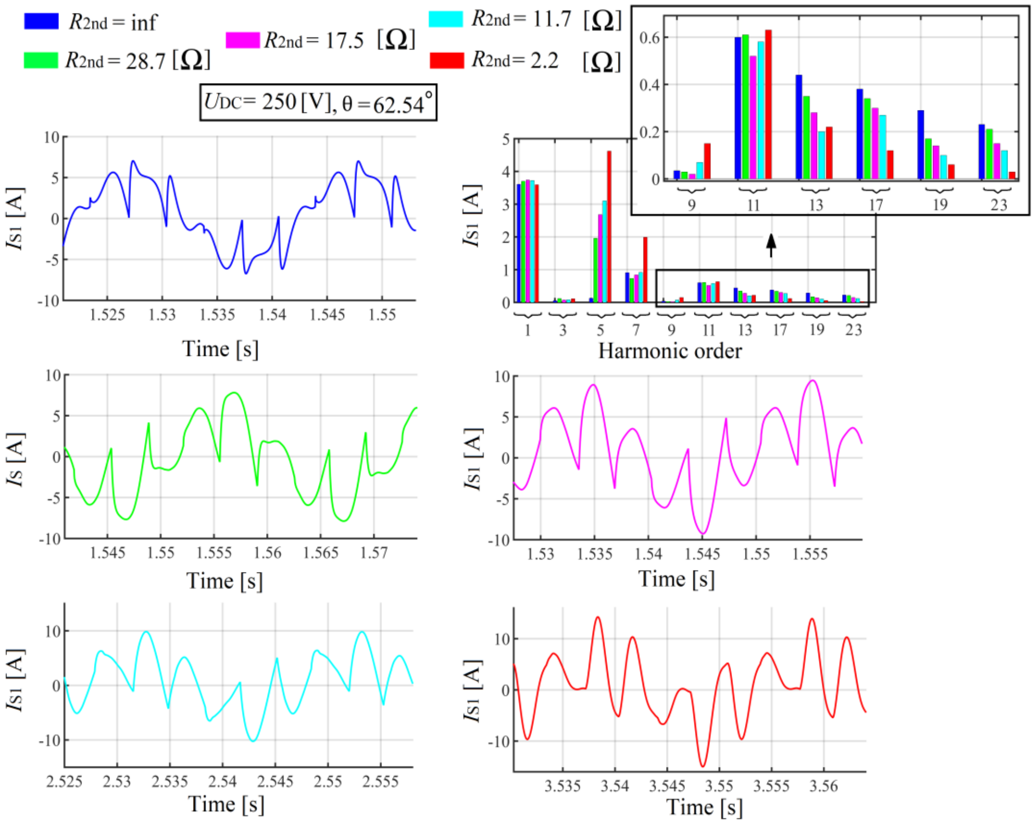

Figure 4.74 Grid current waveforms and spectrums (measured)

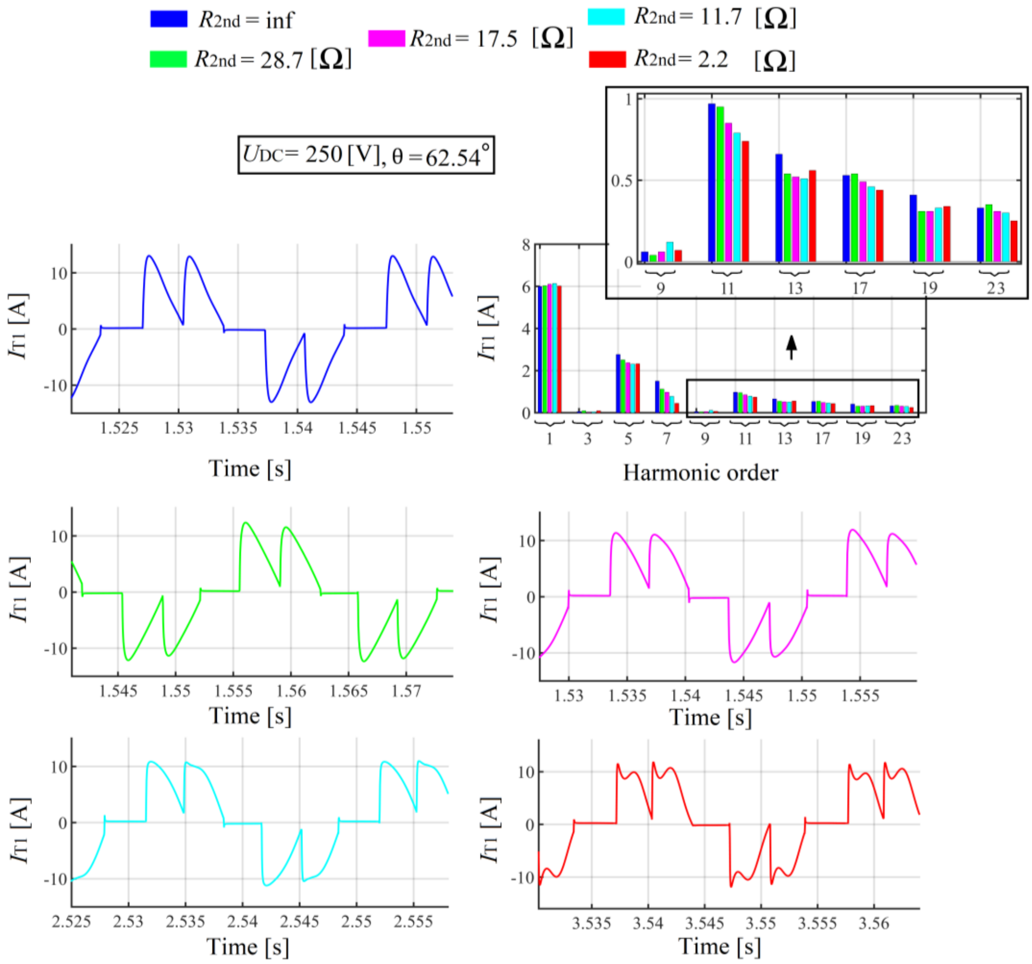

Figure 4.75 Input rectifier current waveforms and spectrum (measured)

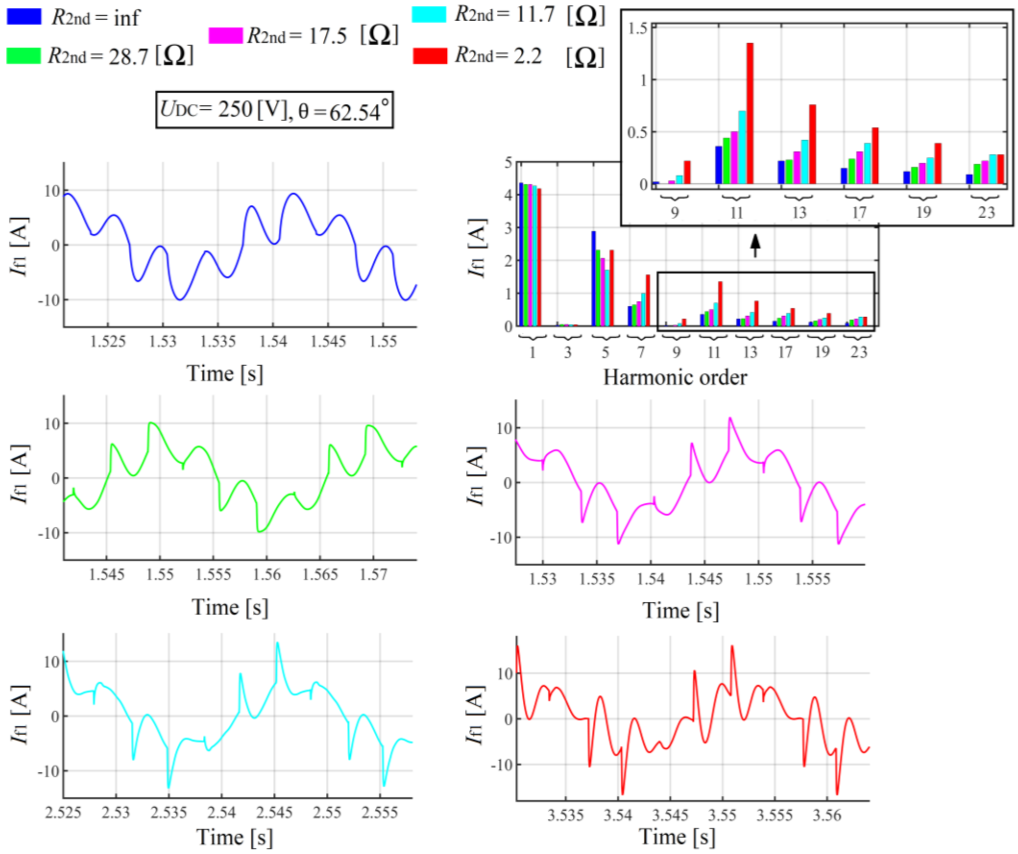

Figure 4.76 Filter current waveforms and spectrum (measured)

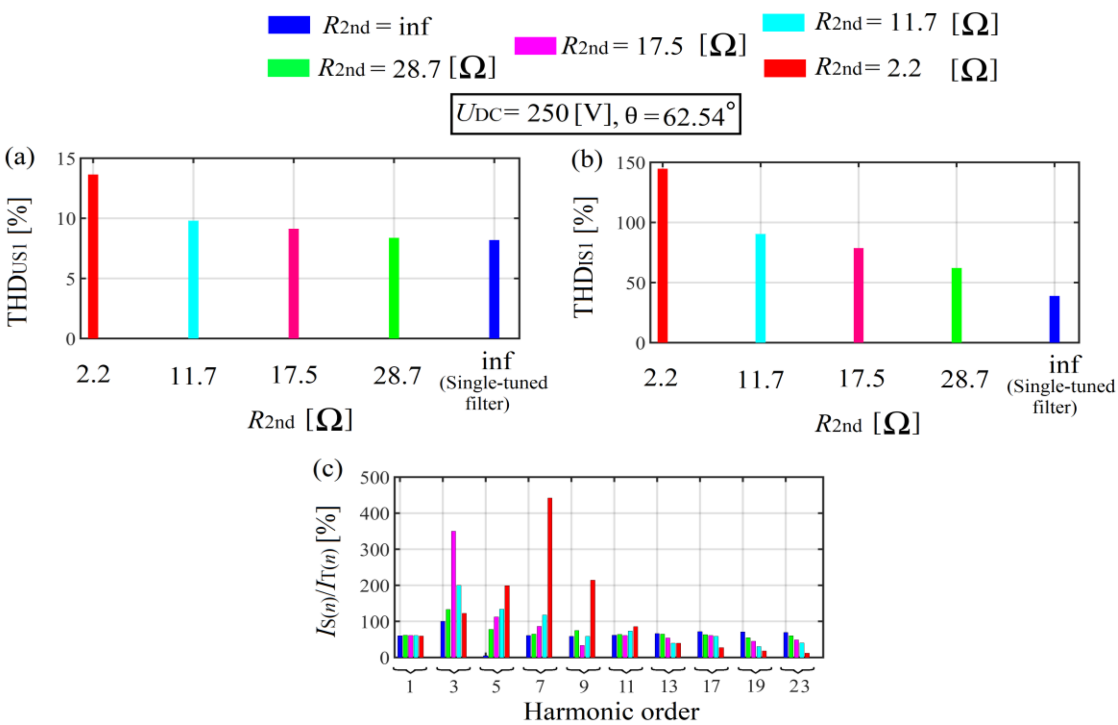

Figure 4.77 THD of grid voltage (a) and current (b), 2nd order filter efficiency (measured)

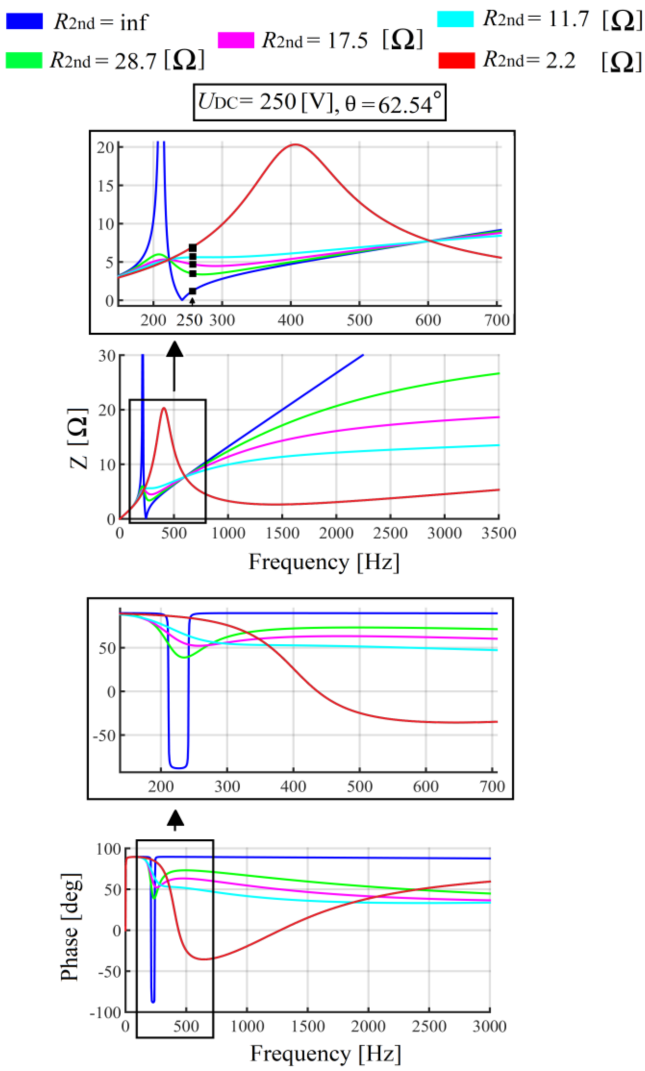

Figure 4.78 Simulated impedance versus frequency characteristics of power system seen from the rectifier input

Chapter 5
Shunt active power filter

This chapter is about the investigation (based on simulations) of SAPF structure presented in Figure 2.11(a) (Chapter 2). A control system algorithm based on the instantaneous *p-q* theory is proposed by the author. The studies of the influence of the electrical grid inductance, the inverter input reactor, DC capacitor and the load input reactor parameters on the SAPF filtration efficiency are presented. The investigated model of SAPF will be used as a part of hybrid active power filter which is presented in Chapter 6 (Figure 6.1).

Some laboratory experiements are also presented in this chapter. The first one is performed on the model of three legs four wires SAPF presenting the influence of the rectifier inpout reactor as well as the grid side line reactor on its efficieny. The second one is perfomed on the hybrid active power filter (model of Figure 2.13(l) – Chapter 2).

5.1 Instantaneous *p-q* theory

The algorithms applied for the SAPF control system exist in several examples. The difference between them (in the most cases) is based on the type of power theory adapted for reference current generation [21, 47, 175]. The control system algorithm under investigation in this chapter is based on the instantaneous *p-q* theory. The time domain instantaneous power theory [10] also called *p-q* theory is widely applied in voltage source inverter (VSI) control system algorithms [152, 254]. It was proposed and published by Akagi Kanazawa et al. in 1983 [7, 8].

The goal of its application in control systems is to deliver the reference current by basing on the determination of the instantaneous real and imaginary powers. With the *p-q* theory, the power system with current disturbances (harmonic, reactive power and asymmetry) can be compensated in steady and transient states [5, 248, 199]. It is not generalized theory of powers because it can only be applied in three phase system [67, 198, 199, 248]. In some papers, its physical interpretation is criticised [66].

In three-phase system ((u_a, u_b, u_c), (i_a, i_b, i_c)) the total instantaneous power is represented by (5.3). In rectangular system (α-β) the total instantaneous real power is represented by (5.4). The total instantaneous power in three-phase system (p_{total}) is conserved during the transformation (from *a-b-c* to α-β), therefore is equal to the instantaneous real power in α-β system ($p_{\text{total}} = p_{\alpha\beta}$ [202, 198].

The concept of instantaneous imaginary power q (5.8) is introduced by supposing an imaginary axis in perpendicular connection with the $\alpha\beta$ plan (Figure 5.2) [7].

The definitions of instantaneous real and imaginary power in the space vector (Figure 5.2) lead to the computation of instantaneous currents in α-β axes. The expressions (5.11) and (5.12) show that the instantaneous currents in α-β axes depends upon the instantaneous voltage and the instantaneous real (p) and imaginary (q) powers.

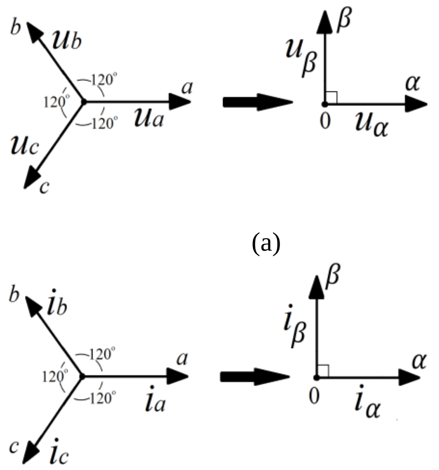

(a)

(b)

Figure 5.1 Vectors representation of voltage (a) and current (b): transformation *a-b-c* into α-β

$$\begin{bmatrix} u_\alpha \\ u_\beta \\ u_0 \end{bmatrix} = \sqrt{\frac{2}{3}} \begin{bmatrix} 1 & -1/2 & -1/2 \\ 0 & \sqrt{3}/2 & -\sqrt{3}/2 \\ 1/\sqrt{2} & 1/\sqrt{2} & 1/\sqrt{2} \end{bmatrix} \begin{bmatrix} u_a \\ u_b \\ u_c \end{bmatrix} \tag{5.1}$$

u_α - instantaneous voltage in α axis
u_β - instantaneous voltage in β axis
u_0 - zero sequence component

$$\begin{bmatrix} i_\alpha \\ i_\beta \\ i_0 \end{bmatrix} = \sqrt{\frac{2}{3}} \begin{bmatrix} 1 & -1/2 & -1/2 \\ 0 & \sqrt{3}/2 & -\sqrt{3}/2 \\ 1/\sqrt{2} & 1/\sqrt{2} & 1/\sqrt{2} \end{bmatrix} \begin{bmatrix} i_a \\ i_b \\ i_c \end{bmatrix} \tag{5.2}$$

i_α - instantaneous current in α axis
i_β - instantaneous current in β axis
i_0 - zero sequence component

$$p_{\text{total}} = u_a i_a + u_b i_b + u_c i_c \tag{5.3}$$

$$p_{\alpha\beta} = u_\alpha i_\alpha + u_\beta i_\beta \tag{5.4}$$

$$\begin{bmatrix} u_\alpha \\ u_\beta \end{bmatrix} = \sqrt{\frac{2}{3}} \begin{bmatrix} 1 & -1/2 & -1/2 \\ 0 & \sqrt{3}/2 & -\sqrt{3}/2 \end{bmatrix} \begin{bmatrix} u_a \\ u_b \\ u_c \end{bmatrix} \tag{5.5}$$

$$\begin{bmatrix} i_\alpha \\ i_\beta \end{bmatrix} = \sqrt{\frac{2}{3}} \begin{bmatrix} 1 & -1/2 & -1/2 \\ 0 & \sqrt{3}/2 & -\sqrt{3}/2 \end{bmatrix} \begin{bmatrix} i_a \\ i_b \\ i_c \end{bmatrix} \tag{5.6}$$

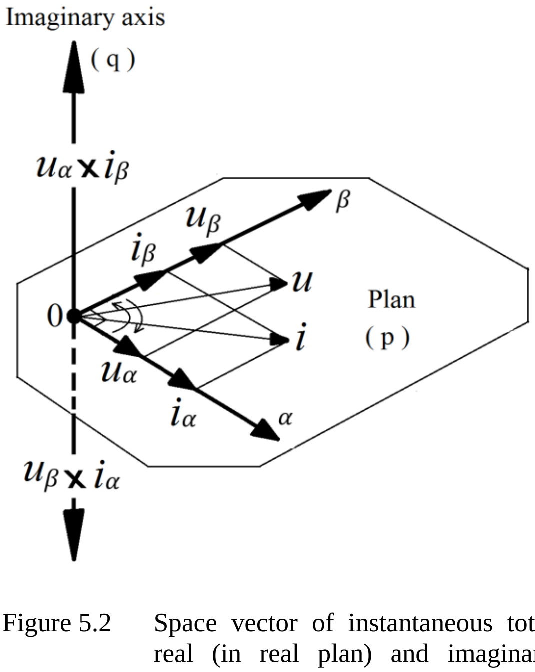

Figure 5.2 Space vector of instantaneous total real (in real plan) and imaginary power (imaginary axis) [7]

$$p = p_{\alpha\beta} = u_\alpha i_\alpha + u_\beta i_\beta \tag{5.7}$$

$$q = u_\alpha \times i_\beta + u_\beta \times i_\alpha = u_\alpha i_\beta - u_\beta i_\alpha \tag{5.8}$$

$$\begin{bmatrix} p \\ q \end{bmatrix} = \begin{bmatrix} u_\alpha & u_\beta \\ -u_\beta & u_\alpha \end{bmatrix} \begin{bmatrix} i_\alpha \\ i_\beta \end{bmatrix} \tag{5.9}$$

$$\begin{bmatrix} i_\alpha \\ i_\beta \end{bmatrix} = \frac{1}{u_\alpha^2 + u_\beta^2} \begin{bmatrix} u_\alpha & -u_\beta \\ u_\beta & u_\alpha \end{bmatrix} \begin{bmatrix} p \\ q \end{bmatrix} \tag{5.10}$$

$$i_\alpha = \frac{u_\alpha}{u_\alpha^2 + u_\beta^2} p + \frac{-u_\beta}{u_\alpha^2 + u_\beta^2} q \tag{5.11}$$

$$i_\beta = \frac{u_\beta}{u_\alpha^2 + u_\beta^2} p + \frac{u_\alpha}{u_\alpha^2 + u_\beta^2} q \tag{5.12}$$

$$p = \tilde{p} + \bar{p} = \tilde{p}_{2\text{n}} + \tilde{p}_{\text{h}} + \bar{p} \tag{5.13}$$

$$\tilde{p} = \tilde{p}_{2\text{n}} + \tilde{p}_{\text{h}} \tag{5.14}$$

$$q = \tilde{q} + \bar{q} = \tilde{q}_{2\text{n}} + \tilde{q}_{\text{h}} + \bar{q} \tag{5.15}$$

$$\tilde{q} = \tilde{q}_{2\text{n}} + \tilde{q}_{\text{h}} \tag{5.16}$$

$$\begin{cases} i_\alpha = \frac{u_\alpha}{u_\alpha^2+u_\beta^2}\bar{p} + \frac{u_\alpha}{u_\alpha^2+u_\beta^2}\tilde{p} + \frac{-u_\beta}{u_\alpha^2+u_\beta^2}\bar{q} + \frac{-u_\beta}{u_\alpha^2+u_\beta^2}\tilde{q} \\ i_\beta = \frac{u_\beta}{u_\alpha^2+u_\beta^2}\bar{p} + \frac{u_\beta}{u_\alpha^2+u_\beta^2}\tilde{p} + \frac{u_\alpha}{u_\alpha^2+u_\beta^2}\bar{q} + \frac{u_\alpha}{u_\alpha^2+u_\beta^2}\tilde{q} \end{cases} \tag{5.17}$$

$$\begin{cases} i_\alpha = +\frac{u_\alpha}{u_\alpha^2+u_\beta^2}\tilde{p}_{2n} + \frac{-u_\beta}{u_\alpha^2+u_\beta^2}\tilde{q}_{2n} + \frac{-u_\beta}{u_\alpha^2+u_\beta^2}\bar{q} + \frac{-u_\beta}{u_\alpha^2+u_\beta^2}\tilde{q}_h \frac{u_\alpha}{u_\alpha^2+u_\beta^2}\tilde{p}_h + \frac{u_\alpha}{u_\alpha^2+u_\beta^2}\bar{p} = i_{\alpha(2n)} + i_{\alpha(\bar{q})} + i_{\alpha(h)} + i_{\alpha(\bar{p})} \\ i_\beta = \frac{u_\beta}{u_\alpha^2+u_\beta^2}\tilde{p}_{2n} + \frac{u_\alpha}{u_\alpha^2+u_\beta^2}\tilde{q}_{2n} + \frac{u_\alpha}{u_\alpha^2+u_\beta^2}\bar{q} + \frac{u_\alpha}{u_\alpha^2+u_\beta^2}\tilde{q}_h + \frac{u_\beta}{u_\alpha^2+u_\beta^2}\tilde{p}_h + \frac{u_\beta}{u_\alpha^2+u_\beta^2}\bar{p} = i_{\beta(2n)} + i_{\beta(\bar{q})} + i_{\beta(h)} + i_{\beta(\bar{p})} \end{cases} \tag{5.18}$$

Table 5.1 Description of the instantaneous real and imaginary current (in $\alpha\beta$ axes) from expression (5.17) [254]

$i_{\alpha(p)} = \frac{u_\alpha}{u_\alpha^2+u_\beta^2}\bar{p} + \frac{u_\alpha}{u_\alpha^2+u_\beta^2}\tilde{p}$ (5.19)	Instantaneous real current in α axis
$i_{\alpha(q)} = \frac{-u_\beta}{u_\alpha^2+u_\beta^2}\bar{q} + \frac{-u_\beta}{u_\alpha^2+u_\beta^2}\tilde{q}$ (5.20)	Instantaneous imaginary current in α axis
$i_{\beta(p)} = \frac{u_\beta}{u_\alpha^2+u_\beta^2}\bar{p} + \frac{u_\beta}{u_\alpha^2+u_\beta^2}\tilde{p}$ (5.21)	Instantaneous real current in β axis
$i_{\beta(q)} = \frac{u_\alpha}{u_\alpha^2+u_\beta^2}\bar{q} + \frac{u_\alpha}{u_\alpha^2+u_\beta^2}\tilde{q}$ (5.22)	Instantaneous imaginary current in β axis

Table 5.2 Instantaneous current components description (in $\alpha\beta$ axes) from expression (5.18) [254]

$i_{\alpha(\bar{p})} = \frac{u_\alpha}{u_\alpha^2+u_\beta^2}\bar{p}$ (5.23)	Instantaneous real current (fundamental harmonic) in α axis	$i_{\beta(\bar{p})} = \frac{u_\beta}{u_\alpha^2+u_\beta^2}\bar{p}$ (5.29)	Instantaneous real current (fundamental harmonic) in β axis
$i_{\alpha(\tilde{p}_{2n})} = \frac{u_\alpha}{u_\alpha^2+u_\beta^2}\tilde{p}_{2n}$ (5.24) $i_{\alpha(\tilde{q}_{2n})} = \frac{-u_\beta}{u_\alpha^2+u_\beta^2}\tilde{q}_{2n}$ (5.25)	Instantaneous asymmetry current in α axis	$i_{\beta(\tilde{p}_{2n})} = \frac{u_\beta}{u_\alpha^2+u_\beta^2}\tilde{p}_{2n}$(5.30) $i_{\beta(\tilde{q}_{2n})} = \frac{u_\alpha}{u_\alpha^2+u_\beta^2}\tilde{q}_{2n}$(5.31)	Instantaneous asymmetry current in β axis
$i_{\alpha(\tilde{p}_h)} = \frac{u_\alpha}{u_\alpha^2+u_\beta^2}\tilde{p}_h$ (5.26) $i_{\alpha(\tilde{q}_h)} = \frac{-u_\beta}{u_\alpha^2+u_\beta^2}\tilde{q}_h$ (5.27)	Instantaneous harmonic current in α axis	$i_{\beta(\tilde{p}_h)} = \frac{u_\beta}{u_\alpha^2+u_\beta^2}\tilde{p}_h$ (5.32) $i_{\beta(\tilde{q}_h)} = \frac{u_\alpha}{u_\alpha^2+u_\beta^2}\tilde{q}_h$ (5.33)	Instantaneous harmonic current in β axis
$i_{\alpha(\bar{q})} = \frac{-u_\beta}{u_\alpha^2+u_\beta^2}\bar{q}$ (5.28)	Instantaneous imaginary current (fundamental harmonic) in α axis	$i_{\beta(\bar{q})} = \frac{u_\alpha}{u_\alpha^2+u_\beta^2}\bar{q}$ (5.34)	Instantaneous imaginary current (fundamental harmonic) in β axis
2n – frequency of harmonic asymmetry component			

The components u_0 and i_0 (zero-phase sequence components) in the expressions (5.1) and (5.2) are not considered in the expressions (5.5) and (5.6), because the neutral wire is neglected (three-phase three wires nonlinear load).

The powers p and q (in α-β coordinates) can be divided into two components as presented in (5.13) and (5.15): $\tilde{p}$, $\tilde{q}$ - variable components, $\bar{p}$, $\bar{q}$ - constant components. According to [198] ($\bar{p}$, $\bar{q}$) are related to the fundamental harmonic (positive sequence) of current and ($\tilde{p}$, $\tilde{q}$) are related to the current harmonics and current asymmetry (negative sequence of fundamental harmonic) as presented in (5.14) and (5.16).The instantaneous currents in α and in β axes are split into different components as shown in (5.17) and (5.18).

Different instantaneous real and imaginary current in α and β axes are presented Table 5.1 to Table 5.3.

The instantaneous asymmetry currents are expressed in α and β axes by (5.24), (5.25), (5.30) and (5.31) in Table 5.2 and by (5.41) and (5.42) in Table 5.3.

The instantaneous harmonic currents are expressed by (5.26) and (5.27) in α axis and by (5.32) and (5.33) in β axis (Table 5.2). The instantaneous reference currents in α-β axes are depicted by (5.43).

After the invers transformation from α-β to a-b-c, the instantaneous active, asymmetry, reactive and harmonic current components are respectively expressed by (5.44), (5.45), (5.46) and (5.47). The needed reference current for the PWM system is expressed by (5.48).

Table 5.3 Instantaneous harmonic, imaginary, real and asymmetry current components in $\alpha\beta$ axes (from Table 5.2) [254]

$i_{\alpha(\mathrm{h})} = \frac{u_\alpha}{u_\alpha^2+u_\beta^2}\tilde{p}_{\mathrm{h}} + \frac{-u_\beta}{u_\alpha^2+u_\beta^2}\tilde{q}_{\mathrm{h}}$ (5.35) $i_{\beta(\mathrm{h})} = \frac{u_\beta}{u_\alpha^2+u_\beta^2}\tilde{p}_{\mathrm{h}} + \frac{u_\alpha}{u_\alpha^2+u_\beta^2}\tilde{q}_{\mathrm{h}}$ (5.36)	Instantaneous harmonic current (for harmonics compensation)
$i_{\alpha(\bar{q})} = \frac{-u_\beta}{u_\alpha^2+u_\beta^2}\bar{q}$ (5.37) $i_{\beta(\bar{q})} = \frac{u_\alpha}{u_\alpha^2+u_\beta^2}\bar{q}$ (5.38)	Instantaneous imaginary current (fundamental harmonic – reactive power compensation)
$i_{\alpha(\bar{p})} = \frac{u_\alpha}{u_\alpha^2+u_\beta^2}\bar{p}$ (5.39) $i_{\beta(\bar{p})} = \frac{u_\beta}{u_\alpha^2+u_\beta^2}\bar{p}$ (5.40)	Instantaneous real current (fundamental harmonic – active power)
$i_{\alpha(2\mathrm{n})} = \frac{u_\alpha}{u_\alpha^2+u_\beta^2}\tilde{p}_{2\mathrm{n}} + \frac{-u_\beta}{u_\alpha^2+u_\beta^2}\tilde{q}_{2\mathrm{n}}$ (5.41) $i_{\beta(2\mathrm{n})} = \frac{u_\beta}{u_\alpha^2+u_\beta^2}\tilde{p}_{2\mathrm{n}} + \frac{u_\alpha}{u_\alpha^2+u_\beta^2}\tilde{q}_{2\mathrm{n}}$ (5.42)	Instantaneous asymmetry current (asymmetry compensation)

$$\begin{cases} i_{\alpha(\mathrm{ref})} = i_\alpha - i_{\alpha(\bar{p})} = i_{\alpha(2\mathrm{n})} + i_{\alpha(\mathrm{h})} + i_{\alpha(\bar{q})} \\ i_{\beta(\mathrm{ref})} = i_\beta - i_{\beta(\bar{p})} = i_{\beta(2\mathrm{n})} + i_{\beta(\mathrm{h})} + i_{\beta(\bar{q})} \end{cases} \tag{5.43}$$

$$\begin{bmatrix} i_{a\_(\bar{p})} \\ i_{b\_(\bar{p})} \\ i_{c\_(\bar{p})} \end{bmatrix} = \sqrt{\frac{2}{3}} \begin{bmatrix} 1 & -1/2 & -1/2 \\ 0 & \sqrt{3}/2 & -\sqrt{3}/2 \end{bmatrix} \begin{bmatrix} i_{\alpha(\bar{p})} \\ i_{\beta(\bar{p})} \end{bmatrix} \tag{5.44}$$

$$\begin{bmatrix} i_{a\_(\mathrm{asymmetry})} \\ i_{b\_(\mathrm{asymmetry})} \\ i_{c\_(\mathrm{asymmetry})} \end{bmatrix} = \sqrt{\frac{2}{3}} \begin{bmatrix} 1 & -1/2 & -1/2 \\ 0 & \sqrt{3}/2 & -\sqrt{3}/2 \end{bmatrix} \begin{bmatrix} i_{\alpha(2\mathrm{n})} \\ i_{\beta(2\mathrm{n})} \end{bmatrix} \tag{5.45}$$

$$\begin{bmatrix} i_{a\_(\bar{q})} \\ i_{b\_(\bar{q})} \\ i_{c\_(\bar{q})} \end{bmatrix} = \sqrt{\frac{2}{3}} \begin{bmatrix} 1 & -1/2 & -1/2 \\ 0 & \sqrt{3}/2 & -\sqrt{3}/2 \end{bmatrix} \begin{bmatrix} i_{\alpha(\bar{q})} \\ i_{\beta(\bar{q})} \end{bmatrix} \tag{5.46}$$

$$\begin{bmatrix} i_{a\_(\mathrm{harmonic})} \\ i_{b\_(\mathrm{harmonic})} \\ i_{c\_(\mathrm{harmonic})} \end{bmatrix} = \sqrt{\frac{2}{3}} \begin{bmatrix} 1 & -1/2 & -1/2 \\ 0 & \sqrt{3}/2 & -\sqrt{3}/2 \end{bmatrix} \begin{bmatrix} i_{\alpha(\mathrm{h})} \\ i_{\beta(\mathrm{h})} \end{bmatrix} \tag{5.47}$$

$$i_{abc\_(\mathrm{ref})} = i_{abc\_(\bar{q})} + i_{abc\_(\mathrm{harmonic})} + i_{abc\_(\mathrm{asymmetry})} \tag{5.48}$$

5.1.1 Example of *p-q* theory application

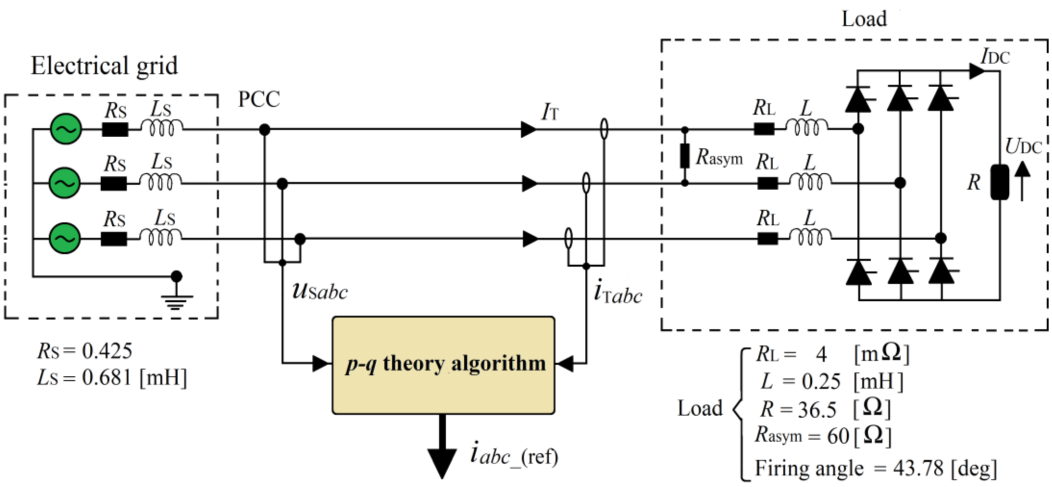

Figure 5.3 Equivalent circuit of the simulated power system

The simulated power system for the *p-q* theory application is presented in Figure 5.3 (see Annex I, Table I.4 for the electrical grid paramters and chapter 4, Figure 4.2 for the load parameters (input rectifier reactor and DC side resistance)). The electrical grid equivalent inductance in Figure 5.3 is around 21.64 times higher than the estimeted laboratory model grid inductance in Figure 4.2 (see also Figure 4.6(b)). The resistor R_{asym} is used to create a current unbalance condition in this example. The goal of applying the *p-q* theory is to split the power system current (I_T) into different components: active, reactive, asymmetry and harmonics.

Two investigation cases are considered. The first one is the application of *p-q* theory under symmetrical but distorted supply voltage and the second one is about the filtration of the supply voltage before its application in the *p-q* theory algorithm (Figure 5.13). Through the two investigated cases, it is demonstrated that the supply voltage distortion affects (or are present in) the obtained reference current ($i_{abc\_(ref)}$). The *p-q* theory algorithm designed in MATLAB-SIMULINK is described in Annex V. The simulated data are recorded for a constant rectifier firing angle (θ = 43.78º).

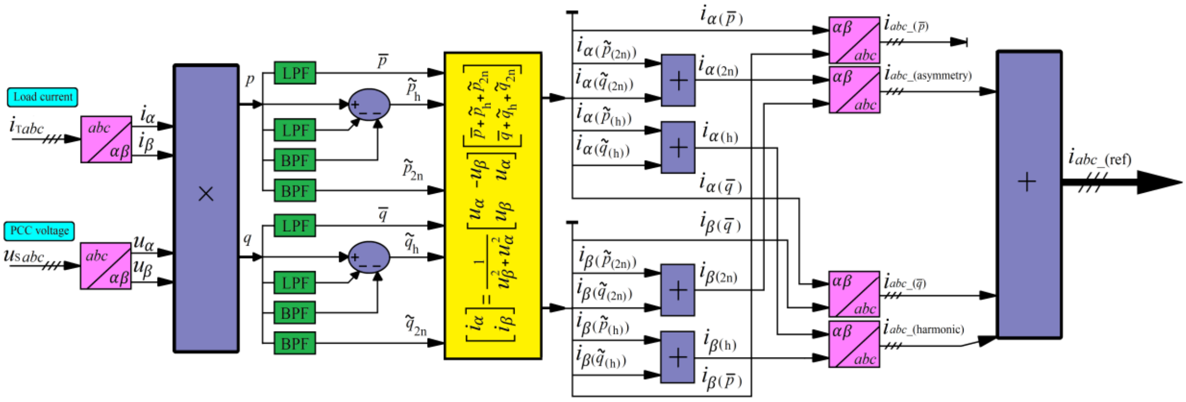

Figure 5.4 *p-q* theory algorithm applied in the system of Figure 5.3. The blocks in green color represent the Butterworth filters (HPF – high pass filter, LPF – low pass filter, BPF – band pass filter) (see Annex V)

5.1.1.1 Application of *p-q* theory under symmetrical but distorted supply voltage

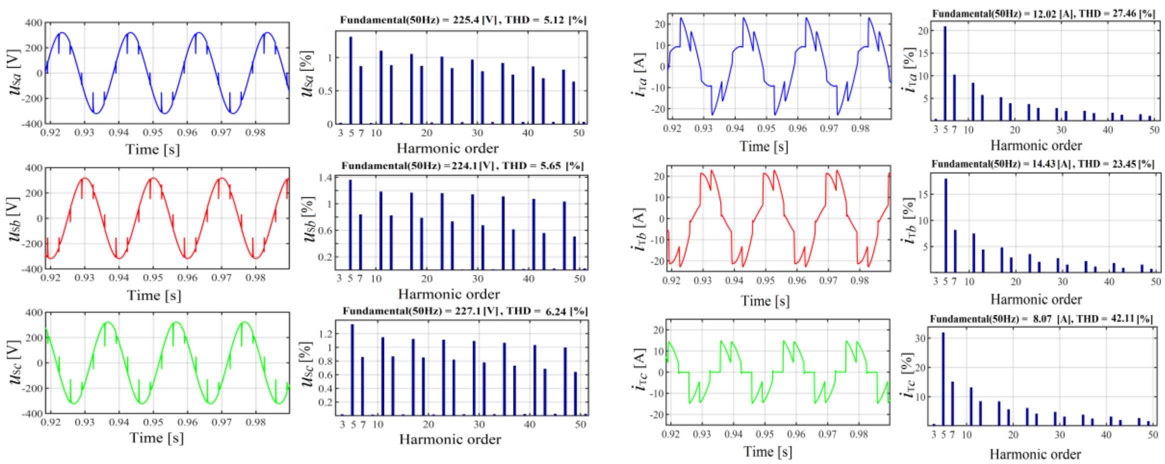

Figure 5.5 Waveforms of supply voltage (a) and load current (b) with spectrums

The input parameters of *p-q* algorithm (Figure 5.4) are the grid voltages (U_{Sabc}) and load currents (I_{Tabc}). The load currents are distorted, unbalance (with the negative sequence of 32.89 % - see also Figure 5.5(b)) and phase shifted with the grid voltage (Figure 5.3 - firing angle). The load current asymmetry has affected also the supply voltage (0.78 % of negative sequence) but in small scale (see spectrum in Figure 5.5(a), the THD and RMS are a little different in each phase). The grid voltage waveforms are also distorted by commutation notches (Figure 5.5(a)).

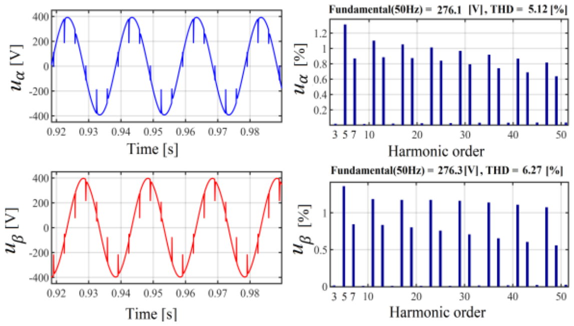

(a)

Figure 5.6 PCC voltage waveforms in α-β coordinates with spectrums

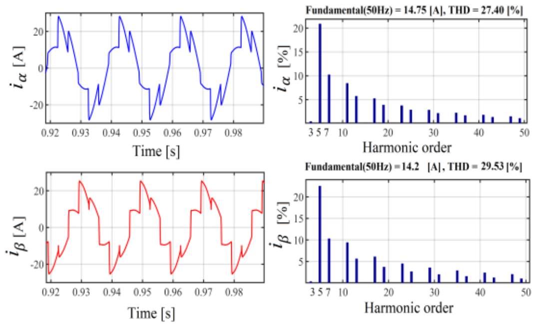

(b)

Figure 5.7 Load current waveforms in α-β coordinates with spectrums

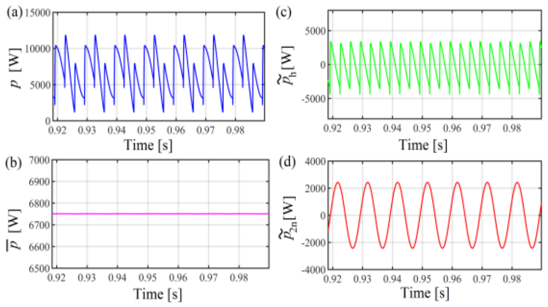

Figure 5.8 (a) instantaneous real powers in α-β coordinates: (b) constant part; (c) part related to the harmonics; (d) part related to the asymmetry

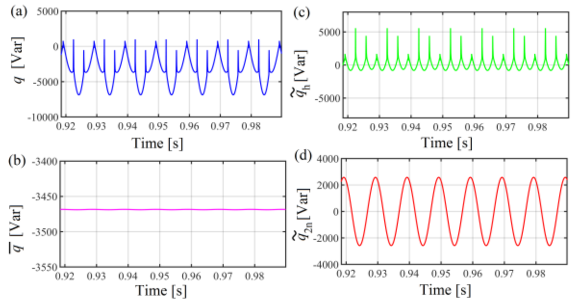

Figure 5.9 (a) instantaneous imaginary powers in α-β coordinates: (b) constant part; (c) part related to the harmonics; (d) part related to the asymmetry

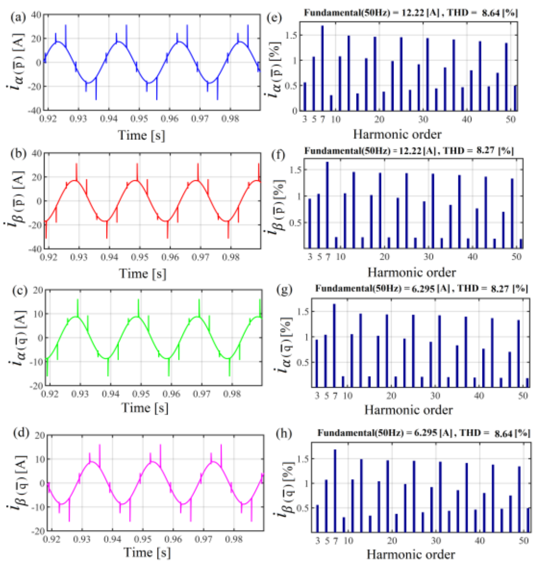

Figure 5.10 (a), (b) waveforms of instantaneous real current in α-β coordinates with their spectrums (e) and (f); (c), (d) waveforms of instantaneous imaginary current in α-β coordinates with their spectrums (g) and (h)

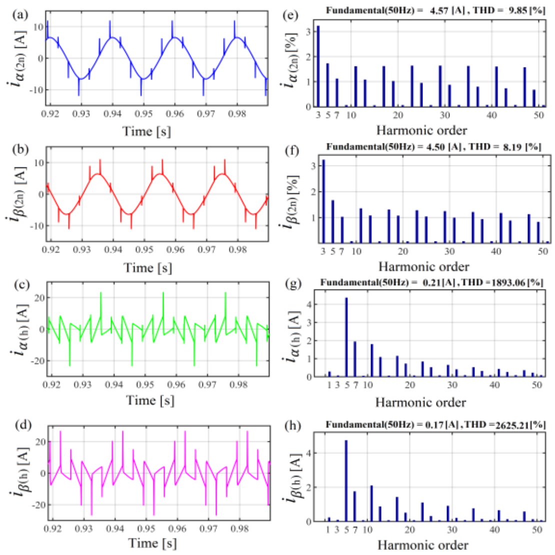

Figure 5.11 (a), (b) waveforms of instantaneous asymmetry current in α-β coordinates with their spectrums (e) and (f); (c), (d) waveforms of instantaneous harmonic current in α-β coordinates with their spectrums (g) and (h)

The disturbances contained in the supply voltage and load current are conserved during the transformation from *a-b-c* to α-β coordinates (comparing Figure 5.6(a)(b) to Figure 5.5(a)(b)).

In α-β coordinates, after the instantaneous real and imaginary powers calculation (see Figure 5.8(a) and Figure 5.9(a)), the low and band pass filters are used to split the powers into different parts: the constant part (Figure 5.8(b) and Figure 5.9(b)), the part related to the harmonics (Figure 5.8(c) and Figure 5.9(c)) and the asymmetry part (Figure 5.8(d) and Figure 5.9(d)) (see Annex V, Figure V.5 to Figure V.8).

The instantaneous real and imaginary current waveforms (in α-β) are respectively constituted by Figure 5.10 with the spectrums. Figure 5.11(a)(b)(e)(f) presents the instantaneous asymmetry current waveforms and spectrums. The instantaneous harmonic current waveforms with spectrums are shown in Figure 5.11 (c)(d)(g)(h).

After the inverse transformation, the reference currents related to the real power ($i_{\mathrm{a}(\bar{p})}$), imaginary power ($i_{\mathrm{a}(\bar{q})}$), harmonics ($i_{\mathrm{a(harmonic)}}$) and asymmetry ($i_{\alpha\mathrm{(asymmetry)}}$) are represented with the spectrum in Figure 5.12(a) to (h). The three-phase reference currents are shown in Figure 5.12(j) together with the spectrums.

The distortions (commutation notches) present in the supply voltage are also observed in all instantaneous currents waveforms after the invers transformation (see the waveforms in Figure 5.12(a) to (h)).

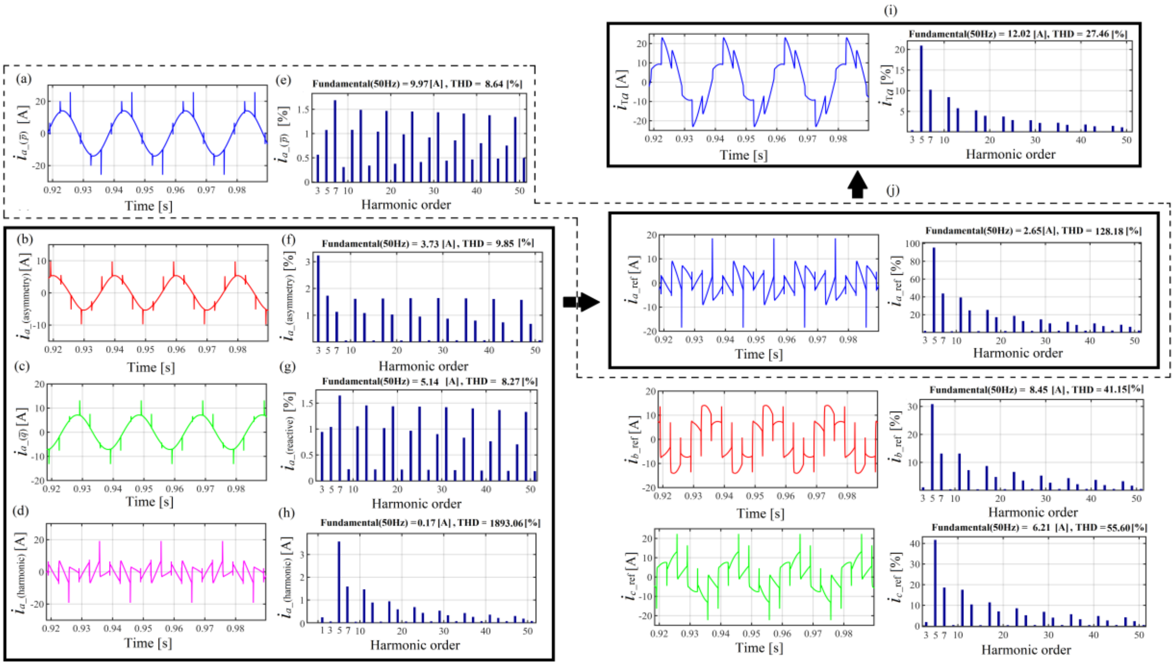

Figure 5.12 One-phase representation of reference currents after inverse transformation: (a) current related to the real power and (e) its spectrum; (b) asymmetry current and (f) its spectrum; (c) current related to the imaginary power constant part and (g) its spectrum and (d) harmonic current with its spectrum (h). (i) current obtained after additing the waveforms from (a) to (d) as well as the spectrums from (e) to (h), (j) reference currents in *a-b-c* (without the current related to the real power ($\bar{p}$)) coordinate with spectrums

5.1.1.2 Application of *p-q* theory after supply voltage filtration

The distorted supply voltage is filtered before being applied at the *p-q* theory algorithm block input (Figure 5.13). The asymmetry (small scale) on the supply voltage is conserved after the filtration (Figure 5.13). For more details of "supply voltage filtration" block see Figure V.4 in Annex V.

The voltage waveforms in Figure 5.14 (in α-βcoordinates) compaired to those in Figure 5.6(a) do not almost contain the supply voltage distortion. In Figure 5.15, the waveforms of instantaneous real and imaginary current in α-β coordinates do not present any distortion as well as the current asymmetry waveforms. The current harmonic waves (in α-β) with spectrums are presented in Figure 5.15(g) to (j).

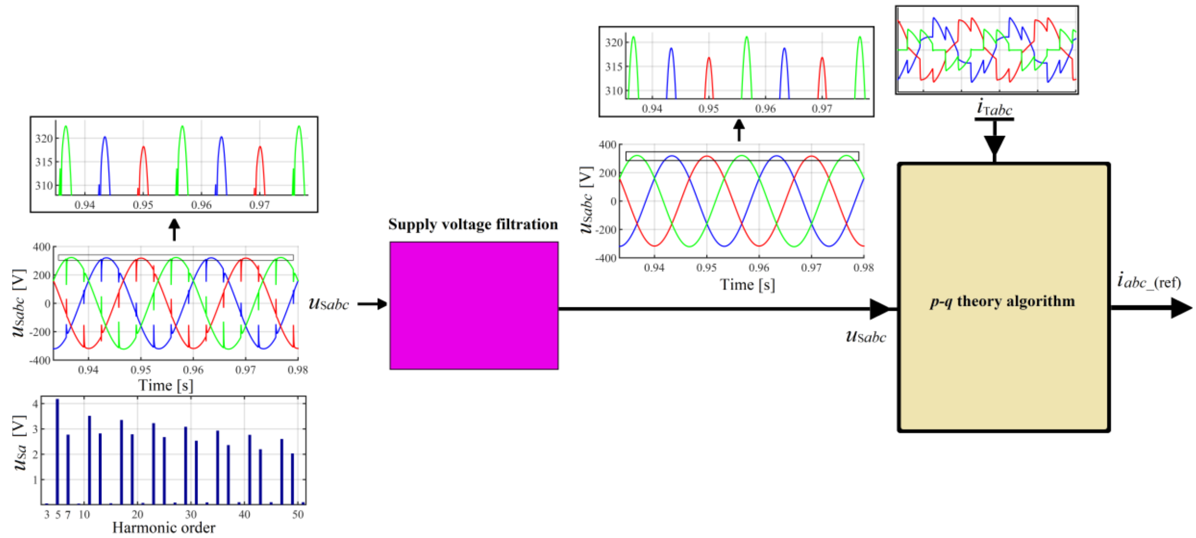

Figure 5.13 *p-q* theory algorithm with supply voltage filter

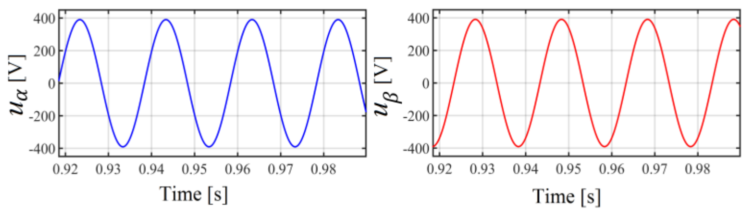

Figure 5.14 Supply voltage in α-β coordinates

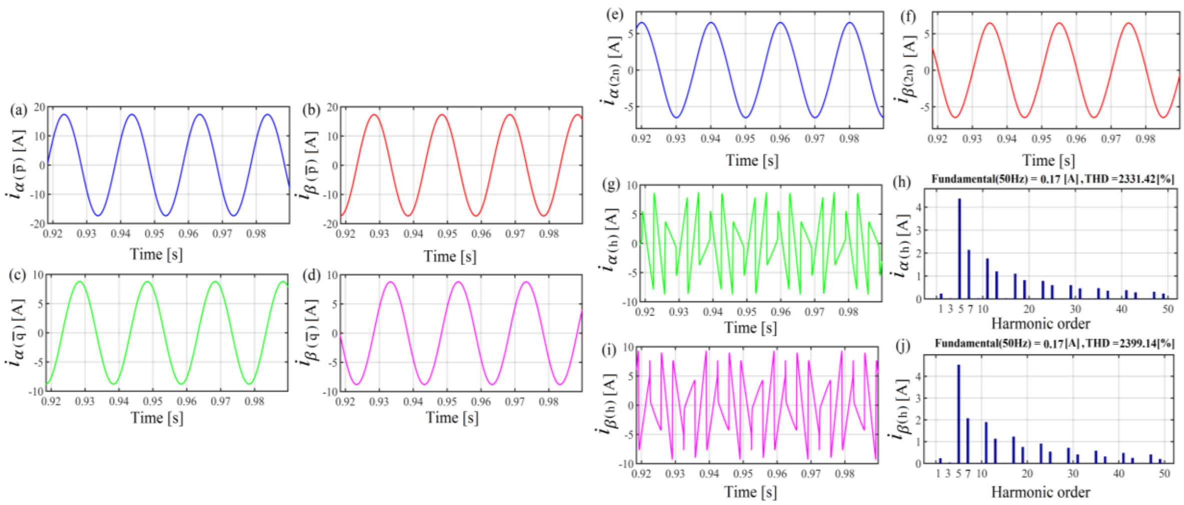

Figure 5.15 Waveforms of instantaneous real current (a)(b), imaginary current (c)(d), asymmetry current (e)(f), harmonics current (g)(i) (with spectrums (h)(j)) in α-β coordinates

The constant component values of instantaneous total real and imaginary power ($\bar{p}$, $\bar{q}$) should be equal to the total active and reactive power values ($P_{S\_total(1)}$, $Q_{S\_total(1)}$) in *a-b-c* coordinates, but according to the data in (Table 5.4) they are almost equal due the slight numerical errors.

Compared to the waveforms in Figure 5.12(a)(b)(c), the waveforms in Figure 5.16(a)(b)(e) are sinusoidal. The reference currents in Figure 5.16(g) have lower THD than those of Figure 5.12(j) (see also Figure 5.17).

Figure 5.17(b) shows that with the "Supply voltage filtration" system (see Figure 5.13); the reference current does not contain the distortion coming from the grid voltage waveforms.

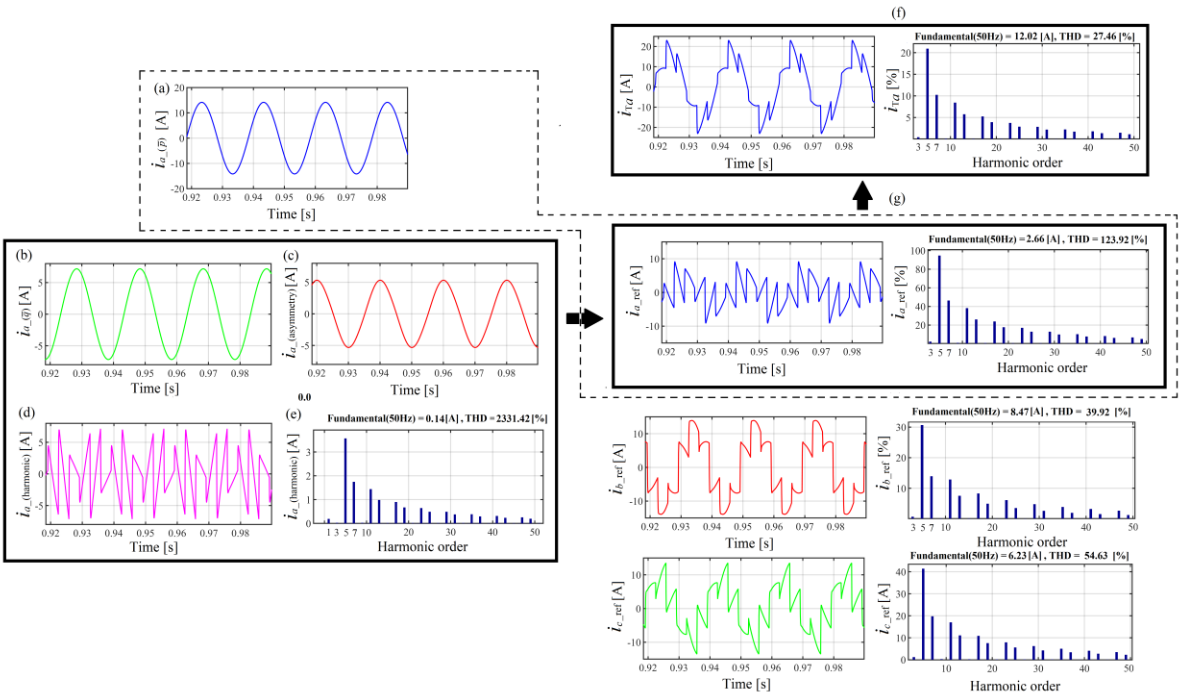

Figure 5.16 One-phase representation of reference currents after inverse transformation: (a) current related to the real power, (b) current related to the imaginary power, (c) asymmetry current, (d) harmonics current with (e) its spectrum, (f) current obtained after additing all the current components from (a) to (d), (g) reference currents (without the current related to the real power) in *a-b-c* coordinate with spectrums

Table 5.4 The real and imaginary power values in α-β coordinates are compared respectively to the total active and reactive powers values in a-b-c coordinates

$P_{S\_total(1)}$ [W]	6766	$Q_{S\_total(1)}$ [Var]	3418.1
$\bar{p}_{\alpha\beta}$ [W]	6774	$\bar{q}_{\alpha\beta}$ [Var]	3432

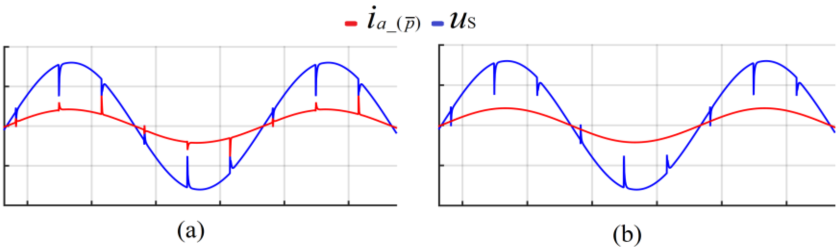

Figure 5.17 Waveforms of the supply voltage together with the reference real current (obtained after *p-q* theory application): (a) case without supply voltage filtration and (b) case with supply voltage filtration

5.2 Investigation of three wires three legs SAPF in MATLAB SIMULINK

The investigation is performed on the simulated laboratory model presented in Figure 4.2 (see also Annex IV, Figure IV.3).

The analysis done on the *p-q* theory algorithm (see Figure 5.4) have permitted the author to propose the SAPF control system presented in Figure 5.19 (see also Figure 5.18). It is organized into three parts (*control loop (1), (2)* and *(3)*) (for more details see Annex V, Figure V.1 to V.13).

The role of the *control loop (1)* is to maintain the inverter DC capacitor voltage to the reference level (U_{DC_ref}) [168, 30]. The reached maximum voltage during the transient state and its duration depends upon the capacitor capacitance value and the PI controller parameters.

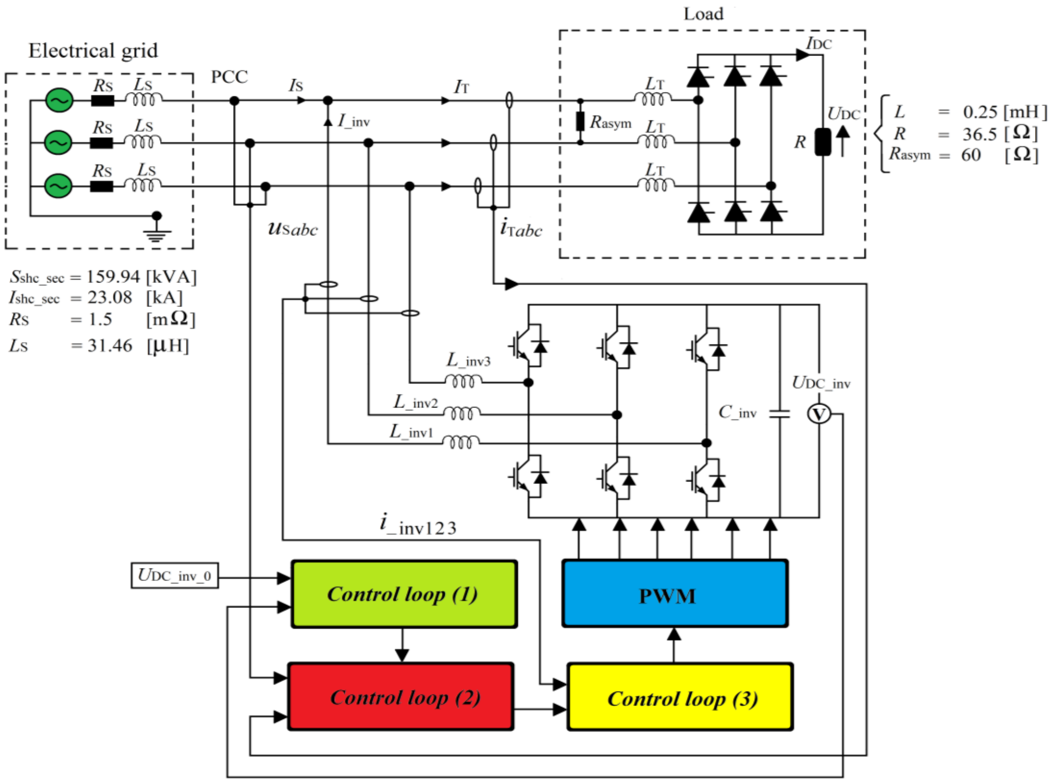

Figure 5.18 Power system representation (see also Annex IV, Figure IV.3)

The *control loop (2)* contains the *p-q* algorithm and its goal is to generate the instantaneous reference current ($i_{abc\_(\mathrm{ref})}$) needed for the *control loop (3)* by basing on the instantaneous PCC voltage (u_{Sabc}) and load current (i_{Tabc}) [30]. In Figure V.5 to V.8 of Annex V, it is presented the way of real and imaginary power components extraction.

In the *control loop (3)*, the reference current ($i_{abc\_(\mathrm{ref})}$) (see example in Figure 5.16(g)) is compared to the feedback loop current coming from the inverter input ($i_{\_\mathrm{inv}123}$). The reference current coming from the *p-q* theory algorithm block is constituted of load current components (harmonics, asymmetry and fundamental harmonic reactive current). The fundamental harmonic active current component is rejected (Figure 5.19).

The time response of the feedback loop current coming from the inverter input should be as fast as possible to make the inverter input current waveforms as close as possible to the reference current waveform. The time response delay can be caused by the discrete PI controller application, fixed sampling frequency of the analogue digital device, the transistor switching frequency, and the inverter input reactor (or other passive filters) [42, 70, 138].

5.2.1 Simulation studies of three wires three legs SAPF

The SAPF is studied in the power system presented in Figure 5.18. Connected between the electrical grid and the load, its role is to extract through the control system the disturbances (harmonics, fundamental harmonic reactive current and asymmetry) contained in load current I_T and injects them back in opposite sign at the PCC, thereby cancelling the original disturbances (leaving the fundamental harmonic active current) and improving in that way the grid current and voltage quality.

Table 5.5 PI controller parameters

	k_p	k_i
control loop (1)	40000	43.75
control loop (3)	250	0.0001

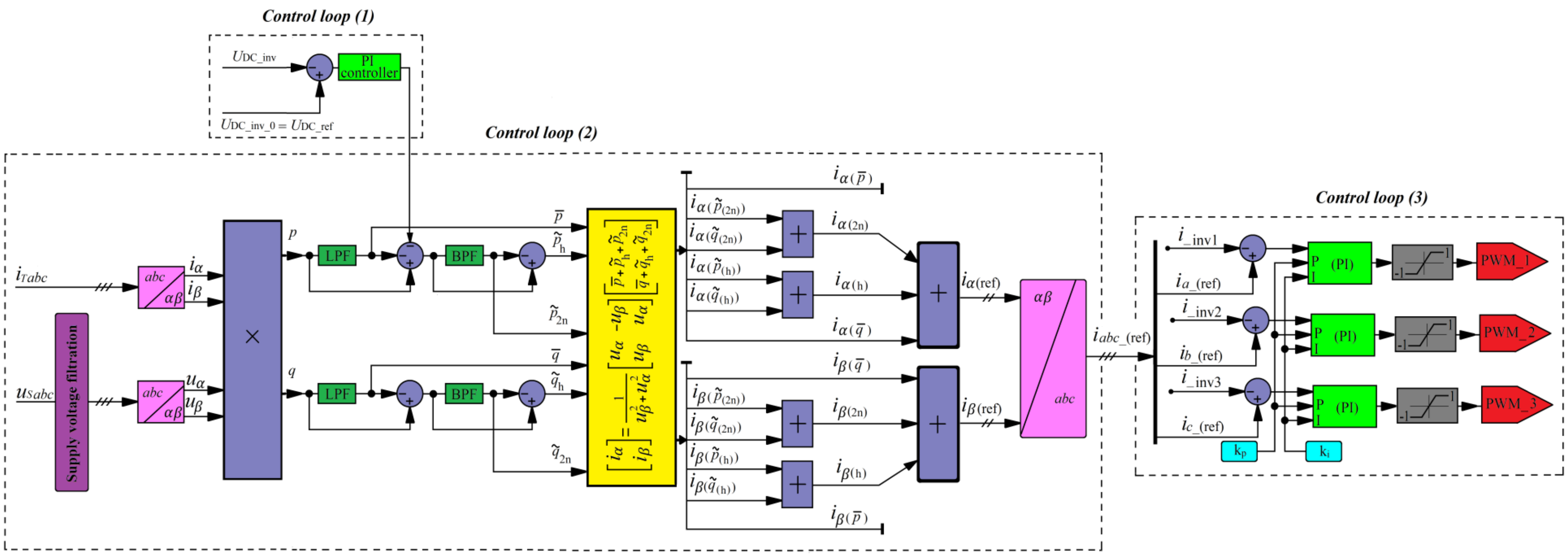

Figure 5.19 Proposed SAPF control system (see Figure 5.18)

$$k_{asym} = \frac{I_{S(1)}^{(-)}}{I_{S(1)}^{(+)}} * 100 \quad (5.50)$$

$$THD_{Us} = \frac{\sqrt{\sum_{n=2}^{50} U_{S(n)}^2}}{U_{S(1)}} * 100 \quad (5.51) \qquad THD_{Is} = \frac{\sqrt{\sum_{n=2}^{50} I_{S(n)}^2}}{I_{S(1)}} * 100 \quad (5.52)$$

$$TTHD_{Us} = \frac{\sqrt{U_{S\_true\_RMS}^2 - U_{S(1)}^2}}{U_{S(1)}} * 100 \quad (5.53) \qquad TTHD_{Is} = \frac{\sqrt{I_{S\_true\_RMS}^2 - I_{S(1)}^2}}{I_{S(1)}} * 100 \quad (5.54)$$

The PI controller parameters of *control loop (1)* and *control loop (2)* presented in Table 5.5 are selected on the base of author practical knowledge (the optimal selection of PI controller parameters is not the subject of this chapter). The rectifier firing angle as well as the PI controller parameters are constant during the simulation studies. The inverter switching frequency is fixed to 20 kHz and the reactors and capacitor resistances are neglected during the studies. The expressions from (5.50) to (5.54) are used to compute the grid current negative sequence in percentage of positive sequence, the grid voltage and current THD and TTHD.

5.2.1.1 Influence of the inverter input reactor on the SAPF performances

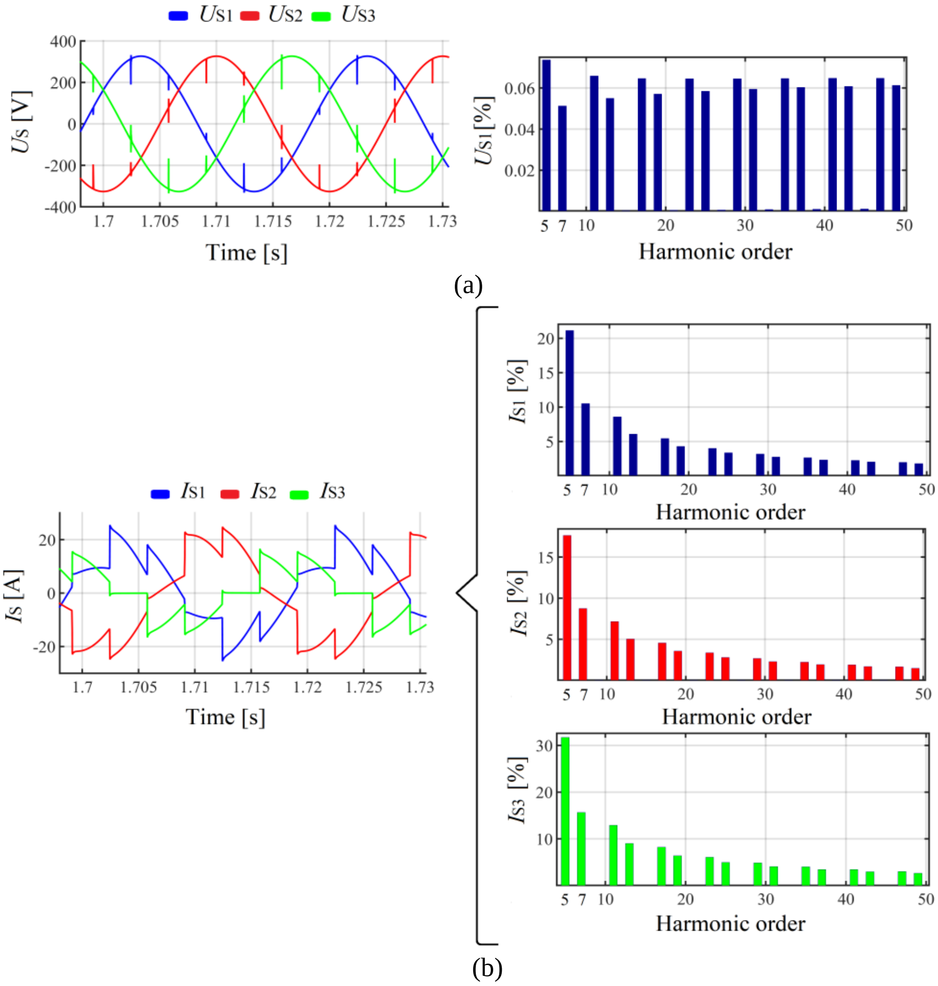

Figure 5.20 Waveforms of PCC voltage (a) and current (b) with their spectrums before the SAPF connection

The SAPF parameters (see Table 5.6) used to study the influence of the input reactor on its efficiency are computed based on the expressions (V.14), (V.22) and (V.36) presented in Annex

V. Two values of SAPF input reactor inductance are considered: $L_{\_inv\_min}$ and $L_{\_inv\_max}$ (see Annex V, Table V.3 for more detailes)

For all study cases the simulation is done with a small value of rectifier input reactor (L_T). The grid voltage and current waveforms (with spectrums) before the SAPF connection are constituted by Figure 5.20(a)(b). The phase unbalance can be observed on the grid current waveforms (which are not identical) and spectrums. In Figure 5.20(a) only one-phase grid voltage spectrum is presented.

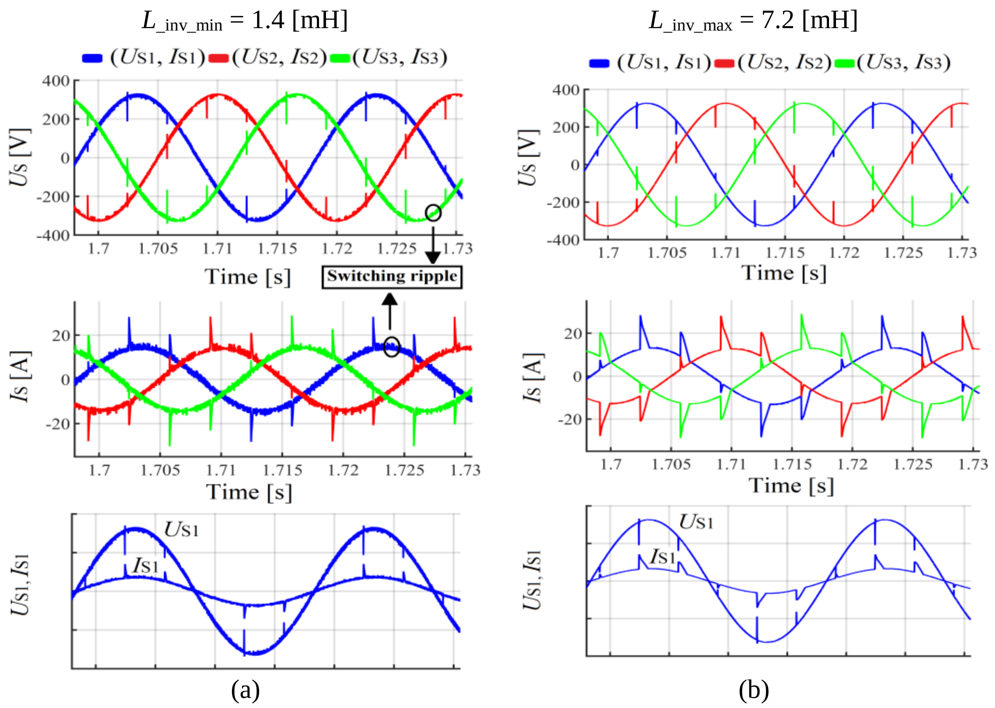

Figure 5.21 Waveforms of PCC voltage and current after the SAPF connection: (a) for $L_{\_inv\_min}$, (b) for $L_{\_inv\_max}$

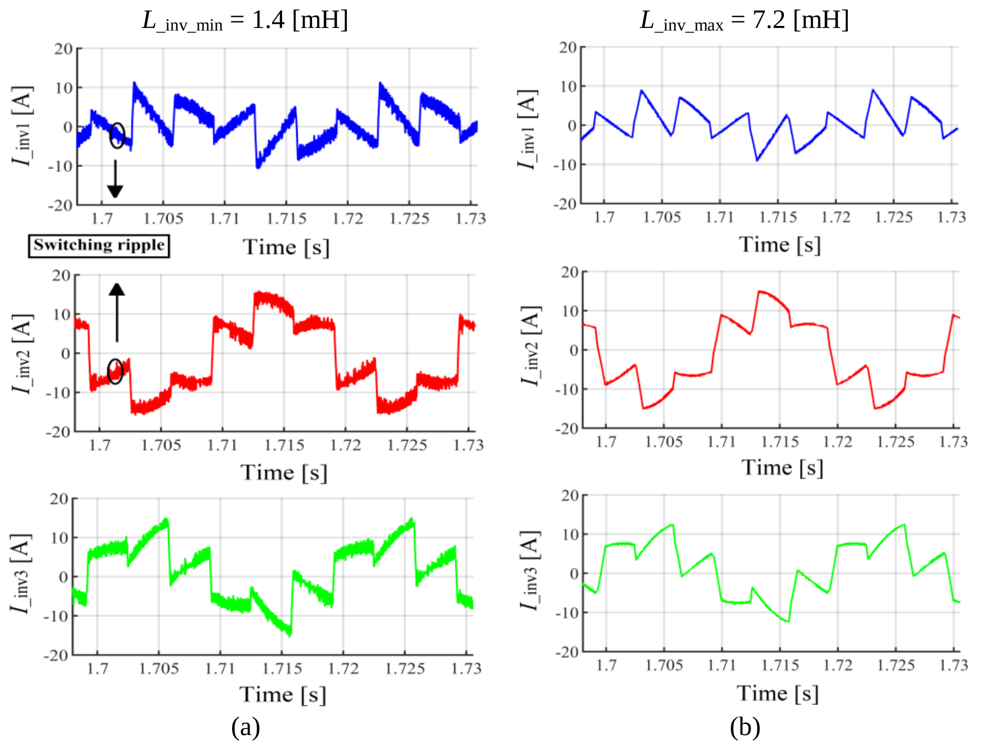

Figure 5.22 Waveforms of SAPF current: (a) for $L_{\_inv\_min}$, (b) for $L_{\_inv\_max}$

Table 5.6 Computed SAPF parameters (see expressions IV.16, IV.24 and IV.38 of Annex IV)

$U_{\text{DC\_inv\_0}} = 750$ V
$C_{\text{\_inv}}$=3 mF
$L_{\text{\_inv\_min}}$=1.4 mH
$L_{\text{\_inv\_max}}$=7.2 mH

After the SAPF connection, the grid current and voltage waveforms as well as the waveforms of injected current are respectively presented in Figure 5.21(a)(b) and Figure 5.22(a)(b). The SAPF with minimum input inductance $L_{\text{\_inv\_min}}$ (Figure 5.21(a) and Figure 5.22(a)) presents higher switching components than the SAPF with the maximum intput inductance $L_{\text{\_inv\_max}}$ (Figure 5.21(b) and Figure 5.22(b)). The grid current waveforms commutation notches are less mitigated in the case of SAPF with $L_{\text{\_inv\_max}}$ than in the case of SAPF with $L_{\text{\_inv\_min}}$ (Figure 5.21(a)(b)).

Table 5.7 Grid voltage and current parameters before and after the SAPF connection

	Before the SAPF connection					
	THD_{US} [%]	THD_{IS} [%]	$Q_{S(1)}$ [Var]	$P_{S(1)}$ [W]	$S_{S(1)}$ [VA]	k_{asym} [%]
L1	0.25	28.07	414.08	2838.4	2868.5	33.25
L2	0.25	23.41	1954.5	2833.1	3441.9	
L3	0.25	42.07	1181.8	1507.2	1915.2	
	$U_{s1(1)} = 230.8\ e^{j30^\circ}$			$I_{s1(1)} = 12.43\ e^{j21.7^\circ}$		
	$U_{s2(1)} = 230.7\ e^{j270^\circ}$			$I_{s2(1)} = 14.92\ e^{j235.4^\circ}$		
	$U_{s3(1)} = 230.7\ e^{j150^\circ}$			$I_{s3(1)} = 8.29\ e^{j111.90^\circ}$		

	After the SAPF connection ($L_{\text{\_inv\_min}}$ = 1.4 [mH])			After the SAPF connection ($L_{\text{\_inv\_max}}$ = 7.2 [mH])		
	THD_{US} [%]	THD_{IS} [%]	k_{asym} [%]	THD_{US} [%]	THD_{IS} [%]	k_{asym} [%]
L1	0.18	10.34	0.59	0.25	26.7	0.75
L2	0.19	10.99		0.25	27.92	
L3	0.18	10.93		0.25	27.7	
	$U_{s1(1)} = 230.8\ e^{j30^\circ}$		$I_{s1(1)} = 10.45\ e^{j28.9^\circ}$	$U_{s1(1)} = 230.80\ e^{j30^\circ}$		$I_{s1(1)} = 10.36\ e^{j27.8^\circ}$
	$U_{s2(1)} = 230.8\ e^{j270^\circ}$		$I_{s2(1)} = 10.99\ e^{j268.7^\circ}$	$U_{s2(1)} = 230.80\ e^{j270^\circ}$		$I_{s2(1)} = 10.48\ e^{j267.7^\circ}$
	$U_{s3(1)} = 230.8\ e^{j150^\circ}$		$I_{s3(1)} = 10.93\ e^{j149.1^\circ}$	$U_{s3(1)} = 230.80\ e^{j150^\circ}$		$I_{s3(1)} = 10.4\ e^{j147.2^\circ}$

Table 5.8 Grid voltage and current TTHD

	After the SAPF connection ($L_{\text{\_inv\_min}}$ = 1.4 [mH])		After the SAPF connection ($L_{\text{\_inv\_max}}$ = 7.2 [mH])	
	$TTHD_{US}$ [%]	$TTHD_{IS}$ [%]	$TTHD_{US}$ [%]	$TTHD_{IS}$ [%]
L1	3.57	16.31	1.70	27.09
L2	2.93	16.19	1.50	27.59
L3	3.60	16.20	2.13	27.89

The values of grid voltage and current fundamental harmonic before and after the filter connection are presented in Table 5.7. The SAPF with $L_{\text{\_inv\_min}}$ has the lowest grid current and voltage THD as well as the lowest coefficient of the grid current asymmetry (Table 5.7).

In Table 5.8, it can be observed that the SAPF with the $L_{\text{\_inv\_max}}$ has the lowest grid voltage TTHD and the highest grid current TTHD in comparison to the SAPF with the $L_{\text{\_inv\_min}}$.

The waveforms of reference current and compensating current (measured from the *control loop (3)*) are compared in Figure 5.23. In the ideal case, the two signals should match each other and by subtracting one from another, the error should be close to zero.

In the case of SAPF with maximum input reactor inductance ($L_{\text{\_inv\_max}}$), the compensating current ($I_{\text{\_inv1}}$) has difficulties to tract the reference current ($I_{a\text{\_(ref)}}$) at the points of commutation notches because of the high rate of reference current change (see Figure 5.23(b)). The reference current (part of input rectifier current) presents a high rate of change at the commutation notches because of the very small value of the rectifier output reactor (L_T). The difficulty of the compensating current to tract the reference current is less accentuated for the inverter with minimum input inductance ($L_{\_inv\_min}$) (see Figure 5.23(a)).

The gap between the reference current and the compensating current observed in Figure 5.23(a)(b) determines how much the inverter can be efficient mostly in term of current harmonics reduction (see grid current THD in Table 5.7). This gap is responsible of high amplitude ripple (points of commutation notches) observed on the grid current waveform (e.g. Figure 5.21(b)). After subtracting the compensating current from the reference current, the input PI controller error of the minimum and maximum inverter input reactor are respectively constituted by Figure 5.24(a)(b).

Observing Figure 5.24 (c), it can be seen that the inverter input reactor has an influence on DC capacitor transient state duration.

The fundamental harmonic active, reactive and apparent powers at the PCC, load and SAPF for the inverter with $L_{\_inv\_min}$ and $L_{\_inv\_max}$ are presented in Table 5.9.

An example of current harmonics spectrums at the rectifier input, SAPF input and grid side is presented in Figure 5.25 (for $L_{\_inv\_min}$).

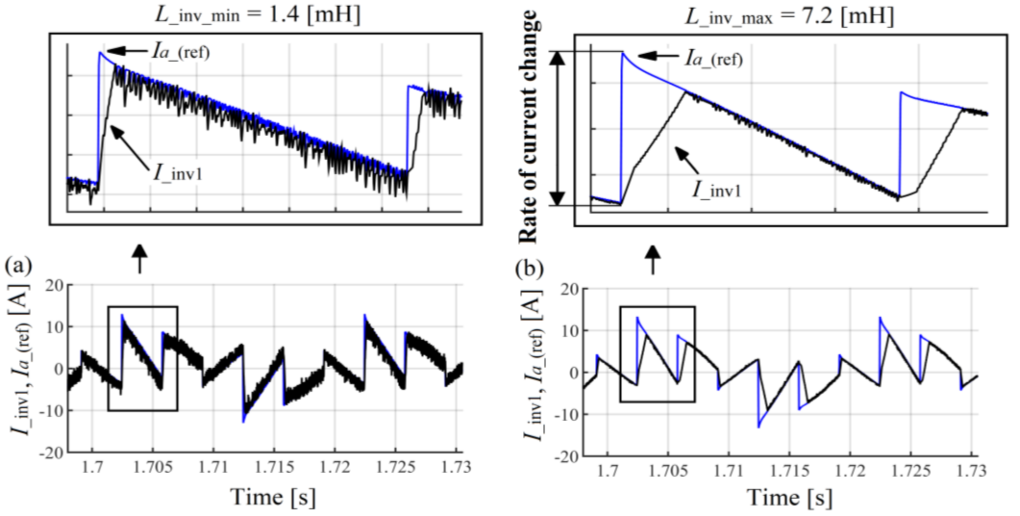

Figure 5.23 Waveforms comparison between the reference and compensating currents of *control loop (3)* (Figure 5.19): (a) for $L_{\_inv\_min}$, (b) for $L_{\_inv\_max}$

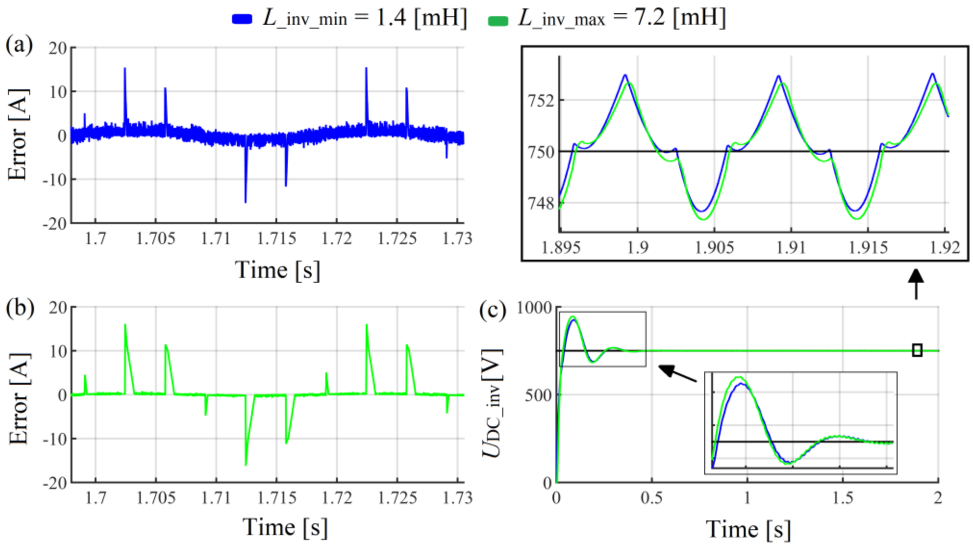

Figure 5.24 (a), (b) errors at the input of PI current *control loop (3)*; (c) DC link voltage

Table 5.9 Active and reactive powers at the PCC, load (rectifier input) and SAPF for the minimum and maximum input inverter reactor inductance

		After the SAPF connection ($L_{\_inv\_min}$ = 1.4 [mH])			After the SAPF connection ($L_{\_inv\_max}$ = 7.2 [mH])		
		PCC	load	SAPF	PCC	load	SAPF
$P_{(1)}$ [W]	L1	2411.4	2838.8	427.40	2389.3	2838.8	449.82
	L2	2535.8	2837.9	438.19	2416.8	2837.9	421.33
	L3	2522.3	1505.7	-890.35	2397.5	1505.7	-891.61
$Q_{(1)}$ [Var]	L1	46.30	414.13	370.22	91.78	414.13	323.23
	L2	57.54	1950.4	1898	97.07	1950.4	1854.5
	L3	39.62	1180.6	1143.7	117.25	1180.6	1062.6
$S_{(1)}$ [VA]	L1	2411.9	2868.8	565.46	2391.1	2868.8	553.92
	L2	2536.5	3443.5	1948	2418.8	3443.5	1.901.8
	L3	2522.6	1913.3	1449.4	2400.3	1913.3	1387.1
	$I_{T1(1)} = 12.43\ e^{j21.7°}$		$I_{\_inv1(1)} = 2.45\ e^{j-10.9°}$		$I_{T1(1)} = 12.43\ e^{j21.7°}$		$I_{\_inv1(1)} = 2.40\ e^{j-5.7°}$
	$I_{T2(1)} = 14.92\ e^{j235.5°}$		$I_{\_inv2(1)} = 8.44\ e^{j193.0°}$		$I_{T2(1)} = 14.92\ e^{j235.5°}$		$I_{\_inv2(1)} = 8.24\ e^{j192.8°}$
	$I_{T3(1)} = 8.29\ e^{j111.9°}$		$I_{\_inv3(1)} = 6.28\ e^{j22.1°}$		$I_{T3(1)} = 8.29\ e^{j111.9°}$		$I_{\_inv3(1)} = 6.01\ e^{j20°}$

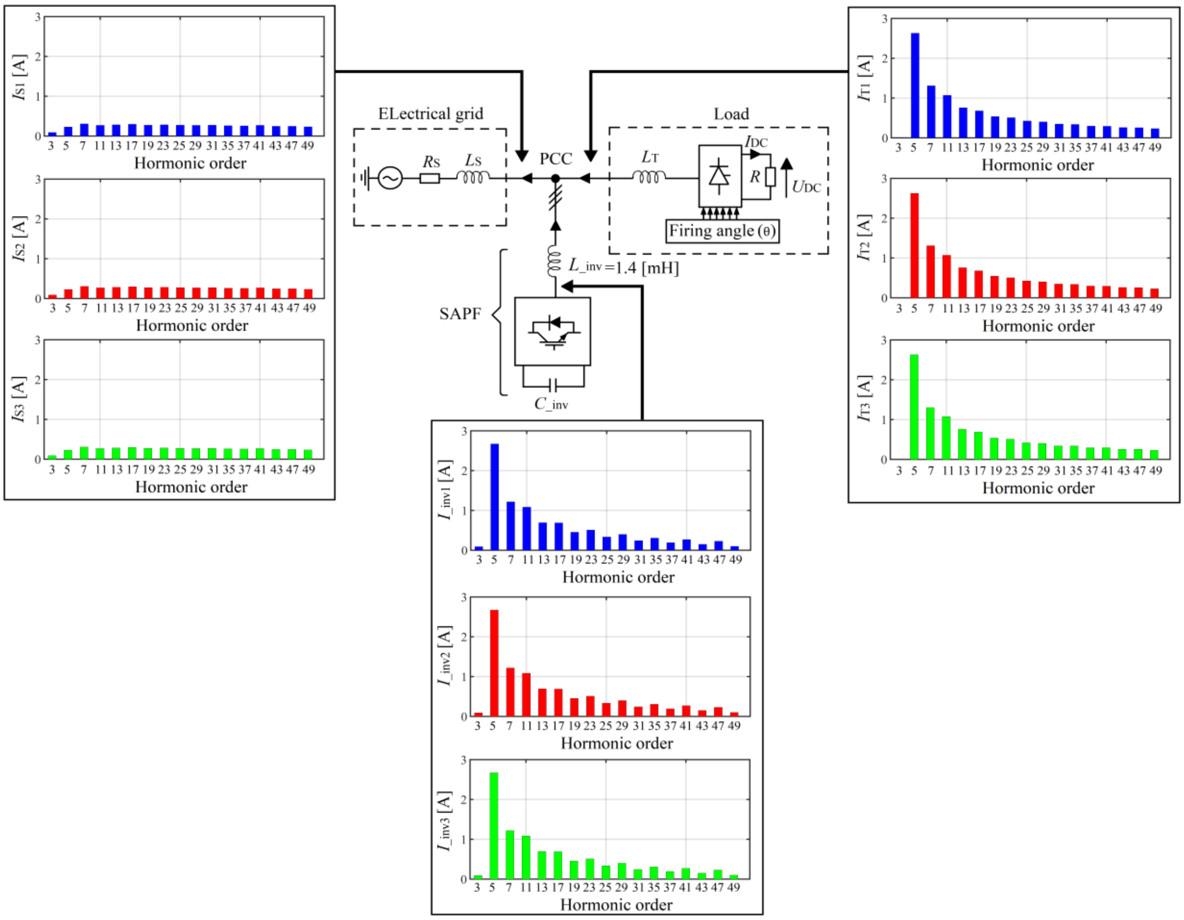

Figure 5.25 Spectrum of input rectifier current (I_T), inverter current ($I_{\_inv}$) and grid current (I_S) for $L_{\_inv}$ equal to 1.4 mH

5.2.1.2 Influence of the thyristor bridge input reactor on the SAPF performances

Basing on the previous experiment, $L_{\_inv\_min}$ has been chosen to study the influence of the rectifier input reactor on the SAPF performances (see Figure 5.26). Three cases of simulation results are compared: (a) the inverter input inductance is higher than the rectifier input inductance ($L_{\_inv} > L_T$), (b) the inverter input inductance is equal to the rectifier input inductance ($L_{\_inv} = L_T$) and (c) the inverter input inductance is smaller than the rectifier input inductance

($L_{\_inv} < L_T$). All the three simulation cases are achieved when the line reactor L_{SS} is not connected at the grid side and when it is connected.

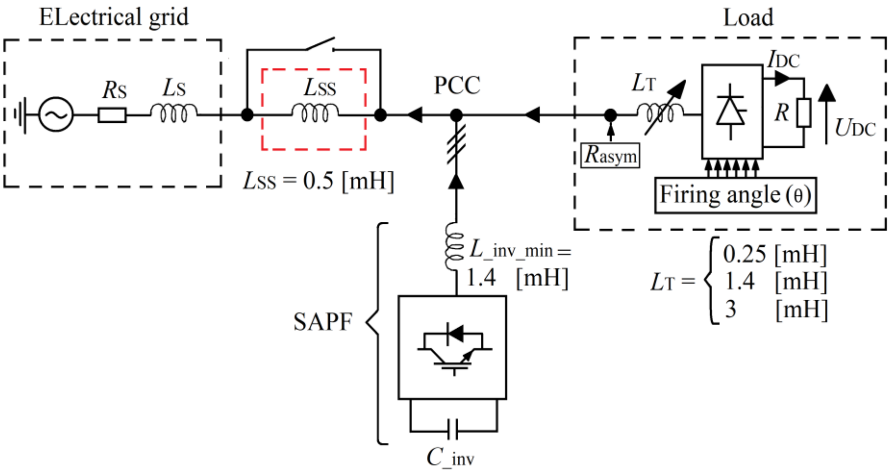

Figure 5.26 Simulated power system. The inverter input reactor is constant and the rectifier input reactor is increased from 0.25 mH to 3 mH

- **Simulation studies when the line reactor L_{SS} is not connected at the grid side**

The grid voltage and current waveforms of Figure 5.27(a)(b)(c) shows that with the thyristor bridge input reactor inductance equal or higher than the inductance at the SAPF input reactor, the ripples (at the points of commutation notches) are reduced (see Figure 5.27(b)(c)).

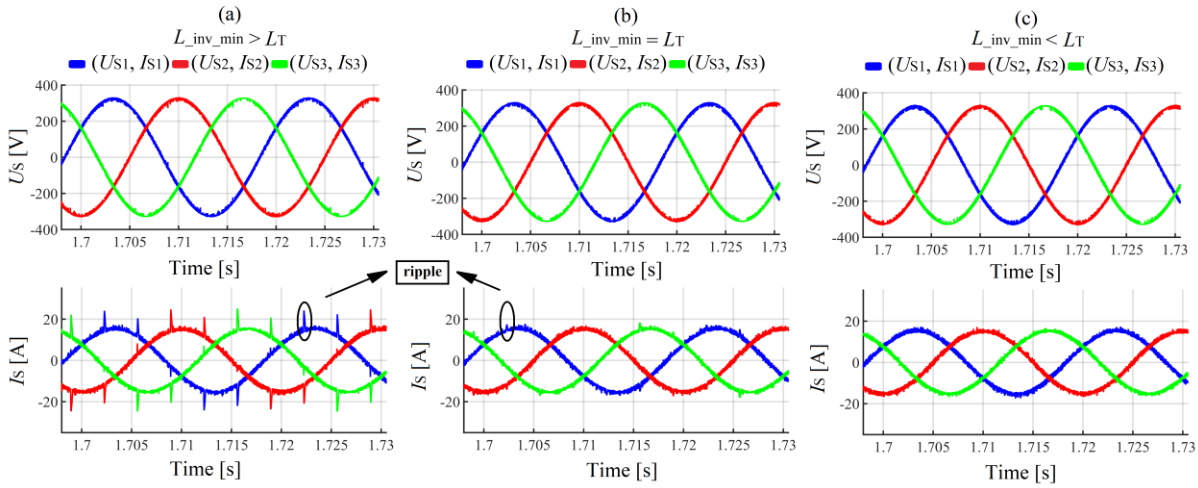

Figure 5.27 Waveforms of PCC voltage and current for different value of input rectifier reactor inductance: (a) $L_{\_inv\_min} > L_T$, (b) $L_{\_inv\_min} = L_T$, (c) $L_{\_inv\_min} < L_T$

The fundamental harmonic parameters of grid voltage and current are presented in Table 5.10. With the input rectifier reactor inductance increase, the grid current has little decreased. The waveform of the reference current compared to the one of the compensating current is presented in Figure 5.28(a)(b)(c). Increasing the rectifier input reactor inductance (L_T) to the value equal or higher than $L_{\_inv\_min}$ has reduced the rectifier input current rate of change at the points of commutation notches making possible the compensating current to track the reference current (Figure 5.28(b)(c)). The error at the PI controller input are presented in Figure 5.29(a)(b)(c) and the waveforms of inverter DC capacitor voltage are considered Figure 5.29(d).

Table 5.11 shows that the best results in term of grid current and voltage THD (as well as TTHD – see Table 5.12); fundamental harmonic reactive power compensation and asymmetry compensation are when the $L_{\_inv\_min}$ is equal or smaller than L_T.

Table 5.10 Grid voltage and current fundamental harmonic before and after the SAPF connection (for different input rectifier reactor value)

	(Before the SAPF connection) L_T = 1 nH				(After the SAPF connection) $L_{\_inv} > L_T$			
	$U_{S(1)}$ [V]		$I_{S(1)}$ [A]		$U_{S(1)}$ [V]		$I_{S(1)}$ [A]	
	RMS	Phase	RMS	Phase	RMS	Phase	RMS	Phase
L1	230.8	30º	12.43	21.7º	230.8	30º	10.41	29.4º
L2	230.7	270º	14.92	235.4º	230.7	270º	10.4	269.2º
L3	230.7	150º	8.29	111.90º	230.7	150º	10.37	149.3º

	(After the SAPF connection) $L_{\_inv\_min} = L_T$				(After the SAPF connection) $L_{\_inv\_min} < L_T$			
	$U_{S(1)}$ [V]		$I_{S(1)}$ [A]		$U_{S(1)}$ [V]		$I_{S(1)}$ [A]	
	RMS	Phase	RMS	Phase	RMS	Phase	RMS	Phase
L1	230.8	30º	10.29	29.4º	230.8	30º	10.14	29.5º
L2	230.7	270º	10.3	269.3º	230.8	270º	10.14	269.3º
L3	230.7	150º	10.28	149.3º	230.8	150º	10.11	149.4º

Table 5.11 Grid voltage and current THD as well as reactive and active power before and after the SAPF connection (for different input rectifier reactor inductance value)

	(Before the SAPF connection) L_T = 1 nH					(After the SAPF connection) $L_{\_inv\_min} > L_T$				
	THD_{US} [%]	THD_{IS} [%]	$Q_{S(1)}$ [Var]	$P_{S(1)}$ [W]	k_{asym} [%]	THD_{US} [%]	THD_{IS} [%]	$Q_{S(1)}$ [Var]	$P_{S(1)}$ [W]	k_{asym} [%]
L1	0.25	28.07	414.08	2838.4	33.25	0.15	8.77	25.15	2402.5	0.30
L2	0.25	23.41	1954.5	2833.1		0.15	8.75	33.51	2400.1	
L3	0.25	42.07	1181.8	1507.2		0.15	8.77	29.24	2393.2	

	(After the SAPF connection) $L_{\_inv\_min} = L_T$					(After the SAPF connection) $L_{\_inv\_min} < L_T$				
	THD_{US} [%]	THD_{IS} [%]	$Q_{S(1)}$ [Var]	$P_{S(1)}$ [W]	k_{asym} [%]	THD_{US} [%]	THD_{IS} [%]	Q_S [Var]	P_S [W]	k_{asym} [%]
L1	0.04	2.47	24.86	2374.8	0.30	0.02	1.22	20.42	2340.2	0.20
L2	0.05	2.91	29.04	2377.1		0.02	1.49	28.59	2340.1	
L3	0.05	2.79	28.98	2372.4		0.02	1.22	24.43	2333.3	

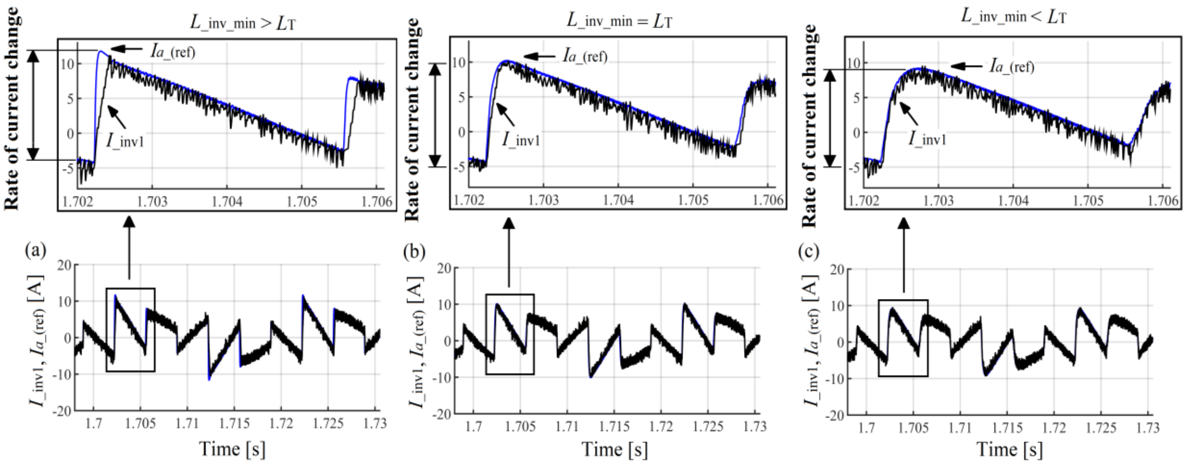

Figure 5.28 Waveforms comparison between the reference and compensating current of *control loop (3)* (Figure 4.24): (a) for $L_{\_inv\_min} > L_T$, (b) for for $L_{\_inv\_min} = L_T$, (c) for $L_{\_inv\_min} = L_T$

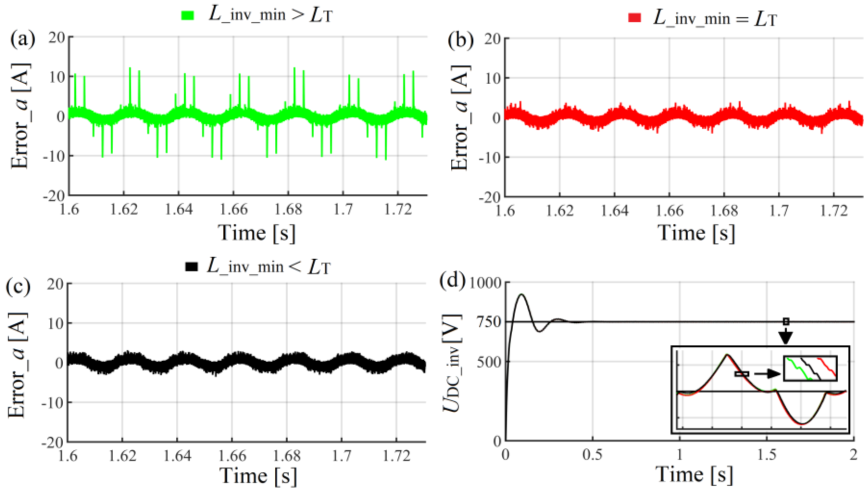

Figure 5.29 (a)(b)(c) error at the input of PI current *control loop (3)*; (d) inverter DC capacitor voltage

Table 5.12 Grid voltage and current TTHD for different value of input rectifier reactor inductance

	(After the SAPF connection) $L_{\_inv\_min} > L_T$		(After the SAPF connection) $L_{\_inv\_min} = L_T$		(After the SAPF connection) $L_{\_inv\_min} < L_T$	
	$TTHD_{US}$ [%]	$TTHD_{IS}$ [%]	$TTHD_{US}$ [%]	$TTHD_{IS}$ [%]	$TTHD_{US}$ [%]	$TTHD_{IS}$ [%]
L1	3.12	12.60	3.18	7.16	3.30	6.59
L2	2.77	13.77	2.85	8.08	2.92	6.82
L3	3.12	13.40	3.23	7.20	3.29	6.11

- **Simulation studies when the line reactor L_{SS} is connected at the grid side**

These studies are about to present the influence of the grid inductance increase on the SAPF performances. The grid inductance is increased by connecting an additional reactor (L_{SS} = 0.5 mH) between the PCC and the electrical grid as presented in Figure 5.26.

The grid voltage and current waveforms as well as the waveforms of compensating and reference current are presented in Figure 5.30. Comparing the grid voltage waveforms of Figure 5.27(a)(b)(c) to those of Figure 5.30(a)(b)(c) it can be noticed that the grid voltage waveforms of Figure 5.30(a)(b)(c) present higher switching ripples (higher THD) because of the additional line reactor L_{SS} voltage drop.

As in the case without the line reactor, the SAPF with $L_{\_inv} = L_T$ and $L_{\_inv} < L_T$ present a better shape of grid current waveforms (lower THD) (see Figure 5.30(b)(c)) than the SAPF with $L_{\_inv} > L_T$. The zoom of the compensating and reference currents are also presented in Figure 5.30(a)(b)(c). Whith L_{SS} connected, the increase of the input reactor inductance L_T from 250 μH to 3 mH has not only reduce the grid current THD but also the grid voltage (Figure 5.30).

The grid voltage TTHD presented in Table 5.13 shows that with grid inductance increase and with the SAPF input reactor inductance smaller than the rectifier input reactor inductance, the grid voltage is more distorted by the switching ripple harmonics.

Table 5.13 Grid voltage and current TTHD for different value of input rectifier reactor inductance when the grid inductance is increased

	L_{SS} = 0.5 mH					
	(After the SAPF connection) $L_{\_inv\_min} > L_T$		(After the SAPF connection) $L_{\_inv\_min} = L_T$		(After the SAPF connection) $L_{\_inv\_min} < L_T$	
	$TTHD_{US}$ [%]	$TTHD_{IS}$ [%]	$TTHD_{US}$ [%]	$TTHD_{IS}$ [%]	$TTHD_{US}$ [%]	$TTHD_{IS}$ [%]
L1	13.98	8.51	17.54	6.20	19.22	6.56
L2	15.64	9.92	17.94	6.78	19.48	6.49
L3	17.61	8.72	22.49	5.20	24.99	4.69

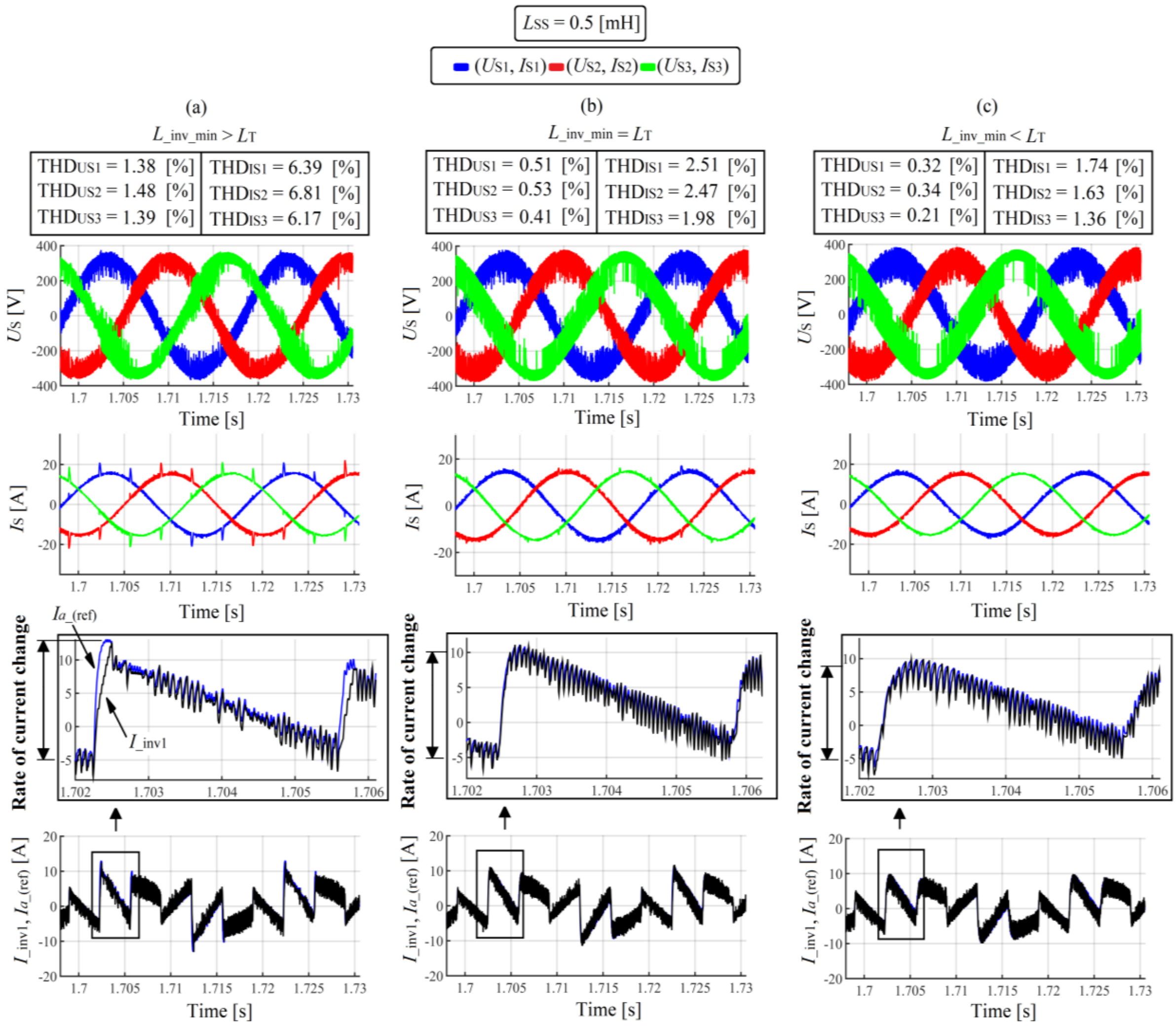

Figure 5.30 Grid voltage and current waveforms (PCC) as well as compensating and reference current waveforms when the line reactor L_{SS} is connected: (a) $L_{\_inv\_min} > L_T$, (b) $L_{\_inv\_min} = L_T$, (c) $L_{\_inv\_min} < L_T$

5.2.1.3 Influence of invert DC capacitor parameters on the SAPF performances

The SAPF performance does not only depend on the parameters of input reactor but also on the parameters of the capacitor at its DC side (capacitance and voltage). Two types of study are under consideration in this chapter: the first one is about the impact of the DC capacitor capacitance on the SAPF efficiency and the second one concerns the inverter DC voltage level importance. During the analysis, the load and inverter input reactor inductances have been chosen (basing on the previous experiments) to be equal (L_T = $L_{\_inv\_min}$ =1.4 mH). The line reactor L_{SS} is not connected.

- **Impact of the DC capacitor size on the SAPF efficiency**

Table 5.14 Inverter DC capacitor parameters

ΔU_{DC_inv} [V]	$U_{DC\_inv\_0}$ [V]	ΔW_{DC_inv} [J]	$C_{\_inv}$ [mF]
140	750	11	0.1
9			1.6
5			3

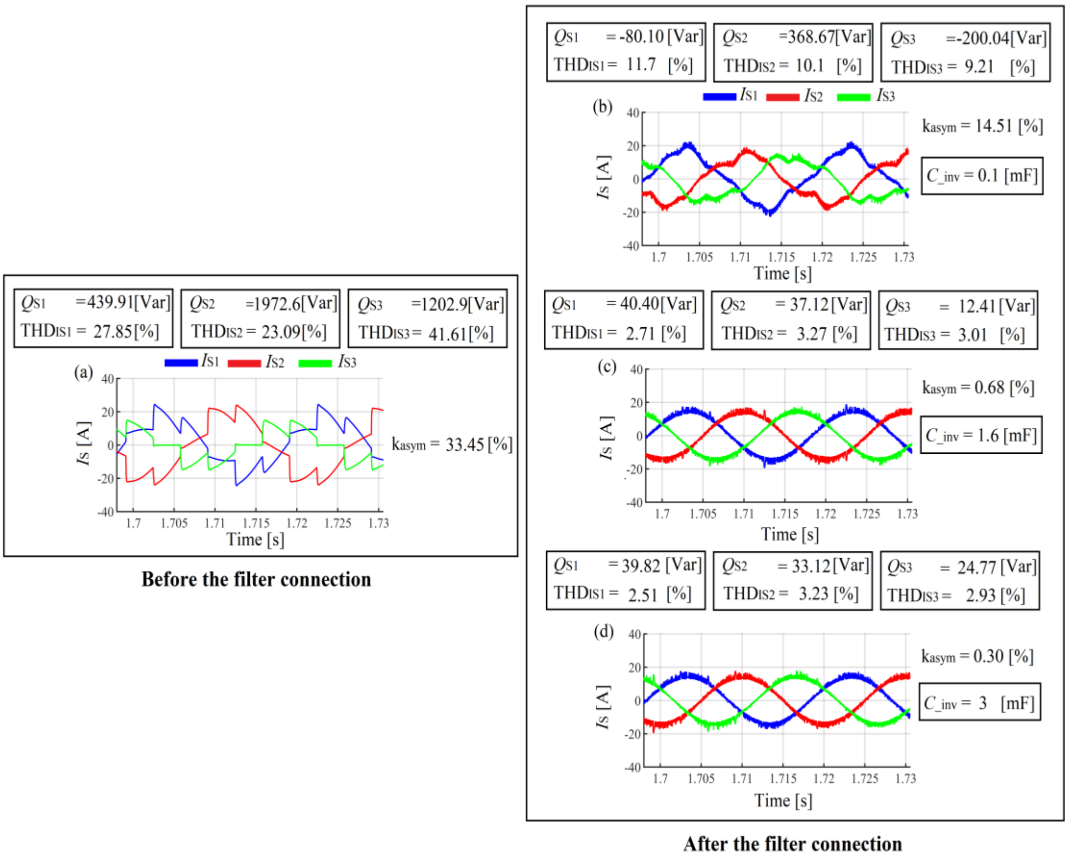

Figure 5.31 Grid current waveforms: (a) before the SAPF connection; (b), (c), (d) after the filter connection (for different values of inverter capacitor capacitance)

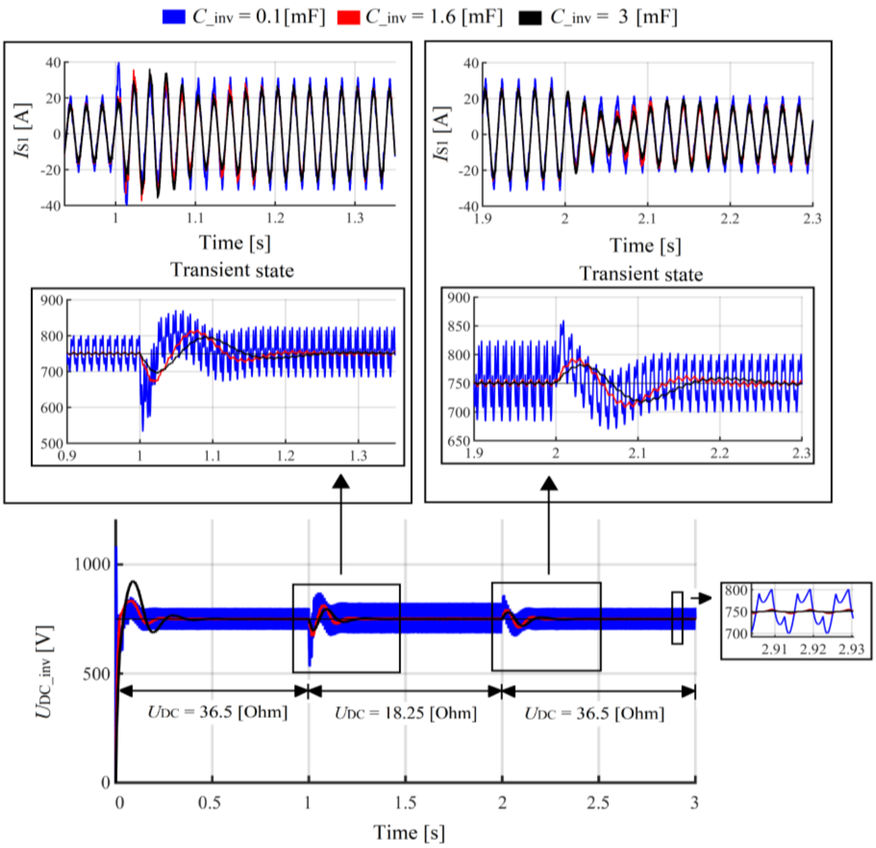

Figure 5.32 Capacitor DC voltage waveforms for different capacitance: transient state observation after the rectifier DC resistance change (R_{DC})

By assuming constant the inverter DC reference voltage (750 V), the capacitor capacitance ($C_{\_inv}$) values are computed for different values of ΔU_{DC_inv} (capacitor voltage fluctuation between the maximum and the minimum) (see Table 5.14). The expression (V.22) of Annex V have been used for that computation.

Comparing Figure 5.31(b) to (c) and (d), it can be noticed that the SAPF with the lowest capacitor capacitance (0.1mF) presents the worst filtration characteristics: highest grid current THD, grid fundamental harmonic reactive power and asymmetry coefficient.

With a large capacitor capacitance, the range of the inverter DC voltage fluctuation varying between the min and the max is reduced (Figure 5.32 e.g. waveform in red colour) and the transient state (e.g. during the load change) is longer than when capacitor capacitance is small (see Figure 5.32).

Table 5.15 Grid voltage and current TTHD for different value of inverter DC side capacitor capacitance

	(After the SAPF connection) $C_{\_inv}$ = 0.1 mH		(After the SAPF connection) $C_{\_inv}$ = 1.6 mH		(After the SAPF connection) $C_{\_inv}$ = 3 mH	
	$TTHD_{US}$ [%]	$TTHD_{IS}$ [%]	$TTHD_{US}$ [%]	$TTHD_{IS}$ [%]	$TTHD_{US}$ [%]	$TTHD_{IS}$ [%]
L1	3.34	16.95	3.27	7.59	3.28	7.16
L2	2.55	18.59	2.87	7.42	2.8	8.08
L3	3.41	20.45	3.22	6.14	3.23	7.20

- **Influence of the DC capacitor voltage on the SAPF efficiency**

Three values of inverter DC reference voltage ($U_{DC\_inv\_0}$) computed basing on the expression (V16) of Annex V are presented in Table 5.16. Three values of the coefficient k_{DC} (e.g. 1; 1.32 and 1.68) have been chosen for that computation. Other power system parameters are constant during the simulation (e.g. $C_{\_inv}$, $L_{\_inv\_min}$, L_T…). The first simulation is done for $U_{DC\_inv\_0}$ equal to 600 V, the second one is done for $U_{DC\_inv\_0}$ equal to 750 V and the third one is done for $U_{DC\_inv\_0}$ equal to 950 V.

Table 5.16 Computed inverter DC voltage for different value of k_{DC} (see expression (V16) Annex V). The values of the inverter DC capacitor capacitance and input reactor inductance as well as the rectifier input reactor inductance are also presented

$1(\sqrt{2})400 = 565.68 \Rightarrow U_{DC\_inv\_0} = 600$ [V]		
$1.32(\sqrt{2})400 = 746.70 \Rightarrow U_{DC_inv_0} = 750$V		
$1.68(\sqrt{2})400 = 944.69 \Rightarrow U_{DC_inv_0} = 950$V		
$C_{\_inv}$ = 3 mF	$L_{\_inv\_min}$ = 1.4 mH	L_T = 0.14 mH

One-phase representation of the compensating current together with reference current are shown in Figure 5.33(a)(b)(c) (from *control loop (3)*) and the grid voltage and current waveforms are presented in Figure 5.34(a)(b)(c). In Figure 5.33, it can be observed that in the case of the SAPF with DC voltage equal 600 V (Figure 5.33(a)), the compensating current has more difficulty to track the reference current than in the case of the SAPF with DC voltage equal 750 V and 950 V (Figure 5.33(b)(c)). The consequences of the compensating current not to track enouth the reference current can be observed in the grid current (see Figure 5.34(a)) which is more distorted and presents the highest THD, TTHD and asymmetry component when compared to the case of the SAPF with DC voltage equal 750 V and 950 V (see Table 5.17 and Table 5.18).

The Figure 5.33(b)(c) is the prove that the DC link capacitor voltage should be high to ensure the SAPF good functionality and efficiency.

The higher is the voltage at the inverter DC side, the longer is the transient state (Figure 5.35(a)(b)(c)).

In Figure 5.36, it is presented a comparative study of grid voltage and current waveforms as well as THD and TTHD when the PCC voltage is filtred before been used in the SAPF algorithm control system and when it is not filtred (see Figure 5.13 as well). The results with non-filtered PCC voltage (Figure 5.36) presents higher grid current THD and TTHD. In the case of hight value of grid indance, the grid current will be much more distorted than in Figure 5.36(b)

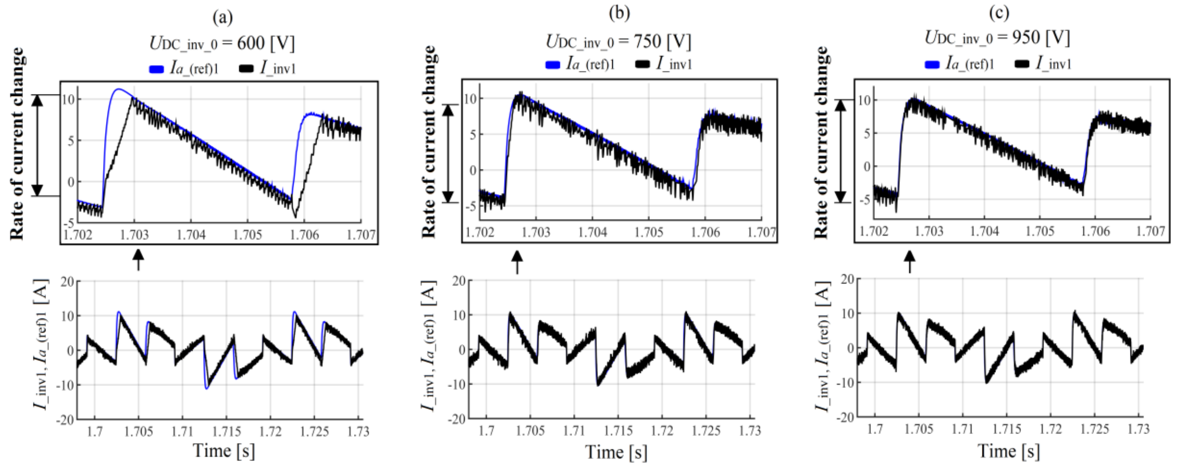

Figure 5.33 One phase waveforms of compensating together with reference currents for: (a) $U_{DC\_inv\_0}$ = 600 V, $U_{DC\_inv\_0}$ = 750 V and $U_{DC\_inv\_0}$ = 950 V

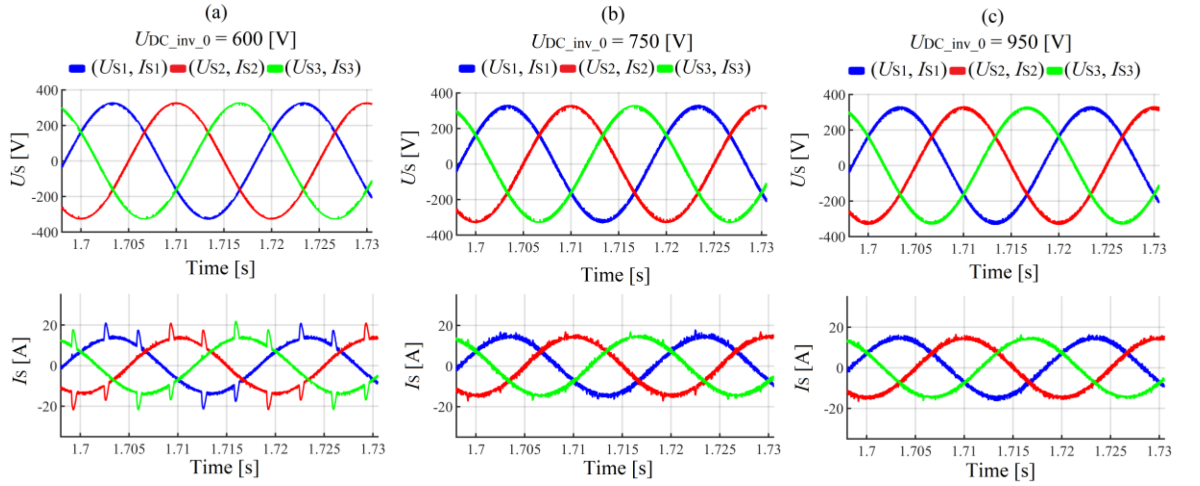

Figure 5.34 Grid current and voltage waveforms when: (a) the SAPF capacitor voltage is equal to the maximum of PCC voltage; (b) and (c) when it is higher than the PCC maximum

Table 5.17 Grid voltage and current THD, reactive and active powers as well as asymmetry coefficient before and after the SAPF connection (for different capacitor voltage values)

	(Before the SAPF connection)					(After the SAPF connection) $U_{DC\_inv\_0}$ = 600 [V]				
	THD_{US} [%]	THD_{IS} [%]	Q_S [Var]	P_S [W]	k_{asym} [%]	THD_{US} [%]	THD_{IS} [%]	Q_S [Var]	P_S [W]	k_{asym} [%]
L1	0.21	27.85	447.89	2809.2	33.45	0.17	15.62	66.18	2369.4	0.39
L2	0.21	23.09	1984.6	2693.4		0.18	15.90	66.24	2371.7	
L3	0.21	41.61	1212.8	1474.9		0.17	15.90	66.18	2369.4	

	(After the SAPF connection) $U_{DC\_inv\_0}$ = 750 [V]					(After the SAPF connection) $U_{DC\_inv\_0}$ = 950 [V]				
	THD_{US} [%]	THD_{IS} [%]	Q_S [Var]	P_S [W]	k_{asym} [%]	THD_{US} [%]	THD_{IS} [%]	Q_S [Var]	P_S [W]	k_{asym} [%]
L1	0.04	2.93	24.89	2377.1	0.30	0.03	1.71	16.59	2377.2	0.31
L2	0.05	3.23	33.12	2372.4		0.03	1.86	33.25	2381.6	
L3	0.05	2.51	24.77	2365.6		0.03	1.75	28.93	2367.8	

Table 5.18 Grid voltage and current TTHD for different value of inverter DC side capacitor voltage

	(After the SAPF connection) $U_{DC\_inv\_0} = 600$ [V]		(After the SAPF connection) $U_{DC\_inv\_0} = 750$ [V]		(After the SAPF connection) $U_{DC\_inv\_0} = 950$ [V]	
	$TTHD_{US}$ [%]	$TTHD_{IS}$ [%]	$TTHD_{US}$ [%]	$TTHD_{IS}$ [%]	$TTHD_{US}$ [%]	$TTHD_{IS}$ [%]
L1	2.00	16.27	3.28	7.16	3.24	7.46
L2	1.62	16.50	2.85	8.08	2.86	7.39
L3	2.04	16.73	3.23	7.20	3.06	6.39

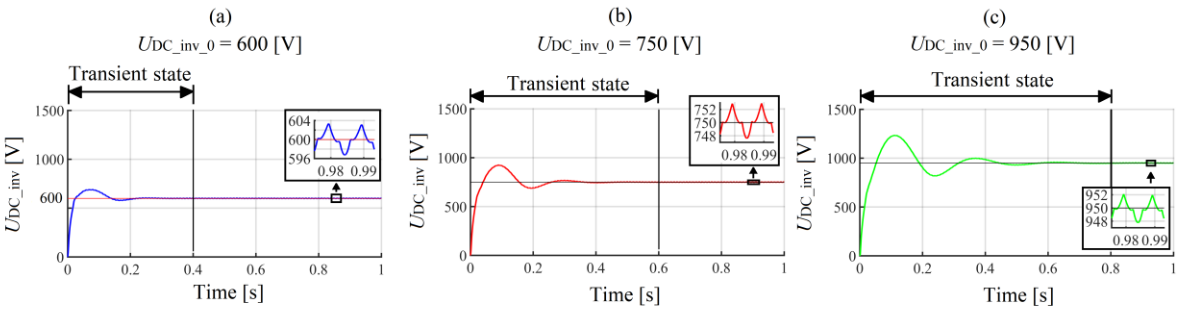

Figure 5.35 Inverter DC side voltage waveforms for $U_{DC\_inv\_0}$ is equal to: (a) 600 V, (b) 750 V and (c) 950 V

$U_{DC\_inv\_0} = 950$ [V]

(With filtred grid voltage) (a) | (Without filtred grid voltage) (b)

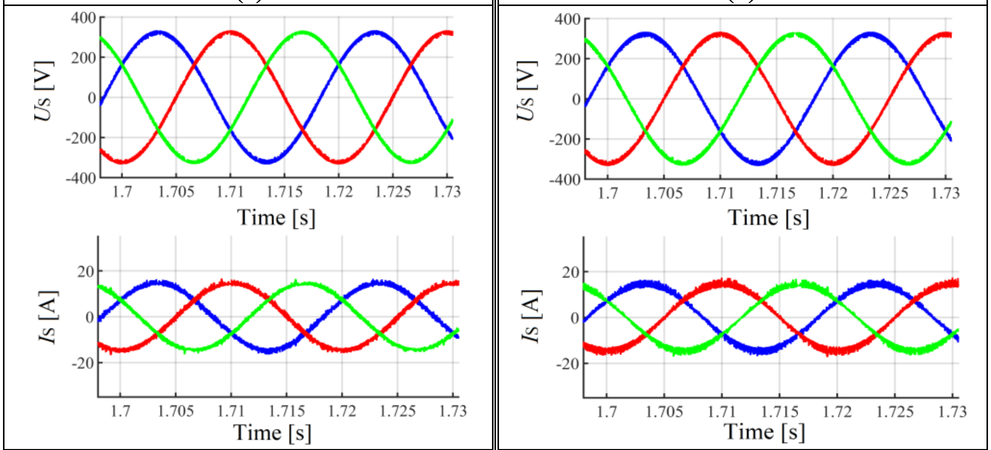

	THD_{US} [%]	THD_{IS} [%]	$TTHD_{US}$ [%]	$TTHD_{IS}$ [%]	THD_{US} [%]	THD_{IS} [%]	$TTHD_{US}$ [%]	$TTHD_{IS}$ [%]
L1	0.03	1.71	3.24	7.46	0.03	1.83	3.04	8.21
L2	0.03	1.86	2.86	7.39	0.03	2.17	2.87	7.86
L3	0.03	1.75	3.06	6.39	0.03	2	3.20	7.27

Figure 5.36 Grid voltage and current waveforms as well as THD and TTHD: (a) the PCC voltage is filtred, (b) the PCC voltage is not filtred (see Figure 5.13)

- **Conclusion**

The performed studies in this chapter allow the author to conclude that the SAPF efficiency did not depend only on its control system and parameters of the elements that constitute it, but also on the electrical grid and load parameters. In the power system with non-sinusoidal voltage and current, the voltage filtration before its use in the algorithm based on instantaneous *p-q* theory is important (from the grid current distortion mitigation point of view).

5.3 Laboratory experiments on the three legs four wires shunt active power filter (model of Figure 2.11(b))

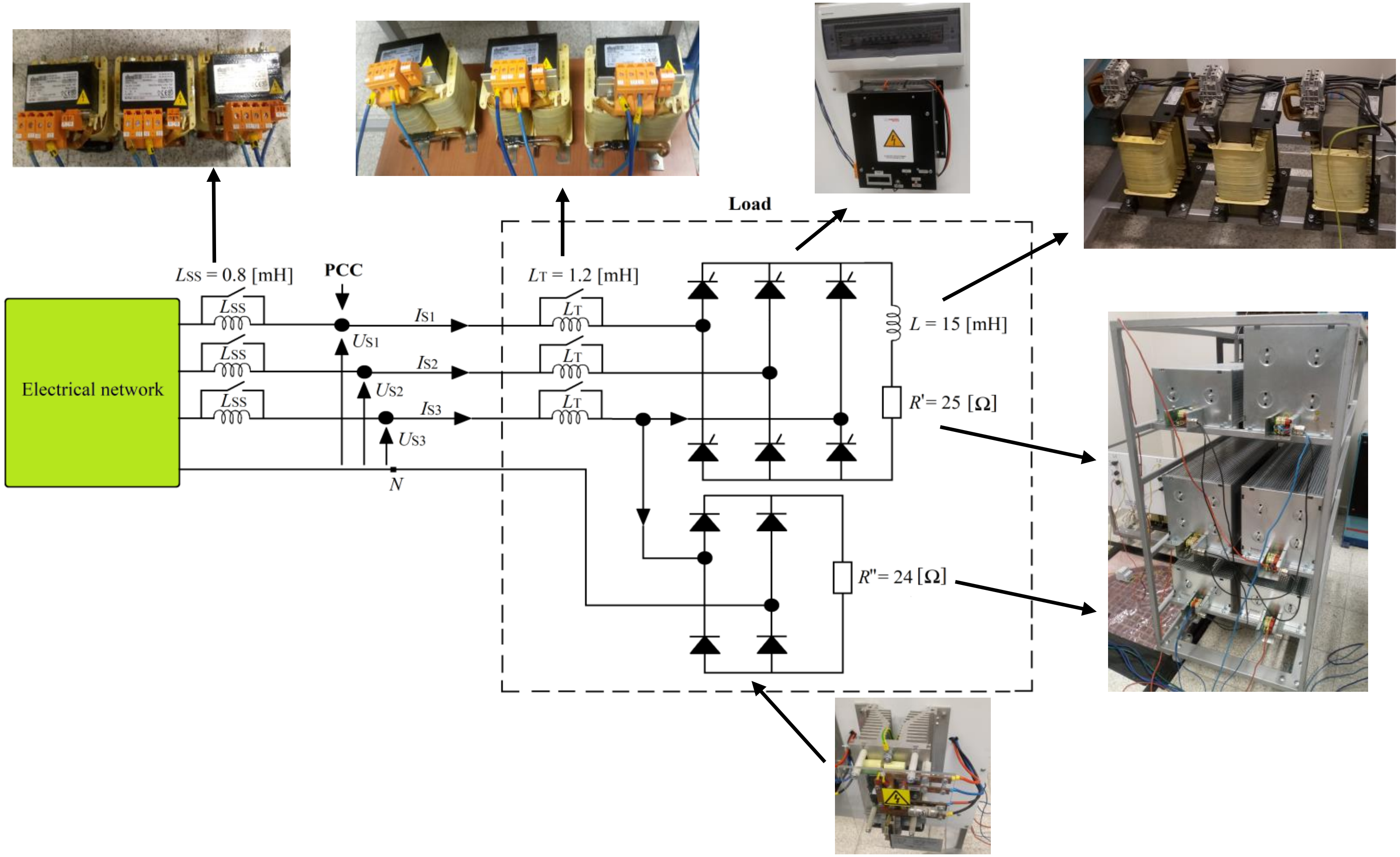

Figure 5.37 Equivalent circuit of the laboratory model with components

The studies of the influence of the rectifier input reactor (L_T) and the grid side line reactor (L_{SS}) on the SAPF performances have been previously presented by basing on the simulation. In this chapter based on the laboratory experiments the same studies are presented.

The laboratory model equivalent circuit is presented in Figure 5.37. The load is composed of three-phase thyristor bridge with resistance R and reactor L at its DC side and reactor L_T at its AC side. The one-phase diode bridge with 24 Ohm resistance at the DC side is used to obtain the current asymmetry. The electrical network parameters were already presented in chapter 4 (Figure 4.6).

The SAPF used in the laboratory to perform the studies is three legs four wires (Figure 5.38). Its control system is based on the instantaneous *p*-*q* theory algorithm and PWM control method. The inverter output current is used as feedback signal.

The laboratory experiments are not focused on the design of the SAPF with its control system, but on the influence of the rectifier commutator reactor (L_T) and line reactor (L_{SS}) (see Figure 5.37) on the SAPF performances. The author did not have influence on the way of SAPF feedback coupling system connection.

The experiments are carried-out by maintaining constant the parameters of SAPF with control system and rectifiers DC components as well.

The measured grid voltage and current spectrums and waveforms before the SAPF connection (L_{SS} and L_T are not connected) is presented in Figure 5.39. It can be seen in that figure the PCC voltage and current distortion, the current asymmetry and the high level of fundamental harmonic reactive power.

5.3.1 Studies of thyristor bridge input reactor influence on the SAPF performance

Three cases of study based on the rectifier input reactor change (L_T) were considered after the SAPF connection: L_T – is not connected, $L_T = L_{\_inv} = 2$ mH and $L_T = 2.5$ mH $> L_{\_inv} = 2$ mH. During the experiments, the grid side line reactor (L_{SS}) was not considered.

Figure 5.40(b)(c) in comparison to Figure 5.40(a) shows that when the inverter input reactor inductance is equal or lower than the rectifier input reactor inductance, the PCC voltage and current waveforms ripples at the commutation are better reduced by the SAPF.

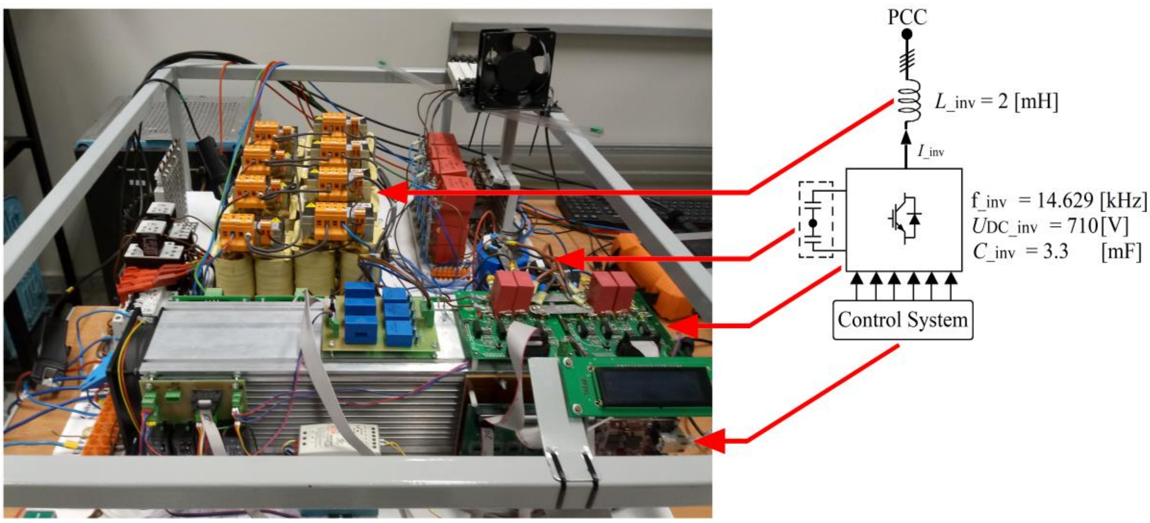

Figure 5.38 Laboratory model of three legs four wires SAPF

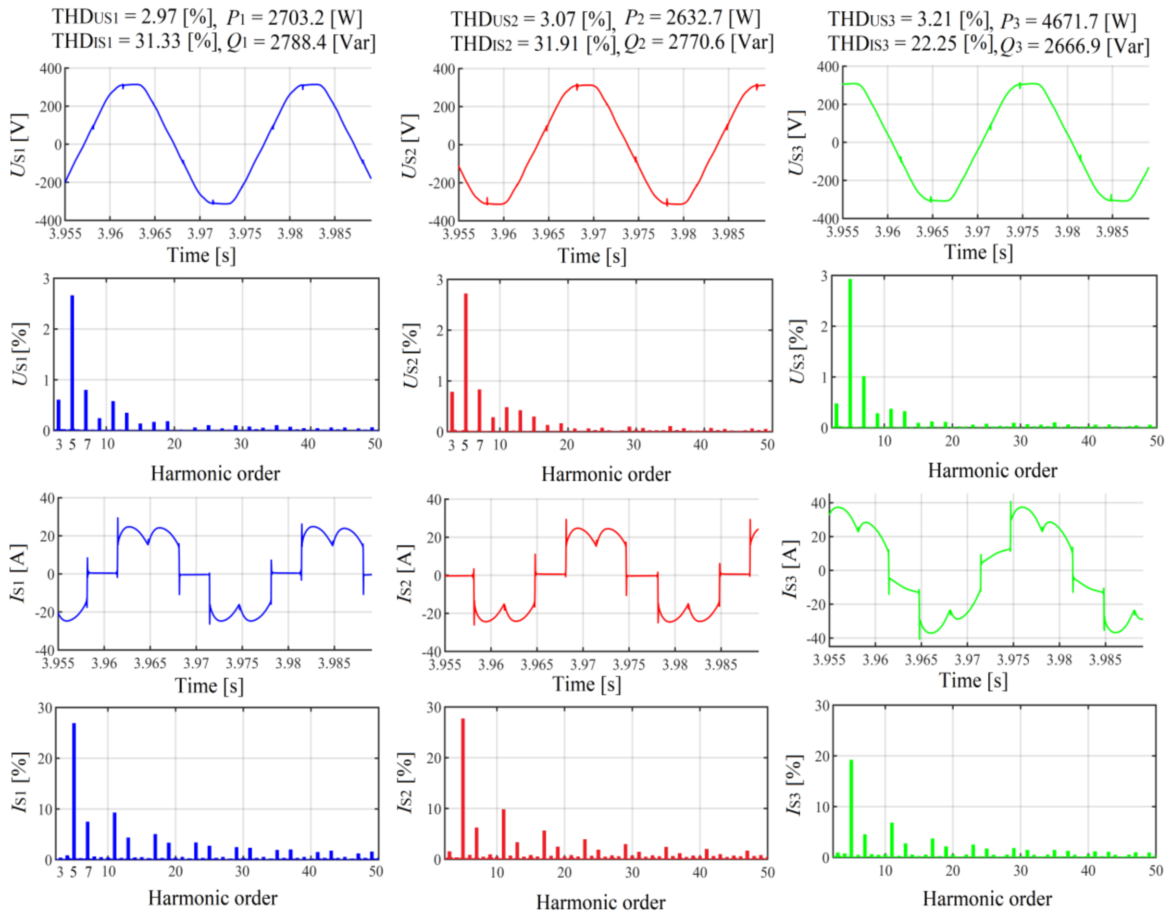

Figure 5.39 Measured grid voltage and current waveforms with spectrums before the SAPF connection (L_{SS} = L_T = 0)

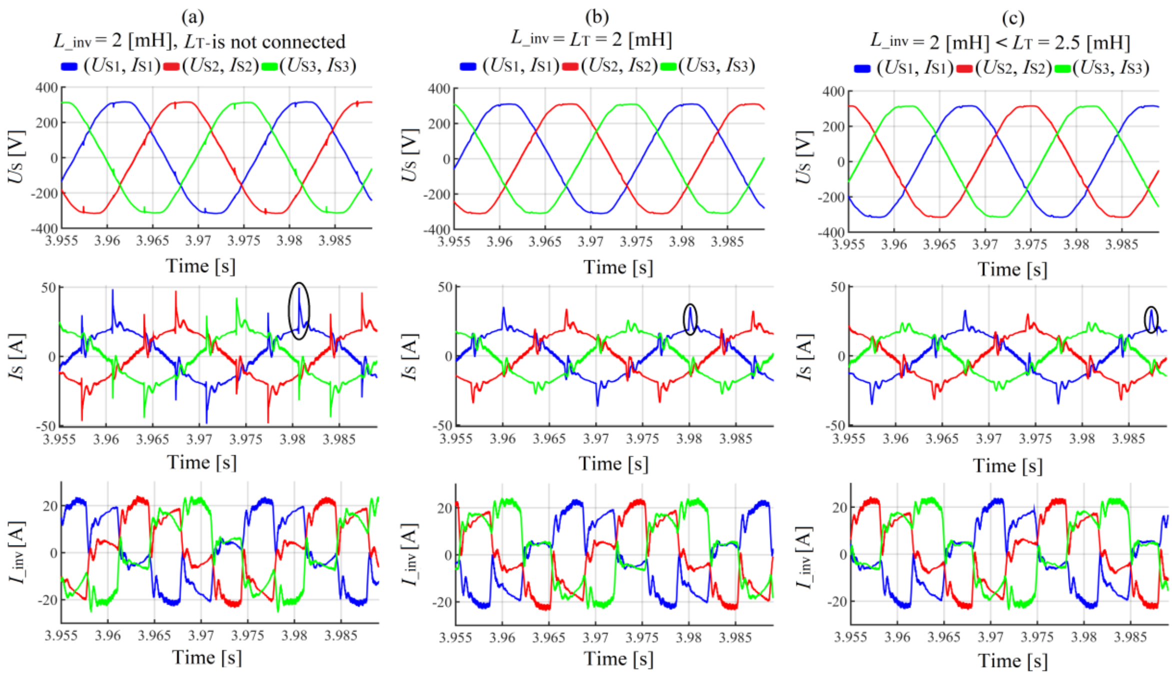

Figure 5.40 Comparison of grid voltage (U_S) and current (I_S) and SAPF current ($I_{\_inv}$) waveforms: (a) L_T is not connected, (b) L_T = $L_{\_inv}$ = 2 mH and (c) L_T > $L_{\_inv}$

Figure 5.41 represents (for the three case studies) a comparison of PCC voltage and current spectrums and THD as well as the PCC active and reactive power. Only one-phase of each case is considered because of the PCC current balance after the SAPF connection. For $L_{\_inv}$ equal or smaller than L_T, the PCC voltage and current 5th harmonic as well as THD are better mitigated (Figure 5.41(a) to (c)). It is important to notice that the PCC voltage contains harmonics, which can affect the results at the PCC.

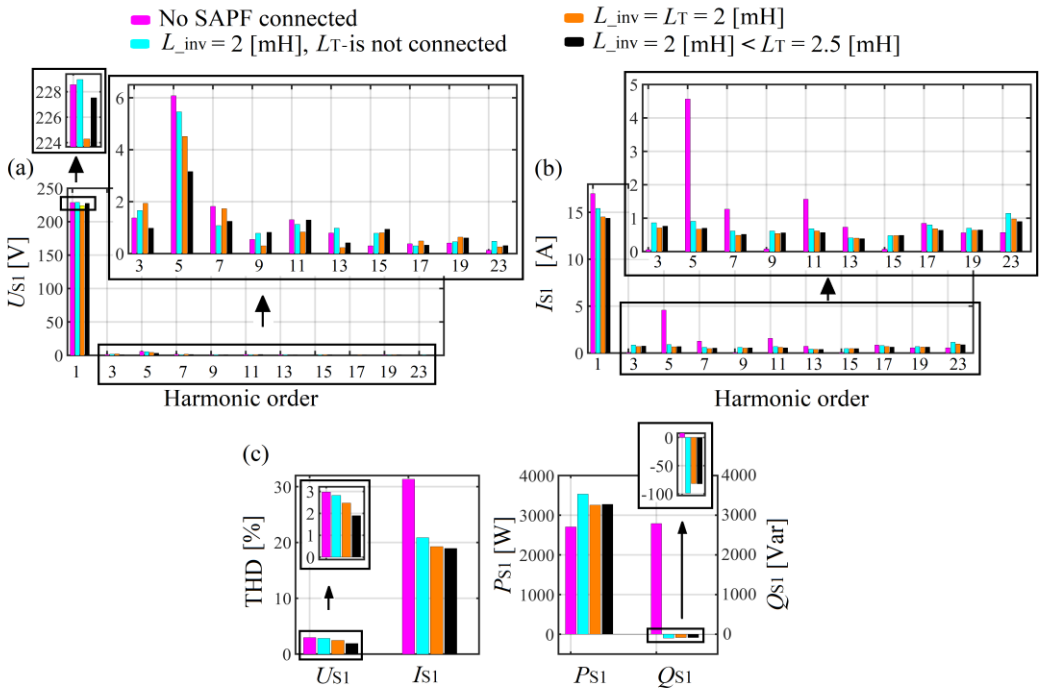

Figure 5.41 Comparison of: (a) PCC voltage spectrums, (b) PCC current spectrums and (c) PCC voltage and current THDs, active (P_1) and reactive powers (Q_1)

5.3.2 Studies of the grid side line reactor influence on the SAPF performances

The goal of these studies is to present what happened if at the PCC (grid side), an additional line reactor (L_{SS} - Figure 5.37) is connected when the SAPF is operating (L_T = 2.5 mH). Three case studies are also compared: (a) the SAPF is not connected, (b) the SAPF is connected but the line reactor L_{SS} is not considered and (c) the SAPF is connected and line reactor L_{SS} is considered.

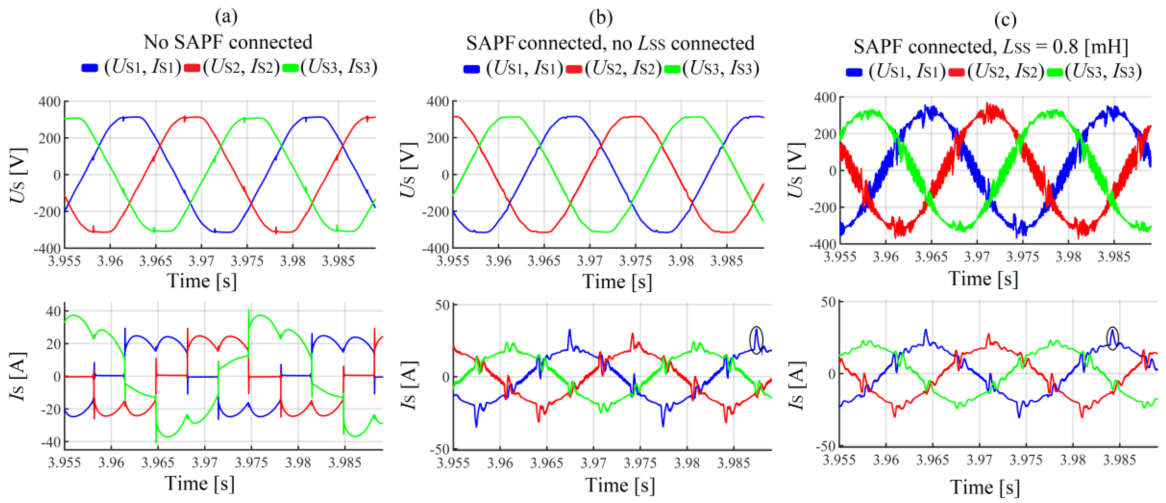

Figure 5.42 Comparison of PCC voltage and current waveforms: (a) the SAPF is not connected, (b) the SAPF is connected but the line reactor L_{SS} is not connected and (c) the SAPF is connected as well as the line reactor

On the one hand, the increase of the grid inductance by adding the line reactor has improved the PCC current waveform (better reduction of ripples at the commutation points

(Figure 5.42(c)) as well as the 5th, 7th and 11th harmonic amplitudes (Figure 5.43(b)) and lower THD (Figure 5.43(c))). On the other hand, it has increased the grid higher voltage harmonics amplitudes from the 13th (Figure 5.43(a)) as well as the THD (Figure 5.43(c)). In comparison to Figure 5.42(a)(b), the grid voltage waveform in Figure 5.42(c) presents the highest switching ripples because of the grid inductance increase. The PCC active and reactive power are presented in (Figure 5.43(c)).

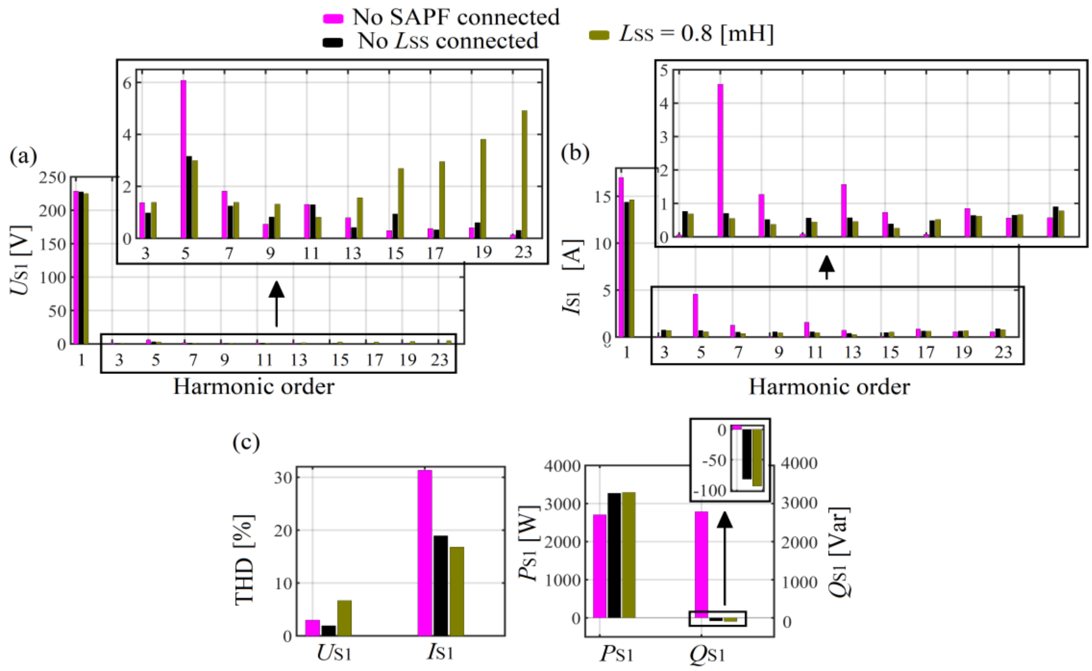

Figure 5.43 Comparison of: (a) grid voltage spectrums, (b) PCC current spectrums and (c) grid voltage and current THDs, active (P_1) and reactive power (Q_1)

- **Conclusion**

The laboratory experiments have shown that:

– for a better reduction of grid voltage and current ripples at the commutation points of waveforms, the inductance of reactor (first-order filter) connected at the SAPF input for switching ripples mitigation, should be smaller or equal to the inductance of the input rectifier reactor so called commutation reactor,

– when the SAPF with reactor at its input is connected at the PCC, the additional line reactor connection between the PCC and the grid is not recommendable, because the PCC voltage will be more distorted with inverter switching ripple.

5.4 Laboratory experiments on the hybrid active power filter: model of Figure 2.13(l)

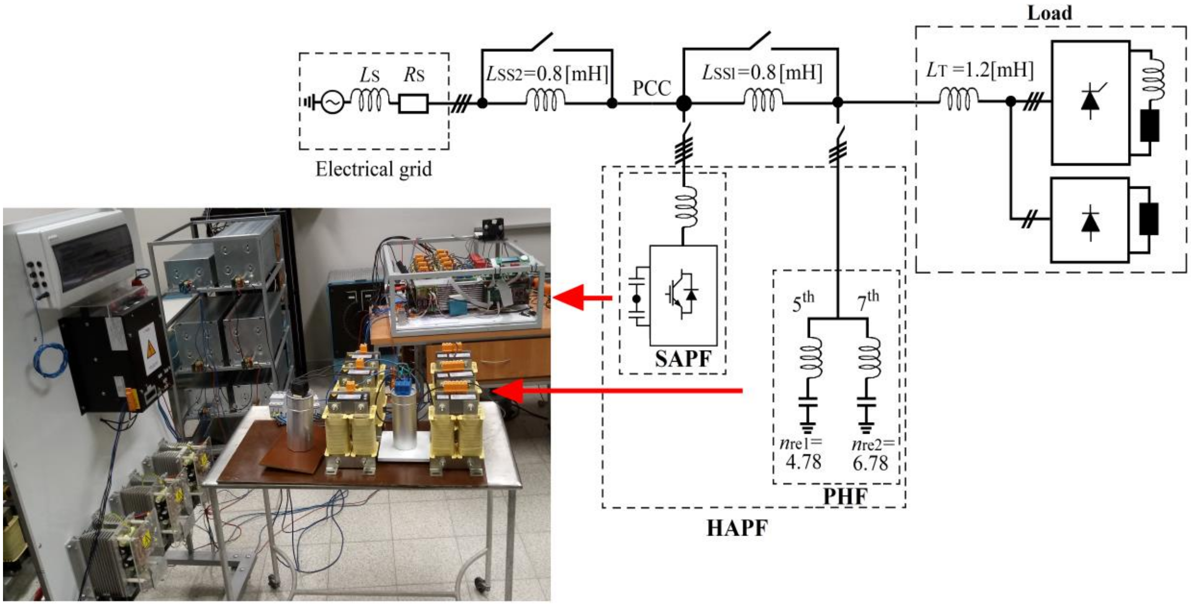

Figure 5.44 HAPF laboratory model

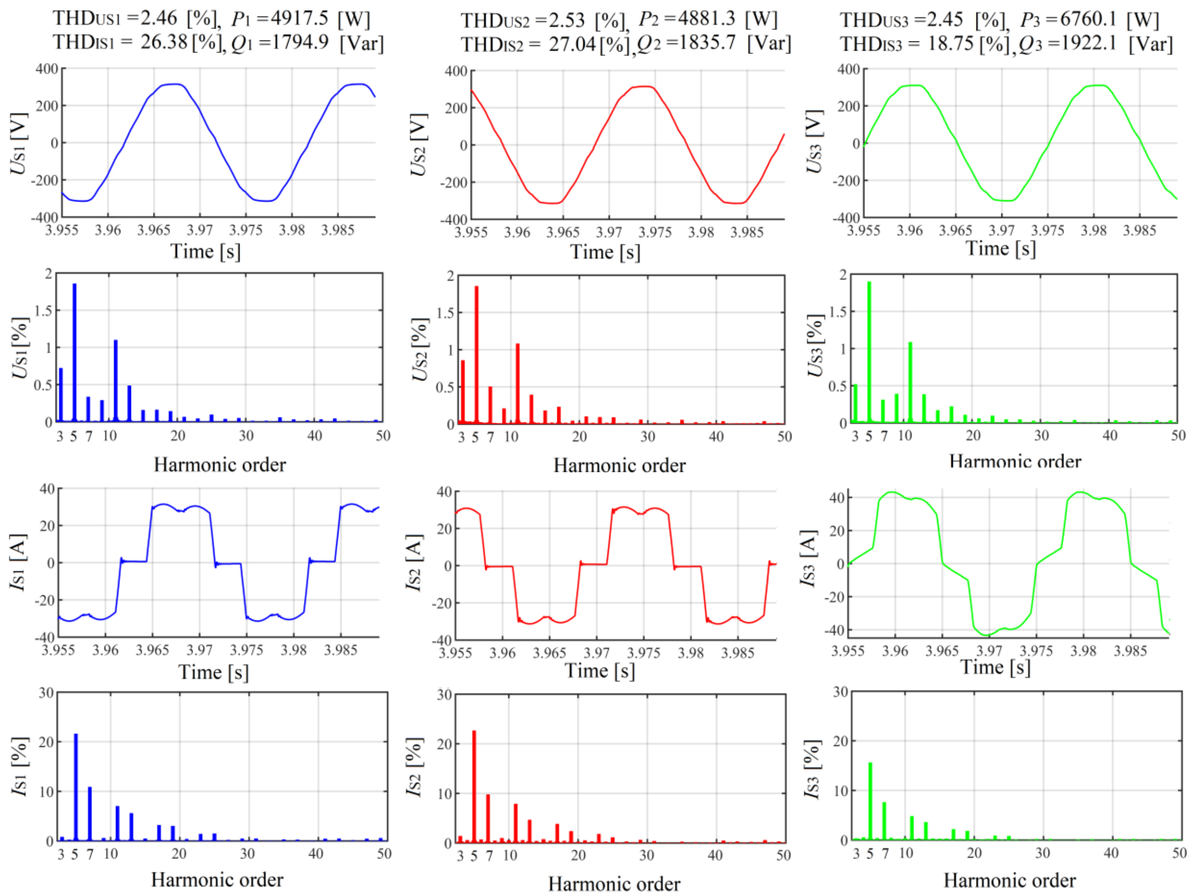

Figure 5.45 PCC voltage and current waveforms and spectrums measured when the HAPF is not connected (with L_T)

The considered laboratory model of HAPF is presented in Figure 5.44 (concerning the load part, see Figure 5.37 for more detail). It is constituted of SAPF (Figure 5.38) connected in parallel with the group of two single-tuned PHFs (Figure 4.59). The PHF group impedance versus frequency characteristics is presented in Figure 4.60(b). The SAPF feedback coupling system was not accessible to the author.

The goal of this laboratory experiments is to confirm the functionality of the considered HAPF topology as described in chapter 2 (Figure 2.12(b) and to show the ability to reduce the SAPF power by connecting the group of PHFs.

Two laboratory experiments are performed: 1) the PHF group, SAPF and HAPF are connected successively and the results (at the PCC) are compared (only the line reactor L_{SS1} is connected to improve the filter group efficiency (L_{SS2} is not connected)); 2) the HAPF (withouth L_{SS1}) is connected to the grid through the line reactor L_{SS2} and the results are compared with those obtained when L_{SS1} (L_{SS2} not connected) were connected between the SAPF and the PHF group (Figure 5.44). The reactors optimization solution is not under concern in this chapter but their influence on the HAPF efficiency.

5.4.1 The first laboratory experiment

In that experiment, the filters are successively connected (firstly no filters is connected, secondly only the PHF is connected, thirdly only the SAPF is connected and finally both of filters are connected (HAPF)) and the measured PCC data are compared (see Figure 5.46 and Figure 5.47).

The PCC voltage and current waveforms and spectrums when no filter is connected are presented in Figure 5.45. The load consumes the fundamental harmonic reactive power and generates the current harmonics and current asymmetry (Figure 5.46(a)).

In Figure 5.46, it can be observed that the SAPF (when operating alone - Figure 5.46(c)) and the HAPF (Figure 5.46(d)) present better shape of grid current waveforms than the group of PHF operating alone (Figure 5.46(b)).

For all considered cases (see Figure 5.47), it can be noticed that the PHF after its connection has mitigated the fundamental harmonic reactive power (Q_{S123} - Figure 5.47(c)) and the current harmonic amplitudes (e.g. 5th, 7th 11th, 13th and 19th - Figure 5.47(b)). The SAPF connected together with the PHF (forming the HAPF) has compensated the remaining grid fundamental harmonic reactive power and mitigated the remaining current harmonics (Figure 5.47(b)(c)).

After the filters connection some PCC voltage harmonic amplitudes have increased (e.g. 5th, 7th - Figure 5.47(a)). This increase is due to the fact that the grid voltage contains harmonics other than the fundamental (e.g. 3rd, 5th, 7th etc. see Figure 4.7, chapter 4) and the grid inductance voltage drops caused by the current harmonics from the grid side and from the remaining load current harmonics after filtration are added (or subtracted). In this case example, these harmonics increase (5th and 7th) is much visible, when the SAPF is operating alone (see the highest PCC voltage THD of Figure 5.47(c)).

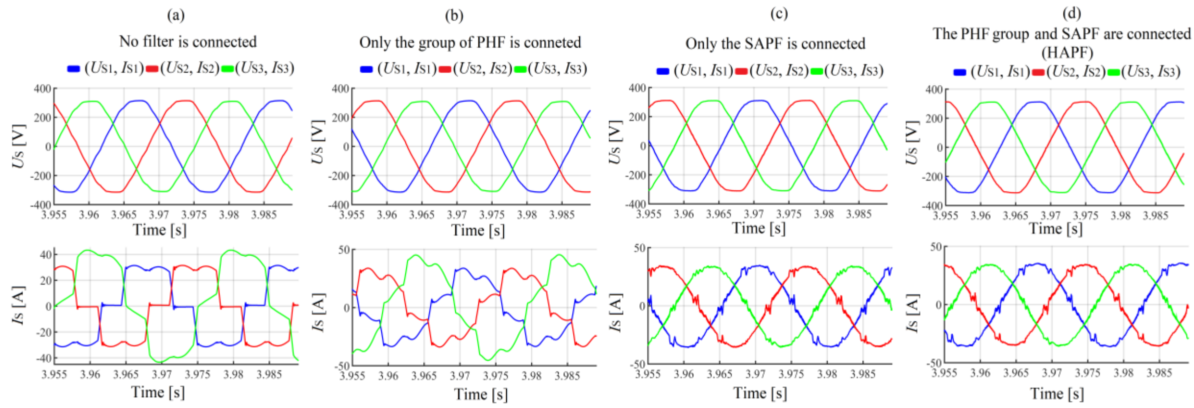

Figure 5.46 PCC voltage and current waveforms: (a) None filter is connected, (b) only the PHF is connected, (c) only the SAPF is connected and (d) the PPF and SAPF are connected (HAPF)

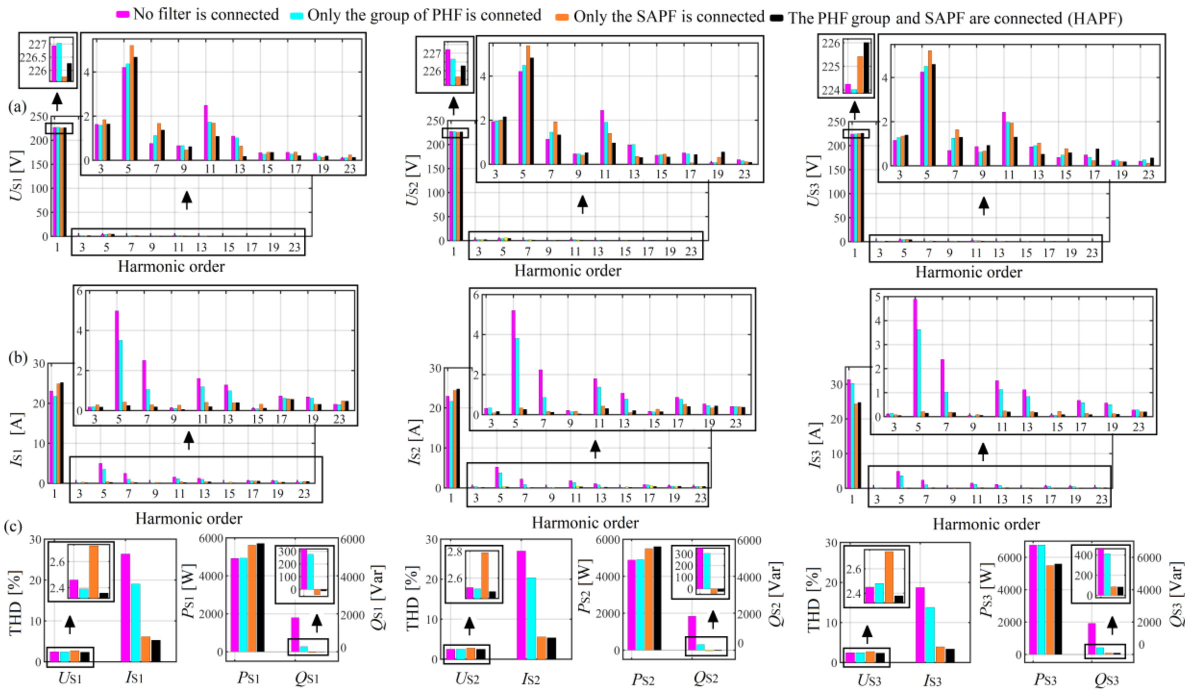

Figure 5.47 (a) PCC voltage (U_{S123}) spectrums, (b) PCC current (I_{S123}) spectrums and (c) PCC voltage and current THD as well as active (P_{S123}) and reactive power (Q_{S123})

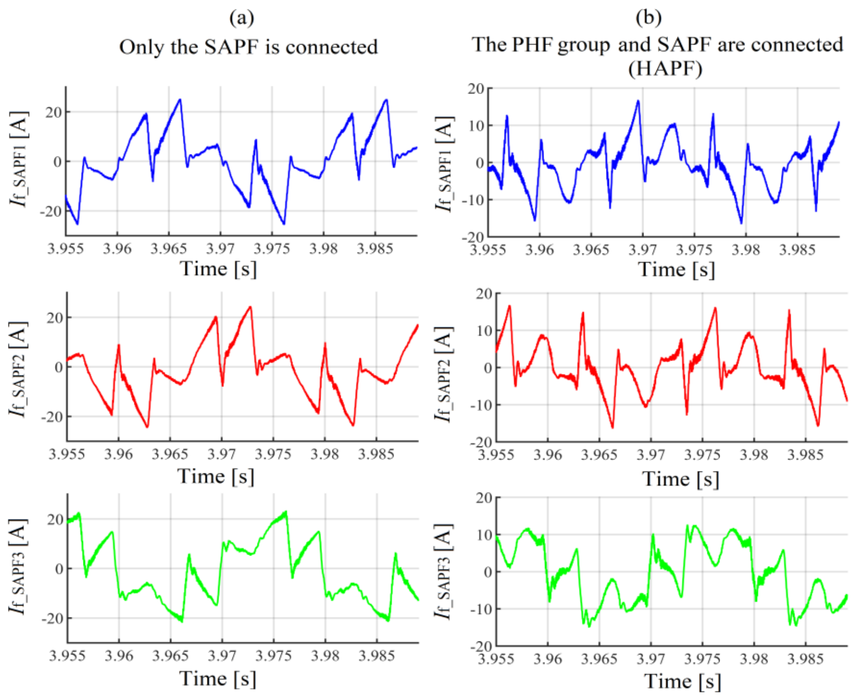

Figure 5.48 SAPF current waveforms: (a) the SAPF is operating alone and (b) the SAPF is operating together with the PHF (HAPF)

Figure 5.48 and Figure 5.49 present a comparison data of SAPF when it is operating alone and when it is operating with the PHF (HAPF). The current waveforms of SAPF (I_{f_SAPF}) when operating alone presents a higher amplitude (around 20 A) than when it is operating with the PHF (around 10 A) (Figure 5.48(a)(b)).

The SAPF when connected alone at the PCC has to generate higher current harmonics amplitudes (Figure 5.49(a)) and fundamental harmonic reactive power (Figure 5.49(b)) than when it is connected with the PHF. The SAPF connected together with the PHF has less power losses (S_{F_SAPF} - Figure 5.49(b)) than when it is working alone.

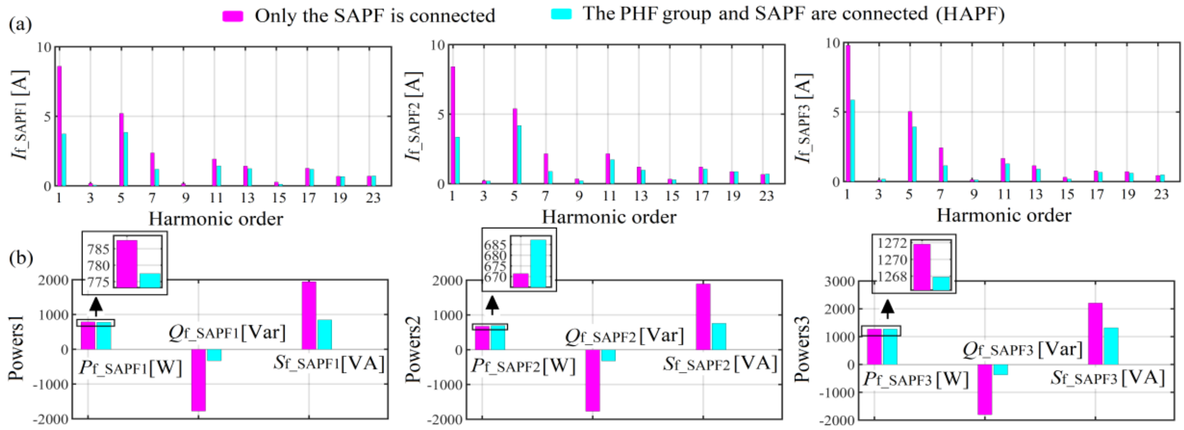

Figure 5.49 (a) SAPF current spectrum and (b) powers

5.4.2 The second laboratory experiment

In the second experiment, the HAPF (without L_{SS1}) is connected to the grid through the line reactor L_{SS2} and the results are compared with those obtained when L_{SS1} (L_{SS2} not connected) were connected between the SAPF and the PHF group (Figure 5.44).

In the case where the HAPF has L_{SS1} connected between the SAPF and the PHF group (without L_{SS2}), the PCC current and voltage waveforms are less distorted (see Figure 5.50(a)).

The connection of the HAPF (without L_{SS1}) to the grid through the line reactor L_{SS2} presents the worst results in term of harmonics mitigation (Figure 5.51(a)-(c)) and fundamental harmonic reactive power compensation (Figure 5.51(d). The PCC voltage and current are more distorted because of the additional voltage drops on the line reactor L_{SS2} (Figure 5.50(b)) (The connection of L_{SS2} at the grid side has decreased the grid short-circuit power, increasing its impedance).

Connected between the filters (SAPF and the PHF group), the line reactor L_{SS1} helps on one hand, the group of PHF to mitigate the 5^{th} and 7^{th} current harmonics and on other hand, it helps the SAPF to mitigate the ripples at the commutation notches of grid voltage and current waveforms.

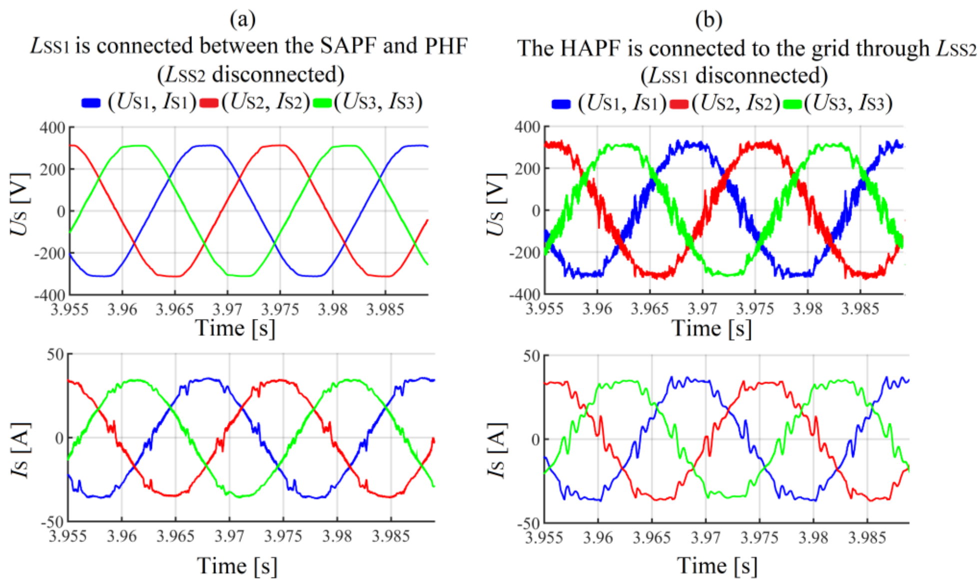

Figure 5.50 PCC voltage and current waveforms: (a) the line reactor L_{SS1} is connected between the SAPF and PHF (L_{SS2} disconnected) and (b) the HAPF is connected to the grid throught L_{SS2} (L_{SS1} disconnected)

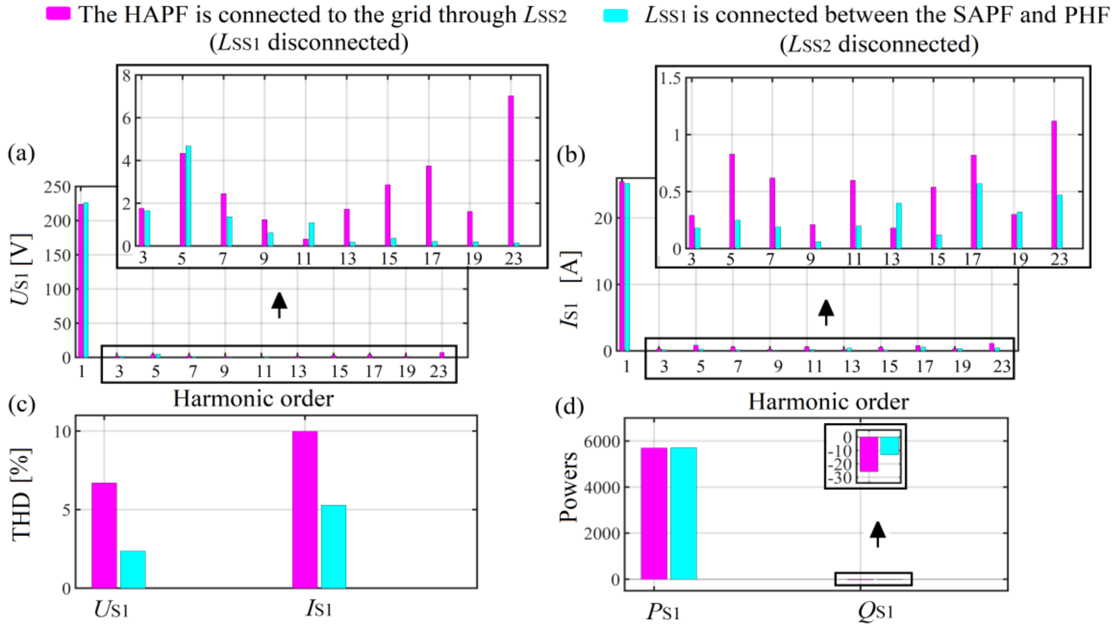

Figure 5.51 (a), (b) PCC voltage and current spectrums, (c) THD and (d) fundamental harmonic active and reactive powers

- **Conclusion**

The laboratory experiments have shown that:

– the SAPF is better than the PHF in term of grid current harmonics mitigation,

– combined with the PHF (HAPF), the SAPF demants less power than when it is operating alone,

– the connection of the SAPF or HAPF to the PCC through a line reactor is not recommendable,

– in the configuration of HAPF where the SAPF and PHF are connected in parallel, if the PHF presents higher impedance of harmonic(s) to be mitigated than in the grid side, the line reactor between the SAPF and PHF is needed.

Chapter 6
Hybrid active power filter (topology nº2)

The shunt active power filter (SAPF) and the passive harmonic filters (PHF) have been studied in the previous chapters (Chapter 3-5). Their disadvantages were notified: high inverter DC voltage demand as well as high cost of its elements (transistor, capacitor etc.) in the case of SAPF and gird impedance dependency, the sensitivity of filter efficiency on LC parameters tolerance, resonance and detuning phenomenon in the case of PHF. The hybrid active power filter is designed to overcome these disadvantages [40, 53, 181].

The hybrid active power filter (topology nº2) (HAPF2) under study (based on simulation) in this chapter is the topology presented in Figure 2.12(c) (Chapter 2). It is composed of PHF connected in series with the active power filter [95]. The SAPF when operating alone is always connected to the full supply phase-to-phase PCC voltage and need (for a good performance) high voltage rate at its inverter DC side (see Figure 5.33). But connected in series with the PHF (HAPF2), the passive filter allows the active power filter to work under small voltage rate at the DC side, therefore reducing its cost [9, 12, 18, 53, 54, 55, 57, 64, 76, 85, 95, 98, 132, 150, 156, 158, 191, 231, 239, 241, 242, 247, 265].

The focus of the author on the topology presented in Figure 2.12(c) is due to the fact that, in the literature there are not many clarifications on the PHF tuning frequency when it is connected in series with the SAPF. The HAPF2 functionality principle and control system as well as the studies based on the PHF tuning frequency are presented in this chapter.

6.1 Functionality principle of HAPF2

The HAPF2 functionality principle is presented in Figure 6.1. The symmetrical load is the source of distorted current which is composed of 3 components: active ($I_{T(1)\_Active}$), inductive reactive ($I_{T(1)\_Inductive\_Reactive}$) and harmonics ($I_{T(h)}$).

Tuned on the frequency of the load characteristic harmonic which in this case is the 7^{th}, (the case of other tuning frequencies will presented in further part of the work) the PHF role is to compensate the load reactive power fundamental harmonic by producing through its capacitor capacitive reactive current ($I_{f(1)\_Capacitive\_Reactive}$) which at the PCC cancel with the load inductive reactive current ($I_{T(1)\_Inductive\_Reactive}$) (in Figure 6.1 it can be seen that, the load induc-

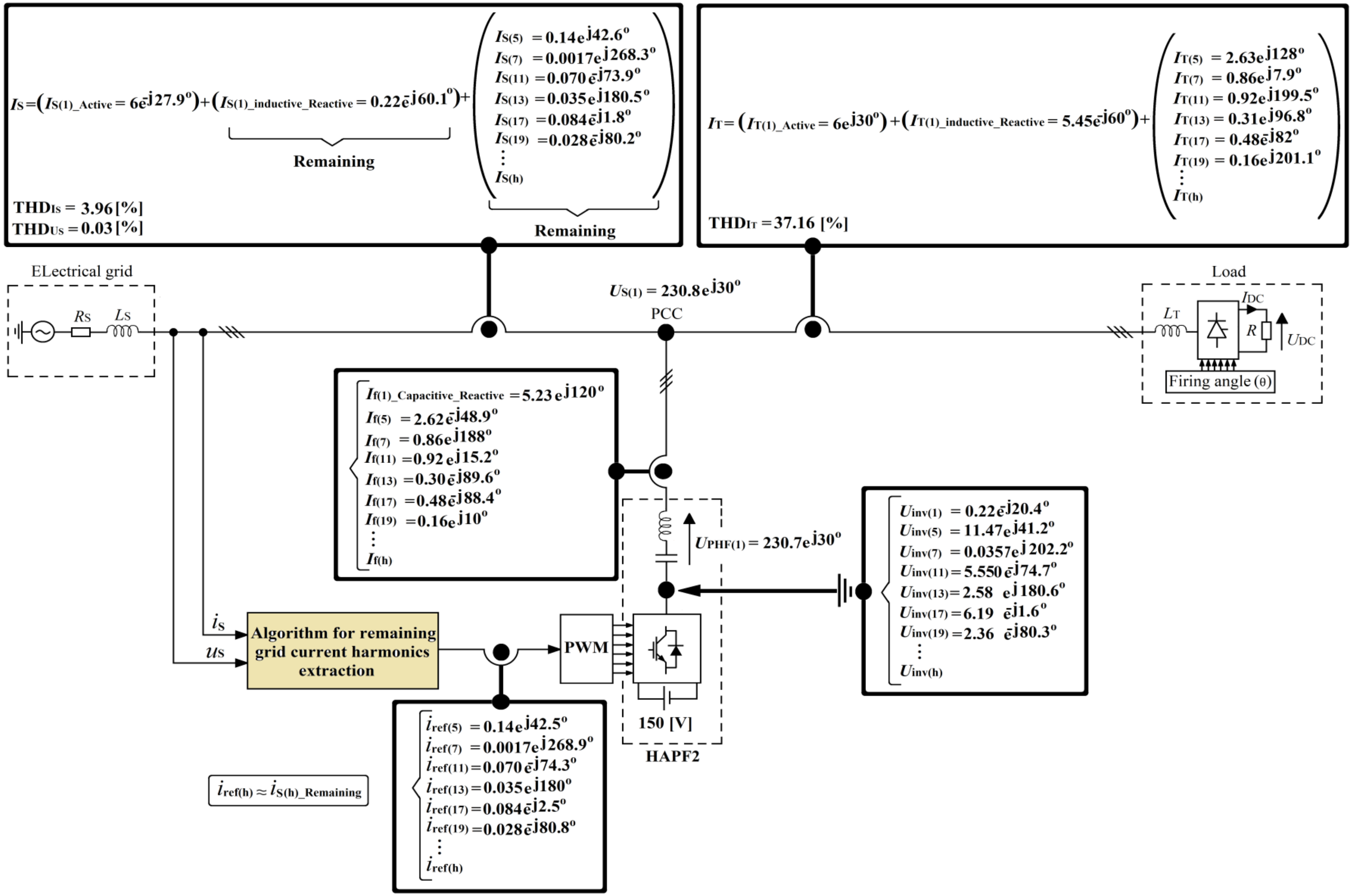

Figure 6.1 HAPF functionality principle

tive reactive current which was 5.45 A is reduced to 0.22 A ($I_{S(1)\_Inductive\_Reactive}$) at the grid side). It plays as well the role of inverter switching ripples attenuation mostly through its reactor. It presents very small impedance for the resonance frequency and frequencies around.

In Figure 6.1, it can be noticed that the grid current remaining harmonics ($I_{S(h)Remaining}$) extracted through the control system algorithm becomes the control system reference harmonics current ($I_{ref(h)}$) which are directly injected to the PWM system without any feedback signal coming from the inverter AC side. Therefore by basing on the reference harmonics current $I_{ref(h)}$ (e.g. $I_{ref(5)} = 0.14e^{j42.5^o}$), the inverter generates current harmonics ($I_{f(h)}$, e.g. $I_{ref(5)} = 2.62e^{-j48.9^o}$) which have the same amplitudes and angle as the load current harmonics (e.g. $I_{T(5)} = 2.63e^{j128^o}$) but in opposite sign so that they cancel each other at the PCC (grid current THD reduction from 37.18% to 4.13% - Figure 6.1). The inverter behaves as a harmonics voltage source ($U_{inv(h)}$). At the end of the compensation, flows at the grid side a current with almost not-change in the active component ($I_{S(1)\_Active}$) and with the remain reactive and harmonic currents (see Figure 6.1).

6.1.1 Description of HAPF2 control system

The HAPF2 control system is presented in Figure 6.3. The applied algorithm to extract the remaining PCC current harmonics is based on the instantaneous *p-q* theory described in chapter 5. The control system structure is almost the same as the one of SAPF described in chapter 5, Figure 5.24. It has three control loops: the control loop (1) for inverter DC side voltage stabilization and maintenance to the desire level, the control loop (2) to extract the harmonics from the PCC current signal and the control loop (3) (open loop without feedback from the inverter AC side) for transistors pulses generation. For more details of HAPF2 control system, see Annex V.

6.2 HAPF2 Simulation studies

The simulated power system is presented in Figure 6.4. The load and the electrical grid parameters are the same as those of the laboratory model presented in chapter 4 (Figure 4.2 and Figure 4.6). The HAPF2 is connected at the PCC to compensate the grid current harmonics and fundamental harmonic reactive power. The voltage at the HAPF2 DC side (U_{DC_inv}) has been fixed to the value of 150V and can be less than that value (e.g. 70V (see [30])).

In papers (e.g. [12, 191, 231] etc.) the authors have presented the same consideration about the PHF tuning frequency. The 7th harmonic frequency is selected to be the HAPF2 passive harmonic filter resonance frequency and the mentioned reason are: the PHF is then less bulky and shipper than when it is tuned to the 5th harmonic frequency, the PHF presents lower impedance for the 11th and 13th harmonic frequencies than when it is tuned to the 5th harmonic frequency etc. In this chapter, the experimental studies are carried out after tuning the PHF in three different frequencies.

It is well explained in chapter 3 and 4 that the PHF (when operating alone) should be tuned to the frequency a little bit lower than the frequency of the lowest load characteristic harmonic in order to slow down its natural detuned phenomenon which can be caused by the aging or damage of its elements. This principle is taken into account during the HAPF2 passive harmonic filter design in the experimental studies.

Three simulation cases studies are compared: in the first one, the PHF of HAPF2 is tuned to the frequency a little bit lower (e.g. 243.5Hz, 4.87) than the frequency of the first load characteristic harmonic (the 5th); in the second one, it is tuned to the frequency a little bit lower (e.g. 343.5Hz, 6.87) than the frequency of the second load characteristic harmonic (the 7th) and in the third one, it is tuned to the frequency a little bit lower (e.g. 543.5Hz, 10.87) than the frequency of the third load characteristic harmonic (the 11th).

6.2.1 Simulation assumption and parameters computation

The PHF parameters of Table 6.1 has been computed by basing on the formula of Table 3.2. (see chapter 3) and the reactor resistances are computed by using of quality factor equation (see Table 3.2.). The PHF reactive power is chosen on the base of the load highest reactive power which is in this case example around 1210 Var (see chapter 4, Figure 4.12). The load, the inverter and the control system parameters are the same for each simulated case and some of them can be seen in Figure 6.4. The HAPF2 will been working with a constant reactive power in the symmetrical power system.

Observing the Table 6.1, it can be seen that, with the resonance frequency increase, the PHF reactor inductance has decreased whereas its capacitor capacity has increased. From the power losses point of view, the PHF with the resonance frequency (n_{re} = 10.87 (543.5Hz)) near the frequency of the 11th harmonic will generate less power losses because of its lowest resistance value. The PHF impedance versus frequency characteristics are presented in Figure 6.2.

Table 6.1 HAPF passive harmonic filter parameters

n_{re}	L_f [mH]	C_f [μF]	R_{Lf} [mΩ]	Q_f [Var]	q'	L_T [mH]
4.87	6.1	69.74	12.8	1210	150	3.5
6.87	3.0	71.27	6.3			
10.87	1.2	72.19	2.5			

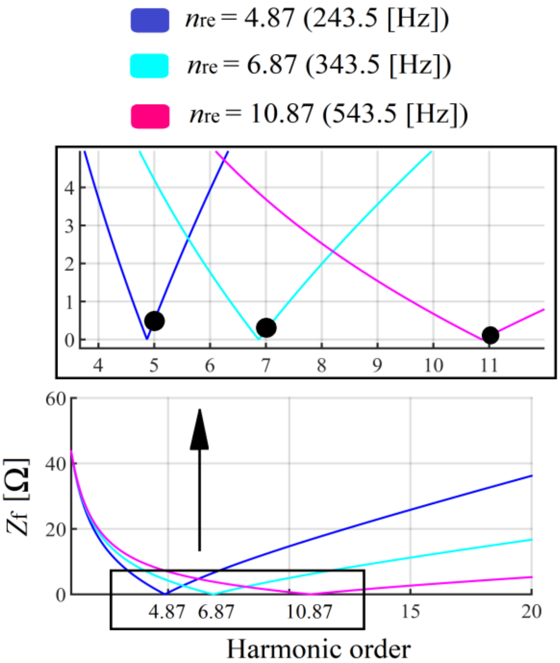

Figure 6.2 PHF impedance versus frequency characteristics. The PHF is tuned to the resonance frequencies of 243.3 Hz, 343.5 Hz and 543 Hz

6.2.2 Simulation results

The grid voltage and current waveforms with the spectrums before the HAPF2 connection are presented in Figure 6.5. Because of the symmetrical power system, some results are presented only for one-phase. Because of the electrical grid rigidity in the laboratory model (very small inductance in comparison to the rectifier and HAPF2 input inductance), the PCC voltage is very less distorted.

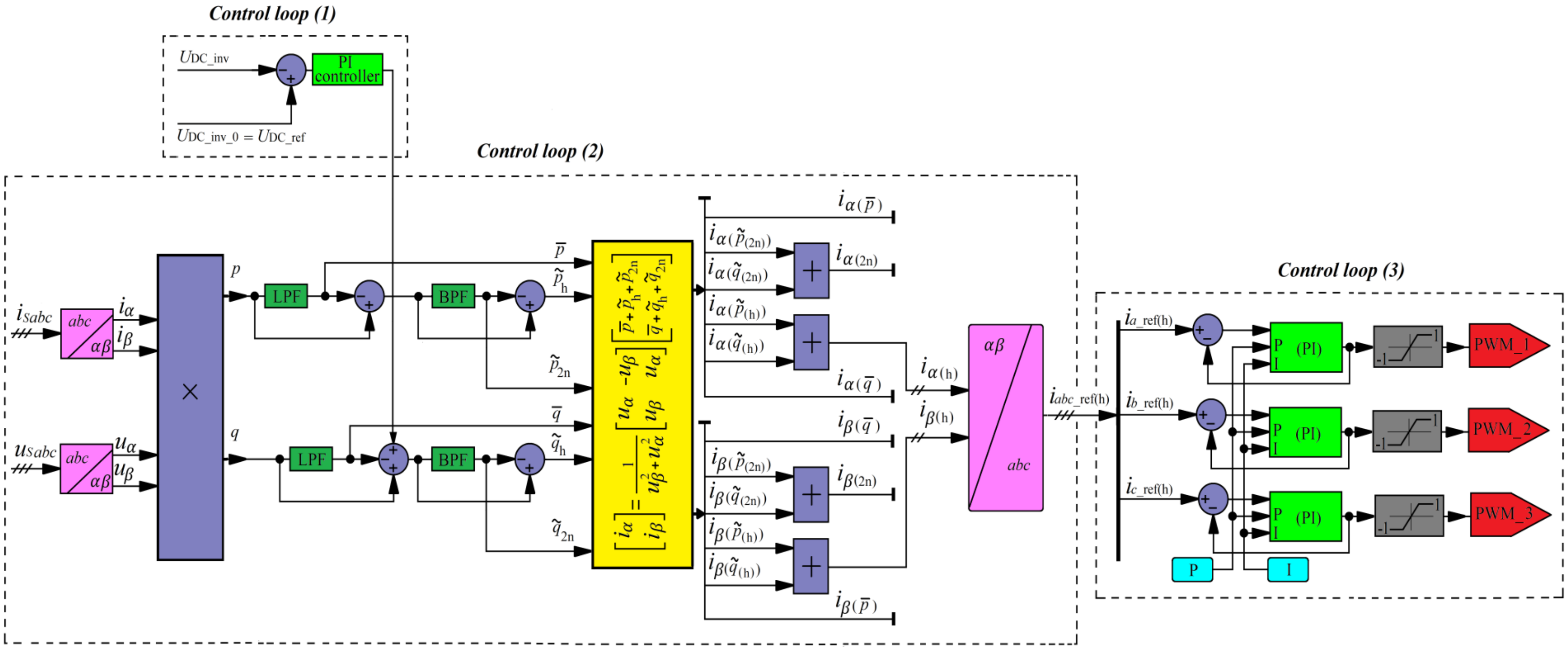

Figure 6.3 HAPF2 control system

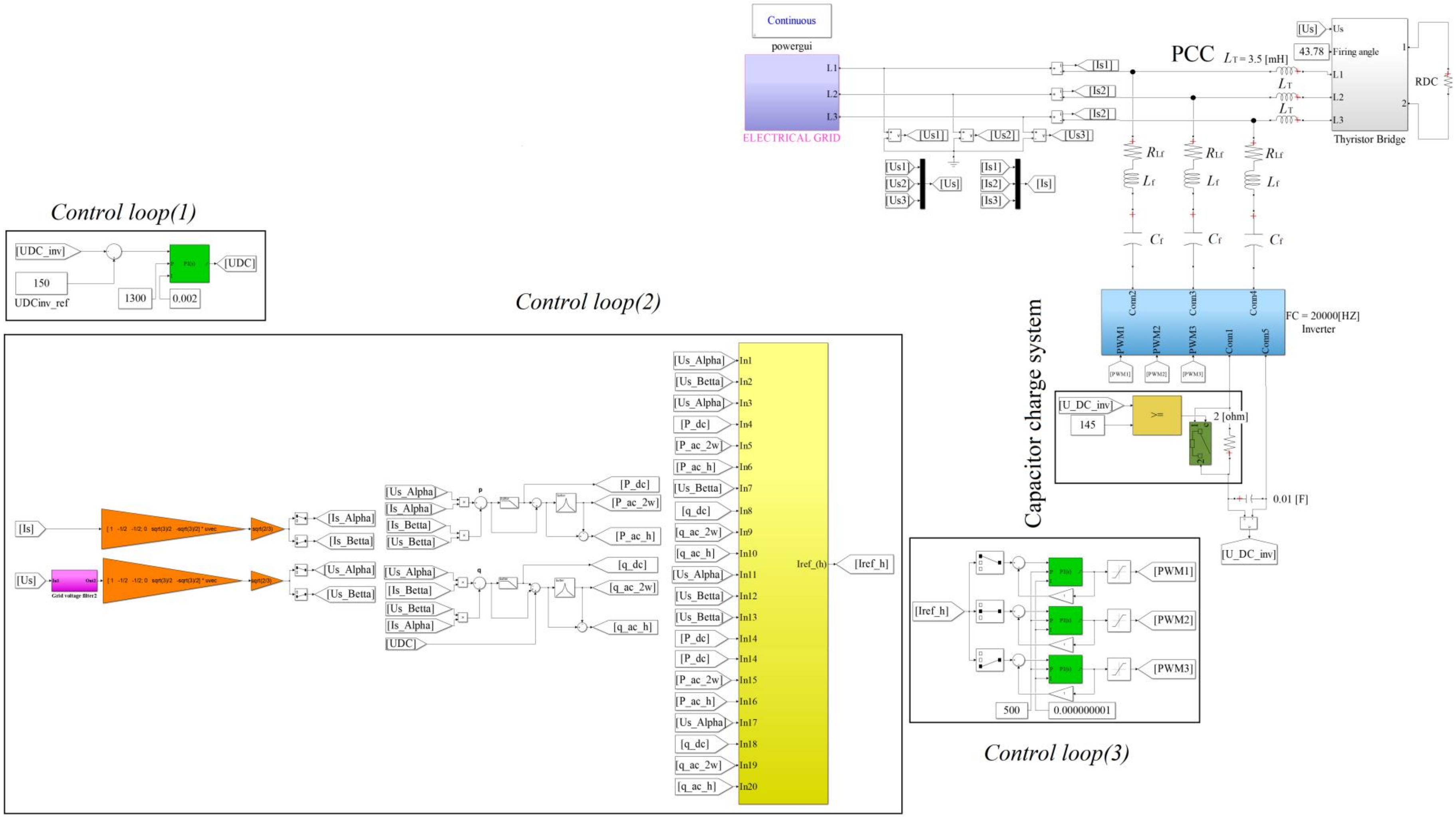

Figure 6.4 Simulated power system in Matlab-Simulink

In Figure 6.6, the waveforms of grid voltage and current and HAPF2 current after the HAPF2 connection are presented and it can be noticed that the HAPF with PHF tuned to the frequency a little bit lower (e.g. 543.5Hz, 10.87) than the frequency of the 11th harmonic presents the best reduction of the PCC current ripples at the waveforms commutation points (see also Figure 6.7(b)). Nevertheless, it presents the highest PCC voltage THD (Figure 6.6).

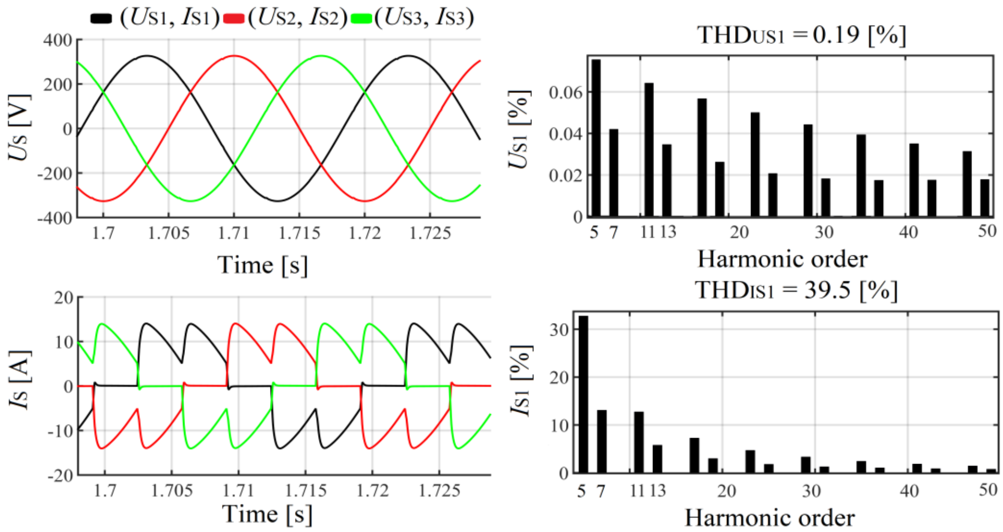

Figure 6.5 Grid voltage (Us) and current (Is) waveforms with their spectrums before the HAPF2 connection

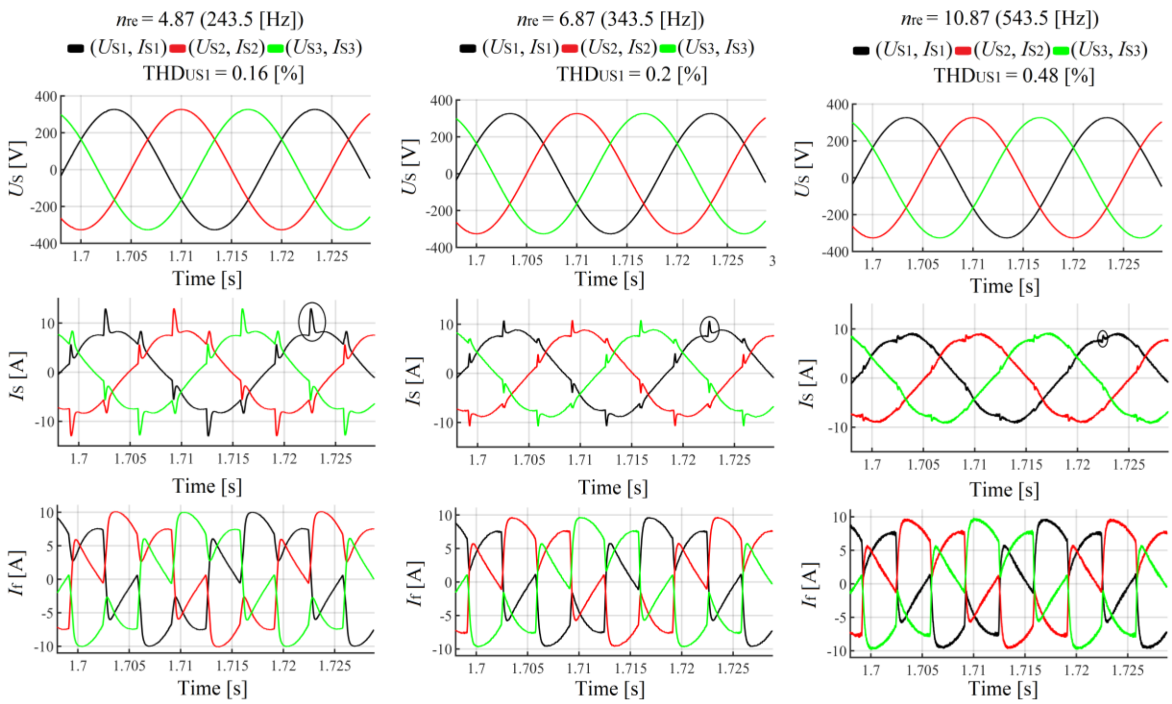

Figure 6.6 Waveforms of grid voltage (Us) and current (Is) and HAPF2 current (I_f) for the PHF tuned to the harmonic component frequency of: 4.87, 6.87 and 10.87

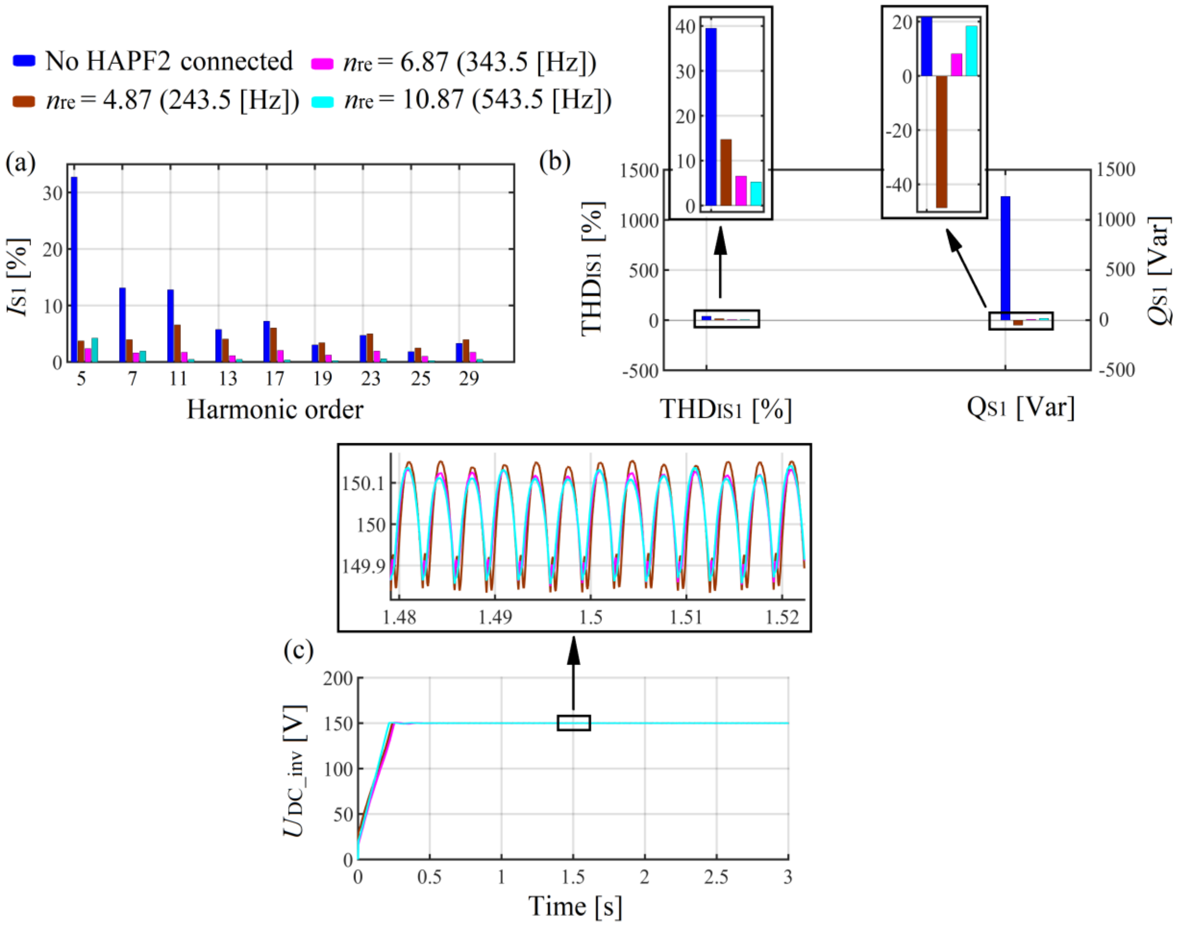

Figure 6.7 (a) grid current spectrum, (b) grid current THD and fundamental harmonic reactive power and (c) HAPF2 DC voltage

Table 6.2 Fondamental harmonic active, reactive and apparent powers at the load (Q_{load}), HAPF (Q_f) and grid (Q_S) side (from the simulation – one-phase)

	No filter	n_{re} = 4,87	n_{re} = 6,87	n_{re} = 10,87
$Q_{S1(1)}$ [Var]	1234	-48.7	8,16	18,31
$P_{S1(1)}$ [W]	1435	1438	1437	1435
$Q_{f1(1)}$ [Var]	-	-1283	-1226	-1216
$S_{f1(1)}$ [VA]	-	1282,83	1225,70	1217,54
$P_{load1(1)}$ [W]	-	1437	1437	1437
$Q_{Load1(1)}$ [Var]	-	1234	1234	1234

In the PCC current comparison spectrums of Figure 6.7(a), the HAPF2 with the PHF tuned to the harmonic component resonance frequency of 10,87 presents the best reduction of the higher harmonics from the 11th (according to the impedance versus frequency characteristics in Figure 6.2, the PHF presents the lowest impedance for the higher harmonics) as well as the lowest THD (see Figure 6.7(b)). But it presents the highest 5th harmonic impedance.

The HAPF with the PHF tuning frequency (n_{re} = 6.87) around the frequency of the 7th harmonic presents the lowest amplitude of the grid current 5th and 7th harmonics (Figure 6.7(a)).

In Figure 6.7(b), it can also be noticed that the PCC fundamental harmonic reactive power (Q_S) is the best compensated for the HAPF with the PHF tuned to the harmonic component resonance frequency of 6.87. The difference observed in the results of the grid fundamental reactive powers after the HAPF2 connection (Figure 6.7(b)) is du to the fact that, for different PHF tuning frequency, the HAPF2 has generated different fundamental harmonic reactive power (little different than the one used to compute the PHF paramters in Table 6.1) for the compensation at the PCC (see Q_f in Table 6.2).

In comparison to the SAPF (when operating alone) DC side voltage (which is around 750V), the HAPF inverter DC voltage is considerably reduced (around 150V, see Figure 6.7(c)).

The simulated power system transient ability during the load parameters change (e.g. decrease of the rectifier DC resistance R_{DC} from 36.5 Ω to 18.25 Ω) is presented in Figure 6.8. It can be seen that after the power system current increase (see Figure 6.8(a) after the rectifier DC side resistance decrease), the HAPF has mitigated the grid current harmonics, but did not totally compensate the fundamental harmonic reactive power because of its PHF reactive power which is sized to around 1210 Var. The invert DC side voltage is shown in Figure 6.8(b).

Figure 6.9(a)(b) presents respectively the waveforms of rectifier input (I_T) and grid side (I_S) current during the asymmetry. The asymmetry was obtained by connecting the resistance beween phases as presented in Figure 5.18 (R_{asym}). The HAPF2 with the proposed control system, does not have ability to compensate the asymmetry component (see also the SAPF in Chapter 5, Figure 5.20(b) and Figure 5.21).

The impedance versus frequency observed at the rectifier terminals (Figure 6.10) shows that the power system is purely inductive. The parallel resonance between the PHF (when operating alone) and the electrical gird is completely eliminated as well the dependency of the PHF performances (when operating alone) on the grid impedance.

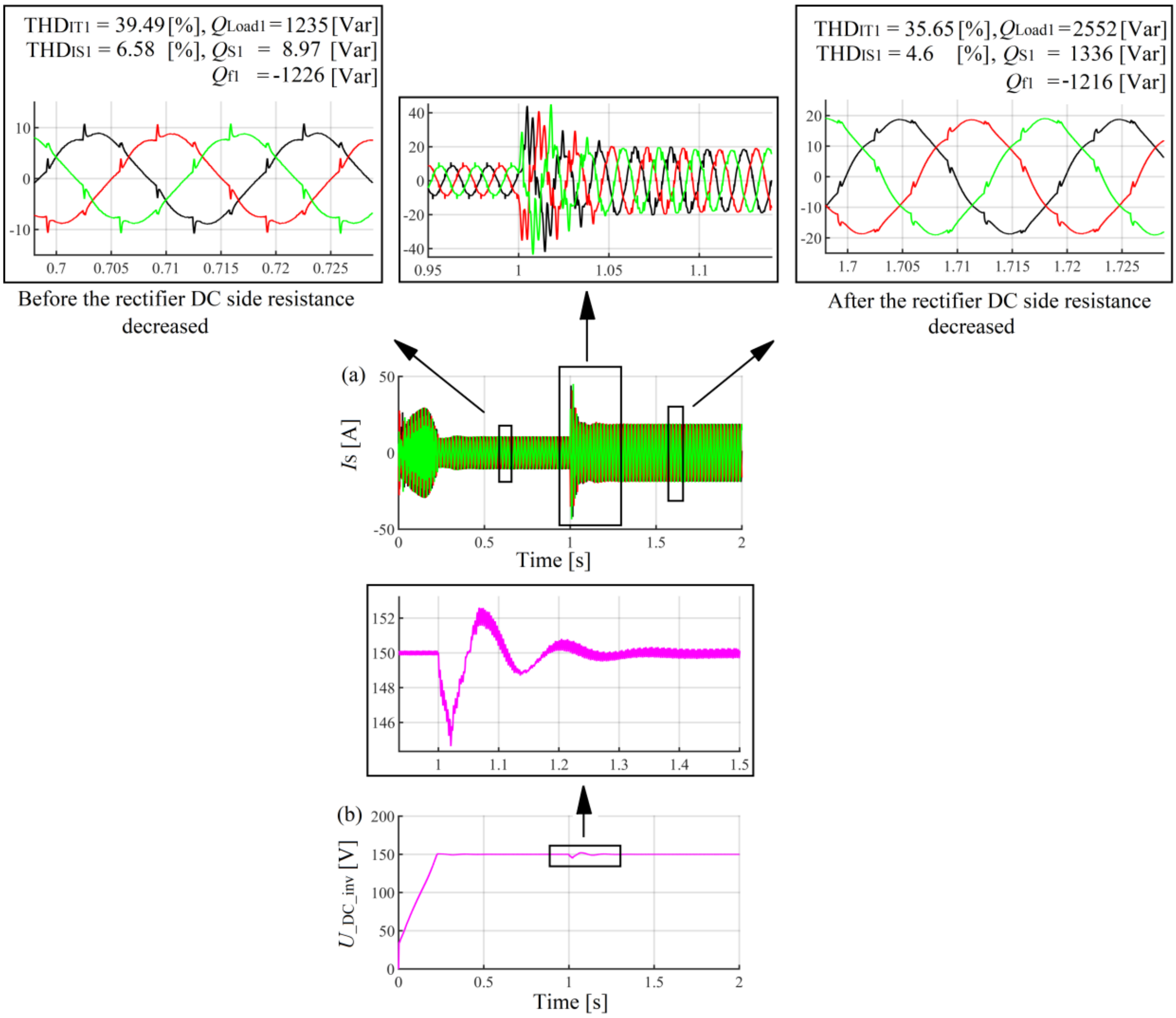

Figure 6.8 (a) grid current waveforms and (b) HAPF2 inverter DC side voltage during the reduction of R_{DC}

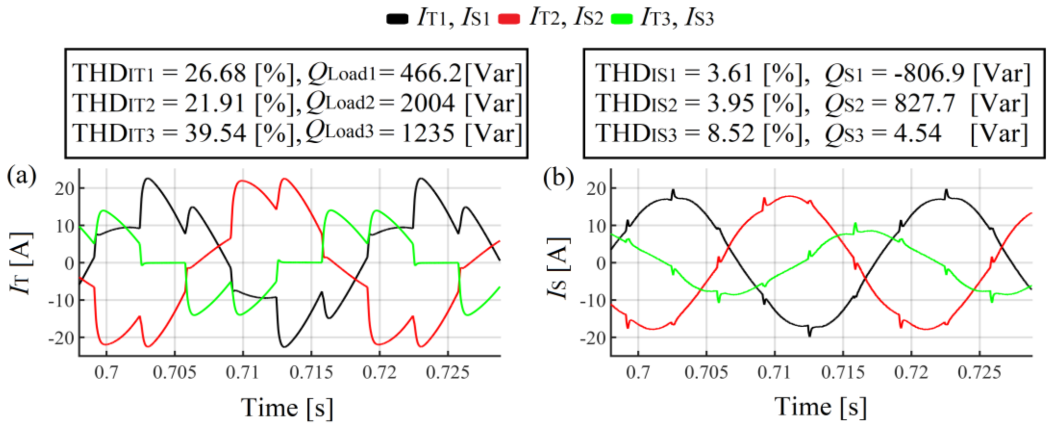

Figure 6.9 Waveforms of (a) input rectifier current and (b) grid current during the load side asymmetry

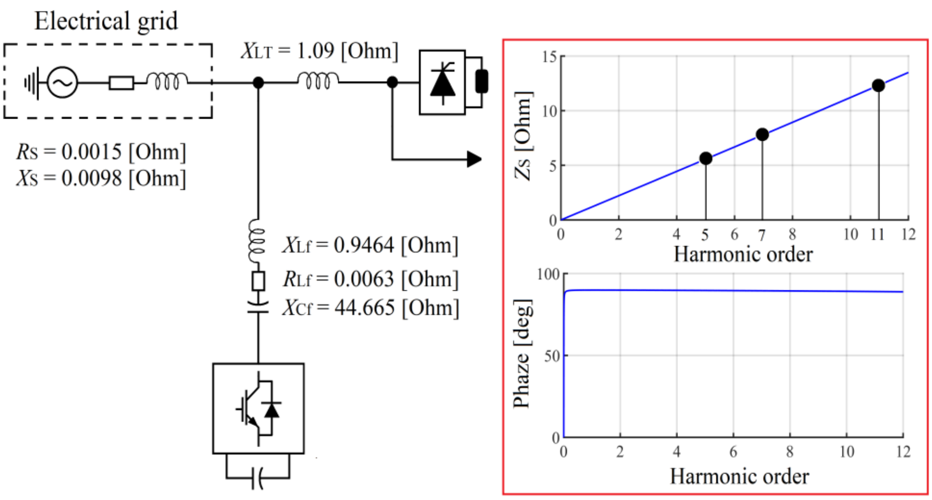

Figure 6.10 Impedance versus frequency of power system observed from thyristor bridge terminals

- **Conclusion**

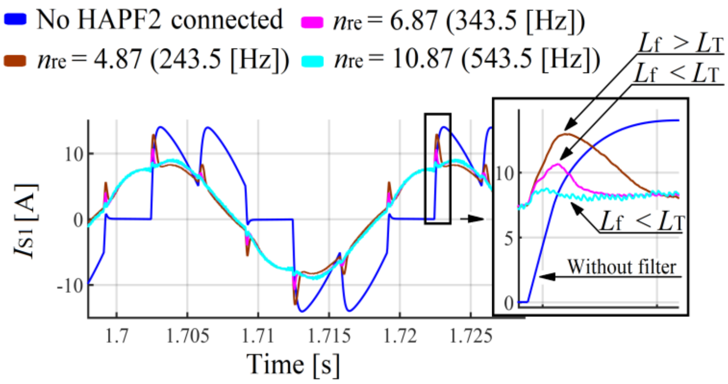

Figure 6.11 Grid current waveforms before and after the HAPF connection.

The HAPF2s with passive harmonic filter tuned to the resonance frequency (n_{re} = 6.87 (543.5Hz)) near the frequency of the 7th harmonic and to the resonance frequency (n_{re} = 10.87 (543.5Hz)) near the frequency of the 11th harmonic have the best result in term of grid current THD reduction because the inductances of their reactors which are 3 mH and 1.2 mH respectively are smaller than the input thysristor bridge reactor inductance which is 3.5 mH (see Figure 6.11). Therefore as it has been experimentally demonstrated in chapter 5 that the SAPF input reactor inductance (first-order filter) should be chosen with the value equal or little bit lower than the input rectifier reactor inductance value for a better mitigation of grid current ripple at the waveforms commutation points, that principle should also be applied during the design of HAPF passive harmonic filter.

The choose of the HAPF2 passive harmonic filter resonance frequency should not be focused only on the rectifier (load to be compensated) characteristic harmonics but also on the value of the rectifier input reactor inductance. The PHF of HAPF2 can be tuned to any frequency provided that, its reactor inductance has a value equal or smaller than the one of the rectifier input reactor so called commutation reactor.

The performed experiments have also shown that when the PHF is tuned to the resonance frequency higher than the frequencies of the 5th and 7th harmonic: the HAPF reduces (at the grid side) better the higher current harmonics (e.g. from the 13th) because the PHF presents smaller impedance for that harmonics (Figure 6.2.), the 5th and 7th current harmonics are worse reduced and the PHF reactor value is smaller in comparison to the case when it was tuned to the frequency near the 5th or 7th harmonics, therefore low cost. If the PHF reactor value is too small, the HAPF can face the problem of switching ripple mitigation

There are many topologies of PHF that can be connected in series with the SAPF as in the structure of HAPF2 [30].

Chapter 7

Conclusion

The techniques used to reduce the voltage and current distortion caused by power electronic converters in the electrical power systems exist in large numbers. Some of them were selected and presented in this work. The thesis objective focused on the hybrid active power filter (HAPF) which is the combination of active power filter (APF) and passive harmonic filter (PHF). To achieve the thesis objective, the author performed different studies (simulation and laboratory) on the selected PHF and SAPF structures.

The acquired knowledge from the studies of the PHF and SAPF structures allowed the author to design and analyzed the hybrid active power filter (HAPF) structures: model of SAPF (three legs three wires) connected in series with the single-branch filter (simulation) and model of SAPF (three legs four wires) connected in parallel with the group of two single-branch filters (laboratory).

7.1 Simulation study results

The following PHF structures were considered: the single-tuned filter, the series PHF, the double-tuned filter, the broad-band filters (first, second, third-order and C-type filter) and Hybrid passive harmonic filter (HPHF). The author analyzed the PHF topologies basing on their impedance versus frequency characteristics, detuning phenomenon (due to the filter elements parameters (LC) change over the time or due to fault or atmospheric conditions), and damping resistance. All the quoted elements have an influence on PHF filtration efficiency. The comparison of some PHF structures (group of two single-filters & double-tune filter, series PHF & HPHF) as well as the methods of sharing the total reactive power in the filter group were also considered. The structures were tested as a stand-alone device as well as a part of the entire system including non-linear load and supply network with its internal equivalent impedance.

Basing on the impedance versus frequency characteristics, the author showed that the variation of the series PHF parameters decreases its efficiency on the harmonic to be blocked. Connected between the PCC and the rectifier load, it can be the source of harmonics amplification at the grid side. The disadvantages (e.g. harmonics amplification etc.) of the series PHF can be overcome by the shunt PHF (HPHF).

The author demonstrated that:

- the shunt PHFs (single-tuned, double-tuned and broad-band filters) should by tuned to the frequency a bit lower than the frequency of harmonic to be eliminated because of the aging of their elements (*LC*) which can caused the filter detuned. The harmonic to be eliminated should be the load (e.g. rectifier) characteristic harmonic after the fundamental harmonic. The bad choice of the shunt PHF resonance frequency can cause the amplification of harmonics at the electrical grid side and filter terminals,
- the increase of single-tuned filter resistance reduces its efficiency on the mitigation of harmonic to be eliminated at the grid side and increases its power losses,
- the filter group (two single-tuned filters) in comparison to the double-tuned filter (the same fundamental harmonic reactive power, reactor quality factor and voltage at their terminals) presentes higher value of inductances (more expensive in practice) and lower impedance for harmonics higher than the harmonics to which it is tuned,
- the first-order filter designed for the fundamental harmonic reactive power compensation, in the electrical power system with distorted voltage and current, can be a source of harmonics amplification (at the grid side),
- the second-order, third-order and C-type filter efficiency depends upon the choice of the damping resistance value. They can be the source of harmonics amplification (mostly the characteristic harmonics near the fundamental) at the grid side if the damping resistance is not well chosen. Depending on their damping resistance value, they are better on the reduction of harmonics in wide band than the single-tune filter (grid side),
- the single-tuned filter compared to the broad-band filters (equal fundamental reactive power, equal reactor quality factor, and equal resonance frequency) and regardless of damping resistance value, is better on the mitigation (grid side) of harmonic which the frequency is near its resonance frequency,
- the second-order filter in comparison to the single-tuned filter and other the broad-band filters (equal fundamental reactive power, equal reactor quality factor, and equal tuning frequency) and regardless of damping resistance value, present higher power losses,

Six methods (Method A to F) of sharing the total fundamental reactive power in the filter group were presented and compared in this work. Despite the fact that the efficiency of filters whose individual components have been selected by different methods is very similar, method A (equal reactive for filters in the group) remains more attractive than other method because it demands less caculation and presents better resuls in term of filter group power losses.

The goal of designing the SAPF (three wires three legs structure) was to compensate the load fundamental harmonic reactive power, harmonics, and asymmetry and it was achieved using the original control algorithm – based on *p-q* theory - prosed by author. The influence of the line reactor (connected between the PCC and the grid side), rectifier input reactor and SAPF input reactor and DC capacitor on its efficiency, was also considered.

In the description of the *p-q* theory algorithm used in the SAPF control system, the author demonstrated that the distortion contained in the PCC voltage, if not filtred, affects the reference current and can be found in the grid current after compensation (the grid current waveform is then the replica of the PCC voltage waveform).

In the electrical system with rectifier load, the choice of the SAPF input reactor (*L*-filter) inductance value should be also based on the input rectifier reactor inductance value. It should be lower or equal to the input rectifier reactor inductance value for better mitigation of the grid current ripples at the commutation notches points. The connection of the line reactor between the PCC and the grid is not recommendable because of the PCC voltage distortion increased.

The analyzed HAPF was the topology of SAPF connected in series with the PHF (single-tuned filter). The goal of studying such of topology was to show that it is possible to reduce the power of SAPF (active part). The HAPF was applied to compensate the load fundamental harmonic reactive power and harmonics. The author demonstrated that the choice of the single-branch filter tuning frequency of that topology should not only depend on the rectifier (load to be compensated) characteristic harmonics but also on rectifier input reactor size. The author also proposed a control system algorithm based on *p-q* theory for that topology.

7.2 Laboratory study results

Basing on the investigations in the laboratory, the author demonstrated that the shunt PHFs efficiency depends upon the electrical grid impedance (the filter impedance of the harmonic to be eliminated should be smaller than the grid impedance of that harmonic), the supply voltage quality (with the distorted electrical grid voltage, after the filter connection, the harmonics flow from the grid to the filter (amplification of harmonics at the grid and filter side)) and the tolerance of the filter elements (*LC*). Before the shunt PHF design, the following infromations are needed:

- the load current characteristic harmonics and fundamental harmonic reactive power,
- the electrical grid estimeted impedance,
- the supply voltage spectrum at the PCC when the load to be compensated is not connected.

In the case of the distorted supply voltage (when the load to be compensated is not connected) and filter impedance of the harmonic to be eliminated not enaugh lower than the grid impedance of that harmonic, the author has demonstrated that the connection of the line reactor between the grid and the PCC can be the solution with the disadvantage that the PCC voltage will be more distorted.

The author also demonstrated that after receiving the filter elements from the producer, it is important to verify (by measuring) if their parameters (reactor inductance and resistance, capacitor capacitance and resistance as well as filter resonance frequency) are within the tolerance or are the expected ones. The measured filter parameters can be a bit different from the nominal parameters because of the elements (*LC*) tolerance.

The investigation of the single-tune filter, group of two single-tuned filters, first and second-order filters in the laboratory confirmed the simulation studies.

The laboratory experiments of the SAPF were performed on the structure of four wires three legs with input reactors *L*. Based on that structure, the author presented the influence of the rectifier input reactor as well as the grid side line reactor on the SAPF efficiency (confirming the simulation).

The laboratory experiments of the HAPF were performed on the structure of SAPF (four wires three legs with *L* filter at the input connected in parallel with the group of two single-tuned filters. The author presented the advantages (the SAPF used less power) of that structure as well as the interest (improvement of the PHF efficiency) of connecting the line reactor between the SAPF and the group of PHF.

7.3 Further work direction

The further part of this work will be focussed on the HAPF (model of SAPF connected in series with the single-branch filter):

- the laboratory investigations
- design of new control system algorithm, allowing the active part to compensate the harmonics, reactive power (despite the passive part reactive power) and asymmetry (so far in the literature, it is difficult to find cases where the active part compensate the load reactive power and asymmetry).

References

A

1 Abu-Rubu H., Iqbal A., Guzinski J.: High Performance Control of AC Drives with MATLAB/SIMULINK Models. John Wiley & Sons, Chichester, United kingdom, 2012.

2 Adel M. S., El-Gammal A. A. A.: A novel discrete multi-objective particle swarm optimization (MOPSO) of optimal shunt power filter, IEEE Power Systems Conference and Exposition, 15-18 March 2009.

3 Abdelmadjid C., et al.: On the design of shunt active filter for improving power quality, IEEE International Symposium on Industrial Electronics, 18 November 2008.

4 Adly A. G., W. Bin Chang., Elham B. M.: A digital recursive measurement scheme for on-line tracking of power system harmonics, IEEE Transaction on Power Delivery, July 1991.

5 Afonso J., Couto C., Martins J.: Active filters with control based on the p-q theory, IEEE Industrial Electronics Society Newsletter, 47, 3, September 2000, pp. 5-10.

6 Ajinkya B., Prit., Jadhav H.T., Wanjari R. A.: An inbuilt passive harmonic filtration transformer for low voltage distribution network, IEEE International Conference on circuits Power and Computing Technologies [ICCPCT], 20-21 April 2017.

7 Akagi H., Kanazawa Y., Nabea A.: Instantaneous reactive power compensators comprising switching devices without Energy storage components, IEEE transactions on industry applications, May/June 1984, pp. 625-630.

8 Akagi H., Kanazawa Y., Fujita K., Nabae A.: Generalized theory of instantaneous reactive power and its application, UDC 621.3.016.25 Electrical Engineering in Japan, 1983.

9 Akagi H., Tamai Y.: Comparisons in Circuit Configuration and Filtering Performance between Hybrid and Pure Shunt Active Filters, IEEE Conference Record of the Industry Applications, 38th IAS Annual Meeting, 12-16 October 2003.

10 Akagi H., Watanabe H E., Aredes M.: Instantaneous power theory and applications to power conditioning, Wiley-IEEE Press, April 2007. 10

11 Akagi H., Ogasawara S., Kim H.: The therory of instantaneous power in three-phase four-wire systems: A comprehensive approach, IEEE Conference of the 1999 Industry Applications, 3-7 October 1999.

12 Akagi H.: Modern active filters and traditional passive filters, Bulletin of the Polish Academy of Sciences Technical Sciences, 54, 3, 2006.

13 Alexandre B. N., Wilsun X., Walmir F.: An investigation on the selection of filter topologies for passive filter applications, IEEE Transaction on Power Delivery, July 2009.

14 Alexandru B., et al.: LCL interface filter design for shunt active power filters, 3rd international Symposium on Electrical Engineering and Energy Converters, Suceava, 24-25 September 2009.

15 Alireza S et al.: Three-phase harmonic detection methods for grid-connection converters, Twenty-Sixth Annual IEEE Applied Power Electronics Conference and Exposition (APEC), 6-11 March 2011.

16 Alireza J., Kamal A.-H.: Unfunctionality of the instantaneous *p-q* theory for the control of series active filters, IEEE Conference on Electrical Power and Energy, 3-5 October 2011.

17 Almonte R. L., Ashley W.: Harmonics at the utility industrial interface: A real world example, IEEE Transactions on Industry Applications, 31, 6, November/December 1995, pp. 1419-1426.

18 Amarjeet K., Bhole A.A.: Design of hybrid filter for elimination of current harmonics, 2nd IEEE International Conference on Recent Trends in Electronics, Information & Communication Technology (RTEICT), 2017.

19 Amirhossein M., Hossein I-E., Mohamadkazem B.: Selective harmonic mitigation-pulse-width modulation technique with variable DC-link voltages in single and three-phase cascaded H-bridge inverters, IET Power Electronics, 7, 4, 2014, pp. 924-932.

20 An L et al.: Development of hybrid active power filter based on the adaptive fuzzy dividing frequency-control method, IEEE Transaction on Power delivery, Vol. 24, NO. 1, January 2009.

21 Anthoula M., Thomas Z., Milias-Argitis J.: Optimal sizing and limitations of passive filters in the presence of background harmonic distortion, Springer, Electrical Engineering, August 2009, pp. 89-100.
22 António M., José F., Helder A.: Active power filters for harmonic elimination and power quality improvement. In power quality, ed Andreas E., InTech, April 2011.
23 Areerak K-L., Areerak K-L.: The comparison study of harmonic detection methods for shunt active power filters, World Academy of Science, Engineering and Technology International Journal of Energy and Power Engineering, 2010.
24 Arrillaga J., Bradley D.A., Bodger P.S.: Power System Harmonics, John Wiley & Sons, Chichester, 1985.
25 Aissani M., Aliouane K.: Three-dimensional space vector modulation for four-leg voltage-source converter used as an active compensator, IEEE International Symposium on Power Electronics Electrical Drives Automation and Motion, Pisa, Italy 14-16 June 2010.
26 Azebaze M.C.S., Hanzelka Z.: Application of C-type filter to DC adjustable speed drive, IEEE International Conference - Modern Electric Power Systems, Poland, Wroclaw, 6–9 July, 2015, pp. 1-7.
27 Azebaze M.C.S., Hanzelka Z.: Different approaches for designing the passive power filters, Przegląd Elektrotechniczny, ISSN 0033-2097, 91, November 2015, pp.102-108.
28 Azebaze M.C.S., Hanzelka Z., Mondzik A.: Different LC power filter topologies - effectiveness of reducing voltage distortion, International Conference on Renewable Energies and Power Quality, Spain, Madrid 4–6 May 2016.
29 Azebaze M.C.S., Hanzelka Z.: Different approaches for designing the passive power filters, VI Conference, Poland, Białka Tatrzańska, 9–10 June 2015.
30 Azebaze M.C.S., Hanzelka Z.: Hybrid power active filter – Effectiveness of passive filter on the reduction of voltage and current distortion, IEEE International Conference on Electric Power Quality and Supply Reliability, Estonia, Tallinn, 29-31 August 2016, pp.91-96.
31 Azebaze M.C.S., Hanzelka Z.: Different approaches for designing the passive power filters, IEEE International Conference on International School on Nonsinusoidal Currents and Compensation, Poland, Łagów, 15-18 June 2015.
32 Azebaze M.C.S.: Rectifiers network with a higher power factor (in polish), AGH University of Science and Technology, Master theses, Poland, Cracow, 2012.
33 Azebaze M.C.S., Hanzelka Z.: Passive harmonic filters. In Power quality in future electrical power systems, 1st ed Zobaa A.F., Shady H.E.A.A., IET the Institution of Engineering and Technology, London, United Kingdom, 2017, 77-127.

B

34 Babak B., Kenneth S. S, Roddy C.W.: Designing passive harmonic filters for an aluminium smelting plant, IEEE Transactions on Industry Application, 47, 2, March/April 2011, pp. 973-983.
35 Babu G. M.: Simulation study of indirect current control technique for shunt active filter, International Journal of Engineering Research and applications (IJERA), 3, 4, July/August 2013, pp. 831-851.
36 Balaji R., Faizal M.: Design of shunt active filters based on phase locked loop and PI controller, International Journal of Soft Computing and Engineering (IJSCE), ISSN: 2231-2307, 4, 3, July 2014.
37 Balci M. E., Hocaoglu M. H.: Effects of source voltage harmonic distortion on power factor compensation in triac controlled AC chopper circuits, IEEE International Conference on Power Electronics and Drives Systems, 28 November/1 December 2005.
38 Bartosz K.: Reducing inverter power rating in active power filters using proposed hybrid power filter topology, IEEE 15th International Conference on Environment and Electrical Engineering (EEEIC), 10-13 June 2015.
39 Bartosz K.: Comparison of an active and hybrid power filter devises, IEEE international Conference on Harmonics and Quality of power (ICHQP), 25-28 May 2014.
40 Bartosz K et al.: Hybrid power filter with reduced inverter power rating, ResearchGate, September 2016.

41 Bartzsch C et al.: Triple tuned harmonic filters – Design principle and operating experience, Proceedings. International Conference on Power System Technology, 13-17 October 2002.
42 Bartosz K., Tomasz K.: Hybrydowe układy filtrów aktywnych – analiza wybranej konfiguracji, AGH University of Science and Technology, Master theses, Poland, Cracow, 2006.
43 Benchaita L., Saadate S., Nia A. S.: A comparison of voltage source and current source shunt active filter by simulation and expermentation, IEEE Transactions on Power Systems, 14, 2, May 1999.
44 Benysek G., Pasko M.: Power Theories for Improve Power Quality, Springer-Verlag London 2012, DOI 10.1007/978-1-4471-2786-4.
45 Bernet S., Ponnaluri S., Teichmann ralph.: Design and loss comparison of matrix converters and voltage-source converters for modern AC drives, IEEE Transactions on Industrial Electronics, April 2002.
46 Bhattacharya S., Frank T. M., Divan D. M., Banerjee B.: Active filter implementation, IEEE industry Application Magazine, 1998.
47 Bhim S., Ambrish C., Kamal Al-H.: Power quality: problems and mitigation techniques, John wiley & sons Ltd, United Kingdom, 2015.
48 Bhim S., Vishal V., Vipin G.: Passive hybrid filter for varying rectifier loads, IEEE International Conference on Power Electronics and Drives Systems, PEDS, 28 November/1 December 2005.
49 Bhim S., et al.: Multipulse AC-DC converters for improving power quality: A review, IEEE Transactions on Power Electronics, 23, 1, January 2008.
50 Bhim S., et al.: A review of three-phase improved power quality AC-AC converters, IEEE transactions on industrial Electronics, 51, 3, June 2004.
51 Bhim S., Kamal A-H., Ambrish C.: A review of active filters for power quality improvement, IEEE Transaction on Industrial Electronics, vol. 46, NO. 5, October 1999.
52 Boudrias J.-G.: Harmonic mitigation, power factor correction and Energy saving with proper transformer and phase shifting techniques, IEEE Canadian Conference on Electrical and Computer Engineering, 2-5 May 2004.
53 Buła D.: Hybrydowe energetyczne filtry aktywne, Doctoral thesis in polish, Poland, Gliwice 2011.
54 Buła D., Pasko M.: Hybrydowy energetyczny filtr aktywny w układzie z filtrem pasywnym dla jednej harmonicznej, Przegląd Elektrotechniczny, ISSN 0033-2097, R. 86, March 2010.
55 Buła D., Pasko M.: Stability analysis of hybrid active power filter, Bulletin of the Polish Academy of Science, Technical Sciences, 62, 2,2014.

C

56 Cavini A., Ronchi F., Tilli A.: Four-wires shunt active filter: optimized design methodology, IEEE conference on Industrial Electronics Society, 2-6 November 2003.
57 Candela J. I.; Teodorescu R.: Proposal of a resonant controller for a three phase four wire grid-connected shunt hybrid filter, IEEE Conference on Energy Conversion Congress and Exposition, 20-24 September 2009.
58 Chiang S.J., Chang J.M.: Design and implementation of the parallelable active power filter, 30th Annual IEEE power Electronics Specialists Conference, pp 406-411, 1999.
59 Chen B., Zeng X., Xv Y.: Three tuned passive filter to improve power quality, IEEE International Conference on Power System Technology, PowerCon, 22-26 October 2006.
60 Chi-Seng L., Man-Chung W.: A novel b-shaped L-type transformerless hybrid active power filter in three-phase four-wire systems, IEEE Conference on the 38th North American Symposium, 17-19 September 2006.
61 Chih-Ju C et al.: Optimal planning of large passive-harmonic-filters set at high voltage level, IEEE Transactions on Power Systems, 15, 1, February 2000, pp. 433-441.
62 Chi-Jui W et al.: Investigation and mitigation of harmonic amplification problems caused by single-tuned filter, IEEE Transactions on Power Delivery, 13, 3, July 1998, pp. 800-806.
63 Chi Z., et al.: Resonance damping techniques for grid-connected voltage source converters with *LCL* filter – A review, Energycon, Dubrovnik, Croatia, 13-16 May, 2014.

64 Cleary-Balderas A., Medina-Rios A., Cruz-Hernéndez O.: Hybrid active power filter based on the IRP theory for harmonic current mitigation, IEEE International Autumn Meeting on Power, Electronics and Computing (ROPEC), 9-11 November 2016.
65 Constantin V. S., Cristiana A. P., Mahaita L.: The synchronous fundamental *dq* frame theory implementation and adaptation for active filtering, IEEE International Conference on Applied and Theoretical Electricity (ICATE), 23-25 October 2014.
66 Czarnecki L. S.: Comments to the paper: instantaneous p-q theory for compensating nonsinusoidal systems, Przegląd Elektrotechniczny, ISSN 0033-2097, 85, June 2009.
67 Czarnecki L. S.: On some misinterpretations of the instantaneous reactive power *p-q* theory, IEEE Transactions on power electronics, 19, 3, May 2004.
68 Czarnecki L. S.: Instantaneous reactive power p-q theory and power properties of three-phase systems, IEEE Transaction on power Delivery, January 2006.
69 Czarnecki L. S., Ginn H.L.: The effect of the design method on efficiency of resonant harmonic filters, IEEE Transactions on Power Delivery, 2005, 20, 1, pp. 286-291.

D

70 Dai K et al.: Harmonic compensation characteristics of active power filter to nonlinear loads based on impedance analysis, IEEE International Symposium on Industrial Electronics (ISIE), 28-31 May 2012.
71 Das J.C.: Power system analysis – Short-circuit load flow and harmonics, New York, USA, 2002.
72 Das J. C.: Passive filters – potentialities and limitations, IEEE Transactions on Industry Applications, January/February 2004, pp. 232-241.
73 Dave B., Case M., Wilsun X.: Mitigation of harmonics in oil field electric systems using a centralized medium voltage filter, IEEE International conference on Harmonics and Quality of power, 1-4 October 2000.
74 de Metz-Noblat B., Dumas F., Poulain C.: Calculation of short-circuit currents, Schneider Electric, Cahier technique no. 158, September 2005.
75 Dekka A. R., Beig A. R., Poshtan M.: Comparison of Passive and Active Power Filters in Oil Drilling Rigs, IEEE International Conference on Electrical Power Quality and Utilization (EPQU), 17-19 October 2011.
76 Demirdelen T., et al.: Review of hybrid active power filter topologies and controllers, 4th International conference on Power Engineering, Energy and Electrical Drives, Istanbul, Turkey, 13-17 May 2013.
77 Divesh P., Sanket P., Aditya P.: Analysis of different techniques used in harmonic reduction for converter rectifier, International Journal of Advance Foundation and research in Science & Engineering, 2, 2016, pp. 226-240.
78 Djeghloud H.: Filtrage actif de puissance, dissertation doctoral, Université des Frères Mentouri Constantine 2007.78.
79 Duarte L. H. S., Alves M. F.: The degradation of power capacitors under the influence of harmonics, IEEE on 10th International Conference on Harmonics and Quality of Power, 6-9 October 2002.

E

80 EN 50160: voltage characteristics of electricity supplied by public electricity network, 2010.
81 Edward J. C., Theodore R. S.: the ANSI 49 rectifier with phase shift, IEEE Transactions on Industry Applications, 20, 3, May/June 1894.
82 Ehsan P., Masood A. A.: Efficient procedures to design and characterize passive harmonic filters in low power applications, IEEE International Symposium on Industrial Electronics (ISIE), 4-7 July 2010.
83 EI-Habrouk M., Darwish M.K., Mehta P.: Active power filters: A review, IEEE Proceedings – Electric power Applications, 147, 5 September 2000.
84 Elmathana M. T., Zobaa A. F., Abdel Aleem S. H. E.: Economical design of multiple-arm passive harmonic filters for an industrial firm-case study, IEEE 15th International Conference on Harmonics and Quality of Power (ICHQP), 17-20 June 2012.
85 Emre D.: Adaptive fuzzy hysteresis band current control for reducing switching losses hybrid active power filter, IET Power Electronics 2018.

86 Eric B., Jean N. F.: Harmoniques: convertisseurs propres et compensateur actifs, cahier technique 183, Schneider Electric, 2000, pp. 1-32.

F

87 Fabio R., Andrea T.: Design methodology for shunt active filters, https://www.researchgate.net/publication/228893534_Design_methodology_for_shunt_active_filters.

88 Fang Z., Akagi H., Nabae A.: Compensation characteristics of the combined system of shunt passive and series active filters, IEEE Transactions on Industry Applications, 29, 1, January/Februart 1993.

89 Firlit A.: Analiza porównawcza algorytmów sterowania filtrów aktywnych opartych na wybranych teoriach mocy, Rozprawa Doktorska, Poland, Kraków 2006.

90 Firlit A., Kołek K., Piątek K.: Heterogeneous active power filter controller, IEEE International Symposium ELMAR, 18-20 September 2017.

91 Flemming A., Alain D.: Adjustable speed drive active filtering capability for harmonic current compensation, IEEE Proceedings of PESC '95 - Power Electronics Specialist Conference, 18-22 June 1995.

92 Folker R., Analytic calculation of the DC-Link capacitor current for pulsed three-phase inverters, http://cpdee.ufmg.br/~paulos/sei_arquivos/analytic%20calculation%20of%20the%20dc%20link.

93 Francesco G., Andrea F., Alessandro U.: New harmonics current mitigation technique in induction motor driving reciprocating compressor, IEEE International Symposium on Systems Engineering, 28-30 September 2015.

94 Francisco K et al.: A comparison between a single and a double tuned hybrid power filter under power quality analysis, Power Electronics Conference (COBEP), 2013 Brazilian, 27-31 October 2013.

95 Fujita H., Akagi H.: A practical approach to harmonic compensation in power systems - series connection of passive and active filters, IEEE Transaction on Industry Applications, 27, 6 November/December 1991.

G

96 Gonzalo S., John H.: A review of harmonic mitigation techniques, http://www.apqpower.com/assets/files/AReviewOfHarmMitigTech.pdf.

97 Grzegorz B.: Power theories for improved power quality, ed Grzegorz B., Pasko M., Springer – pp- 13-47, Verlab London 2012.

98 Gutierrez B., Kwak S.-S.: Finite set model predictive control method of shunt hybrid power filter, 9th International Conference on Power Electronics and ECCE Asia, Seoul, Korea June 1-5, 2015.

H

99 Hanzelka Z.: Jakość energii elektrycznej: Część 6 – Proces łączenia baterii kondensatorów, Twelve Electric, http://www.twelvee.com.pl/42767005.php?c=%D0%B5.

100 Hanzelka Z.: Jakość energii elektrycznej: część 4 – wyższy harmoniczne napięć i prądów, Twelve Electric.

101 Hanzelka Z.: Jakość energii elektrycznej: Część 4 – Wyższy harmoniczne napięć i prądów (c.d.), Twelve Electric, http://www.twelvee.com.pl/42767005.php?c=%D0%B5.

102 Hanzelka, Z.: Selected aspects of the design of passive harmonic filters (in Polish - Wybrane zagadnienia projektowania pasywnych filtrów wyższych harmonicznych), Automatyka, Elektryka, Zakłócenia, Infotech conference, Jurata 23-26 June 2010.

103 Harmonic reduction methods, Eaton Corporation, USA, 2012.

104 Harmoniques et convertisseurs de fréquence, Guide Technique, 6, ABB, 2012.

105 Harmonics in power system – Siemens Industry, Inc. 2013.

106 Harmonic mitigation for AC variable frequency pump drives, World PUMPS, December 2002.

107 He N., Huang L., Wu J., Xu D.: Study on optimal design method for passive power filters set at high voltage bus considering many practical aspects, IEEE Applied Power Electronics Conference and Exposition, February 2008, Austin, TX, pp. 396-401.

108 Helder J.A et al.: Direct current control of an active power filter for harmonic elimination, power factor correction and load unbalancing compensation, https://repositorio-aberto.up.pt/bitstream/10216/202/2/54965.pdf.
109 Helmo K. M. P., Fernando P. M, Luiz C. P. da S.: A comparative analysis of FBD, PQ, and CPT current decompositions – Part I: Three-phase Three-wire systems, IEEE Bucharest Power Tech 2009.
110 Herbert L. G., Czarnecki L.S.: An optimization based method for selection of resonant harmonic filter branch parameters, IEEE Transactions on Power Delivery, 21, 3, July 2006, pp. 1445-1451.
111 Hiranandam A.: Calculation of cable ampacities including the effects of harmonics, IEEE Industry Applications Magazine, 4, 2, Mar/April 1998, pp. 42-51
112 Huang L., He N., Xu D.: Optimal design for passive power filters in hybrid power filter based on particle swarm optimization, IEEE International Conference on Automation and Logistics, August 18 – 21, 2007, Jinan, China.
113 Hussein A. K.: Harmonic mitigation techniques applied to power distribution networks, Hindawi Publishing Corporation Advances in Power Electronics, 2013.

I

114 IEC 60909-0.: Short-circuit in three-phase a.c. systems – Part 0: Calculation of currents, first edition – 2001, http://www.academia.edu/7213550/IEC_60909-0-Short-circuit_currents_in_three phase_a_c._systems_-_Calculation_of_currents_ENG.
115 IEC 61000-4-30: Electromagnetic compatibility (EMC) – part 4-30: testing and measurement techniques – power quality measurement methods, 2014.
116 IEC 61000-3-11: Limitation of voltage changes, voltage fluctuations and flicker in low-voltage supply systems for equipment with rated current ≤ 75 A and subject to conditional connection.
117 IEC 61000-3-12: Limits for harmonic currents produced by equipment connected to public low-voltage systems with input current ≤ 75 A per phase and subject to restricted connection, 2011.
118 IEC 61000-3-6: Assessments of emission limits for distorting loads in MV and HV power system.
119 IEC 61000-4-7 General guide of harmonic distortion and inter-harmonics measurement and instrumentation, for power supply systems and equipment connected thereto.
120 IEEE Standard 1159™-2009: IEEE recommended practice for monitoring electric power quality.
121 IEEE Recommended Practice for Electric Power Distribution for Industrial Plants, IEEE Std 141™-1993(R1999) (Revision of IEEE Std 141-1986).
122 Iman L., et al.: Active damping technique for *LCL*-filtered inverters-based microgrids, IEEE 10th international Symposium on Diagnostics for Electrical Machines, Power electronics and Drives, 1-4 September 2015.

J

123 Jacek K.: Practical application of series active compensators. In power theories for improved power quality, ed Grzegorz B., Pasko M., Springer – pp- 13-47, Verlab London 2012. 199
124 Jacques S.: the singular of the third harmonic, Chneider Electric Cahier technique no. 202, February 2001.
125 Jain S.K., Agrawal P., Gupta H.O.: Fuzzy logic controller shunt active power filter for power quality improvement, IEE Proceedings - Electric Power Applications, September 2002.125
126 Jamali S., Masoum M.A.S., Mousavi S.A.: Influence of controller high pass filter on the performance of shunt hybrid power filter, IEEE Power Engineering Conference, AUPEC '08. Australasian Universities, 14-17 December 2008.
127 James K. P.: A transfer function approach to harmonic filter design, IEEE Industry Application Magazine, January/February 1997, 3, pp. 68-82.
128 Javier N., et al.: Selective harmonic mitigation technique for multilevel cascaded H-bridge converters, IEEE 35th Annual Conference of Industrial Electronics, 3-5 November 2009
129 Javier N., et al.: Selective harmonic mitigation technique for cascaded H-bridge converters with nonequal DC link voltages, IEEE Transactions on Industrial Electronics, 60, 5, July 2013.
130 Javier M et al.: Design of an asymmetric multilevel shunt active power filter, IEEE 24th International Symposium on Industrial Electronics (ISIE), 2015.

131 Jih-Sheng L., Pabbathi V.: A shunt-connected phase-shift transformer for shipboard harmonic eliminating rectifiers, IEEE Asian Conference on Energy, Power and Transportation Electrification, 25-27 October. 2016.
132 Jou H.-L., Wu J.-C., Wu K.-D., Parallel operation of passive power filter and hybrid power filter for harmonic suppression, IEE Proceedings - Generation, Transmission and Distribution, 148, 1, January 2001.
133 Juan W. D., Gustavo V., Luis A. M.: A series active power filter on a sinusoidal current-controlled voltage-source inverter, IEEE Transactions on Industrial Electronics, 44, 5, October 1997.
134 Juan W. D., Contardo J.M., Moran L.A.: A Fuzzy-controlled active front-end rectifier with current harmonic filtering characteristics and minimum sensing variables, IEEE Transactions on Power electronics, July 1999.
135 Junpeng Ji et al.: Research on selection method of passive power filter topologies, IEEE International Conference on Power Electronics and Motion Control, China, Harbin, 2-5 June, 2012.
136 Juan J. P. Á et al.: Optimization of passive filtering systems used for mitigating harmonics in distribution networks, IEEE 17th International Conference on Harmonics and Quality of Power (ICHQP), 16-19 October 2016.
137 Julio C. C-B., Jose M-O.: Comprehensive design methodology of tuned passive filters based on a probabilistic approach, IET Generation, Transmission & Distribution, 30 January 2014.

K

138 Kazmierkowski M. P., Malesani L.: Current control techniques for three-phase voltage-source PWM converters: A survey, IEEE Transactions on Industrial Electronics, 45, 5, October 1998.
139 Khaled H. A., Stephen J. F., Barry W. W.: Passive filter design for three-phase inverter interfacing in distributed generation, Electrical Power Quality and Utilisation, 2007.
140 Kim H., Akagi Hirofumi.: The instantaneous power theory on the rotating p-q-r reference frames, IEEE International Conference on Power Electronics and Drive Systems, Hong-Kong, 27-29 July 1999.
141 Klempka R.: Designing a group of single-branch filters taking into account their mutual influence, Archives for Electrical Engineering, , 63, 1, ISSN 1427 – 4221, March 2014, pp. 81-91.
142 Klempka R.: A New Method for the C-Type Passive Filter Design, Przegląd Elektrotechniczny, 2012, ISSN 0033-2097, 88, 7, pp. 277-281.
143 Klempka R.: Designing a group of single-branch filters, 7th International Conference on Electrical power quality and utilisation, Sept. 17-19, Poland, Cracow 2003.
144 Klempka R.: Passive power filter design using genetic algoritm, Przegląd Elektrotechniczny, ISSN 0033-2097, 89, May/2013
145 Klempka R.: Poprawa jakości dostawy energii elektrycznej z użyciem algorithmóm genetycznych passive power filter design using genetic algoritm, AGH University of Science and Technology, Poland, Cracow 2013.
146 Klempka R.: Passive power filter design using genetic algorithm. Przegląd Elektrotechniczny, May/2013.
147 Klempka R., Hanzelka Z., Varetsky Y.: Bank harmonic filters operation in power supply system - cases studies, INTECH. 17 April 2013, Power Quality Issues, ed. Zobaa A. F, Rijeka INTECH, ISBN 980-953-307-532-2, pp. 201-23.
148 Kovernikova L. I., Nguyen C. T.: An optimization algorithm for calculating optimal parameters of the third-order passive filter, IEEE International Conference on Electrical Power Quality and Utilisation, 17-19 October 2011.
149 Kovernikova L. I., Nguyen C. T.: An optimization approach to calculation of passive filter parameters based on particle swarm optimization, International Conference on Renewable Energies and Power Quality (ICREPQ'12), Spain Santiago de Compostela, 28th to 30th March 2012.
150 Krzeszowiak T et al.: Comparison of active and hybrid power filters for mitigation of harmonic currents, Research postal, International Symposium on Modern Electric Power Systems (MEPS'06), Poland, Wroław 2006.

151 Kuldeep K. S., Saquib S., Nanand V. P.: Harmonics & its mitigation technique by passive shunt filter, International Journal of Soft Computing and Engineering (IJSCE), 3, 2, May 2013.
152 Kumar P., Niranjan K,: Simulation of three-phase three-wire active power filter using *p-q* theory, International Journal of Innovative Research in Electrical, Electronic, Instrumentation and Control Engineering, 4, 3, March 2016.
153 Kwak S., Toliyat H.A.: Design and rating comparison of PWM voltage source rectifiers and active power filters for AC drives with unity power factor, IEEE Transaction on Power Electronics, September 2005.

L

154 Lam C.-S., Wong M. C., Han Y. D.: Hysteresis current control of hybrid active power filters, IET Power Electron, 5, 7, 2012, pp. 1175–1187.
155 Lam C.-S et al.: Minimum DC-Link Voltage Design of Three-Phase Four-Wire Active Power Filters, IEEE 13th Workshop on Control and Modelling for Power Electronics, 10-13 June 2012.
156 Lamich M et al.: New structure for three phase four wires hybrid active filters, 32nd Annual Conference on IEEE Industrial Electronics, 6-10 November 2006.
157 Leopoldo G.F et al.: A flexible selective harmonic mitigation technique to meet grid codes in three-level PWM converters, IEEE Transaction on Industrial Electronics, 54, 6, December 2007.
158 Lijun C., Annette V. J.: A comparison and assessment of hybrid filter topologies and control algorithm, IEEE 32nd Annual Power Electronics Specialists Conference, 17-21 June 2001.
159 Lin L., Yuanbo G., Xiahua Z.: Analysis and application of passive damping LLCL filter in active filter, IEEE International Conference on Cyber Technology in Automation, Control and Intelligent Systems, China, Shenyang, 8-12 June 2015.
160 Lin C.E., Chen C.L., Huang C.L.: Calculating approach and implementation for active filters in unbalanced three-phase system using synchronous detection method, IEEE International conference on Industrial Electronics, Control, Instrumentation, and Automation, 13-13 November 1992.
161 Lina H., Na H., Dianguo X.: Optimal design for passive power filter in hybrid power filter based on particle swarm optimization, IEEE International Conference on Automation and Logistics, Jinan, China, 18 - 21 August 2007.
162 Low voltage drives harmonic mitigation comparison: AC line reactors vs. DC link chokes, Eaton Corporation, USA, 2015.
163 Lucas F. E et al.: Improved structure for three-phase four-wires hybrid active power filters, International Conference on Energies and Power Quality (ICREPQ'13), March 2013.
164 Lucian A., Frede B., Steffan H.: Evaluation of harmonic detection methods for active power filter application, Twentieth Annual IEEE Applied Power Electronics Conference and Exposition, 6-10 March 2005.
165 Lucian A., Frede B., Steffan H.: Evaluation of harmonic detection methods for active power filter applications, IEEE 30th Annual Conference on Applied Power Electronics, 6-10 March 2005.
166 Lucian A., Frede B., Steffan H.: Detection is key - harmonic detection methods for active power filter applications, IEEE Industry Applications Magazine, July-August 2007.
167 Lucian A., Wojciech W., Frede B., Tomasz K., Bartosz K.: A new control structure for hybrid power filter to reduce the inverter power rating, 32nd Annual Conference on IEEE Industrial Electronics, 16 April 2007.
168 Luis A.M., Juan W.D., Rogel R.W.: A three-phase active power filter operating with fixed switching frequency for reactive power and current harmonic compensation, IEEE Transactions on Industrial Electronics, August 1995.
169 Lui M., Juan D.: Active filter. In Power electronics handbook, ed. Muhammad H. Rashid, Academic press, San Diego, San Francisco, New York, Boston, London, Sydney, Tokyo, 2001.
170 Luis T.M., Phoivos D.Z., Geza J.: Analysis and design of a novel 3-ϕ solid-state power factor compensator and harmonic suppressor system, IEEE Transactions on Industrial Application, July/August 1989.

M

171 Maciążek M, Posko M.: skutki oddziaływania wyższych harmonicznych na sieć zasilającą oraz wybrane metody ich eliminacji, Praca instytutu Elektrotechniki, zeszyt 242, 2009.

172 Mahesh S., Padiyar K. R., Ramanarayanan.: Digital simulation of a hybrid active filter – an active filter in series with a shunt passive filter, IEEE Power Quality '98, 18-18 June 1998.
173 Martin b.: Advance control of active filter in a battery charge application, Lund University, Sweden, 1999.
174 Masatoshi et al.: Harmonic current and reactive power compensation with an active filter, PESC ’88 Record., 19th Annual IEEE Power Electronics Specialists Conference, 11-14 April 1988.
175 Massoud A.M., Finney S.J., Williams B.W.: Predictive current control of a shunt active power filter, IEEE 35th Annual Conference on Power Electronics Specialists Conference, Aachen, Germany 2004.
176 Massoud A. M., Finney S. J., Williams B. W.: Review of harmonic current extraction technique for an active power filter, IEEE International Conference on Harmonics and Quality of Power, 2004.
177 Matyjasek K.: Pasywne filtry drugiego rzędu typu „C” kompensacja mocy biernej pieców łukowych, Elma Energia Olsztyn, Certyfikat ISO 9001:2000.
178 Matyjasek K.: Filtry pasywne, Elma Energia Olsztyn, Certyfikat ISO 9001:2000.
179 Mehemet B., et al.: Analysis and comparison of passive damping methods for shunt active power filter with output LCL filter, IEEE International Conference on Electrical Machines and Power Electronics, 2-4 September 2015.
180 Metody ograniczania wpływ wyższych harmonicznych, Danfoss Drives, 2010.
181 Mesbahi N.: Contribution à l’étude des performances des onduleurs multiniveaux sur les réseaux de distributions, Doctorate Dissertation, Université Badji Mokhtar Ar Annaba, Algeria, 2014.
182 Micheal D., Nirod C.S.: On resonance and frequency response characteristics of electrical circuits, International Journal of Electrical Engineering Education, Manchester, October 2013, 50, 4, pp. 368–383.
183 Mikkili S., Panda A. K.: Instantaneous active and reactive power and current strategies for current harmonics cancellation in 3-ph 4-wire SHAF with both PI and fuzzy controllers, Scientific Research and Academic publisher, 3, 3, July 2011, PP. 285-298.
184 Min-cia K., Xinzhou D.: The parameters calculation and simulation research of two-type double-tuned Filter, IEEE Transmission and Distribution Conference and Exposition, Asia and Pacific, 26-30 October 2009.
185 Ming-cai K., Jia-hua Z.: Compensates the double tuned filter element parameter change based on the controllable reactor, IEEE International Conference on Electricity Distribution, CICED, China, 10-13 December 2008.
186 Mingcai K., Zhiqian B., Xiping Z.: The parameters calculation and simulation research about two types structure of double-tuned Filter, IEEE 45th International Conference on Universities Power Engineering, 31 August/3 September 2010.
187 Mohammad A. S. M., Ewald F.F.: Power quality in Power Systems and Electrical Machines, Second edition, ELSEVIER, 125 London Wall, London, EC2Y 5AS, United Kingdom, 2015.
188 Muhammad H. R.: Power Electronics handbook, Elsevier, USA, 2011.
189 Muhammad R., Muhammad I., Danang S.: Single tuned harmonic filter as total harmonic distortion (THD) compensator, CIRED, 23rd International Conference on Electricity Distribution, Lyon, June 15-18, 2015, p. 0056.
190 Murat E. B., Aslan D. K.: Optimal design of C-type passive filters based on response surface methodology for typical industrial power systems, Electrical power Components and systems, 14:653-668, 2013.
191 Mustapha S et al.: Control strategy of a transformerless three phase shunt hybrid power filter using a robust PLL, IEEE 38th Annual Conference on Industrial Electronics Society, IECON, 25-28 October 2012.
192 Mustafa E. M., Salih T., Ahmet Z.: Simulated annealing based passive power filter design for a medium voltage power system, IEEE International Symposium on Innovations in Intelligent Systems and Applications, 2-4 July 2012.

N

193 Nor H. B. Abdul Kahar., Ahmed F. Zobaa.: Optimal single tuned damped filter for mitigation harmonic using MIDACO. IEEE International Conference on Environment and Electrical

Engineering and IEEE Industrial and Commercial Power Systems Europe (EEEIC/I&CPS Europe), 6-9 June 2017.
194 Nekkar D.: Contribution a l' étude des strategies de commande des filters actifs triphasés, Magister memory, Université Mohamed Chérif Messaadia de Souk-Ahras, Algieria, 2013-2014.
195 Ning-Yi D., Man-Chung W.: Design considerations of coupling inductance for active power filter, 6th IEEE Conference on Industrial Electronics and Applications, 21-23 June 2011.

O

196 Olszowiec P.: Zwarcia mniej groźne, Energia Gigawat, 1/2011.

P

197 Pasko M., Maciążek M.: Teoria mocy p-q - poprawna teoria czy użyteczny algorytm sterowania kompensatorów kluczujących, Przegląd Elektrotechniczny, ISSN 0033-2097, R. 82 NR 6/2006.
198 Pasko M., Maciążek M.: Teoria mocy p-q - poprawna teoria czy użyteczny algorytm sterowania kompensatorów kluczujących - podsumowanie, Przegląd elektrotechniczny, ISSN 0033-2097, 82 October 2006.
199 Pasko M., Maciążek M.: Principles of electrical power control. In power theories for improved power quality, ed Grzegorz B., Pasko M., Springer – pp- 13-47, Verlab London 2012. 199
200 Peng F. Z., Akagi H., Nabea A.: A new approach to harmonic compensation in power systems – A combined system of shunt passive and series active filters, IEEE Transactions on industry, 26, 6 November/December 1990.
201 Peng F. Z., Akagi H,. Nabae A.: Compensation characteristics of the combined system of shunt passive and series active filters, IEEE Transactions of Industry Applications, 29, 1, January/February 1993.
202 Peng F. Z., Lai J-S.: Generalized instantaneous reactive power theory for three-phase power systems, IEEE Transactions on Instrumentation and Measurement, 45, 1, Febryuary 1996, PP. 293-297.
203 Piróg S.: Energoelektronika – Układy o Komunikacji Sieciowej i o Komutacji Twardej, AGH University of Science and Technology, Poland, Cracow 2006.
204 Ponnaluri S., Krishnamurthy V., Kanetkar V.: Generalized system design and analysis of PWM based power electronic converters IEEE conference on Industry Application, 8-12 October 2000.
205 Po-Tai C., Subhashish B., Deepak M. D.: Hybrid solutions for improving passive filter Performance in high power applications, IEEE Transactions on Industry Applications, 33, 3, May/June 1997.
206 Przewodnik techniczny Merlin Gerin.: Podstawy projektowania i doboru aparatury w sieciach średniego napięcia, Schneider Electric, January 2004.

Q

207 Qingxin Shi et al.: Passive filter installation for harmonic mitigation in residential distribution systems, IEEE Power & Energy Society General Meeting, 16-20 July 2017.

R

208 Reza S.: Mehmet K.: Optimal design of passive harmonic filters using bee colony optimization, IEEE conference on HONET-ICT, 13-14 October 2016.
209 Rivas D et al.: Improving passive filter compensation performance with active techniques, IEEE Transactions on Industrial Electronics, 50, 1, February 2003, pp. 161-170.
210 Rivas D., Moran L., Duxon J., Espinoza J.: A simple control scheme for hybrid active power filter, IEE Proceedings – Generation, Transmission and Distribution, 07 November 2002.
211 Rinaldi et al.: United States Patent, US 3,340,851 B1, 22 January 2002.
212 Rockwell A., Mequon W.: Line reactors and AC drives, http://literature.rockwellautomation.com/idc/groups/literature/documents/wp/drives-wp016_-en-p.pdf.
213 Rodriguez J., Jih-Sheng L., Fang Z. P.: Multilevel inverters: A survey to topologies, controls, and applications, IEEE transactions on Industrial Electronics, 49, 4, August 2002.
214 Ruixiiang F et al.: Configuration of a novel hybrid active power filter and its control method, IEEE Conference on Power and Energy Engineering, Asia-Pacific, 27-31 March 2009.

215 Reynaldo R., Gregory A. F.: Optimal harmonic filter topology applied in HV and EHV networks using particle swarm optimization, IEEE Electrical Power and Energy Conference (EPEC), 12-14 October 2016.

216 Sanae R et al.: A comparative study of harmonic detection algorithm for active filters and hybrid active filters, IEEE Conference on Power Electronics Specialists, 2002.

S

217 Sakar S., Abdel A. S. H. E., Balci M. E., Zobaa A. F.: A filter design approach to maximize ampacity of cables in nonsinusoidal power systems, IEEE International Conference, ISNCC 15-18 June 2015, Poland, Lagów, pp. 1-4.

218 Sakar S et al.: Optimal design of single-tuned passive filter using response surface methodology, IEEE International Conference, ISNCC, Łagow, Poland, 15-18 June 2015.

219 Sam A-R., Franz S., Ken S.: PFC boost converter design guide, Infineon, 2016.

220 Sasaki H., Machida T.: A new method to eliminate AC harmonic currents by magnetic flux compensation-considerations on basic design, IEEE Transaction on Power Apparatus and Systems September 1971.

221 Sekar T. C., Rabi B. J.: A review and study of harmonic mitigation techniques, IEEE International Conference on Emerging Trends in Electrical Engineering and Energy Management, 13-15 December 2012.

222 Shady H.E.A.A., Zobaa A. F., Mohamed M.A.A.: Optimal C-type passive filter based on minimization of the voltage harmonic distortion for nonlinear loads, IEEE Transactions on Industrial Electronic, 59, 1, January 2012, pp. 281-289.

223 Shengqiang L., Xiaodond L., Wilsun X.: Modeling DC motor drive systems in power system dynamic studies, IEEE Transactions on Industry Applications, 51, 1, January/February. 2015, pp. 658-668.

224 Shady H.E. Abdel. Aleema., Ahmed F. Zobaa., Murat E. Balcica.: Optimal resonance-free third-order high-pass filters based on minimization of the total cost of the filters using Crow Search Algorithm, ELSEVIER, Electric power Systems Research, October 2017.

225 Shengqing Li et al.: Multi-objective optimization design for passive power filters in hybrid power filter system based on multi-island particle swarm optimization, IEEE 7th International Power Electronics and Motion Control Conference - ECCE Asia, China, Harbin, 2-5 June 2012.

226 Singh B., Chandra A., Al-Haddad K. Power Quality: Problems and Mitigation Techniques, John Wiley & Sons Ltd, 2015.

227 Singh B., Verma V., Chandra A., Al-Haddad k.: Hybrid filters for power quality improvement, IEE Proceedings – Generation, Transmission and Distribution, 6May 2005.

228 Singh G. K.: Power system harmonic research: a survey, Wiley InterScience, European Transactions on Electrical Power, 2009.

229 Soomro D. M., Almelian M. M.: Optimal design of a single tuned passive filter to mitigate harmonics in power frequency, ARPN Journal of Engineering and Applied Sciences, October 2015.

230 Sozański P. K.: Harmonic compensation using the sliding DFT algorithm for three-phase active power filter, Electrical Power Quality and Utilisation, Journal Vol. XII, 2006.

231 Srianthumrong S., Akagi H.: A medium-voltage transformerless AC/DC power conversion system consisting of a diode rectifier and a shunt hybrid filter, IEEE Transactions on Industry Applications, 39, 3, May/June, 2003.

232 Stalec L.: Analysis of selected structures of passive filters (in polish), AGH University of Science and Technology, Master theses, Poland, Cracow, 2016.

233 Strojny J., Strzałka J.: Zbiór zadań z sieci elektrycznych, część I, AGH University of Science and Technology, Poland, Cracow 1990.

234 Strojny J., Strzałka J.: Zbiór zadań z sieci elektrycznych, część II, AGH University of Science and Technology, Poland, Cracow 1990.

235 Strzelecki., Benysek G.: Power Electronics in Smart Electrical Energy Networks, Springer-Verlag London Limited, 2008.

236 Subhashish B., Deepak D.: Synchronous frame based controller implementation for a hybrid series active filter system, IEEE Conference Record on Industry Applications, Thirtieth IAS Annual Meeting, IAS '95, 8-12 October 1995.
237 Subjak J. S., McQullkin J. S.: Harmonic – causes, effects measurements and analysis – update, IEEE Conference on Industrial and Commercial Power Systems Technical, 7-11 May 1989.
238 Sung J.-H., Park S., Nam K., New hybrid parallel active filter configuration minimising active filter size, IEE Proceedings - Electric Power Applications, 147, 2, March 2000, pp. 93-98.
239 Sut-Ian H., Chi-Seng L., Man-Chung W.: Comparison among PPF, APF, HAPF and a combined system of a shunt HAPF and a Shunt Thyristor controlled LC, IEEE Region 10 Conference TENCON, 1-4 November 2015.
240 Syed. M. P., Creg W. P. C.: Application, Design and Specification of Harmonic filters for variable frequency drives, IEEE Transactions on Industry Applications, 31, 4, July/August 1995.

T

241 Tangtheerajaroonwong W et al.: Design of a transformerless shunt hybrid filter integrated into a Three-Phase diode rectifier, IEEE 37th Power Electronics Specialists Conference 2006.
242 Taruna J., Shailendra J., Ganga A.: Comparison of topologies of hybrid active power filter, IET-UK International Conference on Information and Communication Technology in Electrical Sciences (ICTES 2007).
243 Thekla N. B., Stavros A. P.: Short-circuit calculations in networks with distributed generation, Elsevier, Electric Power Systems Research 78, 2008, pp. 1181-1191.
244 Thierry T et al. : Performance evaluation of three phase three and four wire active filter, IEEE Conference Record on Industry Applications Conference, Thirty-First IAS Annual Meeting, IAS '96, 6-10 October 1996.
245 Tian j., Chen Q., Xie B.: Series hybrid active power filter based on controllable harmonic impedance, IET Power Electron, 5, 1, January 2012, pp. 142-148.
246 Tiago D. C. B., José A. P., Marcelo G. S.: Passive filter aided by shunt compensators based on the conservative power theory, IEEE Transaction on Industry Applications, July/August 2016.

U

247 Ucak O., Kocabas I., Terciyanli A.: Design and implementation of a shunt active power filter with reduced DC link voltage, ResearchGate, 27 May 2015.
248 Udgave R.S., Atre Y. R.: Active filters with control based on the P-Q theory, IOSR Journal of Electronics and Communication Engineering (IOSR-JECE), ISSN: 2278-2834, PP. 27-30.
249 Upadhye S.D., Atre Y. R.: Determination of the design parameters of passive harmonic filters using nonlinear optimization, IEEE Conference on Industrial and Commercial Power Systems Technical, 3-8 May 1998.

V

250 Visintini R.: Rectifiers, https://cds.cern.ch/record/987551/files/p133.pdf.
251 Vijayakumar G., Nitin G., Gupta R. A.: Mitigation of power quality using shunt active power filters: A comprehensive review, IEEE Conference on Industrial Electronics and Applications (ICIEA), 2017.

W

252 Wagner V.E.: Effects of harmonics on equipment, IEEE Transactions on Power Delivery, 8, 2, April 1993, pp. 672-680.
253 Wasiak I.: Elektroenergetyka w zarysie, Przesył i rozdział energii elektrycznej, Politechnika Łądzka, Poland, Łódź 2010.
254 Watanabe E. H., Akagi H., Aredes M.: Instantaneous *p-q* power theory for compensating nonsinusoidal systems, IEEE International School on Nonsinusoidal Currents and Compensation, Łagów, Poland, 10-13 June 2008.
255 Wen-guan W. et al.: Ant colony optimization algorithm for design of analog filters, IEEE Congress on Evolutionary Computation, 10-15 June 2012.
256 Włas M.: Design of high harmonic passive filter (in polish - Projektowanie filtrów pasywnych wyższych harmonicznych, Zeszyty Naukowe Wydziału Elektrotechniki i Automatyki Politechniki Gdańskiej), Poland, Lecture Nr 29.

257 Wojciechowski D.: Równoległe kompensator aktywne dużej mocy, Akademia Morska w Gdyni, Poland, Gdynia, 2013.

X

258 Xiang-Yang X., Xu H.: A novel active power filter for harmonic suppression and reactive power compensation, IEEE Conference on Industrial Electronics and Applications, 24-26 May 2006.

259 Xiao Y.: The method for designing the third order filter, IEEE International conference on Harmonics and quality of Power Proceedings, China, Wuhan, 14-16 October 1998.

260 Xiao Y.: Algorithm for the parameters of double tuned filter, IEEE 8th International conference on Harmonics and Quality of Power Proceedings, 14-16 October 1998.

261 Xiaodong L., William J., Ryan L.: Transformer winding connections for practical industrial applications, IEEE conference on Petroleum and Chemical Industry Technical, PCIC'07, 17-19 September 2007.

262 Xiaoming Y et al.: Stationary-frame generalized integrators for current control of active power filters with zero steady state error for current harmonics of concern under unbalanced and distorted operation conditions, IEEE transaction on industry applications, March/April 2002.

263 Xin L., Xu W., Yu Y.: A fast harmonic detection method based on recursive DFT, IEEE International Conference on Electronic Measurement and Instruments, 2007.

264 Xing Z., et al.: An LCL-LC power filter for grid-tied inverter, IEEE Region 10 Conference, TENCON, 22-25 October 2013.

265 Xu Y et al.: Parallel operation of hybrid active power filter with passive power filter or capacitors, IEEE Transmission and Distribution Conference and Exhibition: Asia and Pacific, 18-18 August 2005.

Y

266 Yi-hong H.E., Heng S.U.: A new method of designing double-tuned filter, International Conference on Computer Science and Electronics Engineering, , Hangzhou, 22-23 March, 2013.

267 Ying-Pin C., Chi-Jui W.: Optimal multiobjective planning of large-scale passive harmonic filters using hybrid differential evolution method considering parameter and loading uncertainty, IEEE Transactions on Power Delivery, 20, 1, January 2005.

268 Yoa X., Jie Z., Shijie M.: Theory for the design of C-type filter, IEEE International Conference on Harmonics and Quality of Power, 12-15 September 2004, pp. 11-15.

269 Yoichi H., Noriaki S., Kinzo T.: A novel control of a current-source active filter for ac power system harmonic compensation, IEEE transactions on Industry application, 27, 2, March/April 1991.

270 Young-Sik C., Hanju C.: Single-tuned passive harmonic filter design considering variances of tuning and quality factor, Journal of International Council on Electrical Engineering, pp. 7-13, 2011.

271 Yousif S. N. AL., Wanik M. Z. C.: Implementation of different passive filter designs for harmonic mitigation, IEEE Conference on National Power and Energy, PECon, 29-30 November 2004.

272 Yu M et al.: A double tuned filter based on controllable reactor, IEEE International Symposium on Power Electronics, Electrical Drives, Automation and Motion, SPEEDAM, 23-26 May 2006.

Z

273 Zacharia P., Menti A., Zacharis Th.: Genetic algorithm-based optimal design of shunt compensators in the presence of harmonics, Elsevier, Electric Power Systems Research, April 2008, 78, pp. 728-735.

274 Zainal S., Tan P. C., Awang J.: Harmonics mitigation using active power filter: A technological review, Elektrika, Vol. 8, NO. 2, 2006, 17-26.

275 Zamani M. A., Mohseni M.: Damped-type double tuned filters design for HVDC systems, 9th International Conference on Electrical Power Quality and Utilisation, Spain, Barcelona, 9-11 October 2007.

276 Zhang R et al.: Three-dimensional space vector modulation for four-leg voltage-source converters, IEEE Transactions on Power Electronics, May 2002.

277 Zhang R., Liu Y., Li Y.: Optimal parameters for filter using improved genetic algorithms, IEEE International Conference on Sustainable Power Generation and Supply, 6-7 April 2009.

278 Zobaa A. F.: The optimal passive filters to minimize voltage harmonic distortion at a load bus, IEEE Transactions on Power Delivery, 20, 2, April 2005.
279 Zobaa A. F.: A new approach for voltage harmonic distortion minimization, Elsevier, Electric Power Systems Research, 70, 3, August 2004, pp. 253-260.
280 https://www.schaffner.com/products/power-quality/ecosine-passive-harmonic-filter/all-products/
281 https://www.electronicdesign.com/power/igbts-or-mosfets-which-better-your-design
282 http://charlesbrownrecruitment.com/igbt-versus-mosfet-design/
283 https://www.a-eberle.de/en/product-groups/pq-mobile/devices/pq-box-200
284 http://www.chromaate.com/
285 http://www.simpax.pl/pl/budowa-rezystorow/rezystory-cementowe-rc
286 https://www.dacpol.eu/pl/produkty
287 https://library.e.abb.com/public/6dd11a0cd8e1cf9a83257be8005772f0/C_EL25P1_1.pdf
288 https://www.elhand.pl/produkty/transformatory
289 https://sklep.elma-energia.pl/kondensatory-niskich-napiec/19-printed-dress.html
290 https://www.zez-silko.com/en/products/low-voltage-power-capacitors

Annex I. Electrical grid model design in MATLAB/SIMULINK

The electrical network model in Figure I.1 is applied for the simulation studies presented in chapter 3. The equivalent circuit presented in Figure I.1(a) has its computed parameters as well as computation formulas in Table I.1, Table I.2, Table I.3 and Table I.4 [233, 234].

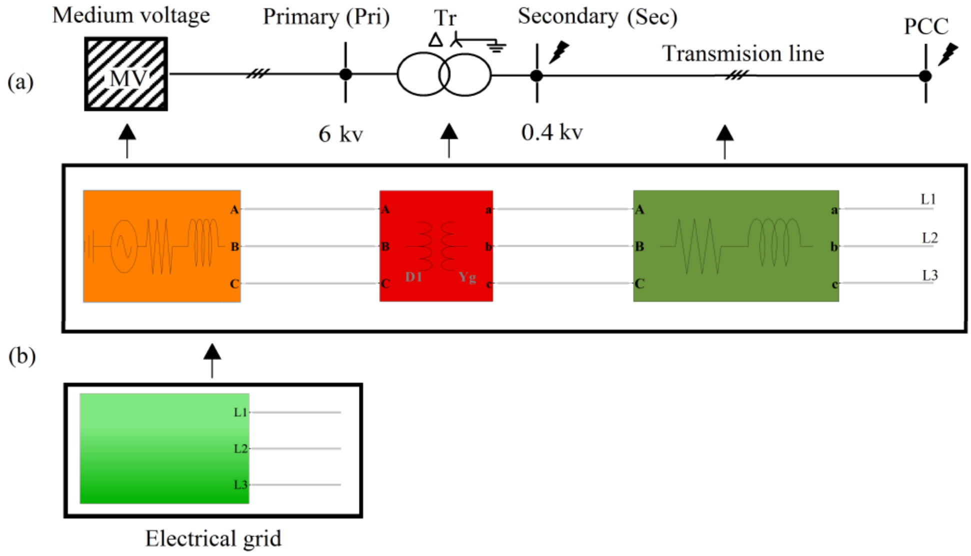

Figure I.1 Supply network equivalent circuit (a) and (b) its model in MATLABE/SIMULINK [1]

Table I.1 Medium voltage parameters (6 kV)

Substitute parameters	Formulas	Computed parameters
U_{MV_N} = 6 kV S_{MV_N} = 200 MVA	$X_{MV} = 1.1\frac{U_{MV\_N}^2}{S_{MV\_N}}$ For the medium voltage system with $U_{MV\_N} \leq 35$ kV [114]: $R_{MV} = 0.1\ X_{MV}$ $X_{MV} = 0.995\ Z_{MV}$	Z_{MV} = 0.1989 Ω X_{MV} = 0.198 Ω R_{MV} = 0.0198 Ω L_{MV} = 630 μH

Table I.2 Transformer parameters (two windings) at the primary side

Substitute parameters	Formulas	Computed parameters
S_{Tr_N} = 500 kVA ΔP_{Tr_N} = 8.5 kW ΔP_{Fe_N} = 2.5 kW $I_{0\%}$ = 5.3 % $\Delta U_{SC\%}$ = 4.5 % $U_{Tr\_Pri\_N}$ = 6 kV $U_{Tr\_Sec\_N}$ = 0.4 kV	$R_{Tr\_Pri} = \frac{\Delta P_{CU\_N} U_{Tr\_Pri\_N}^2}{S_{Tr\_N}^2}$ $Z_{Tr\_Pri} = \frac{\Delta U_{SC\%} U_{Tr\_Pri\_N}^2}{100 S_{Tr\_N}}$ $\vartheta = \left(\frac{U_{Tr\_Sec\_N}}{U_{Tr\_Pri\_N}}\right)^2$	Z_{Tr_Pri} = 3.24 Ω X_{Tr_Pri} = 3 Ω R_{Tr_Pri} = 1.224 Ω L_{Tr_Pri} = 9550 μH

S_{Tr_N} - nominal power of transformer
ΔP_{Cu_N} - nominal copper losses of transformer
ΔP_{Fe_N} - Iron losses of transformer
$I_{0\%}$ - no-load current of transformer
$\Delta U_{Shc\%}$ - short-circuit voltage of transformer
$U_{Tr\_Pri\_N}$ - transformer nominal voltage (primary side)
$U_{Tr\_Sec\_N}$ - transformer nominal voltage (secondary side)

Two points of the supply network (secondary side of transformer and transmission line end) are chosen for the short-circuit power calculation (Figure I.1(a)). The computation equations are shown in Table I.4 [74, 114, 206, 233, 234]. Figure I.1(b) represents the supply network model in MATLAB/SIMULINK [1].

Table I.3 Transmission line parameters

Substitute parameters		Formulas	Computed parameters	
γ_{AL}	$=34\,\frac{\mathrm{m}}{\Omega\mathrm{mm}^2}$	$R_{\mathrm{L}} = \frac{\ell}{\gamma_{\mathrm{AL}} x}$	Z_{L}	= 0.465 Ω
x	= 35 mm^2		X_{L}	= 0.2 Ω
X_0	$=0.4\,\frac{\Omega}{\mathrm{km}}$	$X_{\mathrm{L}} = X_0 \ell$	R_{L}	= 0.420 Ω
ℓ	= 500 m		L_{L}	= 636.6 μH

X_0 - reactance per unit length of transmission line
ℓ - length of transmission line
x - cross-section area of transmission line

Table I.4 Computed equivalent parameters of the simulated power system

$Z_{\mathrm{SC\_Sec}} = (Z_{\mathrm{MV}} + Z_{\mathrm{Tr\_Pri}})\vartheta$	$Z_{\mathrm{SC\_Sec}}$	= 0.01528 Ω
$I_{\mathrm{SC\_Sec}} = \frac{U_{\mathrm{Tr\_Sec\_N}}}{\sqrt{3} Z_{\mathrm{SC\_Sec}}}$	$I_{\mathrm{SC\_Sec}}$	=15.109 kA
$S_{\mathrm{SC\_Sec}} = \sqrt{3} U_{\mathrm{Tr\_Sec\_N}} I_{\mathrm{SC\_Sec}}$	$S_{\mathrm{SC\_Sec}}$	=10.468 MVA
$Z_{\mathrm{S}} = Z_{\mathrm{SC\_PCC}} = Z_{\mathrm{SC\_Sec}} + Z_{\mathrm{L}}$	Z_{S}	= 0.480 Ω
$I_{\mathrm{SC\_PCC}} = \frac{U_{\mathrm{Tr\_Sec\_N}}}{\sqrt{3} Z_{\mathrm{S}}}$	$I_{\mathrm{SC\_PCC}}$	= 481.12 A
$S_{\mathrm{SC\_Sec}} = \sqrt{3} U_{\mathrm{Tr\_Sec\_N}} I_{\mathrm{SC\_PCC}}$	$S_{\mathrm{SC\_PCC}}$	= 0.33 MVA
$X_{\mathrm{S}} = (X_{\mathrm{MV}} + X_{\mathrm{Tr\_Pri}})\vartheta + X_{\mathrm{L}}$	X_{S}	= 0.2142 Ω
$R_{\mathrm{S}} = (R_{\mathrm{MV}} + R_{\mathrm{Tr\_Pri}})\vartheta + R_{\mathrm{L}}$	R_{S}	= 0.4255 Ω
	L_{S}	= 681.82 μH

$Z_{\mathrm{Shc\_Sec}}$ - equivalent impedance (from the MV system to the transformer secondary side)
$I_{\mathrm{SC\_Sec}}$ - initial short-circuit current at the transformer secondary side
$S_{\mathrm{SC\_Sec}}$ - short-circuit power at the transformer secondary side
Z_{S}, $Z_{\mathrm{Shc\_PCC}}$ - power system equivalent impedance (from the MV system to the PCC)
$I_{\mathrm{SC\_PCC}}$ - initial short-circuit current at the transmission line end (PCC)
$S_{\mathrm{SC\_PCC}}$ - short-circuit power at the transmission line end (PCC)

Annex II. Model of the electrical grid with the load (MATLAB/SIMULINK)

In this annex, the two electrical circuits models designed in MATLAB/SIMULINK to perform the analyses in chapter 3 are presented. The first electrical model is constituted of three-phase adjustable speed drive (Figure II.1) and the second one is constituted of one-phase diode bridge with *R* load at the DC side (Figure II.6).

A. Electrical circuit model with three-phase adjustable speed drive

The three-phase thyristor bridge with DC motor drive at its DC side and reactor (L) at its AC side constitutes the non-linear load of Figure II.1. The block in dark green is the DC motor drive (see Figure II.2) and the block in cyan represents the DC motor control speed (see Figure II.3).

The blocks in orange and light blue are respectively the scopes, voltage and current measurement blocks (Figure II.1).

The DC motor drive block is presented in Figure II.2 with more details. The block in red colour is the DC motor, the torque is given by the block named “Load torque” and the blocks named “Mean1” and “Mean2” are respectively used to compute the mean value of rotor speed and current for the feedback control system loops. The “Armature current” is the current of rotor coils and the “Field current” is the current of the wound stator.

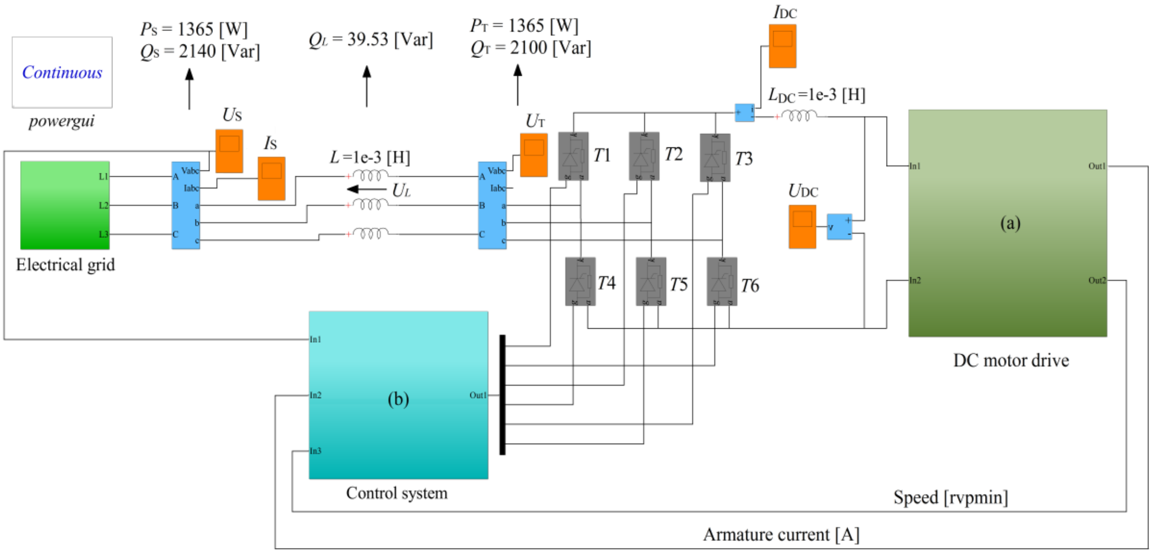

Figure II.1 Three-phase thyristor rectifier connected to the electrical grid

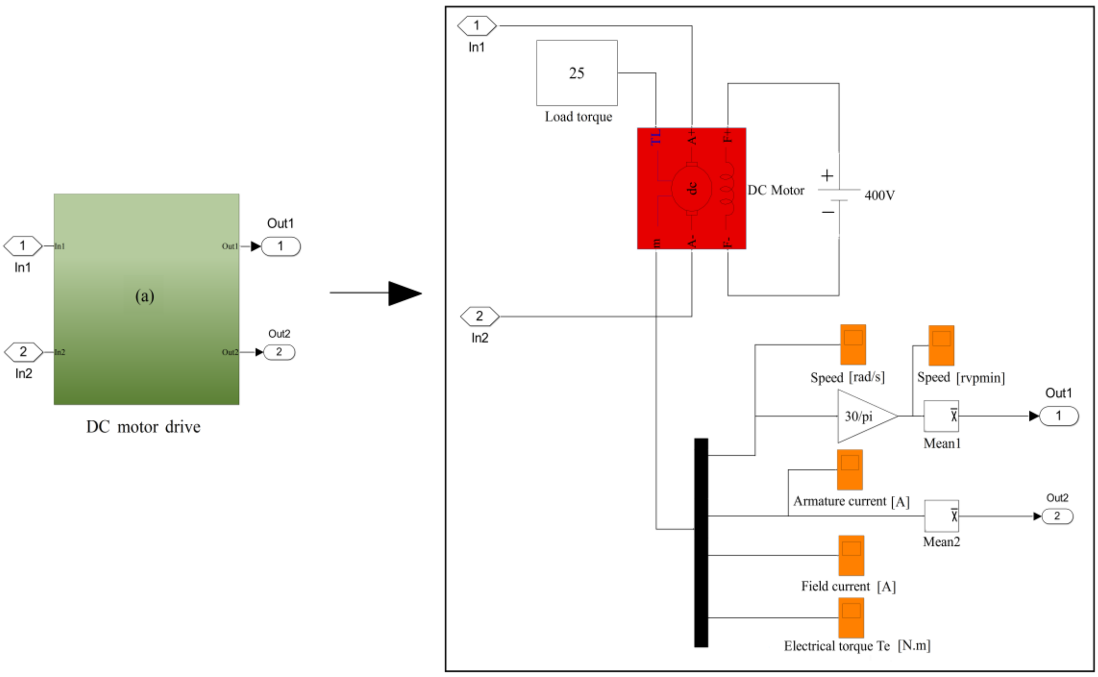

Figure II.2 DC motor drive

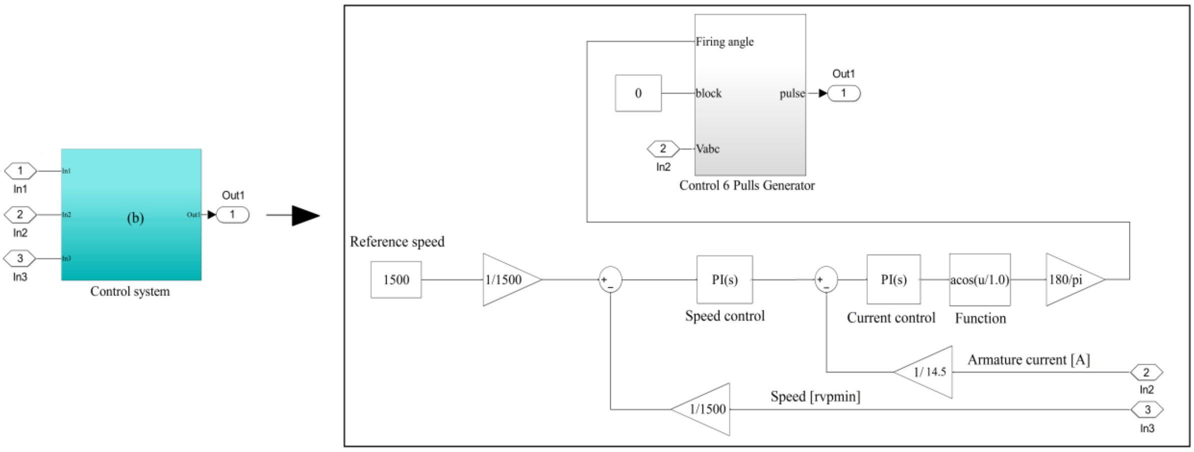

Figure II.3 DC motor control speed

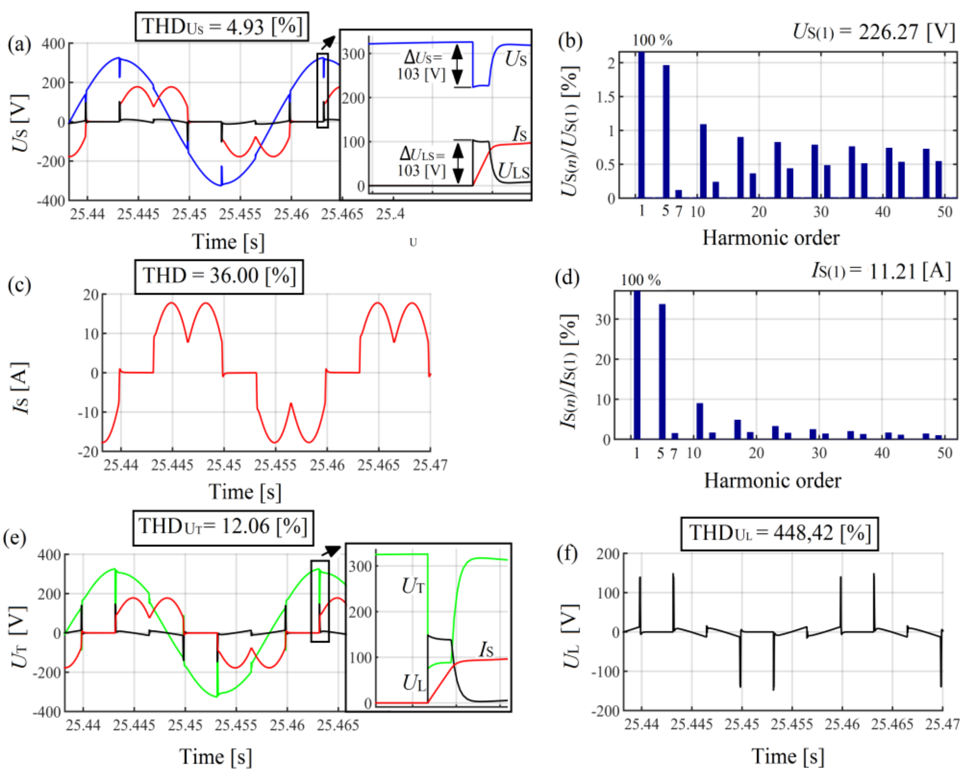

Figure II.4 Examples of waveforms and spectrums obtained after simulation of power system of Figure II.1 (AC side): (a) grid voltage and (b) its spectrum; (c) grid current and (d) its spectrum; (e) voltage at the thyristor bridge input; (f) reactor (L) voltage

The DC motor control speed system is presented with more details in Figure II.3. It is constituted of two control loops (rotor speed and current), two PI controllers and one pulls generator [1, 123]. The optimization of the PI controllers ("Speed control" and "Current control") is not taking into account. The block named “Function” is used to inverse the signal at the output current controller (the firing angle is between 90º and 0º). At the end the two control loops, the generated firing angle is used by the generator to generate pulses.

The waveforms and spectrums examples obtained after simulating the power system of Figure II.1 are presented in Figure II.4 (AC side) and Figure II.5 (DC side).

At the AC side, the grid voltage and current with their spectrums are presented in Figure II.4(a) to (d). The input thyristor rectifier voltage is presented in Figure II.4(e) and the voltage reactor in Figure II.4(f). When the grid current is increasing (during the thyristors commutation), the grid reactor (L_S) voltage also increases at the same time and the voltage dips appear on the grid voltage as show on Figure II.4(a). The voltage increase (ΔU_{LS} = 103 V) on the grid reactor is equal to the voltage dip on the grid voltage (ΔU_S = 103 V – see the commutation dip of Figure II.4(a)). The input thyristor bridge voltage (U_T) is more distorted than the grid voltage (U_S) because the reactor (L) presence (Figure II.4(a) and (e)).

At the DC side, Figure II.5(a) and (b) shows respectively the voltage and current feeding the DC motor rotor and Figure II.5 (c) and (d) constitutes respectively the rotor drive speed and firing angle.

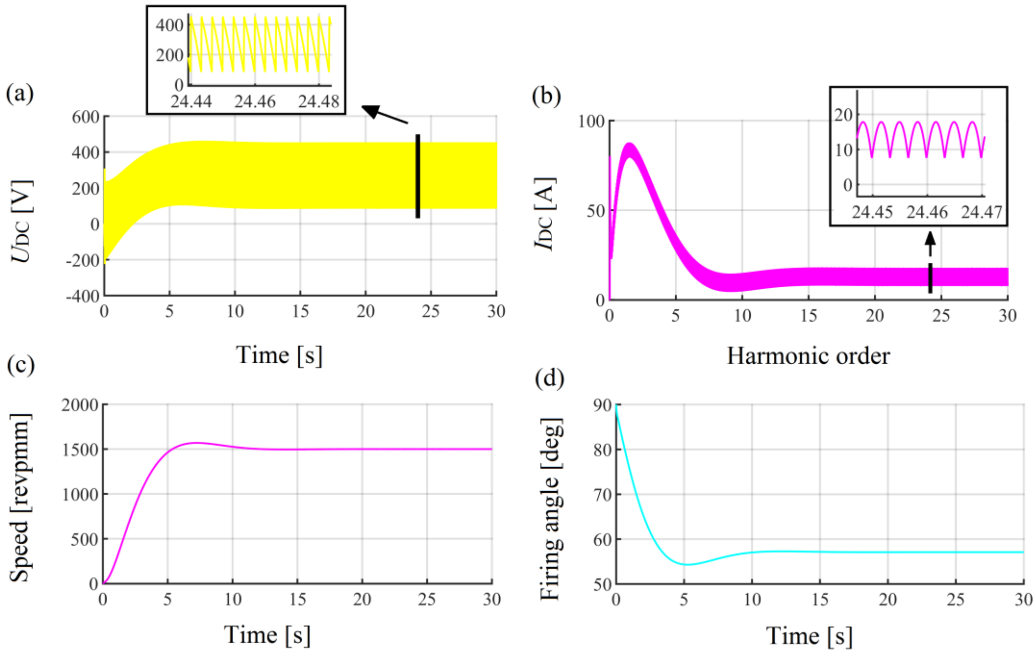

Figure II.5 Examples of characteristics obtained after simulation of power system of Figure II.1 (DC side): (a) voltage and (b) current feeding the motor drive rotor; (c) motor drive speed; (d) firing angle obtained at the end of the control system

B. Electrical circuit model with one-phase diode rectifier

The one-phase diode bridge with *RC* load at the DC side and reactor (*L*) at the AC side is presented in Figure II.6. The blocks *D*1 to *D*4 represent the diodes bridge. The blocks named "Flip-Flop", "Breaker1", "Comparator", "Constant" and "Breaker2" are used to charge the capacitor C_{DC}. When the simulation starts, the capacitor C_{DC} is securely charged through the resistance *r* ("Breaker1" and "Breaker2" are switched *off*). When the capacitor C_{DC} is charged to a value higher or equal to the value inside the block name "constant" (e.g. 300 V), "Breaker1" and "Breaker2" are switched *on* and the current stopped to flow through the resistance *r*. The block named "Flip-Flop" is used to maintain the blocks "Breaker1" and "Breaker2" *on* during the rest of simulation. The blocks in orange colour represents the scope and the blocks in light blue colour are voltage and current measurements.

The examples of waveforms and spectrums obtained after simulation of Figure II.6 are presented in Figure II.7. The grid voltage and current with their spectrums are presented in Figure II.7(a) to (d), the input diode rectifier voltage in Figure II.7(e) and the voltage at the DC side of rectifier in Figure II.7. The input diode rectifier voltage (U_r) is more distorted than the grid voltage (U_S).

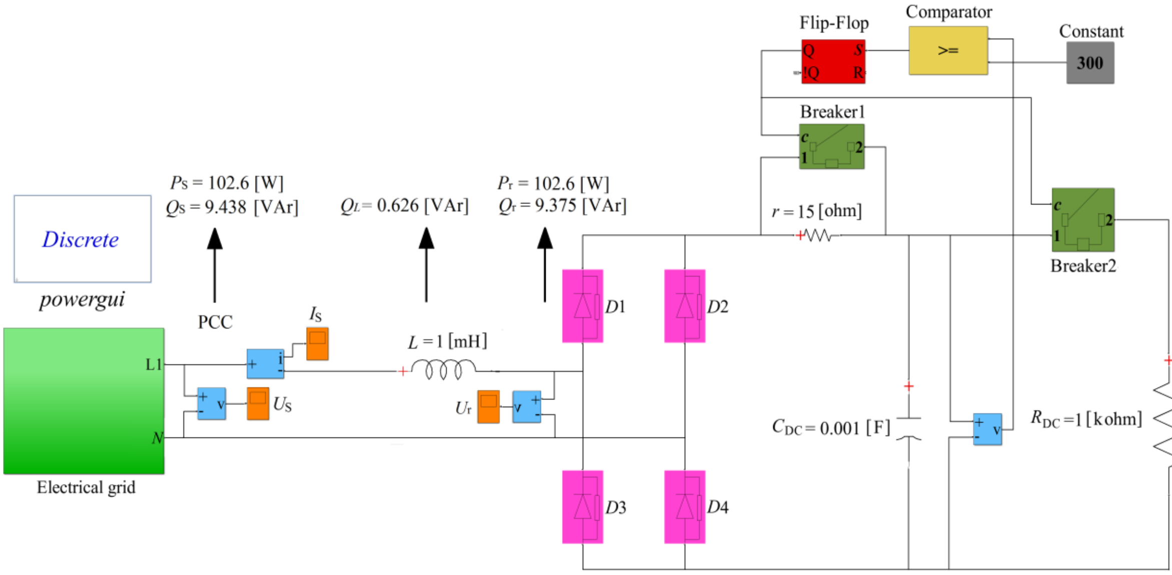

Figure II.6 Single-phase rectifier with R_{DC}-C_{DC} load at the DC side and reactor L at the AC side (MATLAB/SIMULINK).

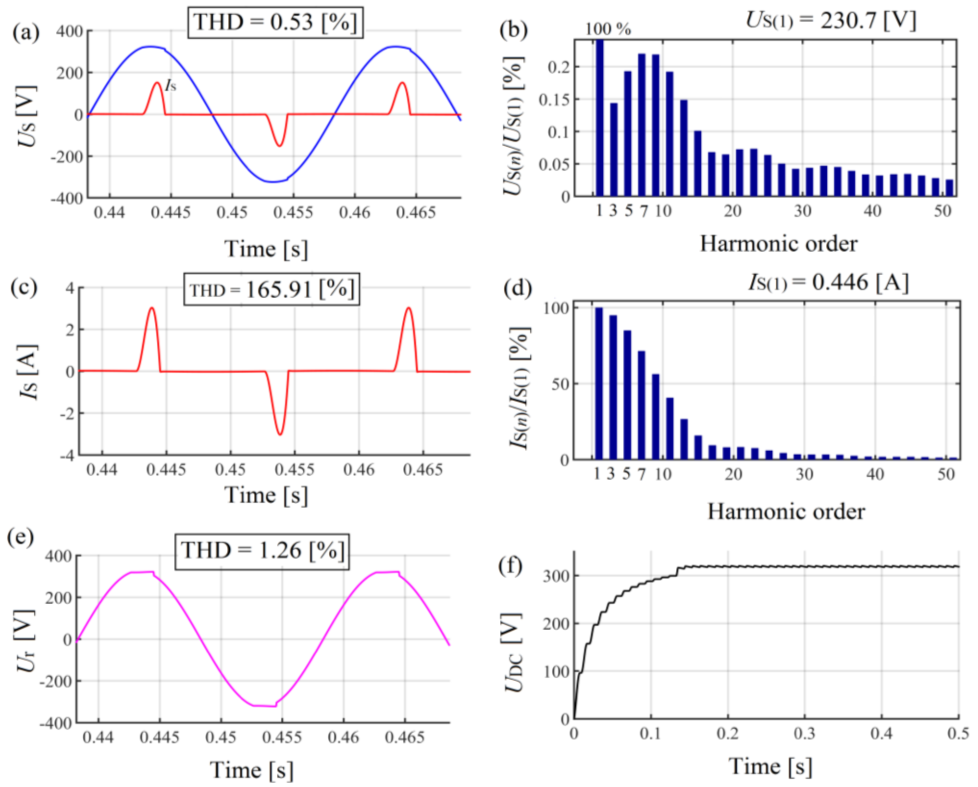

Figure II.7 Examples of waveforms and spectrums obtained after simulation of single-phase diode bridge of Figure II.6: (a) grid voltage and (b) its spectrum; (c) grid current and (d) its spectrum; (e) voltage at the input of rectifier; (f) voltage at the DC side of rectifier

Annex III. Data from chapter 3

III.1 Series passive harmonic filters

Table III.1 The series PHF parameters for different values of the fundamental harmonic impedance ($Z_{f(1)}$)

n_{re} =5			
$Z_{f(1)}$ [Ω]	$Z_{f(5)}$ [TΩ]	$C_{f(1)}$ [μF]	$L_{f(1)}$ [mH]
0.0795	2251.8	1700	0.24
1.0795	36029	122.86	3.3
2.0795	36029	63.779	6.4
4.0795	*Inf*	32.511	12.5

Table III.2 The series PHF parameters for different values of tuning frequency

$Z_{f(1)}$ = 0.0795[Ω]			
n_{re}	$Z_{f(5)}$ [Ω]	$C_{f(1)}$ [μF]	$L_{f(1)}$ [μH]
4.7	2.8809	1900	241.60
5	*Inf*	1700	242.93
5.2	5.0740	1500	243.70

Table III.3 The series PHF parameters. Increase and decrease of filter reactor inductance by ± 10%

n_{re} =5					
$L_{f(1)(+10\%)}$ [μH]	L_f [μH]	$L_{f(1)(-10\%)}$ [μH]	$C_{f(1)}$ [μF]	$Z_{f(1)}$ [Ω]	$Z_{f(5)}$ [Ω]
267.23	-	-	1700	0.0878	4.1976
-	242.93	-		0.0795	2.2518e+15
-	-	218.64		0.0713	3.4344

Table III.4 The series PHF parameters. Increase and decrease of filter capacitor capacitance by ± 10%

n_{re} =5					
$Z_{f(1)}$ = 0.0795[Ω]					
$C_{f(1)(+10\%)}$ [μF]	$C_{f(1)}$ [μF]	$C_{f(1)(-10\%)}$ [μF]	$L_{f(1)}$ [μH]	$Z_{f(1)}$ [Ω]	$Z_{f(5)}$ [Ω]
1800	-	-	242.93	0.0798	3.8160
-	1700	-		0.0795	2.2518e+15
-	-	1500		0.0792	3.8160

Table III.5 The series PHF parameters. Increase of reactor resistance (R_{Lf})

n_{re} =5				
$Z_{f(1)}$ =0.0795 [Ω]				
q'	$Z_{f(5)}$ [Ω]	$C_{f(1)}$ [μF]	$L_{f(1)}$ [mH]	R_{Lf} [mΩ]
inf	2.2518e+15	1700	0.24293	0
100	190.80			0.76
85	162.18			0.89
35	66.78			2.2

Table III.6 The series PF parameters. Increase of damping resistance (R)

n_{re} =5				
$Z_{f(1)}$ [Ω]	$Z_{f(5)}$ [Ω]	$C_{f(1)}$ [μF]	$L_{f(1)}$ [mH]	R [Ω]
0.0795	2.2518e+15	1700	0.24293	-
	5			5
	10			10
	20			20

Table III.7 Parameters after simulation

$U_{s\ max}$ [V]					$I_{s\ max}$ [A]			
n	Without filter		With filter		Without filter		With filter	
	Ampl.	Phase	Ampl.	Phase	Ampl.	Phase	Ampl.	Phase
1st	319.96	30.6	320.06	30.6	15.86	-26.8	15.50	-25.9
5th	6.29	-67.5	0.01	133.2	5.35	43.8	0.01	224.2
7th	0.37	9.5	9.35	250.5	0.24	116.4	5.88	-3.9
11th	3.49	-34.5	4.88	-28.9	1.42	65.5	1.99	71.2
13th	0.77	-74.3	4.48	-79.3	0.27	24.7	1.56	19.2
17th	2.89	-11.4	3.38	-3.3	0.77	85.0	0.90	93.3
19th	1.17	-60.4	3.12	-54.8	0.28	35.6	0.75	41.1
23th	2.65	8.9	1.98	19.0	0.52	103.7	0.39	114.0
25th	1.40	-43.8	1.83	-32.7	0.25	50.8	0.33	61.9
29th	2.53	28.0	0.69	34.2	0.4	121.8	0.11	128.3
THD [%]	4.94		4.21		36		42.19	

Table III.8 Continuity of Table III.7

$U_{T\ max}$ [V]				
n	Without filter		With filter	
	Ampl.	Phase	Ampl.	Phase
1st	315.75	30.2	314.98	30.0
5th	14.45	-55.3	211.26	-46.2
7th	0.88	18.6	18.85	258.5
11th	8.40	-28.6	11.30	-23.2
13th	1.87	-69.3	10.56	-74.4
17th	7.02	-7.6	8.07	0.6
19th	2.84	-57.0	7.50	-51.4
23th	6.45	11.8	4.78	21.9
25th	3.41	-41.2	4.42	-30.1
29th	6.15	30.3	1.66	36.4
THD [%]	12.07		67.73	

Table III.9 Reactive and active power of power system (the SPHF resistance was neglected)

	$P_{S(1)}$ [W]	$Q_{S(1)}$ [Var]	$Pf_{(1)}$ [W]	$Q_{f(1)}$ [Var]	$Q_{L(1)}$[Var]	$P_{T(1)}$ [W]	$Q_{T(1)}$[Var]
Before	1365	2140	-	-	39.52	1365	2100
After	1369	2068	-	9.549	37.73	1369	2021

III.2 Shunt Passive Filter

III.2.1 Single-tuned filter

III.2.1.1 Analysis of single-tuned filter for different tuning frequencies

Table III.10 Parameters of single-branch filter

f [Hz]	*n*	$C_{f(1)}$ [µF]	$L_{f(1)}$ [mH]	$Z_{f(5)}$ [Ω]	$Z_{f(1)}$ [Ω]	$Q_{f(1)}$ [Var] (Compensation)
205	4.1	122.95	4.9	2.52	24.35	-2172.5
235	4.70	124.81	3.7	0.67		
245.5	4.85	125.17	3.4	0.32		
250	5	125.49	3.2	0.00		

Table III.11 Reactive and active power of simulated power system

n	Measured values							
	Grid (PCC)			Single filter		Input reactor (L)	Input of thyrystor bridge	
	P_S [W]	Q_S [Var]	*DPF*	P_f [W]	Q_f [Var] (capacitive)	Q_L [Var]	P_T [W]	Q_T [Var] (inductive)
Without filter	1365	2140	0.5378	-	-	39.53	1365	2100
4.1	1362	25.21	0.9998	-	2145	39.54	1362	2131
4.70	1360	30.01	0.9998	-	2142	39.56	1360	2132
4.85	1359	32.68	0.9997	-	2140	39.59	1360	2133
5	1359	31.94	0.9997	-	2141	39.6	1359	2134

Table III.12 Grid voltage ($U_{S\,max}$ [V]) and current ($I_{S\,max}$ [A]) parameters

n	Without filter		n = 4.1		n = 4.70		n = 4.85		n = 5	
	Voltage	Current	Voltage	Current	Voltage	Current	Voltage	Current	Voltage	Current
1st	319.97	15.86	322.93	8.43	322.92	8.42	322.91	8.42	322.91	8.42
5th	6.28	5.34	4.48	3.82	2.46	2.09	1.17	0.99	0.02	0.01
7th	0.38	0.24	0.41	0.25	0.42	0.27	0.43	0.28	0.45	0.29
11th	3.48	1.42	2.98	1.22	2.81	1.15	2.75	1.12	2.71	1.10
13th	0.77	0.27	0.59	0.21	0.53	0.19	0.51	0.18	0.49	0.17
17th	2.89	0.77	2.48	0.67	2.36	0.63	2.32	0.62	2.29	0.61
19th	1.17	0.28	0.95	0.23	0.88	0.21	0.86	0.20	0.83	0.20
23rd	2.65	0.52	2.28	0.45	2.17	0.43	2.13	0.42	2.11	0.41
25th	1.4	0.25	1.16	0.21	1.09	0.20	1.06	0.19	1.04	0.19
29th	2.52	0.4	2.17	0.34	2.07	0.33	2.03	0.32	2.01	0.31
THD [%]	4.93	36	4.24	49.70	3.94	31.54	3.84	22.35	3.79	18.74

III.2.1.2 Optimization technique in MATLAB (method f)

The optimization technique (method f) applied to share the total reactive power in the group of two single-tuned filters is clarified in Table III.13.

Table III.13 Program used to obtained the objective function (y) and Q_{f1}

File name: dwafiltry500var.m

```
function [y]=dwafiltry500var(Qf1)
if Qf1>0 && Qf1<500
  Qf2=500-Qf1;
  nre_f1=2.9;    % resonance frequency of filter (f1)
  nre_f2=4.85;   % resonance frequency of filter (f2)
  nf1 =3;        % characteristic harmonic to be eliminated
                   by (f1)
  nf2=5;         % characteristic harmonic to be eliminated
                   by (f2)
  q=85;          % reactor quality factor
  U=230;         % filter voltage
  w1=100*pi;
  Cf1=(nre_f1^2-1)*Qf1/(w1*nre_f1^2*U^2);
  Cf2=(nre_f2^2-1)*Qf2/(w1*nre_f2^2*U^2);
  Lf1=1/(w1^2*nre_f1^2*Cf1);
  Lf2=1/(w1^2*nre_f2^2*Cf2);
  R_Lf1=w1*Lf1/q;
  R_Lf2=w1*Lf2/q;
```

File name: gl.m

```
clc
clear
Qf1=1:499;
n=length(Qf1);
d=zeros(n,3);
for i=1:length(Qf1)
d(i,:)=dwafiltry500var(Qf1(i));
end
hold on
plot(Qf1,d(:,1),'b')  % optimization function
characteristic
grid on
Q3opt=fminsearch('dwafiltry500var',260)%
= Qf1 % reactive power of filter (f1)
```

```
   zs_nf1=0.425+1i*0.214*nf1;    % electrical grid system
                                 impedance for the 3rd
                                 harmonic
   zs_nf2=0.425+1i*0.214*nf2;    % electrical grid system
                                 impedance for the 5th
                                 harmonic
   zf1_nf1=R_Lf1+1i*w1*nf1*Lf1-1i/(w1*nf1*Cf1);   % 3rd
                        harmonic impedance (f1)
   zf1_nf2=R_Lf1+1i*w1*nf2*Lf1-1i/(w1*nf2*Cf1); % 5rd
                        harmonic impedance (f1)
   zf2_nf1=R_Lf2+1i*w1*nf1*Lf2-1i/(w1*nf1*Cf2); % 3rd
                        harmonic impedance (f2)
   zf2_nf2=R_Lf2+1i*w1*nf2*Lf2-1i/(w1*nf2*Cf2); % 5rd
                        harmonic impedance (f2)
   zF_nf1=zf1_nf1.*zf2_nf1./(zf1_nf1+zf2_nf1);
                        % 3rd harmonic impedance (f2 and f1)
   zF_nf2=zf1_nf2.*zf2_nf2./(zf1_nf2+zf2_nf2);
                        % 5th harmonic impedance (f2 and f1)
   zF_Zs_nf1=zs_nf1.*zF_nf1./(zs_nf1+zF_nf1);
                        % 3rd harmonic impedance for (f2, f1
                         and grid)
   zF_Zs_nf2=zs_nf2.*zF_nf2./(zs_nf2+zF_nf2);
                        % 5th harmonic impedance for (f2, f1
                         and grid)
    y=1-((1-abs(zF_Zs_nf1./zs_nf1)).*(1-
abs(zF_Zs_nf2./zs_nf2))); % optimization function

else
    y=1e5;
end
```

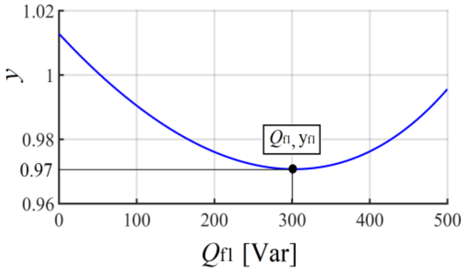

Optimization function

Annex IV. Technical data of the PHFs laboratory components (chapter 4)

IV.1 Load data

The load technical data are presented in Table IV.1, Table IV.2, Figure IV.1 and Figure IV.2.

Table IV.1 Technical data of resistances (R_1, R_2) at the thyristor bridge DC side [285]

SIMPAX DAWNIEJ SIMET S.A. PIASKI		
Parameter	**Value**	**Unit**
Nominal voltage U_N	840	V
Nominal current I_N	35.4	A
Nominal resistance R_N	8	Ω ± 5%
Type of work	S-1	%
Protection degree	IP-20	IP

Table IV.2 Technical data of the thyristor rectifier [286]

Technical data: DACPOL SERVICE Sp. Z O.O.	
Thyristor type	ST3F
Supply voltage	3x 400 V, 50 Hz (L1, L2, L3, N)
Tolerance of supply voltage	+10% to -15%
Method of adjusting the firing angle	phase
Adjusting angle range	0 to 170° el
Control signal	0-10V or 4-20mA
Lock signal	0V blocking a logic zero or +24V blocking a logical one
Work temperature range	0°C, +40°C
Storage temperature range	-25°C to +55°C
Relative humidity	to 90% (without condensation)
Insulation electrical strength	2500V AC
Protection degree	IP20
Cover	metal
Control mode	- External control with control signal - Internal control with potentiometer

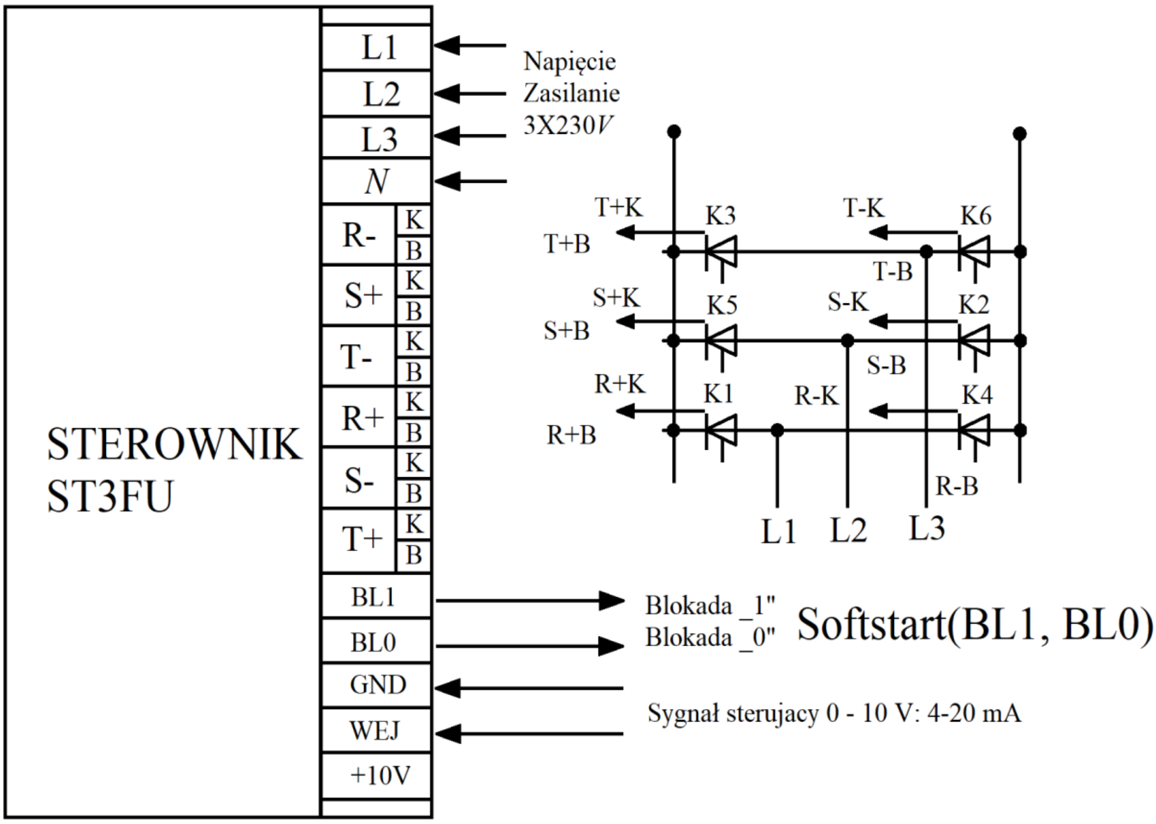

Figure IV.1 Connection diagram of thyristor bridge rectifier [286]

ABB France 3, rue Jean Perrin 69680 Chassieu, FRANCE Tel : +33 (0)4 72 22 17 22 Fax : +33 (0)4 72 22 19 84	SENSOR / *CAPTEUR* Commercial reference *Référence commerciale* **EL25P1**	 Order code *Référence de commande* **1SBT132500R0001**	Issued: 1995.03.23 Modification : Date : Page 2/2

CHARACTERISTICS	*CARACTERISTIQUES*		
Nominal primary current (I_{PN})	*Courant primaire nominal (I_{PN})*	A r.m.s. *(A eff.)*	: 25
Measuring range (I_P max)	*Plage de mesure (I_P max)*	A peak *(A crête)*	: ±55 (@ ±15V (±5%))
Max. measuring resistance (R_M max)	*Résistance de mesure max. (R_M max)*	Ω	: 142 (@Ipmax / ±15V (±5%))
Min. measuring resistance (R_M min)	*Résistance de mesure min. (R_M min)*	Ω	: 100 (@I_{PN} / ±15V (±5%))
Min. measuring resistance (R_M min)	*Résistance de mesure min. (R_M min)*	Ω	: 0 (@I_{PN} / ±12V (±5%))
Turn ratio (N_P/N_S)	*Rapport de transformation (N_P/N_S)*		: 1/1000
Secondary current (I_S) at I_{PN}	*Courant secondaire (I_S) à I_{PN}*	mA	: 25
Accuracy at I_{PN}	*Précision à I_{PN}*	%	: ≤ ±0.5 (-20°C … +70°C)
Offset current (I_{S0})	*Courant résiduel (I_{S0})*	mA	: ≤ ±0.2 (@ +25°C)
Linearity	*Linéarité*	%	: ≤ 0.1
Thermal drift coefficient	*Coefficient de dérive thermique*	µA/°C	: ≤ 7 (-20°C … +70°C)
Delay time	*Temps de retard*	µs	: ≤ 0.1
di/dt correctly followed	*di/dt correctement suivi*	A/µs	: ≤ 200
Bandwidth	*Bande passante*	kHz	: 0 … 200 (-1dB)
No-load consumption current (I_{A0}) (Consumption = $I_{A0} + I_S$)	*Courant de consommation à vide (I_{A0})* *(Consommation = $I_{A0} + I_S$)*	mA	: ≤ 20 (@ ±15V (±5%))
Voltage drop (e)	*Tension de déchet (e)*	V	: ≤ 3
Secondary resistance (R_S)	*Résistance secondaire (R_S)*	Ω	: ≤ 63 (@ +70°C)
Dielectric strength	*Rigidité diélectrique*		
Primary / Secondary	*Primaire / Secondaire*	kVr.m.s. *(kV eff.)*	: 3 (50Hz, 1min)
Supply voltage	*Tension d'alimentation*	V d.c.	: ±12 … ±15 (±5%)
Mass	*Masse*	Kg	: 0.02
Operating temperature	*Température de service*	°C	: -20 … +70
Storage temperature	*Température de stockage*	°C	: -25 … +85
Temperature of primary conductor in contact with the sensor	*Température du conducteur primaire en contact avec le capteur*	°C	: ≤ 100

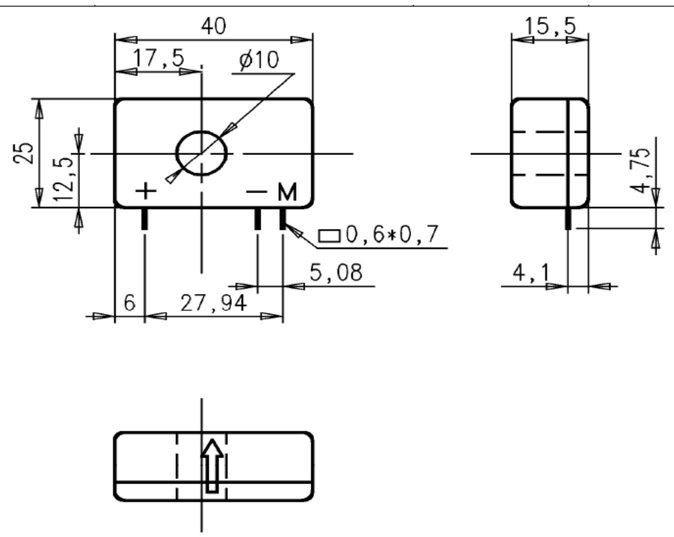

Figure IV.2 Current sensor technical data [287]

IV.2 Electrical grid parameters

The parameters of the electrical grid (from the MV to the LV) feeding the laboratory model are presented in Table IV.3, Table IV.4 and Table IV.5. The simulated blocks of laboratory model is presented in Figure IV.3.

Table IV.3 Medium voltage network side parameters

Given parameters	Computed parameters
U_{MV_N} = 15.750 kV	Z_{MV} = 1.0970 Ω X_{MV} = 1.0915 Ω
	R_{MV} = 0.1091 Ω
S_{MV_N} = 250 MVA	L_{MV} = 0.0035 H

Table IV.4 Transformer parameters (two windings)

Given parameters	Computed parameters (secondary side)
S_{Tr_N} = 1000 kVA ΔP_{Cu_N} = 9067 W	Z_{Tr_Sec} = 0.0093 Ω
ΔP_{Fe_N} = 1610 W $\Delta U_{Shc\%}$ = 5.81 %	X_{Tr_Sec} = 0.0092 Ω
$I_{Tr\_Pri\_N}$ = 36.66 A $U_{Tr\_Pri\_N}$ = 15.750 kV	R_{Tr_Sec} = 0.0015 Ω
$U_{Tr\_Sec\_N}$ = 0.4 kV $I_{Tr\_Sec\_N}$ = 1443,38 A	L_{Tr_Sec} = 29.228 μH

Table IV.5 Computed equivalent parameters of the electrical grid (calculated at the PCC point) feeding the laboratory model

S_{SC_Sec} = 0.15994 MVA X_S = 0.0099 Ω	Z_S = 0.0100 Ω I_{SC_Sec} = 23.086 kA
$Z_{S(5)} = \sqrt{R_S^2 + (5X_S)^2}$ $X_{S(5)} = 5X_S$	R_S = 0.0015 Ω L_S = 31.468 μH $Z_{S(5)}$ = 0.0495 Ω $X_{S(5)}$ = 0.0494 Ω

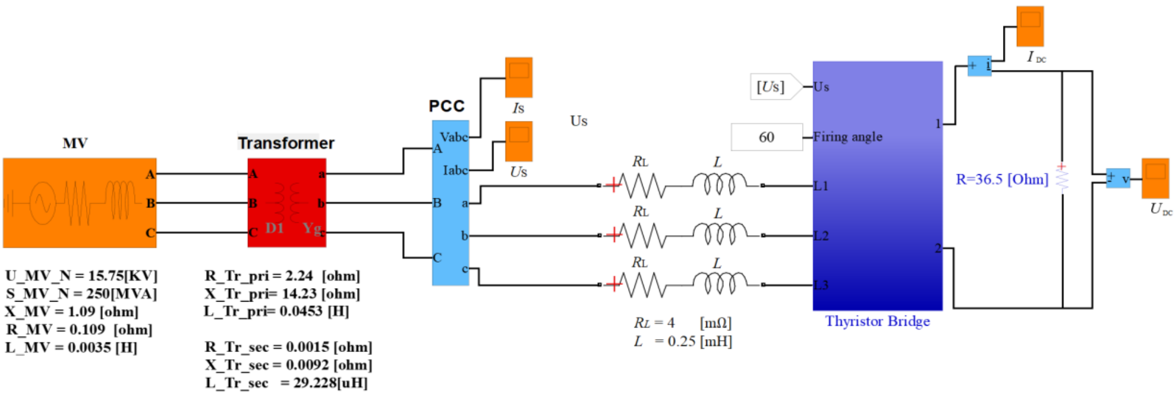

Figure IV.3 Simulated model of laboratory setup

IV.3 PHF reactors and capacitors technical data

Lubliniec, 28.06.2017r.

Sz. P. mgr inż. Marek Litewka

Akademia Górniczo-Hutnicza

Wydział Elektrotechniki, Automatyki, Informatyki i Inżynierii Biomedycznej
Katedra Energoelektroniki i Automatyki Systemów Przetwarzania Energii

Al. Mickiewicza 30
30-059 Kraków
kom.: +48 12 617-34-03
e-mail: litewka@agh.edu.pl

elhand TRANSFORMATORY
ELHAND TRANSFORMATORY Sp. z o.o.
PL 42-700 Lubliniec ul. Klonowa 60
tel. +48 34 34 73 100
fax +48 34 34 70 207
info@elhand.pl
www.elhand.pl
NIP: PL 5751862934

Oferta nr OFPL-2017-1293 na dławiki typu ED1-8,03-7,7-7,3-7,0-6,6; IP00

Szanowny Panie,
w nawiązaniu do przesłanego zapytania w dniu 19.06.2017r. niniejszym przedstawiam naszą ofertę na interesujące Państwa dławiki naszej produkcji w wykonaniu lądowym, wykonane zgodnie z wymaganiami normy PN-EN 60076-6 oraz przekazanymi danymi technicznymi:

typ	ED1-8,03-7,7-7,3-7,0-6,6; IP00
nr obliczeń / nr kalkulacji	OBL33476 / KALK/2017/0411
indukcyjność L	8,03 – 7,7 – 7,3 – 7,0 – 6,6 mH
prąd I	15 A
częstotliwość	50 Hz
napięcie pracy Un	400 V
napięcie próby Upr	3 kV_{AC} (1 min)
praca	S1 (ciągła)
wykonanie	C1/E0
klasa izolacji	T40F
chłodzenie	AN (naturalne, powietrzne)
położenie	stojące
materiał uzwojeń	miedź
impregnacja	lakier elektroizolacyjny
stopień ochrony	IP00, klasa I
wymiary LxBxH [mm]	~ 165 x 110 x 240
masa [kg]	~ 12
ilość [szt.]	3
Tolerancja indukcyjności	*±10%*
cena netto	**717,00 PLN/szt.**

OFERTA WAŻNA DO: 30.09.2017r.

WARTOŚĆ OFERTY NETTO: 2 151,00 PLN

WARUNKI HANDLOWE:

1. Termin realizacji zlecenia: 3 - 5 tygodni od otrzymania pisemnego zamówienia,
2. Warunki dostawy: FCA (wg Incoterms) - spedycją na koszt Odbiorcy,
3. Sposób zapłaty przelewem na nasze konto z terminem wpływu 14 dni od daty sprzedaży,
4. Okres gwarancji: 24 miesiące od daty sprzedaży.

Oczekując zainteresowania ofertą, łączę serdeczne pozdrowienia.
Z poważaniem
Adam Jonczyk
ELHAND TRANSFORMATORY Sp. z o.o.
tel. +48 34 3473 111
fax +48 34 3470 207
e-mail: marketing@elhand.pl

W przypadku zamówienia proszę powołać się na numer oferty.

KRS: 0000342480
Sąd Rejonowy w Częstochowie,
XVII Wydz. Gospod. KRS
Kapitał zakładowy: 7.211.850 PLN
NIP: PL 5751862934;

Konto bankowe:
ING Bank Śląski S.A.O/Lubliniec
PL 29 1050 1142 1000 0023 5194 3747 (PLN)
PL 12 1050 1142 1000 0023 5194 3762 (EUR)
PL 20 1050 1142 1000 0023 5336 5832 (USD)

Konto bankowe:
Deutsche Bank PBC S.A.
PL 78 1910 1048 2518 4670 6589 0001 (PLN)
PL 51 1910 1048 2518 4670 6589 0002 (EUR)
SWIFT/BIC: DEUTPLPX

Figure IV.4 Technical data of reactor with six terminals. This rector is used to present the detuning phenomenon of single-tune filter applied to mitigate the 5th harmonic in the grid current and voltage [288]

Form.3/P10-01

ELHAND TRANSFORMATORY Sp. z o.o. Lubliniec dn. 2017-08-22

Zamówienie : PL/1295 / 2017 / 1 Nr obliczeń : 33476

PROTOKÓŁ KONTROLI DŁAWIKA

PKW

I. Dane techniczne :

Typ : ED1 - 8,03-7,7-7,3-7,0-6,6/15 Nr fabr. 13637 Rok prod.: 2017

Moc znamionowa 0,57 kVAr
Indukcyjność 8,03-7,7-7,3-7,0-6,6 mH Prąd znamionowy 15 A Napięcie pracy 400 V
Najwyższe napięcie pracy 750 V Częstotliwość 50 Hz Klasa izol. T40F
Napięcie prob. 2,5 kV w ciągu 60 sek. 50 Hz Rezystancja izolacji 7,112 GΩ
Rodzaj pracy S1 Chłodzenie AN Stopień ochr. IP00
Wykonanie C1/E0 wg przepisów PN-EN 61558-2-20

Straty czynne przy I_N 29,8 W

II. Wymiary, waga :

Waga: miedzi 2,9 kg żelaza 6,73 kg dławik 10,6 kg
Wymiary zewnętrzne dławika (L×B×H) 157 mm 133 mm 235 mm
Rozstaw i średnica otworów montażowych (d × e × f) 115 mm 106 mm 11x21 mm

III. Wyniki pomiarów (temp. uzw. = 22 °C; częstotliwość 50 Hz)

Pomiar rezystancji izolacji (2500V_{DC});

	R_{60s} [GΩ]	R_{15s} [GΩ]	R_{60s} / R_{15s}
uzwojenie – rdzeń	7,112	6,980	1,01

Próba napięciowa izolacji;

	Napięcie probiercze [kV]	Czas [s]	Wynik
uzwojenie – rdzeń	2,5	60	pozytywny

Pomiar rezystancji uzwojeń:

Zaciski	Rezystancja [Ω]
1.1 – 1.2	0,10568
1.3 – 1.2	0,10364
1.4 – 1.2	0,10158
1.5 – 1.2	0,09955
1.6 – 1.2	0,09702

Pomiar indukcyjności (częstotliwość 50 Hz):

Tepping	Voltages	Currents	Inductance	Deviations of inductance
1.1 - 1.2	39,183 V	14,965 A	8,35673 mH	4,07 %
Reactive power 1-ph	588,089 VAr			
Active power 1-ph	29,778 W			
Tepping	Voltages	Currents	Inductance	Deviations of inductance
1.1 - 1.3	37,506 V	14,94 A	8,01685 mH	4,11 %
Reactive power 1-ph	562,191 VAr			
Active power 1-ph	28,98 W			
Tepping	Voltages	Currents	Inductance	Deviations of inductance
1.1 - 1.4	36,467 V	15,187 A	7,65514 mH	5 %
Reactive power 1-ph	555,665 VAr			
Active power 1-ph	29,406 W			
Tepping	Voltages	Currents	Inductance	Deviations of inductance
1.1 - 1.5	35,095 V	15,286 A	7,33705 mH	4,81 %
Reactive power 1-ph	538,598 VAr			
Active power 1-ph	29,043 W			
Tepping	Voltages	Currents	Inductance	Deviations of inductance
1.1 - 1.6	33,056 V	15,211 A	6,94721 mH	5,26 %
Reactive power 1-ph	505,251 VAr			
Active power 1-ph	27,682 W			

Orzeczenie:
Wyniki prób i pomiarów fabrycznych pozytywne. Urządzenie nadaje się do eksploatacji.

Uwagi
Urządzenia pomiarowe: INW/11350/ELH, INW/11450/ELH, INW/10750/ELH, INW/11110/ELH, INW/11550/ELH.

ELHAND TRANSFORMATORY Sp. z o.o.
Specjalista Kontroli Jakości

Dudek M.
kontroler

inż. Wojciech Machnik
sprawdził

Figure IV.5 Technical data of the reactors with six terminals: control protocol [288]

Lubliniec, 18.10.2017r.

Sz. P. Stephane Azebaze

Akademia Górniczo-Hutnicza

Wydział Elektrotechniki, Automatyki, Informatyki i Inżynierii Biomedycznej
Katedra Energoelektroniki i Automatyki Systemów Przetwarzania Energii

Al. Mickiewicza 30
30-059 Kraków
e-mail: stephane@agh.edu.pl

elhand
TRANSFORMATORY
ELHAND TRANSFORMATORY Sp. z o.o.
PL 42-700 Lubliniec ul. Klonowa 60
tel. +48 34 34 73 100
fax +48 34 34 70 207
info@elhand.pl
www.elhand.pl
NIP: PL 5751862934

Oferta nr OFPL-2017-1957 na dławiki typu ED1-7,3; IP00

Szanowny Panie,
w nawiązaniu do przesłanego zapytania w dniu 18.10.2017r. niniejszym przedstawiam naszą ofertę na interesujące Państwa dławiki naszej produkcji w wykonaniu lądowym, wykonane zgodnie z wymaganiami normy PN-EN 60076-6 oraz przekazanymi danymi technicznymi:

typ	ED1-7,3; IP00
nr obliczeń / nr kalkulacji	OBL33476* / KTD/2017/0708
indukcyjność L	7,3 mH
prąd I	15 A
częstotliwość	50 Hz
napięcie pracy Un	400 V
napięcie próby Upr	3 kV_{AC} (1 min)
praca	S1 (ciągła)
wykonanie	C1/E0
klasa izolacji	T40F
chłodzenie	AN (naturalne, powietrzne)
położenie	stojące
materiał uzwojeń	miedź
impregnacja	lakier elektroizolacyjny
stopień ochrony	IP00, klasa I
wymiary LxBxH [mm]	~ 160 x 135 x 240
masa [kg]	~ 11
ilość [szt.]	3
cena netto	**596,00 PLN/szt.**

OFERTA WAŻNA DO: 31.01.2018r.

WARTOŚĆ OFERTY NETTO: 1 788,00 PLN

WARUNKI HANDLOWE:

1. **Termin realizacji zlecenia:** 4 - 5 tygodni od otrzymania pisemnego zamówienia,
2. **Warunki dostawy:** FCA (wg Incoterms) - spedycją na koszt Odbiorcy,
3. **Sposób zapłaty** przelewem na nasze konto z terminem wpływu 14 dni od daty sprzedaży,
4. **Okres gwarancji:** 24 miesiące od daty sprzedaży.

Oczekując zainteresowania ofertą, łączę serdeczne pozdrowienia.
Z poważaniem
Adam Jonczyk Jonczyk A.
ELHAND TRANSFORMATORY Sp. z o.o.
tel. +48 34 3473 111
fax +48 34 3470 207
e-mail: a.jonczyk@elhand.pl

ELHAND TRANSFORMATORY Sp. z o.o.
Kierownik Działu Handlowego
mgr ... Nowotarska

W przypadku zamówienia proszę powołać się na numer oferty.

KRS: 0000342480
Sąd Rejonowy w Częstochowie,
XVII Wydz. Gospod. KRS
Kapitał zakładowy: 7.211.850 PLN
NIP: PL 5751862934;

Konto bankowe:
ING Bank Śląski S.A.O/Lubliniec
PL 29 1050 1142 1000 0023 5194 3747 (PLN)
PL 12 1050 1142 1000 0023 5194 3762 (EUR)
PL 20 1050 1142 1000 0023 5336 5832 (USD)

Konto bankowe:
mBank S.A. o/Opole
PL 80 1140 1788 0000 4359 4600 1001 (PLN)
PL 53 1140 1788 0000 4359 4600 1002 (EUR)
SWIFT/BIC: BREXPLPWOPO

Figure IV.6 Technical data of reactors used to design the 7th harmonic single-tuned filter [288]

THREE-PHASE GAS INSULATED POWER CAPACITORS MKG TYPE

General rated data

	Type	Voltage V	Power kVar	Rated current A	Capacitance 3xμF	Cubicle
U_{CN}=525V	MKG 525-2,5	525	2,5	2,7	9,6	A
	MKG 525-5	525	5	5,5	19,2	A
	MKG 525-7,5	525	7,5	8,2	28,9	B
	MKG 525-10	525	10	11,0	38,5	B
	MKG 525-12,5	525	12,5	13,7	48,1	C
	MKG 525-15	525	15	16,5	57,7	D
	MKG 525-20	525	20	22,0	77,0	E
	MKG 525-25	525	25	27,5	96,2	F
	MNG 525-30	525	30	33,0	115,5	G

General rated data:

Rated voltage:	400, 440, 450, 480, 525, 690 V
Rated power:	2,5….40 kVar
Frequency:	50Hz
Capacitance tolerance:	-5…+10%
Active power losses:	≤0,2W/kVar
Permissible continuous current:	$1{,}3I_N$
Permissible short-time current (0,5 period):	$200I_N$
Discharge:	50V/1min.
Altitude:	≤2000m a.s.l.
Mounting position:	vertical
Ambient temperature:	-25…+50°C
Humidity:	95%
Internal protection:	overpressure
Standards:	IEC60831

Figure IV.7 Technical data of capacitor used in the design of single-tune filter for the 5th harmonic mitigation in the grid current [289]

Low Voltage Power Capacitors
Three-phase capacitors: 525V, 50Hz, IP 20, MKP

TYP *Type*	Výkon *Power* Q_N [kvar]	Kapacita *Capacitance* C_N [μF]	Proud *Current* I_N [A]	Hmotnost *Weight* *[kg]*	Rozměry *Dimension* *øDxH [mm]*
CSADG 1-0,525/2,5N	2,5	3 x 9,6	3 x 2,7	0,6	85 x 175
CSADG 1-0,525/5N	5	3 x 19,3	3 x 5,5	0,7	
CSADG 1-0,525/8N	8	3 x 30,8	3 x 8,8	0,9	
CSADG 1-0,525/10N	10	3 x 38,5	3 x 11,0	1,0	
CSADG 1-0,525/12,5N	12,5	3 x 48,1	3 x 13,7	1,1	85 x 245
CSADG 1-0,525/15N	15	3 x 57,8	3 x 16,5	1,2	
CSADG 1-0,525/20N	20	3 x 77,0	3 x 22,0	1,7	110 x 245
CSADG 1-0,525/25N	25	3 x 96,3	3 x 27,5	1,9	
CSADG 1-0,525/30N	30	3 x 116	3 x 33,0	2,1	

Rated voltage:	U_N	230 - 800 V
Frequency:	f_N	50/60 Hz
Standards:		IEC 60831-1+2, EN 60831-1+2, UL No. 810, GOST 1282-88, VDE 0560 46+47
Max overvoltage:	U_{max}	U_N + 10 % (up to 8 hours daily) U_N + 15 % (up to 30 minutes daily) U_N + 20 % (up to 5 minutes) U_N + 30 % (up to 1 minute)
Overcurrent (according to above standards):	I_S	1,5 - 2,0 * I_N
Capacitance tolerance:		-5 / +10 %
Test voltage, terminal/terminal:	U_{TT}	2,15 * U_N, AC, 2 s
Test voltage, terminal / case:	U_{TC}	U_N < 500 V: 3000 V AC, 10 s U_N > 500 V: 2 x U_N + 2000 V AC, 10 s
Inrush current:		Max 400 x I_N
Dielectric losses:	tan δ	cca 0,2 W/kvar
Statistical life expectancy:		150 000 - 200 000 hours (depended on voltage, temper.)
Degree of protection:		IP 20, on request IP 54
Ambient temperature category:		-50 °C / D - maximum is 65 °C - highest mean over any period of 24 h is 45 °C - highest mean over any period of 1 year is 35 °C
Cooling:		natural or forced
Permissible relative humidity:		95 %
Max above sea level:		4 000 m above sea level
Mounting position:		any
Mounting:		Stud M12 at the bottom
Case:		Aluminium
Dielectric:		MKP - metallized PP film
Impregnant:		Dry type, inert gas N_2
Discharge resistors:		Included - 50 V, 1 minute or 75 V, 3 minutes

Figure IV.8 Technical data of capacitor used in the design of single-tune filter for the 7th harmonic mitigation in the grid current [290]

IV.4 Connection of the capacitors bank to the PCC

In Figure IV.9, the capacitor bank is supplied by the PCC voltage (0.4 kV) which contains a little quantity of harmonics (see Figure 4.7, chapter 4). The capacitor bank parameters are presented in Table IV.6 and Table IV.7. The grid voltage THD has decreased after the capacitor connection (Form 2.66% before to 2.38% after the capacitor connection - Table IV.7).

Figure IV.10(c) shows that the capacitor bank current waveform (supposed to be pure sinusoidal) is distorted, therefore contains harmonics coming from the grid voltage (Figure IV.10(d)).

The grid current 5th and 7th harmonics represent respectively 9.59 % and 6.15 % of the supplied current.

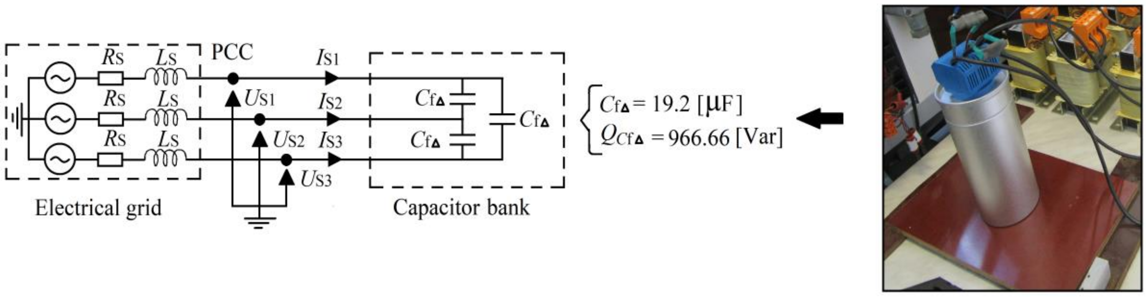

Figure IV.9 Laboratory equivalent circuit with the capacitors bank connected to the PCC

Table IV.6 Capacitor parameters

$U_{N\_Cf\Delta}$ [V]	400	525
$I_{N\_Cf\Delta}$ [A]	4.185	5.5
$Q_{N\_Cf\Delta}$ [Var]	966.6	1666.66

Table IV.7 PCC voltage and current parameters

Phase to ground voltage						
n	U_{S1} [V] (No load connected)		(load connected)			
			U_{S1} [V]		I_{S1} [A]	
	r.m.s	phase	r.m.s	phase	r.m.s	phase
1st	224.71	83.08	225.9	-77.04	4.15	14.06
3th	2.61	-5.23	2.15	244.86	0.028	-3.32
5th	4.76	241.60	4.35	162.19	0.399	251.42
7th	2.13	251.66	1.85	212.67	0.255	-54.92
9th	0.49	179.57	0.40	175.55	0.015	66.12
11th	0.60	123.73	1.23	154.73	0.244	247.62
13th	0.13	-0.64	0.25	63.57	0.068	137.72
17th	0.39	-38.54	0.25	99.03	0.088	186.85
19th	0.26	-35.71	0.17	154.74	0.072	-85.31
23th	0.26	116.78	0.166	36.01	0.067	120.05
THD [%]	2.66		2.38		13.97	
True r.m.s	224.80		226		4.2	
Q_S [Var]	-		-937.31			

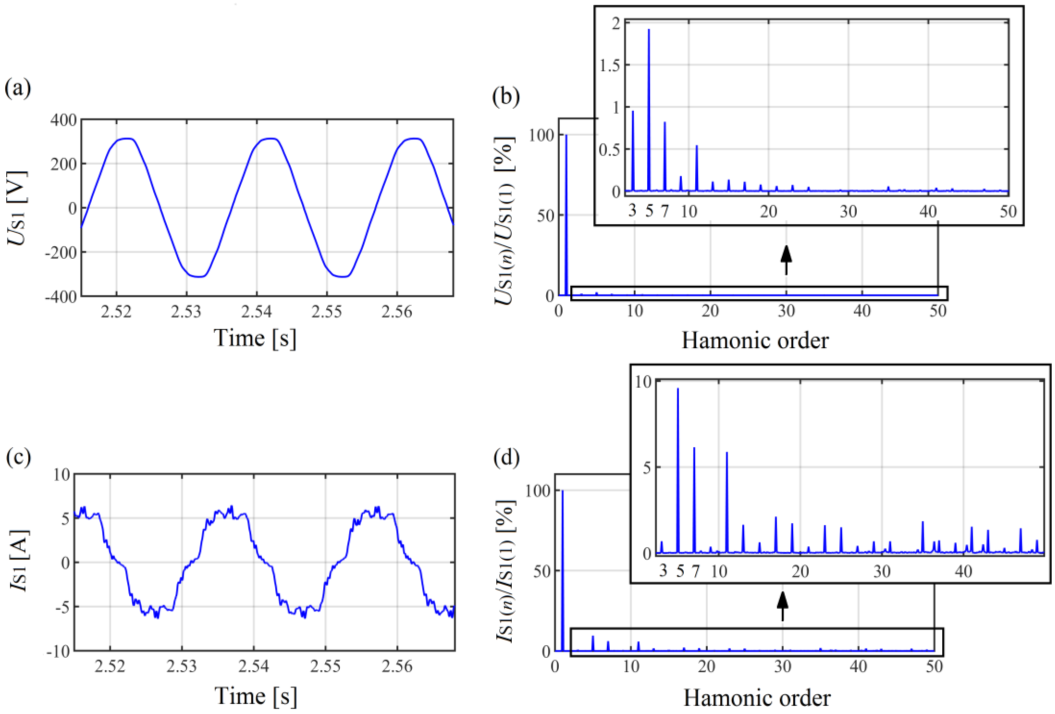

Figure IV.10 One-phase PCC voltage (a) and current (b) with the spectrum respectively in (b) and (d)

Annex V. Presentation of the simulated power system with SAPF

V.1 Description of shunt active power filter (SAPF) simulated blocks

The electrical power system designed in MATLAB environment to analyze the SAPF in chapter 5 is presented in Figure V.1. It is constituted of three parts (see also chapter 5, Figure 5.18): the electrical network, the load (rectifier with resistance at its DC side and reactor at its AC side) and the SAPF with its control system. The electrical grid and load are described in Chapter 4. This chapter is focused on the SAPF control system simulated blocks which are: *control loops (1)* to *(3)* and block using PWM control method (Figure V.1).

The DC side capacitor of the inverter is pre-charged by the “Battery charging” system in Figure V.2. After the capacitor reaches the fixed voltage (e.g. 700 V – see the capacitor voltage characteristic of Figure V.2), the resistor “r” is eliminated from the circuit by closing the contact “A”. The *control loop (1)* is used to stabilized and maintain constant (around 750 V) the inverter DC voltage (Figure V.2).

The *control loop (2)* presented in Figure V.3 has six blocks: the electrical grid voltage filtration block (Figure V.4) (for the reconstitution of pure sinusoidal voltage waveforms, synchronized with the grid voltage by the phase-locked loop (PLL) block); the *a-b-c* to α-β coordinates conversion block (Figure V.5) to convert the PCC voltage U_S and load current I_T from *a-b-c* coordinates to α-β coordinates; the powers division block (Figure V.6) from which the constant ($\bar{p}$, $\bar{q}$), asymmetry ($\tilde{p}_{2n}$, $\tilde{q}_{2n}$) and harmonic ($\tilde{p}_h$, $\tilde{q}_h$) components of power in α-β coordinates are obtained; the current computation blocks in α-β coordinates (Figure V.7(a)(b)) and the invers conversion block (Figure V.8) from α-β to *a-b-c* coordinates.

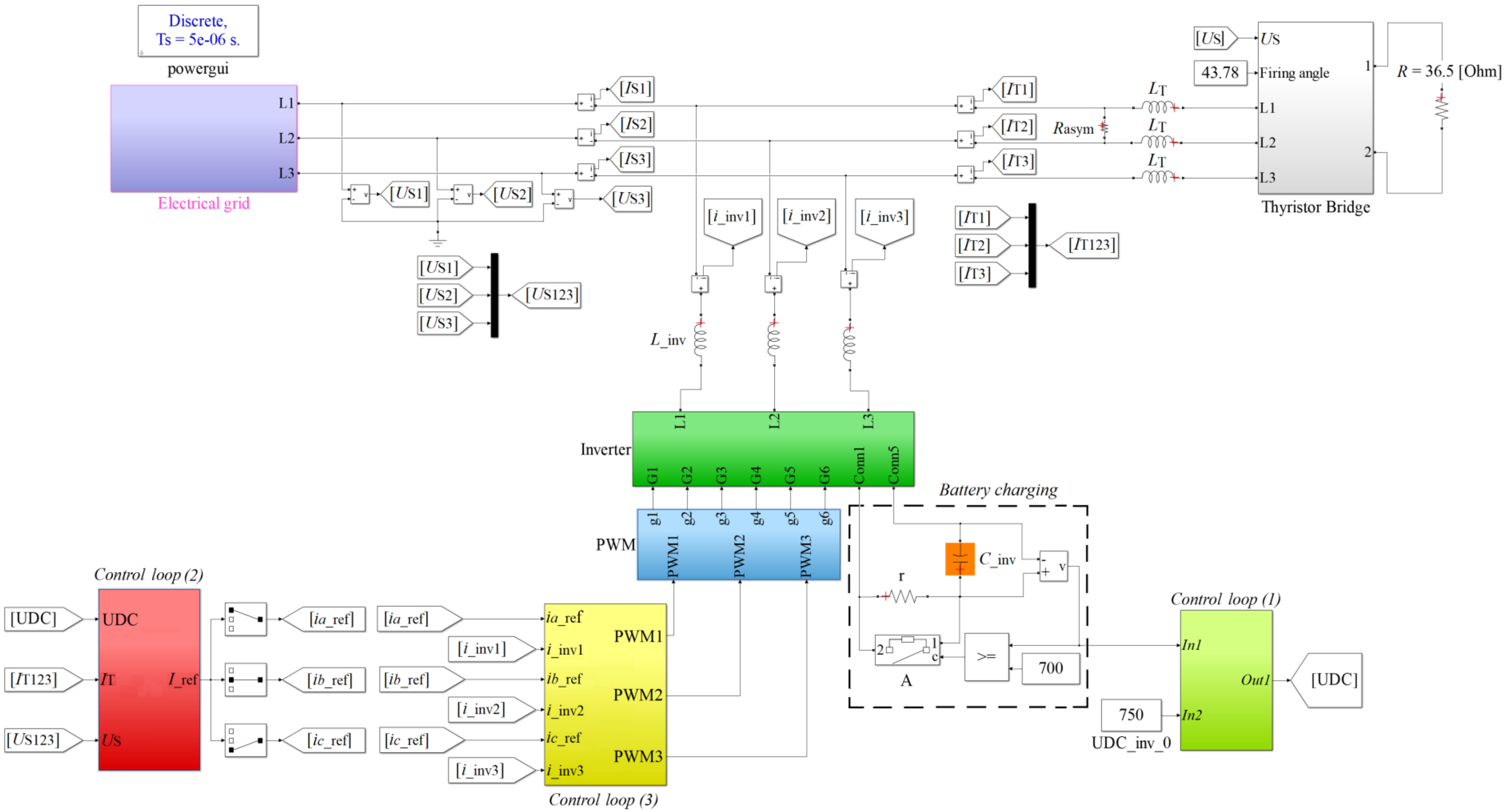

Figure V.1 Simulated power system in MATLAB environment (see also the equivalent circuit of chapter 5, Figure 5.18)

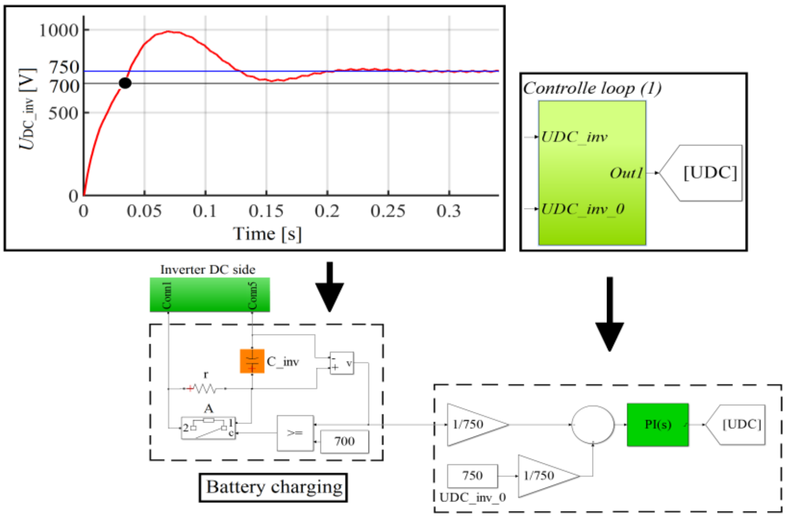

Figure V.2 DC inverter battery charging system and *Control loop (1)*

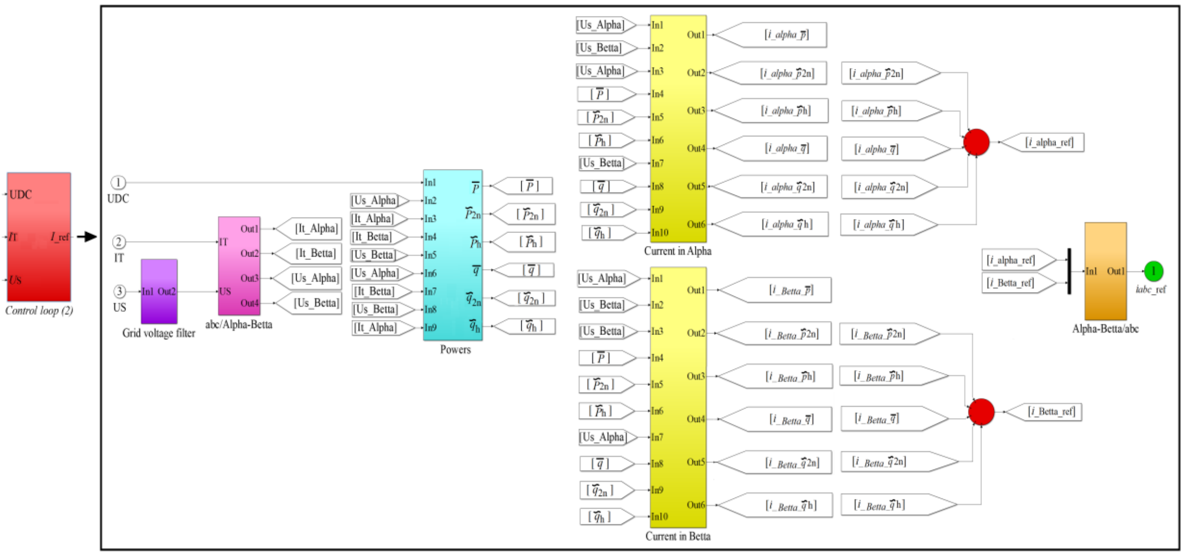

Figure V.3 *Control loop (2)*

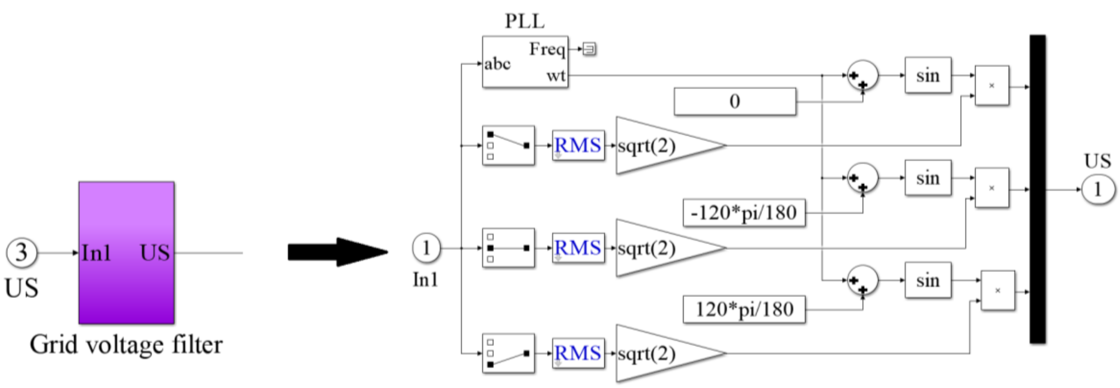

Figure V.4 Grid voltage filtration from *Control loop (2)*

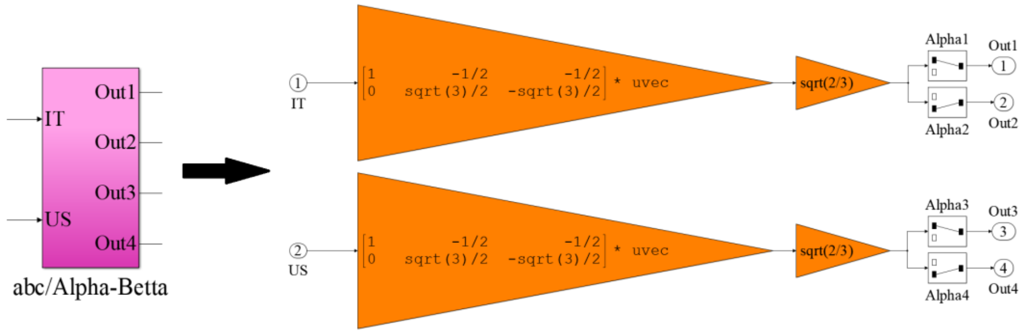

Figure V.5 Conversion from *a-b-c* to α-β coordinates (from *Control loop (2)*)

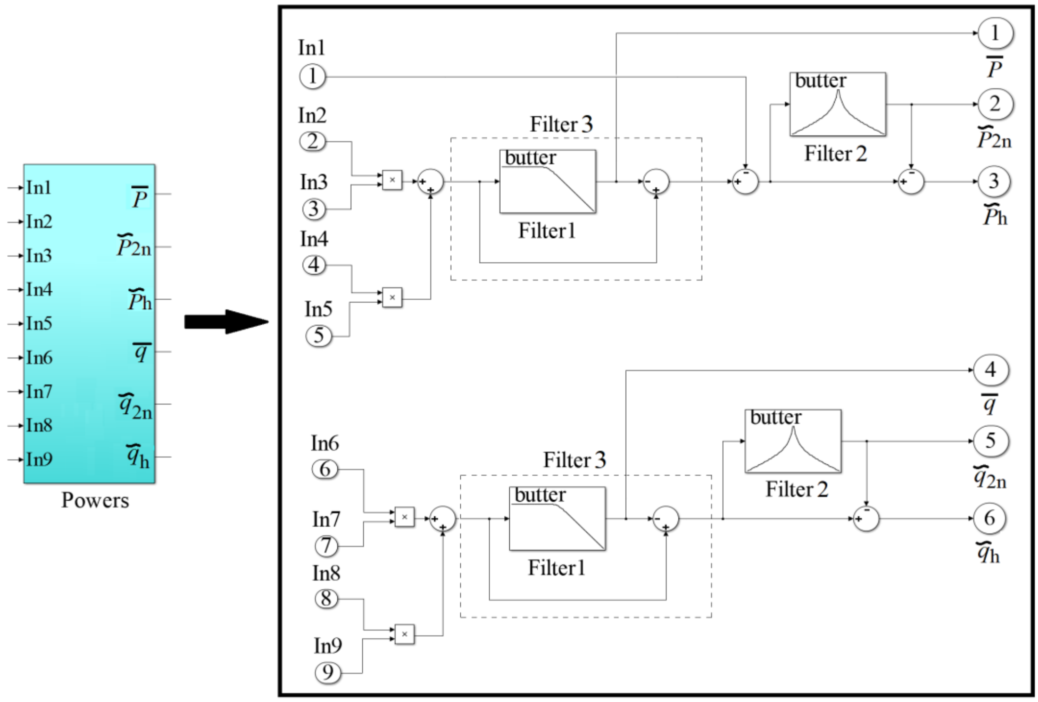

Figure V.6 Powers filtration in α-β coordinates (from *Control loop (2)*)

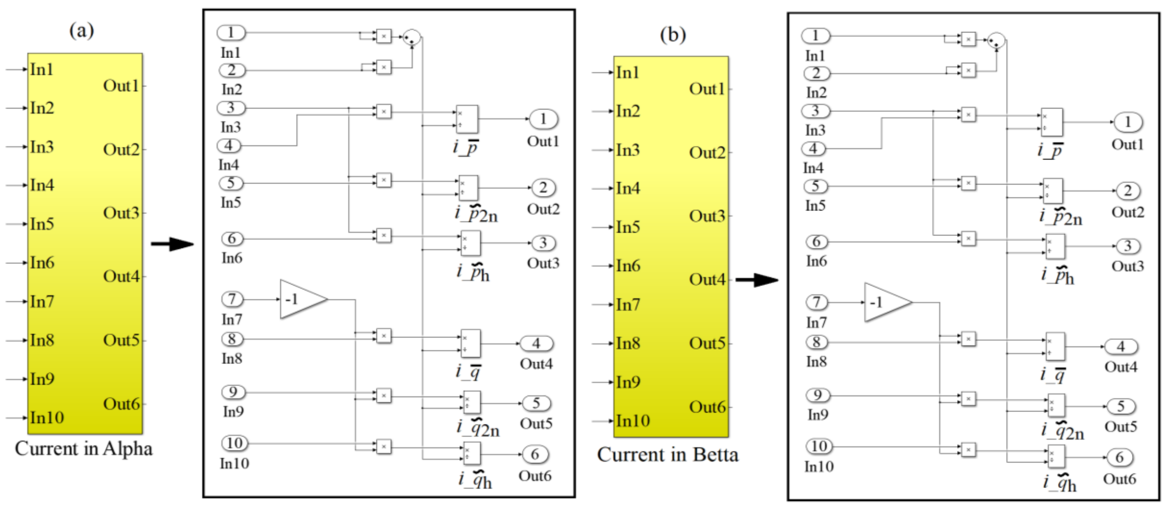

Figure V.7 (a) current computation in α axis (from *Control loop (2)*), (b) current computation in β axis (from *Control loop (2)*)

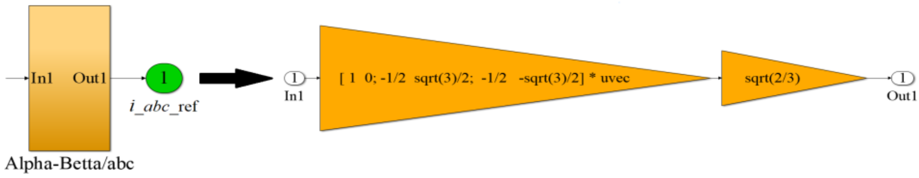

Figure V.8 α-β to *a-b-c* coordinates conversion from *Control loop (2)*

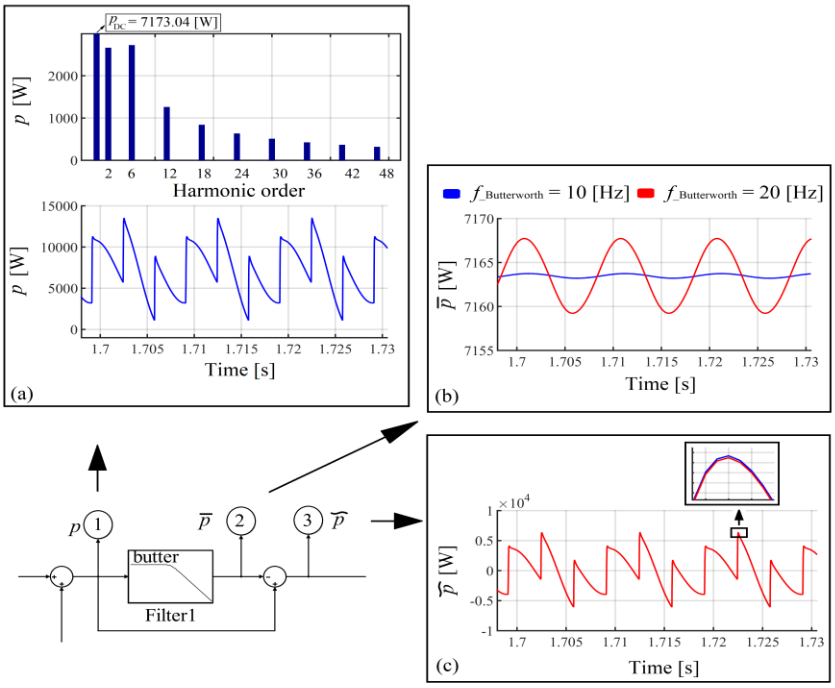

Figure V.9 Instantaneous real power in α-β coordinates: (a) before the filtration; (b) constant part for different cutoff frequencies; (c) variable part

The power filtration block in Figure V.6 is constituted of three types of Butterworth filters: the low pass filter (Filter1), the pass band filter (filter2) and high past filter (Filter3).

The fourth-order low past filter (Filter1) with the cut off frequency ($f_{\_Butterwoth}$) equal to 10 Hz is used to obtain the constant part (e.g. $\bar{p}$) of the power (e.g. *p*) as presented in Figure V.9(a). The higher is the cut-off frequency, the higher are the fluctuating components in the power constant part (see Figure V.9(b)).

The real power variable part (e.g. $\tilde{p}$ in Figure V.9(a)) is obtained by using the high past filter (Filter3 – see Figure V.6).

The asymmetry component ($\tilde{p}_{2n}$) of real powers is obtained through the second-order band pass filter and the harmonic components is obtained basing on the following equation: $\tilde{p}_h = \tilde{p} - \tilde{p}_{2n}$ (see Figure V.10) [89, 197].

The waveforms and spectrums of the instantaneous real power variable part are shown in Figure V.10(a) and Figure V.11(a) (from Figure V.9(c) for f_Buterworth =10 Hz). In the both spectrums, the 2nd order harmonic represents the asymmetry component. The band pass filter has two frequencies (upper (e.g. 105 Hz) and lower (e.g. 95 Hz) pass band frequency) that should be well chosen (near 100 Hz) in order to separate the 100 Hz component from the harmonics component.

In Figure V.10(b)(c), after increasing the upper pass band frequency from 105 Hz to 200 Hz (lower passband frequency (95 Hz) is constant), the harmonics other than the 2nd order (e.g. 6th etc.) appeared. In Figure V.11(b)(c) the upper pass band frequency is maintained constant (105 Hz) and the lower pass band is decreased from 95 Hz to 50 Hz. The observations done on the instantaneous real power (*p*) are the same for the instantaneous imaginary power (*q*).

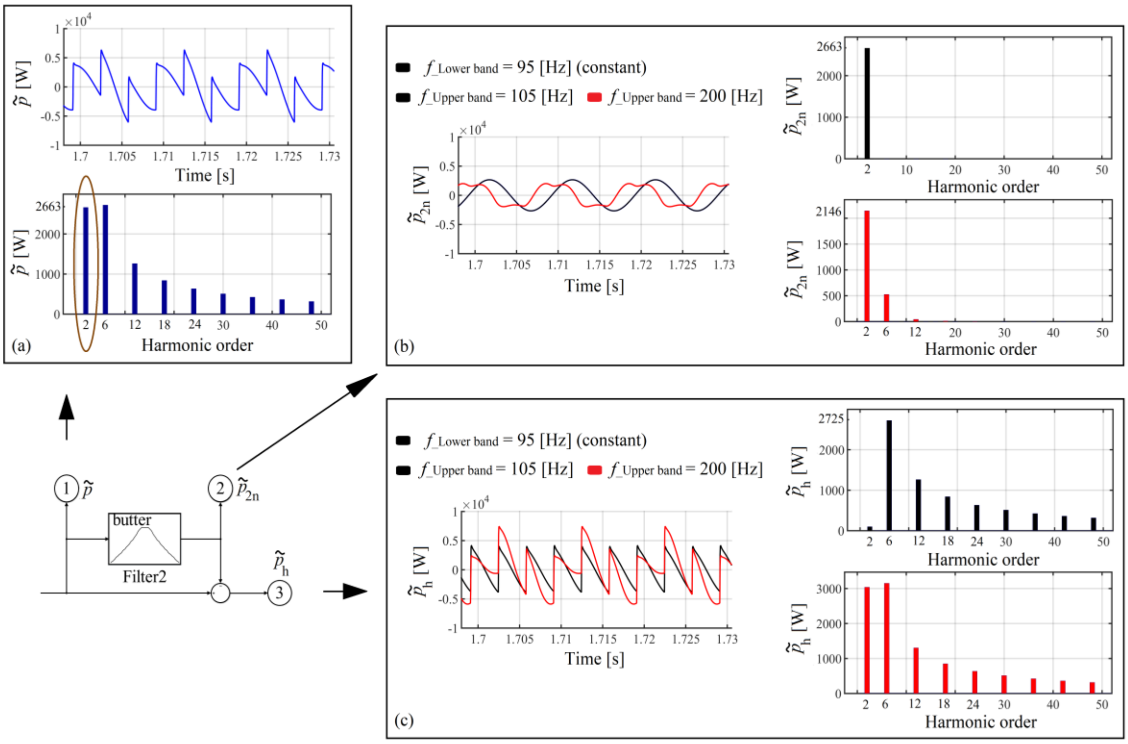

Figure V.10 Variable part (with spectrums) of instantaneous real power in α-β coordinates (from Figure V.9(c) for $f_{\_Buterworth}$ =10 Hz): (a) before the filtration; (b) asymmetry and (c) harmonic component after increasing the upper passband frequency from 105Hz to 200Hz by maintaining the lower passband constant

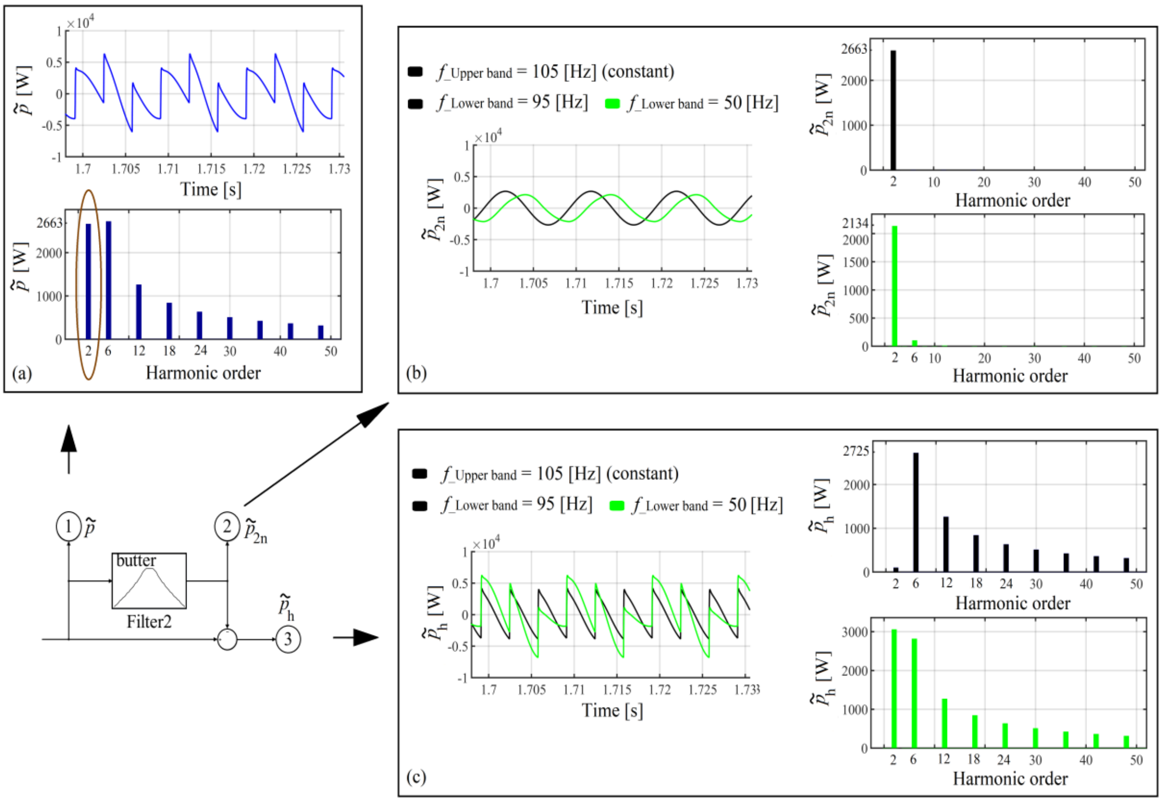

Figure V.11 Variable part (with spectrums) of instantaneous real power in α-β coordinates (from Figure V.9(c) for $f_{\_Buterworth}$ =10 Hz): (a) before the filtration; (b) asymmetry and (c) harmonic component after decreasing the lower passband frequency from 95Hz to 50Hz by maintaining the upper passband constant

In Figure V.10(b) and Figure V.11(b) it can be noticed a significant influence of the filtration bandwidth on the 2nd harmonic elimination.

The block of *control loop (3)* is constituted by Figure V.12. It contains three PI controller blocks and despite the current unbalance in the power system, their parameters (k_p = 250, k_i = 1e-4) are the same (The PI controller parameters optimization was not the subject under consideration of the work theses).

The MATLAB blocs used to obtain transistors pulses is shown in Figure V.13(a) and an example of transistors pulses generation is presented in Figure V.13(b). The output PI controller signal is compared to the carrier signal and from that comparison, the pulses are generated. The upper and lower PI controller output signal limits are set to ±0.95 and the upper and lower carrier signal boundary are fixed to ±1 [1].

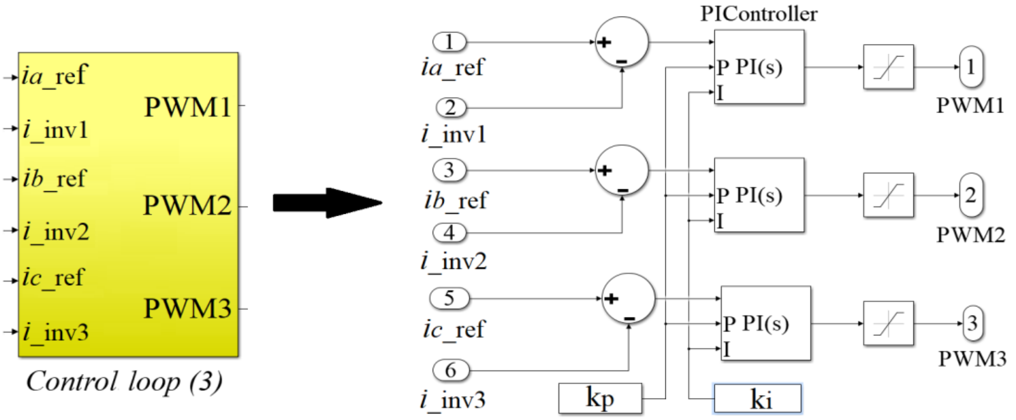

Figure V.12 *Control loop (3)*

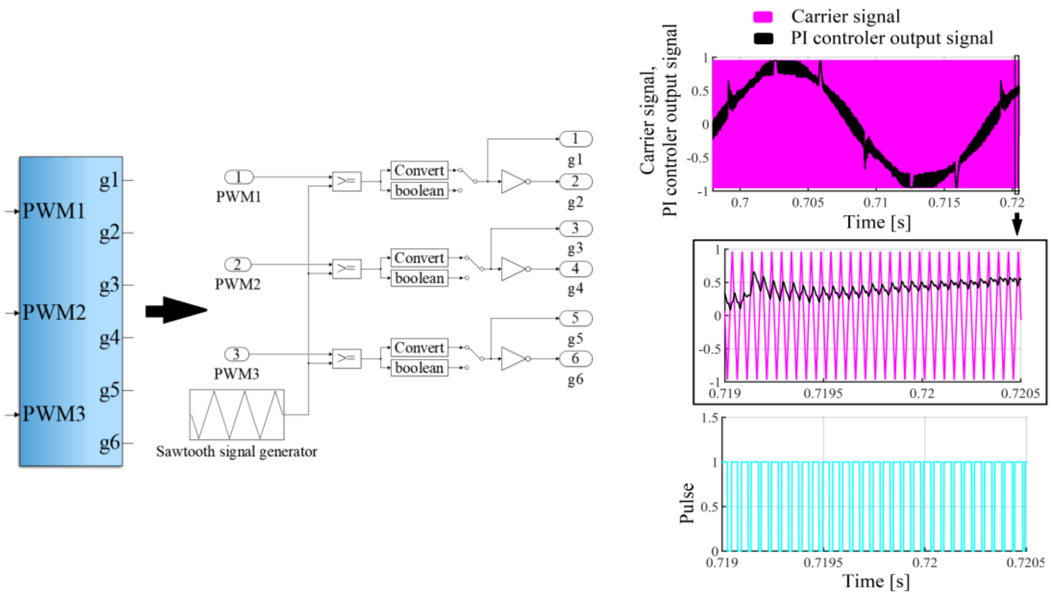

(a) (b)

Figure V.13 (a) PWM blocks from MATLAB-SIMULINK, (b) carrier signal together with output PI controller signal and IGBT transistor gate pulses

V.2 Proposed expressions to compute the three-wire three legs SAPF input reactor and DC side capacitor parameters

The computation of the SAPF input reactor and DC capacitor parameters are very controversial in the literature (there are many expressions). In this chapter, a literature revue is presented and the new expressions are proposed by the author.

V.2.1 SAPF DC capacitor parameters computation

For an efficient functionality of the SAPF, the DC link capacitor plays an important role [92, 125, 168]. Its parameters (voltage and capacitance) define the SAPF (power) compensation capability. The capacitor capacitance must be chosen in such a way to maintain the DC voltage ripples as small as possible because of their negative influences (e.g. THD increase etc.) on the grid current.

There are two constrains while computing the DC inverter capacitor capacitance: one is based on the capacitor voltage ripple amplitude, which should be as small as possible (large capacitor capacitance) and the second is based on the fast capacitor voltage stabilization (short transient state – small capacitor capacitance).

In [125], the inverter DC capacitor is designed to generate less DC voltage ripples. The expression (V.1) (Table V.1) proposed in that literature depends upon the peak voltage ripple ($U_{\mathrm{DC\_inv\_peak\text{-}peak(max)}}$) and the rate of inverter input current ($I_{\mathrm{AC\_inv\_rated}}$).

In the power system with the SAPF connected between the PCC and the load, the transient state due to the load change, causes fluctuation on the inverter DC side voltage. The voltage fluctuation amplitude (during that transient state) can be control by designing the appropriate inverter DC capacitor [78, 168] (see the expression (V.2) in Table V.1 - $U_{\mathrm{DC\_inv\_max}}$ is the maximum voltage achieves by the capacitor during the transient state, $U_{\mathrm{DC\_inv}}$ is the mean value of capacitor voltage at the steady state, $i_{\mathrm{DC\_inv}}$ (t) is the instantaneous DC inverter current at the transient state and ($\theta1$, $\theta2$) the chosen period.

The inverter DC capacitor capacitance is expressed in [170] by assuming that the DC inverter voltage ripple factor (K_v) is inferior or equal to 5% of the capacitor mean voltage $U_{\mathrm{DC\_inv}}$ and the inverter input current is sinusoidal and balance. The expression (V.3) (Table V.1) is more clarified in [170] ($I_{\mathrm{DC\_inv(h)}}$ is the RMS value of the given current harmonic crossing and h is the DC current harmonic.

The determination of SAPF DC capacitor capacitance presented in [173] is based on the inverter nominal power ($S_{\mathrm{\_inv}}$). The expression (V.4) presented in Table V.1 is well defined in [108, 173] ($\Delta U_{\mathrm{DC\_inv}}$ is the inverter DC voltage ripples and $U_{\mathrm{DC\_inv}}$ is the mean value of the inverter capacitor voltage).

In [56, 87] the inverter DC capacitor maximum energy ($E_{\max}$) constituted the main criteria of inverter capacitor capacitance calculation (V.5) (Table V.1) ($U_{\mathrm{DC\_inv\_ref}}$ is the reference value of inverter DC capacitor voltage and $U_{\mathrm{DC\_inv\_min}}$ is the inverter DC capacitor minimum voltage).

The inverter DC capacitor should be design in such a way to maintain the DC voltage ripple between certain limit (1 to 2% of the nominal voltage according to [244]). The expressions (V.6) and (V.7) (Table V.1) are described in [244] and the expressions (IV.8), (V.9) and (V.10) are computed from (IV.6) basing on the type of system and load disturbances to be compensated ($U_{\mathrm{S},j}$ is the grid voltage, $i_{j,\mathrm{h}}$ is the load generated current harmonics (without fundamental harmonic) and r_υ is the inverter DC voltage ripple).

The inverter DC voltage level determines the capability of SAPF to work efficiently in term of grid disturbances compensation. According to [239] its value should be more than two-time the source peak voltage value.

The expression (V.11) (Table V.1) relating the inverter DC voltage ($U_{\mathrm{DC\_inv}}$) to the inverter input voltage ($U_{\mathrm{AC\_inv(1)}}$ – fundamental harmonic) is proposed in [155] (for three legs four wires inverter).

In [3] the estimation of the DC inverter reference voltage ($U_{\mathrm{DC\_inv\_ref}}$) is based principle that the voltage at the inverter DC side should be higher or equal to the line to line PCC voltage (V.12) (Table V.1). Another expression to estimate the inverter DC voltage value is presented in (V.13).

Table V.1 Expression examples of inverter DC capacitor capacity and voltage (from literature)

$C_{\_\text{inv}} = \frac{\pi I_{\text{AC\_inv\_rated}}}{\sqrt{3}\,\omega\, U_{\text{DC\_inv\_peak-peak(max)}}}$ (V.1)	$C_{\_\text{inv}} = \frac{1}{(U_{\text{DC\_inv\_max}} - U_{\text{DC\_inv}})} \int_{\theta1/\omega}^{\theta2/\omega} i_{\text{DC\_inv}}(\text{t})\text{dt}$ (V.2)
$C_{\_\text{inv}} = \frac{\sqrt{\left\{\sum_{\text{h}=6}^{\infty}\left(\frac{I_{\text{DC\_inv (h)}}}{\text{h}}\right)^2\right\}}}{\omega_{(1)}\,\text{K}_{\text{v}}\, U_{\text{DC\_inv}}}$ (V.3)	$C_{\_\text{inv}} = \frac{S_{\_\text{inv}}}{2\Delta U_{\text{DC\_inv}}\omega_{(1)} U_{\text{DC\_inv}}}$ (V.4)
$C_{\_\text{inv}} = \frac{2\text{E}_{\max}}{\left(U^2_{\text{DC\_inv\_ref}} - U^2_{\text{DC\_inv\_min}}\right)}$ (V.5)	$C_{\_\text{inv}} = \frac{\Delta\left[\int \sum_{j=\text{a,b,c}}\{U_{\text{S},j} i_{j,\text{h}}\}\text{dt}\right]}{\left(\text{r}_{\upsilon} U^2_{\text{DC\_inv}}\right)}$ (V.6) $\text{r}_{\upsilon} = \frac{U_{\text{DC\_inv\_max}} - U_{\text{DC\_inv\_min}}}{U_{\text{DC\_inv}}} = \frac{\Delta U_{\text{DC\_inv}}}{U_{\text{DC\_inv}}}$ (V.7)
$C_{\_\text{inv}} = \frac{1.24}{\Delta U_{\text{DC\_inv}} U_{\text{DC\_inv}}}$ (V.8) $C_{\_\text{inv}} = \frac{0.32}{\Delta U_{\text{DC\_inv}} U_{\text{DC\_inv}}}$ (V.9) $C_{\_\text{inv}} = \frac{0.776}{\Delta U_{\text{DC\_inv}} U_{\text{DC\_inv}}}$ (V.10)	$U_{\text{DC\_inv}} = \sqrt{2}\, U_{\text{AC\_inv(1)}}$ (V.11) $U_{\text{DC\_inv\_ref}} = \frac{2\sqrt{2}\, U_{\text{S(1)}}}{1.155}$ (V.12) $U_{\text{AC\_inv\_max}} < m_{\text{a\_max}} \frac{U_{\text{DC\_inv\_ref}}}{\sqrt{3}}$ (V.13)

V.2.1.1 Proposed expressions to compute the inverter DC capacitor parameters

The relation between the inverter reference DC voltage ($U_{\text{DC\_inv\_0}}$) and the PCC phase to phase AC voltage ($U_{\text{S\_p-p}}$) is proposed by the author in (V.14). The DC capacitor reference voltage is proposed to be higher than the maximum phase to phase PCC voltage (IV.14).

$$\boxed{U_{\text{DC\_inv\_0}} > \text{k}_{\text{DC}}(\sqrt{2}\, U_{\text{S\_p-p}})} \quad \text{k}_{\text{DC}} \geq 1 \text{ is a coefficient} \tag{V.14}$$

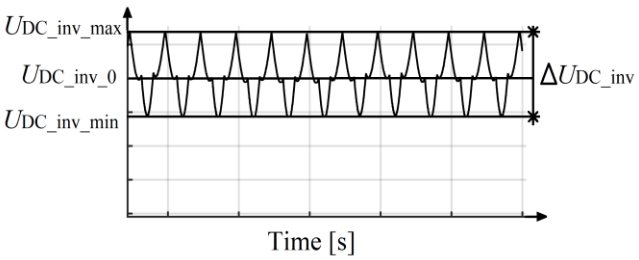

Figure V.14 Waveforms of inverter DC voltage

The capacitor DC inverter voltage ripple varies between the extremums ($U_{\text{DC\_inv\_max}}$ and $U_{\text{DC\_inv\_min}}$) as presented in Figure V.14. The capacitor DC voltage variation ($\Delta U_{\text{DC\_inv}}$) also corresponds to energy variation ($\Delta W_{\text{DC\_inv}}$) as presented in (IV.19).

The reference energy of inverter DC capacitor is expressed by (V.15) and the maximum and minimum energy are expressed respectively by (IV.16) and (V.17). The DC capacitor energy variation between the max and the min is presented by (V.19) and (V.20). By using the expression (V.21) in (V.20), the inverter DC capacitor capacity is obtained in (V.24).

The inverter DC capacitor maximum capacitance is obtained by assuming the energy variation ($\Delta W_{\text{DC\_inv}}$) tending to infinity and its minimum capacitance is obtained by assuming the voltage variation ($\Delta U_{\text{DC\_inv}}$) tending to infinity (see expressions (V.23) and (V.24)).

$$W_{\text{DC\_inv\_0}} = \frac{1}{2} C_{\_\text{inv}} U^2_{\text{DC\_inv\_0}} \tag{V.15}$$

$$W_{\text{DC\_inv\_max}} = \frac{1}{2} C_{\_\text{inv}} U^2_{\text{DC\_inv\_max}} \tag{V.16}$$

$$W_{\text{DC\_inv\_min}} = \frac{1}{2} C_{\_\text{inv}} U^2_{\text{DC\_inv\_min}} \tag{V.17}$$

$$U_{\text{DC\_inv\_min}} = U_{\text{DC\_inv\_max}} - \Delta U_{\text{DC\_inv}} \tag{V.18}$$

$$W_{\text{DC\_inv\_max}} - W_{\text{DC\_inv\_min}} = \Delta W_{\text{DC\_inv}} = \frac{1}{2} C_{\_\text{inv}} (U^2_{\text{DC\_inv\_max}} - U^2_{\text{DC\_inv\_min}}) \tag{V.19}$$

$$\Delta W_{\text{DC\_inv}} = \frac{1}{2} C_{\_\text{inv}} (2U_{\text{DC\_inv\_max}} \Delta U_{\text{DC\_inv}} - \Delta U^2_{\text{DC\_inv}}) \tag{V.20}$$

$$U_{\text{DC\_inv\_max}} = U_{\text{DC\_inv\_0}} + \frac{\Delta U_{\text{DC\_inv}}}{2} \tag{V.21}$$

$$\boxed{C_{\text{\_inv}} = \frac{\Delta W_{\text{DC\_inv}}}{U_{\text{DC\_inv\_0}}\,\Delta U_{\text{DC\_inv}}}} \tag{V.22}$$

$$\text{For}\begin{cases}\Delta U_{\text{DC\_inv}} = \text{const}\\ \Delta U_{\text{DC\_inv}} = \text{const} \Rightarrow C_{\text{\_inv\_max}}\\ \Delta W_{\text{DC\_inv}} \to \infty\end{cases} \quad (\text{V.23}) \qquad \text{For}\begin{cases}\Delta W_{\text{DC\_inv}} = \text{const}\\ \Delta U_{\text{DC\_inv}} = \text{const} \Rightarrow C_{\text{\_inv\_min}}\\ \Delta U_{\text{DC\_inv}} \to \infty\end{cases} \quad (\text{V.24})$$

V.2.2 Computation of SAPF input reactor inductance

As well as the DC side inverter capacitor, the choice of the inverter input reactor ($L_{\text{\_inv}}$) also influences the SAPF performances. Like other interface passive filters for power inverters (see chapter 2), the mean goal of its application is to mitigate the inverter switching ripples contained in the PCC voltage and current [168]. In the literature there is not fixed rule on how to compute the inverter input reactor inductance and because of that many mathematic expressions are proposed (see some examples in Table V.2).

The reduction of switching ripple harmonic depends upon the inverter input reactor size, which also have an influence on the compensation performances of SAPF in term of harmonics, asymmetry and reactive power mitigation.

The expression (V.25) (Table V.2) of inverter input reactor inductance proposed in [168] is based on the constraint that for a given inverter switching frequency ($f_{\text{\_inv}}$), the inverter input reactor minimum slope ($(dI_{\text{\_inv}}/dt)_{\text{min}}$) should be smaller than the triangle saw waveforms slope [194]. In the expression (V.25), ξ is the maximum current ripple value.

The expression (V.26) of Table V.2 is proposed in [21, 108]**.** The inverter input reactor minimum inductance ($L_{\text{\_inv\_min}}$) is computed by basing on the maximum value of the compensating current ($I_{\text{\_inv\_max}}$) generated by the inverter to compensate the load inductive current (ΔU_{min} is the minimum reactor voltage drop to keep the ripple current at the small level. It is the different between the RMS value (fundament component) of inverter output voltage and the grid voltage).

In some literatures it can be noticed that, the design of inverter output reactor is based on the inverter capability to compensate the load current harmonics and reactive power fundamental harmonic [195]. However, that approach depends upon the load parameters which can be unavailable or vary with time.

In [195] two methods are proposed to compute the inverter input reactor inductance. The first method is focused on the current ripples suppression (difference between the compensating and the reference current) and the second method is focused on the ability of the inverter input current to track the reference current. From the two methods, the expression (V.27) in Table V.2 is proposed. The expression (V.27) should be for a symmetrical power system in which the SAPF compensates only the load current harmonics and reactive power fundamental harmonic. In that expression, ς is the level of voltage source inverter, ΔI_{ripple} is the maximum current ripple, δ is the coefficient that can be chosen between 0.1 and 0.3 according to [195], n is the order of the most dominating load harmonic, $I_{\text{C\_inv}}$ is the RMS value of current rating flowing at the AC side of inverter, $\Delta I_{ripple\text{\_max}}$ is the maximum ripple chosen and $U_{\text{DC\_inv\_max}}$ is the maximum capacitor voltage. The expression (V.28) is proposed in [87].

According to the expression (V.29) (see Table V.2) presented in [75, 153, 204, 45], the inverter output reactor inductance is computed basing on the maximum current ripples ($I_{\text{\_ripple\_max}}$) permitted to flow through that reactor. That expression is set up by the assumption that the reactor resistance is neglected and the inverter control system is in close loop [204]. A low inverter inductance value gives a better harmonics compensation characteristic [75]. The expression (IV.30) is presented in [239].

The goal of computing the inverter input reactor inductance in [56] is to maintain the switching ripple amplitude below certain limit. The expressions (IV.31) and (IV.32) (Table V.2) are formulated taking into account the current switching ripple maximum amplitude ($\Delta I_{\text{ripple\_max}}$) [56, 195]. In (V.31), k is a constant that can take the value of 0.70 [56].

In [244]**,** the topology of four wires SAPF with capacitors connected to the neutral is considered. The inverter output reactor (V.33) (see Table V.2) is designed by basing on the criteria that the amplitude of current ripples should not be higher than the 5% of the load current rate [244]. In (V.33), $U_{\text{\_inv}}$ is the RMS value of the inverter output voltage, $I_{T(1)}$ is the RMS value of the load fundamental harmonic current, $f_{(1)}$ fundamental harmonic frequency and ζ is the percentage boundary of the switching frequency amplitude (should not excide 5% of the load current load).

Table V.2 Expression examples of inverter input reactor inductance (from literature)

$L_{\text{\_inv}} = \frac{U_{S(1)} + (\frac{U_{\text{DC\_inv}}}{2})}{4\xi f_{\text{\_inv}}}$ (V.25)	$L_{\text{\_inv\_min}} = \frac{\Delta U_{\min}}{\omega_{(1)} I_{\text{\_inv\_max}}}$ (V.26)
$\frac{U_{\text{DC\_inv}}}{8 f_{\text{\_inv}} (\varsigma - 1) \Delta I_{\text{ripple}}} \leq L_{\text{\_inv}} \leq \frac{\delta U_{\text{DC\_inv}}}{n \omega_{(1)} I_{\text{C\_inv}}}$ for $\varsigma > 0$ and $0.1 \leq \delta \leq 0.3$ (V.27)	
$L_{\text{\_inv}} > \frac{U_{\text{DC\_inv\_max}}}{6 f_{\text{\_inv}} \Delta I_{\text{ripple\_max}}}$ (V.28)	$L_{\text{\_inv}} = \frac{U_{S(1)}}{2\sqrt{6} f_{\text{\_inv}} I_{\text{ripple\_max}}}$ (V.29)
$L_{\text{\_inv}} = \frac{U_{\text{DC\_inv}}}{4 f_{\text{\_inv}} I_{\text{ripple}}}$ (V.30)	$L_{\text{\_inv\_min}} = k \frac{1}{2\sqrt{3}} \frac{U_{\text{DC\_inv}}}{f_{\text{\_inv}} \Delta I_{\text{ripple\_max}}}$ (V.31)
$L_{\text{\_inv}} \geq \frac{3 U_{\text{DC\_inv}}}{16 f_{\text{\_inv}} \Delta I_{\text{ripple\_}max}}$ (IV.32)	$L_{\text{\_inv}} > \frac{U_{\text{\_inv}}}{I_{T(1)} (f_{\text{\_inv}} / f_{(1)}) \omega \zeta}$ (V.33)

V.2.2.1 Proposed expression for SAPF input reactor inductance

The switching ripples observed on the input inverter voltage and current waveforms can be reduced whether by increasing the switching frequency or applying at the inverter input an reactor with high inductance. In practice the main disadvantage of invert switching frequency increase is the transistors power losses growth.

The inverter input reactor with high value of inductance has the drawback that the SAPF compensation efficiency is reduced, mostly in term of harmonics filtration.

The switching ripple reduction and the compensation performances improve are the two principle criteria that should be taken into account while designing the inverter input reactor.

The author has proposed the expression presented in (V.36). In that expression the reactor inductance size is proportional to its voltage drop.

The input inverter reactor voltage ($\Delta U_{\text{L\_inv}}$) presented in (V.34) is the difference between the RMS (fundamental harmonic) value of the phase to ground output inverter voltage $U_{\text{AC\_inv\_p-g}}$) and the PCC voltage (U_S) ($I_{\text{\_inv}}$ is the inverter input current. By assuming that the RMS value of reference current (output *p-q* theory algorithm current ($I_{\text{\_(ref)}}$) is equal to the RMS value of the inverter input current (in each phase), the expression (V.35) is set up (the number 3 in (V.35) means three-phase). The expressions used to obtained the minimum and maximum inverter input reactor inductance are respectively presented in (V.37) and (V.38) ($I_{\text{a\_(ref)}}$, $I_{\text{b\_(ref)}}$ and $I_{\text{c\_(ref)}}$ are RMS values of reference current in each phase).

$$\Delta U_{\text{L\_inv}} = U_{\text{AC\_inv\_p-g}} - U_S = L_{\text{\_inv}} \omega_{(1)} I_{\text{\_inv}} \quad \text{(V.34)}$$

$$I_{\text{\_inv}} = I_{\text{\_(ref)}} = \frac{I_{a\text{\_(ref)}} + I_{b\text{\_(ref)}} + I_{c\text{\_(ref)}}}{3} \quad \text{(V.35)}$$

$$\boxed{L_{\_\mathrm{inv}} = \frac{3\Delta U_{\mathrm{L\_inv}}}{\omega_{(1)}(I_{a\_(\mathrm{ref})} + I_{b\_(\mathrm{ref})} + I_{c\_(\mathrm{ref})})}} \quad \text{(V.36)}$$

$$L_{\_\mathrm{inv\_min}} = \frac{3\Delta U_{\mathrm{L\_inv\_min}}}{\omega_{(1)}(I_{a\_(\mathrm{ref})} + I_{b\_(\mathrm{ref})} + I_{c\_(\mathrm{ref})})} \quad \text{(V.37)} \quad L_{\_\mathrm{inv\_max}} = \frac{3\Delta U_{\mathrm{L\_inv\_max}}}{\omega_{(1)}(I_{a\_(\mathrm{ref})} + I_{b\_(\mathrm{ref})} + I_{c\_(\mathrm{ref})})} \quad \text{(V.38)}$$

An example of SAPF parameters computation is presented in Table V.3.The expressions V.14, V.22 and V.36 are used to calculate respectively the inverter DC side voltage ($U_{\mathrm{DC\_inv0}}$) and capacitance ($C_{\_\mathrm{inv}}$) as well as input inductance ($L_{\_\mathrm{inv}}$). The minimum value of the inverter input reactor inductance ($L_{\_\mathrm{inv\_min}}$) is obtained after assuming a minimum voltage drop on the inverter input reactor (e.g. $\Delta U_{L\_\mathrm{inv\_min}}$ = 3 V) and the maximum value ($L_{\_\mathrm{inv\_max}}$) is obtained after assuming a maximum voltage drop on the inverter input reactor (e.g. $\Delta U_{L\_\mathrm{inv\_max}}$ = 16 V). The reference current values ($I_{a\_(\mathrm{ref})}$, $I_{b\_(\mathrm{ref})}$, $I_{c\_(\mathrm{ref})}$) are obtained at the end of the control system (output of *control loop (2)*) before the SAPF connection to the PCC.

Table V.3 Computed SAPF parameters

$1.32(\sqrt{2})400 = 746.70 \Longrightarrow U_{\mathrm{DC\_inv\_0}} = 750$ V
$C_{\_\mathrm{inv}} = \frac{11}{750*5}$=3 mF
$L_{\_\mathrm{inv\_min}} = \frac{3*3}{100\pi(4.46+9.38+7.34)}$=1.4 mH
$L_{\_\mathrm{inv\_max}} = \frac{3*16}{100\pi(4.46+9.38+7.34)}$=7.2 mH

OSWIADCZENIE AUTORA PRACY

Oświadczam, świadomy odpowiedzialności karnej za poświadczenie nieprawny, że niniejszą pracę doktorska wykonałem osobiście i samodzielnie, że nie korzystałem ze żródeł innych niż wymienione w pracy.

Azebaze Mboving
……………………………………
Podpis

Kraków, dnia 29.04.2020 r.